ISSN 0289-842X

RIKEN Accelerator Progress Report

1998

vol. 32

理化学研究所
The Institute of Physical and Chemical Research (RIKEN)

RIKEN Accelerator Progress Report 1998
January-December

vol. 32

理化学研究所
The Institute of Physical and Chemical Research (RIKEN)
Wako, Saitama, 351-0198 JAPAN

Editors

T. Abe A. Goto

T. Ichihara K. Ishida

T. Kambara Y. Kobayashi

A. Ozawa I. Shimamura

S. Yamaji Y. Yamazaki

All rights reserved. This report or any part thereof may not be reproduced in any form (including photostatic or microfilm form) without written permission from the publisher.

All reports are written on authors' responsibility and thus the editors are not liable for the contents of the report.

CONTENTS

I. PREFACE

This issue of RIKEN Accelerator Progress Report communicates the research activities of the RIKEN Accelerator Research Facility (RARF) for the 1998 calendar year. The research programs have been coordinated with the framework of a project entitled Multidisciplinary Research on Heavy Ion Science. The project involves a variety of fields such as nuclear physics, atomic physics, nuclear chemistry, radiation biology, condensed matter physics in terms of accelerator or radiation applications, basic studies on energy production, basic studies on accelerator cancer therapy, material characterization, applications to space science, accelerator physics and engineering, laser technology, and computational technology. These activities involve 12 laboratories in RIKEN and more than 400 researchers including outside members from domestic and foreign institutions. Sixty-five universities and institutes from with in Japan and 36 institutes from 12 countries are included.

The major research activities of the RARF are based on the heavy-ion accelerator complex consisting of the K = 540 RIKEN Ring Cyclotron (RRC), the energy-variable heavy-ion linear accelerator (RILAC) and the K = 70 azimuthally variable field cyclotron (AVF), which have altogether provided a beam time (on the target) of more than 8000 h throughout the year.

The three accelerators deliver heavy-ion beams of a variety of elements with energies ranging from a few A MeV to 135A MeV. The two injector machines (AVF and RILAC) are equipped with ECR heavy ion sources. The AVF is additionally equipped with a polarized ion source for vector and tensor polarized deuterons. Recently, the capabilities of the RILAC have been dramatically enhanced by addition of a new 18 GHz ECR ion source followed by a frequency-variable RFQ preaccelerator. Heavy ion intensities have increased from ten to one hundred times that in the original setup. The three accelerators have been used in various configurations. The RRC operates with the AVF or the RILAC as the injector. The AVF provides beams of ions of mass number up to 60 and the RILAC provides beams of ions of large mass number. In addition, the AVF and the RILAC can be used separately, when they are not used as injectors, for low-energy applications.

Two-thirds of the RRC research beam time (~5000 h in total) is allotted to nuclear physics and one-third to atomic physics, material science, nuclear chemistry, radiation biology and others. Incontrast, the RILAC and the AVF beam times were used by fields other than nuclear physics. The research beam times are 2100 h for the AVF and 800 h for the RILAC.

The use of radioactive ion (RI) beams is the main emphasis of the studies at the RRC. Three different types of radioactive beams, i.e., (1) projectile-fragment (PF) radioactive, (2) spin-polarized radioactive, and (3) high-spin isomer beams, have been developed and used in a broad range of nuclear studies. PF beams are most widely used by virtue of their versatility and high intensities. The spin-polarized beams are particularly useful for NMR experiments with radioactive isotopes. The isomer beam intensity has been significantly improved, and is approaching a realistic application level. These beams are primarily used for studies in nuclear physics. Major subjects pursued are (1) exotic nuclear structure and new dynamics of extremely neutron-rich nuclei (such as those with a neutron halo or skin), (2) nuclear astrophysics involving unstable-nucleus reactions, (3) synthesis of new unstable isotopes far from the range of stability, (4) extensive measurements of nuclear moments, and (5) high-spin physics investigated using isomer beams. The characteristic features of intermediate-energy direct reactions are often exploited for such studies.

The RI beams are useful for other domains of science as well. In particular, applications in condensed matter science have been developed to a large extent by exploiting the on-line capability of Mössbauer and PAC spectroscopy techniques which are feasible only with RI beams.

Intermediate-energy heavy ions from the RRC have found their own applications. A strikingly efficient mutagenic effect was observed when the embryo of a Tobacco plant was bombarded by heavy ions. High-energy heavy ions irradiated the plants which were (naturally) placed in air to obtain a desirable amount of Linear Energy Transfer (LET) through the sample. This technique has made available a new scheme of mutant production which is efficient and well controlled. The method is so efficient that it is expected to offer new possibilities in bioscience research through comparison of normal and mutagenized samples. To obtain more detailed information, such as the cross-talks between cells, the development of a microbeam is planned.

Another significant development has been seen in the application of the radioactive tracer technique. High-energy heavy ion reactions facilitate the simultaneous production of a wide variety of isotopes. This feature is exploited to cultivate a novel multitracer methodology in which a radioactive tracer source containing a variety of elements is prepared for injection into a sample. This method enables the study of the circulation behavior of different elements in a common sample, drastically improving the reliability and efficiency

over those of single-tracer experiments. The application of the method is rapidly extending to the fields of bio-inorganic chemistry, dietetics, toxicology, pharmacology, environmental studies, and the medical field in general.

The RARF hosts many international collaborations, among which are two large international collaboration programs using overseas accelerator facilities: One is the muon science project at ISIS in collaboration with the Rutherford-Appleton Laboratory (RAL), and the other is the spin physics program at RHIC in collaboration with the Brookhaven National Laboratory (BNL). The pulsed muon beam facility at ISIS has entered into a stage of steady operation. Great success was achieved in observing the X-rays generated in μ capture by alpha particles produced by muon catalyzed fusion. Studies of quark-gluon spin structure functions at BNL/RHIC are in progress and will be ready for the commissioning of RHIC operation in 1999. The RIKEN/BNL Research Center is in operation and attracts physicists from all over the world.

The RI Beam Factory Project was started this year. The construction of the test sector magnet for the Superconducting Ring Cyclotron (SRC, K = 2500 MeV) has been started. Design work on the booster cyclotron (ISR) and the other facilities are also in progress.

I. Tanihata
Director
RIKEN Accelerator Research Facility

II. OPERATION OF ACCELERATORS

RILAC Operation

E. Ikezawa, S. Kohara, M. Fujimaki, T. Aihara,* T. Ohki,*
H. Hasebe,* H. Yamauchi,* and M. Kase

During this reporting period, RILAC has been in a steady operation and has supplied various kinds of ion beams for various experiments. Table 1 is the statistics of the number of days operated during January through December, 1998. One day of the scheduled beam time was forced to be cancelled owing to the failure in the No. 1 rf amplifier. Table 2 summarizes the number of days allotted to different research groups. The percentage of the beam time used by the group of RIKEN Ring Cyclotron (RRC) was approximately 46% of the total. The ions of ^{16}O, ^{40}Ar, ^{58}Ni, ^{84}Kr, ^{128}Te, ^{136}Xe, ^{181}Ta, ^{208}Pb, and ^{209}Bi accelerated by RILAC were injected to RRC. Tables 3 and 4 are the statistics of the number of days of the RILAC ion beams delivered using the Cockcroft-Walton injector with an 8-GHz ECR ion source (NEOMAFIOS) and those delivered using the new pre-injector (consisting of an 18-GHz ECR ion source and a variable-frequency RFQ equipped with a folded-coaxial resonator), respectively. The ion beams of 18 kinds of element were used for the experiments and beam acceleration tests. The percentage of the beam time to have used metallic ions amounted approximately 35% of the total.

We carried out following machine improvements during this reporting period: (1) Aperture of the rebuncher installed after the RFQ has been enlarged from 40 mm to 50 mm in diameter in order to accept the beam having an emittance larger than the designed value. (2) With NEOMAFIOS, we have tested a method of production of metallic ions by using materials such as Eu_2O_3. As a result, we were successful

Table 1. Statistics of the RILAC operation during January 1 through December 31, 1998.

	Days	%
Beam time	171	46.8
Overhaul and improvement	40	11.0
Periodic inspection and repair	52	14.2
Machine trouble	1	0.3
Scheduled shut down	101	27.7
Total	365	100

Table 2. Beam time allocated for different research groups.

	Days	%
Atomic physics	48	28.1
Nuclear physics	12	7.0
Radiation chemistry	17	9.9
Material analysis and development	4	2.3
Instrumentation	3	1.8
Accelerator research	9	5.3
Beam transport to RRC	78	45.6
Total	171	100

Table 3. Statistics of the RILAC ion beams delivered using the Cockcroft-Walton injector.

Ion	Mass	Charge states	Days
He	4	2	9
B	11	1,3	9
C	12	1,2,4	7
N	15	3,4	9
O	16	3	2
Ne	20	4	3
Mg	24	5	9
Al	27	6	2
Ar	40	8	6
Er	166	18	1
Ta	181	16	7
Pb	208	11	3
Bi	209	16	4
		Total	71

Table 4. Statistics of the RILAC ion beams delivered using the new pre-injector.

Ion	Mass	Charge states	Days
He	4	1	1
Al	27	7	3
Ar	40	5,8,9,11,12	23
Fe	56	15	4
Ni	58	9	9
Kr	78	18	2
Kr	84	11,13,19,20	5
Te	128	19	8
Xe	136	18,20,27	45
		Total	100

* Sumijyu Accelerator Service, Ltd.

to obtain the beam intensity of 28 eμA for Eu^{12+} and 4 eμA for Eu^{18+}. The ions of 10 kinds of gaseous elements and those of 51 kinds of solid elements have been produced by the NEOMAFIOS till today. (3) The beam slits, Faraday cups, and beam profile monitors of the beam transport line A were replaced with new ones in order to improve their strengths against the high beam intensity extractable from an 18-GHz ECR ion source. They were normally mounted on a diagnostic chamber.

We experienced following machine troubles during this reporting period: (1) In the resonator No. 6, a thin copper sheet (of 10 cm wide, 7 cm long, and 0.3 mm thick) used for electric contact was melted down due to the excessive rf current and parasitic oscillation. (2) A potential transformer was worn out in a high voltage power supply (440 kW) for the final vacuum tube (No. 1 and No. 2), and we replaced it with a new one. (3) Power supplies for the screen grid (1.5 kV, 2.2 A) of the final vacuum tube (No. 6), for the filament (4.5 V, 1640 A) of the final vacuum tube (No. 1), and for the plate (5 kV, 2 A) of the driving vacuum tube (No. 3) had troubles, and we replaced it with spare ones. (4) Three heat exchangers in a water cooling system were overhauled because of a deterioration in the thermal efficiency.

RRC and AVF Cyclotron Operations

M. Kase, A. Goto, T. Kageyama, M. Nagase, S. Kohara, T. Nakagawa, K. Ikegami, J. Fujita, N. Inabe, O. Kamigaito, M. Kidera, M. Komiyama, A. Yoneda, I. Yokoyama, H. Isshiki,* H. Akagi,* R. Abe,* R. Ichikawa,* N. Tsukiori,* K. Takahashi,* T. Maie,* T. Homma,* K. Kobayashi,* and Y. Yano

During one year of 1998, the RIKEN Ring Cyclotron (RRC) and AVF cyclotron were in a favorable condition as in other years. Many kinds of beams were accelerated with RRC as shown in Fig. 1. Among them, nine kinds of beams were newly accelerated in 1998. They are listed in Table 1 together with their acceleration data.

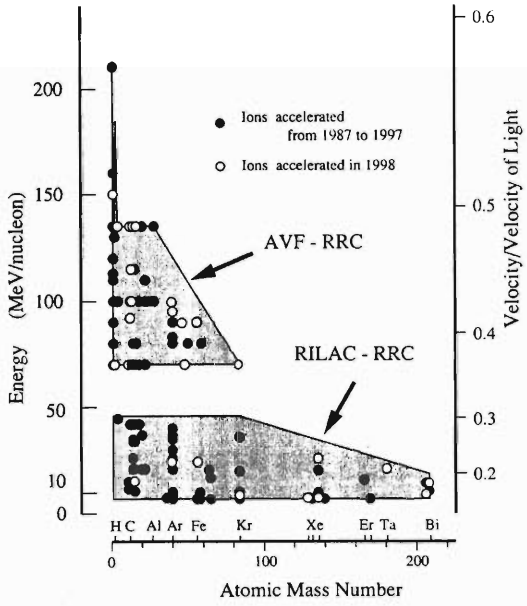

Fig. 1. The performance of RRC. The beams which were accelerated newly during the year 1998 are shown by open circles and those which have been accelerated since 1987 are shown by solid circles.

Table 1. List of new beams in 1998.

Particle	Charge state IS	Charge state RRC	Energy (MeV/n)	Frequency (MHz)	Harmonic No. (RRC)	Injector	Beam Intensity (pnA)
^{16}O	+3	+3	16	24.6	10	18ECR+RFQ+RILAC	>2000
^{40}Ar	+9	+9	24	27.0	9	18ECR+RFQ+RILAC	2100
^{40}Ca	+11	+18	100	29.0	5	10ECR+AVF	33
^{46}Ti	+12	+20	90	27.6	5	10ECR+AVF	12
^{58}Ni	+19	+9	25	27.5	9	18ECR+RFQ+RILAC	23
^{58}Ni	+16	+24	90	27.6	5	10ECR+AVF	6
^{128}Te	+19	+19	8.3	27.6	11	18ECR+RFQ+RILAC	3
^{136}Xe	+18	+18	7.6	18.8	11	18ECR+RFQ+RILAC	550
^{208}Pb	+11	+30	9.5	19.1	10	?N-ECR+RILAC	1.7

10ECR : 10GHz ECR Ion Source
18ECR : 18GHz ECR Ion Source
N-ECR : Neomafios ECR Ion Source

* Sumijyu Accelerator Service, Ltd.

A total of operation hours of the year 1998 amounted 6600 hr, and among those, 4840 hr were spent for so-called "beam time" for various experiments. 73% of the beam time were devoted to the nuclear physics experiments and 27% to the other fields such as: medical science, radio-chemistry, health physics, material science, biology, and atomic physics.

Figure 2 shows the operation statistics of twelve years from 1987 to 1998. The fraction of the nuclear physics experiments had a peak of 4300 hr in 1996, and then decreased by 15% after that. This is due to the fact that an experiment in search of the super-heavy element has been stopped since 1997. On the other hands, the share to non-nuclear physics experiment is increasing gradually, since the application for biological and biomedical reserach are being expanded. As the results, a total of beam time have been kept around 4700 hr since 1994.

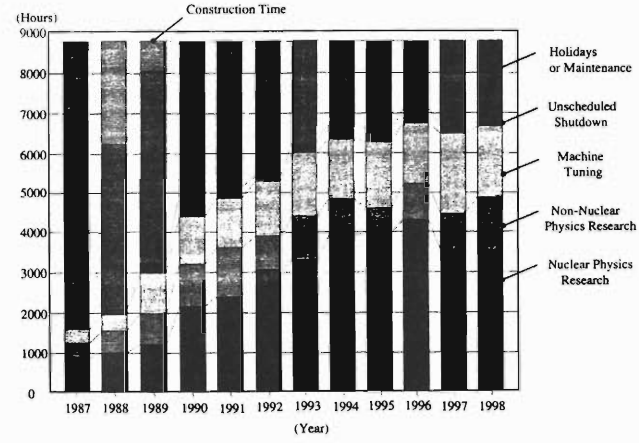

Fig. 2. Statistics of the RRC operation during these twelve years from 1987 to 1998.

A total of the unscheduled shutdown due to machine troubles was 157 hr in 1998, the minimum in these 12 years. In this year, machine troubles were mainly related to the low-level circuits of rf system, and any big troubles relating to the vacuum leak did not occur.

AVF cyclotron was used as the stand-alone for 700 hr in 1998. Kinds of beam were limited to proton and polarized-deuteron. They were used for nuclear physics, in-beam Mössbauer, and for slow positron beam production.

In the end of 1997, the official limit for the maximum beam intensities was raised for low-energy beams at RRC. According to the new permission, the maximum beam intensity is inversely proportional to a beam en-

ergy. For example, it has become 10 pμA for beams with energy of 13.5 MeV/nucleon, while it is still 1 pμA for 135 MeV/nucleon same as before. In February 1998, a 24 MeV/nucleon ^{40}Ar beam was accelerated with the intensity more than 2 pμA and was used for a simulation test of the rotation target prototype for BigRIPS in RIBF. The input beam power was more than 2 kW.

A gas target of RIPS for production of a high spin isomer beam became ready to use and was tested several times using a beam of 7.6 MeV/nucleon ^{136}Xe with the intensity of 0.5 pμA.

A drift of the magnetic fields in RRC sector magnets has been frequently problem. In search of causes of the drift, two kinds of devices were newly installed in the summer 1998. A dc current transformer (DCCT) was added to monitor an output of the main coil power supply. A precise measurement of dc current has become possible independent of a feedback loop in the power supply. And also NMR probes were installed in every sector magnet at the radius of around 3500 mm. In the S- and W-sectors, the probe position is fixed and in the N- and E-sectors the probes can be removed remotely because they intercept the orbits of an extracted beam. Using also data of temperatures around the sector magnets, the monitoring of the magnetic field has now completed.

A sextupole magnet in 10 GHz ECR ion source was converted into a new type of N38H permanent magnets in the summer 1998. The maximum field strength of the new one is about 1.6 times that of the old. Since the confining magnetic field was strengthened, the beam intensity as well as the stability of plasma has been improved. A new ECR ion source using a super-conducting solenoid are being fabricated in factories, and will be completed in the summer of 1999.

In order to prepare the space for RIBF, most of the building on the east side of Nishina Memorial Building will be removed in the spring of 1999. In advance to it, the power substation for the all existing machines is going to be moved to the west side of the Nishina Memorial Building. Moreover, the houses for RF power supply for both RRC and RILAC will be changed to new ones on this side. For two months from February to April 1999, the whole machine will be shutdown due to these changes of power line.

During the shutdown period, improvement of injection system of RRC is scheduled. Two sets of Magnetic Inflection Channels (MIC1 & MIC2) will be replaced with new ones and the size of beam pipe will be enlarged slightly. Beam monitors along the injection line will be replaced with new types preparing for the high intense beam injection in the future.

Design of cavity for Charge State Multiplier (CSM) is now in progress. In the summer of 1999, the first unit of CSM consisting of three cavities (two accelerators and one decelerator) will be installed in the second target room of RILAC, along the injection beam line to RRC.

The Tandem Operation

K. Ogiwara, E. Yagi, and T. Urai

The 1.7 MV tandem accelerator was operated for 95 days, except for the machine inspection, beam test, and so on, during the annual reporting period from Nov. 1, 1997 to Oct. 31, 1998.

Experimental studies on the following subjects have been performed, and some of them are in progress:

(1) Rutherford Backscattering Spectroscopy (RBS)

(a) Behavior of the Xe atoms implanted into iron.

(b) Channeling analysis of dopants in II-VI compound semiconductors.

(c) RBS study of multilayer films, welded steel, and oxides.

(d) RBS analysis of the polystyrene surfaces and glassy carbon films modified by means of ion implantation.

(2) Nuclear Reaction Analysis (NRA)

(a) Study on the lattice location of hydrogen in niobium alloys by a channeling method.

(3) Particle-Induced X-ray Emission (PIXE)

(a) Application of PIXE to the biomedical and material sciences: Trace element analysis using energy-dispersive X-ray spectrometry, and chemical state analysis using wave-dispersive X-ray spectrometry.

(b) Trace element analysis of feathers for monitoring the environmental pollusion.

(c) Development of an in-air high-resolution PIXE system for chemical state analysis.

(d) Characterization of II-VI ternary semiconducting crystals.

III. RESEARCH ACTIVITIES

1. Nuclear Physics

Structure of $N \sim 20$ Unstable Nuclei Studied by Monte Carlo Shell Model

Y. Utsuno, T. Otsuka, T. Mizusaki, and M. Honma

[Monte Carlo shell model, Shell closure]

The neutron-rich $N \sim 20$ region is referred to as the "island of inversion", where the $N = 20$ closed shell structure vanishes. For instance, the $N = 20$ nucleus ^{32}Mg has been proven to be well deformed as confirmed by a observed $B(E2; 0_1^+ \rightarrow 2_1^+)$ value.[1] We study the structure of nuclei around the "island" within the framework of the large-scale shell-model calculation by the Quantum Monte Carlo Diagonalization (QMCD) method.[2,3]

The model space is the same as the one in Ref. 3. We have already confirmed the feasibility of the QMCD method in this model space and shown that the spurious center-of-mass motion can be removed.[3] We then refine the effective interaction, paying attention to the monopole terms and the paring interaction. We have found that the interplay between the $T = 0$ and $T = 1$ monopole interactions plays an important role in the binding energy and the deformation especially for the oxygen and the neon isotopes. The heaviest bound of the oxygen isotopes is ^{24}O, which is reproduced by the modified interaction.

In order to see competition between the normal and the intruder configurations intuitively, we calculate the potential energy sueface (PES) within the shell-model space. The PES is calculated by the constrained Hartree-Fock method[4] with the constraints of $<J_x> = \sqrt{I(I+1)}$, $<Q_0> = q$, and $<Q_{\pm 1}> = <Q_{\pm 2}> = 0$. Figure 1 shows the PES of ^{32}Mg. We see several local minima in Fig. 1, which suggest the shape coexistence. The lowest-energy state corresponds to the $2p2h$ excited state from the $N = 20$ core. We utilize these minima as starting points of the sampling in the QMCD method.

Figure 2 shows yrast energy levels of the magnesium isotopes compared with the experiment. The excitation energies by the QMCD method are in agreement with experimental ones, while the sd-shell model does not reproduce the $E_x(2_1^+)$ of ^{32}Mg. We predict large deformation structure for the $N = 22$ and 24 nuclei. For these nuclei, the particle-hole excitation from the $N = 20$ core is still important.

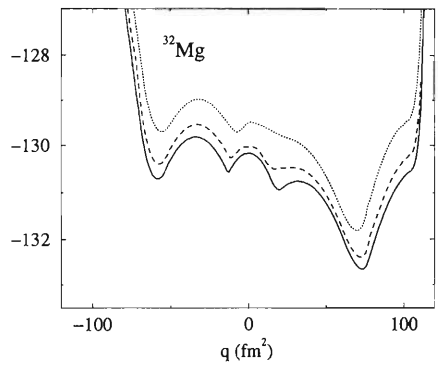

Fig. 1. Potential energy surface of ^{32}Mg. The solid, dashed, and dotted lines denote $I = 0, 2, 4$, respectively.

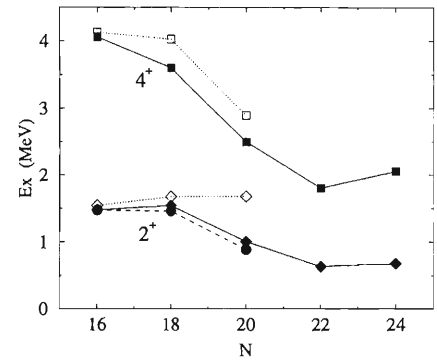

Fig. 2. Yrast energy levels of the magnesium isotopes. The circles correspond to the experiment. The closed (open) symbols are the QMCD calculation (sd-shell model).

References

1) T. Motobayashi et al.: Phys. Lett. B **346**, 9 (1995).
2) T. Otsuka, M. Honma, and T. Mizusaki: Phys. Rev. Lett. **81**, 1588 (1998) and references therein.
3) Y. Utsuno et al.: RIKEN Accel. Prog. Rep. **31**, 15 (1998).
4) For instance, P. Ring and P. Schuck: in *The Nuclear Many-Body Problem* (Springer, New York, 1980).

Monte Carlo Shell Model Calculation and Computers

N. Shimizu, T. Otsuka, Y. Watanabe, A. Taketani,
T. Mizusaki, and S. Haruyama

[Shell model, Nuclear structure, Computational physics]

The nuclear shell model is the most useful approach in describing the various nuclear properties: energy levels, quadrupole moments, electromagnetic transition probabilities, and so on. In this model, Hamiltonian matrix in the full valence-nucleon Hilbert space has to be diagonalized. It requires, in many cases, enormous time even with the latest computers, because of huge dimension. For example, the matrix Hamiltonian for ^{154}Sm with the ^{132}Sn closed core has a 4×10^{13} J = 0 basis dimension.

In order to overcome this difficulty, the Monte Carlo approach incorporating both the diagonalization method and the auxiliary field technique has been developed.[1-4] Because this approach handles a small number of bases, it does not only decrease time to calculate, but also makes parallel computation easier drastically.

In Oct. 1998, we introduced the computer system which consists of 34 Alpha CPUs in order to perform the above-mentioned large-scale calculations. As well, this system is a prototype of larger system named "High Performance Personal Computer System" to be installed in March, 1999.

The framework of the prototype system is illustrated in Fig. 1 and several features are listed as follows:

- 8 Alpha CPUs (Red Hat Linux) at 533 MHz and 24 Alpha CPUs (Red Hat Linux) at 600 MHz serve as slave computers. They have no magnetic disks and perform only parallel calculations.
- One Alpha CPU (Digital UNIX) at 667 MHz is the front-end computer and is able to integrate 32 slave computers. The front-end computer always monitors their individual state (power supply and temperature) under watch respectively with controller (referred as PS/T cont. in Fig. 1).

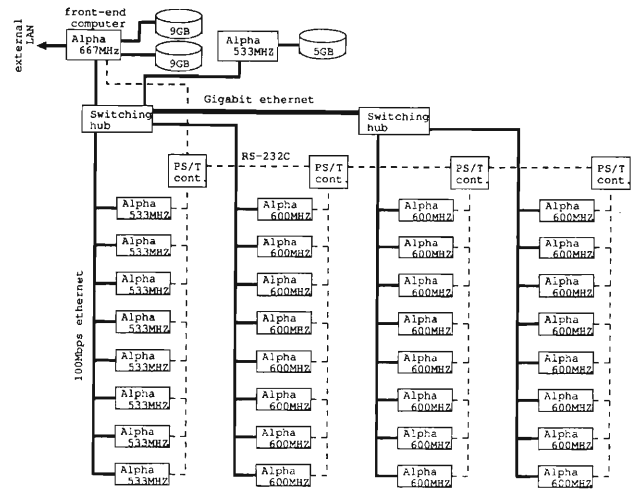

Fig. 1. Framework of computer system introduced in Oct. 1998.

- One Alpha CPU (Red Hat Linux) at 533 MHz is prepared for the slave computers to boot through the network by using the Network File System.
- They are connected with each other by 100 Mbps Ethernet. Although it is slower than many other recent parallel-computing systems, this is sufficient for the present Monte Carlo calculations.

References

1) M. Honma, T. Mizusaki, and T. Otsuka: Phys. Rev. Lett. **75**, 1284 (1995).
2) T. Mizusaki, M. Honma, and T. Otsuka: Phys. Rev. C **53**, 2786 (1996).
3) M. Honma, T. Mizusaki, and T. Otsuka: Phys. Rev. Lett. **77**, 3315 (1996).
4) T. Otsuka, M. Honma, and T. Mizusaki: Phys. Rev. Lett. **81**, 1588 (1998).

Relativistic Continuum Hartree-Bogoliubov Theory with Both Zero Range and Finite Range Gogny Force and Their Application†

J. Meng

[Relativistic continuum Hartree-Bogoliubov, Pairing correlation, Drip-line nuclei]

The Relativistic Mean Field (RMF) theory has received wide attention as a successful description for many nuclear phenomena during the past years. The RMF has been used to describe binding energies, nuclear radii, nuclear density distribution, single particle spectra, magnetic moments, collective excited states, the dipole sum rule, shell effects in finite and exotic nuclei; scattering processes of nucleons on nuclei at intermediate energies; collective excitations such as giant resonances and identical bands in rotating superdeformed nuclei, etc. Obviously, the RMF is one of the best candidates for application to exotic nuclei. In all the RMF studies mentioned above, however, the pairing correlation has been neglected or simply treated by BCS approximation. In order to describe open shell nuclei, the pairing correlation must be taken into account properly. This is particularly noteworthy since describing the coupling to the continuum for exotic nuclei, which is very crucial for the description of drip line nuclei, can only be done in the coordinate representation. This is because the expansion in a localized harmonic oscillator basis provides a poor approximation to the continuum, even when a large number of oscillator shells are taken into account. For stable nuclei, the BCS approximation is simple and practical. But for exotic nuclei it will lead to a partial occupation of unphysical states in the continuum and therefore to a gas of evaporating neutrons.

Recently a fully self-consistent Relativistic Continuum Hartree-Bogoliubov (RCHB) theory, i.e., RHB theory in coordinate representation, has been proposed.[1)] It is relativistic in that it is able to take into account the proper isospin dependence of the spin-orbit term, which is crucial for a accurate reproduction of recent measurements of the isotopic shifts in the Pb-region and for a reliable description of nuclei far away from the line of β-stability. In addition this theory provides a self-consistent treatment of pairing correlations in the presence of the continuum. As has been shown in Ref. 1, the scattering of Cooper pairs into the continuum containing low-lying resonances of small orbital angular momentum plays an important role for the formation of a neutron halo. The dependence of the results on the box size was discussed in Ref. 2, in which the formation of giant halos is discussed for the first time.

Here we report on the RCHB theory and provide details of the relevant numerical techniques. We have undertaken a systematic study of the pairing correlation in the RCHB theory by considering the density-dependent δ-force and finite range Gogny force. The techniques for the coupled differential equations and coupled integro-differential equations are also included. A preliminary application of the solution for the halo in ^{11}Li has been reported in Ref. 3. After taking into account the pairing and blocking effect, the ground state properties of Na nuclei has been well reproduced, including the binding energies and *rms* radii, and the development of the halo and shell structure has been discussed.[4)]

The formalism for Relativistic Continuum Hartree-Bogolyubov (RCHB) theory, which is the extension of the Relativistic Mean Field (RMF) and the Bogoliubov transformation in the coordinate representation is presented. As the formalism allows for the proper description of the coupling between the bound state and the continuum by the pairing force, it is suitable not only for stable nuclei but also the nuclei near the drip line. The pairing correlations are taken into account by both a density-dependent force of zero range and the finite range Gogny force. The development of the formalism and the numerical techniques involved are discussed in detail. The physics from the RCHB and its understanding in the canonical basis are presented. The RCHB theory is used to describe the chain of nickel isotopes extending from the proton drip line to the neutron drip line. The comparisons of the two neutron separation energies S_{2n} as well as the neutron, proton and matter *rms* radii yield excellent agreement between the calculations with both interactions and the experimental values where they exist. Predictions have also been made for the drip-line nucleus ^{100}Ni. The pairing energies and single particle levels in the canonical bases and their corresponding occupation probabilities turn out to be similar.

References

1) J. Meng and P. Ring: Phys. Rev. Lett. **77**, 3963 (1996).
2) J. Meng and P. Ring: Phys. Rev. Lett. **80**, 460 (1998).
3) J. Meng et al: Z. Phys. A **358**, 123 (1997).
4) J. Meng et al: Phys. Lett. B **419**, 1 (1998).

† Condensed from the article in Nucl. Phys. A **635**, 3 (1998).

The Proton and Neutron Distributions in Na Isotopes: The Development of Halo and Shell Structure†

J. Meng, I. Tanihata, and S. Yamaji

[Relativistic continuum Hartree-Bogoliubov, Neutron halo, Shell structure]

With the exotic matter distribution near the drip line, many questions are still open; e.g., the relation between the halo and the shell effect, the difference about the proton and neutron distributions on the stability line and away from the stability line. How is the halo formed? Are there a rapid change from the normal nuclear density to the halo density or a gradual change in the particle number? Because the matter distribution is not measurable directly, a series of experiments at different incident beam energy is necessary in order to determine the density distribution of both proton and neutron model-independently. Among all the experiments carried out so far, Na isotopes provide a good opportunity to study the density distributions over a wide range of neutron numbers.[1] We report in this article a systematic study of the nuclear density distributions in Na isotopes within the Relativistic Mean Field (RMF) theory, properly describing the pairing and the blocking effect of odd particle system by Hartree-Bogoliubov theory in coordinate representation, and try to answer some of the general questions in these low-density nuclear matter.

People have applied so far rather different techniques to describe halo phenomena in light nuclei. As for instance: the exact solution of few-body equations treating inert sub-clusters as point particles; the density dependent Hartree-Fock method in a localized mean field taking into account all the particles in a microscopic way; or a full shell model diagonalizations based on the oscillator spaces with two different oscillator parameters for the core- and halo-particles. Recently, however, a fully self-consistent calculation within the Relativistic continuum Hartree-Bogoliubov (RCHB) theory for the description of the chain of lithium isotopes ranging from ^{6}Li to ^{11}Li was reported.[2] Here the matter distributions from the proton drip line to the neutron drip line in Na isotopes have been systematically studied and presented. The relation between the shell effects and the halos has been examined. Tail of the matter distribution shows a strong dependence on the shell structure.

Summarizing our investigations, the development of a proton skin as well as neutron skin has been systematically studied with a microscopic RHB model, where the pairing and blocking effect have been treated self-consistently. A systematic set of calculations for the ground state properties of nuclei in Na isotopes is presented using the RHB theory together with standard Glauber theory. The RHB equations are solved self-consistently in coordinate space so that the continuum and the pairing have been better treated.[3] The calculated binding energies are in good agreement with the experimental values. A Glauber model calculation has been carried out with the density obtained from RHB. A good agreement has been obtained with the measured cross sections for ^{12}C as a target, and a rapid increase of the cross sections has been predicted for neutron rich Na isotopes beyond ^{32}Na. Systematics of the proton and neutron distributions are presented. After a systematic examination of the neutron, proton, and matter distributions in the Na nuclei from the proton drip-line to the neutron drip-line, the connection between the tail part of the density and the shell structure has been found. The tail of the matter distribution is not so sensitive to how many particles are filled in a major shell. Instead, it is quite sensitive to whether this shell has occupation or not. The physics behind the skin and halo has been revealed as a spatial demonstration of shell effect: simply the extra neutrons are filled in the next shell and sub-shell. This is in agreement with the mechanism observed so far in the halo system but more general. As the $1f_{7/2}$ is very close to the continuum, the $N = 28$ closed shell for stable nuclei fails to appear due to the coming down of the $2p_{3/2}$ and $2p_{1/2}$ levels. Another important conclusion here is that, contrary to the usual impression, the proton density distribution is less sensitive to the proton to neutron ratio. Instead, it is almost unchanged from the proton drip-line to the neutron drip-line. Similar conclusion has been obtained recently by charge exchange reaction experimently.[4] Influence of the deformation, which is neglected in the present investigation, is also interesting to us; more extensive study to extend the present study for deformed cases are in progress.

References

1) T. Suzuki et al.: Phys. Rev. Lett. **75**, 3241 (1995).
2) J. Meng and P. Ring: Phys. Rev. Lett. **77**, 3963 (1996). J. Meng: Nucl. Phys. A **635**, 3 (1998).
3) J. Meng and P. Ring: Phys. Rev. Lett. **80**, 460 (1998).
4) O. Bochkarev et al.: submitted to Z. Phys.

† Condensed from the article in Phys. Lett. B **419**, 1 (1998).

A Giant Halo at the Neutron Drip Line†

J. Meng and P. Ring*

[Relativistic continuum Hartree-Bogoliubov, Giant halos, Zr-isotopes]

With perpetual improvement in the techniques of producing radioactive beams, the study of exotic nuclei very-far away from the line of β-stability has now become feasible. Experiments of this kind may cast a new light on nuclear structure, and novel and entirely unexpected features may appear: Neutron rich nuclei can have a structure very different from that of normal nuclei. They consist of a normal core surrounded by a skin of neutron matter. Close to the drip line, where the coupling to the continuum becomes important, a neutron halo can develop, as it has been observed in several light nuclei. However, in all of the halos observed so far, only one has a small number of neutrons: namely, one or two are outside of the normal core. Even in the chain of He-isotopes, only ^{6}He shows indications of a possible halo containing 2 neutrons, whereas ^{8}He with its large 2-neutron separation energy of 2.24 MeV has only a neutron skin.

In order to study the influence of correlations and many-body effects it would be very interesting to find also the nuclei with a larger number of neutron distributed in the halo. Here, the Relativistic continuum Hartree-Bogoliubov (RCHB) theory[1)] has been used for the present investigation. It is a relativistic extension of conventional Hartree-Fock-Bogoliubov theory in coordinate space. Being relativistic, it is able to take into account at the same time the proper isospin dependence of the spin-orbit term, which is very crucial for an accurate reproduction of recent measurements of the isotopic shifts in the Pb region and for a reliable description of the nuclei far away from the line of β-stability. In addition, this theory provides a self-consistent treatment of pairing correlations in the presence of the continuum. As it has been shown in Ref. 1, the scattering of Cooper pairs into the continuum containing low-lying resonances of small angular momentum plays an important role for the formation of a neutron halo. By using a density-dependent zero range interaction, the halo in ^{11}Li has been successfully reproduced in this self-consistent picture. To obtain these results, a full solution of the RCHB equations is necessary. The expansion in a harmonic oscillator basis, which is quite useful only for the nuclei close to the line of β-stability, provides only a very poor approximation in the continuum, even if a large number of oscillator shells is taken into account. The simple "BCS"-approximation leads to a partial occupation of unbound states in the continuum, and therefore leads to a gas of evaporating neutrons. Here, we report on calculations where the same method as in Ref. 1 has been used to investigate the halos in Zr nuclei at the neutron drip line.

Because this theory takes into account the proper isospin dependence of the spin-orbit term, it is able to provide a good description of global experimental data not only for stable nuclei but also for exotic nuclei throughout the nuclear chart.[2)] In this report we describe on the theoretical prediction of a giant neutron halo for the Zr isotopes close to the neutron drip line. Up to six neutrons are formed outside of the ^{122}Zr core with the magic neutron number $N = 82$.

Summarizing our investigations, we predict neutron halos in the Zr nuclei close to the neutron drip line, which are composed not only by one or two neutrons, as is the case in the halos investigated so far in light p-shell nuclei, but which contain up to 6 neutrons. This is a new phenomenon, which has not been observed experimentally so till today. It would allow the study of collective phenomena in neutron matter of low density. This prediction is based on relativistic Hartree-Bogoliubov theory in the continuum. It combines the advantages of a proper description of the spin orbit term with those of full Hartree-Bogoliubov theory for the continuum, which allows in the canonical basis the scattering of Cooper pairs into low-lying resonances for the continuum. A density-dependent force of zero range has been used in the pairing channel. It contains no free parameter, because its strength is adjusted for the isotope ^{116}Zr to a similar calculation with Gogny's force D1S in the pairing channel. The halos are formed by two to six neutrons scattered as Cooper-pairs mainly to the levels $3p_{3/2}$, $2f_{7/2}$, $3p_{1/2}$, and $2f_{5/2}$. This is made possible by the fact that these resonances in the continuum come down very close to the Fermi level in these nuclei and is made possible by their coupling with the loosely bound levels just below the continuum limit.

References

1) J. Meng and P. Ring: Phys. Rev. Lett. **77**, 3963 (1996).
2) J. Meng: Nucl. Phys. A **635**, 3 (1998).

† Condensed from the article in Phys. Rev. Lett. **80**, 460 (1998)

* Technische Universität München, Germany

Landau-Migdal Parameters, $g'_{\rm NN}$ and $g'_{\rm N\Delta}$

T. Suzuki and H. Sakai

[Gamow-Teller giant resonances, Landau-Migdal parameters]

The Landau-Migdal parameters for nucleon-nucleon ($g'_{\rm NN}$), together with the nucleon-Δ($g'_{\rm N}\Delta$) and Δ-Δ($g'_{\Delta\Delta}$) couplings, play a crucial role in spin-dependent structure of nuclei. They dominate nuclear spin response functions for hadron and electron scattering[1] and the pion-condensation in high-density nuclear matter.[2] Experimentally, however, those values are not known yet. Because of this fact, the so-called universality ansatz,[2,3] $g'_{\rm NN} = g'_{\rm N\Delta} = g'_{\Delta\Delta}$, has been widely used.

We therefore try to estimate the values of $g'_{\rm NN}$ and $g'_{\rm N\Delta}$ from recent experimental data on the excitation energy and strength of the Gamow-Teller (GT) state.[4] For this purpose, we use the quark model[5] where the interaction is assumed to be

$$V = (V_{\rm NN} + V_{\rm N\Delta} + V_{\Delta\Delta})V_q, \tag{1}$$

with

$$V_q = \frac{1}{2}\left(\frac{f_\pi}{m_\pi}\right)^2 \sum_{i,j}^{A} \delta(\boldsymbol{r}_i - \boldsymbol{r}_j)\{(\boldsymbol{\tau}_i\cdot\boldsymbol{\tau}_j)(\boldsymbol{\sigma}_i\cdot\boldsymbol{\sigma}_j)\}_q, \tag{2}$$

where $(f_\pi/m_\pi)^2 = 392$ MeV $\cdot$ fm^3. The spin and isospin operators are given by the sum over the three quarks inside the baryons as usual,

$$(\sigma\tau)_q = \sum_{i=1}^{3} \sigma^{(i)}\tau^{(i)}. \tag{3}$$

The relationship between the above and Landau-Migdal parameters is given by

$$g'_{\rm NN} = \left(\frac{5}{3}\right)^2 V_{\rm NN}, \quad g'_{\rm N\Delta} = \left(\frac{5}{3}\right)^2 V_{\rm N\Delta},$$
$$g'_{\Delta\Delta} = \left(\frac{5}{3}\right)^2 V_{\Delta\Delta}. \tag{4}$$

Using the above interactions, we solve the equation of the random phase approximation in the space of the particle-hole and Δ-hole states, which yields the GT strength:

$$|\langle {\rm GT}|\sum \tau_-\sigma_-|0\rangle|^2 = Q\sum_{ph}|\langle p|\tau_-\sigma_-|h\rangle|^2, \tag{5}$$

where Q stands for the quenching factor and is given by

$$Q = \left\{\frac{1+\beta(g'_{\Delta\Delta} - g'_{\rm N\Delta})}{1+\beta g'_{\Delta\Delta}}\right\}^2, \tag{6}$$

with $\beta = 0.280$.

Experimentally, the value of Q has been observed to be 0.90 ± 0.05 for ^{90}Nb,[4] which yields

$$g'_{\rm N\Delta} = 0.18 + 0.05 g'_{\Delta\Delta}, \tag{7}$$

where the uncertainty in Q is not considered. Then, if the value of $g'_{\Delta\Delta}$ is assumed to be < 1.0,[3] we obtain

$$0.18 < g'_{\rm N\Delta} < 0.23. \tag{8}$$

On the other hand, the excitation energy of the GT states provides us with

$$A\kappa_{\tau\sigma} = g'_{\rm NN}\left(\frac{f_\pi}{m_\pi}\right)^2 \rho_0\gamma \cdot \frac{1+\beta g'_{\Delta\Delta}\{1-(g'_{\rm N\Delta})^2/(g'_{\Delta\Delta}g'_{\rm NN})\}}{1+\beta g'_{\Delta\Delta}}. \tag{9}$$

Here, $A\kappa_{\tau\sigma}$ is the strength of the spin-isospin interaction in the nucleon space, which has been already estimated to be 19.8 MeV from the excitation energy,[6] and γ and ρ_0 denote the attenuation factor of the nuclear surface effects and the nuclear matter density, respectively.[6] Inserting Eq. (8) into Eq. (9), we obtain:

$$0.591 < g'_{\rm NN} < 0.594. \tag{10}$$

Equations (8) and (10) clearly show that the universality ansatz does not hold.

In conclusion, we have estimated the values of the Landau-Migdal parameters, $g'_{\rm NN}$ and $g'_{\rm N\Delta}$, from recent experimental data on the excitation energy and strength of the GT state.[4] They are about 0.6 and 0.2, if $g'_{\Delta\Delta} < 1$, respectively. The value of $g'_{\Delta\Delta}$ is not known, but the GT strength depends weakly on it. As a result, the GT strength yields a strong constraint on the value of $g'_{\rm N\Delta}$. Moreover, because of the small value of $g'_{\rm N\Delta}$, the excitation energy of the GT state is dominated by $g'_{\rm NN}$. The universality ansatz cannot explain the strength and excitation energy simultaneously.

References

1) K. Nishida and M. Ichimura: Phys. Rev. C **51**, 269 (1995).
2) J. Meyer-ter-Vehn: Phys. Rep. **74**, 323 (1981).
3) E. Oset and M. Rho: Phys. Rev. Lett. **42**, 47 (1979).
4) T. Wakasa et al.: Phys. Rev. C **55**, 2909 (1997).
5) T. Suzuki and M. Kohno: Prog. Theor. Phys. **68**, 690 (1982).
6) T. Suzuki: Nucl. Phys. A **379**, 110 (1982); T. Suzuki: Ann. Phys. Fr. (Paris) **9**, 535 (1984).

Excitation of Two-Phonon States through Exchange Current

T. Suzuki

[Double giant resonances, Exchange current]

We have investigated photo-excitation of the two-phonon states through exchange current. The photo-absorption cross section for dipole states is given in natural units by[1)]

$$\sigma = \frac{16e^2\pi^3}{3k}|\langle f|\int drrY_{10}(\hat{r})(\nabla\cdot\boldsymbol{j}_{\rm N}+\nabla\cdot\boldsymbol{j}_{\rm ex})|i\rangle|^2, \quad (1)$$

where k denotes the photon energy and $\boldsymbol{j}_{\rm N}$ the isovector nuclear current,

$$\boldsymbol{j}_{\rm N} = -\frac{1}{4m}\sum_i^A\{\boldsymbol{p}_i, \delta(\boldsymbol{r}-\boldsymbol{r}_i)\}\tau_{3i}. \quad (2)$$

If the nuclear interactions contain the isospin-isospin interaction:

$$V = \frac{1}{2}\sum_{i,j}^A V(\boldsymbol{r}_i,\boldsymbol{r}_j)\boldsymbol{\tau}_i\cdot\boldsymbol{\tau}_j, \quad (3)$$

the exchange current is given by

$$\nabla\cdot\boldsymbol{j}_{\rm ex} = -\frac{1}{4i}\sum_{i,j}V(\boldsymbol{r}_i,\boldsymbol{r}_j) \times\{\delta(\boldsymbol{r}-\boldsymbol{r}_i)-\delta(\boldsymbol{r}-\boldsymbol{r}_j)\}\{\tau_{-i}\tau_{+j}-\tau_{+i}\tau_{-j}\}. \quad (4)$$

We estimate the cross section for the two-phonon states by assuming the Bohr-Mottelson force,[2,3)]

$$V = \frac{1}{2}\chi\sum_\mu\sum_i^A r_iY^*_{1\mu}(\hat{r}_i)\boldsymbol{\tau}_i\cdot\sum_j^A r_jY_{1\mu}(\hat{r}_j)\boldsymbol{\tau}_j, \quad (5)$$

where the strength, χ, of the interaction is determined so as to reproduce the excitation energy, 2ω, of the giant dipole states,

$$\chi = 4\pi\frac{m\omega^2}{A}, \quad (\omega = \frac{41}{A^{1/3}}\ \text{MeV}). \quad (6)$$

This interaction yields the exchange current which can excite two-phonon states with $[0^+\times1^-]1^-(T=1,\ T_z=0)$ and $[2^+\times1^-]1^-(T=1,\ T_z=0)$, where the one-phonon states with $0^+, 1^-$ and 2^+ have the isospin quantum number, $T=1$ and $T_z=\pm1$. The cross sections for these states are calculated to be

$$\sigma([0^+\times1^-]1^-) = 8\pi^2e^2\frac{\omega^4\langle r^2\rangle}{(\omega_0+\omega_1)\omega_0\omega_1}, \quad (7)$$

$$\sigma([2^+\times1^-]1^-) = 40\pi^2e^2\frac{\omega^4\langle r^2\rangle}{(\omega_2+\omega_1)\omega_2\omega_1}, \quad (8)$$

where ω_0, ω_1 and ω_2 stand for the excitation energies of the one-phonon states with $0^+, 1^-$ and 2^+, respectively, and the one-phonon states are assumed to exhaust the values of the classical energy-weighted sum rule. When we use the experimental values,[4)]

$$\omega_0\approx\omega_2 = 3\omega,\ \omega_1 = 2\omega,\ \langle r^2\rangle = \frac{3}{5}(1.2A^{1/3})^2, \quad (9)$$

we obtain from the sum of Eqs. (7) and (8),

$$\sigma_{\rm ex} = \frac{16m\omega\langle r^2\rangle}{5A}\sigma_0 \approx \frac{2.74}{A^{2/3}}\sigma_0, \quad (10)$$

where σ_0 denotes the cross section for the giant dipole state to exhaust the value of the classical energy-weighted sum rule and is given by

$$\sigma_0 = \pi^2e^2\frac{A}{2m}. \quad (11)$$

For an example, Eq. (10) gives the cross section for the two-phonon state to be about 23% of σ_0 in ^{40}Ca.

Recently, the double giant dipole and quadrupole states have been observed through relativistic heavy ion reactions and through double charge-exchange reactions.[5)] Since their isospin is $T=0$ or $T=2$, the exchange current cannot excite them, owing to the isospin selection rule. It is very interesting to excite the two giant resonance states with $T=1$ through the exchange current.

References

1) T. de Forest and J. D. Walecka: Adv. Phys. **15**, 1 (1966).
2) A. Bohr and B. R. Mottelson: *Nuclear Structure*, Vol. II (Benjamin, Massachusetts, 1975).
3) T. Suzuki: Nucl. Phys. A **289**, 461 (1977).
4) F. E. Bertrand: Ann. Rev. Nucl. Sci. **26**, 457 (1976).
5) Ph. Chomaz and N. Frascaria: Phys. Rep. **252**, 275 (1995).

Variational Approach to Collective Excitations

M. Sambataro* and N. Dinh Dang

[Variational approach, Random-phase approximation, BCS]

In this work we have examined a variational approach to collective excitations within a boson formalism.[1] Aiming at providing a simultaneous treatment of particle-hole and particle-particle(hole-hole) correlations, we have first introduced quasi-particles. Bosons have been defined in correspondence with pairs of these quasi-particles. By means of a mapping procedure of Marumori-type we have constructed boson images of fermion operators truncating the expansion of the boson operators at four-boson terms. RPA-type phonons have been introduced as Bogolyubov transformations of the above bosons and we have also defined the ground state of the system as the vacuum of these phonons. The minimization of the expectation value of the boson Hamiltonian in this vacuum with respect to the variables defining the quasi-particles and the phonons operators has allowed to fix these variables.

Important features of this boson procedure are that (1) no RPA-type inconsistency occurs, (2) no explicit knowledge of the ground state wave function is required and (3) no ambiguities related to the non-commutativity of the phonon operators exist. Also the variational aspect of the procedure is an important feature always allowing to identify the exact ground state energy as a lower bound of the calculation.

As a test for our approach we have chosen an exactly solvable two-level model characterized by a pairing Hamiltonian. Ground state energies have been found in a quite good agreement with the exact results, always remaining located between these and the BCS ones. We have also calculated the energy of the first 0^+ excited state and compared it with the BCS and QRPA values. Also in this case our approach has offered a quite good agreement with the exact results providing globally the best results.

References

1) M. Sambataro and F. Catara: Phys. Rev. C **51**, 3066 (1995); M. Sambataro and J. Suhonen: Phys. Rev. C **56**, 782 (1997).

* National Institute of Nuclear Physics, Catania Section, Italy

Relativistic and Non-Relativistic Mean Field Investigation of the Superdeformed Bands in ^{62}Zn

H. Madokoro and M. Matsuzaki

[Relativistic mean field, Superdeformed band, ^{62}Zn]

We study the superdeformed(SD) bands in ^{62}Zn, which were recently discovered, using a Relativistic Mean Field (RMF) model. This model starts from the Lagrangian which contains nucleonic and mesonic degrees of freedom. We can extend this model to the rotating frame by combining it with the cranking assumption. For detail, see Refs. 1 and 2.

In this study, the occupation numbers of protons in each parity-signature block ($\pi = \pm$, $r = \pm i$) are fixed to $\pi[8++;8+-;7-+;7--]$. As for the neutron occupations, we consider followings,

A: $\nu[8++;8+-;8-+;8--](\pi_{\rm tot}=+, r_{\rm tot}=+1)$,
D1: $\nu[8++;9+-;8-+;7--](\pi_{\rm tot}=-, r_{\rm tot}=+1)$,
D2: $\nu[8++;9+-;7-+;8--](\pi_{\rm tot}=-, r_{\rm tot}=-1)$,
D3: $\nu[9++;8+-;8-+;7--](\pi_{\rm tot}=-, r_{\rm tot}=-1)$,
D4: $\nu[9++;8+-;7-+;8--](\pi_{\rm tot}=-, r_{\rm tot}=+1)$,
C: $\nu[9++;9+-;7-+;7--](\pi_{\rm tot}=+, r_{\rm tot}=+1)$,

where the total parities and signatures were also shown. As for the parameter sets, we adopt the ones called NL1, NL3, NL-SH, and TM1. Figure 1 shows the calculated and experimental moments of inertia of the several SD bands in ^{62}Zn. Calculation used the set NL1. Several discontinuities are caused by the crossing between the [303 7/2] and [310 1/2] orbits. Apart from these crossings, the bands D3, D4, and C reproduce the experimental data fairly well. From the analysis of the effective alignments, the band C seems to be the best candidate for the experimentally observed one. However, we can not exclude the possibility of the band D4 because this band also gives good results if we adopt the set TM1. As these two bands have different parities, we can determine which one corresponds to the experimentally observed one if the parity-signature assignments are performed experimentally.

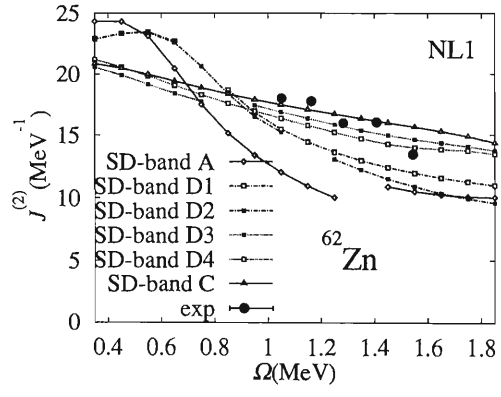

Fig. 1. The moments of inertia calculated by using the set NL1. The experimental data are shown by black circles.

For comparison, we have also performed the Skyrme Hartree Fock(SHF) calculations using the code HFODD.[3] The parameter sets adopted are SIII, SkM*, SkP, and SLy4. Figure 2 shows the moments of inertia of the same SD bands as those of RMF calculations. Calculation here used the set SLy4. Here we found good agreements for the bands D1, D3, and C. The analysis of the effective alignments tells us that the band C corresponds to the experimental data.

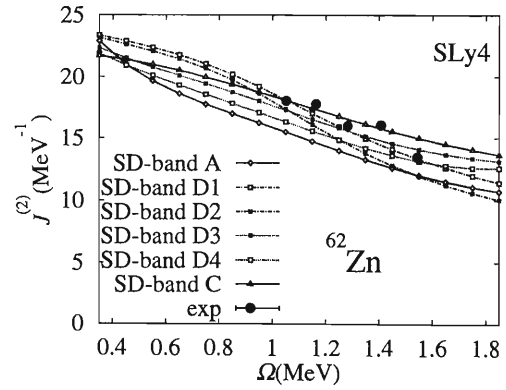

Fig. 2. The moments of inertia calculated by using the set SLy4. The experimental data are shown by black circles.

We find that these SD bands which reproduce the experimental moments of inertia fairly well are located more than 1 MeV higher than the lowest SD band in both RMF and SHF calculations. This may be connected with the unexpectedly high position of the $g_{9/2}$ single neutron orbit. It seems that all the parameter sets examined in this work have this feature, which is unresolved yet. In future, we will examine the effects which are not taken into account in the present investigations. They are, for example, the pairing interactions, which may solve the problem discussed above.

References

1) W. Koepf and P. Ring: Nucl. Phys. A **493**, 61 (1989).
2) H. Madokoro and M. Matsuzaki: Phys. Rev. C **52**, R2934 (1997).
3) J. Dobaczewski and J. Dudek: Comput. Phys. Commun. **102**, 183 (1997).

SD Pair Approximations of the Nuclear Collective Motion

Y. M. Zhao, S. Yamaji, N. Yoshinaga, and A. Arima

[*SD* pair approximation, Excitations of medium-heavy nuclei]

Through the success of the IBM[1] and the FDSM,[2] it was recognized that the *SD* pairs play a dominant role in the collective motions. In the IBM, *SD* pairs are approximated as *sd* bosons. In the FDSM, *SD* pairs are the SP(6) or SO(8) symmetry-dictated *SD* pairs. Recently, Chen proposed a nucleon-pair shell model[3,4] (NPSM). When one restricts the angular momenta by 0 and 2, the NPSM is reduced to the *SD* pair shell model (*SD*PM).

Numerical calculation in the *SD*PM is very time-consuming (when nuclear pair number N $\geq$ 4). The reason is that one can not use CFP (coefficients of fractional parentage) techniques since the subspace is not closed. However, we point out that one may use similar techniques which can be expected to reduce the cpu time drastically. Taking the overlap calculation as an example, since we construct the subspace using only two kinds of nucleon pairs (i.e., collective *SD* pairs), it is not difficult to see that there is only one pair which goes beyond the subspace in the (N-1)-pair overlaps. All the matrix elements with the same building blocks are related to each other via coupling coefficients. Therefore, one needs only a very small part of the (N-1)-pair overlaps in the recursion formulae. Modification of the numerical code is still in progress.

We have calculated ^{132}Te, ^{130}Te, ^{128}Te, ^{134}Xe, ^{132}Xe, ^{130}Xe, ^{136}Ba, ^{134}Ba, and ^{132}Ba. The Hamiltonian includes the single-particle term, monopole and quadrupole pairing between like valence nucleons, and Q-Q force for both like- and unlike-valence nucleons. We use BCS pair for the S pair, and then construct D pair by $D^\dagger = \frac{1}{2}[Q, S^\dagger]$. The calculational results reproduce the experimental data very well.

Extension of the *SD*PM to describe odd nuclei is straightforward. We have developed several algorithms which are suitable for numerical calculations. The program is under development.

References

1) F. Iachello and A. Arima: *The Interacting Boson Model*, (Cambridge Univ., 1987).
2) C. L. Wu et al.: Phys. Rev. C **36**, 1157 (1987).
3) J. Q. Chen: Nucl. Phys. A **626**, 686 (1990).
4) J. Q. Chen et al.: Nucl. Phys. A **639**, 615 (1990).

The Pseudo-Spin Symmetry in Zr and Sn Isotopes from the Proton Drip Line to the Neutron Drip Line†

J. Meng, K. Sugawara-Tanabe, S. Yamaji, and A. Arima

[Pseudo-spin symmetry, Relativistic continuum Hartree-Bogoliubov, Drip-line nuclei]

The concept of pseudo-spin was originally found in spherical nuclei 30 years ago,[1,2] but later proved to be a good approximation in deformed nuclei and remains an important physical concept even in the case of triaxiality as well.

Since the suggestion of the pseudo-spin symmetry, much efforts has been made to understand its origin. Based on the single particle Hamiltonian of the oscillator shell model the origin of pseudo-spin was proved to be connected with the special ratio in the strength of the spin-orbit and orbit-orbit interactions[3] and the unitary operator performing a transformation from normal spin to pseudo-spin space was discussed. However, it was not explained why this special ratio is allowed in nuclei. The relation between the pseudo-spin symmetry and the relativistic mean field (RMF) theory was first noted in Ref. 4, in which Bahri et al. found that the RMF explains approximately the strengths of spin-orbit and orbit-orbit interactions in the non-relativistic calculations. In a recent paper Ginocchio took a step further and revealed that pseudo-orbital angular momentum is nothing but the "orbital angular momentum" of the lower component of the Dirac wave function.[5]

By relating the pseudo-spin symmetry back to the Dirac equation through the framework of Relativistic Continuum Hartree-Bogoliubov (RCHB) theory,[6] the pseudo-spin approximation in real nuclei was shown to be connected with the competition between the pseudo centrifugal barrier (PCB) and the pseudo-spin orbital potential (PSOP), which is mainly decided by the derivative of the difference between the scalar and vector potentials. This is general for any Dirac spinors system with spherical symmetry. With the scalar and vector potentials derived from a self-consistent Relativistic Hartree-Bogoliubov calculation, the pseudo-spin symmetry and its energy dependence have been discussed in Ref. 7.

The highly unstable nuclei with extreme proton and neutron ratio are now accessible with the help of the radioactive nuclear beam facilities. The physics connected with the extreme neutron richness in these nuclei and the low density in the tails of their distributions have attracted more and more attention not only in nuclear physics but also in other fields such as astrophysics. It is very interesting to investigate the pseudo-spin symmetry approximation both in normal and exotic nuclei. For this purpose, we use the RCHB theory, which is the extension of the RMF and the Bogoliubov transformation in the coordinate representation, and provides not only a unified description of the mean field and pairing correlation but also the proper description for the continuum and its coupling with the bound state.[6,8,9]

The pseudo-spin symmetry is found to be a good approximation even for the exotic nuclei with highly diffused potential. The above conclusion has been well supported by RCHB calculations for Zr and Sn isotopes from the proton drip line to the neutron drip line. From the simple Dirac equation, it has been shown that there are two equivalent ways to solve the coupled Dirac equation for the upper and lower components: i.e., the normal spin formalism and pseudo-spin formalism. Both formalisms are equivalent as far as the energies and wave functions are concerned. The pseudo-spin symmetry is a good approximation for normal nuclei and become much better for exotic nuclei with highly diffuse potentials. The pseudo-spin symmetry has strong energy dependence. The energy splitting between the pseudo-spin partners is smaller for orbitals near the Fermi surface. The lower components of the Dirac wave functions for the pseudo-spin partners are very similar and almost equal in magnitude. The similarity in the lower components of the wave function for the pseudo-spin partners near the Fermi surface is closer than for the deeply bound ones.

References

1) A. Arima, M. Harvey, and K. Shimizu: Phys. Lett. B **30**, 517 (1969) .
2) K. T. Hecht and A. Adler: Nucl. Phys. A **137**, 129 (1969).
3) A. Bohr, I. Hamamoto, and B. R. Mottelson: Phys. Scripta **26**, 267 (1982).
4) C. Bahri, J. P. Draayer, and S. A. Moszkowski: Phys. Rev. Lett. **68**, 2133 (1992).
5) J. Ginocchio: Phys. Rev. Lett. **78**, 436 (1997).
6) J. Meng: Nucl. Phys. A **635**, 3 (1998).
7) J. Meng, K. Sugawara-Tanabe, S. Yamaji, P. Ring, and A. Arima: Phys. Rev. C **58**, R628 (1998).
8) J. Meng and P. Ring: Phys. Rev. Lett. **77**, 3963 (1996).
9) J. Meng and P. Ring: Phys. Rev. Lett. **80**, 460 (1998).

† Condensed from the article in Phys. Rev. C **59** (1999), in press

The Pseudo-Spin Symmetry in Relativistic Mean Field Theory†

J. Meng, K. Sugawara-Tanabe, S. Yamaji, P. Ring,* and A. Arima

[Pseudo-spin symmetry, Relativistic mean field, Relativistic continuum Hartree-Bogoliubov]

The concept of pseudo-spin is that the single particle orbitals with $j = l + 1/2$ and $j = (l + 2) - 1/2$ lie very close in energy and can therefore be labelled as pseudo-spin doublets with quantum number $\tilde{n} = n - 1$, $\tilde{l} = l - 1$, and $\tilde{s} = s = 1/2$. This concept is originally found in spherical nuclei,[1,2] but later proved to be a good approximation in deformed nuclei as well.[3,4] The origin of pseudo-spin is proved to be connected with the special ratio in the strength of the spin-orbit and orbit-orbit interactions[5,6] and the unitary operator performing a transformation from normal spin to pseudo-spin space have been discussed.[5] However, it is not explained why this special ratio is allowed in nuclei. The relation between the pseudo-spin symmetry and the relativistic mean field (RMF) theory[7] was first noted in Ref. 8. In a recent paper Ginocchio taked a step further and revealed that pseudo-orbital angular momentum is nothing but the "orbital angular momentum" of the lower component of the Dirac wave function.[9]

He also built the connection between the pseudo-spin symmetry and the equality in the scalar and vector potentials. Here we will show that the quality of pseudo-spin symmetry is connected with the competition between the centrifugal barrier (CB) and the pseudo-spin orbital potential (PSOP), which is mainly decided by the derivative of the difference between the scalar and vector potentials.

Here the Relativistic continuum Hartree-Bogoliubov (RCHB) theory[10] has been used for the present investigation. As this theory takes into account the proper isospin dependence of the spin-orbit term, it is able to provide a good description of global experimental data not only for stable nuclei but also for exotic nuclei throughout the nuclear chart.[11] Starting from the RCHB, instead of assuming the equality in magnitude of the scalar and vector potentials, we treated the equation exactly and obtained a general formalism leading to the pseudo-spin symmetry.

We use the non-linear Lagrangian parameter set NLSH[12] which could provide a good description of all nuclei from oxygen to lead. As we study not only the closed shell nuclei, but also the open shell nuclei, the inclusion of the pairing is necessary. The pairing interaction is the same as Ref. 13. As shown in Ref. 11, the particle levels for the bound states in canonical basis are the same as those by solving the Dirac equation with the scalar and vector potentials from RCHB.

In conclusion, the pseudo-spin symmetry is examined in realistic calculation in the framework of RCHB theory. We have proved that if $dV/dr = 0$ is satisfied, the pseudo-spin symmetry is exact. Further, the new condition $\frac{1}{E-V}\frac{\kappa}{r}\frac{dV}{dr} \ll \frac{\kappa(1-\kappa)}{r^2}$ is found under which the symmetry is preserved approximately. We have examined under this condition how good approximation the pseudo-spin symmetry is in RCHB. For a given angular momentum and parity channel, the effective CB, $(E-V)\frac{\kappa(\kappa-1)}{r^2}$, becomes stronger for the less bound level, so the pseudo-spin symmetry for the weakly bound state is better than that for the deeply bound state, which is in agreement with the experimental observation.[1,2] The pseudo-spin symmetry is found to be a good approximation even for exotic nuclei. The above conclusion has been well supported by the examples of ^{88}Zr and ^{120}Zr. From the simple Dirac equation, it has been shown that there are two equivalent ways to solve the coupled Dirac equation for the upper and lower components: i.e., the normal spin formalism and pseudo-spin formalism. Both formalisms are equivalent as long as the energies and wavefunctions are concerned.

References

1) A. Arima, M. Harvey, and K. Shimizu: Phys. Lett. B **30**, 517 (1969).
2) K. T. Hecht and A. Adler: Nucl. Phys. A **137**, 129 (1969).
3) R. D. Ratna Raju, J. P. Draayer, and K. T. Hecht: Nucl. Phys. A **202**, 433 (1973); J. P. Draayer and K. J. Weeks: Ann. Phys. (N. Y.) **156**, 41 (1984).
4) J. Y. Zeng et al.: Phys. Rev. C **44**, R1745 (1991).
5) A. Bohr, I. Hamamoto, and B. R. Mottelson: Phys. Scripta **26**, 267 (1982).
6) O. Castañov, M. Moshinsky, and C. Quesne: Phys. Lett. B **277**, 238 (1992).
7) B. D. Serot and J. D. Walecka: in *Advances in Nuclear Physics*, edited by J. W. Negele and E. Vogt, Vol. 16 (Plenum, New York, 1986) p. 1.
8) C. Bahri, J. P. Draayer, and S. A. Moszkowski: Phys. Rev. Lett. **68**, 2133 (1992).
9) J. Ginocchio: Phys. Rev. Lett. **78**, 436 (1997).
10) J. Meng and P. Ring: Phys. Rev. Lett. **77**, 3963 (1996).
11) J. Meng: Nucl. Phys. A **635**, 3 (1998).
12) M. Sharma, M. Nagarajan, and P. Ring: Phys. Lett. B **312**, 377 (1993).
13) J. Meng and P. Ring: Phys. Rev. Lett. **80**, 460 (1998).

† Condensed from the article in Phys. Rev. C **58**, R628 (1998)

* Technische Universität München, Germany

The Pseudo-Spin Symmetry in Dirac Equation

K. Sugawara-Tanabe, J. Meng, S. Yamaji, and A. Arima

[Pseudo-spin symmetry, Deformed Dirac equation]

The origin of the pseudo-spin symmetry[1] has been investigated with the purpose to find its root to the relativistic Dirac equation.[2-4] By extending Ginnocchio's method,[2] we found the more general and realistic condition for the hidden symmetry of pseudo-spin approximation in the lower component (f) of Dirac wave function in the spherical potentials.[3,4] The Dirac equation for a nucleon with mass M moving in the vector potential ($V_V(\vec{r})$) and scalar potential ($V_S(\vec{r})$) is given by,

$$[\vec{\alpha}\cdot\vec{p}+V_V(\vec{r})+\beta(M+V_S(\vec{r}))]\psi(\vec{r})=\epsilon\psi(\vec{r}). \quad (1)$$

Here $\vec{\alpha}$ and β are Dirac matrices. The spinor $\psi(\vec{r})$ is composed of the upper component (g) and the lower component (f). In the spherical potential case, these two components g and f are decomposed into the product of the radial part and the vector spherical harmonics with quantum numbers j, ℓ and j_z, where j is the single-particle angular momentum and ℓ is its orbital angular momentum.

Now we extend our theory to the deformed case with axially symmetric shape. In this case j is no longer a good quantum number, but there still remains a symmetry around the symmetry axis z characterized by $j_z=\Omega$. We use the cylindrical coordinate $(r_\perp, z, \varphi)$ to solve the Dirac equation. Each of g and f has now two components,

$$g=\frac{1}{\sqrt{2\pi}}\begin{pmatrix} ig_+^\Omega e^{i(\Omega-1/2)\varphi} \\ ig_-^\Omega e^{i(\Omega+1/2)\varphi}\end{pmatrix},$$
$$f=\frac{1}{\sqrt{2\pi}}\begin{pmatrix} f_+^\Omega e^{i(\Omega-1/2)\varphi} \\ f_-^\Omega e^{i(\Omega+1/2)\varphi}\end{pmatrix}. \quad (2)$$

Here $f_\pm^\Omega$ and $g_\pm^\Omega$ are the functions of $r_\perp$ and z, and $\pm$ corresponds to $\pm 1/2$ of s_z. Inserting Eq. (2) into Eq. (1) and eliminating $f_\pm^\Omega$ ($g_\pm^\Omega$), we get the coupled equations between g_+^Ω and g_-^Ω and also between f_+^Ω and f_-^Ω. Here we show the coupled equations for f_+^Ω and f_-^Ω.

$$\begin{aligned}-V_2V_1f_+^\Omega &= \frac{\partial^2 f_+^\Omega}{\partial r_\perp^2}-\frac{(\Omega-1/2)^2}{r_\perp^2}f_+^\Omega \\ &+\frac{1}{r_\perp}\frac{\partial f_+^\Omega}{\partial r_\perp}+\frac{\partial^2 f_+^\Omega}{\partial z^2} \\ &-\frac{1}{V_1}\frac{\partial V_1}{\partial r_\perp}\left(\frac{\partial f_+^\Omega}{\partial r_\perp}-\frac{\Omega-1/2}{r_\perp}f_+^\Omega-\frac{\partial f_-^\Omega}{\partial z}\right) \\ &-\frac{1}{V_1}\frac{\partial V_1}{\partial z}\left(\frac{\partial f_-^\Omega}{\partial r_\perp}+\frac{\Omega+1/2}{r_\perp}f_-^\Omega+\frac{\partial f_+^\Omega}{\partial z}\right), \end{aligned} \quad (3)$$

$$\begin{aligned}-V_2V_1f_-^\Omega &= \frac{\partial^2 f_-^\Omega}{\partial r_\perp^2}-\frac{(\Omega+1/2)^2}{r_\perp^2}f_-^\Omega \\ &+\frac{1}{r_\perp}\frac{\partial f_-^\Omega}{\partial r_\perp}+\frac{\partial^2 f_-^\Omega}{\partial z^2} \\ &-\frac{1}{V_1}\frac{\partial V_1}{\partial r_\perp}\left(\frac{\partial f_-^\Omega}{\partial r_\perp}+\frac{\Omega+1/2}{r_\perp}f_-^\Omega+\frac{\partial f_+^\Omega}{\partial z}\right) \\ &-\frac{1}{V_1}\frac{\partial V_1}{\partial z}\left(\frac{\partial f_+^\Omega}{\partial r_\perp}+\frac{\Omega-1/2}{r_\perp}f_+^\Omega+\frac{\partial f_-^\Omega}{\partial z}\right), \end{aligned} \quad (4)$$

where $E=\epsilon-M$, $V_1=E-V$, $V_2=E+2M^*-V$ with $V=V_V(\vec{r})+V_S(\vec{r})$ and $M^*=M+V_S(\vec{r})$. The coupled equations between g_+^Ω and g_-^Ω are given by exchanging $f_\pm^\Omega$ by $g_\pm^\Omega$, and V_1 by V_2 and vice versa. In the non-relativistic theory, the levels labeled by $(\ell_z=\Lambda, s_z=1/2, j_z=\Omega)$ and by $(\ell_z=\Lambda+2, s_z=-1/2, j_z=\Omega+1)$ become the pseudo-spin pair of $(\tilde{\ell}_z=\Lambda+1, \tilde{s}_z=-1/2, j_z=\Omega)$ and $(\tilde{\ell}_z=\Lambda+1, \tilde{s}_z=1/2, j_z=\Omega+1)$. Comparing Eqs. (3) and (4), we find that f_+^Ω and $f_-^{\Omega+1}$ become pseudo-spin doublets as long as $\partial V_1/\partial r_\perp=0$ and $\partial V_1/\partial z=0$. Thus, we find the condition for the pseudo-spin symmetry in the deformed potential as

$$(a)\quad \frac{\partial V_1}{\partial z}=0,\quad \frac{\partial V_1}{\partial r_\perp}=0; \quad (5)$$

$$\begin{aligned}(b)\quad &\left|\frac{1}{V_1}\frac{\partial V_1}{\partial r_\perp}\frac{\tilde{\Omega}}{r_\perp}\right| \ll \left|\frac{\tilde{\Omega}^2}{r_\perp^2}\right|, \\ &\left|\frac{1}{V_1}\frac{\partial V_1}{\partial z}\frac{\tilde{\Omega}\pm 1}{r_\perp}\right| \ll \left|\frac{\tilde{\Omega}^2}{r_\perp^2}\right|. \end{aligned} \quad (6)$$

By applying the similar technique used in the spherical potentials, we found the condition for the hidden-symmetry of pseudo-spin in deformed nuclei for the first time. The condition (a) in Eq. (5) is not always satisfied in the real nuclei, but (b) in Eq. (6) is a more plausible condition. Our next work is to evaluate (b) in Eq. (6) for the deformed nuclei with a realistic parameter set similar to the spherical case shown in Refs. 3 and 4.

References

1) A. Arima, M. Harvey, and K. Shimizu: Phys. Lett. B **30**, 517 (1969).
2) J. N. Ginocchio: Phys. Rev. Lett. **78**, 436 (1997).
3) J. Meng, K. Sugawara-Tanabe, S. Yamaji, P. Ring, and A. Arima: Phys. Rev. C **58**, R632 (1998).
4) J. Meng, K. Sugawara-Tanabe, S. Yamaji, and A. Arima: Phys. Rev. C **59**, 154 (1999).

Triaxial Deformation of Medium Heavy Nuclei in Relativistic Mean Field Theory with Pairing Correlation

S. Sugimoto, K. Sumiyoshi, D. Hirata, I. Tanihata, and H. Toki

[Relativistic mean field theory, Triaxial deformation, Pairing]

We study the properties of medium heavy mass nuclei including the possibility of triaxial deformation in the relativistic mean-field theory with pairing correlation. We calculate the energy surfaces of the even-even nuclei around ^{122}Xe in the β-γ plane on the Fujitsu VPP500/28 Supercomputer of the Computation Center in RIKEN.

The relativistic many body theory has been extensively applied to nuclei and nuclear matter with remarkable successes in recent years. The relativistic mean-field (RMF) theory has been employed in large scale to study the properties of stable and unstable nuclei. The description of the ground state properties of stable and unstable nuclei with axial deformation in terms of the RMF has been found to be very satisfactory.[1] However, it was found necessary to extend the theory to include higher order deformations. In many cases, the axial symmetric calculations give minima on both the prolate and oblate shapes with energies very close to each other. In those cases, the ground state configuration cannot be well distinguished and the shape coexistence or another type of deformation should be also explored. The inclusion of triaxial deformation(γ degree of freedom) to the RMF approach was worked out and applied to study the properties of light mass sulfur nuclei.[2] It was found a smooth transition from prolate to oblate shapes through triaxial shapes and eventually to the spherical shape. Similar behavior can be expected in other region of the nuclear chart. Here, we applied this framework to the medium heavy region around ^{122}Xe. We found that in this region many nuclei have the possibility of the triaxial shapes in their ground state. We also found the smooth shape transitions in the sulfur region.

However, in those calculations we did not take into account the effect of pairing correlations. This correlation may have large effect on nuclear deformations. We include it in the calculation of the triaxial deformation in terms of the BCS theory. We use the extended RMF theory which include the triaxial deformation degree of freedom. The theory contains the meson masses, the meson-nucleon coupling constants, and the meson self-coupling constants as free parameters. The calculations are carried out using the parameter set TMA, which was determined by fitting the experimental data of masses and charge radii of nuclei in a wide mass range, so as to reproduce nuclear properties quantitatively in the entire mass region.[3] The wave functions of nucleons and mesons are expanded in terms of the eigenfunctions of an triaxially deformed harmonic oscillator potential. The expansion method is described in detail in the paper by Gambhir et al.,[2,4] but one more degree of freedom (γ deformation) is included newly.[2] In the present calculation, we work with basis of the 12 major shells for fermions and 10 major shells for bosons. In order to obtain the energy surfaces, we perform the quadratic constrained calculations on the quadrupole moments of nucleon distribution, Q_{20} and Q_{22}.[2,5] In the pairing channels we use the BCS scheme by the constant gap approach. We note that in this scheme pairing correlations are not treated on the ground of relativistic framework. We are now investigating the theory which treats the pairing correlations consistent with the relativistic framework.

We shall show one result. Figure 1 shows the energy surface of ^{124}Xe in β-γ plane. The horizontal axis ($\gamma = 0°$) denotes the prolate shape and the tilted axis ($\gamma = 60°$) denotes the oblate shape. The region among these axes denotes triaxially deformed shape. The larger value of β indicates the stronger defomation. The energy difference between the contour is about 1 MeV. In Fig. 1 the position of the absolute minimum is denoted by the black area. From the Figure we see ^{124}Xe has the axial deformed shape in the ground state. The other nuclei are still under study.

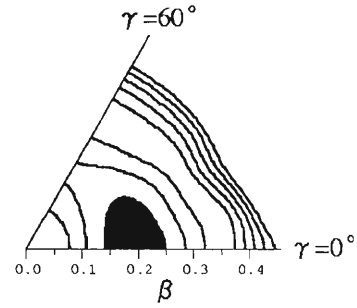

Fig. 1. The energy surface in the β-γ plane of ^{124}Xe. The positon of the absolute minimum is denoted by the black area.

References

1) D. Hirata et al.: Nucl. Phys. A **616**, 438c (1997) .
2) D. Hirata et al.: Nucl. Phys. A **609**, 131 (1996).
3) Y. Sugahara: Doctor thesis, Tokyo Metropolitan University (1995).
4) Y. K. Gambhir et al.: Ann. Phys. **198**, 132 (1990) .
5) H. Flocard et al.: Nucl. Phys. A **203**, 433 (1973).

SU(3) Symmetry in Oblate and Triaxial Nuclei

K. Sugawara-Tanabe and A. Arima

[SU(3) symmetry, Oblate deformation, Triaxial shape]

We have previously shown that the new dynamical SU(3) symmetry exists at the prolate deformed nuclei when the two harmonic oscillator frequencies $\omega_\perp$ and ω_z have the rational ratio.[1] In this paper we show that we can similarly extend our discussion to the oblate deformed nuclei and also to the triaxial shaped nuclei.

We adopt the harmonic oscillator Hamiltonian with a rational ratio $a : b : c$ between three frequencies ω_x, ω_y and ω_z. Then the energy eigenvalue becomes $\hbar\omega_{sh}(N_{sh}+(a+b+c)/2)$ with the shell quantum number $N_{sh} = an_x + bn_y + cn_z$ and the shell energy $\hbar\omega_{sh}$. At first we consider the case of oblate superdeformation, in which $\omega_x : \omega_y : \omega_z = 1 : 1 : 2$, and the deformation parameter $\delta = 3(a-c)/(2a+c) = -0.75$. We construct new boson operators d and $d^\dagger$ as a biproduct of the harmonic oscillator bosons, $c_\pm$ and $c_\pm^\dagger$, where $c_\pm = \mp(c_x \mp c_y)/\sqrt{2}$. Because of the biproduct of $c_\pm$, we have two kinds of bosons corresponding to $n_d = n_\pm/2$ or $n_d = (n_\pm - 1)/2$:

$$d = \frac{1}{\sqrt{2(1+\hat{n}_\pm)}}c_\pm^2, \quad d = \frac{1}{\sqrt{2(2+\hat{n}_\pm)}}c_\pm^2, \tag{1}$$

where $\hat{n}_\pm = c_\pm^\dagger c_\pm$. Both bosons do not mix each other as they belong to different N_{sh}. We obtain a new set of group operators, $\tilde{Q}$ and $\tilde{\ell}$ in the same way as in the prolate superdeformed case. In contrast to Elliott's case[2] where $\pm 2\hbar\omega_0$ excitations are excluded, our group operators exclude $\pm 2\hbar\omega_{sh}$ excitations. Moreover, this new SU(3) has a dual nature because of two kinds of bosons. Then we can summarise the clasification of the single-particle states in a superdeformed oscillator of $\tilde{Q}_0$ and $\tilde{\ell}_z$, which becomes completely the same as shown in Table 1 in Ref. 1. Similarly, we can get the same classification of the single-particle levels for the case of $a : b : c = 1 : 1 : 3$ as $a : b : c = 3 : 3 : 1$ in prolate hyperdeformation. In this case we introduce three kinds of g-bosons corresponding to $n_g = n_\pm/3$ or $n_g = (n_\pm - 1)/3$ or $n_g = (n_\pm - 2)/3$:

$$g = \frac{1}{\sqrt{3(\hat{n}_\pm+2)(\hat{n}_\pm+1)}}c_\pm^3,$$
$$g = \frac{1}{\sqrt{3(\hat{n}_\pm+3)(\hat{n}_\pm+1)}}c_\pm^3,$$
$$g = \frac{1}{\sqrt{3(\hat{n}_\pm+3)(\hat{n}_\pm+2)}}c_\pm^3. \tag{2}$$

In this case SU(3) is triplicate. Similarly we can get the same classification for $a : b : c = 2 : 2 : 3$ as $a : b : c = 3 : 3 : 2$, in which SU(3) has six-fold degeneracy. In this case we adopt g bosons for $\pm$ axis and d bosons for z axis. Thus, we can conclude that there exists SU(3) symmetry even in the oblate deformation as long as two frequencies have rational ratios.

Now we consider the triaxial case with $a : b : c = 1 : 2 : 3$. We use g bosons for the x axis ($c_\pm$ in (3) should be replaced by c_x), d bosons for the y axis ($c_\pm$ in (2) should be replaced by c_y), and the usual harmonic oscillator boson c_z for the z axis. The Casimir operator becomes,

$$C = 2(\hat{n}_g + \hat{n}_d + \hat{n}_z)(\hat{n}_g + \hat{n}_d + \hat{n}_z + 3). \tag{3}$$

Although it has the nature of SU(3) for the triaxial case with rational ratio of three frequencies, but there is no degeneracy of SU(3) in different N_{sh}. Moreover, the single-particle levels are qualified only by $\tilde{Q}_0$, and $\tilde{\ell}_z$ is no longer diagonal in this representation. Instead we can use $\tilde{Q}_2 + \tilde{Q}_{-2} = \sqrt{6}(\hat{n}_g - \hat{n}_d)$ as a order of triaxiality. We can summarize the classification of the single-particle levels in the Table 1.

Table 1. Single particle levels for triaxial ($a : b : c = 1 : 2 : 3$) shape.

N_{sh}	n_g	n_d	n_z	$< C >$	$< Q_0 >$
0	0	0	0	0	0
1	0	0	0	0	0
2	0	0	0	0	0
3	1	0	0	8	−1
	0	0	0	0	0
	0	0	1	8	2
4	1	0	0	8	−1
	0	0	0	0	0
	0	0	1	8	2
	0	0	1	8	−1

References

1) K. Sugawara-Tanabe and A. Arima: Nucl. Phys. A **619**, 88 (1997).
2) J. P. Elliott: Proc. Roy. Soc. A **245**, 128 (1958); **245**, 562 (1958).

Relativistic Mean Field Investigation of the Identical Bands and Band Crossing in the Superdeformed Eu-Gd Nuclei

H. Madokoro, J. Meng, M. Matsuzaki, and S. Yamaji

[Relativistic mean field, Identical band, ^{148}Eu, ^{149}Gd]

8 new superdeformed(SD) bands in ^{148}Eu were discovered in recent experiment,[1] some of which have nearly identical transition energies and therefore identical moments of inertia to those in ^{149}Gd, that is, they form the so-called identical bands. In addition, there is another interesting observation of the $\pi 6^1$-$\pi 6^3$ band crossing which is the first experimental observation of this crossing. As for the identical bands, there have been so many experimental observations of the identical pairs in the $A \sim 130$, 150 and 190 mass regions. From the theoretical side, there have been several attempts to explain the mechanism of these identical bands, for example, the one using the concept of pseudo-spin symmetry.[2] Why the transition energies of these two bands become so identical within an accuracy of 0.1%, however, is still under debate.

In 1993, Munich group proposed a new explanation of the identical bands within the context of Relativistic Mean Field (RMF) model. They calculated the lowest SD band in ^{152}Dy and one of the excited SD bands in ^{151}Tb which form the identical pair of bands. In addition to the usual calculation, they performed two types of calculations, one with neglecting the polarization effect induced by the neutron hole, another one with neglecting the effect of the space components of the vector mesons (nuclear magnetism). Both calculations did not give the identical transition energies but acted in the opposite direction with approximately the same magnitudes. Finally they concluded that a cancellation occurred between the effect of the polarization and that of the nuclear magnetism, resulting in the nearly identical transition energies. Up to now, this new mechanism has been examined only for the pair of ^{152}Dy-^{151}Tb nuclei. To see whether this mechanism is a general one or not, it is necessary to perform the same calculations for other pairs of bands. Therefore, as a first step, we investigate the identical pair of ^{148}Eu-^{149}Gd nuclei, including recently discovered SD bands in ^{148}Eu, using RMF model.

RMF model contains nucleons and several kinds of mesons as basis components. Starting from the Lagrangian containing these degrees of freedom, we can derive the equations of motion for nucleons and mesons after applying the variational principle. In the application to rotating nuclei, we combine the RMF model and the cranking assumption. Then the Lagrangian in the laboratory frame is generalized to the uniformly rotating frame, from which the equations of motion in this frame are derived. For detail, see Refs. 3 and 4.

In the numerical calculations, the parameter set NL1 is adopted. At first we calculate the moments of inertia of the lowest SD band in ^{149}Gd and the lowest two SD bands in ^{148}Eu. Apart from small deviations at lower frequencies, we obtain good agreements between the calculated and the experimental values. Besides, we find that the moments of inertia(or equivalently the transition energies) become nearly the same values between ^{149}Gd and ^{148}Eu. Next, we perform two different kinds of calculations following the previous investigation of Munich group. (1) We calculate the SD bands in ^{148}Eu using the wave functions of ^{149}Gd, without assuming self-consistency. This corresponds to the calculation neglecting the effect of the polarization induced by a neutron hole. The resulting transition energies do not become identical at all. (2) We perform a self-consistent calculation of the SD bands in ^{148}Eu, but the space components of the vector mesons, are neglected. Again the transition energies in this case do not become the same. We find that, contrary to the case of ^{152}Dy-^{151}Tb pair, both effects act not in the opposite direction but in the same direction. Thus a cancellation between (1) and (2) does not occur. It should be noticed that the usual calculation where both the polarization effect and the nuclear magnetism are included does give the identical transition energies, as we stated before. This implies that the usual calculation is not a simple summation of (1) and (2), and there may be other effects which also contribute to the difference of the transition energies. Including these other effects, together with (1) and (2), will finally lead to the identical transition energies. Anyway we can say that the cancellation between the effect of the polarization and that of the space components of the vector mesons does not occur in the case of ^{149}Gd-^{148}Eu pair. Clearly it is necessary to perform further systematic investigations to give a definite conclusion, and such investigations in this mass region, together with those of the $\pi 6^1$- $\pi 6^3$ band crossing, are now in progress.

References

1) D. S. Haslip et al.: Phys. Rev. C **57**, 2196 (1998).
2) W. Nazarewicz, P. J. Twin, P. Fallon, and D. Garrett: Phys. Rev. Lett. **64**, 1654 (1990).
3) W. Koepf and P. Ring: Nucl. Phys. A **493**, 61 (1989).
4) H. Madokoro and M. Matsuzaki: Phys. Rev. C **52**, R2934 (1997).

Band Structures of ^{182}Os Studied by GCM Based on 3D-CHFB

T. Horibata, M. Oi, N. Onishi, and A. Ansari[*1,*2]

[Tilted rotation, Generator coordinate method, γ-deformation]

We have carried out the angular momentum and particle number constrained generator coordinate method(GCM) calculations based on the three-dimensional cranked Hartree-Fock-Bogoliubov approach (3D-CHFB). Compared to our previous works,[1,2] we have refined the force parameters carefully so as to reproduce the characteristic features of the yrast states for the mass region of interest. With our new set of force parameters the neutron gap parameter Δ_n vanishes almost, whereas the proton gap parameter Δ_p survives still with the size of the ground state one at $J = 18\hbar$. In our calculation the band crossing occurs at $J = 20\hbar$. After choosing the set of force parameters we have performed the 3D-CHFB calculation along the prime meridian on the globe of $J = 18\hbar$ sphere. We know from our previous study that a calculation along the prime meridian always gives a lower energy compared with the calculation performed on the whole surface of the globe. Like the previous calculation, we have confirmed the existence of a stable tilted axis rotating(TAR) potential curve for this time also. The TAR minimum appears at $\psi = 24°$. Furthermore, we have found a negative potential curve near the north pole. We have performed the GCM calculation based on this new potential curve and discussed properties of the band structure of ^{182}Os. The results can be summarized by stressing following three points.

First point is that by including the constrained terms in the Hill-Wheeler equation the stability of the solutions is much increased and we can recognize in the GCM solutions the appearance of wide-range plateaus even in such a high angular momentum region as $J = 18\hbar$. This was not the case in our previous work. The reason is that we can suppress a drift of the mean value of the square of angular momenta by the constrained term in the Hill-Wheeler equation and can prevent a contamination by the lower angular momentum components that are present in the cranking wave function.

Second point is that from the symmetry property of the lowest GCM solution we can expect that this nucleus should be a tilted-rotor at $J = 18\hbar$ yrast state. The tilt angle is about $\psi = 12°$. As discussed in Ref. 3 the TAR potential minimum will not be a necessary condition for an occurrence of the tilted axis rotation. In our approach, only the GCM solutions can properly predict the characteristic features of exotic collective motions. In the fourth and sixth solutions we have found an s-band character in the principal axis rotational(PAR) region. We have found a sign of multi-band mixing in this nucleus. If the s_n-band states, such as the fourth or sixth solutions, come into energetically-lower positions in the higher angular momentum region, we can say that the band mixing[4] will become a key concept in understanding the band structure of the nucleus.

The last point is that we have found the new 3D-CHFB solutions along the prime meridian, which have been obtained by the tilt-back calculation at $J = 18\hbar$ state. From the characteristic features of the solution, we can say that a new type of seesaw vibrational mode of the proton and neutron pairing occurs in the backbending region in ^{182}Os. This mode accompanies a large γ-oscillation. Thus, a wobbling motion is expected to mediate a band crossing between the g-band and s-band in this nucleus. The GCM calculation which includes these new solutions to explore the band structure of $A \sim 180$ mass region will be the next attractive subject. The preliminary results will be appeared on Ref. 5 and the detailed discussions are given in Ref. 3.

References

1) T. Horibata, M. Oi, and N. Onishi: Phys. Lett. B **355**, 433 (1995).
2) T. Horibata and N. Onishi: Nucl. Phys. A **596**, 251 (1996).
3) T. Horibata, M. Oi, N. Onishi, and A. Ansari: Nucl. Phys. A **646**, 277 (1999) (RIKEN-AF-NP-297).
4) P. M. Walker: Proc. Future of Nuclear Spectroscopy, Crete (1993).
5) T. Horibata, M. Oi, and N. Onishi: J. Phys. G **25**, 1 (1999) (RIKEN-AF-NP-287).

*1 Institute of Physics, Graduate School of Arts and Sciences, University of Tokyo
*2 Institute of Physics, Doordarshan Marg, India

Width and Shape of the Hot Giant Dipole Resonance

N. Dinh Dang, K. Tanabe, and A. Arima

[Single-particle levels, Thermal and statistical models, Giant resonances]

We have developed an approach to study the width and shape of the GDR at various temperatures, which includes all the forward-going processes up to two-phonon ones in the second-order of the interaction strength. The present paper shows that: (1) the total width Γ_{GDR} of the hot GDR arises mainly from the coupling of the GDR vibration to all *ph*, *pp* and *hh* configurations. It increases sharply as temperature increases up to $T \sim 3$ MeV. At higher temperatures the width increase is slowed down to reach a saturated value of around 12 MeV in ^{120}Sn and around 10.5 MeV in ^{208}Pb at $T \sim 4$–6 MeV; (2) the quantal width Γ_Q of the GDR due to coupling of GDR vibration to only *ph* configurations decreases as T increases. Neglecting the two-phonon processes in the expansion to higher-order propagators results in a quantal width, which is almost independent of T; (3) the calculated GDR shape in our model agrees reasonably well with the data. The numerical calculations are limited within a schematic case whose parameters were selected to reproduce the empirical values of the GDR width and its energy at $T = 0$. More refined microscopic studies in this direction are highly desirable since the actual complexity of the wave functions can clarify in detail the relationship between the eigenstates of the model Hamiltonian and the representation basis, and, therefore, may shed more light on the physics of the problem. Other ingredients such as the temperature dependence of the single-particle energies, the contribution of the evaporation width at high temperatures, and the effects of high values of the angular momentum have been also left out in the present study. While there have been some indications on that these effects may not be crucial within the temperature region under consideration and/or in nuclei with mass number A $\geq$ 120, they certainly deserve thorough studies in the future.

More details about our study of the hot GDR can be found in the series of our papers in Ref. 1.

References

1) N. Dinh Dang and A. Arima: Phys. Rev. Lett. **80**, 4145 (1998); Nucl. Phys. A **636**, 443 (1998); N. Dinh Dang, K. Tanabe, and A. Arima: Phys. Rev. C **58**, 3374 (1998); Nucl. Phys. A **645**, 536 (1998); N. Dinh Dang and F. Sakata: Phys. Rev. C **55**, 2872 (1997); Phys. Rev. C **57**, 3032 (1998); N. Dinh Dang: Phys. Rep. **264**, 123 (1996); N. Dinh Dang: Nucl. Phys. A **504**, 143 (1989).

Contribution of Higher-Order Processes to the Damping of Hot Giant Dipole Resonance†

N. Dinh Dang, K. Tanabe, and A. Arima

[Single-particle levels, Thermal and statistical models, Giant resonances]

The giant dipole resonance (GDR) is one of the most spectacular and best known responses of nuclei. It is generated by collective motion of protons against neutrons in the nucleus. Apart from the GDR built on the ground state (g.s. GDR), the GDR built on compound nuclear states (hot GDR) has been the subject of a considerable number of experimental and theoretical studies during the last fifteen years.

Recently we have proposed an approach to the width of the hot GDR, which has shown that the coupling of the collective dipole vibration (GDR phonon) to the incoherent particle-particle (pp) and hole-hole (hh) configurations appearing at non-zero temperature (the thermal damping) is responsible for the width increase at low temperature T and its saturation at high T. It has also been concluded that the quantal damping due to coupling only to ph configurations decreases slowly as the temperature increases. The application of this approach to a systematic study of the quantal and thermal dampings of the hot GDR in ^{90}Zr, ^{120}Sn, and ^{208}Pb has shown a reasonable agreement with the experimental data.[1)] In this work a systematic study is presented for three characteristics of the giant dipole resonance (GDR): (1) its width, (2) its shape and (3) the integrated yield of emitted γ rays in ^{120}Sn and ^{208}Pb as a function of temperature T. The double-time Green function's method has been used to derive a complete set of equations, which allows us to calculate explicitly the GDR width due to coupling to all forward-going processes up to two-phonon ones at most in the second order of the interaction strength. An overall agreement between theory and experiment is found for all the three characteristics. The results show that the total width of the GDR due to coupling of the GDR phonon to all ph, pp and hh configurations increases sharply at low temperatures up to $T \sim 3$ MeV and saturates at $T \sim 4$–6 MeV. The quantal width Γ_Q due to coupling to ph configurations decreases slowly with increasing T. It becomes almost independent of T only when the contribution of two-phonon processes at $T \neq 0$ is omitted. The observed saturation of the integrated yield above $E^* \sim 300$ MeV is reproduced in both the GDR region and in the region above it.

References

1) N. Dinh Dang and A. Arima: Phys. Rev. Lett. **80**, 4145 (1998); Nucl. Phys. A **636**, 443 (1998).

† Condensed from the article in Phys. Rev. C **58**, 3374 (1998)

Damping of Hot Giant Dipole Resonance Due to Complex Configuration Mixing

N. Dinh Dang, K. Tanabe, and A. Arima

[Single-particle levels, Thermal and statistical models, Giant resonances]

A central problem in the study of giant dipole resonance (GDR) in highly-excited nuclei (hot GDR) during the last fifteen years has been the behavior of the GDR width and shape as a function of temperature T. The main part of the total GDR at $T = 0$ width comes from the spreading width due to coupling to complicated configurations such as $2p2h$ and even more complex ones. It turns out that the spreading width depends weakly on T within the extension of well-known microscopic theories to non-zero temperature.[1] This contradicts the experimental systematic which shows a rapid increase of the full width at half maximum (FWHM) at low excitation energies E^* (or T). At higher E^* the width increases slowly and even saturates at $E^* \geq 130$ MeV in Sn isotopes. It has been pointed out that not only the FWHM and energy, but also the complete shape of the GDR should be considered to achieve a meaningful comparison between theory and experiment. The saturation of the yield of γ rays at $E^* \geq 300$ MeV also requires further studies to give an adequate answer on the persistence or disappearance of the GDR at high T. Recently we have proposed a microscopic approach to the damping of the hot GDR,[2] which shows that the coupling of the collective dipole vibration (GDR phonon) to particle-particle (pp) and hole-hole (hh) configurations appearing at $T \neq 0$ is decisively important for a consistent description of the width's increase and its saturation. This work presents for the first time a complete approach, including explicitly all the forward-going processes up to two-phonon ones at $T \neq 0$. Its application will address all three issues: (1) the GDR width, (2) its shape and (3) γ-ray yield in ^{120}Sn and ^{208}Pb. The calculated total width, strength function and the integrated yield of γ rays of the GDR in ^{120}Sn and ^{208}Pb are found in reasonable agreement with the data. Including two-phonon processes, the quantal width Γ_Q due to coupling to ph configurations alone decreases with increasing T. It is shown that the GDR still persists up to $T \sim 6$ MeV.

References

1) P. F. Bortignon et al.: Nucl. Phys. A **460**, 149 (1986); N. Dinh Dang: Nucl. Phys. A **504**, 143 (1989).
2) N. Dinh Dang and A. Arima: Phys. Rev. Lett. **80**, 4145 (1998); Nucl. Phys. A **636**, 443 (1998).

Shape Evolution of the Hot Giant Dipole Resonance†

N. Dinh Dang, K. Tanabe, and A. Arima

[Single-particle levels, Thermal and statistical models, Giant resonances]

A systematic description of the evolution of the giant dipole resonance (GDR) at non-zero temperature T is given within the framework of two versions PDM1[1] and PDM2[2] of the Phonon Damping Model (PDM). The numerical calculations have been performed for the GDR width, the strength function and the integrated yield of the γ rays in ^{120}Sn and ^{208}Pb at $0 \leq T \leq 6$ MeV. The results obtained agree reasonably

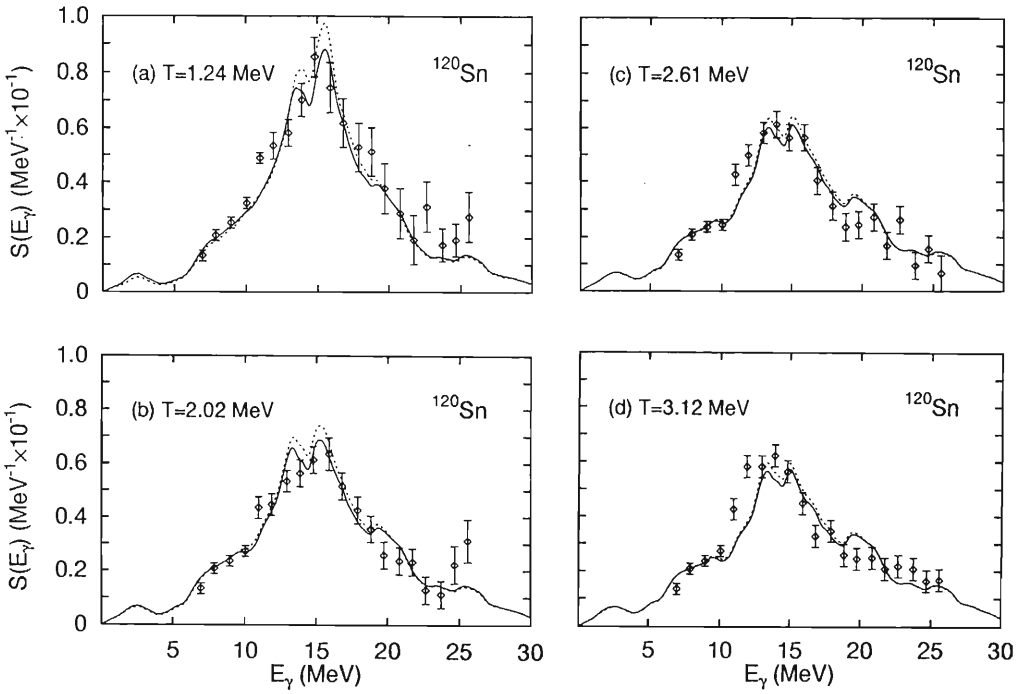

Fig. 1. GDR strength function in ^{120}Sn calculated within PDM-1 at several temperatures. *Solid*: results obtained with the effect of single-particle damping. *Dashed*: results without the effect of single-particle damping. *Diamonds*: inelastic α-scattering data adapted in Ref. 3.

well with the most recent experimental data for all these three characteristics including the saturation of the yields within the GDR region and in the region above it. An example is shown in Fig. 1. Predictions have been made for the GDR shape in both nuclei at T up to 6 MeV and for the integrated yield of γ rays in ^{208}Pb.

References

1) N. Dinh Dang and A. Arima: Phys. Rev. Lett. **80**, 4145 (1998); Nucl. Phys. A **636**, 443 (1998).
2) N. Dinh Dang, K. Tanabe, and A. Arima: Phys. Rev. C **58**, 3374 (1998).
3) T. Baumann et al.: Nucl. Phys. A **635**, 428 (1998).

† Condensed from the article in Nucl. Phys. A **645**, 536 (1998)

Damping of Double Giant Dipole Resonance

N. Dinh Dang, K. Tanabe, and A. Arima

[Giant resonances, Thermal and statistical models, Relativistic heavy-ion collision]

An unambiguous signature of the double giant dipole resonance (DGDR) has been obtained in pion-induced charge exchange reactions and in relativistic heavy-ion reactions via Coulomb excitation.[1] In the harmonic picture a multiphonon excitation is considered as composed of independent phonons. Hence, the energy of a multiphonon state is just the sum of energies of the constituting single-phonon (boson) states. In reality the main features of the observed DGDR can be summarized as follows. (1) The energy E_{DGDR} of the DGDR is about twice as large compared to the giant dipole resonance (GDR): $E_{DGDR} \simeq 2E_{GDR}$, i.e. well described by the harmonic picture. (2) The observed width Γ_{DGDR} of the DGDR is in between $\sqrt{2}\Gamma_{GDR}$ and $2\Gamma_{GDR}$, where Γ_{GDR} is the GDR width. (3) The magnitude of the measured total electromagnetic excitation cross section is found to be enhanced up to more than three times larger than the one obtained in the harmonic limit, depending on nuclei.

In this work a microscopic approach is proposed to the damping of the DGDR. The double-time Green's function method is used to derive a closed set of coupled equations for the propagation of two-phonon excitation through the field of incoherent nucleon pairs. The analytical expressions for the width and energy shift of the DGDR are obtained. The numerical calculations are performed for ^{90}Zr, ^{90}Sn, and ^{208}Pb for several characteristics of the DGDR at zero as well as nonzero temperatures T. The results are found in reasonable agreement with existing experimental systematics for the width and energy of the DGDR. As compared to the estimation within the harmonic picture, the anharmonicity leads to a noticeable enhancement of the integrated photoabsorption cross section (IPACS) over the DGDR region. The DGDR width is found to increase sharply with increasing T at $T \leq 3$ MeV, but comes to a saturation at $T > 3$ MeV. The harmonic limit for the DGDR width is restored already at $T \geq 1.5$ MeV. It is shown that the IPACS of the DGDR can also be enhanced compared to its harmonic value if it is built on a hot GDR.

References

1) S. Mordechai et al.: Phys. Rev. Lett. **61**, 531 (1988); H. Emling: Part. Prog. Nucl. Phys. **33**, 629 (1994); K. Boretzky et al.: Phys. Lett. B **384**, 30 (1996).

Reaction Cross-Sections in the Quantum Molecular Dynamical Approach

T. Maruyama

[Reaction cross-section, QMD]

Radii of exotic nuclei are experimentally determined from measuring reaction cross-sections σ_R in nucleus-nucleus collisions using the equation as

$$\sigma_R = \pi(R_P + R_T)^2, \quad (1)$$

where R_P and R_T indicate projectile and target radii, respectively. This equation is, however, satisfied only for collisions above several hundred MeV/u, where the elementary NN cross-section does not have strong energy-dependence, and the trajectory of a projectile nucleus is well approximate to be straight.

On the other hand we need to make theoretical analysis of experimental results with the beam energy below 100 MeV/u, where a lot of data is available from RIKEN. In this calculation we must consider effects of energy-dependence of the NN cross-section and curved trajectory of initial nuclei in reaction around 50–100 MeV/u energy region.

The Quantum Molecular Dynamics (QMD) approach[1,2] must be a powerful theoretical method for this purpose. This approach is a semi-classical numerical simulation including a mean-field and elastic and ineleastic NN collisions, and it can give consistent results in wide energy region: from several ten MeV/u to several GeV/u. Furthermore this approach have successfully explained many kinds of experimental results in nucleus-nucleus collisions,[1] proton-induced reactions,[2] and so on. In this work we make initial nulcei with correct root-mean-square radii while one has not carefully treated them, and examine reaction cross-sections in the QMD approach.

First we determine parameters of a mean-field to give correct root-mean-square radii of ground state nuclei where each nucleon moves feeling force from other nucleons. Figure 1 shows calculation results of time-averaging root-mean-square radii of several nulcei, whose binding energies are given as experimental data.

As a next step we calculate energy-dependencs of reaction cross-sections in the QMD approach. We define a reaction event where one NN collision occures, and evaluate the reaction cross-section by summing reaction probabilities for all impact-parameters.

In Fig. 2 we draw target-mass-number dependence of reaction cross-sections for the carbon beam at 83 and 300 MeV/u. We can see that the QMD approach nicely reproduce exerimentl results[3] even below 100 MeV/u. Then we can conclude that our approach is effective for the present purpose. Now we are testing reactions with isotope beams. After that we will extend this approach to controle initail distribution and to determine the radii of exotic nuclei.

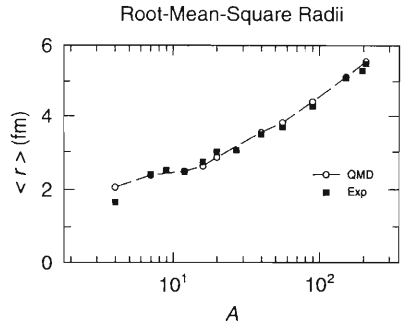

Fig. 1. Time averaging root-mean-square radius of ground state nuclei. Open circles show the results of QMD and the full squares indicate experimental results.

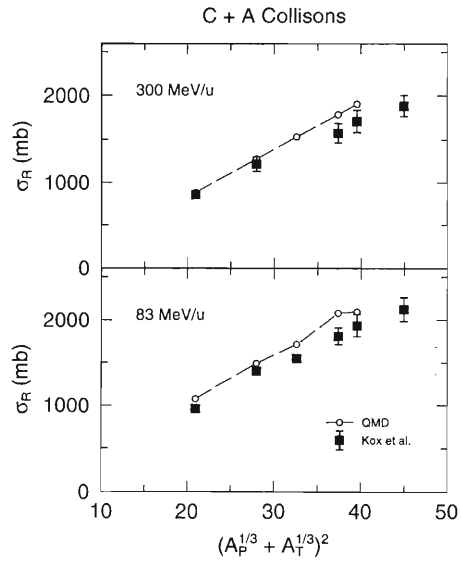

Fig. 2. Target-mass dependence of the reaction cross-sections of collisions with the carbon beam at the incident energies 300 MeV/u (upper column) and 83 MeV/u (lower column). The experimental data are taken from Ref. 3.

References

1) J. Aichelin: Phys. Rep. **202**, 233 (1991).
2) K. Niita, S. Chiba, T. Maruyama, T. Maruyama, H. Takada, T. Fukahori, Y. Nakahara, and A. Iwamoto: Phys. Rev. C **52**, 2620 (1995).
3) S. Kox et al.: Phys. Rev. C **35**, 1678 (1987).

Relativistic EOS Table Constrained by Unstable Nuclei for Supernova and r-Process Simulations

K. Sumiyoshi, H. Shen, K. Oyamatsu, S. Yamada, H. Suzuki, and H. Toki

[Dense matter, Supernova, r-process, Heavy elements]

The physics of supernova is fascinating since it is the key to understand the stellar evolution and the origin of the heavy elements. The mechanism of supernova explosion is still one of big mysteries in astrophysics. Whether the r-process nucleosynthesis to create heavy elements happens in the supernova is also an important question to be answered at the same time. To attack these problems, one has to perform sophisticated numerical simulations with the reliable information of nuclear physics at extreme conditions.

One of essential ingradients from nuclear physics is the equation of state (EOS) of dense matter. The challenge is to describe both unstable nuclei and dense matter covering the wide region of high density, neutron-rich and high temperature during supernova explosion. Because of the lack of the EOS table to cover all conditions, it has been difficult to perform simulations to follow the series of phenomena: gravitational collapse, core bounce, the birth of a neutron star, neutrino wind to lead r-process, and explosion.

To provide the properties of unstable nuclei and dense matter in supernova conditions within a reliable nuclear many body framework, we have completed the EOS table for supernova simulations within the relativistic mean field (RMF) framework. The RMF framework has been successful to describe the structure of unstable nuclei as well as stable ones. The effective lagrangian with non-linear σ and ω terms is constructed based on the relativistic Brückner Hartree-Fock theory. The parameters of the lagrangian are constrained by fitting the experimental data of mass and charge radii of stable and unstable nuclei. We apply the same RMF framework to calculations of the EOS table in the wide region of the environment by adopting the Thomas-Fermi approach.[1,2]

This relativistic EOS table enables us to perform the full simulations of supernova phenomena from the gravitational core collapse to the cooling of the neutron star newly formed. We are applying the relativistic EOS table to the hydrodynamical calculations of core collapse, the supernova neutrinos from the birth of neutron star, and the neutrino wind from proto-neutron star.[3] Here we show an example of the application of the EOS table to hydrodynamical calculations.

Figure 1 shows the calculated trajectory of mass elements in the collapse of the core of a massive star as a function of time. After the core collapses gravitationally, the bounce occurs at high density, leaving a compact object at center. The shock wave is launched

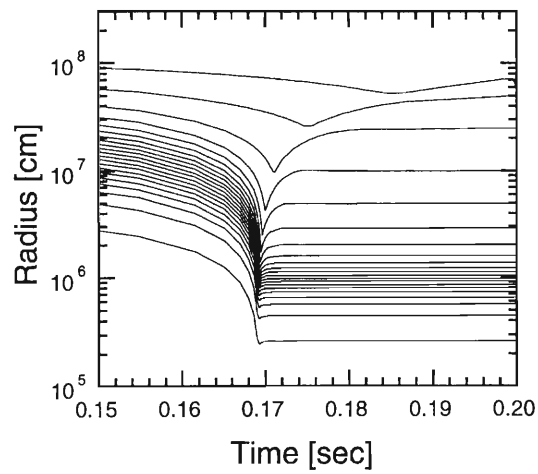

Fig. 1. Trajectory of mass elements during gravitational core collapse.

at the bounce, and propagates towards the surface, leading to a successful explosion. Although this is a test calculation treating only hydrodynamics without the neutrino transfer, which is an another key part, we have found that the EOS table works quite well even for dynamical situations. We are currently working on the full simulations of hydrodynamics with the neutrino transfer to clarify the mechanism of explosion.

We have performed also the numerical simulations of the neutrino wind from a proto-neutron star born right after the core bounce. At the surface of the proto-neutron star, the matter is heated up due to neutrinos and escapes as a wind. This wind between the stellar surface and the shock front is believed to be a site for the r-process nucleosynthesis. However, the hydrodynamical condition of the wind, such as entropy, electron fraction and dynamical time scale, has a large uncertainty in previous studies. We are now exploring the dynamics of the wind by hydrodynamical simulations to determine these conditions and to clarify whether the r-process occurs and how r-process products are.

References

1) H. Shen, H. Toki, K. Oyamatsu, and K. Sumiyoshi: Nucl. Phys. A **637**, 435 (1998).
2) H. Shen, H. Toki, K. Oyamatsu, and K. Sumiyoshi: Prog. Theor. Phys. **100**, 1013 (1998).
3) K. Sumiyoshi, H. Suzuki, and S. Yamada; in preparation.

The Long Half-Life of Highly Ionized ^{44}Ti

Y. Mochizuki

[Nucleosynthesis, Supernova remnants]

The half-life of ^{44}Ti measured in laboratory cannot be applied directly to the astrophysical situation. This is because the half-life values measured so far are for neutral atoms. Since ^{44}Ti decays by electron capture only, the ionization can affect on the decay rate. In this paper, I discuss the ionization effect on the half-life, taking into account the evolution of a supernova remnant in which ^{44}Ti was synthesized. A simple model is taken to demonstrate the retardation of the decay as the first step.

The binding energy of the K-shell electrons of ^{44}Ti is calculated to be 6.6 keV. Hence it is obvious that ^{44}Ti is fully ionized when it is synthesized in a supernova explosion. After the explosion, the temperature of the ejected material decreases rapidly due to the adiabatic cooling as the ejecta freely expands. Consequently, it is expected that the created nuclei become neutral within about 1000 sec.

However, there is a possibility that ^{44}Ti is made to be ionized again: This is due to a reverse-shock heating. The reverse shock is produced by the high pressure behind the blast-wave shock interacting with the surrounding circumstellar medium. The reverse shock goes back into the ejecta and heats up and ionizes it during the free expansion phase on the evolutional course of a supernova remnant (SNR). The reverse shock becomes important, say, from $\sim$100 yrs after the explosion.

^{44}Ti is radioactive, and the nuclear γ-rays from its decay have been detected with COMPTEL in SNR Cassiopeia-A (Cas-A). The flux detection has a strong impact, since we can check the theory of collapse-driven supernova explosions through the conversion of the flux into the initial abundance of ^{44}Ti at the time of the explosion, using the other observed values of the half-life, the distance, and the age of Cas-A.

A hindrance here is the half-life, which is not easy to be determined experimentally, because the value is of the time scale of human life. For this and for the astrophysical importance, several measurements of the ^{44}Ti half-life have been done so far. The latest half-life values determined from experiments converge into $t_{1/2}^{lab} = 60 \pm 1$ yrs.

We emphasize here that the laboratory half-life measurements are for the *neutral* atoms. As mentioned before, ^{44}Ti can be ionized during the evolution of a SNR. In this case, the resulting "effective" half-life becomes longer than the experimental value. This is because ^{44}Ti decays 100% by electron capture. The orbital-electron-capture decay (observed in laboratory) is suppressed, when the nucleus possesses no or a few electrons in astrophysical situation.

In Fig. 1, the calculated results of the effective half-life, using $t_{1/2}^{lab} = 60$ yrs, are shown as a function of the post-shock electron temperature. In the figure, we have assumed that the reverse shock hits a layer of ^{44}Ti at 100 yrs after the explosion. The age of Cas A and the electron density are assumed to be 320 yrs and 20 cm^{-3}, respectively. The initial ionization structure of the shocked ^{44}Ti has been taken to be complete 0-, 1-, 2-, 3-electron system, or that under the Collisional Ionization Equilibrium condition. It is clear from Fig. 1 that the effective half-life becomes longer because of the retardation of the electron-capture decay.

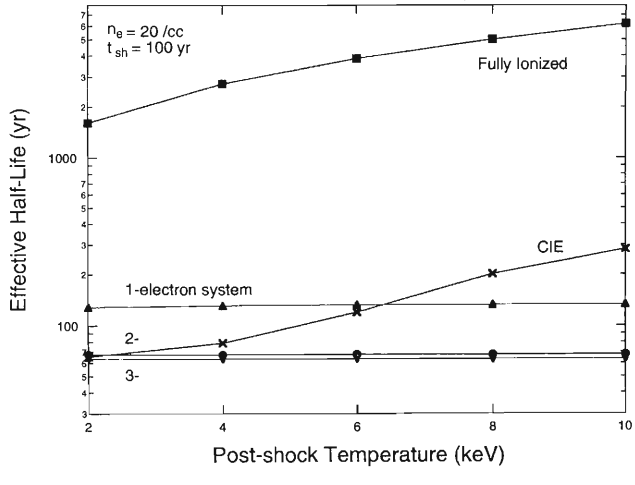

Fig. 1. The effective half-life of ^{44}Ti as a function of post-shocked electron temperature.

The Half-Life of ^{44}Ti and SN 1987A†

Y. Mochizuki, S. Kumagai,* and I. Tanihata

[Nucleosynthesis, Supernovae]

The radioactive nuclei, ^{56}Ni, ^{57}Ni, and ^{44}Ti, are believed to be synthesized in the α-rich freeze-out process, which occurs in neutrino-driven winds within about one second after core bounce in supernovae.[1] These nuclei are proton rich, and hence decay by positron emission or by electron capture. The γ-ray photons coming out from the decay sequence of ^{44}Ti is now a strong candidate to explain the late light curve of SN 1987A. In this paper, we discuss the abundance of ^{44}Ti in relation with its unestablished half-life value by comparing the theoretical light curves with the observed luminosity of SN 1987A.

It is noted that the production of ^{44}Ti is important to understand the dynamics of core collapse supernova explosions. The ^{44}Ti yield at the time of an explosion depends strongly on the location of the mass cut, electron fraction, and entropy condition in the α-rich freezeout. Hence, the initial yield of ^{44}Ti provides unique information to constrain the explosion models. In the above, the mass cut is the position in a star that separates the supernova ejecta and the materials which collapse into a central compact object, a neutron star or a blackhole.

In Fig. 1, we show the calculated UV-IR light curves of SN 1987A and the observed luminosities. Our calculation of the light curve is based on Kumagai et al.[2] It has been established that the observed of light curve of SN 1987A in early time is first governed by the decay sequence ^{56}Ni $\rightarrow^{56}$Co $\rightarrow^{56}$Fe, and then by ^{57}Ni $\rightarrow^{57}$Co $\rightarrow^{57}$Fe. As we can see in Fig. 1, the slowness of the observed decline of the light curve becomes especially distinguished after ~1500 days from the explosion. The dominant energy source at this time can be attributed to the ^{44}Ti decay; ^{44}Ti decays by electron capture to ^{44}Sc, emitting 67.9 keV (100%) and 78.4 keV (98%) lines. ^{44}Sc then decays mainly by the positron emission into ^{44}Ca, which emits a 1157 keV (100%) line.

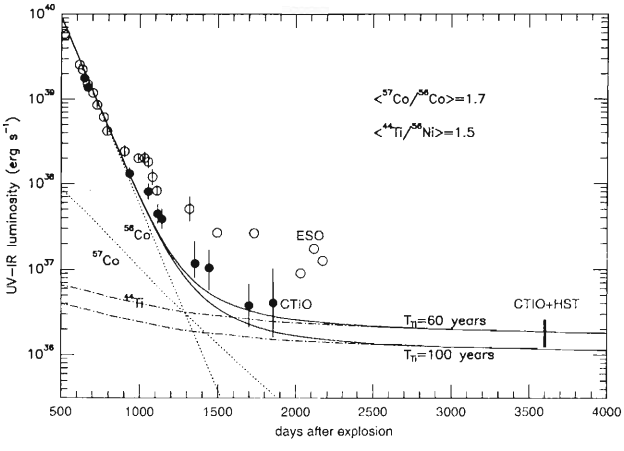

Fig. 1. The observed luminosities of SN 1987A and the calculated light curves.

The energy release from the ^{44}Ti decay depends strongly on its half-life. However, the published experimental values for the half-life display a large spread, ranging from ~35 to ~68 years. In Fig. 1, the half-life of ^{44}Ti is assumed as 60 yrs and as 100 yrs. The solid lines in the figure denote the calculated evolution of the total luminosity, corresponding to each value of the half-life. Contributions from the decays of ^{56,57}Co and ^{44}Ti are also shown, respectively, with the labeled dotted lines and the dash-dotted lines.

To explain the latest observed luminosity[3] which is abbreviated with CTIO + HST in Fig. 1, $\langle^{44}\mathrm{Ti}/^{56}\mathrm{Ni}\rangle = 1.5$ has been assumed as for the initial abundance of ^{44}Ti. Here, $\langle^{44}\mathrm{Ti}/^{56}\mathrm{Ni}\rangle$ is defined as the ratio of ^{44}Ti/^{56}Ni in amounts in the supernova remnant to ^{44}Ca/^{56}Fe in the solar neighborhood, i.e., $\langle^{44}\mathrm{Ti}/^{56}\mathrm{Ni}\rangle \equiv [X(^{44}\mathrm{Ti})/X(^{56}\mathrm{Ni})] \,/\, [X(^{44}\mathrm{Ca})/X(^{56}\mathrm{Fe})]_{\odot}$.

We have found that the deduced synthesized mass of ^{44}Ti is consistent with recent nucleosynthesis calculations for the half-life value of 60 yrs, which is the latest suggested value from experiments, within the uncertainty of the observed luminosity (Fig. 1). It has been also found that the observed luminosity can be reasonably explained by the energy release from the ^{44}Ti decay under the above-mentioned range of the half-life values obtained experimentally so far.

Finally, we note that further observations of the luminosity of SN 1987A a few years later are greatly encouraged to reduce the uncertainty that comes from observations. It is also noted that the half-life of ^{44}Ti should be pursued not only for the neutral atom under usual laboratory conditions, but also from the theoretical point of view to study the effect of ionization on the half-life under possible supernova conditions.

† Condensed from the article in *Origin of Matter and Evolution of Galaxies*, edited by S. Kubono et al. (World Scientific), in press; RIKEN-AF-NP-289 (preprint)

* Department of Physics, College of Science and Technology, Nihon University

References

1) S. E. Woosley et al.: Astrophys. J. Suppl. **26**, 231 (1973).
2) S. Kumagai et al.: Astron. Astrophys. **273**, 153 (1993).
3) N. B. Suntzeff: in *SN1987A: Ten Years After*, edited by M. M. Phillips and N. B. Suntzeff, in press.

Correlation and Finite Interaction-Range Effects in High Energy Electron Inclusive Scattering

A. Kohama, K. Yazaki, and R. Seki*

[Glauber approximation, Electron inclusive scattering]

We calculate cross sections of high energy electron inclusive scattering off nuclear matter in a new and consistent formulation based on the Green's function method[1] with the Glauber approximation. We suggest the superiority to other formulation[2] for a description of this kind of process. Our formulation is an extension of our previous work on the nuclear transparency in $(e, e'p)$ reaction.[3]

Since we are interested in the nucleon quasi-elastic region, the elementary process is considered to be mostly the eN elastic scattering, $e + N \rightarrow e + N$. The energy loss, ω, is roughly 2 [GeV]. We do not intend to explain the inelastic channel of the eN cross section, which takes part in the data in high-ω region.

The inclusive cross section is written as

$$\frac{d\sigma_{\mathrm{eA}}}{d\Omega d\omega} = \langle \frac{d\sigma_{\mathrm{eN}}}{d\Omega} \rangle_{\mathrm{cl,on}} S(\omega, \mathbf{q}),$$

where $S(\omega, \mathbf{q})$ is the response function. The cross section on the r.h.s. is the *on-shell* eN elastic scattering cross section, and $\langle \ldots \rangle$ implies averaging over spin, isospin, and the Fermi motion.

We examine two zero-range approximations for the N-N potential, which is constructed from the N-N amplitude obtained experimentally. One is the zero-range approximation in z-direction only (ZR1), and another is the zero-range approximation in the whole direction (ZR2). We find out that the ZR1 is a good approximation for the finite-range interaction.

The numerical results of the inclusive cross section are shown in Fig. 1. The incident electron has the energy, $\epsilon = 3.595$ [GeV], and its scattering angle is $\theta = 30°$. The PWIA result directly reflects the momentum distribution of a nucleon in the nuclear matter. Including only the final-state interaction (FSI) broadens the cross section, but adding the nuclear correlation (ZR1 and ZR2) reduces the broadening, that is, the effect of the FSI.

Although ZR1 includes the major part of the finite-range interaction, the cross section of ZR1 still overestimates the experimental cross section for low-ω region. It seems to contradict our insistence that our formulation is a consistent treatment of the FSI for the inclusive process. Furthermore, ZR2 comes closer to the experimental data than ZR1 does, though ZR2 is more approximate expression than ZR1.

* Department of Physics and Astronomy, California State University, Northridge, and W. K. Kellogg Radiation Laboratory, Caltech, USA

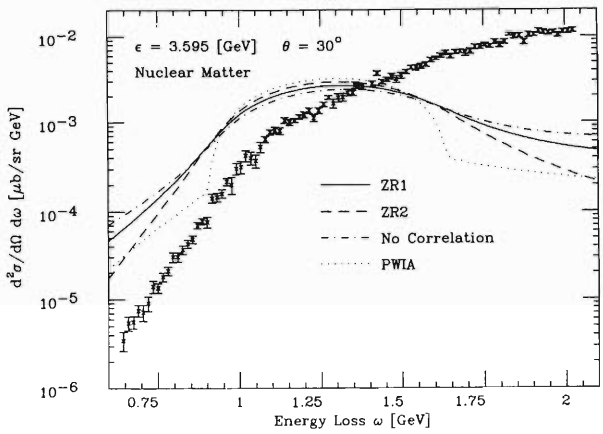

Fig. 1. The cross sections of the inclusive scattering off nuclear matter. The dotted curve is the case of PWIA. The dash-dotted curve is the case of only the FSI (no correlation effect). The solid curve (ZR1) and the dashed curve (ZR2) are the results of the calculations including both the FSI and the nuclear correlation with each zero-range approximation. The experimental data are from Ref. 4.

One reason why this comes about is our use of the *on-shell* eN cross section. Since the electron hits a bound nucleon, we should use an *off-shell* eN cross section, but in principle we cannot determine it by experiments. In order to see the *off-shell* behavior of the cross section, we should consider it theoretically by making a model for the bound nucleon taking account its internal structure. Since it is beyond the scope of this work, we just use the *on-shell* cross section for the calculations in order to avoid to bring about other ambiguity in our discussion here. Thus, we concentrate on a consistent treatment of the FSI of the struck nucleon in the Glauber approximation, and the agreement of the numerical results with the experimental data is not necessarily our objective of this work. These facts push us to study the *off-shell* cross section, and we leave the study in our future work.

References

1) O. Morimatsu and K. Yazaki: Prog. Part. Nucl. Phys. **33**, 679 (1994).
2) H. A. Gersch, L. J. Rodriguez, and P. N. Smith: Phys. Rev. A **5**, 1547 (1972).
3) A. Kohama, K. Yazaki, and R. Seki: Nucl. Phys. A **551**, 687 (1993).
4) D. B. Day et al.: Phys. Rev. C **40**, 1011 (1989).

Transversity Distributions and Spin Asymmetries at RHIC

S. Hino, M. Hirai, S. Kumano, and M. Miyama*

[Parton distribution, Structure function]

Transversity distributions, $\Delta_T q$, will be measured by using the Drell-Yan process at RHIC (Relativistic Heavy Ion Collider). Major reasons for studying the $\Delta_T q$ are following. Because the transversity Q^2 evolution is quite different from the longitudinal Q^2 evolution, perturbative QCD could be tested by finding the difference between the transversity and longitudinally-polarized distributions. Furthermore, this difference could shed light on the relativistic aspect of nucleon structure in the sense that nonrelativistic quark models predict the same distributions.

First, we have investigated the Q^2 evolution equation for the transversity distributions and obtained its numerical solution.[1] Because of the chiral-odd nature of the transversity distributions, the gluon does not participate in the Q^2 evolution equation. Even though a distribution is not flavor-nonsinglet, the evolution equation looks like the "usual" nonsinglet one without a coupling to the gluon term. Therefore, the results of Q^2 evolution are quite different from the longitudinal ones. For example, although the identical singlet distributions are assumed at $Q^2 = 4$ GeV^2, the evolved-transversity distribution, $\Delta_T q_s$, at $Q^2 = 200$ GeV^2 is significantly smaller than the longitudinal distribution, Δq_s, in the region $x \sim 0.1$. The magnitude of $\Delta_T q_s$ itself is also smaller than that of Δq_s at a very small $x(< 0.07)$ at $Q^2 = 200$ GeV^2.

Second, we have studied antiquark flavor asymmetry, $\Delta_T \bar{u}/\Delta_T \bar{d}$, by two different descriptions: a meson-cloud model and an exclusion model.[2] The ρ-meson clouds could contribute to the flavor asymmetry, for example, because of the $\bar{d}$-quark excess in ρ^+. Exclusion effects also affect on the asymmetry because of the difference in polarized quark probabilities in the SU(6) quark model. Although these mechanisms are much different, it is interesting to find that both models predict $\Delta_T \bar{d}$ excess over $\Delta_T \bar{u}$. Next, the obtained flavor-asymmetric distributions are used for calculating the transverse double spin asymmetry, A_{TT}. In comparison with the flavor symmetric double spin asymmetry, significant deviation was found in the proton-proton (pp) reaction. However, the single process is not sufficient for investigating the flavor asymmetry. We therefore proposed that the flavor asymmetry can be measured by using the polarized proton-deuteron (pd) Drell-Yan process in combination with the polarized pp reaction.

Because the Drell-Yan formalism with the spin-1 deuteron had not been available, we have investigated the general formalism of the Drell-Yan processes with spin-1/2 and spin-1 hadrons.[3] Imposing Hermiticity, parity conservation, and time-reversal invariance, we found that 108 structure functions exist in the Drell-Yan processes. The number reduces to 22 after integrating over the virtual-photon transverse momentum, $\vec{Q}_T$, or after taking the limit $Q_T \to 0$. It was also shown that fifteen spin asymmetries can be investigated. Because the deuteron is a spin-one hadron, there are additional structure functions to those of the proton. In particular, it is interesting to measure the quadrupole spin asymmetry, A_{UQ_0}, which is related to the tensor polarized distributions, δq. The δq should be interesting quantities because the tensor structure is not clarified within the parton model. If the deuteron acceleration is realized at RHIC in the future, The δq can be measured. The polarized hadron reactions have an important advantage over the lepton reactions in measuring the antiquark tensor polarization.[3] Because the essential pd formalism is now completed, it is possible to study the $\Delta_T \bar{u}/\Delta_T \bar{d}$ by measuring the A_{TT} and then by taking the difference between the polarized pp and pd cross sections.

References

1) S. Kumano and M. Miyama: Phys. Rev. D **56**, 2504 (1997); M. Hirai, S. Kumano, and M. Miyama: Comput. Phys. Commun. **108**, 38 (1998); **111**, 150 (1998).
2) S. Kumano: Phys. Rep. **303**, 183 (1998); S. Kumano and M. Miyama: research in progress.
3) S. Hino and S. Kumano: preprints SAGA-HE-136-98, SAGA-HE-139-98.

*1 Department of Physics, Saga University, http://www2.cc.saga-u.ac.jp/saga-u/riko/physics/quantum1/structure.html.

A New Parametrization of Polarized Parton Distributions in the Nucleon

Y. Goto, N. Hayashi, M. Hirai, H. Horikawa, S. Kumano, M. Miyama, T. Morii, N. Saito, T. Shibata, E. Taniguchi, and T. Yamanishi

[Polarized partons, NLO analysis, Nucleon spin structure]

To study how the partons polarize in the nucleon is crucially important to understand the spin structure of the nucleon. Recently there has been a renewed interest on polarized parton distributions in the nucleon, largely stimulated by acquisition of the high-precision polarized data on various targets[1] and by development of the next-to leading order (NLO) QCD calculations of polarized parton distribution functions.[2]

In this work, introducing reasonable physical conditions, i.e., the positivity condition and the counting rule for the helicity-dependent parton distribution functions, we propose a new parametrization[3] of the polarized parton distribution with initial scale Q_0^2,

$$\Delta f_i(x,Q_0^2) = A_i\ x^{\alpha_i}\ (1+\gamma_i\ x^{\lambda_i})\ f_i(x,Q_0^2)\ . \qquad (1)$$

Here, $i = u_v$(valence u quark), d_v(valence d quark), $\bar{q}$(sea quark) and g(gluon); $\Delta f_i(x,Q_0^2)$ and $f_i(x,Q_0^2)$ are the polarized and unpolarized distribution functions, respectively; and α_i, γ_i and λ_i are the free parameters; and A_i is a normarization factor. The counting rule naturally leads to the condition for polarized distribution functions[4]

$$f_i^+(x,Q_0^2) \gg f_i^-(x,Q_0^2) \quad \text{for} \quad x \to 1, \qquad (2)$$

where $f_i^+(f_i^-)$ represents the distribution function of the parton helicity parallel(anti-parallel) to the nucleon helicity. This condition, together with a reasonable assumption that the first moment of each polarized parton distribution should not become infinite at Q_0^2, constrains the parameters in Eq. (1) as $A_i = \frac{1}{1+\gamma_i}$, $\alpha_i \geq 0$, $\gamma_i \neq -1$, $\lambda_i > -\alpha_i$. Further constraints are given for the valence quark distributions: From the weak decay constants, F and D, obtained from the β-decays of neutron and hyperons, we can determine the first moment of the polarized valence u and d quark distributions by assuming the SU(3) flavor symmetry, thus constraining the free parameters for Δu_v and Δd_v. Then, we have finally 10 remaining parameters, $\alpha_{u_v}, \gamma_{u_v}, \alpha_{d_v}, \gamma_{d_v}, \alpha_{\bar{q}}, \gamma_{\bar{q}}, \lambda_{\bar{q}}, \alpha_g, \gamma_g, \lambda_g$, which can be determined by the χ^2–analysis of the experimental data of a virtual photon asymmetry, $A_1(x,Q^2)$, for the proton, neutron, and deuteron targets.

Using the Glück-Reya-Vogt(GRV) parametrization for unpolarized parton distribution functions[5] and using the R_{1990}[6] for the value of R which is the ratio of the longitudinal to transversal virtual-photon nucleon cross sections, we have carried out the χ^2–analysis to the data. The obtained parameters can reproduce well the experimental data. The results of χ^2–analysis are substantially better for the NLO(χ^2/d.o.f = 0.897) than for the LO(χ^2/d.o.f = 1.088). Thus, the NLO analysis is absolutely necessary to extract information on the polarized parton distribution. We have also compared our results of $x\Delta d_v(x)$ and $\Delta d_v(x)/d_v(x)$ with the Spin-Muon-Collaboration(SMC) data[7] at $Q^2 = 10$ GeV^2 as shown in Fig. 1.

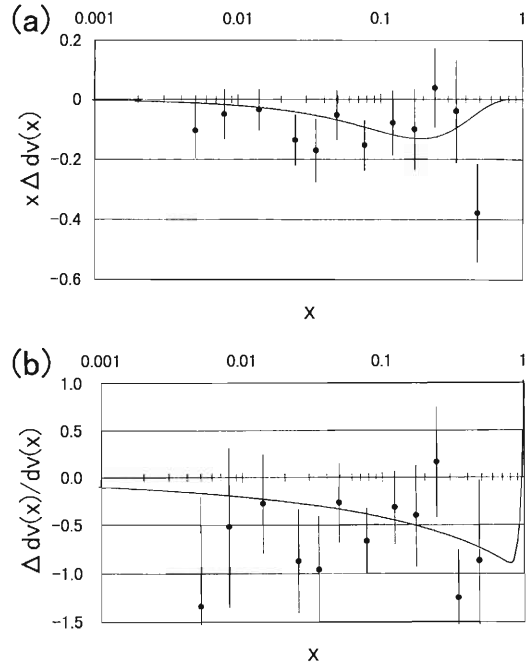

Fig. 1. Calculated distributions of (a) $x\Delta d_v(x)$ and (b) $\Delta d_v(x)/d_v(x)$ at $Q^2 = 10$ GeV^2. Data shown by closed circles are from Ref. 7.

Our parametrization looks promising. We have proposed an input polarized distribution by introducing physical conditions of positivity and counting rule, and obtained better results than other works done so far.

References

1) D. Adams et al.: CERN-EP/98–85 (1998); B. Adeva et al.: Phys. Lett. B **412**, 414 (1997); K. Abe et al.: SLAC-PUB-7753 (1998); A. Airapetian et al.: hep-ex/9807015 (1998).
2) R. Mertig and W. L. van Neerven: Z. Phys. C **70**, 637 (1996); W. Vogelsang: Phys. Rev. D **54**, 2023 (1996).
3) Y. Goto et al.: in preparation.
4) S. J. Brodsky, M. Burkardt, and I. Schmidt: Nucl. Phys. B **441**, 197 (1995).
5) M. Glück, E. Reya, and A. Vogt: Z. Phys. C **67**, 433 (1995).
6) L. W. Whitlow et al.: Phys. Lett. B **250**, 193 (1990).
7) B. Adeva et al.: Phys. Lett. B **420**, 180 (1998).

RIKEN Accel. Prog. Rep. **32** (1999)

Semi-Classical Sine-Gordon Solitons on a Finite Interval

T. Matsuki

[Topological soliton, 1+1 D, Sine-Gordon model]

Recently, a non-perturbative method based on treating the system on a light-like finite interval has attracted much attention. A vast number of theories have been treated, starting from the 1+1 dimensional(D) Yukawa model,[1] upto QCD_{1+1}.[2]

The Sine-Gordon model has also been studied in the soliton charge $Q = 0$ sector,[3] from which one observes the soliton-antisoliton threshold, but cannot derive the conclusive evidence of existence of the one-soliton state. If the method is truly non-perturbative, it must be capable of incorporating the nonperturbative states, the solitons, which arise in theories with topology or spontaneous symmetry breakdown (SSB).

One of the problems of the formalism is that we are working on a finite interval. Care must be taken due to the boundary conditions(B.C.) which are clearly different from the infinite interval problem. In order to investigate this problem, we concentrate on a semi-classical description in the equal time formulation, and see if one can deduce the quantum mass of the one soliton state. The linearized eigenfunction can be utilized for the light-front formulation.

We first construct the one soliton classical solution in the Sine-Gordon model. The Lagrangian is given by

$$\mathcal{L} = \partial_\mu \phi \partial^\mu \phi - \frac{\mu^2}{\beta^2}(1 - \cos(\beta\phi)).$$

The static solution is given by solving the Lagrangian $\mathcal{L} = -\phi'(x)^2 - V(\phi(x))$ under the boundary condition that is periodic modulo $2\pi/\beta$, which is a B.C. that conserves momentum. This can be interpreted as the single particle mechanics with the Hamiltonian $H = \dot{x}^2 - V(x)$, if we do the replacements $x \to t$ and $\phi \to x$. Let the energy of the particle be given by $H = E$. Then, the finite interval problem corresponds to $E > 0$. Solving

$$\frac{1}{2}\dot{x}^2 - \frac{\mu^2}{\beta^2}(1 - \cos(x)) = E,$$

and with the original notation, we obtain

$$\phi(x) = \frac{2}{\beta}\cos^{-1}\left(\mathrm{Sn}(-\frac{\mu}{k}[x - x_0], k)\right).$$

Here, $k = \sqrt{\frac{2\mu^2}{E+2\mu^2}}$, and $\mathrm{Sn}(u,k)$ denotes the Jabobian form of the elliptic function. In order to determine k, we look at the boundary condition $\frac{\mu}{k}2L = 2K(k)$, where $K(k)$ is the first complete elliptic integral. Solving this equation for k, we have $k = k(L)$.

Now that we have the classical solution, we can calculate the classical mass of the soliton:

$$\begin{aligned} M &= \int [\frac{1}{2}\phi'^2 + V(\phi)] \\ &= \frac{2}{\beta^2}\frac{2\mu}{k}[2\tilde{E}(k) - (1-k^2)K(k)] \\ &= \frac{8\mu}{\beta^2}[1 + 4e^{-2\mu L} + O(e^{-6\mu L})](L \to \infty) \\ &= \frac{\pi^2}{\beta^2}\frac{1}{L}[1 + 2\xi^2 - \frac{1}{2}\xi^4 + ..], (L \to 0), \end{aligned} \tag{1}$$

where $\tilde{E}(k)$ is the complete elliptic integral of the second kind, and $\xi = (\mu/\pi)L$. Notice that it gives the correct limit at $L \to \infty$, and that the expression diverges as $L \to 0$

We may discuss the semi-classical nature of the soliton by expanding the field around the classical solution. The linearized equation of motion of the fluctuation becomes

$$[-\partial_x^2 + \mu^2\{2\mathrm{Sn}^2(-\frac{\mu}{k}x, k) - 1\}]\psi_n = \omega_n^2\psi_n.$$

Replacing x by $u = -(\mu/k)x$, we have

$$[\partial_u^2 + \{h_n - 2k^2\mathrm{Sn}(u,k)^2\}]\psi_n = 0,$$

where $h_n = k^2(1 + \frac{\omega_n^2}{\mu^2})$. This equation is known as the Lamé equation of order one.

The eigenfunction for $L \sim 0$ can also be obtained by perturbing with the parameter k. For example in the case of the even Lamé function $\mathrm{Ec}(u)$, expand it as $\psi(v) = A_0 + \Sigma_n A_{2n}\cos(2nv)$ where $\sin v \equiv \mathrm{Sn}(u,k)$. The Lamé equation then becomes equivalant to the following recursion relation[4,5]

$$\begin{aligned} &1/2[(2-2n)(2n+3)k^2]A_{2n+2} \\ &+[2(h-k^2) - 4n^2(2-k^2)]A_{2n} \\ &+1/2[2n(-2n+3)k^2]A_{2n-2} = 0 \end{aligned}$$

Perturbing with small k^2, i.e. with small L, it gives

$$\omega_n = \frac{n\pi}{L}\left(1 + \frac{1}{4n^2-1}\xi^4 + ...\right),$$

where $\xi = (\mu/\pi)L$. We can treat the odd Lamé function in a similar way.

The eigenvalues allows us to calculate the quantum mass correction for $L \sim 0$. Taking care of the vacuum energy and the boson mass renormalization,[6]

$$\Delta M = \frac{\pi}{L}\left(-\frac{1}{2}\xi^2 + \left[\frac{1}{2}\ln 2 - \frac{13}{24} + \frac{1}{8}\zeta(3)\right]\xi^4 + ...\right)$$

we can finally obtain a finite result. Notice that the dependence of ΔM on L differs significantly from that of the classical mass given by Eq. (1). It is impossible, unlike the infinite interval case, to include the quantum effect by redefining the coupling constant as $\beta^2 \to \beta^2/(1-\beta^2/8\pi)$, at least not in a L-independent fashion.

To summarize, we have obtained the classical one-soliton solution on a finite interval. We have obtained the dependence of the classical soliton mass on the interval length. The classical solution is at the same time the solution on the light-front. Moreover, we have performed the semi-classical quantization of the soliton, by taking into account the fluctuation around the classical solution. Thus we have shown that the semi-classical treatment is indeed possible on a finite interval. It is uncertain, however, whether the system still maintains its semi-classical exactness.

References

1) H-C. Pauli et al: Phys. Rev. D **32**, 1993 (1985).
2) K. Hornbostel et al: Phys. Rev. D **41**, 3814 (1990).
3) M. Burkardt: Phys. Rev. D **47**, 4628 (1993).
4) E. L. Ince: Proc. Royal Soc. Edinburgh **60**, 47 (1940).
5) E. L. Ince: Proc. Royal Soc. Edinburgh **60**, 83 (1940).
6) Kikkawa and Sakita: in *Quantum Mechanics of Many Body Systems by Path Integral* (Iwanami Publ., 1986), p. 181 (in Japanese).

Muon Catalyzed Fusion and Muon to ^{3}He Transfer in Solid T_2 Studied by X-ray and Neutron Detections

T. Matsuzaki, K. Nagamine, K. Ishida, S. N. Nakamura, N. Kawamura, M. Tanase, M. Kato, K. Kurosawa, M. Hashimoto, H. Sugai, K. Kudo,*1 N. Takeda,*1 and G. H. Eaton*2

[Muon catalyzed fusion, Exotic atom, Muonic X-ray, t-t fusion neutron]

After a series of muon catalyzed fusion experiments with a liquid/solid D-T mixture at RIKEN-RAL Muon Facility by detecting the X-ray and neutrons originated from the d-t fusion process,[1] we have conducted a similar measurement of muon catalyzed t-t fusion and of the related phenomena with a solid T_2 target. This experiment is important not only for the back-up to analyze the data of muon catalyzed d-t fusion, but also for a study of the new type of physics related to the t-t fusion.

The experiment has been conducted at RIKEN-RAL Muon Facility by using the same set-up already installed for the d-t muon catalyzed fusion experiment.[1] The T_2 gas target (T: 99.1% and H: 0.9%, 56 TBq: 1500 Ci) prepared at JAERI was installed to the tritium gas handling system[2] which can purify the target gas at the site of experiment by removing ^{3}He impurity just before the measurement.

The muon catalyzed t-t fusion reactions in the solid T_2 target are expressed as following,

$$t + t + \mu^- \longrightarrow \alpha + 2n + \mu^- + Q(11.33\ \mathrm{MeV}) \quad (1)$$

$$\longrightarrow (\mu^-\alpha) + 2n + Q. \quad (2)$$

Regarding the reaction (2) as the muon-to-α sticking process, we have directly deduced the X-ray yield related to the sticking probability (ω_s) by observing K_α X-ray from the $(\mu^-\alpha)$ atom, where the Doppler width of observed K_α X-ray line has also given us an information on the motion of $(\mu^-\alpha)$ atom in solid T_2 medium. The observed X-ray spectrum is shown in Fig. 1. We have also deduced the $(tt\mu)$ molecule formation rate, $\lambda(tt\mu)$, and effective sticking probability, $\omega_s(tt\mu)$, for the t-t muon catalyzed fusion process by combining the X-ray and neutron data.

It is known in a series of our experiments that ^{3}He, a decay product of tritium, is accumulated in the solid T_2 target, and muon does transfer from $(t\mu^-)$ to ^{3}He through the $(t^3He\mu^-)$ molecule formation while emitting the characteristic 6.7 keV photons. As shown in Fig. 1, we have observed the photons to deduce the molecule formation rate $\lambda(t^3He\mu^-)$ and radiative decay branching ratio of the $(t^3He\mu^-)$ molecule.

A strange ^{3}He accumulation effect in solid T_2 was observed in the time dependence of t-t fusion neutron disappearance rate, λ_n, after solidification, as shown in Fig. 2. The λ_n, determined by the time spectrum of t-t fusion neutron, increases linearly (as shown by filled circles) with time in the beginning, and then depicts a leveling-off behavior at around 20 h, followed by a gradual decrease until 60 h. The strange turnover of λ_n at around 20 h should be compared with the similar phenomena in the $D_{0.3}T_{0.7}$ data (shown by open circles) at 30 h. This phenomenon can probably be explained by a ^{3}He bubble formation through a rapid diffusion of ^{3}He in solid T_2 or D-T mixture to find out another ^{3}He. The critical ^{3}He concentration of around 125 ppm in both cases seems to be an important parameter for the phenomenon.

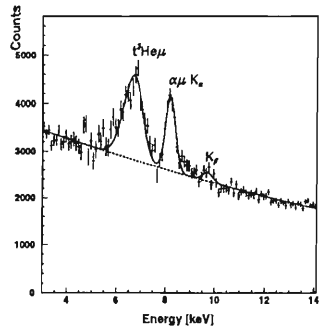

Fig. 1. Observed X-ray spectrum for μ^- in solid T_2 target in the time domain from 80 to 2080 nsec after μ^- pulse. The clear peaks at 6.7, 8.2 and 9.7 keV are assigned as radiative-decay photon from the $(t^3He\mu)$ molecule, and the K_α and K_β X-rays from the $(\mu^-\alpha)$ atom.

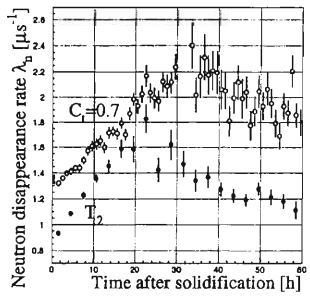

Fig. 2. Time dependent fusion-neutron disappearance rate, λ_n, in T_2 as a function of the time after the solidification which can be considered as the time after the ^{3}He removal. As a reference, the same data for the $D_{0.3}T_{0.7}$ mixture is shown.

References

1) K. Ishida et al: RIKEN Accel. Prog. Rep. **31**, 49 (1998).
2) T. Matsuzaki et al: RIKEN Accel. Prog. Rep. **30**, 151 (1997).

*1 Electrotechnical Laboratory (ETL)
*2 Rutherford Appleton Laboratory (RAL), UK

Measurements of ^{3}He Accumulation Effect on Muon Catalyzed Fusion in the Solid/Liquid D-T Mixtures†

N. Kawamura, K. Nagamine, T. Matsuzaki, K. Ishida, S. N. Nakamura, Y. Matsuda, S. Sakamoto, M. Tanase, M. Kato, K. Kurosawa, H. Sugai, K. Kudo,*1 N. Takeda,*1 and G. H. Eaton*2

[Muon catalyzed fusion, Fusion produced neutron]

Through the D-T muon catalyzed fusion (μCF) experiments carried out at the RIKEN-RAL Muon Facility,[1] we found the ^{3}He accumulation phenomenon: the ^{3}He originating from tritium β decay was trapped in the solid D-T system, while that in liquid was diffused and evaporated into the D-T gas.

In the present work, the D-T target was initially purified by the tritium gas handling system,[2] for the ^{3}He concentration to be reduced to <1 ppm. Afterwards, ^{3}He concentration increases by the rate of $1.55 \times 10^{-4} \times C_t$ per day, where C_t is the original tritium concentration.

Figure 1 shows typical timing spectra of fusion neutrons. Clear difference is seen between solid and liquid, i.e. the neutron disappearance rate λ_n increases with time in solid, while no visible change was observed in liquid. Further analysis gives us the following feature of this phenomenon: (1) only in solid, the neutron disappearance rate increased with the time after condensation; (2) by melting solid, the neutron disappearance rate returns to the original value measured at the time right after solidification.

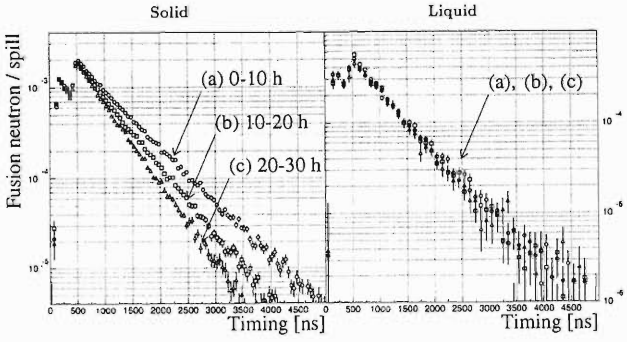

Fig. 1. Typical time spectra of fusion neutrons of μCF in D-T mixture: solid and liquid with $C_t = 0.7$ at (a) τ = 0–10 h, (b) 10–20 h and (c) 20–30 h after condensation.

The λ_n is dissolved into two parts as $\lambda_n = \lambda_0 + W\phi\lambda_c$, where λ_0 is the muon decay rate, W is the total muon loss probability per cycle, ϕ is the D-T target density normalized by the liquid hydrogen density, and λ_c is the muon cycling rate in dt-μCF. In the intended system, only the concentration of the ^{3}He originating from tritium β-decay, $C_{\rm He}$, changes with time in a unit of hour, and a muon trapped by such a ^{3}He is lost out of the μCF cycle, and W increases. Thus increase of λ_n is explained by the ^{3}He accumulation effect. By using the muon transfer rate from $(d\mu)$ and $(t\mu)$ to ^{3}He, $\lambda_{d{\rm He}\mu}$ and $\lambda_{t{\rm He}\mu}$, and the capture rate to ^{3}He from free muon, λ_a, the increase of λ_n defined as $\lambda_{\rm He}$ ($\equiv \lambda_n(\tau) - \lambda_n(\tau = 0)$) is dissolved as:

$$\lambda_{\rm He} = \phi\,(f_{d\mu}\lambda_{d{\rm He}\mu} + f_{t\mu}\lambda_{t{\rm He}\mu} + f_a\lambda_a)\,C_{\rm He}(\tau),$$

where, f_x is the ratio of muon residing time in the state x ($= d\mu$, $t\mu$, a(free)). During the typical experimental periods of 4–5 days, $C_{\rm He} = \lambda_t \tau C_t$ is a good approximation, in which λ_t is the tritium decay rate.

In Fig. 2, $\lambda_{\rm He}$ is plotted with various C_t as a function of the time after solidification and after liquefaction, τ. The tendency shown in this figure is consistent with the model supposing the ^{3}He accumulation. Namely, λ_n increases linearly in each C_t, and the slope of the τ-$\lambda_{\rm He}$ plot increases with C_t only in solid.

According to our further analysis,[2] $f_{d\mu}$, $f_{t\mu}$ and f_a were determined, and we obtained the result of $\lambda_{d{\rm He}\mu} = (6 \pm 2) \times 10^8$ s^{-1} and $\lambda_{t{\rm He}\mu} = (4.2 \pm 0.3) \times 10^9$ s^{-1}, which is consistent with the theoretical prediction.[3]

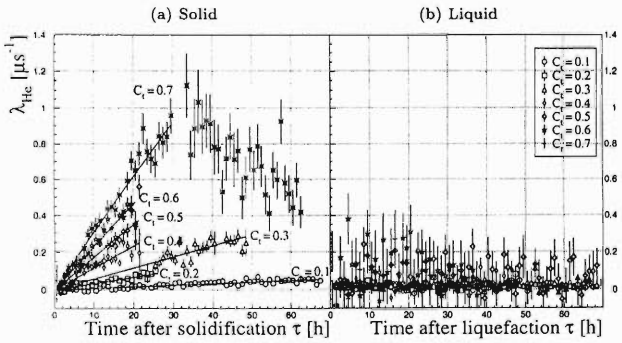

Fig. 2. The plot of $\lambda_{\rm He}$ in (a) solid and (b) liquid with various C_t.

† Condensed from the article in Hyperfine Interact. **118/119** (1999), in press.

*1 Electrotechnical Laboratory (ETL)
*2 Rutherford Appleton Laboratory (RAL), UK

References

1) K. Nagamine et al.: Hyperfine Interact., **118/119** (1999), in press.
2) K. Ishida et al.: Hyperfine Interact., **118/119** (1999), in press.
3) A. V. Kravtsov et al.: J. Phys. B **19**, 2579 (1986).

Muon to Alpha Sticking K_β/K_α X-ray Ratio in Muon Catalyzed D-T Fusion at the RIKEN-RAL Muon Facility†

S. N. Nakamura, K. Nagamine, T. Matsuzaki, K. Ishida, N. Kawamura, Y. Matsuda, S. Sakamoto, M. Iwasaki, M. Tanase, M. Kato, K. Kurosawa, H. Sugai, K. Kudo,[*1] N. Takeda,[*1] and G. H. Eaton[*2]

[Muon catalyzed fusion, Exotic atom, Muonic X-rays]

The negative muon (μ^-) to α initial sticking probability (ω_s^0) calculated with nuclear reaction theory cannot be compared directly with the experimentally observable effective sticking probability (ω_s).

In order to associate these two quantities, detailed knowledge about atomic processes of the $\mu^-\alpha$ atom is essential. In reality, the value of experimentally observed ω_s is smaller than that of theoretically predicted one.[1)] However, it was difficult to identify which causes the discrepancy, ω_s^0 calculation or atomic process calculations.

Study of the intensity ratio between K_β and K_α X-rays from $\mu^-\alpha$ atom can contribute much to answer the above question; because such a ratio is nearly independent of the initial sticking process, but is very sensitive to the atomic process. However, the observation of K_β X-ray had been impossible thus far due to a large bremsstrahlung background from the tritium β decay. Measurement of the X-rays and neutrons from muon catalyzed *d-t* fusion was carried out at the RIKEN-RAL Muon Facility.[1)] The world highest intensity pulsed muon beam has enabled us to observe K_β X-ray for the first time.

Experiments to measure the K_β/K_α intensity ratio were performed for D-T mixtures with different tritium concentrations.

The area of K_β and K_α X-ray signals in the energy spectrum was obtained for each tritium concentration, and it was corrected for a difference of attenuation by the materials between D-T target and Si(Li) X-ray detector. Figure 1 shows the result. The averaged K_β/K_α intensity ratios for liquid and solid were $7.5 \pm 1.0\%$ and $6.0 \pm 1.2\%$ (the errors are purely statistical), respectively. The preliminary experimental result tends to give smaller K_β/K_α intensity ratio than the theoretical values, though the K_β / K_α ratio is sensitive to the way of background subtraction.

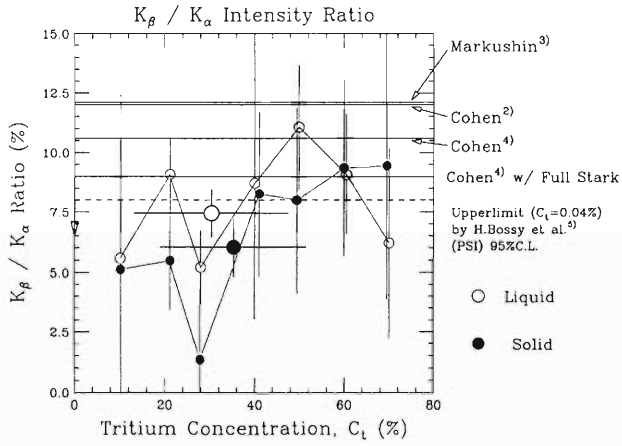

Fig. 1. The K_β/K_α X-ray intensity ratio. Open circles are liquid data points and closed ones solid. Solid lines are theoretical predictions and dashes line is an upper-limit obtained by the previous experiment. The larger points show our averaged results.

In order to obtain more reliable data, a high precision experiment for the K_β/K_α X-ray intensity ratio is in progress at the RIKEN-RAL Muon Facility.

References

1) K. Nagamine et al.: Contribution to EXAT98, Hyperfine Interact., in press; T. Matsuzaki et al.: Contribution to EXAT98, Hyperfine Interact., in press; K. Ishida et al.: Contribution to EXAT98, Hyperfine Interact., in press; N. Kawamura et al.: Contribution to EXAT98, Hyperfine Interact., **118/119** (1999), in press.
2) J. S. Cohen: Muon Catal. Fusion **3**, 421 (1988).
3) V. E. Markushin: Muon Catal. Fusion **3**, 395 (1988).
4) J. S. Cohen: private communication (1998).
5) H. Bossy et al.: Phys. Rev. Lett. **55**, 1870 (1987).

† Condensed from the article in Hyperfine Interact. **118/119** (1999), in press.

*1 Electrotechinical Laboratory (ETL)
*2 Rutherford Appleton Laboratory (RAL), UK

X-ray and Neutron Measurement of α-Sticking Probability in Muon Catalyzed *dt* Fusion at the RIKEN-RAL Muon Facility

K. Ishida, K. Nagamine, T. Matsuzaki, S. N. Nakamura, N. Kawamura, S. Sakamoto, Y. Matsuda, M. Tanase, M. Kato, K. Kurosawa, H. Sugai, K. Kudo,[*1] N. Takeda,[*1] and G. H. Eaton[*2]

[Muon catalyzed fusion, Muonic X-ray]

The muon to alpha sticking probability (ω_s) is the main component of muon loss in muon catalyzed fusion (μCF) and thus determines the maximum number of fusions catalyzed per muon. However, the measurements so far, mainly by fusion neutron detection, have always shown smaller value of ω_s than that by theoretical calculations and this has been the most significant puzzle in μCF. To solve this problem, we started measurement of X rays from the $(\alpha\mu)^+$ ion, which is a direct product of the sticking.

Measurements were made for liquid and solid $D_{1-x}T_x$ mixtures with x = 0.1, 0.2, 0.28, 0.4, 0.5, 0.6 and 0.7.[1)] With the use of the world strongest pulsed muon beam at the RIKEN-RAL Muon Facility, a clear Doppler broadened X-ray peak was sucsessfully observed[2)] above the bremstrahlung background from tirtium β-decay.

The effective sticking probability ω_s was determined by subtracting the $dd\mu$ and $tt\mu$ side channel contributions from the muon loss probability W obtained by neutron detection. The obtained value of ω_s was consistent with the measurements done at PSI and LAMPF and the discrepancy between experiments and theories was again confirmed.

The K_α X-ray yield per *dt*-fusion $Y(K_\alpha)$, as shown in Fig. 1, was determined by dividing the X-ray yield by the number of fusion neutron (Y_x/Y_n) and subtracting contributions due to $dd\mu$ and $tt\mu$ side channel (Y_{dd} and Y_{tt}):

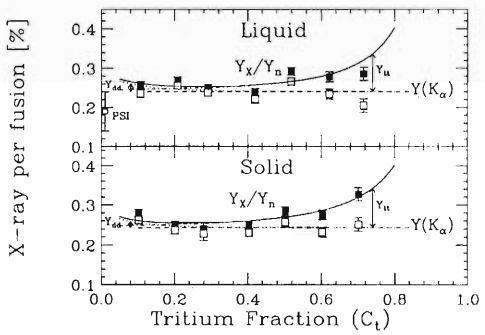

Fig. 1. The K_α X-ray yield per fusion. The filled squares are the measured number of X-rays per fusion neutron. The open squares are the values with $dd\mu$ and $tt\mu$-contributions (Y_{dd} and Y_{tt}) subtracted.

The obtained values of ω_s and $Y(K_\alpha)$ are plotted in Fig. 2 and are compared with theories. The theoretical values were calculated by combining the initial sticking probability calculation (ω_s^0 = 0.912%)[3)] and the atomic process calculations[4-6)] (R: regeneration probability, γ_{K_α}: X-ray yield per initial sticking). The measured $Y(K_\alpha)$ was smaller than most of the theoretical calculations, but the deviation was not as significant as the case for the effective sticking ω_s. This suggests that there might be some unknown factor in $\alpha\mu$ atomic process that makes the regeneration probability R larger than expected.

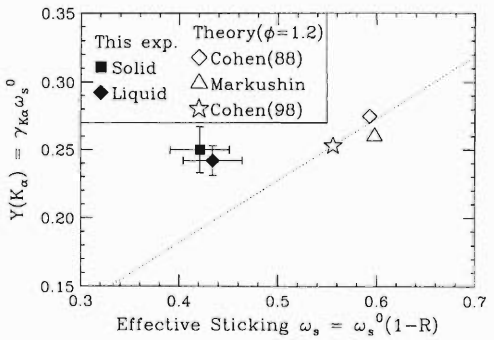

Fig. 2. Comparison of our measurement and calculations[4-6)] of effective muon sticking probability ω_s and the sticking $\mu\alpha$ X-ray yield $Y(K_\alpha)$.

This X-ray result, in combination with additional finding for the K_β/K_α intensity ratio,[7)] will be used to solve the puzzle of muon to alpha sticking.

References

1) K. Ishida et al.: Proc. of Monte Vertia Workshop on Exotic Atoms, Molecules and Muon Catalyzed Fusion (EXAT98), Ascona (1998); Hyperfine Interact. **118/119** (1999), in press.
2) K. Ishida et al.: RIKEN Accel. Prog. Rep. **30**, 39 (1997); K. Ishida et al.: RIKEN Accel. Prog. Rep. **31**, 49 (1998).
3) Chi-Yu Hu, G. M. Hale, and J. S. Cohen: Phys. Rev. A **49**, 4481 (1994).
4) M. Struensee and J. S. Cohen: Phys. Rev. A **38**, 44 (1988).
5) V. E. Markushin: Muon Catal. Fusion **3**, 395 (1988).
6) J. S. Cohen: RIKEN Rev. No. 20, p. 8 (1999).
7) S. N. Nakamura et al.: RIKEN Accel. Prog. Rep. **32**, 42 (1999).

*1 Electrotechnical Laboratory (ETL)
*2 Rutherford Appleton Laboratory (RAL), UK

RHIC Spin Project

Y. Batygin, H. En'yo, Y. Goto, N. Hayashi, T. Ichihara, K. Imai, M. Ishihara, T. Katayama, T. Kawaguchi, K. Kurita, Y. Kondo, Y. Mao, A. Masaike, R. Muramatsu, J. Murata, Y. Nakada, M. Nakamura, H. Okamura, M. Okamura, N. Saito, H. Sakai, Y. Sakemi, T. Sakuma, H. Sato, H. Sato, T-A. Shibata, H. Takahashi, A. Taketani, E. Taniguchi, J. Tojo, T. Tominaka, H. Torii, T. Wakasa, Y. Watanabe, H. Wu, M. Xiao, K. Yamamoto, and M. Yosoi

[pp interaction, Structure function, Spin, Asymmetry, Polarized beam]

RHIC Spin project is the integrated efforts of accelerator, experimental, and theoretical physics to study the polarization phenomena in high energy hadron reactions using polarized proton beams at RHIC. This is a report of the forth year of this project.

For the accelerator part, a major progress was the completion of the design of the RHIC as a polarized collider, which is now summarized in design manual.[1] The polarized ion source from KEK has been modified at TRIUMF to strengthen its current by a factor of 10 or more. In addition, the beam transport from the ion source to RFQ is being designed to minimize depolarization of the proton beam. Furthermore, the first full-length helical dipole magnet is being fabricated at BNL, and the field analysis method has been developed using three dimensional model calculations.

The polarization of the beam will be measured with two methods in the RHIC polarized-beam commissioning. One is to utilize the asymmetry $\mathcal{A}_N$ for inclusive pion production at large-x_F (pion polarimeter). Another is to use the theory prediction on $\mathcal{A}_N$ for elastic scattering of the proton on carbon in Coulomb-nuclear-interference (CNI) region: CNI Polarimeter. The idea of pion polarimeter has been verified using a 22 GeV/c polarized proton beam extracted from AGS in the experiment E925.[2] The CNI polarimeter will be installed in AGS at BNL soon for the test as the experiment E950. We have finalized the detector setup based on the test experiments at Kyoto University and Indiana University Cyclotron Facility.[3]

The magnet for PHENIX Muon Arm has been fabricated at MELCO, Japan, and assembled at BNL (Fig. 1). It was successfully excited up to the full field, and the field will be mapped precisely soon.

A major progress on the detector construction has been marked by the completion of the installation of muon identifier (MuID). The MuID panels are fabricated in a Japanese factory and in BNL. The details of the fabrication are described in Refs. 4 and 5.

We have exposed the PHENIX electromagnetic calorimeter to high-energy beams (6.0 to 80 GeV) at CERN to investigate the performance at high energy. Its linearity, shower profile, and hadron response have been studied. The analysis is still going on, and the preliminary results are presented in Ref. 6.

A computing center for the PHENIX data analysis and simulation in Japan is proposed. We have finalized its conceptual design[7] and it has been reviewed by the RHIC Computing Facility review committee. A prototype of the CPU farm and file server system has been successfully built at BNL. Most of the PHENIX standard software has been installed, and they are running on the CPU farm for the evaluation of the prototype.

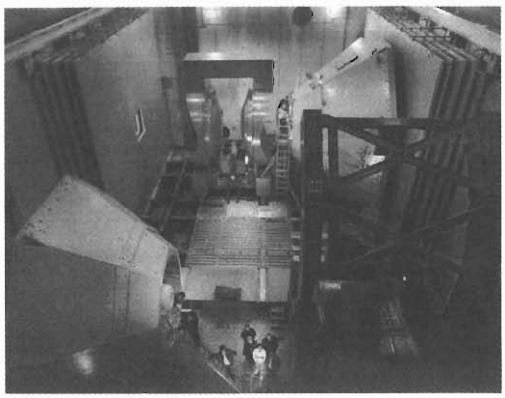

Fig. 1. Recent photograph of PHENIX detector system.

In addition to the previous simulation works on prompt photon and W productions, we have extended our studies to include the J/ψ production, which should be sensitive to the gluon polarization $\Delta g(x)$ in the proton. $\mathcal{A}_{LL}$ has been evaluated[8] using models on $\Delta g(x)$. This study will be extended to determine the production mechanism of J/ψ and to evaluate the sensitivity to $\Delta g(x)$.

We have formed a working group on polarized parton distribution with theorists to perform a global fit of existing experimental data to the formulae in both leading order and next-to-leading order in perturbative QCD. Preliminary results are discussed in Ref. 9.

References

1) Design Manual of Polarized Proton Collider at RHIC, July 1998.
2) N. Hayashi et al.: RIKEN Accel. Prog. Rep. **32**, 46 (1999).
3) J. Tojo et al.: RIKEN Accel. Prog. Rep. **32**, 52 (1999).
4) A. Taketani et al.: RIKEN Accel. Prog. Rep. **32**, 50 (1999).
5) K. Kurita et al.: RIKEN Accel. Prog. Rep. **32**, 48 (1999).
6) Y. Goto et al.: RIKEN Accel. Prog. Rep. **32**, 47 (1999).
7) Y. Watanabe et al.: RIKEN Accel. Prog. Rep. **32**, 53 (1999).
8) T. Sakuma et al.: RIKEN Accel. Prog. Rep. **32**, 45 (1999).
9) Y. Goto et al.: RIKEN Accel. Prog. Rep. **32**, 37 (1999).

Simulation of the J/ψ Production in Polarized Proton-Proton Collision

T. Sakuma, Y. Goto, K. Kurita, N. Hayashi, N. Saito, and T-A. Shibata

[RHIC, Spin, Asymmetry, J/ψ, Color-octet, MuID]

We have studied the J/ψ production in polarized proton-proton pp collision for the RHIC-Spin[1] in order to probe the gluon inside the polarized proton. Although the J/ψ production is sensitive to the gluon distribution function, the production mechanism has not yet known completely. There is Color-Octet Model[2] (COM) that is considered as the most powerful model and is successful in explaining the direct J/ψ cross section at the CDF which is one of $p\bar{p}$ collider experiment. We performed the J/ψ Monte Carlo simulation with modified PYTHIA[3] event generator in which COM was implemented.[4] We considered the $gg \rightarrow gJ/\psi$ subprocess only as the first step.

We generated direct J/ψ events in $p\bar{p}$ collision at $\sqrt{s} = 1.8$ TeV and extracted color-octet matrix elements

$$\left\langle 0|\mathcal{O}_8^{J/\psi}(^3S_1)|0\right\rangle = 4.0 \times 10^{-3}$$

$$\left\langle 0|\mathcal{O}_8^{J/\psi}(^1S_0)|0\right\rangle + \frac{3}{M_c^2}\left\langle 0|\mathcal{O}_8^{J/\psi}(^3P_0)|0\right\rangle = 6.1 \times 10^{-3}$$

from CDF data.[5] Using this matrix elements, we predicted the direct J/ψ cross section and spin asymmetry in pp collision at RHIC energies ($\sqrt{s} = 200, 500$ GeV).

Expected direct J/ψ cross sections are shown in Fig. 1. All points were multiplied by the muon branching fraction $B(J/\psi \rightarrow \mu^+\mu^-) = 0.0601$. PHENIX Muon Arms acceptance cut ($1.2 \leq |\eta| \leq 2.4$) was also applied.

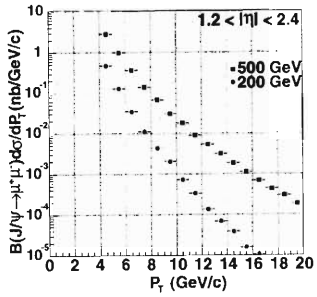

Fig. 1. Prediction of J/ψ cross section.

The asymmetry $\mathcal{A}_{LL}$ can be written in terms of cross section,

$$\mathcal{A}_{LL} = E\frac{\mathrm{d}^3\Delta\sigma}{\mathrm{d}^3p} / E\frac{\mathrm{d}^3\sigma}{\mathrm{d}^3p}.$$

To extract the spin dependent cross section $E\dfrac{\mathrm{d}^3\Delta\sigma}{\mathrm{d}^3p}$, yield of an unpolarized event was weighted by

$$\frac{\Delta G(x_1,Q^2)}{G(x_1,Q^2)}\frac{\Delta G(x_2,Q^2)}{G(x_2,Q^2)}\hat{a}_{LL},$$

since the PYTHIA is an unpolarized generator. $G(x,Q^2)$ ($\Delta G(x,Q^2)$) is the gluon (helicity) distribution function at a given Bjorken's x and momentum scale Q^2. x_1 and x_2 are fractions of the proton momentum carried by the gluon. The quantity $\hat{a}_{LL}$ is the $gg \rightarrow J/\psi g$ subprocess asymmetry at COM.[6] In fact, to determine $\hat{a}_{LL}$, one has to disentangle $^1S_0$ and $^3P_0$ contributions to the matrix elements. Figure 2 shows the asymmetries with three different ΔG inputs,[7] but neglecting $^3P_0$ contribution. From these asymmetries, one can show the experimental sensitivities. Although the size of asymmetries are rather small (1 to 1.5% at maximum), there is significant statistic at lower p_T region, $p_T < 11$ or 7 $(\mathrm{GeV}/c)^2$ for $\sqrt{s} = 500$ and 200 GeV, respectively.

We will extend this work further. For example, we can evaluate an analysis program and method by showing how well one can recover an input gluon and its helicity distribution.

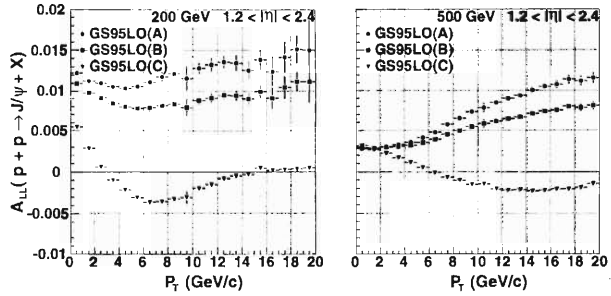

Fig. 2. Prediction of J/ψ spin asymmetry at PHENIX.

References

1) H. En'yo et al.: RIKEN Accel. Prog. Rep. **31**, 52 (1998).
2) P. Cho and A. K. Leibovich.: Phys. Rev. D **53**, 150 (1996); Phys. Rev. D **53**, 6203 (1996).
3) T. Sjöstrand.: Comput. Phys. Commun. **82**, 74 (1994).
4) B. Cano-Coloma et al.: Nucl. Phys. B **508**, 753 (1997).
5) CDF Collaboration.: Report No. Fermilab-Conf-95/128-E (1995).
6) A. Tkabladze and O. Teryaev.: Phys. Rev. D **56**, 7331 (1997).
7) T. Gehrmann and W. J. Stirling.: Phys. Rev. D **53**, 6100 (1996).

Measurement of the Proton Polarization at 21.6 GeV/c for AGS E925

N. Hayashi, H. En'yo, Y. Goto, T. Ichihara, Y. Kondo, Y. Nakada, M. Nakamura, N. Saito, H. Sakai, H. Sato, H. Okamura, M. Okamura, and T. Wakasa

[RHIC, AGS, Spin, Asymmetry, Polarized beam, Polarimeter]

The polarization measurement of the proton beam up to 250 GeV/c is very important to lead the RHIC/Spin project[1] into success. One of proposed methods utilizes the transverse spin asymmetry, $\mathcal{A}_N$, in $p^\uparrow + C \to \pi^\pm + X$. The experiment E925 of the AGS was proposed to confirm independence of this asymmetry from the target material and beam energy. The experiment uses the polarized proton beam extracted from the AGS and the beam polarization is determined by measuring the $\mathcal{A}_N$ in p-p elastic scattering. The first E925 run with the carbon target was performed on November 1997. This article describes the measurement of the beam polarization.

The design concept of the polarimeter was described previously.[2] We measured the p-p elastic scattering asymmetry at $t = -0.15$ (GeV/c)^2, where t represents the square of the momentum transfer. Analyzing power in this momentum region was obtained to be $\mathcal{A}_N = 0.040 \pm 0.004$ from a phenomenological analysis based on previous experimental data.[3] The present set-up is shown in Fig. 1. From the previous set-up only the position of the forward counters (FRA, FLA, FRB, and FLB) were modified. Since we used a polyethylene (CH_2) target, we subtracted carbon contributions from the raw data.

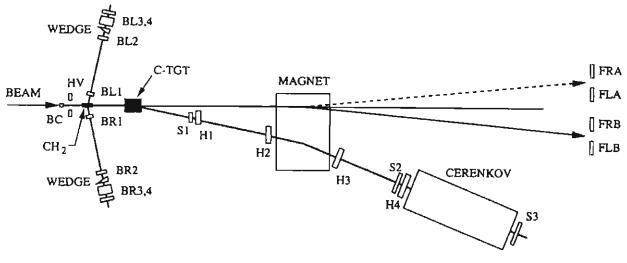

Fig. 1. A schematic drawing of the E925 set-up. The C-TGT (Carbon target) and Cerenkov counter arm is for the pion detection part. The other parts, CH_2 target, two backward arms, and four forward counters consist p-p elastic part.

Initially, the proton beam momentum was 22.75 GeV/c, but a rather strong depolarization resonance in the AGS was found at this energy. Thus, we set the beam momentum at 21.6 GeV/c in order to preserve the beam polarization. Beam intensity was about 10^7–10^8 per burst. (one burst every 3 seconds.) The events were triggered by only the backward (recoil) arm counters, namely $B1 \otimes B2 \otimes B3 \otimes \overline{B4}$ ($B1$ denotes $BL1$ and/or $BR1$, and $B2$, $B3$ and $B4$ denote similarly). Trigger rate was up to 70–80 events/burst. We reversed the magnet polarity of π spectrometer occasionally in order to take both π^+ and π^- for the pion arm.

Raw asymmetries ϵ were extracted from the following formula:

$$\epsilon \equiv \frac{\sqrt{N_L^\uparrow \times N_R^\downarrow} - \sqrt{N_L^\downarrow \times N_R^\uparrow}}{\sqrt{N_L^\uparrow \times N_R^\downarrow} + \sqrt{N_L^\downarrow \times N_R^\uparrow}}. \quad (1)$$

N_L (N_R) is the number of counts detected in the left (right) arm and the superscript $^\uparrow$ ($^\downarrow$) indicates up (down) polarization. Systematic asymmetry errors, detector acceptance, and beam intensity for each polarization state are almost canceled by using this formula.

We have obtained the asymmetry for the CH_2 target:

$$\epsilon_{CH_2} = 0.0107 \pm 0.0023. \quad (2)$$

The error indicated above is only statistical one. The asymmetry ϵ_p of the proton was deduced from the ϵ_{CH_2} after subtracting the carbon contributions as:

$$\epsilon_p = 0.0108 \pm 0.0024(stat.) \pm 0.0003(syst.). \quad (3)$$

The first and second uncertainties are the statistical and systematic errors, respectively. The systematic error depends on the asymmetry ϵ_C for the carbon target, which we had to assume.

The polarization P was determined from $P = \epsilon_p / \mathcal{A}_N$ as

$$P = 0.271 \pm 0.059(stat.) \pm 0.028(syst.). \quad (4)$$

The error of $\mathcal{A}_N$ contributes to the systematic error.

References

1) H. En'yo et al.: RIKEN Accel. Prog. Rep. **31**, 52 (1998).
2) H. En'yo et al.: RIKEN Accel. Prog. Rep. **31**, 173 (1998).
3) D. G. Crabb et al.: Nucl. Phys. B **121**, 231 (1977); M. Borghini et al.: Phys. Lett. B **36**, 501 (1971); A. Gaido et al.: Phys. Lett. B **61**, 103 (1976).

Performance of PHENIX EM-Calorimeter for Spin Physics

Y. Goto, K. Imai, N. Saito, and H. Torii

[pp interaction, Structure function, Spin, Asymmetry, Polarized beam]

EM calorimeter plays an important role in both the heavy ion physics and the spin physics in the PHENIX experiment at RHIC.[1,2] To cover both physics topics, it is required to cover a wide range of energies with good linearity, resolution, and hadron rejection. The heavy ion physics wants an access to the low p_T region extending down to a few hundred MeV/c in order to detect the soft photon signal from the quark gluon plasma (QGP) state. The detection of soft plural photons in this region requires rejection of low energy anti-neutrons and other hadrons with the timing measurement. It requires the threshold energy as low as possible. In the spin physics at $\sqrt{s} = 500$ GeV, a copious weak bosons are produced and the maximum energy of decay electron/positron reaches approximately 80 GeV. Prompt photon measurement also requires a p_T range up to 30 GeV/c.

The EM calorimeter was originally designed for the heavy ion physics. The spin physics requires the nonlinearity less than 1% for the steep slope cross section measurement of prompt photon and π^0 production. To fulfill the requirements, we have to perform a high energy beam test of the EM calorimeter, a test of the electronics, and a development of the necessary software. We also need a good calibration system. We have a cosmic muon system for the absolute and relative energy scale determination, and a laser system to correct the time dependence.

The high energy beam test was already done at the CERN/SPS H6 beam line. One lead–scintillator (PbSc) super module and 4 lead glass (PbGl) super modules were placed on a movable platform to change the position and angle of the incident beam on the calorimeter. All the necessary data which we planned were obtained, although some of them had a less statistics than expected. The following is the summary of our data sets:

- Energy scan data (6, 10, 15, 20, 30, 40, and 80 GeV/c e^- beams at 0 degree on the calorimeter)
- Non-perpendicular incident beam data (10, 15, 20, 30, and 40 GeV/c e^- beams at 10 and 20 degrees on the calorimeter)
- Position scan data (20 GeV/c e^- beam)
- Hadron response data (40 GeV/c π^+ beam)
- Energy calibration data (10 GeV/c μ^- beam for PbSc and 10 GeV/c e^- beam for PbGl)

The energy scan data will serve for the energy linearity and resolution measurements. The non-orthogonal incident beam data and the position scan data are necessary mainly for the software development: e.g., shower reconstruction program and shower simulation program. Hadron response data can be used for the hadron background estimation. We took energy calibration data with a purpose to calibrate the energy scale tower by tower.

The data analysis is now in progress. Figure 1 shows a preliminary result of the PbSc response for the 40 GeV/c e^-, π^+ and μ^+ beams. Preliminary muon and laser calibration have been done. The peak position for the 40 GeV/c e^- beam and the peak positions for π^+ and μ^+ beams are all consistent with the predictions by calculation.

Further work we have to do is the test of electronics for the calorimeter. Some parts of electronics design were modified to cover the high energy region. We have to check the front-end-module to confirm the energy coverage and linearity of the calorimeter. As for the software development, a fast Monte Carlo simulation program is necessary to make our simulation program run faster. We have to utilize the results of our high energy beam test, such as the shower shape, to make the simulation program reproduce the real shower shape precisely. Shower reconstruction program also has to be checked and developed to obtain a good γ/π^0 discrimination and a good electro-magnetic-shower/hadron-shower discrimination at the higher energy region.

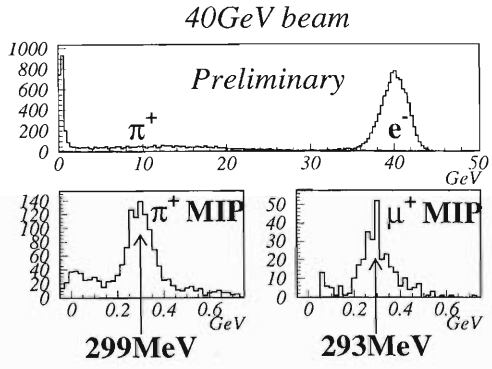

Fig. 1. Preliminary result of PbSc response for the 40 GeV/c e^-, π^+ and μ^+ beams.

References

1) H. En'yo et al.: RIKEN Accel. Prog. Rep. **31**, 52 (1998).
2) Y. Goto et al.: RIKEN Accel. Prog. Rep. **31**, 54 (1998).

Construction and Quality Assurance of the Large Muon Identifier Panels for PHENIX at BNL

K. Kurita, A. Taketani, Y. Goto, M. Ishihara, T. Ichihara, Y. Watanabe, N. Saito, N. Hayashi, H. En'yo, Y. Nakada, H. Sato, K. Imai, Y. Mao, and W. Tian

[PHENIX experiment, Muon Identifier, Production factory]

We have built, installed, and tested forty PHENIX Muon Identifier (MUID) large panels in Brookhaven National Laboratory (BNL) as shown in Fig. 1.[1-3] Twenty small MUID panels which cover the large panel gaps were fabricated in Japan and shipped to BNL for installation during the large panel construction period. The detail of the MUID fabrication procedure at Japanese factory is described elsewhere in this report.[4] Since the same fabrication procedure was adopted in both MUID factories, in present article we report our quality assurance (QA) test results of MUID tubes and the installed panel test in PHENIX Experimental Hall (PEH).

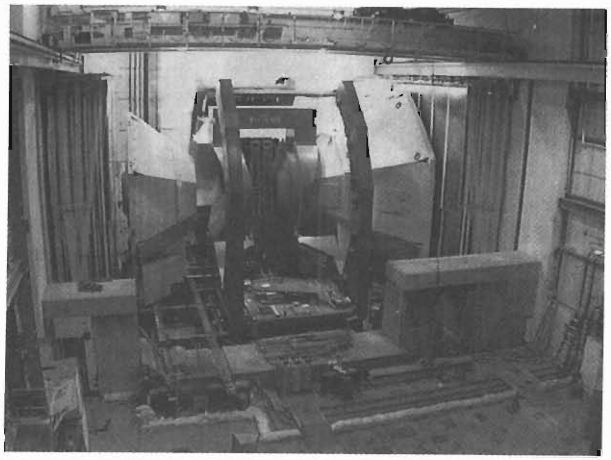

Fig. 1. Photograph of PHENIX Experimental Hall(PEH): MUID panels are located behind the lamp-shade shape MUON magnets.

The MUID detector's sensitive element is the rectangular shape plastic tubes (8.3 cm (W) × 1 cm (H) × 510/502 cm (L)) supplied by an Italian company, pol.hi.tech. The same company supplied the tubes to the Japanese factory. However, we had a major problem with the tubes, which Japanese factory did not experience.

It was a large leakage current between the cathode and anode when a high voltage was applied on them. The cause turned out to be the humidity inside the tubes. When pol.hi.tech tested the gas tightness before the shipment of the tubes to BNL, they submerged the tubes under water. If a certain amount of air bubbles a tube was observed from a tube, it was marked as a leaky tube and thus rejected. They then packed the tubes which passed the leak test into wooden crates before they are dried. Therefore the water vapor was trapped in the crates and diffused into the tubes on their way to BNL.

It turned out that the bad tubes can be spotted by simply measuring the resistance (R_{ac}) with a mega-Ohm meter between the anode and cathode of a tube. Normal tubes had resistance above 100 GΩ but the bad tubes showed much lower values as low as 10 MΩ. We could recover bad tubes by flowing a large volume of dry gas before our QA procedure. Most tubes recovered to 100 GΩ in a day or two. The tubes which were recovered by this method were about 4000 out of 10000 total tubes we used for the large panel construction. When we informed this problem to the Italian factory, they changed the shipping procedure so that little water is left in the tube container. The low R_{ac} problem disappeared after the alteration of tube shipment procedure.

Though most bad tubes were recovered, their failure rate in our QA test was about twice higher than that of a good batch of tubes. Final QA results are summarized in the Table 1 above. Once passed the QA test, the recovered tubes had the same efficiency as that of other good tubes.

Table 1. Summary of the results of tube QA test.

Tube length	Total #	# failed	Failure rate
510cm	4,876	764	15.7%
502cm	5,256	740	14.1%
total	10,132	1,504	14.8%

The construction and installation of all the MUID panels were finished in late September 1998, and currently the installed panel test is under way. We brought in two portable gas supply stations: one in south and another in north of PEH. We flow pure CO_2 into panels. Due to the limitation of the number of supply lines, we can supply gas only to three large panels at a time.

The panel-check procedure in PEH is following: (1) Flow enough CO_2 to flush all unwanted components, such as oxygen and humidity, through tubes which normally takes two days. (2) Slowly raise the HV allowing over current no more than 10 μA. (3) Look at the signal shape on an oscilloscope for each channel at full operating voltage 4.3 kV. (4) Measure the counting rate of

cosmic ray and compare with the panel test result in the factory.

We have checked 36 large panels and all 20 small panels. In general the panel performance turned out to be good, but we found a few minor problems. They are: (1) We have to flow more gas to the panels with bad tubes before applying high voltage. (2) We can not apply high voltage at all on one segment of a small panel which corresponds to 1/6 of a panel. (3) There are about 20% of tubes which show sparks of various levels. They are expected to be suppressed by further conditioning with more gas flow and high voltage cleaning.

References

1) H. En'yo et al.: RIKEN Accel. Prog. Rep. **30**, 33 (1997).
2) Y. Mao et al.: RIKEN Accel. Prog. Rep. **30**, 36 (1997).
3) A. Taketani et al.: RIKEN Accel. Prog. Rep. **31**, 172 (1998).
4) A. Taketani et al.: RIKEN Accel. Prog. Rep. **32**, 50 (1999).

Installation and Quality Test of Muon Identifier in Japan for PHENIX

A. Taketani, K. Kurita, M. Ishihara, T. Ichihara, Y. Watanabe, N. Saito, N. Hayashi, H. En'yo, Y. Nakada, H. Sato, K. Imai, H. Torii, T-A. Shibata, T. Sakuma, E. Taniguchi, Y. Mao, Z. Li, J. Tojo, M. Sekimoto, and H. Funahashi

[PHENIX experiment, Muon Identifier, Production factory]

The fabrication of muon identifier (MUID) was done at KEK and at BNL. This paper will summarize the 20 of small panels fabricated in KEK. The muon identification plays quite important role at RHIC spin project.[1] The muon detector will cover from 10 to 35 degrees in azimuthal angle. The MUID panel consists of Iarocci tubes,[2] electronics, frame, and covers. The size is 2.9 m(H) $\times$ 4.4 m(V) and weight is 600 kg, which is fabricated in KEK.

The Iarocci tubes were fabricated in Italy and shipped to KEK factory. There are two types of tubes. One is 2.5 m and another 3.82 m long, so called short and long tubes, respectively. We have tested 2031 short tubes and 1165 long tubes.

At first, the resistances of anode-anode, anode-cathode, cathode-cathode, and capacitance of anode-cathode are measured. The tubes which are identified as broken wire or broken connection are rejected. The electrically qualified tubes are tested with 30 cm-water equivalent overpressure and measured for their leakage. The tubes with relatively small leakage are fed with pure CO2, and then a high voltage up to 4.8 KV has been applied for five days. At the end of the burn in, the pulse height spectrum of cosmic ray signal is taken. Also, single count rate by the cosmic ray is measured for each tube. These values are used to identify the operational tubes.

105 tubes are recovered by adding glue in the cracks between jacket and end plug. The tubes which are rejected by too much current during burn in or by bad signal-to-noise ratio were recovered with 5 more days of conditioning.

About 150 tubes were processed per week. The processes of tube quality assurance are proceeded independently from panel assembling. Table 1 shows the reasons of final failure and number of tubes. Finally, 2840 tubes were qualified for the installation.

Table 1. Number of failed tubes and the reasons.

Reason	Short Tube	Long Tube	Total
electrically	24	41	65
gas leak	58	173	231
over current	8	4	12
signal	35	13	48

The assembling procedure has been described before.[3] Figure 1 shows a photo of flipping panel. At KEK factory there are no air conditioners to maintain stable temperature and low humidity. Humidity causes problems with high voltage(HV) circuit. We try to keep clean and dry all HV equipments during the burn in period, especially for HV connectors. To avoid the humidity in the panel volume, dry nitrogen gas was fed into the space among tubes, panel frame, and covers at the end of every single panel fabrication. It prevents high voltage sparks at outside tubes quite well.

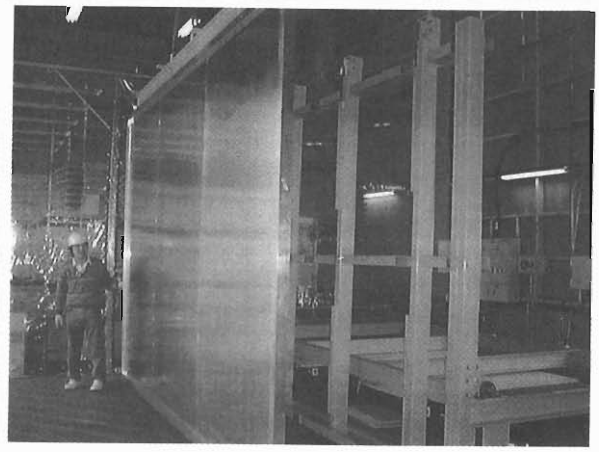

Fig. 1. Photo of flipping panel.

Temperature excursion affects during day and night on the accuracy of the tube leakage rate measurement. When temperature of the tube changes, pressure in the tubes might be changed since tubes are closed systems. We evaluates the relationship among the inside pressure, outside pressure, and temperature by simple measurements. The leakage rates were corrected.

The signal shapes are checked by the oscilloscope and the single count rate from cosmic ray are measured for individual tubes. About 5 percent of the two packs are noisy due to the discharging in the tubes. We try burn in at first panels for additional hours, and then the problem goes away. These discharging are regarded as recoverable by additional burn in, thereby at this moment.

It takes for almost one month to assemble the first panel by five physicists and two technicians. We reviewed all procedure to reduce the time very carefully. At the end of the fabrication, it takes 3 days typically.

Most of the efforts are reducing the total number of steps of person walking during the assembling and installing of two packs of tubes. Also a time sharing method works it well. In the morning, technicians install two packs, then a physicist checks gas leakage in the early afternoon. In the late afternoon, technicians install the preamps. The burin in takes another few hours and another physicist checks all signals. We were succeed to reduce the fabrication time and man power.

The panel is relatively heavy, big and not rigid. Three aluminum rods of square cross-section are attached under the panel. They across the panel to support the tube weight through the cover. Two rods are attached over the longer frames. In order to attach the rods, the blocks are installed in the frame permanently. Rods are fixed by bolts that are easy to install and remove. A single crane can lift the panel by 3 person safely in 30 minutes.

We chose the surface shipping although the delivery time is quite different. The biggest concern to reject the airplane is an environmental pressure change during the take-off and landing. The pressure decreases from 1 to 0.8 atoms in 15 minutes at take-off. We are afraid that tubes might expand with rapid pressure change and break. Also, during the landing the tubes may suck the dusty environmental air.

Five panels are stacked in the same package due to the crane capacity at the factory. The 10 cm thick styrofoam separates each panel. Three squared cross-section aluminum rods are attached under the each panel to enable a horizontal handling. An aluminized plastic bag wraps five panels together. The bag is pumped out and then closed in order to shut the dirty and humid air out during the transportation.

We shipped four times. Each shipment lasts for one month. After arriving at BNL, 10 out of 20 panels are opened and investigated. One percent of the tubes had broken wire.

We started the fabrication in December 1997 and finished at June 1998. The last 5 panels are shipped to BNL in early July 1998.

References

1) H. En'yo et al.: RIKEN Accel. Prog. Rep. **30**, 34 (1997).
2) Y. Mao et al.: RIKEN Accel. Prog. Rep. **30**, 36 (1997).
3) A. Taketani et al.: RIKEN Accel. Prog. Rep. **31**, 172 (1998).

R & D of CNI Polarimeter with Carbon Target

J. Tojo, A. Ichikawa, K. Imai, Y. Kondo, R. Muramatsu, J. Murata,
M. Nakamura, H. Takahashi, K. Yamamoto, Y. Goto, N. Hayashi,
M. Ishihara, K. Kurita, M. Okamura, and N. Saito

As a RHIC polarimeter, the pC Coulomb Nuclear Interference (CNI) polarimeter using the elastic proton-carbon scattering in the CNI region was recently proposed.[1,2] The maximum analyzing power of 2 to 4% is expected at the kinematic region where the energy of the recoil carbon ion is below 1 MeV. This region is suitable for polarimetry. The energy of such carbon ions has to be measured in coincidence with the beam pulse in order to identify the elastic scattering as a function of the momentum transfer squared. We proposed to use the combination of two microchannel plates (MCP) and a silicon strip detector (SSD) for the detection of recoil carbon ions as shown in Fig.1. Both the time-of-flight (TOF) measurement between two MCPs and the pulse height measurement with the SSD provide the particle identification and the energy of recoil carbon ions. With the proposed polarimeter, the beam polarization can be measured within a few minutes at an accuracy of 10%. Uncertainty on the hadronic spin flip amplitude dominates the ambiguity of this measurement. The quality of the RHIC polarized proton program heavily depends on the success of the development of the polarimeter.

Test experiments to detect such low energy carbon ions with the MCP were carried out at the Tandem Van de Graaff in Kyoto University. A 10 MeV proton beam and a thin carbon target of 5 μg/cm^2 in thickness were used to measure the elastic proton-carbon scattering. The scattered protons were detected with a plastic scintillator mounted on a photomultiplier. In order to maximize the detection efficiency and to design the polarimeter, the recoil carbon ions were detected with the detector system including MCP. Three configurations were tested as the detector system; (1) only MCP, (2) combination of MCP and SSD(Au surface) with an electrostatic mirror, and (3) combination of MCP and a thin carbon foil (5 μg/cm^2) with an electrostatic mirror. From the TOF measurement, which can be converted to the energy spectra of the carbon ions, the low energy carbon ions as low as 200 keV were successfully detected with each setup. From the efficiency measurement, the method shown in Fig. 1 was found suitable for detecting lower energy carbon ions.

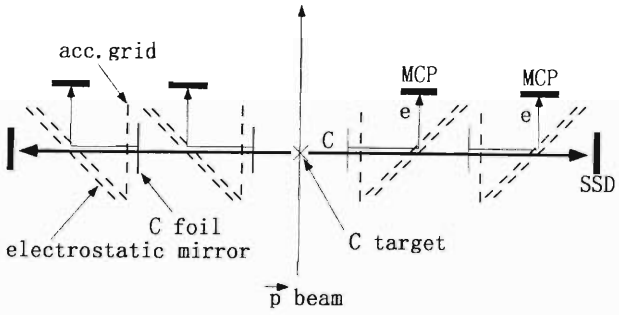

Fig. 1. Schematic view of the recoil arm.

We are developing a Si strip detector and a fast preamplifier in collaboration with BNL instrumentation division. Si detector simulation shows that we can detect the recoil Carbon down to 200 keV. The purpose of the customized design is to minimize the noise due to the large capacitance of commercially available Si detectors. A minor modification to one of the preamplifiers which were developed by the instrumentation division earlier will be made to accommodate our Si detector. The performance of the Si detector and the preamplifier will be evaluated on a test bench prior to the beam test at the BNL-AGS.

The Si detector is expected to be fabricated by the middle of Dec. 1998. Then, the Si detector in combination with MCP will be tested using the proton beam at the Kyoto Tandem for the carbon detection in early Jan. 1999. Then, finally the polarization measurement with the proposed setup will be performed at BNL-AGS using the polarized proton beam expected to be available in Mar. 1999. The experiment E950 will use two recoil arms to measure the analyzing power for proton-carbon elastic scattering in the CNI region $-t$ = 0.003–0.01 (GeV/c)^2 at beam momentum of 23 GeV/c.

References

1) Proc. Workshop on Hadron Spin-Flip at RHIC Energies, RIKEN BNL Research Center, July 21-Aug. 22, edited by T. D. Lee., Vol. 3 (1997).
2) B. Kopeliovich: High-Energy Polarimetry at RHIC, hep-ph/9801414.

Plan for the PHENIX Computing Center in Japan

Y. Watanabe and T. Ichihara

Now the start of experiments with RHIC[1] (Relativistic Heavy Ion Collider) is close, within a year. As the construction of accelerators and detectors is going at a high pace, the computer system has to be prepared in real earnest since the most important part is data analysis once the experiments start. As we reported in the last issue of this report,[2] the RCF[3] (RHIC Computing Facility) is going to be established at BNL[4] (Brookhaven National Laboratory) which is the central computer center for all four experiments at RHIC, and we are also preparing to build a similar facility named CC-J (PHENIX Computer Center in Japan) at RIKEN Wako campus as a base of analysis for Japanese and Asian colleagues.

The purposes of the CC-J are focused to the following three points:

- Detector simulations and theoretical model calculations: These CPU intensive tasks are invaluable for the extraction and understanding of results from PHENIX measurements. The CC-J will handle the bulk of the simulation tasks of PHENIX, and it should be noted here that both the RCF and the PHENIX collaboration already assume the CC-J to provide this service.
- PHENIX regional computing center in Asia: The CC-J is intended to be a regional center for the simulation and analysis of PHENIX physics results. Existence of a regional access to the computing and physics data will encourage a strong participation from the PHENIX collaborators of Japanese and Asian regions. Primary DST (Data Summary Tape) production will take place in the RCF directly from the raw data, and so the CC-J will emphasize micro-DST production and later physics analysis. The CC-J will significantly enhance the prospects in timely production of physics results from PHENIX.
- SPIN physics analysis: Although the workforce for carrying out the SPIN physics program at RHIC is centered at the RIKEN BNL Research Center, it is very important to keep maintain a strong locus of activity in Japan. The importance of this principle has long been accepted by the RIKEN BNL Research Center and by the RIKEN headquarters. The CC-J should help draw the attention of Japanese people, attract new people, and serve in its home ground as a showcase of this RIKEN project.

In order to realize such purposes, we wrote a proposal[5] stating RBRC[6] (RIKEN BNL Research Center) should build a strong channel with SPIN physics at RIKEN, and intends to establish the CC-J after JFY 1999 by three years. We let the proposal be reviewed by an advisory committee consisting of four excellent physicists who have also a good ability in computers. Some important numbers which describe a planed capability of the CC-J are following Table 1.

Table 1. Planed scale of the CC-J.

Total CPU power	~10,000 SPECint95
Fixed disk	15 TBytes
Tape robots capacity	100 TBytes
Speed of data archive	110 MBytes/s
Total capacity of tapes	250 TBytes/year

These numbers indicate that the size of CC-J will become about 1/3–1/2 of the RCF's.

We are making two prototype facilities in this year. One is the simulation and data analysis facility, and another is the data duplication facility to transfer data from BNL to RIKEN. The former consists of 10-unit LINUX boxes (each box has two Pentium II CPUs) as a PC farm and one-unit SUN E450 as a RAID file server. For the latter, we will purchase a tape drive (STK Redwood) to attach to the STK silo of RCF.

We acknowledge Prof. Hideto En'yo, Prof. Hideki Hamagaki, Prof. Jyunsei Chiba, and Prof. Ryugo Hayano for their earnest discussions with us.

References

1) *http://www.rhic.bnl.gov/*
2) Y. Watanabe et al.: RIKEN Accel. Prog. Rep. **31**, 171 (1998).
3) *http://www.rhic.bnl.gov/html/RDG.html*
4) *http://www.bnl.gov/*
5) *http://spin.riken.bnl.gov/ccj/doc/plan/*
6) *http://www.rarf.riken.go.jp/rarf/rhic/bnl/*

A High-spin Isomer in ^{143}Nd

X. H. Zhou, H. Tsuchida,* Y. Gono, A. Odahara, E. Ideguchi, T. Morikawa, M. Shibata, H. Watanabe, M. Miyake,* T. Tsutsumi,* S. Motomura,* T. Kishida, S. Mitarai, and M. Ishihara

[NUCLEAR REACTION: ^{18}O + ^{130}Te at E_{lab} = 80 MeV; γ-γ-t coincidence measurement]

High-spin isomers were observed systematically in the $N = 83$ isotones with proton number Z from 68 to 61,[1] the characteristics of these high-spin isomers can be well described in the framework of a deformed independent particle model (DIPM).[2] The DIPM calculations assigned the isomers to be of the stretched configurations $[\nu(f_{7/2}h_{9/2}i_{13/2})\pi(h^2_{11/2})]^+_{49/2}$ and $[\nu(f_{7/2}h_{9/2}i_{13/2})\pi(d^{-1}_{5/2}h^2_{11/2})]^+_{27}$ in the odd and odd-odd $N = 83$ isotones, respectively.[1] These configurations may induce oblate deformations, while the lower-spin states have near spherical shapes. Therefore, the high-spin isomers in the $N = 83$ isotones were interpreted to be caused by sudden changes in nuclear shape, which was confirmed by the deformation parameters of the yrast isomers in ^{147}Gd deduced from the experimental quadrupole moments.[3,4] The purpose of the present investigation is to search for the corresponding high-spin isomer in ^{143}Nd with a proton number of 60. The level structure of ^{143}Nd was studied by several groups,[5-8] but no high-spin isomer has been reported so far.

The excited states in ^{143}Nd were populated using the ^{130}Te(^{18}O, 5n)^{143}Nd reaction at a beam energy of 80 MeV. Measurements of delayed γ-γ coincidences, γ-ray angular distributions, and γ-ray linear polarizations were performed. Linear polarization measurements are useful in determining the electric or magnetic character of γ radiation. By combining the results of γ-γ coincidences, linear polarization, and angular distribution measurements, a new level scheme is proposed to ^{143}Nd as shown in Fig. 1. The level at 8989 keV with spin and parity values of $49/2^+$ is identified to be an isomer. Above the 8989-keV isomer the γ rays have considerable populations. This makes it possible to extract the half-life of the 8989-keV isomer from the γ-γ-t data. Figure 2(a) shows the time distribution between the two γ-ray groups, which lie above and below the isomeric state, respectively. And the time distribution between prompt coincidence γ rays is presented in Fig. 2(b) for comparison. The latter distribution represents the time jitter of the detection system and its associated electronics. A half-life of 35 ± 8 ns was extracted for the isomer at 8989 keV from an exponential fit to the curve in Fig. 2(a).

The deformation parameters β for the yrast states in ^{143}Nd are calculated with the deformed independent particle model. The calculation shows that, below the $49/2^+$ isomer, the yrast states have near spherical

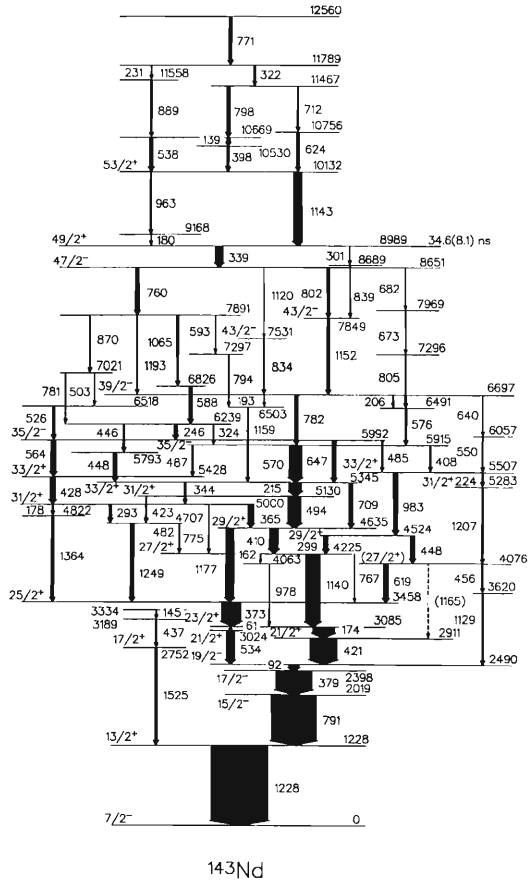

^{143}Nd

Fig. 1. Level scheme of ^{143}Nd proposed in the present work.

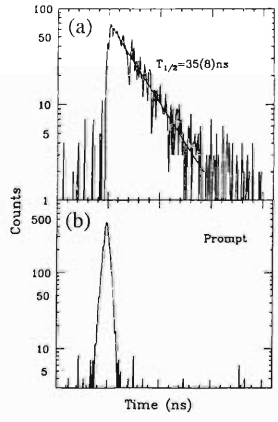

Fig. 2. (a) The time distribution between the two γ-ray groups lying above and below the isomeric state, respectively, and (b) the time distribution between prompt coincidence γ rays.

* Department of Physics, Kyushu University

shapes with small deformations ranging from 0 to -0.1, but the deformation is increased suddenly at the $49/2^+$ isomeric position. A β value of -0.18 is obtained for the $49/2^+$ isomer in ^{143}Nd. In ^{143}Nd the $49/2^+$ isomer has a full neutron configuration of $[(d_{3/2}^{-2})_0 f_{7/2} h_{9/2} i_{13/2}]$, the large deformation of the $49/2^+$ isomers is caused by the two $(d_{3/2}^{-2})_0$ neutron holes in this configuration, since the large quadratic term in the dependence of the energy of the $d_{3/2}$ orbit on β drives the nucleus towards a large oblate deformation.[2] As the isomers in the heavier isotones, the occurrence of the $49/2^+$ isomer in ^{143}Nd can be interpreted as a shape isomer.

References

1) A. Odahara et al.: Nucl. Phys. A **620**, 363 (1997).
2) T. Dossing et al.: Phys. Scr. **24**, 258 (1981).
3) O. Hausser et al.: Nucl. Phys. A **379**, 287 (1982).
4) E. Dafni et al.: Nucl. Phys. A **443**, 135 (1985).
5) O. J. Tekyi-Mensah et al.: Phys. Rev. C **50**, R1759 (1994).
6) S. M. Aziz et al.: Phys. Rev. C **41**, 1268 (1990).
7) D. D. Caussyn et al.: Phys. Rev. C **43**, 2098 (1991).
8) M. Fauerbach et al.: Phys. Rev. C **58**, 826 (1998).

In-Beam Gamma-Ray Study with HSIB of ^{145m}Sm

E. Ideguchi, Y. Gono, T. Kishida, T. Kubo, X. H. Zhou, T. Morikawa, A. Odahara, H. Tsuchida, M. Shibata, H. Watanabe, M. Miyake, S. Motomura, T. Tsutsumi, K. Yoneda, B. Cederwall, T. Bäck, T. Murakami, and M. Ishihara

[NUCLEAR REACTIONS ^{16}O(^{136}Xe, 7n)^{145m}Sm, ^{12}C(^{145m}Sm, xn)$^{157-x}$Er, High spin isomer beam]

Recently, the search for the hyperdeformed states has collected much attention after they were predicted in the extremely high spin states.[1] Large Ge arrays such as EUROBALL and Gammasphere have been constructed in order to investigate such high spin states.[2] However, unambiguous experimental evidence to confirm the existence of the hyperdeformed states has not been found yet. The most important experimental difficulty seems to be how to make such an extremely high spin state.

The High Spin Isomer Beam (HSIB) was developed in RIKEN Accelerator Research Facility in order to excite very-high spin states. Since the HSIB itself has a high angular momentum, the secondary fusion induced by HSIB will excite much higher spin states.

The secondary fusion experiment induced by HSIB was carried out by using the ^{12}C(^{145m}Sm, xn)$^{157-x}$Er reaction. HSIB was produced by using the ^{16}O(^{136}Xe, 7n)^{145m}Sm reaction. ^{136}Xe beam was accelerated to 7.6 MeV/u by RIKEN Ring Cyclotron and maximum beam intensity of ^{136}Xe was about 100 pnA.

In order to avoid a melting problem possible with usual thin metal foil due to the high intensity of primary beam, the CO_2 gas target system, which was originally developed in Kyushu University,[3] was used. Pressure inside the gas cell of the system was kept 50 Torr during its operation. This condition corresponds to the thickness 1mg/cm^2 of ^{16}O. The length and diameter of the cell were 10 cm and 6 mm, respectively. After the gas target the HSIB was focused on the usual primary target position of RIPS[4] by using a solenoidal magnet, and it was separated from the primary beam and transported to the final focal plane by using RIPS.

At the final focal plane the ^{145m}Sm isomer beam was obtained at the intensity of more than 10^5pps. The secondary target of ^{12}C was used with the thickness of 1.86 mg/cm^2. The Ge telescope system[5] was used to detect γ-rays with high efficiency and to correct Doppler effects. In the secondary reaction to use HSIB the velocity of the secondary beam is expected to be about 10% of the speed of light, which will cause a serious Doppler broadening. The Ge telescope system consists of a segmented Ge and a Clover Ge detector. The segmented Ge detector, which was a planar type Ge and was segmented into 25 pieces, was set in front of the Clover detector. This setup can determine the angle of a γ ray emitted from the target with the information which segment was fired. These results were utilized for Doppler correction. Sixteen Ge detectors were also used to make a $\gamma\gamma$ coincidence measurement together with the telescopic Ge system.

In the secondary fusion experiment a large background level in the γ-ray spectrum is due to the decay γ-rays from the high spin isomer. In order to reduce this background of isomer the neutron detectors from Gettingen University[6] were used as a gate together with the Ge detectors because the neutrons and γ-rays are emitted at the same time in the secondary fusion reaction.

In Fig. 1, the γ-ray spectra without (a) and with (b) the information gated by the neutron detectors are shown, respectively. The background from the high spin isomers were much reduced by the neutron gate. In the spectrum gated by neutron detectors, Doppler shifted γ peaks are observable. These peaks were corrected by using the Ge telescope as shown in the frame (c) in Fig. 1.

Data analysis of the secondary reaction experiment is still in progress.

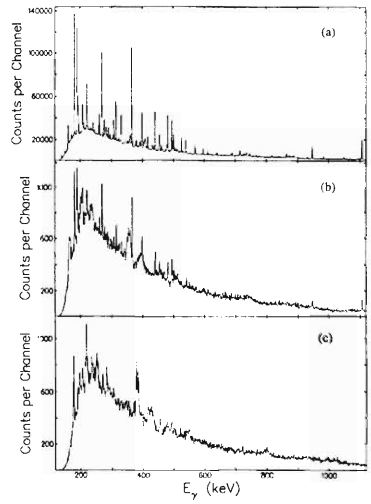

Fig. 1. Gamma-ray spectra obtained at the secondary target position. (a) Without a neutron gate, (b) With a neutron gate, and (c) Doppler corrected spectrum.

References

1) S. Aberg: Nucl. Phys. A **557**, 17c (1993).
2) C. W. Beausang and J. Simpson: J. Phys. G **22**, 527 (1996).
3) K. Sagara et al.: Nucl. Instrum. Methods Phys. Res. A **378**, 392 (1996).
4) T. Kubo et al.: Nucl. Instrum. Methods Phys. Res. B **70**, 309 (1992).
5) E. Ideguchi et al.: RIKEN Accel. Prog. Rep. **27**, 121 (1993).
6) V. Kunze et al.: Nucl. Instrum. Methods Phys. Res. A **361**, 263 (1995).

α-Decays of ^{195g,m}At and ^{199}Fr

Y. Tagaya, S. Hashimoto, K. Morita, A. Yoshida, Y. Pu, T. Ariga, K. Ohta,
T. Ishizuka, T. Minemura, I. Hisanaga, T. Motobayashi, and T. Nomura

[NUCLEAR REACTION, ^{169}Tm(^{36}Ar, α6n), ^{169}Tm(^{36}Ar, 6n), ^{195g,m}At, ^{199}Fr, α-decays, Gas-filled separator]

The α-decay of ^{195}At was first studied by Treytl and Valli [1] and later by Leino.[2] Although possible assignment of the ground-state α-decay was reported in Ref. 2, it has not been adopted in recent compilations[3] presumably due to the poor statictics and complicated nature of the observed decays. We have therefore reinvestigated the ^{195}At, and have successfully identified the α-decays from both the ground-states (g) and isomeric-states (m) produced in the ^{169}Tm(^{36}Ar, α6n) reaction. In addition, the first evidence for the α-decay of ^{199}Fr produced in the ^{169}Tm(^{36}Ar, 6n) reaction has been found.

Metallic ^{169}Tm targets of about 0.44 mg/cm^2 thickness evaporated onto a 13 μm thick aluminium foil were fixed on a rotating disk, which was 150 mm in diameter and rotated at 10 rps. Each piece of the target effectively covered 30°, and there was 30° dead space between two neighbouring targets. The pulsed ^{36}Ar beam with 8.3 ms duty-on and 8.3 ms duty-off periods was used. The bombarding energy and beam intensity were monitored by measuring the elastically-scattered ^{36}Ar with a small Si-detector placed at 46.1° with respect to the beam direction. The beam intensity was 1.0×10^{12} s^{-1} on the average, while the beam energy of 273.6 MeV from the cyclotron was degraded through an aluminium foil down to 215 ± 5 MeV.

Reaction products recoiling out of the target were separated from the primary beam with a gas-filled recoil separator GARIS,[4] and were detected with a two dimensional position sensitive detector (PSD) placed at the focal plane of the GARIS. A Si detector of almost same size placed 0.5 cm behind the PSD was used as a veto counter, which turned out quite effective in order to reduce the backgrounds such as light particles coming into the PSD. A micro-channel-plate (MCP) assembly was also placed 70 cm upstream of the PSD.

In the analysis, all the PSD signals in coincidence with MCP signals were regarded as the evaporation residues (ER), while those without MCP signals were treated as the possible α-decay events. Three successive events consisting of ER, first α-decay (α1), and second α-decay (α2) in this time sequence were searched on condition that they occured within the small area on the PSD at adequate time intervals, Δt_1 and Δt_2, which are those between the first two and second two events, respectively. The present assignment is based on the agreement of the α2-decay properties (energies E_α and lifetimes $T_{1/2}$) with the properties previously known.

All the decay properties concerned with ^{195g,m}At and ^{199}Fr were tabulated in Table 1. Assignment of the ^{195m}At was based on the observation of the ER-^{195m}At-^{191m}Bi correlations with a low background (See Fig. 1) and on the agreement of the ^{191m}Bi α-decay energy and lifetime with literature values.[5,6] Assignment of the ^{195g}At was based on the observation of the ER-^{195g}At-^{191g}Bi correlations with a low background and on the agreement of the ^{191g}Bi α-decay energy and lifetime with literature values.[5] Assignment of the ^{199}Fr was based on the observation of the ER-^{199}Fr-^{195g}At correlations with a low background and the agreement of the ^{195g}At α-decay energy and lifetime with the measured values in this experiment.

Table 1. The α-decay properties measured in present experiment.

	Present		Literature	
Nuclide	E_α (keV)	$T_{1/2}$ (ms)	E_α (keV)	$T_{1/2}$ (ms)
^{195m}At	6960±20	385^{+69}_{-51}	—	—
^{191m}Bi	6869±20	156^{+27}_{-20}	6876±5[5]	150±15[6]
^{195g}At	7091±40	144^{+21}_{-16}	—	—
^{191g}Bi	6316±20	13±2 s	6311±5[5]	12±1 s[5]
^{199}Fr	7655±40	12^{+10}_{-4}	—	—

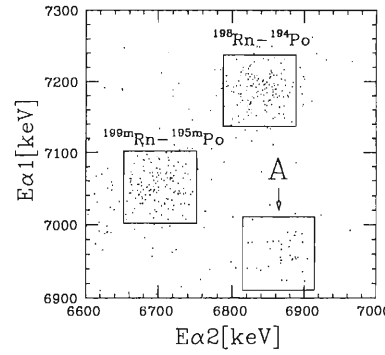

Fig. 1. The ER-α1-α2 correlations. $\Delta t_1 \leq 1.0$ s, $\Delta t_2 \leq 0.5$ s. Group A: ER-^{195m}At-^{191m}Bi.

References

1) W. Treytl and K. Valli: Nucl. Phys. A **97**, 405 (1967).
2) M. Leino: Ph. D. thesis, Dept. of Phys., Univ. of Helsinki (1983).
3) For example, see Table of *Isotopes*, 8th edition, Vol. 2, edited by R. B. Firestone and V. S. Shirley (John Wiley & Sons. Inc., 1996).
4) K. Morita et al.: Nucl. Instrum. Methods Phys. Res. B **70**, 220 (1992).
5) E. Coenen et al.: Phys. Rev. Lett. **54**, 1783 (1985).
6) M. Leino. et al.: Phys. Rev. C **24**, 2370 (1981).

Experimental Result of the $^{40}Ar + ^{238}U$ Fusion Reaction

Y. Tagaya, K. Morita, K. Uchiyama, T. Ariga, T. Hirakawa, K. Suda, M. Okada, K. Ohta, T. Ishizuka, K. Sueki,*1 T. Motobayashi, H. Miyatake, S. Jeong, and T. Nomura*2

[NUCLEAR REACTION, $^{238}U(^{40}Ar, \alpha 2n)$, ^{272}Hs, Deformed closed shell, Gas-filled recoil separator]

Existence of the deformed closed shell near N = 162 was predicted in the shell model calculation.[1] Although the α-decay energies (E_α) near N = 162[2] have been measured a few times, more data beyond N = 162 are necessary to prove the existence of such shell. We have therefore performed an experiment to produce ^{272}Hs (Z = 108) from the $^{238}U(^{40}Ar, \alpha 2n)$ reaction and to determine the E_α and the half-life ($T_{1/2}$) of ^{272}Hs. The same reaction experiment was performed previously,[3] but the result was ambiguous due to the poor statistics. In the current setup, both the beam intensity and the position resolution of the detector have been improved significantly.

The 0.5 mg/cm^2 thick UO_3 target material was electro-deposited on the aluminum foils, and these pieces of target were mounted on a disk. The disk was rotated at 10 rps for the irradiation of the pulsed ^{40}Ar beam (duty factor 0.7) from the RIKEN Ring Cyclotron. Bombarding energies at the half thickness of the target were 209 ± 3 MeV and 201 ± 3 MeV. Beam intensity was 0.3 pμA on average, and the total dose was 9.0×10^{34}cm^{-2} for 209 MeV bombardment. They were 0.4 pμA and 4.0×10^{35} cm^{-2} respectively for 201 MeV bombardment. The evaporation residue was separated from the primary beam by using the gas-filled recoil separator (GARIS).

Two dimensional position sensitive detector (PSD) was placed at the focal plane, and the energy, position and absolute time of all events were measured at the place. Another silicon detector was placed behind the PSD to reduce the event triggers originated from the arrivals of light particles. A micro-channel-plate (MCP) assembly was placed 70 cm upstream of the PSD, and its signals were used for the time-of-flight measurement between the MCP and PSD and for the discrimination of arrival events from decay events. The beam energy, intensity, and status of the target were monitored by measuring the elastically scattered projectiles with a silicon detector.

Firstly, the correlations consisting of the arrival of the evaporation residue (ER) and the first α-decay (α_1, ^{272}Hs) were searched on the conditions that the time difference between ER and α_1 (Δt) is smaller than 2 s, the E_α is between 9.0 and 9.5 MeV, the horizontal position difference (Δx) is smaller than 320 μm, and the vertical one (Δy) is smaller than 500 μm. Then, one correlation was found, whose E_α was 9352 ± 40 keV and Δt was 40 ms. The α_1 event of this correlation was during the beam-on period in 201 MeV bombardment. Secondly, all the events following the above correlation were searched for the second α-decay (α_2, ^{268}Sg) and for the spontaneous fission (SF, ^{264}Rf), within the same position gate as ER-α_1. However, no correlation was found. Observed E_α and Δt were consistent with the properties of two correlations in the previous experiment (E_α = 9353 keV, Δt = 16 ms; E_α = 9376 keV, Δt = 47 ms[3]) which formed a short half-life group. Other three candidates (E_α = 9347 keV, Δt = 949 ms; E_α = 9357 keV, Δt = 949 ms; E_α = 9401 keV, Δt = 953 ms[3]) which formed a long half-life group were also observed in the previous experiment , but no corresponding correlation was found in present experiment. If the observed event comes from ^{272}Hs, the E_α sytematics suggests a manifestation of the shell effect (Fig. 1). The experimental cross-section of the observed event was calculated to be 0.1 nb assuming that the transmission efficiency of the GARIS was 5%.

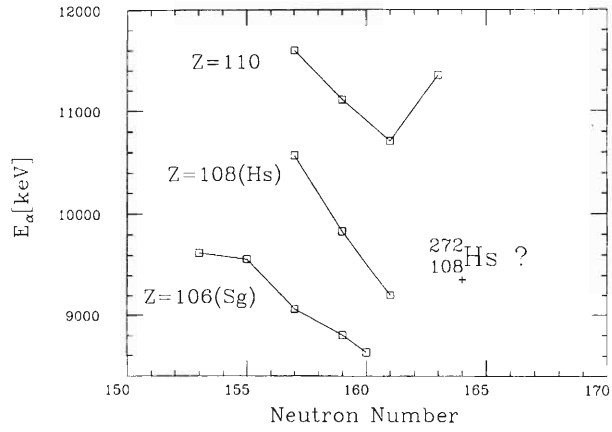

Fig. 1. E_α systematics for heavy elements. The data shown by square markers were taken from the eariler works. The datum of cross marker is from present work.

References

1) Z. Patyk and A. Sobiczewski: Nucl. Phys. A **533**, 132 (1991).
2) For example, Yu. A. Lazerev et al.: Phys. Rev. C **54**, 620 (1996).
3) T. Nomura et al.: RIKEN Int. Workshop on Heavy-Ion Reactions with Neutron-Rich Beams, Wako, p. 269 (1993).

*1 Tokyo Metropolitan University
*2 KEK Tanashi

Plan for Lifetime Measurements of Excited States Using the Recoil Decay Tagging Technique with Gas-Filled Recoil Separator

K. Uchiyama, K. Morita, K. Furuno, and Y. Tagaya

[Lifetime measurement, Recoil decay tagging, Gas-filled recoil separator]

We propose in-beam γ-ray spectroscopy experiments using the recoil decay tagging[1] and also lifetime measurements of excited states with RIKEN GAs-filled Recoil Isotope Separator (GARIS). The main purpose is to study the nuclear structure of the low-lying states in neutron deficient isotopes near and beyond the lead region. The study of nuclear structure in this region is quite challenging. For instance, Dracoulis et al. reported the irregular yrast sequence in ^{174}Pt.[2] They had to identify the nuclides based on γ-X coincidence informations. The recoil decay tagging technique makes isotope identifications easier. So it will become possible to use more complex reaction channels which are needed to produce more neutron deficient isotopes by fusion-evaporation reaction. The recoil decay tagging is suitable for systematic study of this irregular sequence. This is the reason why we propose the recoil decay tagging experiments using GARIS.

In addition to the energy level schemes, the reduced transition probability deduced from the lifetime of excited states is indispensable especially for studying anomalous behavior of the low-lying states like mentioned above. In the Ba isotopes, for an example of the extreme case, pairwise proton transfer causes to enhance the $B(E2 : 0_1^+ \rightarrow 2_1^+)$ values of the isotopes in mid-shell region *without* a concomitant change in the energies of low-lying states.[3] An intrusion of the proton core orbit into valence shells is concerned with this phenomenon. So it is impossible to indicate this without an information of reduced transition probability. More complex phenomena are expected near and beyond the lead region. Therefore, it is necessary to measure not only γ-ray spectra but also lifetimes of excited states. Fortunately, the lifetime measurements can be performed using almost the same setup as of the recoil decay tagging, in principle. We will briefly describe here about the concept of this lifetime measurement combined with the recoil decay tagging technique.

Our plan of lifetime measurements is a modified recoil distance method, like the differential plunger proposed by Dewald et al.[4] The conventional recoil distance method is performed using target and stopper, and the decay curves are determined by the following relation:

$$R(D) = \frac{I_u(D)}{I_u(D) + I_s(D)}, \qquad (1)$$

where D is the distance between target and stopper, I_s and I_u are the Doppler shifted and unshifted peak intensities, respectively. The stopper should be thick enough to stop the recoiling nuclei because the Doppler unshifted peak intensity is needed to make the decay curves. In the case of using the mass separator, the stopper must be replaced by the "retardation" foil for introducing the recoiling nuclei into the mass separator. A schematic drawing of the setup is shown in Fig. 1. The recoiling nuclei are separated from the primary beam by the GARIS, and then are implanted into a two dimensional position sensitive silicon detector (PSD). The implantation of the evaporation residues and their α decays are detected by this PSD. The time of flight measurement is additionally performed using a micro-channel plate assembly (MCP) and the PSD. The γ-ray detectors around the target are used to measure both the fully Doppler shifted and the reduced Doppler shifted γ rays which are in coincidence with the implantation signal of the PSD. Distance between the target and the retardation foil can be varied by moving the position of the retardation foil to determine decay curves of the excited states.

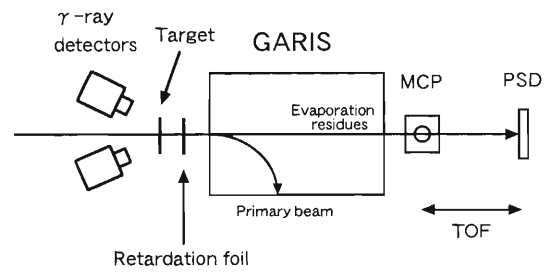

Fig. 1. Schematic drawing of a setup for lifetime measurements using the recoil decay tagging with the GARIS.

The main purpose of using the retardation foil is to determine the fully Doppler shifted peak. Therefore the retardation foil must be thin enough for the recoiling nuclei to pass through and to make the signal in the focal plane detector. But it must be thick enough to reduce the velocity of the recoiling nuclei. For instance, the schematic γ-ray spectra of the fully Doppler shifted peak and the reduced Doppler shifted peak of $2_1^+ \rightarrow 0_1^+$ transition in ^{174}Pt, produced by the reaction ^{115}In (^{63}Cu, 4n), are shown in Figs. 2 and 3. These spectra are the results of drastically simplified Monte Carlo simulation, where assumed are the following conditions: the distance between the target and the retardation foil is 200 μm, the retardation foil is a gold one, the energy of the γ ray is 394.2 keV, the detector angle is 150° with respect to the beam axis, the lifetime

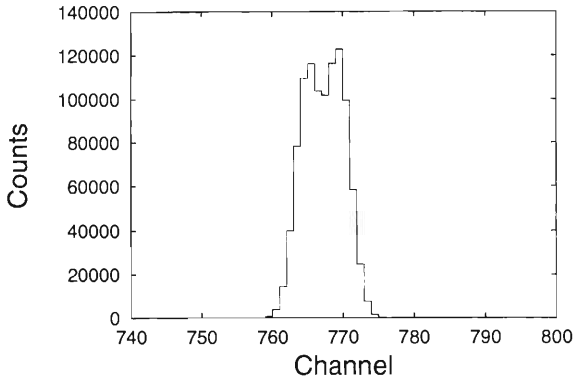

Fig. 2. A spectrum consisting of the fully Doppler shifted peak and the reduced Doppler shifted peak of $2_1^+ \rightarrow 0_1^+$ transition in ^{174}Pt. The thickness of the retardation foil was 2 mg/cm^2. Other parameters are described in the text.

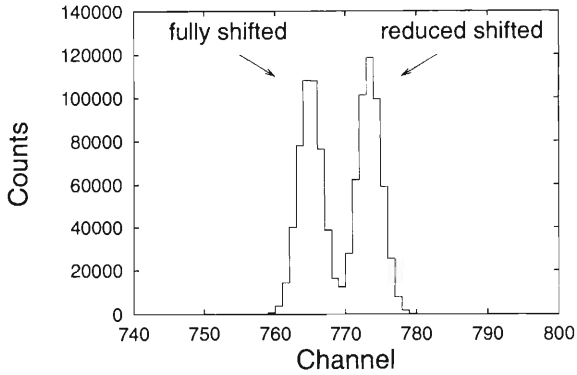

Fig. 3. A spectrum consisting of the fully Doppler shifted peak and the reduced Doppler shifted peak of $2_1^+ \rightarrow 0_1^+$ transition in ^{174}Pt. The thickness of the retardation foil was 4 mg/cm^2. Other parameters are same as Fig. 2.

is 28.1 ps estimated by empirical relations,[3,5] and the energy of recoiling nuclei is 103.7 MeV in the laboratory frame. The energy loss in the retardation foil was estimated using the stopping-power table[6] and some corrections; however, the energy straggling, multiple scattering in foils etc., were not included in these simulation. Figure 2 shows the schematic spectrum when a 2 mg/cm^2 thick gold foil was used as the retardation foil. Obviously, it is impossible to divide the spectrum into two peaks when the thinner foil is used as a retardation foil. Figure 3 shows the schematic spectrum when a 4 mg/cm^2 thick gold foil was used as a retardation foil. In this case, it is possible to divide it into two peaks. The kinetic energy of the recoiling nuclei is about 48 MeV in the laboratory frame after passing through the 4 mg/cm^2 retardation foil. This value 48 MeV is enough high.

In present case, γ decay occurs not only near the target position but also inside the GARIS. So the decay curve $R(D)$ cannot be determined by Eq. (1) because the total intensity, that is the denominator of Eq. (1), cannot be determined correctly. This situation is similar to the conventional recoil distance measurement with inverse reaction made by H. Emling et al.[7] In their case, it is difficult to determine the intensity of the unshifted peak due to the long slow-down time in the stopper foil. So, they used the equivalent relationship:

$$R(D) = 1 - \frac{I_s(D)}{I_s(\infty)}. \tag{2}$$

Consequently, in present case, the decay curve $R(D)$ can be determined simply by the fully Doppler shifted component $I_{fs}(D)$ and by using the following relationship:

$$R(D) = 1 - \frac{I_{fs}(D)}{I_{fs}(\infty)}, \tag{3}$$

where D is the distance between the target and the retardation foil. The normalization to $I_{fs}(D)$ at every distance can be performed using the total number of the recoiling nuclei, which can be deduced from the α-decay spectrum detected by the PSD. We should mention that the value of $I_{fs}(\infty)$ can be measured from the setting without a retardation foil. This is just the normal recoil decay tagging setup. More detail on the setup, method of data analysis, and so on are under discussion.

References

1) K. Helariutta et al.: Phys. Rev. C **54**, R2799 (1996).
2) G. D. Dracoulis et al.: Phys. Rev. C **44**, R1246 (1991).
3) M. Sugita et al.: Phys. Lett. B **440**, 239 (1998).
4) A. Dewald et al.: Z. Phys. A **334**, 163 (1989).
5) S. Raman et al.: Phys. Rev. C **37**, 805 (1988).
6) L. C. Northcliffe and R. F. Schilling: Nucl. Data Tables A **7**, 233 (1970).
7) H. Emling et al.: Phys. Lett. B **98**, 169 (1981).

Reaction Products from the ^{208}Pb + ^{208}Pb Reaction at 15A MeV

K. Yoshida, M. Shimooka, R. Wada, T. Nakagawa, K. Nakagawa, I. Tanihata, Y. Aoki, J. Kasagi, and W. Q. Shen*

[^{208}Pb + ^{208}Pb, 15A MeV, Fission]

The energies and velocities of reaction products have been measured for the ^{208}Pb + ^{208}Pb reaction at 15A MeV to investigate the formation of a very heavy compound nucleus. Due to the strong Coulomb repulsion, it has been thought that the formation of a compound nucleus is strongly hindered in the collision between heavy nuclei such as ^{208}Pb + ^{208}Pb. However, recent theoretical calculations suggest that a heavy compound nucleus can be formed in heavy nucleus-nucleus collision at sufficiently high incident energies to overcome the strong Coulomb repulsion. Such a heavy compound nucleus, if it is formed, will decay to plural fragments by fission. In the experiment, we focused on the detection of all the fragments from a ternary fission of the heavy compound nucleus, since the fragments from usual binary fission are known to distribute in space similar to the reaction products of a deep inelastic reaction.

The experiment was performed at the RIKEN Ring Cyclotron. ^{208}Pb beams with an energy of 15A MeV was bombarded on a 99.9% enriched ^{208}Pb foil of 1 mg/cm^2 in thickness backed with 20 μg/cm^2 collodion. Fission fragments were detected with the large PPAC/IC chamber[1] which covered 25–75° laboratory angles around the beam axis. The chamber is divided azimuthally into 12 identical units with a minimum dead space in between. A backward hemisphere was covered with BaF_2 phoswich detectors[2] to detect charged particles as well as γ-rays.

Figure 1 shows the correlation of relative azimuthal angles among the three fragments detected by the PPAC/IC chamber. As seen, most events have an asymmetric character: one of the angle is about 60° and the others are about 150°. In these events, the two fragments with a small folding angle have a strong correlation in their velocities. This suggests that the events come from the fission of projectile or target nuclei after the deep inelastic scattering.

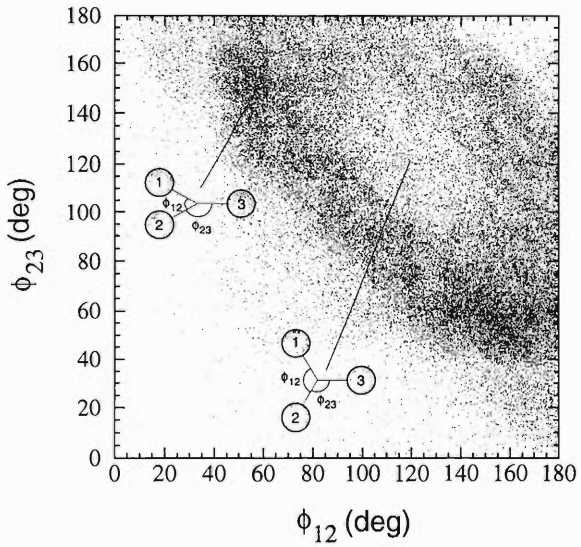

Fig. 1. Correlation of relative azimuthal angles between two fragments from the three-fragment events in the ^{208}Pb + ^{208}Pb reaction at 15A MeV. The definition of the relative azimuthal angles is schematically shown in inset.

Yield of the symmetric event, of which all three folding angles are nearly 120°, is about 1% of the total three-fragments events. There is no strong correlation in velocities of these fragments. This can be interpreted as a signature of the simultaneous break up of three fragments. Analysis of the deduction of mass of the fragments and analysis of the charged particle spectra are now in progress.

References

1) K. Yoshida et al.: RIKEN Accel. Prog. Rep. **31**, 165 (1998).
2) Y. Futami et al.: Nucl. Instrum. Methods Phys. Res. A **329**, 513 (1993).

* Shanghai Institute of Nuclear Research, Chinese Academy of Science, Shanghai, China

Measurement of the Cross Sections and the Vector and Tensor Analyzing Powers for *d-p* Elastic Scattering at E_d = 270 MeV

K. Sekiguchi, N. Sakamoto, H. Okamura, A. Tamii, T. Uesaka, Y. Satou, T. Ohnishi, T. Wakasa, K. Yakou, S. Fukusaka, S. Sakoda, K. Suda, H. Kato, Y. Maeda, K. S. Itoh, T. Niizeki, and H. Sakai

[NUCLEAR REACTIONS, ^{1}H($\vec{d}$, d), E_d = 270 MeV measured : $\sigma(\theta), A_y(\theta), A_{yy}(\theta), A_{xx}(\theta), A_{xz}(\theta)$]

The measurement of the cross sections and the vector and tensor analyzing powers A_y, A_{yy}, A_{xx}, A_{xz} for the deuteron-proton (d–p) elastic scattering at 270 MeV has been reported by Sakamoto et al.[1] Their results are shown in Figs. 1 and 2 by the open squares. The solid curves are the three-body Faddeev calculations which take into account the *NN* interactions of $j \leq 4$. Although the fit of the analyzing powers is generally good, the calculated differential cross sections are smaller by 30% than the observed values at the angles where the differential cross sections become minimum. Recently it is pointed out that this discrepancy might be due to the effect of three nucleon force (3NF).[2,3] Since the previous measurement covers only the limited angular range $\theta_{c.m.}$ = 57.0°–137.8°, we extended the measurement to a wide angular range.

The differential cross sections and the vector and tensor analyzing powers A_y, A_{yy}, A_{xx}, A_{xz} were measured at E_d = 270 MeV for the forward angles 10°–60° and for the backward angles 125°–180°. The CH_2 target with a thickness of 46.7 mg/cm^2 was bombarded by a polarized deuteron beam and either scattered deuterons or protons were detected by the spectrograph SMART depending on the scattering angle.

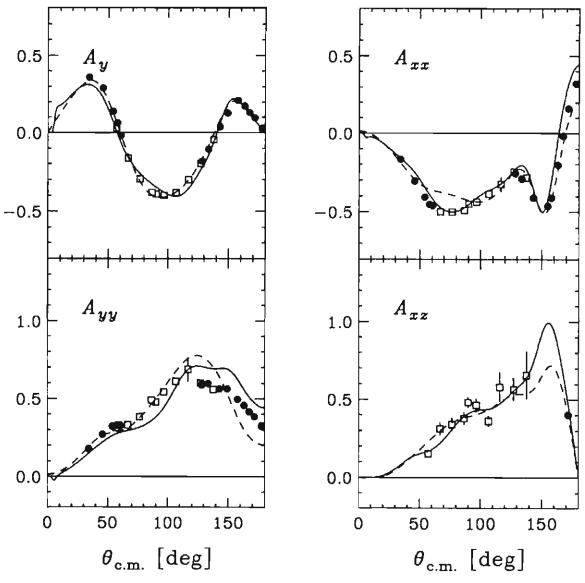

Fig. 1. A_y, A_{yy}, A_{xx}, A_{xz} for the *d-p* elastic scattering at E_d^{lab} = 270 MeV. The solid circles are the results of this experiment and the open squares are those of Ref. 1. The solid curves are the theoretical predictions of the Faddeev calculation taking into account *NN* partial waves $j \leq 4$. The dashed lines are theoretical predictions including the effect of 3NF.

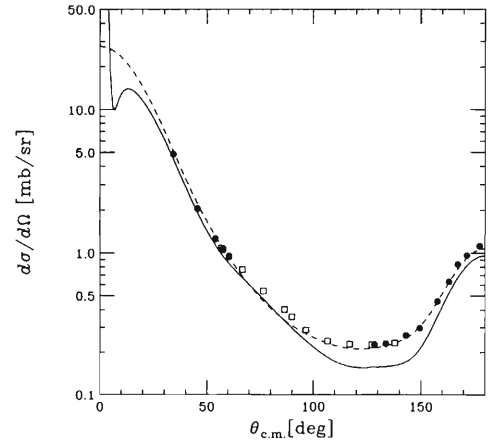

Fig. 2. The differential cross sections for the *d-p* elastic scattering at E_d^{lab} = 270 MeV. The solid circles are the results of this experiment and the open squares are those of Ref. 1. The solid and dashed curves are the same as Fig. 1.

Present results of the analysis are shown with solid circles in Figs. 1 and 2. The errors are statistical ones only and their sizes are smaller than the symbols. Since the two independent measurements provide almost the same values in the overlapping region, the systematic errors seem to be small. The dashed curves in Figs. 1 and 2 are the calculations by Witala et al.[2,4] which take into account the effect of 3NF. Note that the Coulomb interaction is not included in this calculation. The calculation with 3NF shows an excellent fit over the whole observed angular range. Thus the discrepancy in the cross section minimum seems to be accounted for by 3NF. The observed vector analyzing powers A_y are also in good agreement with the calculations with 3NF. However the agreements in the tensor analyzing powers A_{yy} and A_{xx} are rather poor.

Further analysis for the very forward angles are in progress together with those for the A_{xz} data.

References

1) N. Sakamoto et al.: Phys. Lett. B **367**, 60 (1996).
2) H. Witala et al.: Phys. Rev. Lett. **81**, 1183 (1998).
3) S. Nemoto et al.: Phys. Rev. C **58**, 2599 (1998).
4) H. Kamada: private communications.

The $^3\vec{H}e(\vec{d},p)^4He$ Reaction at E_d = 140 and 270 MeV

T. Uesaka, H. Okamura, Y. Satou, T. Ohnishi, K. Sekiguchi, K. Yakou, S. Sakoda, N. Sakamoto, T. Wakasa, K. S. Itoh, K. Suda, and H. Sakai

[^{3}He$(d,p)^4$He, E_d = 140, 270 MeV, Measured analyzing powers]

The high momentum component of deuteron is of fundamental interest because it is directly connected to the interaction between two bound nucleons in specific quantum states. The ^{3}He$(d,p)^4$He reaction at intermediate energy is considered to provide a way to study the high momentum component of deuteron D-state wave function.[1] A prior study was made at $\theta_{\rm lab}$ = 4° by using a 270 MeV polarized deuteron beam at RARF. The results of this experiment, however, show polarization observables in significant disagreement with both PWBA and DWBA. For the purpose of a detailed theoretical investigation regarding the reaction mechanism of the $^3\vec{H}e(\vec{d},p)^4$He reaction, systematic study is necessary, such as measurement of angular distribution and energy dependence of polarization observables and differential cross section is necessary.

We have measured the angular distributions of differential cross section, vector and tensor analyzing powers for the ^{3}He$(\vec{d},p)^4$He reaction at E_d = 140 and 270 MeV.

The new cryogenic-gas-target was constructed for this experiment. The schematic view of the target is shown in Fig. 1. ^{3}He gas was enclose in a copper container which is contacted to a refrigerator. The target dimensions were 13 mm (20 mm) wide, 15 mm (20 mm) high and 20 mm (10 mm) thick in the case of 270 MeV (140 MeV) measurement. Entrance and exit windows were 6 μm thick Habar foils. The gas container and the second stage of the refrigerator were shaded from thermal radiation of the circumstances with a SUS pipe which is attached to the first stage (77 K) of the refrigerator. The SUS pipe was also wrapped with super-insulator foils. Temperature of the target was measured by using a diode thermo-sensor and found to be about 11 K throughout the experiment. The density of the ^{3}He gas reached 6.6×10^{20} cm^{-3} (6.7 mg/cm^2).

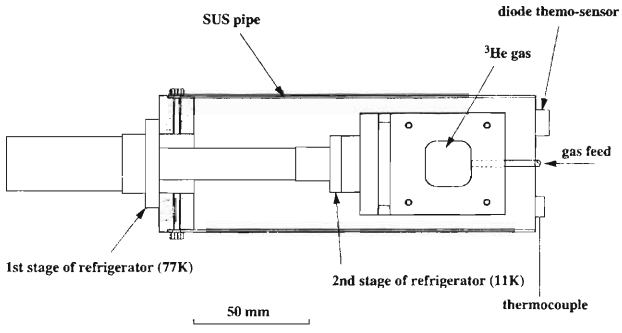

Fig. 1. Schematic view of the cryogenic gas target.

A polarized deuteron beam from the Ring Cyclotron was used to bombard the target. The scattered protons were momentum-analyzed in a magnetic spectrograph SMART and detected at the second focal plane. The detector system consisted of an eight-plane multi-wire drift chamber and three plastic scintillators. Obtained energy spectrum is shown in Fig. 2. The peak at E_x = 0 MeV is from the ^{3}He. Other peaks at higher excitation energies are from Habar foils.

The further analysis is in progress.

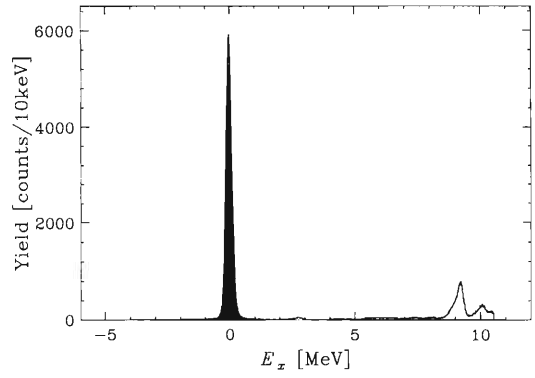

Fig. 2. Excitation energy spectrum for the ^{3}He$(d,p)^4$He reaction at E_d = 270 MeV.

References

1) T. Uesaka et al.: Nucl. Instrum. Methods Phys. Res. A **402**, 212 (1998).

Spectroscopy of ^{11}Be via ^{11}B(d, ^{2}He)^{11}Be Reaction at E_d = 270 MeV

T. Ohnishi, H. Sakai, H. Okamura, T. Niizeki, K. S. Itoh, T. Uesaka, Y. Satou, K. Sekiguchi, K. Yakou, S. Fukusaka, N. Sakamoto, and H. Ohnuma

[NUCLEAR REACTION: ^{11}B(polarized d, ^{2}He)^{11}Be at E_d = 270 MeV; Measured σ, A_y, A_{yy}, and A_{xx}; Neutron halo]

The neutron halo nucleus ^{11}Be has been studied by many experiments and theoretics. Particularly, the ground state is interesting, since it has a spin and parity of $\frac{1}{2}^+$ due to the inversion the 1s- and 0p-shell orbits. The effect of the neutron halo is expected to appear in the dipole transition. From the theoretical calculation for the spin- and isospin-flip dipole transition, the effects of the neutron halo are as follows[1]: Firstly, the peak position of the dipole transition with halo appears at an excitation energy around 10 MeV. It is smaller than that without halo. This is because the smallness of the gap between 1s- and 0p-shells. Secondly, the strength of the dipole transition is enhanced. This is because the operator for the dipole transition has a radial part, r. Therefore, the matrix elements involving a halo have a better overlap at a large radius owing to the large mean square radius compared to that of the core.

In the present measurement, we have studied ^{11}Be excited states by using the ^{11}B(d, ^{2}He)^{11}Be reaction at 270 MeV. ^{2}He indicates proton-proton system coupled to the singlet S-state. The (d, ^{2}He) reaction excites exclusively spin- and isospin-flip excitation: Gamow-Teller (GT) type transitions (ΔL = 0), and spin-flip dipole (SD) transitions (ΔL = 1), and so on. The spectroscopic application of the (d, ^{2}He) reaction at intermediate energy is well tested by the ^{12}C(d, ^{2}He)^{12}B measurement.[2] The measurement using the same reaction was performed at 70 MeV.[3] Though the effects of the neutron halo were measured, some ambiguity of the deduction of ΔL remained. Thus, to deduce ΔL more clearly, we have measured the ^{11}B(d, ^{2}He)^{11}Be reaction at angles where the value of the cross section for the dipole transition becomes largest.

The present measurement was performed at RIKEN Accelerator Research Facility by using the polarized deuteron. The thickness of the ^{11}B self-supporting target was 18.9 mg/cm^2. The contribution of the contamination was negligibly small. The scattered two protons were momentum analyzed by the spectrograph, SMART, and were detected by a multi-wire-drift-chamber and a scintillator hodoscope located at the first focal plane. The angular distributions of the differential cross section and the analyzing powers, A_y, A_{yy}, and A_{xx} were measured in the range θ_L = 0°–16°. The typical spectra of the differential cross section and the tensor analyzing power A_{xx} are shown in Fig. 1.

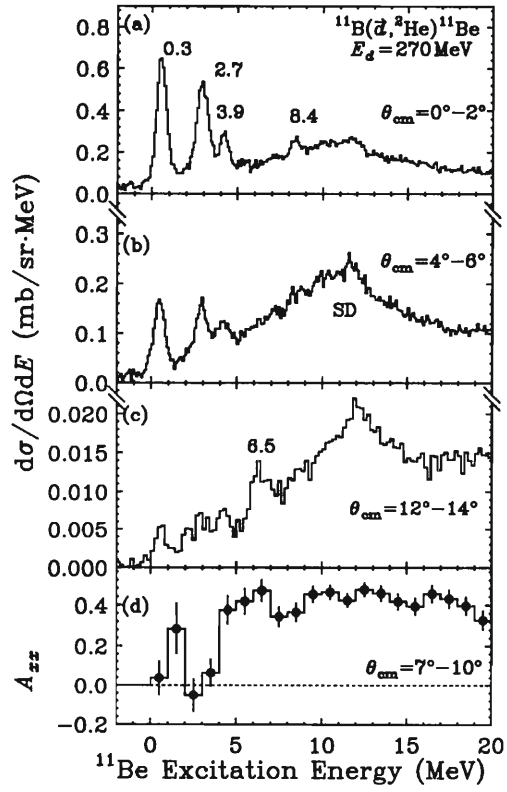

Fig. 1. (a) Spectrum of the differential cross section at θ_{cm} = 0°–2°, (b) θ_{cm} = 4°–6°, and (c)θ_{cm} = 12°–14°. (d) Spectrum of the tensor analyzing power A_{xx} at θ_{cm} = 7°–10°.

In Fig. 1 (a)–(c), several GT transitions are clearly seen at low excited energy region. In addition, a new peak which is considered to be GT transition is found at E_x = 8.4 MeV.

The broad bump appears at around E_x = 10 MeV. Since the broad bump becomes larger at the finite angle, it is considered to be consisted of the spin-dipole transitions and higher ΔL transitions. Further analysis is in progress.

Finally, we thank Bill Lozowski at the Indiana University Cyclotron Facility for making the ^{11}B target for us.

References

1) T. Hoshino et al.: Nucl. Phys. A **523**, 228 (1991).
2) H. Okamura et al.: Phys. Lett. B **345**, 1 (1995).
3) H. Sakai et al.: Phys. Lett. B **302**, 7 (1993).

Measurement of Elastic and Inelastic Scattering of Polarized Deuterons from ^{28}Si at 270 MeV

Y. Satou, S. Ishida, H. Sakai, H. Okamura, N. Sakamoto, H. Otsu, T. Uesaka, T. Wakasa, T. Nonaka, T. Ohnishi, G. Yokoyama, K. Sekiguchi, K. Yakou, S. Fukusaka, K. S. Itoh, T. Ichihara, T. Niizeki, and K. Hatanaka

[NUCLEAR REACTION, ^{28}Si(polarized d, d') E_d = 270 MeV; measured $\sigma(\theta)$, $A_y(\theta)$, $A_{yy}(\theta)$]

Optical model potentials determined from elastic scattering are often necessary inputs for the calculation of inelastic scattering. At intermediate energies (E/A > 100 MeV) deuteron-nucleus elastic scattering data, however, are very scarce and no global optical model potentials are available at present. In order to obtain optical potential parameters, we have measured the elastic scattering of polarized deuterons from ^{28}Si at E_d = 270 MeV. Since ^{28}Si is a strongly deformed nucleus with strong excitation of the first 2^+ state, the channel coupling could be important. The data for the inelastic excitation to the 2^+ level were also acquired.

The measurements were performed in the E4 experimental room using a 270 MeV polarized deuteron beam from the RIKEN Ring Cyclotron, as part of an experiment devoted to the determination of the deuteron spin-flip probabilities, S_1 and S_2, in the ^{28}Si($\vec{d}, \vec{d'}$) reaction.[1)]

In Fig. 1, measured angular distributions of the cross section σ, and analyzing powers, A_y and A_{yy}, for the elastic scattering are shown. The solid lines in Fig. 1 are the results of the optical model (OM) fits. The OM parameters in the notation of Ref. 2 were obtained from the simultaneous analysis of σ, A_y and A_{yy} by using the code ECIS by Raynal.[3)] The data are well reproduced by the OM calculation. In the present OM analysis an imaginary central potential having a Wood-Saxon term (a volume absorption term) as well as a derivative of the WS term (a surface absorption term) in the ratio of about 14 : 1 was required. This is in disagreement with the extrapolation from the lower energy analysis,[2)] in which the surface imaginary term was indicated to decrease as a Gaussian function of the form $W \exp[-(E/100)^2]$, where E is the c.m. kinetic energy.

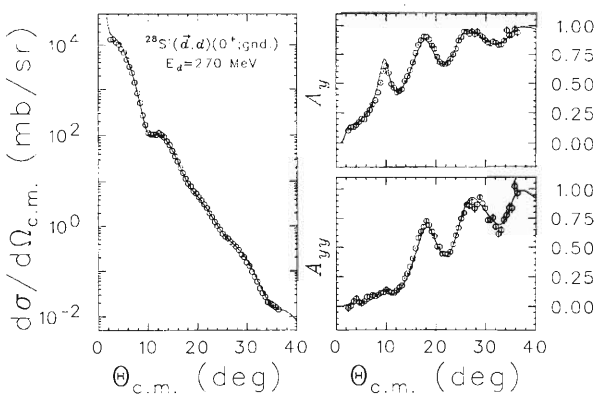

Fig. 1. Deuteron elastic scattering data on ^{28}Si at E_d = 270 MeV. Solid lines are results of the OM calculations.

In Fig. 2, data for the inelastic scattering to the first 2^+ state are displayed. The solid lines in Fig. 2 are the results of the coupled-channel (CC) macroscopic calculation, where the coupling between the ground 0^+ and the first 2^+ states were taken into account under the framework of the rotational model which assumes an oblate deformation for all the potential terms. The agreements between data and theoretical curves are satisfactory. In order to obtain simultaneous fits to all the data, the OM parameters had to be varied from original ones. The most significant of these was the surface imaginary potential, which decreased by about 80%. This may indicate that the surface absorption term required in the present OM analysis is responsible for the absorption due to the 0^+-2^+ channel coupling, and that it no longer plays an important role in the CC calculation in which the channel coupling is explicitly taken into account.

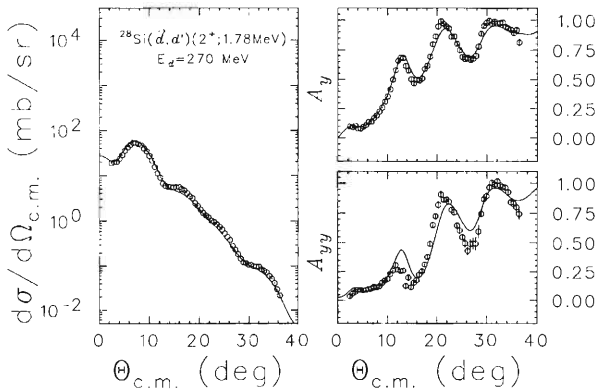

Fig. 2. Data for the ^{28}Si($\vec{d}, d'$)(2^+; 1.78 MeV) reaction at E_d=270 MeV. Solid lines are results of the CC calculation.

References

1) Y. Satou et al.: RIKEN Accel. Prog. Rep. **31**, 62 (1998).
2) W. W. Daehnick et al.: Phys. Rev. C **21**, 2253 (1980).
3) J. Raynal: Computer code ECIS, IAEA-SMR-8/8, p. 75 (1972).

Gamow-Teller Strength of ^{28}Si, ^{32}S, and ^{34}S(d, ^{2}He)

K. S. Itoh, T. Niizeki, T. Ichihara, H. Sakai, H. Okamura, S. Ishida, N. Sakamoto, T. Uesaka, Y. Satou, T. Ohnishi, Y. Tajima, G, Yokoyama, K. Sekiguchi, K. Yakou, S. Fukusaka, H. Ohnuma, and H. Orihara

[NUCLEAR REACTION (d, ^{2}He), GT β decay]

We present preliminary (d, ^{2}He) reaction spectra on the target of ^{28}Si,^{32}S, and ^{34}S at a small angle. We make a comparison of the (d, ^{2}He) spectra with the Gamow-Teller strength from (p,n) reaction for $N = Z$ (^{28}Si, ^{32}S) nuclei. Then, we compare these spactra with shell-model calculations for the $N = Z + 2$ (^{34}S) as well as $N = Z$ nuclei.

The experiment was performed using a 270 MeV deuteron beam available from RIKEN Ring Cyclotron, a large solid-angle and wide momentum-acceptance magnetic spectrometer system, SMART. The ^{2}He nucleus was detected by a pair of Multi-Wire Drift Chambers(MWDC).[1] Since ^{2}He is at unbound state, the pairs of two protons whose relative energy is within 1.0 MeV were actually detected. Targets were self-supporting foils : 25.5 mg/cm^2 thick ^{nat}Si, 38 mg/cm^2 thick ^{nat}S, and 37 mg/cm^2 thick ^{34}S enriched to 99.4%.

For $N = Z$ nuclei the GT$_+$ strength should be equivalent to the GT$_-$ strength. Actually, the (d, ^{2}He) spectra on both of ^{28}Si and ^{32}S seem to be in good agreement with the (p, n) data as shown in Fig. 1.[2,3]

Comparisons of experimental data with shell-model calculation is shown in Fig. 2. Shell-model calculations

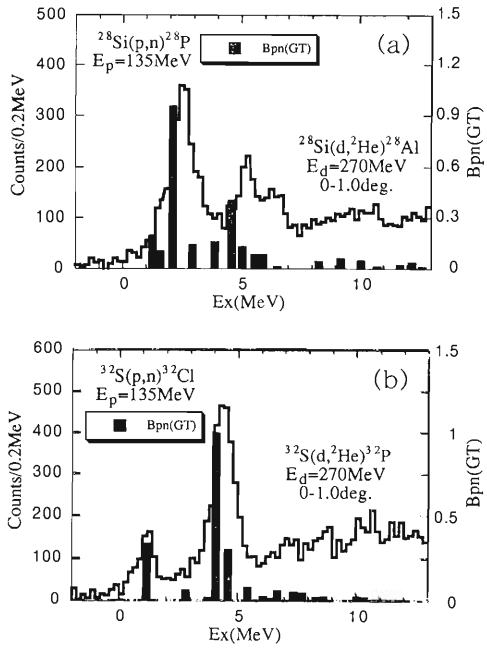

Fig. 1. Spectra (a) and (b) are for comparison of the (d, ^{2}He) with (p,n) reactions on ^{28}Si and ^{32}S, respectively. Bpn(GT) from (p,n) experiments at IUCF.[2,3]

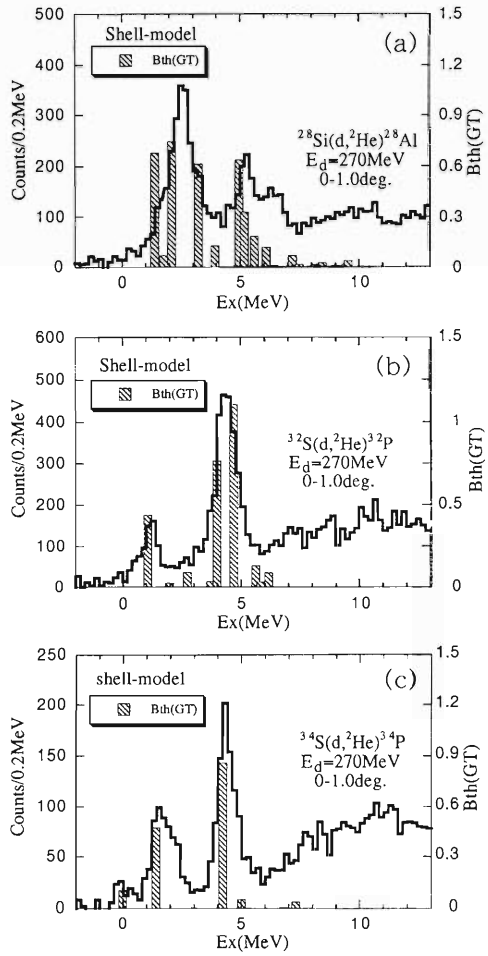

Fig. 2. Comparison of the (d, ^{2}He) excitation-energy spectra with the GT strengths of shell-model calculation by OXBASH on (a) ^{28}Si, (b) ^{32}S, and (c) ^{34}S.

can reproduce well the (d, ^{2}He) spectra on ^{28}Si, ^{32}S and ^{34}S. In Fig. 2(c), the spectrum of (d, ^{2}He) on ^{34}S ($N = Z + 2$ nucleus) agrees well with the shell-model calculation by OXBASH code. Therefore, present data indicates that the (d, ^{2}He) reaction is a useful tool for the study of GT strength in the $N \geq Z$ nuclei.

References

1) H. Okamura et al.: Nucl. Instrum. Methods Phys. Res. A **406**, 78 (1998).
2) B. D. Anderson et al.: Phys. Rev. C **43**, 50 (1991).
3) B. D. Anderson et al.: Phys. Rev. C **36**, 2195 (1987).

Transverse Momentum Distribution of Fragments in Reaction ^{40}Ar + ^{9}Be

S. Momota, M. Notani, N. Fukuda, H. Iwasaki, K. Yoneda, H. Ogawa, N. Aoi, S. Ito, T. Teranishi, N. Inabe, T. Kubo, T. Nakamura, H. Okuno, A. Ozawa, H. Sakurai, T. Suzuki, Y. Watanabe, A. Yoshida, and I. Tanihata

[NUCLEAR REACTIONS: ^{9}Be(^{40}Ar, X), E(^{40}Ar) = 90A MeV, Angular distribution of projectile-like fragments]

The momentum distribution of projectile-like fragments provides us information on the nuclear reaction through which fragments are produced. We have performed a systematic observation of momentum distribution for projectile fragments in the transverse direction.

The projectile fragments were produced by the reaction ^{9}Be(^{40}Ar, X)^{A}Z at the beam energy E(^{40}Ar) = 90A MeV. The produced fragments were selected and analyzed with a RIPS spectrometer.[1] The ^{40}Ar beam was deflected by a swinger magnet before the ^{9}Be target with a recoil angle of θ_x, and its acceptance of RIPS was defined by x-y slits after the ^{9}Be target. The magnetic rigidity of the RIPS was set at 3.71 Tm. The rigidity acceptance of the RIPS was set at $\Delta B\rho/B\rho$ = 1% by a slit at the momentum-dispersive focal plane (F1).

Particle identification (PI) was performed event by event by measuring the time-of-flight (TOF) and the energy loss (ΔE). The detectors for PI, that is two silicon counters (SSD's) and a plastic scintillation counter (PL) were located at the momentum-achromatic focal plane (F2). The TOF of each fragment over the 21.3 m of flight-path between the ^{9}Be target and F2 was determined by the PL timing and the RF timing of RIKEN Ring Cyclotron. The ΔE was measured by SSD's. Observed production rate of fragments was normalized by the beam current monitored by two sets of current-monitor counters, placed on the upstream- and downstream-side of the ^{9}Be target. The profile of the secondary beam at F2 was monitored by the parallel-plate avalanche chamber (PPAC).

Figure 1 shows a typical transverse-momentum distribution of fragments observed. As seen in Fig. 1, the result is well reproducible by a Gaussian distribution, and its dispersion, σ_T can be derived by fitting. Figure 2 shows the σ_T obtained as a function of the longitudinal momentum p_L per unit mass. A correlation between σ_T and p_L is found in Fig. 2. In the region $p_L > 440A$ MeV/c, σ_T is well reproduced by the formulae in Refs. 2 and 3. In the region $p_L < 440A$ MeV/c, σ_T increases as p_L decreases. This correlation suggests the contribution of multi-step process in the nuclear reaction at the intermediate beam energy, $E = 90A$ MeV.

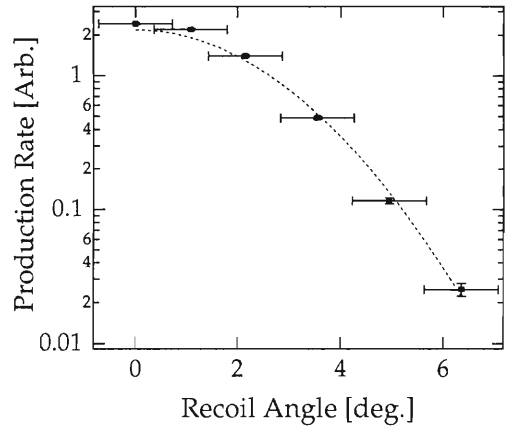

Fig. 1. Observed angular distribution of ^{21}O

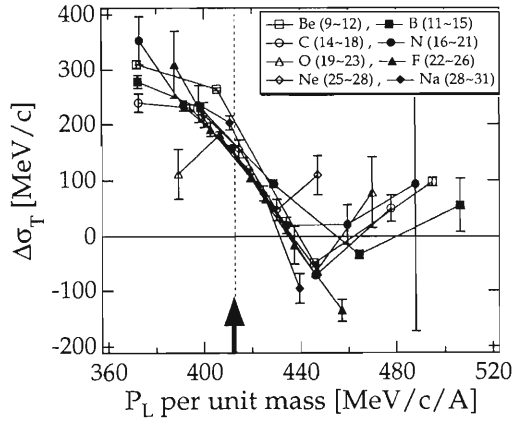

Fig. 2. Correlation between σ_T and p_L The contributions from the Fermi momentum of removal nucleons, σ_F,[2] and from the deflection of projectiles in the field of the target nucleus, σ_D,[3] are subtracted from σ_T to derive $\Delta\sigma_T$.

References

1) T. Kubo et al.: Nucl. Instrum. Methods Phys. Res. B **70**, 309 (1992).
2) A. S. Goldhaber: Phys. Lett. B **53**, 306 (1974).
3) K. van Bibber et al: Phys. Rev. Lett. **43**, 840 (1979).

Projectile-like Fragment Momentum Distributions from ^{40}Ar + ^{nat}Ta Reaction at 94A MeV

Z. Liu, M. Notani, H. Sakurai, S. M. Lukyanov, N. Aoi, D. Beaumel, N. Fukuda, M. Hirai, E. Ideguchi, N. Imai, M. Ishihara, H. Iwasaki, T. Kubo, K. Kusaka, H. Kumagai, T. Nakamura, H. Ogawa, Yu. E. Penionzhkevich, T. Teranishi, Y. X. Watanabe, K. Yoneda, and A. Yoshida

[NUCLEAR REACTIONS: ^{nat}Ta(^{40}Ar, X), E/A = 94 MeV; Measured 0° momentum distributions of projectile-like fragments]

The production of neutron-rich isotopes by projectile-like fragmentation shows a very strong target dependence[1,2] at intermediate energies. To understand underlying mechanism, parallel momentum distributions of projectile-like fragments (PLFs) including transfer reaction products were measured.

The present measurement was performed at RIPS.[3] The ^{40}Ar beam at 94A MeV bombarded a 17 mg/cm^2 ^{nat}Ta target. The beam current was monitored by two plastic hodoscopes around the target. RIPS was operated in a double achromatic mode. The angular acceptance was set to be ±12.5 mrad in both horizontal and vertical direction. At this energy, PLFs were fully stripped. Particle identification was done unambiguously by a combination of time of flight (TOF), energy loss (ΔE) and magnetic rigidity ($B\rho$) measurement. The TOF of a fragment was measured by two plastic detectors at F2 and F3. The ΔE was determined by two 1.1 mm SSD detectors at F3. The $B\rho$ was obtained by position information provided by the PPAC at F1 together with NMR measurements of the RIPS dipole fields. Momentum distributions of PLFs were measured at 30 $B\rho$ settings covering a range of 2.53–3.97 Tm with momentum acceptance $\Delta p/p$ = ±0.5% at lower $B\rho$ settings and ±2.0% at higher $B\rho$ settings. The double differential cross sections $d^2\sigma/dpd\Omega$ around 0° have been deduced by taking into account of PPAC detection efficiency, and dead time correction. The momentum broadening due to the target thickness is only 0.5% for the fragments very close to the projectile. No correction for momenta was performed. To avoid too high count rate on PPACs beam current on the target was adjusted at every $B\rho$ setting. The error in beam current evaluation is less than 20%.

Momentum distributions have been obtained for 70 individual PLFs of elements ranging from B (Z = 5) to K (Z = 17). As an example, the momentum distribution of ^{24}Na is shown in Fig. 1, with the bin size corresponding to $\Delta p/p$ = 1.0%. Only stastical error is shown in Fig. 1. The low-momentum side is wider than the high-momentum side for every fragment. Except the low-momentum tail, the whole of the distribution is resonably described by an asymmetric Gaussian function with different standard deviations σ_h and σ_l on the high and low-momentum side, respectively. The widths σ_h obey very well the Goldhaber law[4] extracted from "pure" fragmentation at relativistic energies. The best fit to σ_hs gives a reduced width of σ_0 = 85.1 MeV/c, in agreement with the systematics in the intermediate energy domain.[5]

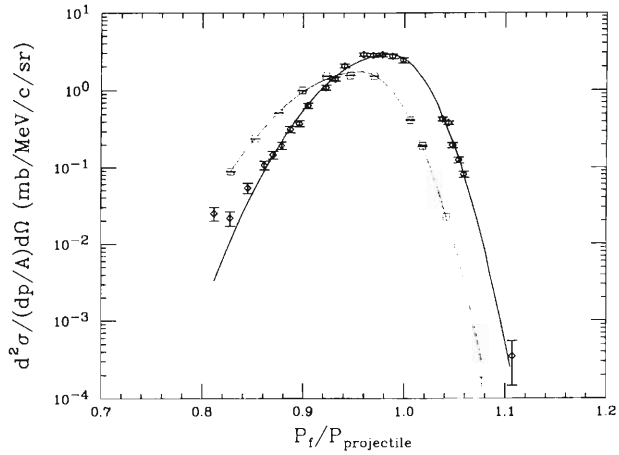

Fig. 1. Momentum (expressed in momentum per nucleon) distributions of ^{24}Na from the ^{40}Ar+^{nat}Ta reaction (diamond) and the ^{40}Ar+^{9}Be reaction (square). Momenta have been normalized to the beam momentum in the middle of the target. Solid lines represent the fittings using the asymmetric Gaussian function.

Some proton pickup PLFs were observed, of which momentum distributions have been obtained for ^{38,39,40}K. Their most probable momenta are lower than those of the neighboring nucleon removal PLFs, due to the dissipative nature of the nucleon transfer process. Interestingly, their most probable momenta and σ_h widths can be well explained by simply assuming that one proton is picked up from the target with a momentum of 270 MeV/c (Fermi momentum of Ta) oriented along the beam direction by the Ar PLFs with the same N. The cross sections of these K isotopes are 1–2 order of magnitude smaller than those of the Ar PLFs with the same N.

Comparison was made between the present data and the Be target data[6] (^{40}Ar beam at 90A MeV). Momentum distrubution of ^{24}Na from the Be target reaction is also shown in Fig. 1. Compared with the Ta target data, the most probable momenta in the Be target are systemactically shifted downwards and the widths are wider, especially on the low-momentum side. These observations indicate that fragments consume more beam energy in the Be target than in the

Ta. Thus the prefragments produced in the reaction with Be target may be hotter, which may hinder the production yields of very neutron-rich isotopes. On the other hand, it has been suggested that transfer process is responsible for the production of very neutron-rich isotopes with heavy targets.[1)] Then larger energy consumption for fragments from Ta target if the reaction mechanism is the same for Be target and Ta target. However, our result is contrary to this hypothesis. For further investigation on the production mechanism of neutron-rich isotopes, we will study product cross section as a function of Z for a given mass A and compare them between light and heavy targets.

References

1) D. Guerreau: Nucl. Phys. A **447**, 37c (1985).
2) H. Sakurai et al.: Nucl. Phys. A **616**, 311c (1997).
3) T. Kubo et al.: Nucl. Instrum. Methods Phys. Res. B **70**, 309 (1992).
4) A. S. Goldhaber: Phys. Lett. B **53**, 306 (1974).
5) V. Borrel et al.: Z. Phys. A **324**, 205 (1986).
6) M. Notani: private communication.

Measurement of Fusion Cross Section of Neutron-Skin Nucleus ^{6}He

Y. X. Watanabe, N. Aoi, N. Fukuda, T. Fukuda, M. Hirai, N. Imai, M. Ishihara, H. Iwasaki, Y. Mizoi, M. Notani, H. Ogawa, H. Sakurai, Y. Watanabe, K. Yoneda, and A. Yoshida

[NUCLEAR REACTION ^{40}Ar(^{6}He,X), E_{CM} = 3–15 MeV]

In the energy region near and below the Coulomb barrier, the fusion cross section of a neutron-rich nucleus is expected to be strongly enhanced as compared to a usual nucleus due to the extraordinary structure of the neutron-rich nucleus.[1,2] We have measured the fusion cross section between a neutron skin nucleus ^{6}He and ^{40}Ar in the vicinity of the Coulomb barrier with RIPS at the RIKEN cyclotron facility. We report the experiment and the present status of the analysis.

A ^{9}Be production target with 1656 mg/cm^2 thickness was bombarded with a ^{11}B beam. The energy and intensity of the primary beam were 70 MeV/u and 200 pnA, respectively. The ^{6}He beam was separated by RIPS from other reaction fragments. The secondary beam was decelerated with an aluminum degrader, and the beam energies in the center of mass system at the reaction were from 3 MeV to 15 MeV. The energy of ^{6}He was determined event by event by measuring a time of flight between two plastic scintillators placed at intervals of 5.3 m. The ^{6}He beam was led into a multiple-sampling and tracking proportional chamber (MSTPC),[3] which had been developed by our group to detect a three-dimensional image of several tracks of charged particles and to detect the energy loss of those particles along their tracks. The MSTPC was filled with a mixed gas (argon:98%, methane:2%) at 100 torr pressure, where the gas acted as a target as well as a detection gas. The positions and energy losses of charged particles were sampled by 64 cathode plates (called PAD's) aligned at 11 mm intervals along the beam line.

Figures 1 and 2 show an example of the energy losses for a fusion event and an elastic scattering event,

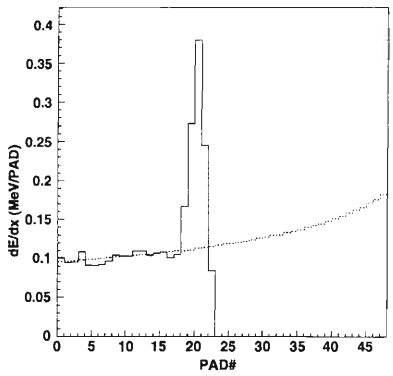

Fig. 1. An example of the energy losses for a fusion event. Abscissa indicates the PAD number. Dotted line shows the energy losses in the case of no reaction.

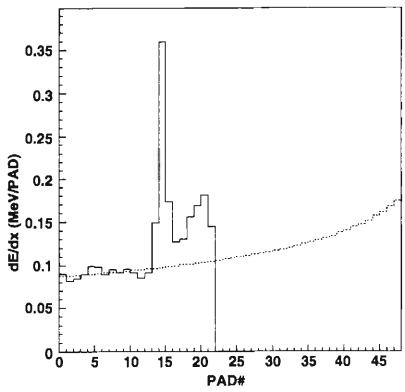

Fig. 2. An example of the energy losses for an elastic scattering event. Abscissa indicates the PAD number. Dotted line shows the energy losses in the case of no reaction.

respectively. In both figures, the abscissas indicate the PAD number, and the ordinates give the energy loss dE/dx. Figure 3 shows an example of the tracks of the projectile and target nuclei in an elastic scattering event. The abscissas indicate the PAD number, and the ordinate of the upper (lower) panel gives the horizontal (vertical) position. Size of the circles is proportional to the magnitude of the energy loss. We can pick up fusion events out of other reaction events by examining the tracks and the energy losses. The further analysis is in progress.

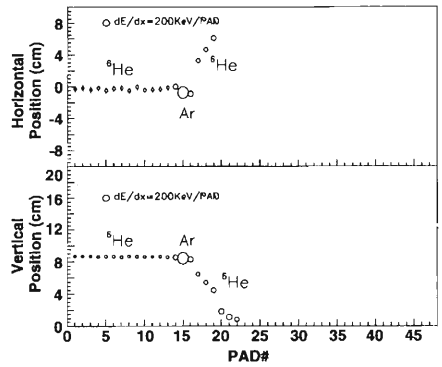

Fig. 3. Horizontal and vertical tracks of elastic scattering event.

References

1) N. Takigawa et al.: Phys. Rev. C **47**, R2470 (1993).
2) J. A. Christley et al.: Nucl. Phys. A **587**, 390 (1995).
3) Y. Mizoi et al.: RIKEN. Accel. Prog. Rep. **30**, 143 (1997).

Observation of Excited State in ^{7}He with Unusual Structure

A. A. Korsheninnikov, M. S. Golovkov, A. Ozawa, E. A. Kuzmin, E. Yu. Nikolskii, K. Yoshida, B. G. Novatskii, A. A. Ogloblin, I. Tanihata, Zs. Fülöp, K. Kusaka, K. Morimoto, H. Otsu, H. Petrascu, and F. Tokanai

[NUCLEAR REACTIONS, Radioactive nuclear beam, p(^{8}He, d), p(^{8}He, d^{6}He), p(^{8}He, d^{4}He), p(^{8}He, dn), p(^{8}He, dn^{6}He), p(^{8}He, dn^{4}He), E/A = 50 MeV]

A novel step in the experiments with exotic nuclear beams, namely, investigation of transfer reactions, is reported. We studied the reaction p(^{8}He, d)^{7}He for the spectroscopy of ^{7}He.

It is well known that nuclei have excited states. There is a famous exception from this rule, the absence of excited states in ^{3}He and ^{3}H. Another kind of exception was considered to be ^{7}He. This nucleus was investigated for 30 years in many reactions with stable beams, and no excited states were found. As a result, ^{7}He began to be considered as a nucleus which may not have excited states.

Exotic nuclear beams are the most promising tool to study as neutron rich systems as ^{7}He. We used beam of ^{8}He at 50 A MeV, that was produced by the RIPS facility, and studied the p(^{8}He,d)^{7}He reaction with the CH_2 and C targets. To study transfer reactions with exotic beams, a special detection system, the RIKEN telescope, was designed (Fig. 1). It represents a stack of solid-state position-sensitive detectors that have large area and annual hole. Using this telescope, we detected deuterons at small angles in the laboratory system (5°–25°) corresponding to a high cross section. Particles from the ^{7}He decay (^{6}He, ^{4}He, and neutrons) were measured by the downstream detectors (Fig. 1).

The obtained deuteron spectra (inclusive and detected in coincidence with ^{6}He, ^{4}He, and neutron) showed not only the well known ground state of ^{7}He, but also an excited state. For example, this excited state is seen in Fig. 2, where we show the spectrum of deuterons detected in coincidence d + ^{4}He + n. The ground state is not seen in this spectrum, because ^{7}He$_{g.s.}$ is lower than the ^{4}He-decay threshold. The most interesting finding is that the revealed excited

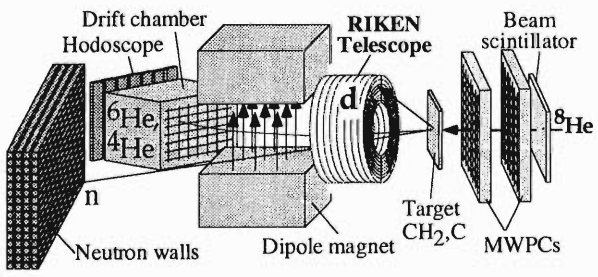

Fig. 1. Scheme of the experimental setup.

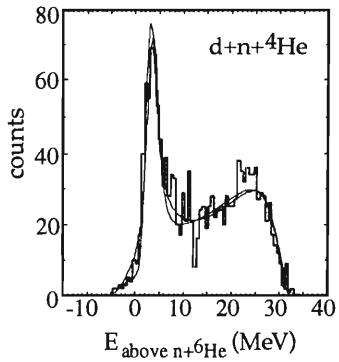

Fig. 2. Deuteron spectrum from reaction p(^{8}He, dnα).

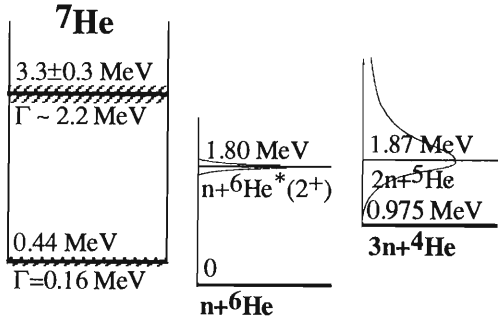

Fig. 3. Decay scheme of ^{7}He.

state decays predominantly into 3n + ^{4}He, but not into n + ^{6}He. The obtained parameters of ^{7}He* are $E = 3.3 \pm 0.3$ MeV (energy above the n + ^{6}He threshold), $\Gamma = 2.2 \pm 0.3$ MeV, and the decay branching $\Gamma\alpha/\Gamma_{tot} = 0.7 \pm 0.2$. The ^{7}He decay scheme is shown in Fig. 3.

Most likely, the ^{7}He excited state has a structure with an excited neutron on the top of ^{6}He-core that is in the excited 2^+-state. It is consistent with the structure of 8He used as a beam: the ^{8}He wave function obtained in the α + 4n model[1] shows[2] that the ^{6}He-subsystem has mainly $J^\pi = 2^+$. The measured decay branching gives a weight of ^{6}He* in ^{7}He* as $P = 0.9 \pm 0.1$.

References

1) M. V. Zhukov, A. A. Korsheninnikov, and M. H. Smedberg: Phys. Rev. C **50**, R1 (1994).
2) M. V. Zhukov: private communication.

Momentum Distributions of Projectile Fragments for Light Proton Drip-Line Nuclei

M. Mihara, M. Fukuda, T. Fukao, M. Tanigaki, T. Onishi, K. Matsuta, Y. Nojiri, T. Minamisono, T. Ohtsubo, M. Ishihara, T. Nakamura, S. Fukuda, S. Ito, T. Kobayashi, S. Momota, A. Ozawa, T. Suzuki, I. Tanihata, and K. Yoshida

[NUCLEAR REACTIONS: ^{9}C + Si, E = 55 MeV/nucleon, ^{7}Be, ^{8}B, ^{9}C + Be, C, Al, E = 30–70 MeV/nucleon; Measured momentum distributions]

In order to elucidate the nature of loosely bound proton, we have measured the longitudinal and transverse momentum distributions of ^{7}Be and ^{8}B fragments resulting from the breakup of ^{9}C on a thin Si target collided at an energy of 55 MeV/nucleon. The transverse momentum distributions of fragments for the (^{7}Be, ^{6}Li), (^{8}B, ^{6}Li), (^{9}C, ^{8}B), and (^{9}C, ^{7}Be) processes were also measured with thick Be, C, and Al targets at 30–70 MeV/nucleon of collision energy.

Unstable secondary nuclear beams of ^{7}Be, ^{8}B, and ^{9}C were produced through the ^{12}C + Be collision of a 135A MeV ^{12}C primary beam with the intensity ~500 pnA provided by the RIKEN ring cyclotron, and were separated by the RIKEN projectile-fragment separator (RIPS). A secondary beam intensity of 200–1000 pps was achieved. The particle detector system was consisted of three parallel-plate avalanche counters (PPACs) placed at intervals of about 30 cm along the beam axis, four thin (100 and 150 μm) Si counters, and a large (60 cm × 60 cm × 3 mm thick) plastic scintillator placed about 2 m away from a vacuum detector chamber within which the most downstream (3rd) PPAC and Si counters were set. For the thin Si target runs, the 2nd and 3rd Si counters were used as a reaction target with the thickness of 250 μm which was enough thin to suppress the energy spread of projectile fragments in the target, and the next (3rd and/or 4th) counters after the target were used for particle identification. For the thick Be, C, and Al target runs, each target was inserted between the 1st and 2nd Si counters so that the incident particles lose their kinetic energy by about 20 MeV/nucleon in the target. The projectile fragments produced in each reaction target were clearly identified by means of ΔE in the Si and plastic counters and by the time-of-flight (TOF) between the PPACs and the plastic counter. The longitudinal momentum of the projectile fragments was deduced from the TOF, and the transverse momentum from the horizontal positions of the PPACs and plastic counter which gave the horizontal emerging angle of fragments.

The widths (FWHM) of the momentum distributions were deduced from the width of present spectra by subtracting that of the system resolutions, which were compared with the Goldhaber model.[1] In Fig. 1, ratios of the present momentum widths to the ones expected from the Goldhaber model are plotted as a function of the separation energy of removed nucleons. The transverse momentum widths for each fragmentation process does not show any dependences on the target and beam energy, so that the averaged values were possible to show in this figure. The result reported previously on the momentum distributions of ^{7}Be observed through the ^{8}B fragmentation[2] is also shown. The widths which become narrower with decreasing the separation energy are, however, much broader than those for the case of neutron rich nuclei[3-5] as seen in Fig. 1. The transverse momentum widths are about 50% larger than the longitudinal ones for the case of the one-proton removal from ^{8}B and ^{9}C.

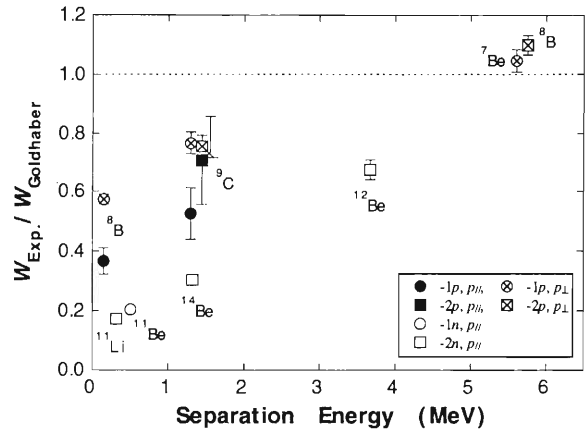

Fig. 1. Ratio of the experimental momentum width to the width expected from the Goldhaber model plotted as a function of the separation energy of removed nucleon(s).

References

1) A. S. Goldhaber: Phys. Lett. B **53**, 306 (1974).
2) M. Mihara et al.: RIKEN Accel. Prog. Rep. **30**, 55 (1997).
3) J. H. Kelly et al.: Phys. Rev. Lett. **74**, 30 (1995).
4) F. Humbert et al.: Phys. Lett. B **347**, 198 (1995).
5) M. Zaher et al.: Phys. Rev. C **48**, R1484 (1993).

Charge Exchange Reaction of ^{14}Be

S. Takeuchi, S. Shimoura, T. Motobayashi, H. Akiyoshi, Y. Ando, N. Aoi, Z. Fülöp, T. Gomi, Y. Higurashi, M. Hirai, N. Iwasa, H. Iwasaki, Y. Iwata, H. Kobayashi, M. Kurokawa, T. Minemura, S. Ozawa, H. Sakurai, M. Serata, T. Teranishi, K. Yamada, Y. Yanagisawa, L. Zhong, and M. Ishihara

[NUCLEAR REACTIONS: ^{1,2}H(^{14}Be, ^{14}B*), 74 A MeV; Charge exchange reaction; Isobaric analog state; Neutron halo]

Charge exchange reaction ^{14}Be(p, n)^{14}B* in inverse kinematics has been performed to investigate the Isobaric Analog State (IAS) of ^{14}Be and its neutron halo structure. The present reaction is useful to excite IAS, as shown in the recent work[1,2] of the neutron halo nucleus ^{11}Li. The IAS of ^{14}Be is characterized by its isospin of $T = 3$ while the other populated states are mostly $T = 2$ states. It is expected that $T = 2$ states of ^{14}B* decays to many channels, but only the ^{12}Be + p + n channel ($T = 3$ and 2) is relevant to the IAS because of the isospin selectivity (see Fig. 1). Thus, the IAS can be revealed by detecting ^{12}Be, proton, and neutron in coincidence.

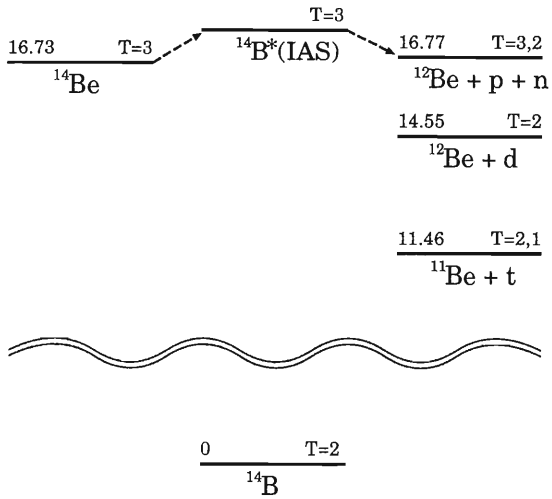

Fig. 1. Energy level scheme associated with the charge exchange reaction and particle decay of ^{14}B*. Energies are shown in MeV.

In order to identify the Fermi transition of ^{14}Be to IAS, the (d, 2n) reaction was also measured in the present experiment. The (d, 2n) reaction does not populate Fermi states, while the (p, n) reaction can cause the Fermi transition and the Gamow-Teller transition. The IAS excited by Fermi interaction can be identified by subtracting the yield of the Gamow-Teller transition.

The ^{14}Be beam was produced by using the projectile fragmentation of a 100 A MeV ^{18}O beam on 1110 mg/cm^2 ^{9}Be target. Energy of the incident ^{14}Be beam was determined event-by-event by measuring the time of flight (TOF) between F2 and F3 plastic scintillators whose thicknesses was 0.5 and 0.3 mm, respectively. After traversing the beam detectors at F2 and F3, the ^{14}Be beam was focused on the $(CH_2)_n$, $(CD_2)_n$, and C targets with the thicknesses of 187, 204, and 152 mg/cm^2, respectively. The average beam energy was 74 A MeV at the middle of the target with a typical intensity of about 10^4 cps. The C target was used for subtracting the contributions from carbon nuclei in the $(CH_2)_n$ and $(CD_2)_n$ targets. Outcoming charged particles were detected by ΔE and E hodoscopes which were located at 492 cm downstream from the target. Those hodoscopes consisted of vertically segmented 5 mm thick plastic scintillators and two layers of horizontally segmented 6 cm thick plastic scintillators. Velocities of charged particles and of neutrons were determined by the TOF over the 492 cm flight path between the target and the hodoscope. Charged particles were identified by using the ΔE-E and TOF-E methods.

The decay particles from ^{14}B* were detected in coincidence, from which the momentum vectors were determined by combining their velocities with hit position on the hodoscope. The energy and width of IAS will be obtained from the decay energies of ^{12}Be, proton, and neutron.

In the present states we are working on the calibration and particle identification. Momentum resolution ($\Delta P/P$) is about 1.5% for charged particles. Further analyses are in progress to determine the energy and width of IAS.

References

1) S. Shimoura et al.: Nucl. Phys. A **630**, 387c (1997).
2) T. Teranishi et al.: Phys. Lett. B **407**, 110 (1997).

Coulomb Dissociation of ^{11}Be and ^{15}C

N. Fukuda, T. Nakamura, T. Kobayashi, H. Otsu, N. Aoi, N. Imai, H. Iwasaki,
T. Kubo, A. Mengoni, M. Notani, H. Sakurai, S. Shimoura, T. Teranishi,
Y. X. Watanabe, K. Yoneda, and M. Ishihara

[^{11}Be + Pb, ^{15}C + Pb, Coulomb dissociation, Direct breakup, Coulomb post-acceleration]

We have measured the Coulomb dissociation of ^{11}Be as well as ^{15}C using the radioactive beam line RIPS at RIKEN Ring Cyclotron Facility.

A significant $E1$ strength at lower excitation energy has been observed by the Coulomb dissociation experiment for the neutron halo nuclei ^{11}Be[1] and ^{11}Li. For the explanation of this characteristic feature, following three intuitive pictures are proposed[2]: a direct breakup mechanism; a resonant breakup mechanism; and a free-particle breakup mechanism. The results of the previous ^{11}Be Coulomb dissociation experiment[1] support the direct breakup mechanism based on the shape of the low-lying strong $E1$ distribution and based on the significant longitudinal momentum difference between the halo neutron and the core nucleus: namely, Coulomb post-acceleration effect.

Though the direct breakup mechanism provides a good discription of the experimetal results, the mixture with the free-particle mechanism cannot be excluded, which can be probed by the transverse Coulomb post-acceleration effect. Aming at the more detailed understanding of the reaction mechanism, we did experiment with emphasis on the measurement of the transverse Coulomb post-acceleration effect. Breakup of ^{15}C as well as ^{11}Be has been measured, scince ^{15}C is similar nucleus to ^{11}Be having a $2s_{1/2}$ valence neutron, whereas, its one-neutron separation energy (S_n = 1.2 MeV) is larger than that of ^{11}Be (S_n = 0.5 MeV). The comparison between these nuclei may give us a knowledge of the dependence of the reaction mechanism on the one-neutron seperation energy .

Another interest is a higer order effect in the Coulomb dissociaion. In the previous experimental results, the angular distribution of the outgoing particle suggests that the $E1$ transition is dominated in the Coulomb dissociation. But, it was difficult to make a quantitative discussion about the mixture with higher order effects due to the insufficient statistics. We have measured the angular distribution of outgoing particles more precisely than measured in previous experiment.

In present experiment, the momentum vectors of the two outgoing particles, ^{10}Be + neutron (^{14}C + neutron), have been measured in coincidence for the reaction of ^{11}Be + Pb (^{15}C + Pb) at 74 MeV/nucleon. The ^{11}Be and ^{15}C ion beams have been produced from the ^{18}O primary beam at 100 MeV/nucleon. The typical secondary beam intensities were about 50 kcps for both nuclei. The experimental setup was almost the same as that for the previous ^{11}Be Coulomb dissociation experiment. The energy of the beam was determined from the time of flight measured with two thin plastic scintillators which were placed 4.65 m apart along the beam line. The position and direction of the beam were measured with two sets of Multi-Wire Drift Chamber (MWDC). The momentum of the outgoing charged particle was measured by the magnetic spectrometer with a tracking drift chamber and by the plastic scintillator hodoscopes. For the neutron detection, a special care was taken to determine the transverse momentum shift with a high precision. We used two layers of the plastic scintillator hodoscope (2.1×0.9 m^2) which is composed of long plastic scintillator bars in order to cover a large angular acceptance. The neutron hodoscopes were placed at the 0 degree position covering angles up to 17 degree, corresponding up to 112 MeV/c in momentum. The number of accumulated events in the current experiment are about twenty times as many as that in the previous experiment. The analysis of the experimental data is in progress.

References

1) T. Nakamura et al.: Phys. Lett. B **331**, 296 (1994).
2) T. Kido et al.: Phys. Rev. C **53**, 2296 (1996).

RIKEN Accel. Prog. Rep. 32 (1999)

Shell Structure Study of the Proton Rich Nucleus ^{17}Ne via the (p, 2p) Reaction

H. Otsu, T. Kobayashi, T. Ujiie, M. Sekiguchi, T. Okuda, A. Ozawa, K. Yoshida, T. Suzuki, I. Tanihata, S. Ito, T. Nakamura, and N. Fukuda

[NUCLEAR REACTIONS ^{1}H(^{17}Ne, 2p)p^{15}O, E/A = 60 MeV/u]

The ^{17}Ne(p, 2p) reaction was measured by means of an inverse kinematics method with the radioactive ^{17}Ne beam.

A variety of new features in nuclear structures have been revealed via studies to use unstable nuclei. Neutron skin or halo structures[1] are the topic of this decade. On the other hand, the proton shell structures should be also studied in order to answer the questions such as: (1) Can protons also form the skin or halo structure? (2) How the Coulomb interaction destructs the isospin symmetry feature?

One of the best ways to obtain the proton shell information is to measure the proton knock-out (p, 2p) reaction.[2,3] The direct knock-out reaction becomes dominant by means of the probes with a high energy enough to interact with individual nucleons in the nucleus. For nucleon probes, such energies are in the region larger than 100 MeV where the de Broglie wavelength becomes the same order of the size of nucleons. By means of the inverse kinematics, the (p, 2p) reaction is utilized to study for structures of unstable nuclei.

A proton rich nucleus like ^{17}Ne is one of the candidates for the proton halo nucleus, while the proton shell configuration of ^{17}Ne is not well known. If a proton s shell is dominant in the ground state configuration, it is possible to form the proton halo structure. On the other hand, if a proton d shell is dominant, the halo structure is not formed because of the centrifugal force. One supporting evidence for the s shell intrusion is indicated from low lying states of the neighborhood nucleus ^{16}F. Note that the s shell intrusion means that the s shell is below the d shell in terms of energy. Figure 1 shows the level schemes of ^{16}F and ^{15}O with a reference of the ^{17}Ne ground state. The ground and 0.193 MeV states correspond to $(2s_{1/2})^{\pi} \oplus (1p_{1/2})^{\nu}$, while the 0.424 MeV and 0.721 MeV states correspond to $(1d_{5/2})^{\pi} \oplus (1p_{1/2})^{\nu}$. In this way, the $2s_{1/2}$ shell is located below the $1d_{5/2}$ shell in ^{16}F. Such an intrusion may also occur in ^{17}Ne.

The proton ground state information can be derived from the final state of the proton knock-out reaction. The ^{16}F nucleus , which is a residual nucleus, decays to p + ^{15}O. A decay to the excited states of ^{15}O is not possible energetically from the states less than 4.65 MeV. The state of ^{16}F can be reconstructed via the invariant mass method from 4-momentum vectors of proton and ^{15}O. The proton shell configuration of ^{17}Ne can be obtained from population to these four states.

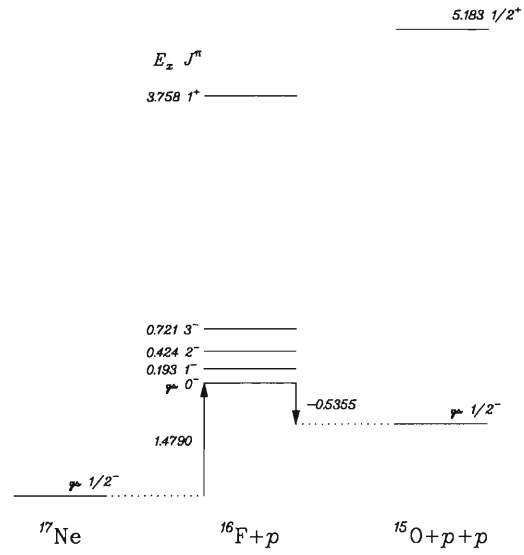

Fig. 1. Low lying states and their spin parity in ^{16}F and ^{15}O with the ^{17}Ne ground state as a reference.

The ^{17}Ne beam around 60 MeV/u on target was provided by the RIPS facility. The typical ^{17}Ne beam intensity was 4×10^4 s^{-1}. The beam was accompanied by other particles, mainly ^{15}O and ^{20}Ne. Then, the total beam intensity was 10 times larger than that of the ^{17}Ne beam. Each beam particle was detected and identified event by event with two plastic scintillators. One of the plastic scintillator was located at F2 position of the RIPS and the other scintillator was located just upstream the target position. Two drift chambers for beam track reconstruction were set between the downstream plastic scintillator and the target position. Each of the drift chamber had 4 planes for x and 4 planes for y. A CH_2 target with a 200 mg/cm^2 thickness was used. A carbon target with equivalent thickness for same beam energy loss was also used for subtraction of carbon contribution from the CH_2 target. Scattered and knocked-out protons were detected in coincidence by two proton telescopes located at ±43.5°, respectively, and 30 cm away from the target. The proton telescope consisted of 8 planes of drift chambers and a NaI scintillator. The residual particles, proton and ^{15}O, were detected in coincidence and particle-identified by $\Delta E - E$ detector hodoscopes located at 0° and 5 m downstream of the target. The ΔE

hodoscope consisted of ten plastic scintillators with size of $100(H) \times 1000(V) \times 5(t)$ mm^3. The E hodoscope consisted of 16 plastic scintillators with size of $1100 \times 60 \times 60$ mm^3. A Helium-bag was inserted along the flight path of the residual particles in order to decrease the multiple scattering effect, especially for ^{15}O. The energies of residual proton and ^{15}O were determined by the time of flight obtained by the signals from the $\Delta E - E$ hodoscopes and from the beam detectors. The momenta were determined from the positions on the detector walls and from the energies.

The analysis is now in progress.

References

1) I. Talmi and I. Unna: Phys. Rev. Lett. **4**, 469 (1960).
2) G. Jacob and Th. A. J. Maris: Rev. Mod. Phys. **38**, 121 (1966).
3) K. Hatanaka et al.: Phys. Rev. Lett. **78**, 1014 (1997); T. Noro et al.: Nucl. Phys. A **629**, 324 (1998).

Magnetic Moment and Electric Quadrupole Moment of the ^{18}N Ground State

H. Ogawa, K. Asahi, K. Sakai, A. Yoshimi, M. Tsuda,[*1] Y. Uchiyama, T. Suzuki, K. Suzuki, N. Kurokawa,[*2] M. Adachi, H. Izumi, H. Ueno, T. Shimoda, S. Tanimoto,[*3] N. Takahashi, W.-D. Schmidt-Ott, M. Schäfer,[*4] S. Fukuda,[*5] A. Yoshida, T. Kubo, H. Okuno, H. Sato, M. Notani, N. Aoi, K. Yoneda, H. Iwasaki, N. Fukuda, M. Ishihara, and H. Miyatake

[$^{18}N_{g.s.}$; β-NMR; Measured magnetic moment, Electric quadrupole moment]

The magnetic moment and electric quadrupole moment of the neutron-rich nucleus ^{18}N have been determined by a β-NMR method, taking advantage of the fragment spin polarization induced in the intermediate-energy projectile fragmentation reaction. To assure the existence of a sufficient polarization prior to the resonance search, a scheme of polarization measurement by means of an adiabatic field rotation has been developed and successfully incorporated in the β-NMR experiment. The polarization $P = 2.2 \pm 0.7\%$ has been obtained for ^{18}N fragments from the ^{22}Ne(110 MeV/u) + ^{12}C reaction at $\theta_L = 3.5 \pm 1.0°$ and $p = 8.07 - 8.32$ GeV/c. And from the observed resonance in a Pt stopper, the magnetic moment for the ^{18}N ground state has been determined to be $|\mu| = 0.3279 \pm 0.0013\ \mu_N$. The ^{18}N fragments have also been implanted in a single crystal Mg stopper. From the observed quadrupole frequency $|eqQ/h| = 73.2 \pm 1.4$ kHz, the electric quadrupole moment $|Q| = 12.3 \pm 1.2$ mb has been deduced by using the field gradient q given Refs. 1 and 2.

Shell model calculations were made using the OXBASH code[3] with the two sets of effective two-body interactions, PSDMK[3,4] and PSDWBT.[3,5] In Fig. 1(a) the experimental magnetic moment (negative in view of the calculated μ values) is compared with the theoretical μ. The agreement is quite good with the PSDMK interaction calculation. On the other hand, the PSDWBT calculation underestimates the $|\mu|$ value slightly. The experimental electric quadrupole moment is compared with the shell model calculations in Fig. 1(b). The calculated Q's seem to be quite stable against the choice of the effective interaction, but there appear substantial deviations from the experimental Q when the standard values for the neutron effective charge e_n are employed. The agreement improves by taking a much smaller value of $e_n = 0.3$. The quenching of e_n in a neutron-rich nucleus was previously indicated in the Q-moment measurement for ^{14}B and ^{15}B.[6]

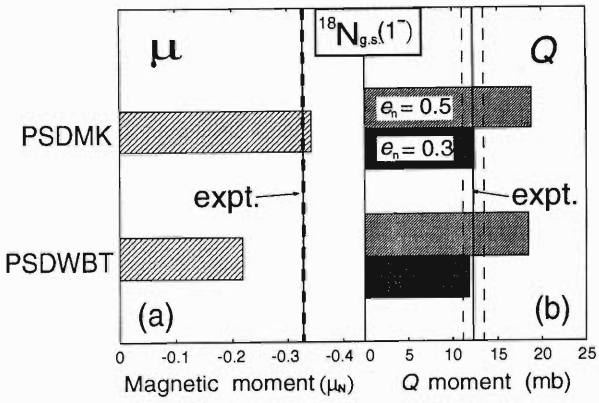

Fig. 1. Comparisons of the experimental (expt.) μ and Q values for the ^{18}N ground state ($I^\pi = 1^-$) with shell-model calculations using two different effective interactions (PSDMK, PSDWBT). Broken lines accompanying the experimental line indicate the experimental error. (For μ the error is so small that these lines may not be well identified). In the Q moment calculations, the effective charge for neutrons was varied from $e_n = 0.3$ to 0.5, while that for protons was fixed at $e_p = 1.3$ (because it hardly affects the Q value).

The μ value recently reported[7] and the Q value inferred in Refs. 7 and 8 from the level mixing resonance experiments by Leuven group are different from the present results by factors of about 0.5 and 3, respectively. Our NMR and NQR spectra, however, clearly indicate that there exist no resonances at the frequencies corresponding to such μ, Q values.

*1 Ultrasound Engineering Department, GE Yokokawa Medical System, Ltd.
*2 Research Laboratory for Nuclear Reactors, Tokyo Institute of Technology
*3 Central Research Laboratory, Hitachi, Ltd.
*4 Roland Berger and Partner GmbH
*5 The Energy Research Center, Wakasa Bay

References

1) T. Minamisono et al.: Phys. Lett. B **420**, 31 (1998).
2) M. Tokman et al.: Chem. Phys. Lett. **265**, 60 (1997).
3) B. A. Brown, A. Etchegoyen, and W. D. M. Rae: OXBASH, MSU Cyclotron Laboratory Report, No. 524, p. 1 (1986).
4) D. J. Millener and D. Kurath: Nucl. Phys. A **255**, 315 (1975).
5) E. K. Warburton and B. A. Brown: Phys. Rev. C **46**, 923 (1992).
6) H. Izumi et al.: Phys. Lett. B **366**, 51 (1996).
7) G. Neyens et al.: Presentation in ENAM98 Conf. (1998).
8) G. Neyens et al.: Phys. Lett. B **393**, 36 (1997).

The First Measurements of Half Lives and Neutron Emission Probabilities of Very Neutron Rich Nuclides of Mg, Al, Si, and P

K. Yoneda, H. Sakurai, N. Aoi, N. Fukuda, T. Gomi, E. Ideguchi, N. Imai, H. Iwasaki, T. Kubo, Z. Liu, S. M. Lukyanov, T. Nakamura, M. Notani, H. Ogawa, Y. E. Penionzhkevich, W.-D. Schmidt-Ott, S. Shimoura, E. Sokol, Y. X. Watanabe, A. Yoshida, X. Zhou, and M. Ishihara

[RADIOACTIVITY $^{31-33}$Na, $^{32-37}$Mg, $^{34-39}$Al, $^{37-42}$Si, $^{41-43}$P; measured $T_{1/2}$, delayed n-emission probabilities]

We report on the measurement of β-decay half lives ($T_{1/2}$) and β-delayed neutron emission probabilities (P_n) for very neutron-rich nuclei with Z = 11–15. This was the first measurement for $^{35-37}$Mg, $^{36-39}$Al, $^{37-42}$Si, and ^{43}P.

The experiment was carried out at RIPS. Neutron-rich nuclei were produced by the projectile fragmentation reaction of 70 MeV/nucleon ^{48}Ca beam with ^{9}Be and ^{181}Ta targets. Each fragment was identified on-line by measuring its time of flight and energy deposits in two Si detectors (0.35 mm^t and 0.5 mm^t). The nuclei were implanted separately into an active stopper, a 3 mm^t Si detector. When a nucleus with $Z \geq 11$ was identified, the primary beam was then turned off for a period much longer than the expected $T_{1/2}$, and during this beam-off period the β decay of the implanted nucleus was observed. The stopper Si detector was used for the detection of β rays. A neutron detector system was placed around the stopper to detect β-delayed neutrons in coincidence with β rays. The neutron detector consisted of 46 proportional counter tubes (32 mm diameter and 300 mm length) filled with 4 atm ^{3}He. The tubes were surrounded by organic glass for moderation of neutrons.

The preliminary results on $T_{1/2}$ are summarized in Fig. 1. $T_{1/2}$ were deduced from the maximum-likelihood fits to the decay curves, obtained from the time difference between the implantation of a nucleus and the detection of β rays.

The tentatively deduced P_n are shown in Table 1. Multiple neutron emission events are clearly indicated by $P_n > 100\%$. The efficiency of the neutron detector was calibrated to be 11.4 ± 2.3% from the measurement of β-delayed neutrons of ^{15}B, which has a known P_n of 100%.[1] The efficiency was also deduced to be 21.5 ± 4.2% from the measurement of β-delayed neutrons of ^{14}Be, which is a low energy neutron emitter (290 keV)[2] compared to ^{15}B.[1] Here we adopted the efficiency obtained from the measurement of β-delayed neutrons of ^{15}B, and it should be noted that the errors do not include ambiguities resulting from the energy dependence of the efficiency.

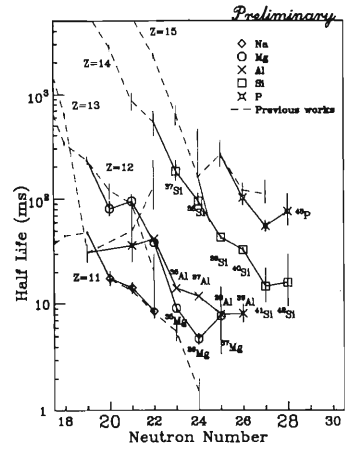

Fig. 1. Plot of half lives versus neutron number. The preliminary results of this work are plotted together with the literature values (dashed lines) compiled in Ref. 3

Table 1. Preliminary results on β-delayed neutron emission probabilities P_n.

nucleus	P_n (%)	nucleus	P_n (%)
^{31}Na	82 ± 42	^{37}Al	55 ± 11
^{32}Na	59 ± 17	^{38}Al	84 ± 19
^{33}Na	136 ± 34	^{39}Al	97 ± 22
^{32}Mg	6 ± 4	^{37}Si	15 ± 8
^{33}Mg	50 ± 18	^{38}Si	28 ± 7
^{34}Mg	58 ± 12	^{39}Si	60 ± 13
^{35}Mg	52 ± 11	^{40}Si	53 ± 12
^{36}Mg	48 ± 12	^{41}Si	103 ± 48
^{34}Al	30 ± 6	^{41}P	71 ± 21
^{35}Al	43 ± 9	^{42}P	57 ± 13
^{36}Al	55 ± 11	^{43}P	84 ± 47

References

1) R. Harkewicz et al.: Phys. Rev. C **44**, 2365 (1991).
2) N. Aoi et al.: Z. Phys. A **358**, 253 (1997).
3) G. Audi et al.: Nucl. Phys. A **624** 1, (1997).

Quadrupole Moment of ^{39}Ca

K. Matsuta, T. Minamisono, M. Fukuda, M. Mihara, T. Onishi, K. Sato, M. Sasaki, K. Minamisono, C. Ha, T. Miyake, H. Akai,[*1] T. Ohtsubo, S. Momota, Y. Nojiri, S. Fukuda,[*2] K. Yoshida, A. Ozawa, T. Suzuki, I. Tanihata, G. F. Krebs,[*3] J. R. Alonso,[*3] and T. J. M. Symons[*3]

[NUCLEAR STRUCTURE, Nuclear magnetic resonance, Measured quadrupole moment of ^{39}Ca ground state]

The electric quadrupole (Q) moment of ^{39}Ca ($I^{\pi} = 3/2^{+}$, $T_{1/2} = 0.86$ s) has been determined for the first time by applying the β-Nuclear Quadrupole Resonance (β-NQR) technique.

The experimental procedure is basically the same as the previous work.[1)] The polarized β-emitter ^{39}Ca was produced through the projectile fragmentation process in the 100A-MeV ^{40}Ca on Au collision and was purified using the fragment separator RIPS. For the optimum polarization, the ^{39}Ca nuclei which were ejected at 2.0° with the momentum higher than that of the beam velocity by 1.0% were selected. Thus polarized ^{39}Ca nuclei were slowed down by an energy degrader of controllable thickness and were implanted into a single crystal $CaCO_3$. The $CaCO_3$ catcher was placed in a strong magnetic field $H_0 = 9$ kOe, in order to maintain the polarization and for the NMR. The crystal c-axis was set perpendicular to the field. For the detection of the quadrupole coupling eqQ/h, the β-NQR method was used. In this method, the polarization was inverted by applying 6 rf oscillating magnetic fields sequentially, while the polarization was monitored through the β-ray asymmetry. The set of frequency was programmed for each quadrupole coupling constant based on the known magnetic moment $\mu = 1.0217\ \mu_N$. The present Larmor frequency is 4.673 MHz.

Figure 1 shows the observed β-NQR spectrum. Although the detected polarization effect for ^{39}Ca in $CaCO_3$ was 10 times smaller than the one in CaF_2, the present resonance is identified for the ^{39}Ca in the substitutional site, since we detect no other significant resonance for $|eqQ|/h$ at frequencies lower than 3.2 MHz. From the chi-square fitting analysis on the spectrum, the quadrupole coupling constant was determined to be $|eqQ|/h(^{39}\text{Ca in } CaCO_3) = 0.60 \pm 0.04$ MHz. The electric field gradient (EFG) at the substitutional site of Ca in the crystal was predicted to be $q = (7.0 \pm 1.0) \times 10^{20}$ V/m^2 from the first principles calculation of

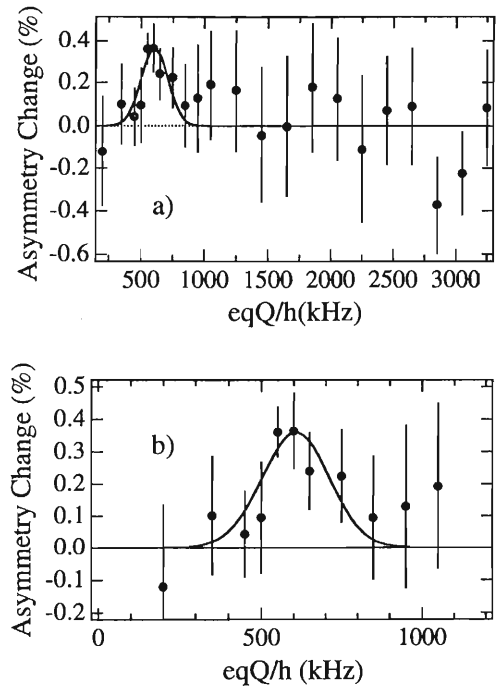

Fig. 1. NQR spectrum for ^{39}Ca in $CaCO_3$. a) Over-all view, b) Close-up view.

electronic band structure based on the KKR method. Since the EFG has not been measured yet, this predicted value of EFG was used for the determination of the Q moment. As a result, the quadrupole moment of ^{39}Ca was determined to be $|Q(^{39}\text{Ca})| = 36 \pm 7$ mb. The shell model value 26 mb predicted by the OXBASH code agrees with the present quadrupole moment.

References

1) K. Matsuta et al.: RIKEN Accel. Prog. Rep. **29**, 60 (1996).

*1 Department of Physics, Osaka University
*2 Energy Research Center, Wakasa Bay
*3 LBL, USA

Production of ^{44}Ti at the RIKEN RIPS Facility

Zs. Fülöp, M. Golovkov, T. Kato, K. Kimura,[*1] H. Kudo,[*2] Y. Mochizuki, H. Otsu, A. Ozawa, H. Petrascu, H. Sakurai, T. Suzuki,[*2] I. Tanihata, Y. Wakasaya, K. Yoshida, R. N. Boyd,[*3] and E. Somorjai[*4]

[Half-life, Nucleosynthesis]

The observation of the E_γ = 1157 keV line —characteristic to the decay of ^{44}Ti— in the Cassiopeia A[1] supernova called for the accurate determination of the half-life of ^{44}Ti ($T_{1/2} \sim 60$ y). In lack of reliable half-life data the initial amount of ^{44}Ti ejected by the Cassiopeia A cannot be given with a precision needed to test the various supernova models. In fact, since ^{44}Ti can also be produced in meteorites by means of cosmic-ray interactions, the half-life of ^{44}Ti also has impact on the galactic cosmic ray flux and its modulation by solar activity.[2] The abundance of ^{44}Ca in the solar system also may depend on the half-life of ^{44}Ti.[3]

In our study we have tested the feasibility of the RIKEN RIPS radioactive beam facility to produce ^{44}Ti beam. In order to estimate the half-life of ^{44}Ti with the implantation method (1) known amount of ^{44}Ti should be implanted to a stopper (or stack of stoppers) and (2) the γ-activity with respect to a ^{44}Ti characteristic line should be determined. During our test measurement the ^{44}Ti was produced by fragmentation of 2 particle nA, 90 A MeV ^{46}Ti on 200 mg/cm^2 thick Beryllium target. The projectile fragments were separated by the RIPS fragment separator with a 221 mg/cm^2 thick Aluminium wedge degrader placed between the two analyser dipole magnets. Through appropriate settings of the fragment separator we achieved high secondary beam intensity ($2 \cdot 10^5$/s) with high ratio of ^{44}Ti nuclei (> 50%) without implanting isotopes contributing to the gamma activity of the sample. Also, we kept the content of ^{42}Sc (same A/Z as ^{44}Ti, i.e. TOF determination is not enough to separate this isotope from ^{44}Ti) to minimum (< 5%).

Plastic scintillators have been mounted at F2 and F3 foci for on-line TOF measurements at full intensity, while a Si-detector at F2 focus for low intensity (200/s) energy loss measurements during the secondary beam tuning. The separated fragments have been implanted into a 1 mm thick plastic scintillator stopper allowing a loss-free determination of the number of implanted ions. Behind the stopper, an additional plastic scintillator served to check the presence of ions penetrating the stopper. In addition, two Parallel Plate Avalanche Counters[4] (PPAC) have been mounted to F3 focus to determine the distribution of the implanted ions in the stopper plastic scintillator. The information on the distribution can be used to take into account the effect of the finite source size on the activity determination.

The γ-activity of the implanted sample has been investigated by high-efficiency (120%) HPGE gamma detector. The laboratory background was suppressed by a 10 cm lead shield with additional 1.5 mm copper and 10 mm steel layers. A Lucite plate with a thickness of 2 mm supported the irradiated scintillator at 27 and 57 mm from the detector. Point-like sources of ^{60}Co and ^{22}Na have been used for efficiency calibration. There is no contamination observed in the gamma spectra of the irradiated sample with the exception of the ^{44}Sc^m isomeric state decay (E_γ = 271 keV, $T_{1/2}$ = 58.6 h). After 12 h of irradiation the decay yield of ^{44}Ti (detected as the gamma-decay of the ^{44}Sc daughter at 1157 keV) is higher than the ^{40}K laboratory background. Due to the excellent shielding of the system and the very small γ-contamination in the irradiated scintillator from the implantation, the 1157 keV peak originating from the decay of ^{44}Ti is the strongest in the spectrum. To follow the errors in the determination of the activity of the implanted ^{44}Ti we compared the yield of the ^{44}Sc daughter 1157 keV γ-line at two source-detector distances, one week and 14 weeks after the implantation. Having taken into the account the contribution of the ^{44}Sc^m isomeric state decay, no difference in the determined activities have been found within the achieved statistical limit (5%). It supports that no loss in the implanted ^{44}Ti occurred via diffusion and also proves the reliability of the efficiency determination.

Since the 1157 keV line is not the only one characteristic to the decay of ^{44}Ti, also an investigation is under course concerning the systematic errors occurring at the determination of the ^{44}Ti half-life using low energy (68, 78 keV) gamma lines from its decay.

References

1) A. F. Iyudin et al.: Astron. Astrophys. **284**, L1 (1994).
2) G. Bonino et al.: Science **270**, 1648 (1995).
3) D. Bodansky et al.: Phys. Rev. Lett. **20**, 161 (1968).
4) H. Kumagai and I. Tanihata: RIKEN Accel. Prog. Rep. **31**, 164 (1998).

*1 Nagasaki Institute of Applied Science
*2 Niigata University
*3 Ohio State University, USA
*4 ATOMKI, Hungary

Development of Polarized ^{129}Xe Solid for Polarization of Unstable Nuclei

K. Sakai, Y. Mizumura, T. Suzuki, K. Asahi, H. Ogawa, A. Yoshimi, Y. Uchiyama, M. Nagakura, H. Sato, A. Yoshida, T. Kubo, H. Okuno, M. Ishihara, K. Yoneda, M. Notani, H. Izumi, and S. Fukuda*

[Polarized ^{129}Xe solid, Cross polarization, Nuclear magnetic moment]

We have developed a polarized ^{129}Xe solid as an implantation medium (stopper) in which unstable nuclei are implanted and and their spins are polarized by the cross polarization process. A stopper for such a purpose should span a sufficiently large volume for the implantation, and should afford a high polarization $P_{\rm solid}$, a long spin relaxation time T_1, and a small spin-depolarization rate $D_{\rm cross}$ during the polarization transfer under a few gauss (G) field. As we reported previously,[1,2] about 80 mg of the ^{129}Xe solid has been obtained with $P_{\rm solid} \sim 1\%$, about 0.27 times the ^{129}Xe gas-phase spin polarization ($P_{\rm gas}$) produced with optically polarized Rb atoms, and $T_1 \sim 25$ min. This result implies that there is a large polarization loss ($D_{\rm loss} \sim 73\%$) during the condensation from the gas to solid phases, suggesting the importance of decreasing $D_{\rm loss}$ as well as of increasing $P_{\rm gas}$ and T_1 for achieving higher $P_{\rm solid}$. In present report, we describe the result of recent improvements aiming at decreasing the $D_{\rm loss}$.

In a typical procedure to produce a polarized ^{129}Xe solid, a ^{129}Xe gas at a pressure $p_{\rm Xe} = 1$–3 atm is introduced into a cylindrical glass cell, 4 cm long and 2 cm in diameter, together with a small amount of Rb vapor. The optical pumping is carried out by warming up to 350 K and illuminating it with a circularly polarized light from diode lasers. After the polarization the $P_{\rm gas}$ reaches 3–10%, the cell is cooled down by putting its bottom part ($8 \times 20 \times 2$ mm^3) into contact with a liquid nitrogen vessel. Thus, the ^{129}Xe gas condenses into a solid, maintaining its polarization in part.

The large $D_{\rm loss}$ observed previously is supposed to have resulted from i) the interaction between the ^{129}Xe and Rb in the gas phase and ii) short relaxation time T_1 after the condensation. The short T_1 may be due to a relatively high final temperature (>140 K) for the solid phase, since T_1 estimated for the solid at such a temperature was less than 4 min.[3] In order to remove the Rb vapor from the gas as soon as the pumping was finished, we cooled the main part of cell without a delay to about 270 K by blowing the cell with a cold nitrogen vapor before a liquid nitrogen was poured in.

Furthermore, in order to cool the ^{129}Xe solid to a lower temperature in a shorter time, the thermal contact between the cell and liquid nitrogen vessel was reinforced by introducing a cold finger and copper wire structure. With such efforts, the ^{129}Xe gas of $p_{\rm Xe} \leq 2$ atm turned to be able to condense within 5 min after the cooling was initiated. The various $P_{\rm solid}$ attained with different initial gas pressures were: $P_{\rm solid} = 5\%$ at 1 atm (~80 mg), 3.6% at 1.5 atm (~120 mg), and 0.13% at 2 atm (~160 mg). The corresponding polarization losses during the condensation process were: $D_{\rm loss} \approx 24\%$ at 1 atm, 20% at 1.5 atm, and 96% at 2 atm. The large $D_{\rm loss}$ observed at 160 mg may be explained by a longer time required for the larger amount of ^{129}Xe to cool down to below 140 K. We also measured the spin relaxation time T_1 after the solid reached an equilibrium temperature, and measured $D_{\rm cross}$ during the cross polarization process. The typical value for T_1 was about 50 min ($T_1 \approx 100$ min at largest), while $D_{\rm cross} \approx 5\%$. The increased T_1 indicates that lower temperatures were attained for ^{129}Xe in the solid phase.

We plan to apply the present cross-polarization technique for the purpose to polarize ^{11}Be nuclei. The presently achieved values for $P_{\rm solid}$ and T_1, both for the 80 and 120 mg ^{129}Xe solids, seem to satisfy the required conditions for the planned experiment with ^{11}Be beam. In respect of the volume available for the implantation, the 120 mg cell would be preferred to the 80 mg one. The time ($T_{\rm meas}$) available for the measurement of the ^{11}Be polarization in such a planned experiment depends largely on $D_{\rm cross}$ as well as on T_1. At present, $T_{\rm meas} \approx 13$ min is essentially determined by $D_{\rm cross}$ rather than T_1. The preparation of the planned experiment with the 120 mg cell is in progress.

References

1) H. Sato et al.: RIKEN Accel. Prog. Rep. **30**, 64 (1997).
2) H. Sato et al.: Nucl. Phys. A **402**, 241 (1998).
3) M. Gatzke et al.: Phys. Rev. Lett. **70**, 690 (1993).

* The Energy Research Center, Wakasa Bay

Coulomb Dissociation of ^{8}B at 254 A MeV

N. Iwasa, F. Boué,[*1,*2] G. Surówka,[*1,*3] K. Sümmerer,[*1] T. Baumann,[*1] B. Blank,[*2] S. Czajkowski,[*2] A. Förster,[*4] M. Gai,[*5] H. Geissel,[*1] E. Grosse,[*1] M. Hellström,[*1] B. Kohlmeyer,[*6] P. Koczon,[*1] R. Kulessa,[*3] F. Laue,[*1] C. Marchand,[*2] T. Motobayashi, H. Oeschler,[*4] A. Ozawa, M. S. Pravikoff,[*2] E. Schwab,[*1] W. Schwab,[*1] P. Senger,[*1] J. Speer,[*6] C. Sturm,[*4] A. Surowiec,[*1] T. Teranishi, F. Uhlig,[*4] A. Wagner,[*4] and W. Walus[*3]

[^{208}Pb(^{8}B, p ^{7}Be)^{208}Pb, Coulomb dissociation]

The Coulomb dissociation of ^{8}B is an alternative method for extracting the astrophysical S_{17} factors for the ^{7}Be(p, γ)^{8}B reaction.[1)] The S_{17} factor at zero energy is the most uncertain input to solar models, and is directly related to predictions of the high-energy ^{8}B-neutrino flux from the sun: relevant to the "solar neutrino problem." Recently, two Coulomb dissociation experiments were performed at $E(^8\mathrm{B}) \approx 50$ A MeV at RIKEN,[1,2)] and the S_{17} factors were successfully extracted for the p-^{7}Be relative-energy (E_{rel}) regions of $E_{\mathrm{rel}} = 0.6$–1.7 MeV and 0.4–3.0 MeV, respectively. These results were found consistent with the results of the direct measurement by Filippone et al., Vaughn et al., and Hammache et al.[3)]

We have studied the ^{8}B Coulomb dissociation process at 254 A MeV at GSI to obtain the S_{17} factors for the E1 multipolarity at low center-of-mass energies, and to extract information on the E2 admixtures. A radioactive ^{8}B beam produced by the Fragment Separator (FRS) at GSI bombarded an enriched ^{208}Pb target with a thickness of 200 mg/cm^2. The outgoing reaction products, proton and ^{7}Be, were analyzed by the Kaon Spectrometer (KaoS) which has a large momentum acceptance of $p_{\mathrm{max}}/p_{\mathrm{min}} \approx 200\%$ and an angular acceptance of 140 and 280 mrad in horizontal and vertical direction, respectively. Two pairs of silicon microstrip detectors were installed at about 14 and 31 cm downstream from the target, respectively, for measuring x- and y-positions of the products before entering the KaoS magnet. The vertex information was used to eliminate a large amount of the background events produced in layers of materials other than the target.

The Coulomb dissociation yields were extracted as a function of the E_{rel} or of the scattering angle θ_8 of the p-^{7}Be center-of-mass with respect to the beam direction. The resultant E_{rel} and θ_8 distributions were well reproducible by Monte-Carlo simulations using the non-resonant-E1 cross section predicted by Typel et al.[4)] as well as the resonant-M1 cross section measured by Filippone et al.[3)] We also have tried to extract the upper limits for a possible E2 contribution by comparing the experimental and simulated θ_8 distributions including E2 contributions. We obtained only a very small E2 amplitude, which is consistent with the Coulomb dissociation result of Kikuchi et al.;[2)] but is not consistent with the result of longitudinal-momentum measurements by Davids et al.[5)] Considering this discrepancy, further experimental and theoretical studies are desirable to clarify the amount of E2 admixture.

By comparing the resultant E_{rel} distribution with the simulation, the experimental S_{17} distribution was extracted. Figure 1 shows our preliminary S_{17} factors at $E_{\mathrm{rel}} = 0.25$–2.8 MeV. We have omitted the data points in the region of the M1 resonance (0.5–0.8 MeV) because we are primarily interested in the E1 component. Our results are consistent with existing (p, γ) data[3)] and with other Coulomb dissociation data.[2)]

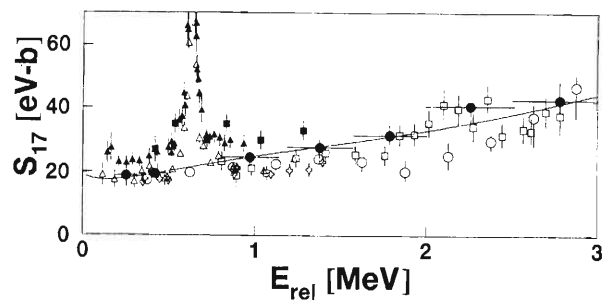

Fig. 1. Preliminary results for the S_{17} factor (filled circles) together with the (p, γ) results[3)] and the Coulomb dissociation results.[2)] The solid curve shows the best fit with the theoretical energy dependence calculated by Typel et al.[4)]

*1 GSI, Germany
*2 CEN Bordeaux, France
*3 Jagellonian University, Poland
*4 Technische Hochschule Darmstadt, Germany
*5 University of Connecticut, USA
*6 Universität Marburg, Germany

References

1) T. Motobayashi et al.: Phys. Rev. Lett. **70**, 2680 (1994); N. Iwasa et al.: J. Phys. Soc. Jpn. **65**, 1256 (1996).
2) T. Kikuchi et al.: Phys. Lett. B **391**, 261 (1997); T. Kikuchi et al.: Eur. Phys. J. A **3**, 209 (1998).
3) B. W. Filippone et al.: Phys. Rev. C **28**, 2222 (1983); F. J. Vaughn et al.: Phys. Rev. C **2**, 1657 (1970); F. Hammache et al.: Phys. Rev. Lett. **80**, 928 (1998).
4) S. W. Typel et al.: Nucl. Phys. A **613**, 147 (1997).
5) B. Davids et al.: Phys. Rev. Lett. **81**, 2209 (1998).

Measurements of Interaction Cross-Sections for Carbon Isotopes at Relativistic Energies and the Halo Structure in ^{19}C

A. Ozawa, O. Bochkarev,[*1] L. Chulkov,[*1] D. Cortina,[*2] H. Geissel,[*2] M. Hellström,[*2] M. Ivanov,[*3] R. Janik,[*3] K. Kimura, T. Kobayashi, A. A. Korsheninnikov, G. Münzenberg,[*2] F. Nickel,[*2] Y. Ogawa, A. A. Ogloblin,[*1] M. Pfützner,[*2] V. Pribora,[*1] H. Simon,[*2] B. Sitar,[*3] P. Strmen,[*3] K. Sümmerer,[*2] T. Suzuki, I. Tanihata, M. Winkler,[*2] K. Yamashita, and K. Yoshida

[NUCLEAR REACTIONS; ^{40}Ar + Be, E $\sim$ 1 A MeV; Secondary beams; $\sigma_I(^{12-20}\mathrm{C})$]

Measurements of the interaction cross-sections (σ_I) at relativistic energies allow us to determine the nuclear matter radii because of the simple reaction mechanism.[1)] Since the nuclear radii are directly related to the density distributions, the measurements of σ_I have been utilized to deduce the density distributions of some halo nuclei. Among the C isotopes, ^{19}C is one of the most interesting candidates for a neutron-halo nucleus. Its one-neutron separation energy (S_n) is the lowest (= 240 $\pm$ 100 keV) among C isotopes. The longitudinal-momentum distribution of ^{18}C, after the one-neutron breakup of ^{19}C, has been measured at 77 A MeV.[2)] The observed narrow width of momentum for ^{18}C indicates a one-neutron halo of ^{19}C. However, the density distribution of ^{19}C has not been determined till today. Therefore, measurements of σ_I are indispensable. Our experimental setup and experimental conditions are readily described in the previous progress report.[3)]

The σ_I plotted as a function of the mass number (A) of the C isotopes are shown in Fig. 1. Observed σ_I increases monotonically with A. The solid line in the figure shows the σ_I calculated by the equation: $\sigma_I = \pi\,[R_I(\mathrm{C}) + r_0 A^{1/3}]^2$, where R_I(C) is the interaction radius of ^{12}C and r_0 is a number selected to reproduce the ^{12}C cross-section. The broken line in Fig. 1 shows a systematic increase obtained by simply fitting the σ_I of ^{17}C, ^{18}C, and ^{20}C. Observed σ_I for the ^{19}C is much larger than the systematic trend by about three σ's. Thus, an anomalous structure is evident for ^{19}C.

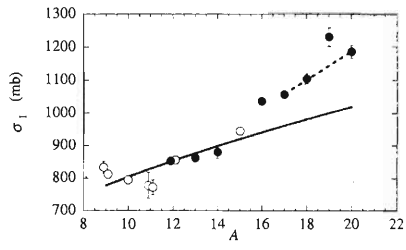

Fig. 1. σ_I for C isotopes on C targets. The filled circles are data points obtained in this work. The blank circles are data from previous studies at LBL.

*1 Kurchatov Institute, Russia
*2 GSI, Germany
*3 Comenius University, Slovak Republic

For further quantitative discussions, we have performed calculations similar to those in Ref. 4. Matter-density distribution of the core (^{18}C) has been parametrized to reproduce the observed σ_I of ^{18}C with a C target. The density distribution for the valence neutron of ^{19}C was calculated by a simple potential model,[4)] where single-nucleon density distributions for the s, p and d orbitals in a core plus nucleon potential were calculated for given values of the separation energies. In the calculations, we assumed a Woods-Saxon shape potential; fixed the radius and diffuseness parameters; and we adjusted the depth of the potential so as to reproduce the S_n of ^{19}C. The resulting single-neutron distribution was added to the core density distribution, taking into account the difference in the center of mass for the composite system. The spin and parity of ^{19}C are not known experimentally. If we assume $J^\pi = 1/2^+$ for ^{19}C, a 46% (54%) occupation probability for the $0^+ \otimes 2s_{1/2}$ ($2^+ \otimes 1d_{5/2}$) configuration is necessary to reproduce the observed σ_I. The matter-density distribution with the above mixed configurations is shown by the solid line in Fig. 2. Since the distribution has a large tail component, a neutron halo structure of ^{19}C is clearly demonstrated in this figure.

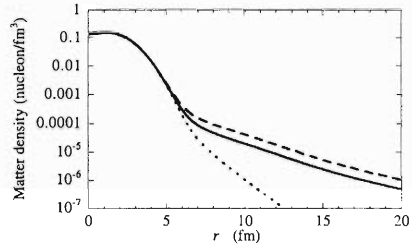

Fig. 2. Density distributions of ^{19}C based on a core plus neutron structure. The dashed, and dotted lines show the density distributions assumed pure $0^+ \otimes 2s_{1/2}$ and pure $2^+ \otimes 1d_{5/2}$ configurations, respectively. The solid line shows the density distribution required to reproduce the observed σ_I for ^{18}C and ^{19}C.

References

1) I. Tanihata et al.: Phys. Rev. Lett. **55**, 2676 (1985).
2) D. Bazin et al.: Phys. Rev. Lett. **74**, 3569 (1995).
3) A. Ozawa et al.: RIKEN Accel. Prog. Rep. **31**, 79 (1998).
4) M. Obuti et al.: Nucl. Phys. A **609**, 74 (1996).

2. Atomic and Solid-State Physics

Charge Transfer Processes in Collisions of H^+ Ions with P Atoms at Low Energies

J.-P. Gu,[*1] G. Hirsch,[*1] R. J. Buenker,[*1] M. Kimura,
C. M. Dutta,[*2] P. Nordlander,[*2] and I. Shimamura

The use of heavy ions in radiation therapy is expected to provide an advantageous therapeutic effect for tumors which are deeply seated and radioresistant provided that an effective dose distribution can be made. In particular, at the near end of the particle track, a sharp Bragg peak is known to be present for heavy ions. This is one of their special features that is considered to be most useful for treating tumors deep inside the body.[1] An efficient exploitation of this advantage of heavy ions in radiation therapy requires a careful treatment plan that enables one to concentrate an efficient and sufficient dose to a target region and spare surrounding critical organs. Since phosphorus (P) atoms are abundant in human bodies, it is important to examine the collision dynamics by proton impact. We have investigated charge transfer and excitation of P atoms in collision with H^+ ions at low-to-intermediate collision energies based on a molecular expansion method. The processes in which we are interested are shown below, together with the corresponding asymptotic energy defects.

(i) Ground − statePatoms :

$$P(3s^23p^3 : {}^4S^0) + H^+ \rightarrow P^+(3s^23p^2 : {}^3P) + H(1s) + 25099\ cm^{-1} \quad (1)$$

(ii) Metastable − statePatoms :

$$P(3s^23p^3 : {}^2D^0) + H^+ \rightarrow P^+(3s^23p^2 : 1S) + H(1s) + 14885\ cm^{-1} \quad (2)$$

In the present CI calculations, the atomic orbital (AO) basis set employed for the phosphorus atom is (12s9p) contracted to [6s5p]. The basis set for the hydrogen atom is a (7s3p1d)/[5s3p1d] contracted set. The first step in the theoretical procedure is to carry out an SCF calculation using the above AO basis sets to generate MOs which are employed as an orthonormal basis for a multireference single- and double excitations (MRD-CI) configuration interaction treatment.[2] A semiclassical MO expansion method with a straight-line trajectory of the incident ion was employed to study the collision dynamics below 10 keV/u.[3] The molecular states included in the dynamical calculations are the two sets of states: (i) quartet states, and (ii) doublet states. First we consider the collision process (1). Below 1 keV/u, $P^+(3s^13p^3 : {}^5S^0)$ state formation becomes a strong channel for charge transfer although below 0.1 keV/u or so, 3 $^4\Gamma^-$ state takes over. Above ~1 keV/u, $P^+(3s^23p^2 : {}^3P)$ is found to be produced more efficiently, but as the energy decreases, $P^+(3s^13p^3 : {}^5S^0)$ production dominates down to 0.03 keV/u. Below this energy, $P^+(3s^23p^2 : {}^3P)$ production takes over again. Around 1 keV/u, both productions are comparable in magnitude. The production of $P^+(3s^23p^2 : {}^3P)$ peaks near 1 keV/u, but is small in the entire energy range calculated here. For the process (2), at higher energy, the 3 $^2\Gamma^-$ state and 4 $^2\Gamma^-$ radial coupling dominates, while as the energy decreases, 2 $^2\Gamma^-$ state and 4 $^2\Gamma^-$ coupling takes over the dynamics. In addition, 2 $^2\Gamma^-$ state and 3 $^2\Gamma^-$ radial coupling play some part at intermediate energy. Naturally, charge transfer from the metastable atom is much larger than that from the ground state in all energies studied.

References

1) Proc. NIRS Int. Seminar on the Application of Heavy Ion Accelerator to Radiation Therapy of Cancer, Chiba, 1994-11, edited by A. Maezono (1994).
2) R. J. Buenker and S. D. Peyerimhoff: Theor. Chim. Acta. **35**, 33 (1974).
3) M. Kimura and N. F. Lane: Adv. At. Mol. Opt. Phys. **26**, 76 (1989).

*1 Theoretische Chemie, Bergische Universität-Gesamthochschule Wuppertal, Germany
*2 Department of Physics, Rice University, USA

RIKEN Accel. Prog. Rep. **32** (1999)

A Comparative Study of Electron- and Positron-Polyatomic Molecule Scattering

M. Kimura, I. Shimamura, O. Sueoka, A. Hamada,[*1] and Y. Itikawa[*2]

The study of positron collisions with molecules has a long history. Interest in positron-molecule collisions arose from a study of positron annihilation in a molecular gas and its related subject, the slowing down of a positron in a molecular gas. Due to rotational and vibrational excitation processes, molecules are more efficient than atoms for slowing down positrons, particularly at low incident energies. With a simple model, rotational excitation cross sections for positron collisions with molecules were estimated and a significant difference between positron collisions and electron collisions in the process was demonstrated. We briefly summarize the characteristics of the problem, first in comparison to positron-atom collisions and then to electron-molecule collisions. The potential generated by a molecule is always anisotropic. Molecules have electric multipole (i.e., dipole, quadrupole,$\cdots$) moments. The interactions of an incident positron with these multipoles are usually anisotropic and of long range. This feature is one of the noticeable differences between the positron-atom and -molecule collisions. Molecules have rotational and vibrational degrees of freedom. If the interaction potential has a strong anisotropy, rotational motion can be easily excited. An anisotropic and long-ranged interaction between the incident positron and molecular multipoles is very effective in the excitation of molecular rotation. Molecular vibration is excited through the distortion of the electronic cloud of the molecule induced by the collision with the incident particle. In this sense, vibrational excitation is more sensitive to the short range part (i.e., near the molecular nuclei) of the interaction. Dissociation of a molecule can be regarded as a limit of vibrational excitation. In many cases the dissociation products are active species (i.e., atoms and radicals). In this regard, the electron impact dissociation is of practical importance and has been studied extensively. Information is rarely available, however, on positron-impact dissociation. In relation to the dissociation process, the following process is of particular interest for a positron collision:

$$e^+ + AB \rightarrow A^+ + PsB. \quad (1)$$

This kind of Ps compounds are interesting objects in atomic physics. They offer another test of many body theory. A more challenging process is

$$e^+ + AB \rightarrow Ae^+ + B. \quad (2)$$

Positron collisions with a Li-containing molecule could give experimental evidence of such an exotic positive ion. It is unlikely for a simple molecule to capture a positron and form a shape resonance. A large polyatomic molecule, however, may have the possibility to capture a positron. A polyatomic molecule has multiple modes of vibration and the dependence on the projectile may be different for different modes. For the same reason, preferable dissociation channels in the positron molecule collision may differ from those in the electron molecule collision. The present study is concerned more with polyatomic molecules than with diatomic and triatomic molecules, which were mainly treated in the earlier review article by Kauppila and Stein.[1)]

References

1) W. E. Kauppila and T. S. Stein: Adv. At. Mol. Opt. Phys. **26**, 1 (1989).

*1 Faculty of Engineering, Yamaguchi University
*2 Institute of Space and Astronautical Science

Low-Energy Positron Collisions with CH_4 Molecule and Ar Atom

T. Nishimura and I. Shimamura

Theoretical work on vibrationally-elastic scattering of positrons (e^+) from two kinds of targets CH_4 and Ar is reported. The present theory is an extension of the previous work on the $e^- + CH_4$ collision.[1] In addition, the fact that the behavior of the differential cross section (DCS) recently measured for the elastic process of $e^+ + CH_4$[2] is quite similar to that of $e^+ + Ar$[3] has stimulated our interest to study these processes theoretically.

The present theory is based on the fixed-nuclei approximation.[1] Then, the wavefunction of the scattered positron satisfies a set of coupled differential equations derived from the Schrödinger equation for the total collision system. By solving these equations, the scattering matrix is obtained from the asymptotic form of the wavefunction, and is transformed into the cross sections. The interaction potential between a positron and a target is represented in the form of a local potential which consists of the electrostatic and the polarization potentials. As for the latter potential, a model potential (V^{corr}) which is based on the correlation energy of a positron in a homogeneous electron gas[4] is adopted for the smaller values of the positron-target distance, **r**. This potential is connected with the long-range asymptotic form (V^{pol}) of the dipole polarization potential ($\propto r^{-4}$) at the position of $r = r_c$ where the two potentials V^{corr} and V^{pol} cross each other. Throughout the present calculation, no positronium (Ps) formation channel is taken into account at collision energies of 0.2–10 eV.

Figure 1 shows the vibrationally-elastic integral cross sections (ICS) for the $e^+ + CH_4$ and $e^+ + Ar$ systems as a function of the collision energy. Below the Ps formation threshold (i.e., 5.80 eV for CH_4 and 8.96 eV for Ar), the present ICSs for both CH_4 and Ar well reproduce the corresponding experimental total cross sections (TCSs).[5,6] Qualitatively, the calculated ICS for CH_4 has a behavior which happens to be similar to that of Ar in the low energy region of 0.2–3 eV. Quantitatively, however, they are quite different. The difference mainly comes from the difference in the magnitude of the potential near r_c, which in turn comes from the difference in the value of r_c, that is, 3.24 au for CH_4 and 2.85 au for Ar. Above the threshold for Ps formation, the TCSs are not appropriate quantities to compare with the present ICSs, since contributions of Ps-formation cross section to the TCSs become rapidly large.

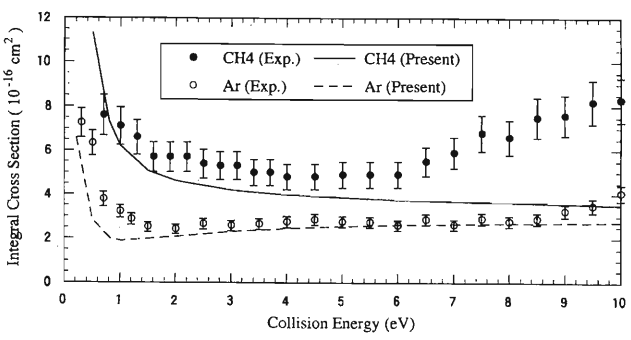

Fig. 1. Integral cross sections of the elastic scattering in the $e^+ + CH_4$ and $e^+ + Ar$ collision systems.

Figure 2 shows the elastic DCS for $e^+ + CH_4$ at energy of 6 eV and for e^++Ar at 5 eV, where the experimental data are available. Since the measured DCSs are on a relative scale, they are normalized at a scattering angle of 90° to those of the calculated DCS. The shapes of the measured [2,3] and calculated DCSs are seen to be similar to each other. Furthermore, we have found similarites between the present DCSs of the two systems for energies of 3–10 eV, which can be attributed to an accidental similarity of the interaction potential between the two systems; not in shape but in magnitude. Further details will be reported elsewhere.

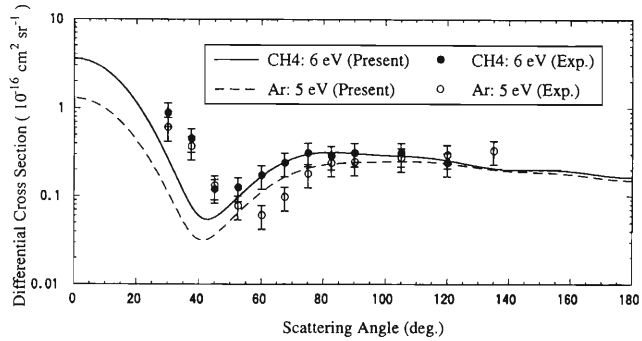

Fig. 2. Differential cross sections of the elastic scattering in the $e^+ + CH_4$ system at energy of 6 eV and in the $e^+ + Ar$ system at 5 eV.

References

1) T. Nishimura and Y. Itikawa: J. Phys. B **27**, 2309 (1994).
2) D. A. Przybyla et al.: Phys. Rev. A **55**, 4244 (1997).
3) S. J. Smith et al.: Phys. Rev. Lett. **64**, 1227 (1990).
4) E. Boronski and R. M. Nieminen: Phys. Rev. B **34**, 3820 (1986).
5) O. Sueoka and S. Mori: J. Phys. B **19**, 4035 (1986).
6) W. E. Kauppila et al.: Phys. Rev. Lett. **36**, 580 (1976).

Close Coupling Calculation for e + Ps Scattering

A. Igarashi

Nowadays the positronium beam has become available, and the collision experiments with protons, atoms, and molecules have been reported.[1)]

Since the positronium consists of two particles with the same mass and opposite charge, the static potential between a positronium and a collision partner vanishes. Therefore, the main interactions in the e + Ps scattering are the electron exchange and polarization.

We apply the usual close coupling or coupled channel method to the e + Ps system, and the integro-differential equations for radial functions are solved with a B-spline method. B-spline function is a piecewise polynomial, which is easy to handle and is quite flexible to interpolate a function. Some applications of the B-spline function in atomic physics are found in Ref. 2.

The total wave function of the Ps^- system is expanded in terms of B-spline functions in the radial range of $0 \leq R \leq R_{max} (R = R_1 \text{ or } R_2)$ as

$$\Psi = \sum_{\mu=1}^{N} \sum_{i} C_i^{\mu} \Big(B_i(R_1)\phi_\mu(\mathbf{r}_1, \hat{R}_1) + (-1)^S B_i(R_2)\phi_\mu(\mathbf{r}_2, \hat{R}_2) \Big) \equiv \sum_{\mu,i} C_i^{\mu} \tilde{B}_{\mu,i}, \quad (1)$$

where $\mathbf{r}_1$ ($\mathbf{r}_2$) is the position vector of electron 1 (2) from positron, $\mathbf{R}_1$ ($\mathbf{R}_2$) the position vector of the other electron from the center of mass of positronium of positron + elecron 1 (2), B_i the B-spline function, ϕ_μ the atomic base, S the total spin of two electrons, N the number of atomic basis functions, and C_i^μ is an expansion coefficient. R_{max} should be chosen as large as the exchange coupling can be neglected.

From $< \tilde{B}_{\nu,j}|H - E|\Psi >= 0$, the homogeneous algebraic equation for the row vector $\mathbf{c} \equiv \{C_i^\mu\}$ is given as

$$\mathbf{Ac} = \mathbf{0}, \quad (\mathbf{A})_{i'j'} =< \tilde{B}_{\mu,i}|H - E|\tilde{B}_{\nu,j} > . \quad (2)$$

In the above equation, N independent solutions of $\mathbf{c}$, that is, N independent sets of radial solutions can be found for $0 \leq R \leq R_{max}$. Because the radial equations are of local potentials for $R_1, R_2 > R_{max}$, they can be solved forward direction in the usual manner. Asymptotic radial solutions are matched with the scattering boundary condition, and hence the scattering matrix is extracted.

Four different Ps-basis sets of real states or Sturmian functions are considered here as following; (i) 1 state: 1s, (ii) 3 states: 1s, 2s, 2p, (iii) 18 states: seven s, six p, and five d orbitals and (iv) 27 states: ten s, nine p and eight d orbitals. The results are tabulated in Table 1 for S- and P-wave phase shifts for some total energies below the Ps(n = 2) threshold. The variational calculation by Ward et al.[3)] is also included for comparison. It is clear that the present phase shifts with basis sets of 18 states and 27 states show good convergence and they are in agreement with the variational values.

To end, the close coupling method was successfully applied to the calculation of the e + Ps scattering phase shifts. This method will be extended to calculate comprehensive cross sections in the e + Ps scattering.

Table 1. Phase shifts in e + Ps scattering at collision momentum k (a.u.) for the symmetry ^{2S+1}L.

k	1 state	3 state	18 state	27 state	Ward et al. [3)]
			^{1}S		
0.1	1.655	1.860	2.056	2.056	2.049
0.2	0.988	1.166	1.378	1.378	1.378
0.3	0.585	0.761	0.983	0.983	0.984
0.4	0.320	0.508	0.746	0.746	0.748
			^{3}S		
0.1	-0.570	-0.538	-0.536	-0.536	-0.536
0.2	-1.064	-1.037	-1.033	-1.033	-1.035
0.3	-1.457	-1.437	-1.430	-1.430	-1.432
0.4	-1.761	-1.745	-1.736	-1.736	-1.739
			^{1}P		
0.1	-0.058	-0.042	-0.038	-0.038	-0.038
0.2	-0.264	-0.241	-0.235	-0.234	-0.235
0.3	-0.498	-0.474	-0.463	-0.463	-0.463
0.4	-0.682	-0.652	-0.634	-0.634	-0.635
			^{3}P		
0.1	0.107	0.166	0.192	0.192	0.192
0.2	0.476	0.628	0.707	0.707	0.707
0.3	0.586	0.699	0.778	0.778	0.778
0.4	0.519	0.608	0.687	0.687	0.687

References

1) A. J. Garner et al.: J. Phys. B **29**, 5961 (1996); J. P. Merrison et al.: Phys. Rev. Lett. **78**, 2728 (1997).
2) *Many-body Theory of Atomic structure and Photoionization*, edited by T.-N. Chang (World Scientific, Singapore, 1993).
3) S. J. Ward et al.: J. Phys. B **30**, 127 (1987).

Protonium Formation in $\overline{p}$-H Collisions

R. J. Whitehead, J. F. McCann, and I. Shimamura

The existence of long-lived antiprotons $\overline{p}$ in liquid helium[1] was explained[2] by the existence of metastable atomic states of antiprotonic helium $He^+\overline{p}$ where $\overline{p}$ is captured into high-n, high-l orbitals. The subsequent decay and annihilation processes of $He^+\overline{p}$ are fairly well understood.[3,4] However, the details of the capture process are less well known.[5] In this work the classical-trajectory Monte-Carlo (CTMC) method has been used to determine ionization and capture cross sections for collisions between $\overline{p}$ and atomic hydrogen H. The results we obtain are an improvement, in terms of accuracy and statistical error, on previous work.[6] For $\overline{p}$ capture (or the production of protonium $p\overline{p}$) the nature of the orbit can be characterized by the quantum numbers (n, l) obtained through the correspondence principle[7] by relating the classical energy and angular momentum to the corresponding quantum numbers. We present some of our results which indicated the $p\overline{p}$ distribution over the n.

Cross sections for $\overline{p}$-H collisions are presented in Fig. 1. For ionization, the results near the peak ($E_{\mathrm{CoM}} \approx 0.65$ a.u.) are substantially higher than data previously obtained by CTMC simulations.[6] The $\overline{p}$ capture cross section rises steeply below the collisional ionization threshold. We have found that the low-energy capture cross section curve can be represented accurately by the Langevin formula[8]: $\sigma = \pi (2\alpha/E)^{\frac{1}{2}}$. A numerical fit to the data found a value of $\alpha \approx 0.15$, substantially less than the static polarizability of the hydrogen atom. In comparison with the data of Cohen,[5,6] our results predict capture cross sections to be slightly larger, though the overall trend is very similar. In order to reduce the statistical error to values smaller than the size of the data points plotted, we used typically 5000–50000 trajectories to construct each point.

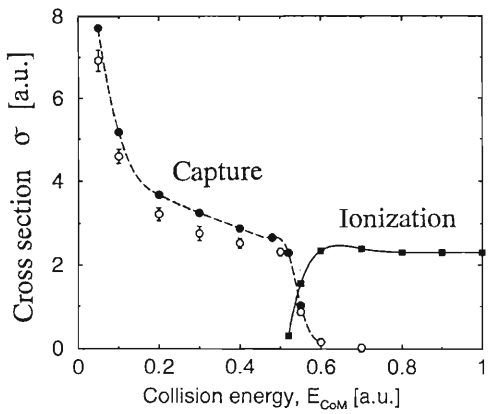

Fig. 1. Capture (•) and ionization (■) cross sections for $\overline{p}$ + H collisions as functions of the center-of-mass collision energy. ○: Cohen's results.[6]

Displayed in Fig. 2 are cross sections for $p\overline{p}$ formation in different shells (σ_n). These distributions indicated the tendency towards high n, a result consistent with classical capture from large impact parameters. Comparison with results obtained by Cohen[6] for the average value of n when capture occurs shows good agreement. However, the results for the l-distributions show significant differences. In particular, we find that our simulations predict larger populations for high-l states.

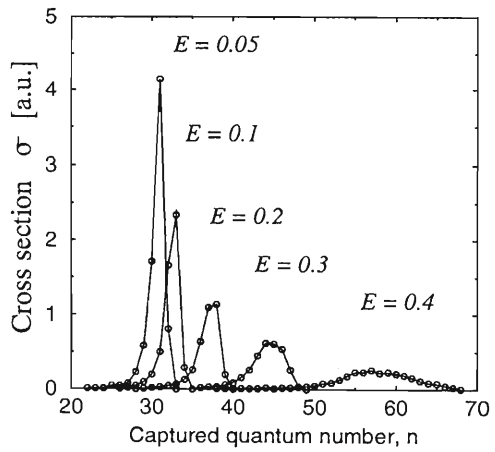

Fig. 2. Partial cross sections σ_n for $p\overline{p}$ formation in $\overline{p}$ + H collisions. E attached to each curve is the center-of-mass collision energy in a.u.

The results show that $p\overline{p}$ is formed in high-n, high-l orbits in support of the Condo hypothesis[2] and in agreement with the conclusion obtained by Cohen.[5,6]

This work was supported by the British Council and the Japan International Science and Technology Exchange Center.

References

1) M. Iwasaki et al.: Phys. Rev. Lett. **67**, 1246 (1991).
2) G. T. Condo: Phys. Lett. **9**, 65 (1964).
3) V. I. Korobov and D. D. Bakalov: Phys. Rev. Lett. **79**, 3379 (1997).
4) V. I. Korobov and I. Shimamura: Phys. Rev. A **56**, 4587 (1997).
5) J. S. Cohen: *Electromagnetic Cascade and Chemistry of Exotic Atoms* (Plenum Press, New York, 1990).
6) J. S. Cohen: Phys. Rev. A **36**, 2024 (1987).
7) R. E. Olson: Phys. Rev. A **24**, 1726 (1981).
8) Y. Kaneko: in *Molecular Processes in Space*, edited by T. Watanabe, I. Shimamura, M. Shimizu, and Y. Itikawa (Plenum Press, New York, 1990), p. 117.

Time-of-Flight Mass Spectroscopy of Product Ions in Fast Ion-C_{60} Collision

Y. Nakai, T. Kambara, A. Itoh, H. Tsuchida, and Y. Yamazaki

A number of measurements of the C_{60} ionization and fragmentation have been performed by using various excitation probes (photon, electron, ion etc). The intensity distributions of product ions strongly depend on the internal energy of precursor of fragmentation. We have reported that only a multiple fragmentation occurs in the hard collision by fast heavy ion.[1] On the other hand, in the case of lower excited energy by electron impact or by very low energy collision with atom and surface, C_{60} emits a small neutral carbon cluster in the micro second time scale after excitation.[2,3] In these cases, the internal energy can be estimated by comparing the experimental intensity ratio between the C_{60} ion and the fullerene-like fragment ion with the theoretical one.

The time-of-flight (TOF) peak profile of each product ion has information of the initial kinetic energy, reaction rate coefficient of fragmentation, and so on. However, a part of such information is often lost because of the poor experimental resolution of TOF measurement. We intend to collect such information by applying a high-resolution TOF mass spectroscopy. The Wiley-McLaren's spatial-focusing condition was used for the TOF measurement. The beams of 2.5 MeV/u He^{2+} and C^{6+} were accelerated by RIken-Linear-ACcelerator(RILAC) and collimated upstream of the target of C_{60} vapor. The C_{60} target was prepared by evaporating the commercial C_{60} powder in a temperature-controlled oven. The effusive C_{60} was collimated by a slit located below the collision region. Base pressure in the collision chamber was kept below 2×10^{-8} Torr. The electrons extracted from collision region were used to trigger the TOF measurement. The ion detector was a three-stage multichannel plate (MCP) and the electron detector was a two-stage MCP. Each detector has an impedance-matched anode for a fast timing read-out. TOF spectra were obtained using a multi-hit time-to-digital converter (TDC). In Fig. 1, the peaks of TOF of C_{60}^+ ions are shown. Each peak is corresponding to C_{60}, which contains the different number of ^{13}C. We can separate the peak with 720 amu($^{12}C_{60}$) and from thet with 721 amu($^{12}C_{59}{}^{13}C$).We suppose that the reason for our high resolution is due to the good collimation of ion beam and the C_{60} molecular beam, and a fast timing readout.

In Fig. 2, the TOF-peak of C_{58}^+ produced by the 2.5 MeV He^{2+} impact is shown. This peak has an asymmetric shape. This asymmmetric shape does not come from the mass difference in C_{60} with different number of ^{13}C. As shown in Fig. 1, the thermal motion of C_{60} target does not cause such a broad peak of C_{58}^+. In Fig. 2, we show the TOF-peaks obtained by Monte Calro simulation for $C_{60}^+ \rightarrow C_{58}^+ + C_2$ with a certain life of fragmentation (0.0 μsec and 2.0 μsec) and a 0.4 eV kinetic energy release. In the case of 2.0 μsec, the simulation result also shows a symilar asymmetric tail on the side of longer TOF as observed by experiment. This means that C_{58}^+ is mainly produced in the delayed emission of C_2 from excited C_{60}^+. We are continuing the analysis of the data now.

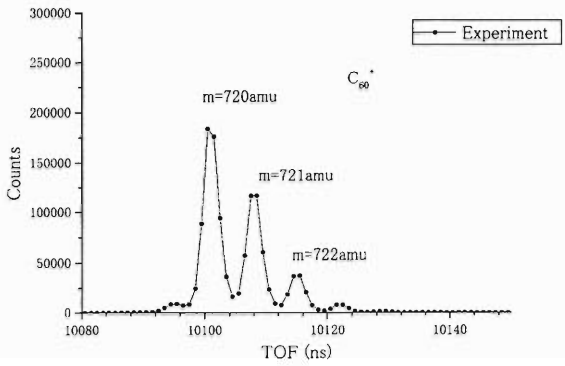

Fig. 1. TOF-peaks of C_{60}^+ ions are shown. Each peak is corresponding to C_{60} which contains the different number of ^{13}C. The width of each peak is considered to be a resolution of our system.

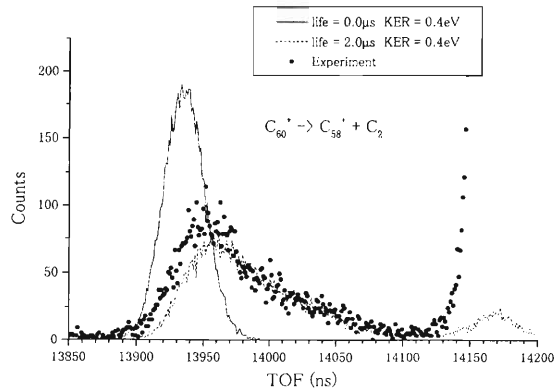

Fig. 2. TOF-peak of C_{58}^+ ions is shown. Solid circle is experimental data. Solid line is the result of Monte Calro simulation with the fragmentation life of 0.0 μsec. Dashed line is the result of Monte Calro simulation with the life of 2.0 μsec. In the case of 2.0 μsec, the simulation result also shows the asymmetric tail on the side of longer TOF similarly to the experimental result. A huge jump of experimental data at the later TOF is a rise of $^{12}C_{60}^+$.

References
1) Y. Nakai et al.: J. Phys. B: At. Mol. Opt. Phys. **30**, 3049 (1997).
2) M. Foltin et al.: J. Chem. Phys. **107**, 6246 (1997).
3) P. Weis et al.: J. Chem. Phys. **104**, 6246 (1996).

Sub-State-Selective Differential Cross Sections of Electron Capture in 10 MeV Ar^{8+}-He Collisions†

T. Kambara, M. Kimura, Y. Awaya, Y. Nakai, T. M. Kojima, V. Mergel,* and H. Schmidt-Böcking*

We have studied the electron capture processes, using atomic target and highly-charged heavy ions, through measurements of the final-state-selective differential cross sections. Constituents of the collision process investigated here are an Ar^{8+} ion and a He target and the reaction is:

$$Ar^{8+}(1s^22s^22p^6) + He(1s^2) \rightarrow Ar^{7+}(1s^22s^22p^6nl) + He^+(n'l'). \quad (1)$$

Here the projectile (Ar^{8+}) energy used was 10 MeV which corresponds to a velocity of 3.17 atomic unit (au). Since an Ar^{8+} ion has a neon-like electron configuration, the electron can only be captured to the $n = 3$ or higher orbital. We have measured the longitudinal momentum (parallel to the projectile momentum) $p_{//R}$ and the transverse one $p_{\perp R}$ of the recoil He^+ ion applying the cold target recoil ion momentum spectroscopy (COLTRIMS)[1] in coincidence with the projectile which captures one electron. To obtain $p_{\perp R}$ dependent differential cross sections of the electron capture to different final states, we fitted the $p_{//R}$ distributions in different $p_{\perp R}$ regions by a sum of Gaussian peaks which correspond to the final states of $n = 3$–5. We have described the measurements and have presented the differential cross sections $d\sigma/dp_{\perp R}$ of electron capture to the $n = 3$–5 states, previously.[2]

A peak-fit analysis of the $n = 3$ final state yields the relative differential cross sections to the substates of $n = 3$: i. e., 3s and 3p. The results are shown in Fig. 1. The experimental cross section to the 3d state is not shown in the figure since the relative uncertainty is high, although it was included in the peak-fit analysis.

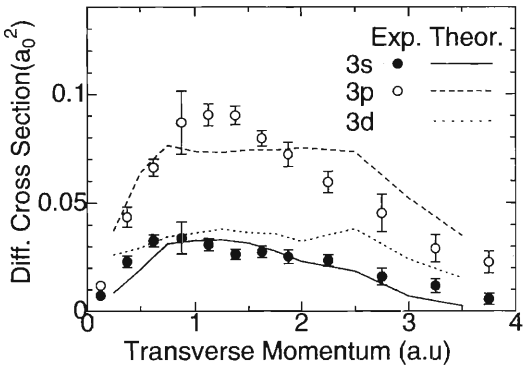

Fig. 1. Differential cross sections of electron capture to $n = 3$ substates. Symbols denote the experimental results for 3s and 3p, and lines are the calculation results.

The experimental results of the differential cross sections are compared with calculations of the close-coupling approximation based on a molecular representation. We have employed the configuration interaction (CI) method to obtain molecular electronic states of the collision system.[3,4] The pseudopotential method was adopted to represent Ar^{8+} core, because it enables us to reduce the many-electron system to more tractable two-electron system. The Slater-type orbitals were used to construct the basis sets, and Slater exponents were given before.[3] The present level of precision of all electronic states considered is less than 2 % compared with experimental asymptotic levels. All states corresponding to Ar^{7+} ($n = 3$, 4 and 5; $l \leq n - 1$) were obtained. The series of avoided crossing between the initial Ar^{8+}/He channel and the final $Ar^{7+}(n = 5)/He^+$, Ar^{7+} $(n = 4)/He^+$, and Ar^{7+} $(n = 3)/He^+$ levels takes place around 8, 7 and 5.5 au, respectively. These crossings play a key role for capture processes depending upon the collision energy.

The calculated $3l$ (l = s, p and d) substate dependence of the capture cross section is compared with the experiment in Fig. 1. Because of diabatic nature of the curve-crossing for higher l partial states with the initial channel such as d and f states, capture to p state is found to be generally dominant, and then followed by d state. For $Ar^{7+}(n = 3)$ formation, capture to the p state is larger than s and d states by a factor of two. There are some differences between the theory and experiment in details; but the theory is in a reasonable accord with the measurement, thus providing a rationale to the observation.

References

1) J. Ullrich, R. Moshammer, R. Dörner, O. Jagutzki, V. Mergel, H. Schmidt-Böcking, and L. Spielberger: J. Phys. B: At. Mol. Opt. Phys. **30**, 2917 (1997).
2) T. Kambara, Y. Nakai, T. M. Kojima, V. Mergel, H. W. Schmidt-Böcking, and M. Kimura: RIKEN Accel. Prog. Rep. **31**, 90 (1998).
3) M. Kimura and R. E. Olson: Phys. Rev. A **31**, 489 (1985).
4) M. Kimura and N. F. Lane: in *Advances in Atomic, Molecular and Optical Physics*, Vol. 26 (Academic Press, 1989) p. 79.

† Condensed from the article in J. Phys. B: At. Mol. Opt. Phys. **31**, L909 (1998)

* Institute for Nuclear Physics, University of Frankfurt, Germany

Effects of the Ion Beam Energy on Atomic Lifetime Measurements Using the Techniques of Beam-Foil Spectroscopy

R. Hutton, Y. Zou,[*1] S. Huldt,[*2] I. Martinson,[*2] K. Ando,
T. Kambara, H. Oyama, and Y. Awaya

In a previous article[1] we have discussed possible inherent problems with atomic life time measurements using the beam-foil technique. These problems are related to contamination of spectral lines by satellite line decays. As an example we have chosen to study the decay of the $1s^2 2s\ ^2S_{1/2}$–$1s^2 2p\ ^2P_{1/2,3/2}$ Li-like transitions. The satellite line contamination will then be from Be-like lines of the form $1s^2 2snl$–$1s^2 2pnl$. In Ref. 2 the fact that for some value of n (depending on the atomic number, Z, of the ion) such configurations will go above the 1st ionisation limit of the Li-like ion is mentioned. For higher n levels these satellites will become less troublesome with regard to Li-like lifetime measurements due to the open autoionisation channels. Another way to minimize the effect of these satellites is to choose the beam energy so as to minimize the Be-like charge state fraction of the ion beam while maintaining a usable Li-like beam fraction. In a recent study of the $1s^2 2p\ ^2P$ levels in Li-like Mg this model was studied by choosing suitable beam energies. Beams of Mg ions were obtained from the RILAC at the energies of 0.4, 1.3 and 2.5 MeV/u. The calculated charge state fractions for Li- and Be like ions at these energies are shown in Table 1 (the tables of Shima et al.[3] are used here). At the highest energy used the satellite contamination should be very small and we would expect almost no contamination of the Li-like resonance line. On the other hand for the 0.4 MeV/u ions we would expect a large satellite contamination, and hence decay curves measured at this energy to be inconsistent with theoretical predictions for the $1s^2 2p\ ^2P$ level lifetimes. In Fig. 1 the decay of the $2p\ ^2P_{3/2}$ level is shown for the three beam energies used. It is clear that the decay curves differ. The date recorded at 0.4 MeV/u decaying faster than that at the higher energies. This would appear to confirm the satellite contamination model as discussed above. More experiments are being performed with other Li-like ions.

Table 1. This shows the charge state distribution for Li- and Be-like Mg ions after stripping by a foil at the energies of 2.5, 1.3 and 0.4 MeV/u.

Ion	E MeV/u	Be-like percent	Li-like percent	Be/Li ratio
	2.5	0.8	15	0.053
Mg	1.3	15	42	0.357
	0.4	17	3	5.67

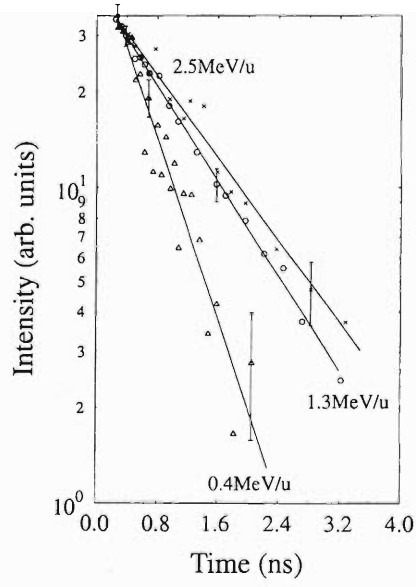

Fig. 1. Decay curves for the Li-like Mg $1s^2 2s\ ^2S_{1/2}$–$1s^2 2p\ ^2P_{3/2}$ transition recorded at three different beam energies, 2.5, 1.3 and 0.4 MeV/u. The decay constant obtained from the 2.5 MeV/u measurement agrees with the theoretical lifetime for the $2p\ ^2P_{3/2}$ level.

References

1) R. Hutton et al.: RIKEN Accel. Prog. Rep. **31**, 94 (1997).
2) R. Hutton et al.: RIKEN Accel. Prog. Rep. **32**, 94 (1998).
3) K. Shima et al.: NIFS-DATA-10, 1991.

*1 Applied Physics Department, Shanghai Jiaotong University, P. R. China
*2 Department of Physics, University of Lund, Sweden

Beam Foil Spectroscopy of Highly Charged Erbium

R. Hutton, Y. Zou,[*1] S. Huldt,[*2] I. Martinson,[*2] K. Ando, T. Kambara, and H. Oyama

Using the techniques of beam-foil spectroscopy at the RILAC we have begun a study of highly-charged very-heavy ions. The reason for these studies is the interest in fusion plasma diagnostics.[1)] It is expected that Xe ($Z = 54$) gas will be injected into the ITER fusion device as a diagnostic element. As it has 54 electrons in the neutral atom and as the last electron has a high ionisation energy, it should give rise to useful charge states throughout the plasma (i.e., different ionic stages appearing at many different temperatures). Also it may be that W ($Z = 74$) will be used as a material in the construction of the ITER device. However the spectroscopy of these elements in many of the charge states is relatively unknown. For a number of charge states, however, the spectroscopy is expected to be relatively simple: e.g., the Cu- and Zn-like charge states. The Cu-like system is effectively a 1 active electron system and the Zn-like system a 2 active electron system. Wavelengths for the resonance lines in these two sequences are already known from laser produced plasma experiments. However, some of the problems in investigating spectra of these elements can be understood from Fig. 1. This shows beam-foil spectra of 1.5 MeV/u Er ($Z = 68$) taken at two different foil positions. Although Erbium is not of interest to ITER diagnostics it was a convenient element to study in terms of accelerator beam currents etc. The results can of course be compared in an isoelectronic way with Xe and W. The spectrum taken where the foil is very close to the spectrometer entrance slit shows a multitude of lines and it is an almost impossible task to identify any single feature. However, as a time delay is introduced between the foil excitation and the observation window a group of quite well resolved lines becomes apparent, see Fig. 1. Closer study shows one of these lines in fairly good wavelength agreement with a calculation of the Zn-like intercombination line ($4s^2\ ^1S_0 - 4s4p\ ^3P_1$) by Beimont.[2)] We subsequently measured decay curves for this group of lines by recording light intensity as a function of foil position. In particular, the intensity decay of the line corresponding to the calculated wavelength of the $4s4p\ ^3P_1$ level decay was analyzed. A decay curve was constructed from which a lifetime for the $4s4p\ ^3P_1$ level was obtained. A decay time of around 1 ns was found for this line. However in previous reports we have discussed problems related to satellite

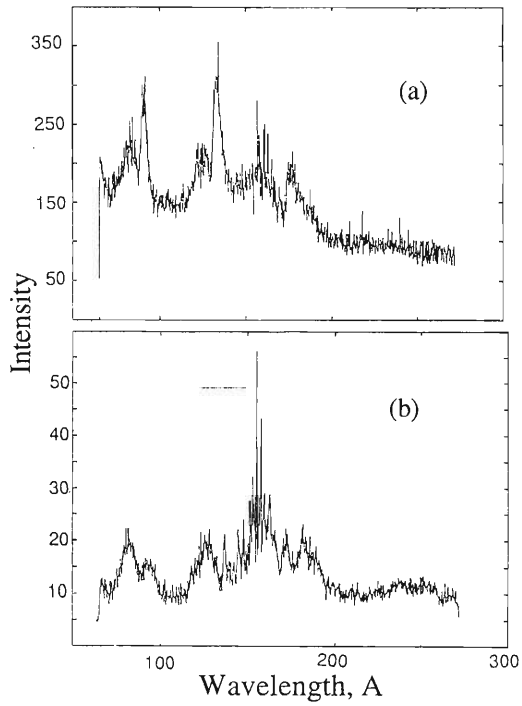

Fig. 1. This shows beam-foil spectra recorded using a beam of 1.5 MeV/u Erbium. The two spectra are taken at different foil positions: (a) very close to the foil and (b) with a time delay of around 0.25 ns between excitation and observation.

line contributions to spectral lines and the influence of such satellites on lifetime measurements.[3)] In particular we have shown a shortening of measured decay times compared to theoretical counterparts due to the satellite contamination. In the experiment done here we expect satellite contamination to be quite large, and therefor our experimental decay time should be shorter than the true level lifetime. However, the theoretical lifetime given in Ref. 2 is 86 ps which is already shorter than our measured value. The only conclusion we can draw at this moment is that more investigation, both theoretical and experimental, is called for.

References

1) F. W. Meyer: Comments At. Mol. Phys. **33**, 193 (1997).
2) E. Biemont: At. Data Nucl. Data Tables **43**, 163 (1989).
3) R. Hutton: RIKEN Accel. Prog. Rep. **32**, 94 (1999).

*1 Applied Physics Department, Shanghai Jiaotong University, P. R. China
*2 Department of Physics, University of Lund, Sweden

Continued Studies of the Beam-Foil Technique for Atomic Lifetime Measurements Using Li-like Ne

R. Hutton, Y. Zou,[*1] S. Huldt,[*2] I. Martinson,[*2] K. Ando, T. Kambara, and H. Oyama

In a previous report we have discussed problems which arise due to satellite contamination of spectral lines in beam-foil spectroscopy and in particular, the influence on lifetime measurements using the Li-like resonance lines of Ar as an example.[1)] There, we showed that at the beam energy used (2.5 MeV/u) the decay of the Li-like Ar resonance line could be contaminated by Be-like satellite line decays. The role the beam energy plays in such measurements is described in Ref. 2. In this report we will describe an experiment to measure the Li-like resonance line lifetime for Neon. It turns out that only a few satellite lines can affect the decay of the resonance line. This is due to (a) wavelength considerations, i.e. the satellite line must blend the transition of interest, also (b), lifetime considerations, i.e. if the initial state of the satellite level decays with a rate very much faster than the excited state giving rise to the resonance line, then the effect is small. The upper satellite level in the cases studied here is 2pnl and this configuration will go above the $1s^2 2s$ ionisation limit for some value of n. Once the initial state of the satellite line is above the ionisation limit, very fast autoionisation channels become open for many of the levels of the 2pnl configuration. This is shown graphically in Fig. 1, where the n value for which the 2pnl configuration goes above the $1s^2 2s$ ionisation limit is shown as a function of Z. From Fig. 1 we see that already for n = 7 the 2pnl levels go above the ionisation limit for Ne. However the 2p6l levels are predicted (Cowan code calculations)[3)] to decay quite fast (at least a factor of 10 faster) compared to the decay of the $1s^2 2p$ level, and therefore the effect of the satellite contamination on the resonance line lifetime may be minimal. To test this we recorded decay data for the Li-like Ne resonance lines. The lifetimes for these levels have been measured in a previous work by Knystautas et al.[4)] In Fig. 2 we show a decay curve for the stronger of the the two resonance lines, the $^2S_{1/2} - {}^2P_{3/2}$ transition. We paid particular attention to recording many points close to the foil zero position as it is in this region that deviations from a single exponential decay can be expected. We found, however, a single exponential decay with a decay constant matching the theoretical lifetime of the $2p\,^2P_{3/2}$ level. This is in agreement with the model described above and in Ref. 1.

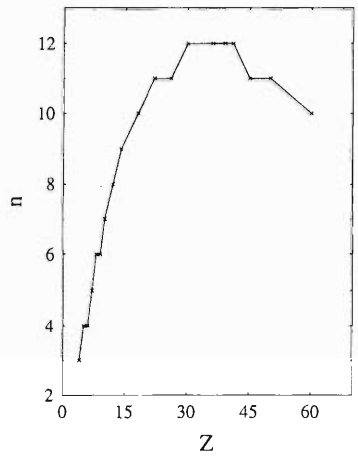

Fig. 1. This shows the value of n in $1s^2 2pnl$ for which autoionisation becomes energetically allowed as a function of Z for Be-like ions. The value of n was obtained from calculations using the Cowan computer code.

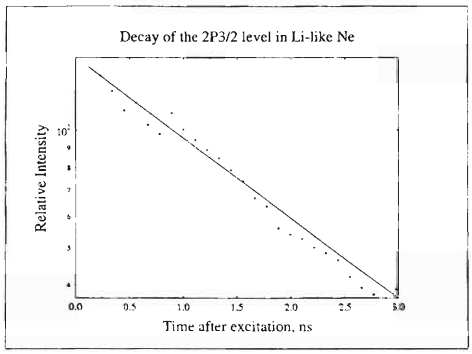

Fig. 2. This shows the decay curve for Li-like Ne measured at a beam energy of 0.4 MeV/u. The decay curve is a straight line, (on a log scale), showing that the decay is probably not contaminated by satellite transitions.

References

1) R. Hutton et al.: RIKEN Accel. Prog. Rep. **31**, 94 (1998).
2) R. Hutton et al.: RIKEN Accel. Prog. Rep. **32**, 93 (1999).
3) R. D. Cowan: *The Theory of Atomic Structure and Spectra* (University of California Press, Berkeley, 1981).
4) E. J. Knystautas et al.: J. Quant. Spectrosc. Radiat. Trasfer **11**, 75 (1971).

*1 Applied Physics Department, Shanghai Jiaotong University, P. R. China
*2 Department of Physics, University of Lund, Sweden

Foil Ageing Problems in Beam-Foil Spectroscopy

R. Hutton, Y. Zou,[*1] S. Huldt,[*2] I. Martinson,[*2]
K. Ando, T. Kambara, and H. Oyama

The target in beam-foil spectroscopy is often a thin carbon foil with a thickness of between 2 and several hundred microgramms per square cm. The status of the foil is very important to the photon generation by the subsequently decaying foil excited ions. In the extreme case of a foil with holes both the current, measured in a Faraday cup (for normalizing the measurement time), and the light yield in a particular line will decrease, and not necessarily in a proportional way. In a series of beam foil spectroscopy experiments performed at RILAC, foils with thickness of either 10 or 40 $\mu g/cm^2$ have been used. It was considered that 1 hour exposure to the beam would be sufficient to prepare the foil for stable use. However, we have found that the foil actually never really stabilizes, or that it does so after more than 20 h which was the longest time we have ever used a single foil. In measuring lifetime decay curves for foil excited ions we chose a fixed foil position to measure the foil aging properties. That is the foil was returned to a fixed slit-foil separation every 1 or 2 h and spectra were recorded. We found that the foil aging property depends on both beam energy and the ion species passing through the foil, and maybe, to some extent, on the type of foil used. We have little data here, so this needs further investigation. Foil aging properties are shown graphically in Fig. 1. In Fig. 2 we show the effect on the spectra at two quite different times, i.e. after 2 h and after 10 h. The beam used here was Mg at an energy of 2.5 MeV/u. The charge state before the foil was Mg^{6+}. It can be seen that not only the intensity but also the charge state distribution changes. The more highly charged ions, e.g. He-like Mg, becoming relatively more predominant at longer times, given that the light intensity from a given charge state follows the charge state fraction in the beam. This may require the ionisation and excitation processes in the ion-foil interaction to be similar which need not be true. These effects can be of course taken into account when measuring lifetimes using the beam-foil method, but such corrections are not often discussed in the literature.

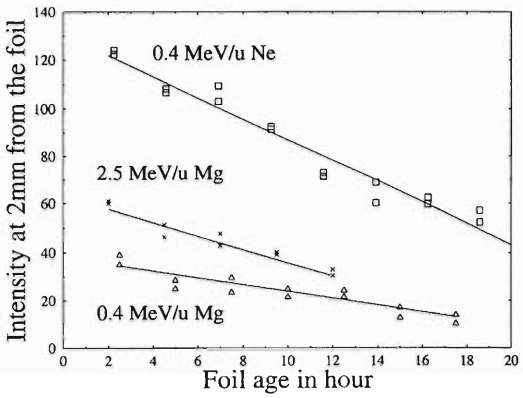

Fig. 1. The measured photon intensity in one of the Li-like resonance decays for different beams plotted as a function of the time after which the foil was first exposed to the ion beam. Here, "foil age in hours" means the number of hours after the foil was first exposed to the ion beam. The data was recorded with foil-spectrometer slit separation of around 2 mm.

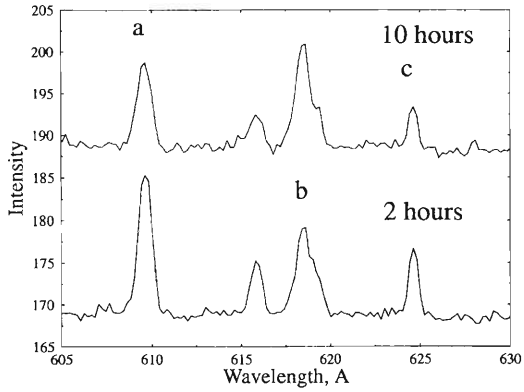

Fig. 2. This shows that the photon intensity in Li-like lines decreases with time after the foil is first exposed to the beam, whereas the photon intensity in He-like transitions increases. The two spectra are recorded at a fixed foil position 2 and 10 h after the foil was exposed to the beam. The two Li-like 2s-2p resonance lines are at 609.5 (a) and 624.5 Å (c). A feature from high nl He-like lines is seen at around 618 Å (b).

*1 Applied Physics Department, Shanghai Jiaotong University, P. R. China
*2 Department of Physics, University of Lund, Sweden

Crossed Beam Experiment of Highly Charged Ion-Atom Collision in the Energy Range below 100 eV/q

M. Kitajima, Y. Nakai, Y. Kanai, Y. Yamazaki, Y. Awaya, and Y. Itoh

The study of multi-electron capture processes in the slow collisions between highly charged ions and atoms or molecules has been the subject of considerable experimental and theoretical investigations. Recently, experimental techniques utilizing a recoil ion source for producing very slow ion beam for the angular differential cross section measurements have been presented.[1,2] The intensity of the very-slow ion beam is, however, extremely small and species of the ions are limited for these experiments.

Here we present an experimental setup for measurementts of the state selective angular differential cross section of multi-electron capture processes in the very-slow collisions between highly charged ions and atoms or molecules. It utilizes the ion beam from the 14.5 GHz Caprice electron cyclotron resonance ion source (ECRIS) at RIKEN.[3] Using the direct ion beam from the ECRIS has the advantage to achieve a high-intensity beam, even after the deceleration of the ion beam. Highly charged ions produced in the ion source are extracted at a beam energy of 2 keV/q into the beam line, and then the mass to charge ratio (m/q) is selected with an analyzing magnet. The ion beam is decelerated down to desired energy in two steps using deceleration lens and energy selected by a double hemispherical analyzer. The target gas is introduced by a multi capillary and intersects with the ion beam at right angles. Scattered ion energies are analyzed by a hemispherical analyzer, which is set on a turntable.

Typical currents of the ion beam measured right after the m/q selection (2 keV/q) and those at the intersection region (decelerated beam) are shown in Table 1. The intensity of very-slow ion beams obtained in the present ECRIS setup is much higher than that obtained with the recoil ion source by a factor of 10^4. An overall energy resolution of about 1/180 of the beam energy was achieved in the present apparatus.

Table 1. Currents and energy widths of ion beams obtained in the present experimental setup.

Ions	2keV/q beam (μA)	Decelerated beam (pA)	Beam energy (eV/q)	Energy width (eV/q)
Ar^{8+}	13	22	35	0.20
Ar^{6+}	9	300	50	0.27
Ar^{4+}	3	135	60	0.66
He^{2+}	20	250	70	0.58
He^{+}	10	300	60	0.33
He^{+}	30	180	40	0.33
He^{+}	20	7	20	0.18

The energy distributions of scattered ion in the 36.6 eV/q (7.3 eV/u) Ar^{8+}-N_2 collisions at the scattering angles from 0° to 10° are shown in Fig. 1. The intense peak seen at 44 eV/q for $\theta_{Lab} = 0°$, originating from single electron capture, rapidly decreases with increasing the scattering angle. The neighboring peak at 46 eV/q also decreases at larger angles. At 53 eV/q, a multi-component peak due to the double electron capture processes is seen, the intensity of which decreases rather slowly. The peak at 56 eV/q does not decrease its intensity with scattering angle in contrast to the other peaks. These different scattering angle dependencies confirm the fact that single electron capture occurs mainly in the glancing collisions with small scattering angle. On the other hand, multiple electron capture occurs in the close collisions with large scattering angle.

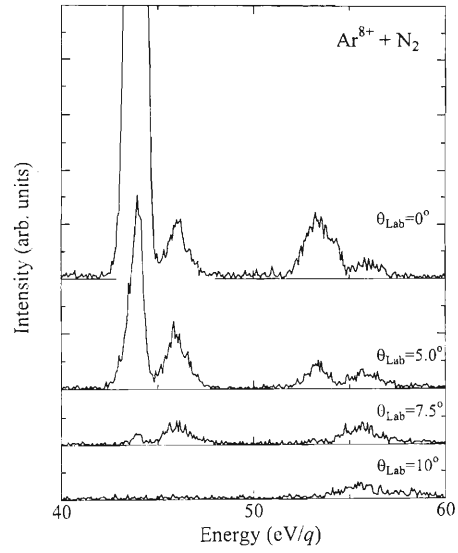

Fig. 1. Energy distributions of scattered ion (Ar^{8+}, Ar^{7+}, and Ar^{6+}) in the 36.6 eV/q (7.3 eV/u) Ar^{8+}-N_2 collisions at the scattering angles θ_{Lab} as indicated.

References

1) H. Cederquist et al.: Phys. Rev. A **39**, 4308 (1989).
2) S. Yaltkaya et al.: Phys. Rev. A **48**, 382 (1993).
3) Y. Kanai et al.: Proc. 12th Int. Workshop on ECRIS, edited by M. Sekiguchi and T. Nakagawa, INS-J-182 (Tokyo, 1995), p. 312.

Angular Distribution of Auger Electrons from Doubly-Excited N^{3+} Produced by the 50 keV N^{5+}-Ar Collisions

T. Kamei, K. Ogura, T. Takayanagi, K. Wakiya, Y. Kanai, and Y. Nakai

To study the double-electron capture processes of highly-charged ions, we have measured Auger electrons emitted from Be-like doubly-excited states.[1,2] In some collision systems, the Auger electron intensities from triplet states were predominant in the spectra measured at 0°.[1,2] To comfirm that the triplet states are indeed produced dominantly in those collision systems, we need the Auger spectra over the whole angular range in the scattering plane. This is because the angular distribution of ejected electrons from multiply excited states produced by the multiple electron capture from target atom is strongly anisotropic.

Here we present the spectra of Auger electrons from the doubly excited $N^{3+**}(1s^2 3l3l')$, which were measured at different observation angles by using a toroidal-type electron energy analyzer.[3] These states were produced by the double-electron capture processes in the collision of the 50 keV N^{5+} ions with Ar atom. The 50 keV N^{5+} ions were extracted from the 14.5 GHz Caprice ECR ion source.[4] Typical spectra measured at 0, 30, and 90 degrees are shown in Fig. 1. Theoretical Auger transition energies are also indicated in Fig. 1.[2] The intensities of the Auger electrons from the triplet states are evidently stronger than those from the singlet states. All spectra measured at 0° to 180° have had this feature. Up to now, we have not calibrated the absolute efficiency of the detector, and therefore we can not extract the production cross sections of the doubly-excited states from our spectra. However, at least we can mention that the intensities of triplet states are predominant at all observation angles. This means that in this collision system, the production of the triplet states are dominant processes in the double-electron transfer processes. To discuss about the mechanism to enhance the production cross sections of triplet states, we need more precise measurements.

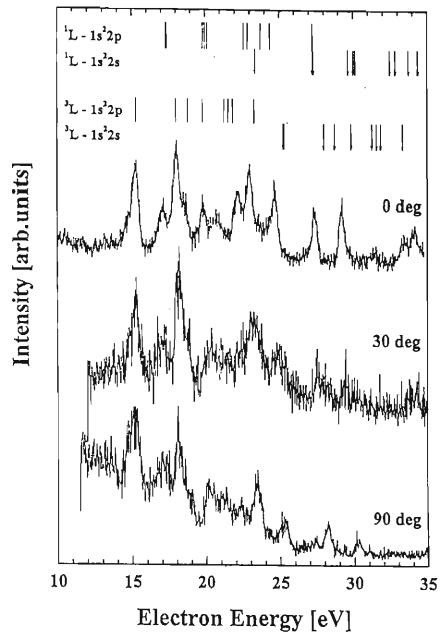

Fig. 1. Ejected electron spectra from the doubly-excited states of $N^{3+**}(1s^2 3l3l')$ produced by collisions of N^{5+} ions with Ar atoms at three observation angles. Arrows and solid lines indicate the theoretical Auger transition energy to the $N^{4+}(1s^2 2s)$ and the $N^{4+}(1s^2 2p)$, respectively. Upper-left descriptions are the singlet doubly-excited states and the triplet doubly-excited states.

References

1) Y. Kanai et al.: Nucl. Instrum. Methods Phys. Res. B **98**, 81 (1995).
2) S. Kitazawa et al.: J. Phys. B **31**, 3233 (1998).
3) Y. Tamagawa et al.: RIKEN Accel. Prog. Rep. **30**, 145 (1997).
4) Y. Kanai et al.: RIKEN Accel. Prog. Rep. **30**, 168 (1997).

Double Electron Capture vs. Target Excitation in Slow He^{2+} + He Collisions

B. Nyström, Y. Nakai, T. Kambara, and Y. Kanai

Photon emission following slow ion-atom collisions has been observed for the collision system He^{2+}+ He. The energy of the incoming beam of helium ions was varied between 18 and 36 keV. In particular, the velocity-dependent photon emission for the $1s^2\ ^1S_0$–$1snp\ ^1P_1$ ($n \leq 4$) resonance series in neutral helium were measured. The measurements were done in such a way that the Doppler shift is used to separate whether the photons originated from the projectile ions or the target atoms. To our knowledge, this is the first time that these two processes, Double-Electron Capture (DEC) and Target Excitation (TE), are separated for this collision system using photon emission spectroscopy. The work has been performed with the 14.5-GHz Caprice ECR ion source at RIKEN[1] by using a recently installed 1-μm grazing incidence VUV-spectrometer.[2]

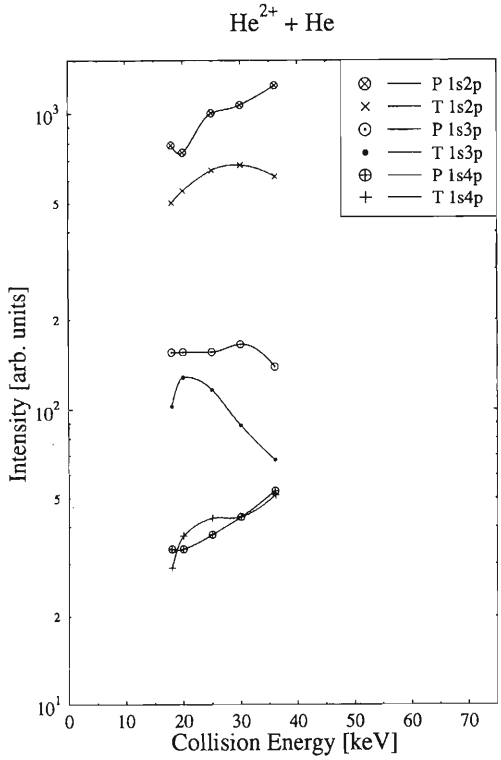

Fig. 1. Beam-energy dependent photon-emission intensities from the lowest singlets in neutral helium. Data for the excited projectiles after double-electron capture processes are plotted with encircled marks and denoted by P in the legend, whereas those for the excited target are plotted without circles and denoted by T. These data points are intensity-calibrated in order to facilitate direct comparison.

Figure 1 shows the development in the measured photon emission intensity with the energy of the impinging beam of He^{2+} ions. The intensity response for the setup is calibrated with the help of known photon emission cross sections[3] for $Xe^{7+,8+}$. Some more work is still needed in order to make a detailed comparison with theory, primarily to correct for possible lifetime effects and for the finite observation window.[4] However, there are resemblance between the measured data and the theoretical calculations.[5]

References

1) Y. Kanai et al.: RIKEN Accel. Prog. Rep. **30**, 168 (1997).
2) B. Nyström et al.: RIKEN Accel. Prog. Rep. **31**, 96 (1998).
3) M. Druetta et al.: Nucl. Instrum. Methods Phys. Res. B **98**, 211 (1995).
4) R. K. Janev et al.: Phys. Rep. **117**, 265 (1985).
5) W. Fritsch.: J. Phys. B: At. Mol. Opt. Phys. **27** 3461 (1994).

Ion-Velocity Effects on Defect Production in an Ion-Irradiated High-T_c Superconductor

N. Ishikawa, Y. Chimi, N. Kuroda, A. Iwase, and T. Kambara

In the present paper, we report our recent results on the defect production by swift heavy ions in high-T_c superconductors $EuBa_2Cu_3O_y$ with the emphasis on the velocity effect. Thin films of the high-T_c superconductor $EuBa_2Cu_3O_y$ (EBCO) were prepared on MgO substrates by an rf magnetron sputtering method. The EBCO thin films were c-axis oriented and thickness of the samples was about 0.3 μm. These samples were irradiated with the following high-energy ions at low-temperature (100 K): 120 MeV $^{35}Cl^{8+}$, 90 MeV $^{58}Ni^{6+}$, 90 MeV $^{127}I^{9+}$, and 200 MeV $^{197}Au^{13+}$ produced from the tandem accelerator at JAERI (Japan Atomic Energy Research Institute)-Tokai, and 3.54 GeV $^{136}Xe^{31+}$ and 3.84 GeV $^{181}Ta^{37+}$ from the Ring Cyclotron at RIKEN (The Institute of Physical and Chemical Research). Using the above ions we varied the values of electronic stopping power S_e from 10 to 47 MeV/(mg/cm^2). In-situ measurements of the fluence dependent electrical resistivity were performed at a fixed temperature (100 K) by employing the conventional four- probe method. It should be noted that the sample thickness (0.3 μm) is much smaller than the ion ranges (> 7.4 μm), meaning that the energy loss of incident ions during their passage through the sample is much smaller than the incident ion-energy, and that the irradiating ions do not remain in the sample as impurities. Since the irradiations and measurements are performed at low temperatures, we can rule out the possibility of thermal annealing of the irradiation-induced defects. Figure 1 shows the resistivity change ($\Delta\rho/\rho$) as a function of the fluence of irradiation for various high-energy ions. Low-energy (~1 MeV) ion irradiations were performed for EBCO thin films previously, and we found that for the low-energy ion irradiation the defect production is dominated by elastic interaction between irradiating ions and target atoms.[1,2] By comparing the results between low and high energy ion irradiations, we find that resistivity change by the high-energy ion irradiations, shown in Fig. 1, is much larger than that by the low-energy ion irradiations. This indicates that mainly the electronic excitation contributes to the defect production in EBCO when irradiated with high-energy (90 MeV–3.84 GeV) ions. Generally the S_e which is defined as an energy transferred from the irradiating ion to the target electrons per unit path length has often been accepted as one of the parameters to characterize the defect production process. However, in this study, the ion-velocity dependence in the defect production has been observed even for the same S_e. In Fig. 2, a comparison of resistivity-fluence curves is made for two irradiations with the same S_e values (~28 MeV/(mg/cm^2)) but with much different velocities. A 3.54 GeV Xe ion is 6.1 times faster than a 90 MeV I ion. From this figure, we see that even for the same S_e value, irradiation effect differs for different velocities: the faster ion causes a smaller change in resistivity, thereby showing the velocity effect.

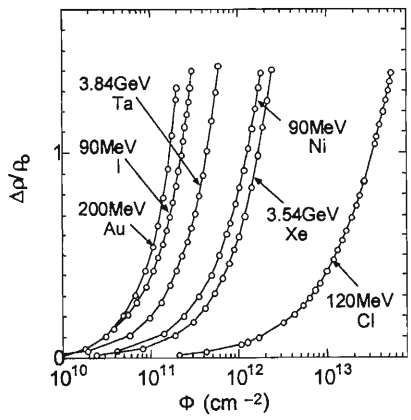

Fig. 1. The resistivity change, $\Delta\rho$, normalized by the resistivity before irradiation, ρ_o, plotted as a function of fluence Φ for the EBCO irradiated with various high energy ions.

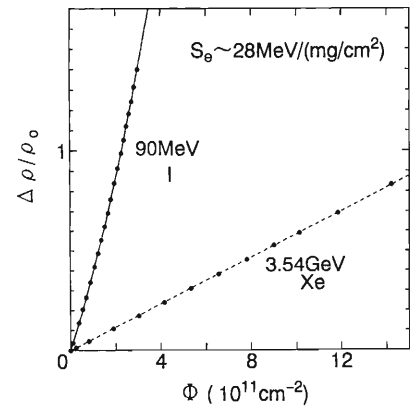

Fig. 2. The value of $\Delta\rho/\rho_o$ plotted as a function of fluence for irradiations with 90 MeV I and 3.54 GeV Xe. These two irradiations have the same S_e values, ~28 MeV/(mg/cm^2). A 3.54 GeV Xe ion is faster than a 90 MeV I ion.

References

1) N. Ishikawa, A. Iwase, Y. Chimi, H. Maeta, K. Tsuru, and O. Michikami: Physica C **259**, 54 (1996).
2) N. Ishikawa, Y. Chimi, A. Iwase, K. Tsuru, and O. Michikami: J. Nucl. Mater. **258/263**, 1924 (1998).

Vortex Pinning of Splayed Columnar Defects in $Bi_2Sr_2CaCu_2O_y$

N. Kuroda, N. Ishikawa, S. Okayasu, A. Iwase, H. Ikeda,* R. Yoshizaki,* and T. Kambara

A limit on technological advances of high temperature superconductors comes from the intrinsically low critical current density J_c stemming from vortex motion. Columnar defects produced by the irradiation with swift (~1 GeV) heavy ions can pin down the magnetic vortices much more effectively than the other kinds of defects such as point defects. Recently, in $YBa_2Cu_3O_{7-\delta}$ (YBCO) a dispersion (or splay) in the orientation of the columnar defects has been found to improve the pinning efficiency strongly, compared to a parallel set of columns,[1] as predicted theoretically.[2] We have investigated the "splayed effect" in $Bi_2Sr_2CaCu_2Oy$ (Bi-2212) single crystals to evaluate the influence of anisotropy on the splayed effect. The anisotropy of Bi-2212 with an anisotropy parameter $\gamma \equiv (m_c/m_{ab})^{1/2} \sim 200$ is much higher than that of the YBCO with $\gamma \sim 6$, where m_c is the effective mass along c-axis and m_{ab} is that in ab-plane.

Bi-2212 single crystals were grown by a traveling solvent floating zone (TSFZ) method and were irradiated with 3.8 GeV $^{181}Ta^{37+}$ at the RIKEN Ring Cyclotron. The three samples used for irradiation were cleaved and cut from one large crystal with T_c of 91 K. Three samples had almost the same dimensions of $1.4 \times 1.7 \times 0.04$ mm^3. The ion beam was tilted from the c-axis by ±20°, +20°, and 0° to produce splayed, inclined, and parallel columnar defects. The pinning properties of Bi-2212 with different configurations of columnar defects were compared with one another. In all cases, the total pin density in ab-plane of the crystal was 8×10^{10}/cm^2, which corresponds to a dose-equivalent matching field $B_\Phi = 1.6$ T. The irradiation reduced T_c by 6 K to be 85 K because of the production of damage.

We found that the splayed effect was not significant in Bi-2212 at low temperatures well below T_c. Figure 1(a) shows the magnetic hysteresis loops at 30 K. The width of hysteresis loop ΔM proportional to the critical current J_c was smaller for splayed configuration (±20°) than that for parallel one (0°) at all measured fields. Moreover, ΔM for ±20° was smaller than that for +20°. The difference in the critical current originates from the difference in the vortex state among splayed, inclined, and parallel columnar defects. The vortex lines at low temperatures for splayed, inclined, and parallel columnar defects[2,3] are illustrated in Fig. 2. The vortex lines are entangled for splayed columnar defects.[2] If the potential barrier to vortex-line cutting U_x[4] is large compared to the thermal energy, entangling vortex lines can lead a viscous behavior with much improved transport properties.

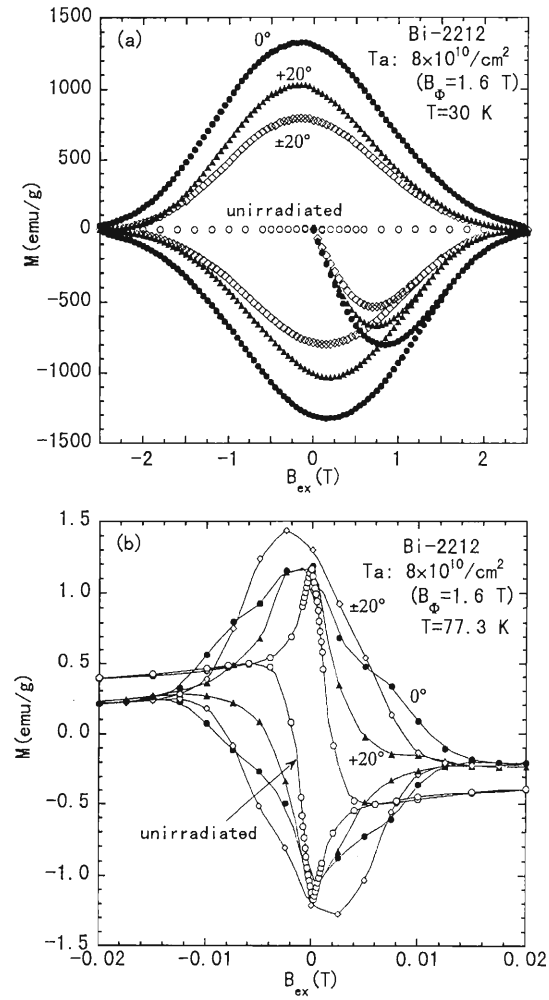

Fig. 1. Magnetic field dependence of magnetization in Bi-2212 with splayed, inclined, and parallel columnar defects (a) at 30 K and (b) at 77.3 K. The external field B_{ex} is parallel to the c-axis.

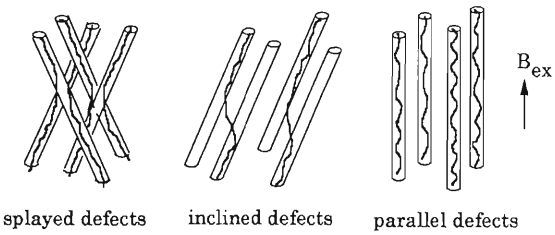

Fig. 2. Illustration of vortex lines for splayed, inclined, and parallel columnar defects.

However, in Bi-2212, the anisotropy is so high that the vortex-line cutting barrier U_x ($\propto 1/\gamma$)is very low. As a result, the "splayed effect" is not significant. Furthermore, in extremely anisotropic Bi-2212, the unpinned

* Cryogenics Center, University of Tsukuba

vortices produced by splay at the defect-defect intersections where two defects cross each other are easy to move, stimulating vortex to creep. A large number of intersections exist in the sample with the density of $2\tan 20°/d^3 \sim 10^{16}/cm^3$, where d is the average spacing between two defects. For the inclined columnar defects, a small part of vortex line cannot be pinned in the columns, owing to the mismatch between the magnetic field direction and the direction of column. This causes the pinning efficiency of the inclined defects (+20°) to reduce less than that of parallel defects (0°).

On the other hand, at 77.3 K, the splayed defects slightly enhance the width of hysteresis loop ΔM, compared with the inclined and parallel columnar defects, as shown in Fig. 1(b). This may be due to the enhancement of c-axis coupling of vortices, resulting from the increase of coherence length along the c-axis near T_c.

References

1) L. Krusin-Elbaum et al.: Phys. Rev. Lett. **72**, 1914 (1994).
2) T. Hwa et al.: Phys. Rev. Lett. **71**, 3545 (1993).
3) G. Blatter et al.: Rev. Mod. Phys. **66**, 1346 (1994).
4) C. Carraro et al.: Phys. Rev. B **51**, 534 (1995).

Columnar Defect-Induced Strain and Superconductivity in $Bi_2Sr_2CaCu_2O_x$ Observed by LT-STS/STM

N. Nishida, H. Sakata, S. Kaneko, Y. Ono, and T. Kambara

Recently, uniaxial strains on high-T_c copper oxide superconductors (HTSC) have attracted much attention, because a thin film of the epitaxially grown $La_{1.9}Sr_{0.1}CuO_4$ single crystal ($T_c \sim 25$ K) on $LaSrAlO_4$ has been reported to show 100% increase in the superconductng transition temperature (T_c) due to the epitaxial compression in *ab*-plane.[1] In HTSC the irradiation of high energy heavy ions can generate columnar defects which are amorphous regions along the ion tracks of 3–12 nm in diameter. We have irradiated $Bi_2Sr_2CaCu_2O_x$ single crystals ($T_c \sim 86$ K) with 3.5 GeV $^{135}Xe^{31+}$ ions, 3.8 GeV $^{181}Ta^{37+}$ ions, and 3.1 GeV $^{209}Bi^{37+}$ ions at RIKEN Ring Cyclotron, and have studied the generated columnar defects by a low-temperature scanning tunneling spectroscopy and microscopy (LT-STS/STM) and by a transmission electron microscope (TEM). A columnar defect has been observed as an insulating and amorphous region as reported before.[2] Columnar defects induce strains in the surrounding crystalline region because the volume in the amorphous region is locally increased. We have succeeded in observing the strain around columnar defects and in measuring the local density of states of quasi-particles, $N_s(E,r)$, by LT-STS/STM. Here we report influence of strain on the superconductivity of $Bi_2Sr_2CaCu_2O_x$ ($x \sim 8$).

The samples were irradiated by heavy ions both in parallel and in perpendicular to the *c*-plane. Figure 1 shows the strain observed by STM on *c*-plane surface of $Bi_2Sr_2CaCu_2O_x$. Heavy ions were injected almost in parallel to the *c*-plane and in the [100] direction The columnar defect runs about 6 nm beneath the surface. The injection angle has been found to be 5° from the elongated shape of the columnar defects on the *c*-plane surface. The white region along the [100] direction in the middle part of Fig. 1 indicates the geometrical protrusion due to the columnar defect running beneath the surface. A superstructure can also be seen as a modulation with about 25 Å cycle along the [010] direction. We have found that the swell of the surface is about a few tenths of nanometer high and 20 nm wide, from the profile shown in Fig. 2. The tensile strain in this region was estimated to be 10^{-3}–10^{-4}.

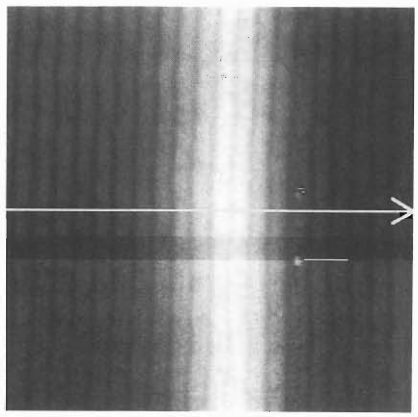

Fig. 1. Constant-current STM topographic image (50 nm × 50 nm) of *c*-plane of $Bi_2Sr_2CaCu_2O_x$ ($x \sim 8$) obtained at 4.2 K with tunneling current of 0.2 nA and bias voltage of 0.5 V. A columnar defect runs along [100] direction 6 nm beneath the surface.

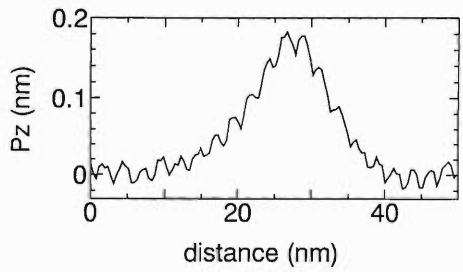

Fig. 2. The STM profile measured along the arrow line marked in Fig. 1.

In the case of the columnar defect running perpendicular to the *c*-plane, on the other hand, a compressive strain of the similar magnitude as the case of the tensile strain is induced on the *c*-plane around it. In both cases we have measured the differential tunneling conductances, dI/dV, around the columnar defects by LT-STS/STM to obtain $N_s(E,r)$. The measured $N_s(E,r)$'s have not exhibited an appreciable change and were the same as those previously observed[3] on the flat *c*-plane surface of $Bi_2Sr_2CaCu_2O_x$. It can be said therefore that in $Bi_2Sr_2CaCu_2O_x$ the strain in the order of 10^{-3}–10^{-4} does not bring about a remarkable change in the superconductivity, whether it is tensile or compressive.

References

1) J. -P. Locquet et al.: Nature **394**, 453 (1998).
2) N. Nishida et al.: RIKEN Accel. Prog. Rep. **30**, 101 (1997).
3) S. Kaneko et al.: Physica C **298**, 105 (1998).

Magnetic Excitations from the Two-Leg Spin Ladder in $La_6Ca_8Cu_{24}O_{41}$

M. Matsuda, K. Katsumata, and R. S. Eccleston*

One- and two-dimensional antiferromagnets show novel phenomena originating from quantum fluctuations. A spin ladder system is important to study a crossover from one- to two-dimensions. Extensive studies have been performed on the spin ladder system both theoretically and experimentally.[1] An interesting property is that the ladders with even-numbers of legs have an excitation gap but those with odd-numbers of legs show gapless excitations. It is also predicted that superconductivity occurs if the ladders with even-numbers of legs are doped with carriers.

We report on the magnetic excitations from $S = \frac{1}{2}$ two-leg ladder (Fig. 1) in $La_6Ca_8Cu_{24}O_{41}$ single crystals.

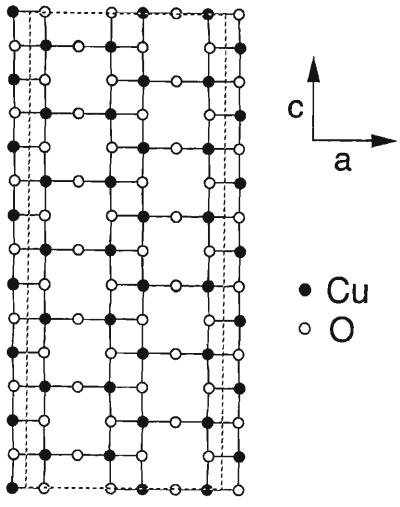

Fig. 1. Structure of the Cu_2O_3 ladders in $La_6Ca_8Cu_{24}O_{41}$.

The neutron scattering experiments were carried out on the High Energy Chopper Spectrometer (HET) on the ISIS Pulsed Neutron Source at the Rutherford Appleton Laboratory. The experiments were carried out with incident neutron energies of 150, 300, 500, 600, and 800 meV which are monochromated by a rotating Fermi chopper which is phased to the source.

Figure 2 shows a summary of the inelastic neutron experiments on $La_6Ca_8Cu_{24}O_{41}$ measured at 20 K. The broken curves are scan loci. The closed circles and the solid straight lines between them represent the positions where peaks are observed in neutron inelastic spectra. Magnetic excitations from the two-leg ladder exist between ~35 and ~200 meV. The solid curves are guides to the eye.

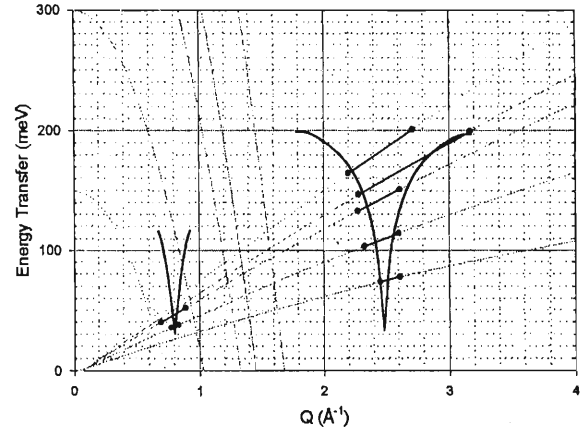

Fig. 2. $\omega - Q$ dispersion relation in $La_6Ca_8Cu_{24}O_{41}$ measured at $T = 20$ K.

We are now completing the measurement of full dispersion curve for the $S = \frac{1}{2}$ two-leg ladders. The experimental curve will then be fitted with a theoretical calculation from which one can determine the exchange interactions between copper spins parallel and perpendicular to the ladder. It is also interesting to see the effect of the holes on the excitation spectrum by comparing the results of $La_6Ca_8Cu_{24}O_{41}$ with those of $Sr_{14}Cu_{24}O_{41}$.[2]

References

1) E. Dagotto and T. M. Rice: Science **271**, 618 (1996).
2) R. S. Eccleston, M. Uehara, J. Akimitsu, H. Eisaki, N. Motoyama, and S. Uchida: Phys. Rev. Lett. **81**, 1702 (1998).

* Rutherford Appleton Laboratory, UK

Laser Spectroscopic Study of Metastable Ne Atoms in Gaseous and Liquid He

Q. Hui, E. B. Gorden, M. Nakamura, and M. Takami

We are currently preparing a CW-laser system for studying the laser induced fluorescence (LIF) spectrum from the singlely-charged atomic ions with one unpaired valence electron, i.e. alkaline earth ions. In the meantime, using a similar experimental setup and pulsed lasers, we are also trying to measure the LIF spectrum of metastable Ne atoms in the gaseous and liquid helium. It is well known that valence electron transitions of neutral atoms in liquid He show a large line-shift and broadening. This is resulted from the interaction between the valence electrons of neutral atoms and the surrounding helium atoms. A so-called "bubble model" has been successfully applied to interpret the observed line-shifts and broadening.[1] Recently experiments by our group and by other groups have revealed non-radiative relaxation in the Ag and alkali atoms excited to a p-state.[2] This observation has been explained as a result of a metal-helium exciplex formation.[3] Metastable Ne atom is similar to the alkali atoms and alkaline earth ions in its electronic structure, and is expected to show a similar dynamics in liquid helium as those observed with alkali atoms and Ag. A preliminary experiment with the metastable Ne atoms dispersed in liquid helium showed almost identical line position and width as in gas phase.[4] Present work is also aimed to clarify this mystery.

The experiments were carried out in a similar cryostat as reported in the last issue of this Progress Report.[5] Instead of a laser-sputtering ion source, a gas-phase discharge in a glass capillary at above liquid helium was used to produce metastable Ne atoms, Ne*. The Ne* atoms were transported into superfluid helium in a glass cell hanging above the bulk liquid helium by a He gas jet through an orifice. A pulsed dye laser was used to excite the Ne atoms from the long-lived $2p^5(^2P_{3/2}{}^o)3s[3/2]_2{}^o$ metastable state. Laser induced fluorescence (LIF) was collected at a right angle by a photomultiplier via a monochromator (Fig. 1).

As the first step of the experiments, we have observed the LIF from metastable Ne atoms in the He gas jet 1-2 cm below the orifice. Excitation spectrum of the $2p^5(^2P_{3/2}{}^o)3p[3/2]_2{}^o \leftarrow 2p^5(^2P_{3/2}{}^o)3s[3/2]_2{}^o$ line (614.3 nm in free spac), recorded by scanning the dye laser wavelength and monitoring the emission at 692.9 nm, shows a nearly symmetric profile with $\sim$1 cm^{-1} line-width (FWHM). We were unable to observe the emission spectrum on the same line because of the strong scattering of laser. Emission spectrum of the 692.9 nm line, which has the same upper state as the 614.3 nm line, shows an asymmetric shape with

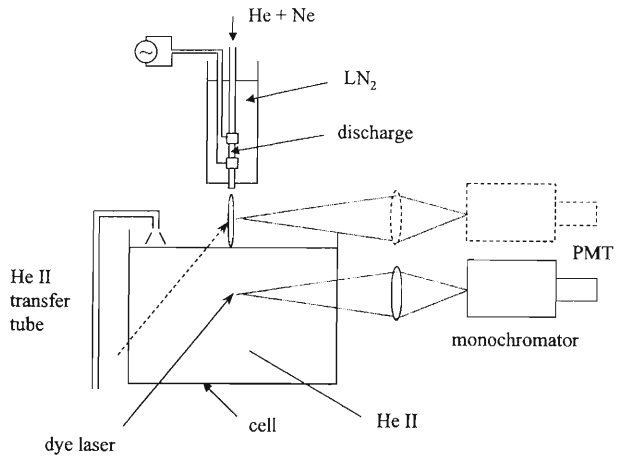

Fig. 1. Experimental setup.

a steep rising edge on the short-wavelength side and a smoother falling edge on the long-wavelength side (Fig. 2). The emission line-width is $\sim$6 cm^{-1}, which is much wider than the excitation line. The asymmetric profile and large broadening of the emission line have not been reported before.

In the upper state of the 692.9 nm line, an unpaired s-electron in the lower state is excited to a p-orbital. According to the theoretical model proposed to explain the LIF spectra of the alkali and Ag atoms in liquid

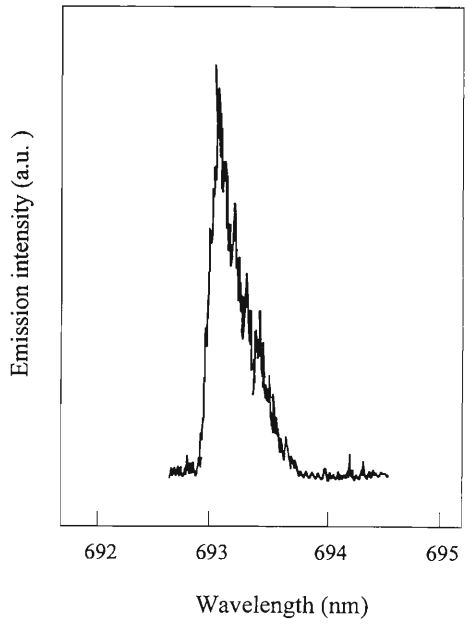

Fig. 2. Emission spectrum of Ne atoms in cold He jet.

helium and cold gas helium,[3] a number of helium atoms are attracted by the charged ion-core of the Ne^* atom to the nodal plane of p-orbital where the electron distribution is zero, thereby forming a Ne^*He_n exciplex. This will reduce the total energy of the system and will result in a red-shift and line-broadening.

We have also observed a narrow excitation line when the excitation laser beam was moved into superfluid helium as in Ref. 4. However, it cannot be excluded that the signal was actually from Ne^* atoms in gas phase, which may be excited by scattered laser light. We plan to improve the setup to reduce this scattering and repeat the experiment.

References

1) A. P. Hickman and N. F. Lane: Phys. Rev. Lett. **26**, 1216 (1971).
2) J. L. Persson et al.: Phys. Rev. Lett. **76**, 1501 (1996).
3) Z. J. Jakubek et al.: Phys. Rev. Lett. **79**, 629 (1997).
4) E. B. Gordon: unpublished material.
5) Q. Hui and M. Takami: RIKEN Accel. Prog. Rep. **31**, 104 (1998).

Channeling Analysis of ZnSeTe†

T. Maruyama, T. Hasegawa,* N. Komuro,* H. Yamada,* W. Ohtsuka,*
K. Akimoto, K. Maeda, and E. Yagi

ZnSeTe is an important material in application to the blue-green laser diodes. However, it is difficult to control the electronic properties in the n-type ZnSeTe even at low content of Te, while ZnSe is generally of the n-type. Our previous extended X-ray absorption fine structure (EXAFS) study suggests that some kind of acceptors not related to Cl atoms are formed in the Cl-doped ZnSeTe layer and that they compensate its n-type conductivity expected to be induced by the Cl-doping.[1] In order to clarify this compensation mechanism, we have carried out Rutherford backscattering spectrometry/ion channeling (RBS/C) and particle induced X-ray emission/ channeling (PIXE/C) measurements for undoped ZnSeTe.

The undoped ZnSeTe thin films were grown on GaAs (100) substrate by means of molecular beam epitaxy. The content of Te atoms in the sample was 27%. Typical thickness of the samples was about 1.5 μm.

The lattice location of the constituent atoms of the ZnSeTe layer was investigated by RBS/C and PIXE/C using a 2 MeV He^+ beam provided from a small tandem accelerator. The backscattering angle was 150° and the characteristic X-rays were collected by a Si (Li) detector placed at an angle of 135° with respect to the incident beam.

Figure 1 shows the channeling angular profiles of the Se K_α and Te L_α X-rays in ZnSeTe across the <100> and <110> axes obtained by the PIXE/C measurements. The intensities of X-ray from the Se and Te atoms give rise to channeling dips in both directions. For both <100> and <110> channels, the angular profiles are much shallower than those in ZnSe and ZnTe. This deterioration reflects the structural inhomogeneity induced by the local distortion in the ternary compounds. Further, the Se and Te X-rays exhibit almost same channeling dips for the <100> channel, whereas the Te-dip is shallower than the Se-dip for the <110> channel, although their angular half-widths are approximately same. These results indicate that for the <100> channel the Te atoms are shadowed by the Se atomic rows, whereas for the <110> channel most of them are shadowed by the Se atomic rows, but some portion of them are displaced from the Se atomic rows. The sites which are shadowed by the <100> atomic rows, but not shadowed by the <110> atomic rows, are tetrahedral (T) interstitial sites. Therefore, it can be said that most of the Te atoms replace the Se atoms and the rest are located at T sites. Previous *ab initio* pseudo-atomic-orbital calculation on native defects in ZnTe showed that Te atoms at T sites act as acceptors in an n-type conductivity, whether Te atoms are surrounded by Zn atoms or by Te atoms.[2] Therefore, it is considered that Te atoms at T sites act as acceptors in ZnSeTe and compensate its n-type conductivity.

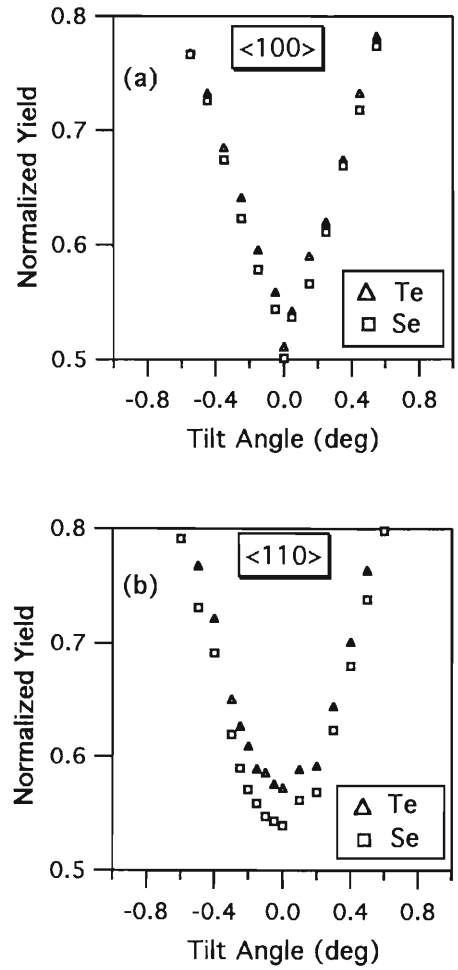

Fig. 1. PIXE angular scans of Se K_α and Te L_α for ZnSeTe across the (a) <100> and (b) <110> axes.

From the PIXE/C and RBS/C results, it was found that some portion of Te atoms are located at T sites in ZnSeTe ternary compounds. This intrinsic defect is a strong candidate of the compensation center in ZnSeTe.

† Condensed from the article in Proc. 2nd Int. Symp. on Blue Laser and Light Emitting Diodes (2nd ISBLLED).

* On leave from Institute of Materials Science, University of Tsukuba

References

1) K. Akimoto et al.: Nonlinear Optics **18**, 235 (1997).
2) R. W. Jansen and O. F. Sankey: Phys. Rev. B **39**, 3192 (1989).

Single Event Burnout in Power MOSFET Caused by High-Energy Ions

S. Matsuda, S. Kuboyama, T. Suzuki T. Hirose, H. Ohira, T. Kohno, and M. Kase

Semiconductor devices to be used for artificial satellites and spacecrafts are affected by the radiation in space. It is well known that the incidence of high energy heavy ions into semiconductor devices causes several kinds of anomalies called single event phenomena (SEP): i.e., single event upset (SEU) on memory device, single event latch up (SEL) on CMOS and LSI etc., and single event burnout (SEB) caused by the heavy ion passing through the active area of Power MOSFET. National Space Development Agency of Japan (NASDA) has studied SEB in Power MOSFET with heavy ions from the RIKEN Ring Cyclotron.[1)]

Power MOSFET's of 200 V class have been developed to be used for the future artificial satellites. To determine the design parameters of the Power MOSFET, we have performed irradiation tests on several types of samples with a beam of Ni^{25+} at 25 MeV/u (total energy of 1450 MeV), and studied the breakdown voltage data concerning with SEB. Because the Ni ion beam passes through the atmosphere, the energy of ion beam on the samples was approximately 286 MeV. Therefore, the linear energy transfer (LET) of the ions in the sample surface(Si) was about 26.7 MeV/(mg/cm^2), and the range was about 44.7 μm in Si.

From our previous study, it is known that SEB tolerance of Power MOSFET depends on the Drain-Source Breakdown Voltage (BV_{DS}) and the cell geometry. But it was not enough to fix all the design parameters. Therefore, several types of samples which were fabricated with various parameters for space applications were prepared. The irradiation test results are shown in Figs. 1 and 2. Figures 1 and 2 show the p-pitch (distance between the two p-layers in Power MOSFET) dependence and n^+ layer As-doping density (in the n^+ layer in Power MOSFET) dependence on SEB threshold, respectively. Cell geometry of all the samples was a stripe cell, because the stripe cell had better SEB tolerance than the square one according to our previous irradiation tests.

Effect of the p-pitch size on the SEB tolerance was studied first. In general, when p-pitch is smaller, the SEB tolerance increases; but the R_{on} (a resistance value when the transistor is "ON" state) characteristic is degraded, in contrast. Therefore, p-pitch size was reduced from 9 μm for our samples. As shown in Fig. 1, as p-pitch was reduced, SEB threshold increased until 6 μm; but SEB threshold decreased at 3 μm of p-pitch size. Therefore it seems that there is an optimum p-pitch size in Power MOSFET.

Effect of the n^+ layer As-doping density was studied

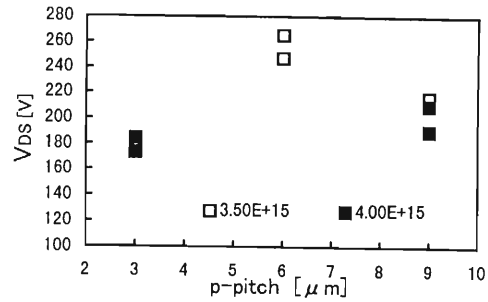

Fig. 1. The p-pitch dependence on SEB threshold.

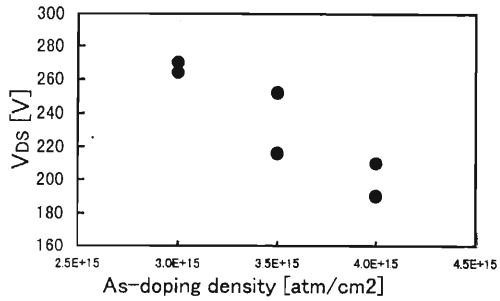

Fig. 2. The n^+ layer As-doping density dependence on SEB threshold.

next. From the previous study, the SEB mechanism of Power MOSFET is known that the parasitic bipolar junction transistor (BJT), inherent to the double-diffused MOS (DMOS) structure, is turned on by incidence of high-energy ions.[2)] It is thus expected that the decrease of current gain (h_{FE}) of the parasitic BJT can increase SEB tolerance. To decrease h_{FE} of parasitic BJT, the As-doping density in the n^+ layer was decreased. As shown in Fig. 2, SEB threshold was increased as As-doping density was decreased. But, decrease of the As-doping density degrades the electrical characteristics such as R_{on}. It is necessary to consider this point.

Considering the several irradiation test results and the electrical characteristics, we found the optimum design parameters, and developed two types of Power MOSFET (2SK3041, 2SK3146) for space applications. 2SK3041 will be used for the artificial satellite named ETS-VIII, which will be launched in 2002.

References

1) S. Kuboyama et al.: IEEE Trans. Nucl. Sci. **NS-39**, 1698 (1992).
2) M. Allenspach et al.: IEEE Trans. Nucl. Sci. **NS-43**, 2927 (1996).

Possibility of the "$\frac{1}{8}$ Effect" in the Zn-Substituted Bi-2212 System Studied by μSR

I. Watanabe, M. Akoshima,* Y. Koike,* and K. Nagamine

Existence of the so-called "$\frac{1}{8}$ effect", meaning that the high-T_c superconductivity (SC) is anomalously suppressed at the hole density of $p = \frac{1}{8}$ per Cu-atom, has been established in the $La_{2-x}Ba_xCuO_4$ system.[1-5] A magnetically ordered state was confirmed by previous muon spin relaxation (μSR) studies when the SC was suppressed.[4,5] Subsequently, a stripe structure of a spin density wave state and a charge density wave state was suggested from a neutron scattering study.[6] Relationship between the magnetically ordered state and the suppression of the SC has been discussed.

Recently, Akoshima *et al.* suggested from transport studies a possibility of the existence of the "$\frac{1}{8}$ effect" in the Zn-substituted Bi-2212 system, $Bi_2Sr_2Ca_{1-x}Y_x(Cu_{1-y}Zn_y)_2O_{8+\delta}$.[7] They found similar anomalous suppression of the SC in the Zn-substituted samples at $p \sim \frac{1}{8}$. They suggested that the substituted Zn played as a pinning center to make a charge and/or a spin ordered state. We applied μSR measurements to investigate magnetic properties of the Zn-substituted Bi-2212 samples. Preparation procedures of sintered samples are written elsewhere.[7] The μSR measurements in the zero-field (ZF) were carried out at the RIKEN/RAL Muon Facility in the UK. A pulsed positive surface muon beam was used. Measured temperature range was from 0.3 to 300 K.

Figure 1 shows the ZF-μSR time spectra of the Zn-substituted sample with $x = 0.3125$ and $y = 0.025$ at 0.30, 1.74 and 19.2 K. The preliminary analysis showed that the depolarization behavior deviates from the Gaussian-type to the exponential-type below 10 K,

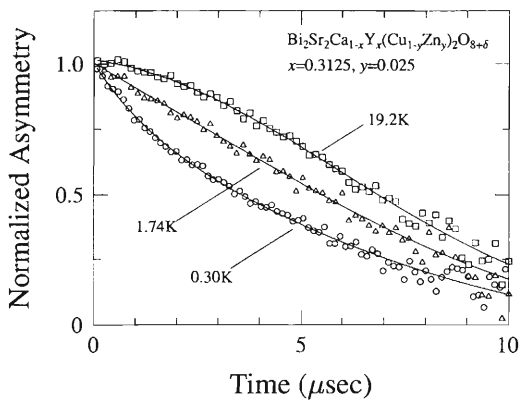

Fig. 1. ZF-μSR time spectra of the Zn-substituted sample with $x = 0.3125$ and $y = 0.025$ at which the high-T_c SC is anomalously suppressed.

indicating the appearance of an effect of dynamically fluctuating internal fields at a muon site.[8]

Figure 2 shows the temperature dependence of the exponential component of the depolarization rate. Enhancement of the depolarization rate was observed below about 10 K in the Zn-substituted sample at $p \sim \frac{1}{8}$ where the SC is anomalously suppressed. The enhancement of the depolarization rate can be regarded as that the Cu spins show the slowing down behavior which is caused by the enhancement of the magnetic correlation between the spins. No enhancement of the depolarization rate was observed in the non-Zn-substituted samples and the Zn-substituted samples with p far from $\frac{1}{8}$. As a result, the present μSR study revealed that both of p being $\frac{1}{8}$ and the Zn-substitution are essential for the suppression of the high-T_c SC and the enahancement of the magnetic correlation. This relationship is similar to that estabilshed in the La-systems.[1-5] Therefore, it can be concluded that the existence of the "$\frac{1}{8}$ effect" in the Bi-2212 is likely.

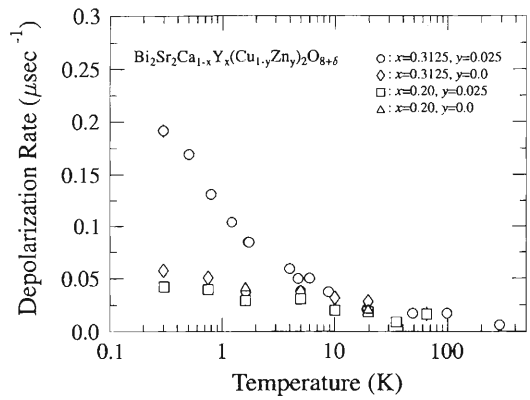

Fig. 2. Temperature dependence of the muon spin depolarization rate of the exponential component of the Zn- and non-Zn-substituted samples.

References

1) A. R. Moodenbaugh et al.: Phys. Rev. B **38**, 4596 (1988).
2) K. Kumagai et al.: J. Mag. Mag. Mater. **76/77**, 601 (1988).
3) K. Kumagai et al.: Physica C **235/240**, 1715 (1994).
4) I. Watanabe et al.: J. Phys. Soc. Jpn. **61**, 3058 (1992).
5) I. Watanabe et al.: Hyperfine Interact. **86**, 603 (1994).
6) J. M. Tranquada et al.: Nature (London) **375**, 561 (1995).
7) M. Akoshima et al.: Phys. Rev. B **57**, 7491 (1998).
8) I. Watanabe et al.: Physica B (1999), in press.

* Graduate School of Engineering, Tohoku University

Muon Spin Resonance in $(Nd_{1-y}Sm_y)_{0.5}Sr_{0.5}MnO_3$

W. Higemoto, K. Nishiyama, I. Watanabe, K. Nagamine,
A. Asamitsu,* H. Kuwahara,* and Y. Tokura*

Recent systematic studies on the perovskite type manganese oxide $(Nd_{1-y}Sm_y)_{0.5}Sr_{0.5}MnO_3$[1,2] have revealed a competitive nature existing between the ferromagnetic double-exchange interaction and the antiferromagnetic charge ordering instability, which gives rise to a temperature, magnetic field, and pressure induced transition from the ferromagnetic metal (FM) to antiferromagnetic insulator (AFI). This transition is accompanied with a change of the resistence by several orders of magnitude, and the phenomenon is known as the colossal magneto resistence (CMR). The competition between the FM state and AFI state is rather sensitive to the Mn-O-Mn bond angle or Sm ratio, y. In particular, a metastable FM phase appears in the $0.85 < y < 1$ region below 100 K. It was suggested that the suppression of ferromagnetic double-exchange interaction by a competing antiferromagnetic charge-ordering instability occur also in paramagnetic phase from the magnetic scesepitibility measurements[2,3] and muon spin relaxation measurements(μ^+SR).[4] Paramagnetic shift measurement is very useful to know the hyperfine coupling constant. To investigate the detail of the magnetic state in the paramagnetic phase, we have applied the RF muon spin resonance technique (RF-μ^+SR).

RF-μ^+SR experiments were carried out at Port-2 of RIKEN-RAL Muon Facility. Multidomain crystals of $(Nd_{1-y}Sm_y)_{1-x}Sr_xMnO_3$ ($x \sim 0.48$, $y \sim 0.875$) were grown by travelling floating zone method and were cut to disk shape.

We have clearly observed the resonance curve under the RF field of 47.0000 MHz as shown in Fig. 1. The local magnetic field B_μ at μ^+ sites can be expressed, in general, as

$$B_\mu = H_{hf} + H_{dip} + (\frac{4\pi}{3} - N)M + H_0. \quad (1)$$

Here, H_{hf} is the hyperfine field, H_{dip} the dipolar field due to the surrounding magnetic atoms inside the Lorentz cavity, N the demagnetization coefficient, M the host magnetization, and H_0 the external field. We define the shift K as

$$K = \frac{H_{hf}}{H_0} = \frac{B_\mu - H_0}{H_0}. \quad (2)$$

Here, we have neglected the term corresponding to the dipolar field because of the symmetry of the crystal. Figure 2 shows the preliminary results of K-χ plot. Surprisingly, the slope of the K-χ plot suddenly changes at ~200 K. This result suggests that the hyperfine coupling constant A_{hf} changes at ~200 K.

* JRCAT

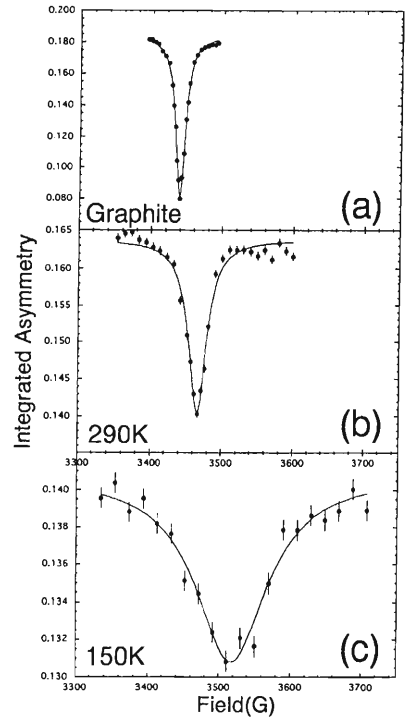

Fig. 1. RF-μSR spectrum in (a)Graphite as a reference and (b, c) in $(Nd_{0.125}Sm_{0.875})_{0.52}Sr_{0.48}$ under the RF-field.

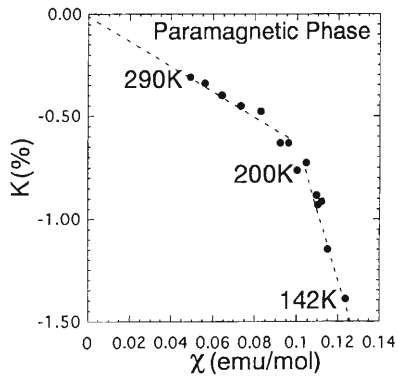

Fig. 2. K-χ plot in the paramagnetic phase.

However, such anomalies at ~200 K are not observed in the other experiments. Possible states are under consideration.

References

1) Y. Tokura et al.: Phys. Rev. Lett. **76**, 3184 (1996).
2) H. Kuwahara et al.: Phys. Rev. B **56**, 9386 (1997).
3) H. Kuwahara et al.: Science **272**, 80 (1996).
4) W. Higemoto et al.: Physica B, in press; RIKEN Accel. Prog. Rep. **31** 106 (1998).

Level Crossing Resonance in *2H*-$NbSe_2$

W. Higemoto, K. Nagamine, S. Kuroda, and K. Takita

The compound *2H*-$NbSe_2$ is a *2H* type transition metal dichalcogenide. As shown in Fig. 1, *2H*-$NbSe_2$ possesses a layered structure with the layers weakly coupled by Van der Waals' forces. Since two dimensionality dominates the system, a weak incommensurate state of the charge-density-wave (CDW) appears below $T_{CDW} \sim 32$ K. Superconductivity (SC) coexists with the CDW state below $T_{SC} \sim 7$ K.[1] It is well known that the behavior of positive muons (μ^+) strongly depends on the conduction electron character in some cases: for example, the muon quantum diffusion phenomena depend critically on the nature of the Fermi surface.[2] We are investigating the relation between the muon behavior and the CDW and the SC states in *2H*-$NbSe_2$ at RIKEN-RAL muon facility. In addition, transition metal dichalcogenides are known to be able to intercalate molecules or atoms into the interlayer. In *2H*-$NbSe_2$, the muon is expected to behave as a hydrogen-like intercalant, and its behavior is also interesting from an intercalation chemistry perspective.

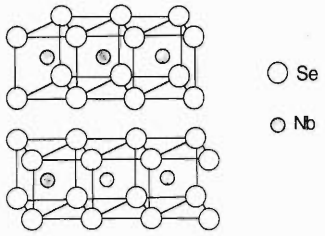

Fig. 1. Crystal structure of *2H*-$NbSe_2$.

In this article, we report the results of muon level crossing resonance experiment (μ-LCR) in *2H*-$NbSe_2$. As we previously reported,[3] microscopic state of the positive muon in *2H*-$NbSe_2$ has been studied using the muon spin relaxation method (μ^+SR). We found that the μ^+SR spectra consist of two components. The ratio of the two components and the dynamics of the muon change both at 140 K, at the charge-density-wave transition temperature (32 K), and again at the superconducting transition temperature (7 K). These facts clearly show that the muon states are affected by the CDW state as well as the SC state. At T_{CDW}, an energy gap appears in the Fermi surface and the density of states (DOS) decreases. It is known that hopping motions of muons in a metal are related to the conduction electrons near the Fermi surface through the electron-drag effect. The hopping rate increases in the SC phase.[2] However, clear explanation of our observation does not exist yet. To know the muon position and the local state of *2H*-$NbSe_2$, we have applied level crossing resonance (LCR) method. ^{93}Nb nuclei has spin $J = \frac{9}{2}$ and quadrupole moment $Q = 0.16 \times 10^{-24}\mathrm{cm}^2$. The quadrupole frequency, ω^Q, is represented by

$$h\omega^Q = \frac{3e^2qQ}{4J(2J-1)}. \quad (1)$$

The level crossing resonance occurs when quadrupolar splitting energy at ^{93}Nb site matches with a corresponding Zeeman splitting energy of muon. Although, electric field gradient (EFG) at ^{93}Nb site is known from the NMR experiment ($e^2qQ/h = 61.98 \pm 0.2$ MHz at 77 K),[4] that of our system was not known because the EFG at ^{93}Nb nucleus site is produced also by muon itself. This contribution is important for determining the muon site in LCR measurement.

Figure 2 shows the dependence of applied longitu-

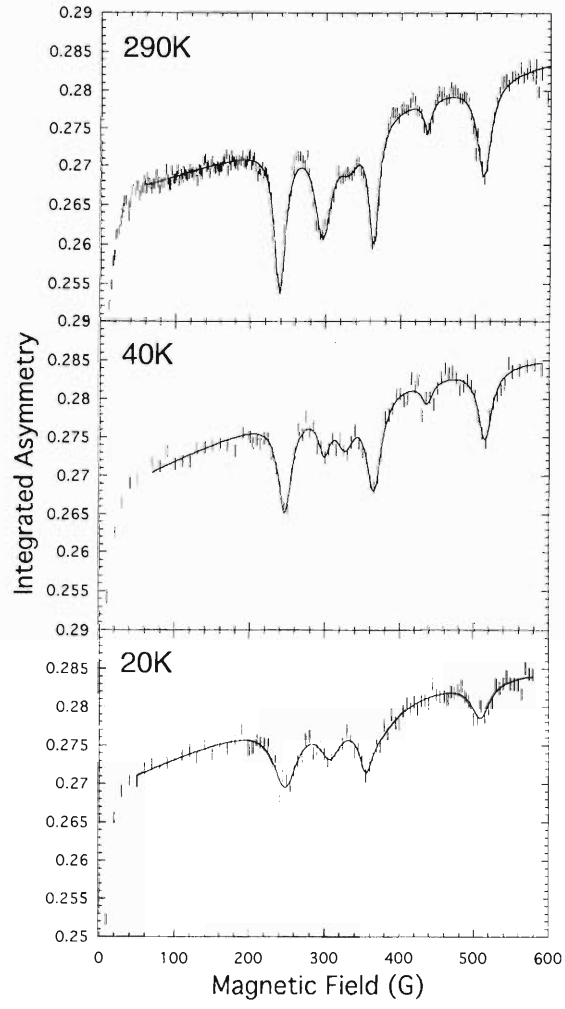

Fig. 2. Longitudinal magnetic field dependence of the muon spin polarization. Six peaks, which are indicating the level crossing resonance, are observable.

dinal field on the integrated asymmetry, $(N_F - N_B)/(N_F + N_B)$, which corresponds to the muon spin polarization. Here, N_F and N_B are the total number of emitted positrons counted at forward counters and backward counters, respectively. We can clearly see the six resonance peaks. We found that the amplitudes of LCR peaks are reduced below 30 K. This feature clearly shows the effects of the state of charge-density-wave. To know the details of the muon position and of the local state of *2H*-$NbSe_2$, theoretical calculation is going on.

In general, microscopic muon state is very important for the μ^+SR studies of matter. We consider that our result can be regarded as a new feature of the muon behavior which will strongly reflect the electric state like CDW state in particular, and will contribute to the understanding of the microscopic muon state in matter.

References

1) R. Sooryakumar and M. V. Klein: Phys. Rev. Lett. **45**, 660 (1980).
2) For example, R. Kadono et al.: Phys. Rev. B **39**, 23 (1989).
3) W. Higemoto et al.: Hyperfine Interact., in press; RIKEN Accel. Prog. Rep. **31**, 110 (1998).
4) H. Ehrenfreund et al.: J. App. Phys. **42**, 1491 (1971).

Muon Spin Resonance in $KCuCl_3$ and $TlCuCl_3$

W. Higemoto, H. Tanaka, I. Watanabe, and K. Nagamine

Recently, a low dimensional magnetic system which possesses the spin singlet ground state has been attracting a great deal of attention. From recent studies by Tanaka et al., it was suggested that the ground state of $KCuCl_3$ and $TlCuCl_3$ are spin singlet state with a finite spin gap.[1] Figure 1 illustrates the exchange interactions. These systems can be described as $S = 1/2$ Heisenberg spin ladder systems with additional interactions. In these systems, because of the spin singlet ground state, non-magnetic state is expected to arize at low temperatures. If the system is non-magnetic state, no muon spin relaxation is expected to occur. However, as we previously reported,[2] muon spin is strongly depolarized in both systems. The origin of the local field at muon site is still unclear. One possible origin is due to the contribution of the impurities or chain ends. In $KCuCl_3$, amount of such impurities or chain ends is too small to induce the large magnetic field to the whole system observed by muon. Thus, it is unlikely that this relaxation phenomena arose from the impurities. One of the other possibility of the origin of the local field is due to the formation of an exotic muon state. Muon spin resonance technique is a strong tool for the investigation of the muon state. In particular, time dependence of the muon state can be investigated. We therefore applied this method on $KCuCl_3$ and $TlCuCl_3$ to know the time dependence of the muon state at RIKEN-RAL muon facility. In $TlCuCl_3$, we have observed the muon spin relaxation which has spectra quite similar shape as the other pure system but of somewhat different from $KCuCl_3$. So, muon spin resonance experiments for these two materials give us much variety of the information about the muon state and magnetism in the spin singlet system. A reference spectrum is shown in Fig. 2(a). Figure 2(b) shows the RF-μ^+SR spectra in $KCuCl_3$ at various temperatures under the RF-field of 47.0000 MHz. We define "integrated asymmetry" as $(N_F - N_B)/(N_F + N_B)$. Here N_F and N_B are total number of emitted positrons counted at forward counters and backward counters, respectively. Above 5 K, we observed the muon spin resonance with a very small paramagnetic shift under the DC-longitudinal field of 3.5 kG which was applied parallel to the initial muon spin direction. However, we could not observe the muon spin resonance below 5 K. This indicates that muon state or magnetic state around muon site is different above and below 5 K. This fact is consistent with the muon spin relaxation results.

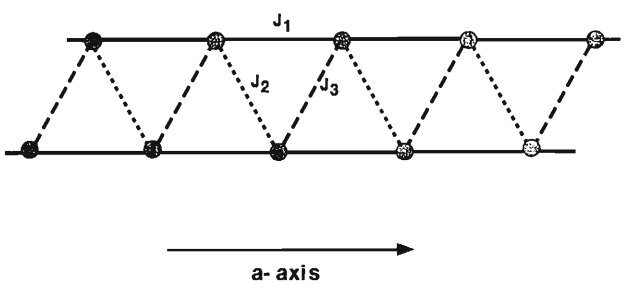

Fig. 1. Spin configuration of the double chain and the interactions J_1, J_2 and J_3.

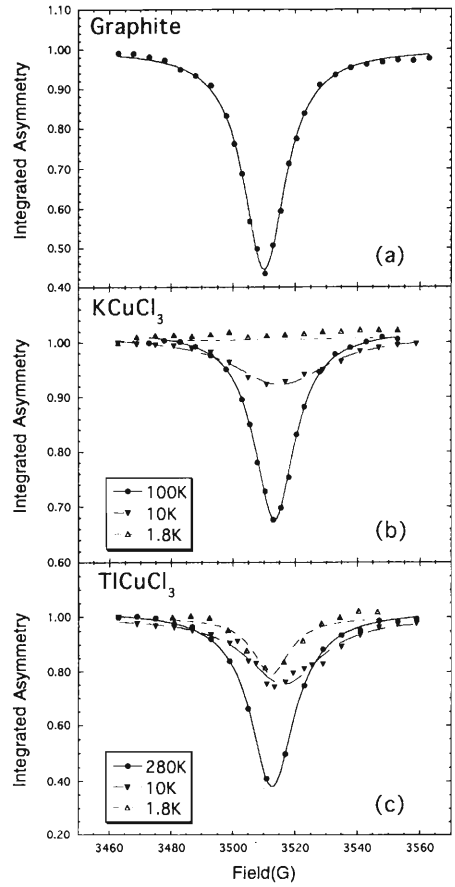

Fig. 2. Muon spin resonance spectra in (a)graphite (reference data), (b)$KCuCl_3$, and (c)$TlCuCl_3$.

In $TlCuCl_3$, the muon spin resonance was observed even in a lower temperature (Fig. 2(c)). We consider that the muon spin relaxation mechanism in $TlCuCl_3$ is different from the case of $KCuCl_3$ at low temperatures.

References

1) H. Tanaka et al.: J. Phys. Soc. Jpn. **65**, 1945 (1996).
2) W. Higemoto et al.: Phys. Lett. A **243**, 80 (1998); RIKEN Accel. Prog. Rep. **31**, 105 (1998).

μ^+SR Investigation of the Magnetic Ordering in $Ce_3Pd_{20}Ge_6$

V. V. Krishnamurthy, I. Watanabe, K. Nagamine, J. Kitagawa,[*1]
M. Ishikawa,[*1] and T. Komatsubara[*2]

The Kondo-lattice compound $Ce_3Pd_{20}Ge_6$ exhibits heavy-fermion behaviour characterized by a huge linear specific heat coefficient C/T $\sim$ 8J/(Ce mol K^2) below 1 K and crystal field split ground state of Ce ions.[1)] This compound forms in a cubic phase with $Cr_{23}C_6$ type superstructure, in which Ce atoms occupy two crystallographically inequivalent sites. The crystal structure consists of a simple cube formed by 8 Ce(2) atoms embedded in a FCC type cubic arrangement of Ce(1) atoms. Magnetic susceptibility χ_{ac}(T) of $Ce_3Pd_{20}Ge_6$ follows a Curie-Weiss law for temperatures above 50 K with an effective moment $\mu_{\rm eff}$ = 2.45 μ_B/Ce and exhibits a sharp cusp at 0.7 K.[1)] Electrical resistivity ρ(T) exhibits a minimum near 10 K, a broad peak around 2 K characterising Kondo lattice behaviour and an inflection point at 0.7 K. The specific heat C(T) demonstrates two anomalies, a sharp peak at 0.7 K and a broad peak at 1.2 K. The anomaly found at 0.7 K in χ(T), ρ(T) and specific heat measurements has been suggested as long range antiferromagnetic (AFM) ordering. By considering the huge value of magnetic entropy $S_{\rm mag}$ ($\sim R$ ln4 at 10 K), the 1.2 K anomaly has been interpreted as quadrupolar ordering due to a crystal field split Γ_8 quartet ground state of Ce^{3+} (J = 5/2) ions. Since there isn't any suitable nuclear probe of Ce for a microscopic investigation of $Ce_3Pd_{20}Ge_6$ single crystal, we have applied μ^+SR to gain knowledge on the magnetic structure of Ce ions in the antiferromagnetic state. Further, if the transition at 1.2 K is a pure quadrupolar ordering, then there should be no anomaly in the local magnetic properties measured by μ^+SR.

$Ce_3Pd_{20}Ge_6$ single crystal was prepared in a triarc furnace. An 8 mm diameter and 1 mm thick disc of the crystal, with its plane perpendicular to the [110] direction was glued to a 25 μm thick silver plate and was cooled in a ^{3}He cryostat. μ^+SR measurements were performed in zero-field, transverse field and longitudinal field conditions in the ARGUS spectrometer following the implantation of μ^+ pulsed beam of momentum 27 MeV/c at RIKEN-RAL muon facility. Figure 1 displays few examples of zero-field spectra measured in the paramagnetic and antiferromagnetic regions. The spectra above 0.7 K could be fitted by an exponential relaxation function with a nearly temperature independent relaxation rate of 0.03 μs^{-1}. The spectra below 0.7 K, clearly shows coherent and spontaneous precession of muons and could be reasonably fitted by

$$G_Z(t) = A_0\exp(-t/T_1) + A\exp(-\lambda t)\cos(\omega t + \phi),$$

where A_0 is the asymmetry of the only-relaxing component and A is the amplitude of the precessing component. $1/T_1$ is the muon spin-lattice relaxation rate. $\nu_\mu = \omega/2\pi$ is the muon spin precession frequency which gives a measure of the strength of the local magnetic field present at the muon site. λ is the line width and ϕ is the phase angle. The temperature dependence of $1/T_1$ and ν_μ are displayed in Fig. 2. $1/T_1$ does not exhibit an anomaly at T_N = 0.7 K and at T_Q = 1.2 K. While the lack of an anamoly in $1/T_1$ at T_Q indicates that the changes in the electronic structure around Ce due to quadrupolar ordering are minimal, the reason for the absence of an anomaly at 0.7 K is not clear. The discontinuous drop of ν_μ at 0.7 K seem to suggest a first order antiferromagnetic transition. The coherent precession of muons below T_N implies a collinear antiferromagnetic structure.

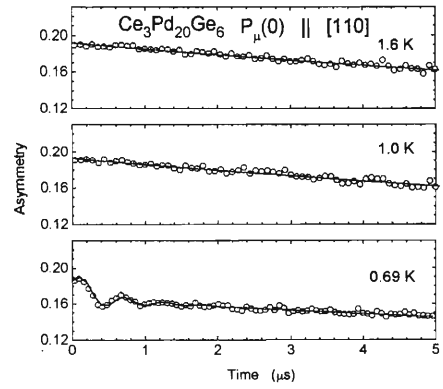

Fig. 1. μ^+SR time spectra in $Ce_3Pd_{20}Ge_6$ measured for the initial muon polarization vector P_μ(0) parallel to [110] direction of the crystal.

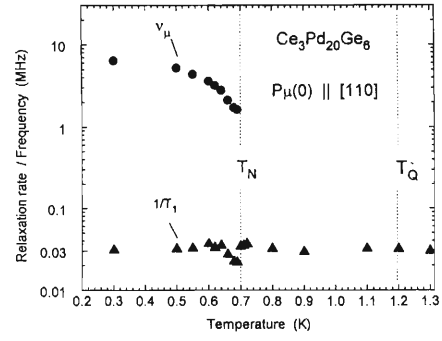

Fig. 2. Temperature dependence of $1/T_1$ and ν_μ in $Ce_3Pd_{20}Ge_6$ single crystal.

*1 Institute for Solid State Physics, University of Tokyo
*2 Tohoku University

References

1) J. Kitagawa et al.: Phys. Rev. B **53**, 5101 (1996).

Muon Spin RF-Resonance of Haldane Gap Systems

A. Fukaya, I. Watanebe, M. Hagiwara, and K. Nagamine

Low-dimensional quantum spin systems with antiferromagnetic interactions, *e.g.* Spin-Peierls and Haldane-gap systems, have attracted much attention. It has been clarified that the ground states of these systems are non-magnetic. However, enhancement of the muon spin relaxation was commonly observed at a low temperature.[1-4] The origin of this enhancement has not been clarified yet.

In order to resolve this problem, it is important to examine the local field at the muon site. We have measured the muon spin resonance with radio frequency (RF-μSR) on the two polycrystalline samples of Haldane gap systems: $Ni(C_2H_8N_2)_2NO_2(ClO_4)$ (NENP) and NiC_2O_4 2·2MIz (2MIz = 2-methylimidazole). In these systems, an enhancement of the muon spin relaxation was observed at low temperatures as usual.[2-4] In this report, we demonstrate only the results of RF-μSR in the NENP (whose gap energy $E_g \sim 14$ K[5]).

The RF-μSR measurements were carried out using a pulsed surface muon beam at the RIKEN-RAL Muon Facility in the UK. The frequency was 47.0 MHz. Double ratio is defined as A^{on}/A^{off}, where $A^{on,off} \equiv (N_F^{on,off} - N_B^{on,off})/(N_F^{on,off} + N_B^{on,off})$. The $N_F^{on,off}$ and $N_B^{on,off}$ denote the integrated positron counts in the forward and backward directions with the RF power on or off, respectively. We analyzed the longitudinal field dependence of the double ratio (resonance curve) using a Lorentzian function. The resonance position is defined as the field at which resonance curve depicts the minimum. In this experimental condition, the resonance position in non-local field is estimated as 3468 G.

In Fig. 1(a), the resonance curves measured at 2.7 K and 80 K are shown. The resonance positions at 2.7 K and 80 K are 3470 G and 3468 G, respectively. Thus, the average local field at the muon site changes only ~2 G even at the low temperature (2.7 K). This is inconsistent with the result of the previous μSR measurement, which showed the magnitude of local field ~90 G.[3] The width of the resonance curve is wider and the depth is much smaller at 2.7 K than at 80 K.

Figure 1(b) shows the temperature dependence of the resonance position. The inset shows the full width at half maximum (FWHM) of the resonance curve. As the temperature decreases below ~20 K, the resonance position shifts to a slightly higher field. The FWHM of the resonance curve becomes wider at the temperature below ~20 K, indicating that the distribution of local fields becomes wide. According to Ref. 4, the temperature at which the muon spin relaxation in zero field starts to be enhanced also is ~20 K.[4]

From these results, we have attempted to consider

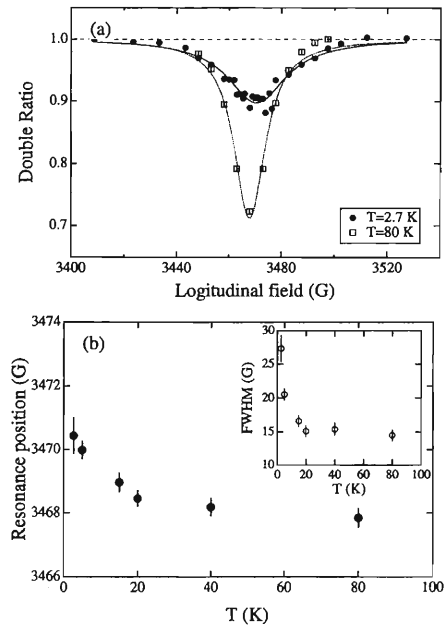

Fig. 1. (a) Resonance curves at 2.7 and 80 K. Solid and dotted lines are the results of fits to a Lorentzian function, and the broken line represents a base line. (b) Temperature dependence of the resonance position. The inset shows the FWHM of resonance curves.

the cause of enhancement of the muon spin relaxation. In some insulators, a part of implanted muons is bound with an electron to form a muonium. In this sample, most of implanted muons is unbound at high temperatures. As temperature decreases, a part of muons is bound with electrons. Such muons do not show resonance in this experimental condition, while they cause a strong muon spin relaxation. The others remain unbounded and the change of local field at the unbound muon site is quite small.

We have measured the RF-μSR also in NiC_2O_4 2·2MIz, and have obtained similar results as the case of NENP.

At present, the cause of a slight change of the resonance position and of the increase of FWHM are still unclear. Further study is necessary in order to clarify the whole picture of the anomalous enhancement of muon spin relaxation in the quantum spin systems.

References

1) A. Sohma et al.: J. Phys. Soc. Jpn. **64**, 3060 (1995).
2) A. Fukaya et al.: Hyperfine Interact., in press.
3) B. J. Sternlieb et al.: J. Mag. Mag. Mater. **104/107**, 801 (1992).
4) M. Motokawa et al.: Physica B **177**, 389 (1992).
5) J. P. Renard et al.: Europhys. Lett. **3**, 945 (1987).

Spin Dynamics of 2D *Kagomé* Antiferromagnet, *m*-MPYNNBF$_4$, Studied by μSR

I. Watanabe, N. Wada,* S. Ohira, and K. Nagamine

Two dimensional (2D) *Kagomé* antiferromagnet, called *m*-MPYNNBF$_4$, shows a spin dimer state with $S = 1$ which is formed below 23 K by two radical electrons through an intra-dimer ferromagnetic interaction.[1,2] The ground state has been found to be non-magnetic by our previous muon spin relaxation (μSR) measurement at KEK-MSL.[3,4] But, because of the restriction of statistics of the muon events, details of the dimer spin dynamics have not become clear yet. We have therefore carried out zero-field (ZF) μSR measurements at the RIKEN-RAL Muon Facility in the UK to clarify these problems by using an intense pulsed muon beam.

Figure 1 shows the ZF-μSR time spectrum of *m*-MPYNNBF$_4$ at 0.30 K. The total number of the muon events was 100 million. Depolarization behavior due to the randomly distributed static fields of ^{19}F nuclear dipoles was observed also in the previous μSR at KEK-MSL.[3] Precession of the muon spin with a small amplitude was clearly observed in this system, proving the existence of the FμF state which is like the hydrogen bonding state.

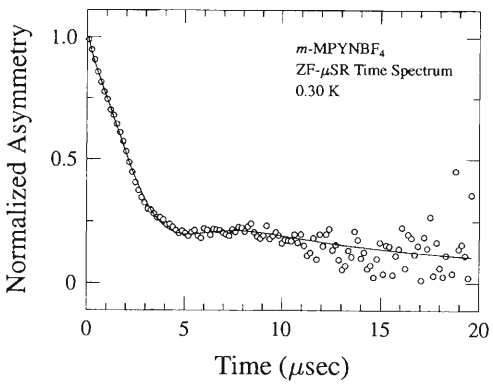

Fig. 1. ZF-μSR time spectrum of *m*-MPYNNBF$_4$ at 0.30 K. The total muon events was 100 million.

Recovery of the asymmetry at the region after 7 μsec was clearly observed. This recovery is described as the "$\frac{1}{3}$-tail" of the Kubo-Toyabe function. The "$\frac{1}{3}$-tail" shows a slow depolarization behavior due to the dynamically fluctuating local fields at a muon site. The time spectrum was analyzed by utilizing the following analysis function: $A_1 e^{(-\lambda_1 t)^\beta} + A_2 G_Z(\Delta, t, \lambda_2)$. The first term describes the muons which interact with surrounding electrons. The second term is the dynamical Kubo-Toyabe function, while λ_2 is the dynamically fluctuating rate of internal fields at the muon site. Solid line in Fig. 1 is the best-fit curve fitted by using the above analysis function.

Figure 2 shows the temperature dependence of the fluctuation rate of dynamical Kubo-Toyabe term in the analysis function. The fluctuation rate is almost constant below about 10 K and shows a linear temperature dependence above 20 K. The linear temperature dependence of the fluctuation rate implies that the origin of fluctuating internal field at the muon site is not due to the thermal activation of muon hopping.

It is suggested from the susceptibility and heat capacity measurements that two radical spins can form the dimer state below about 23 K by the intra-dimer ferromagnetic exchange interaction, J_0.[1,2] In this case, the fluctuation frequency of the internal field below 23 K is dominated by J_0, resulting in the temperature-independent depolarization rate of muon spin. This ferromagnetic exchange energy is overwhelmed by the thermal fluctuation energy above 23 K. In this case, the fluctuation frequency is dominated by the thermal energy of $k_B T$ instead of J_0, resulting in the linear depolarization rate with temperature. The observed temperature dependence of the fluctuating rate of the muon spin shows a good agreement with the spin dynamics feature which is expected from the susceptibility and heat capacity measurements. Thus, our μSR result has revealed the existence of the dimer spin state and its spin dynamics.

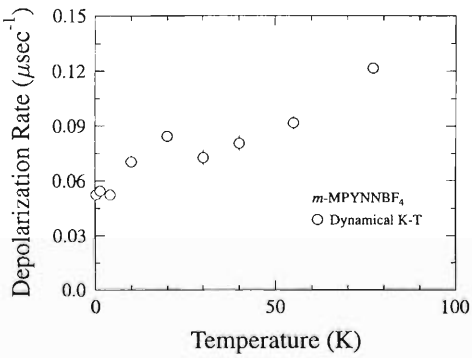

Fig. 2. Temperature dependence of the λ_2 of dynamical Kubo-Toyabe term in the analysis function used.

References

1) K. Awaga et al.: Phys. Rev. B **49**, 3975 (1993).
2) N. Wada et al.: J. Phys. Soc. Jpn. **66**, 961 (1997).
3) I. Watanabe et al.: Phys. Rev. B **58**, 2438 (1998).
4) I. Watanabe et al.: RIKEN Accel. Prog. Rep. **31**, 111 (1998).

* Graduate School of Arts and Sciences, University of Tokyo

μSR Studies on 4-Arylmethyleneamino-TEMPO

S. Ohira, I. Watanabe, T. Ishida,* T. Nogami,* and K. Nagamine

Organic radical magnets having a 2,2,6,6-tetramethylpiperidin-1-yloxyl (TEMPO) group are known to have a strongly 2D structure in their N-O network. Radicals are localized at the N-O site and contribute to the magnetism of the system. A long-range magnetic ordered state in some TEMPO derivatives was observed by various methods.[1)]

Our previous two μSR experiments performed on *p*-chlorobenzylideneamino-TEMPO (*p*-Cl-C_6H_4-CH = N-TEMPO, **1**) and on *p*-phenylbenzylideneamino-TEMPO (*p*-Ph-C_6H_4-CH = N-TEMPO, **2**) showed clear oscillation signals below 275 and 225 mK, respectively; thus indicating the existence of a long-range ferromagnetically ordered state.[2)] These two radicals have a quite similar structure in the N-O sheet. The distance between the sheets of **2** is longer than that of **1**. A mechanism for the intra-sheet ferromagnetic interaction has already been suggested based on the overlap of the molecular orbitals.[3)] On the other hand, the mechanism of the inter-sheet magnetic interaction is still unclear. In order to study critical behavior of these systems, we have carried out longitudinal field (LF) and transverse field (TF) μSR measurements down to about 0.30 K.

The experiments were carried out at the RIKEN-RAL Muon Facility in the UK. Figure 1 (a) and (b) show the LF-μSR time spectra of **1** at 0.30 K and **2** at 0.32 K, respectively. The LF decoupling behavior for **1** reveals the existence of random static internal fields at the muon site. The width of the internal field distribution at 0.30 K increases with increasing LF and eventually saturates.[4)] A random internal field was not observed in the LF spectra of **2**. The muon spin was decoupled under LF above 50 G. The decoupling behavior of **1** at 1.5 K is quite similar to that of **2** as shown in Fig. 1 (b). In the case of **2**, the measured temperature was too high to observe such an LF-induced secondary field.

Because the shapes of both samples are needle-like, two axes directions perpendicular to the longitudinal direction are random for LF, while the other axis can be parallel to TF. In order to clarify the dependence of field direction on the magnetic properties of the system at above the Curie temperature T_C, TF-μSR studies were carried out on these systems. Two precession frequencies of the muon spin were observed under the TF. The muons which precess with the frequency $\gamma_\mu H_{TF}$ make up one large amplitude component, where γ_μ is a gyromagnetic ratio of muon. The other oscillation component showed a higher frequency with a smaller amplitude. Figure 2 shows the temperature depen-

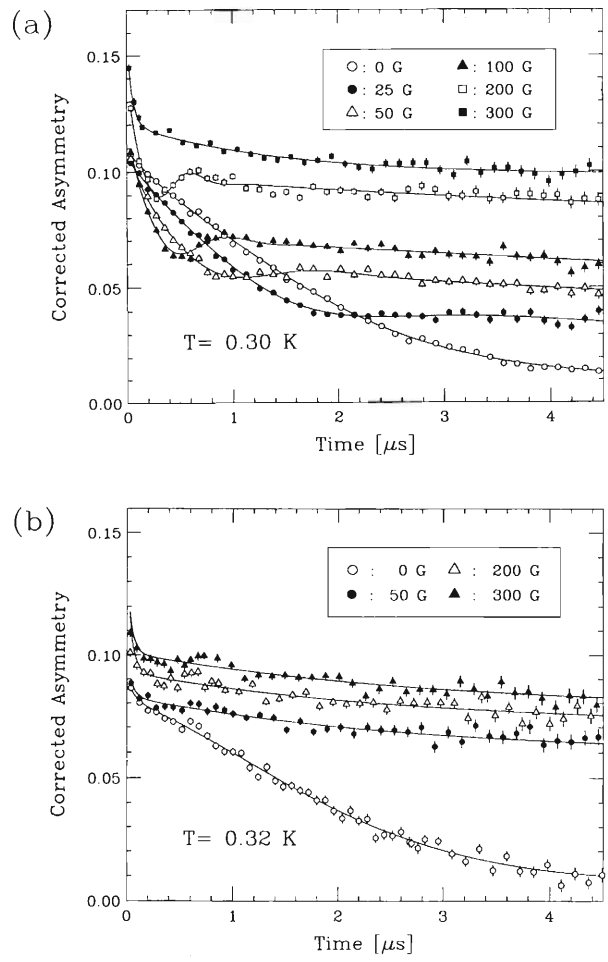

Fig. 1. Time spectra of (a) **1** at 0.30 K and (b) **2** at 0.32 K.

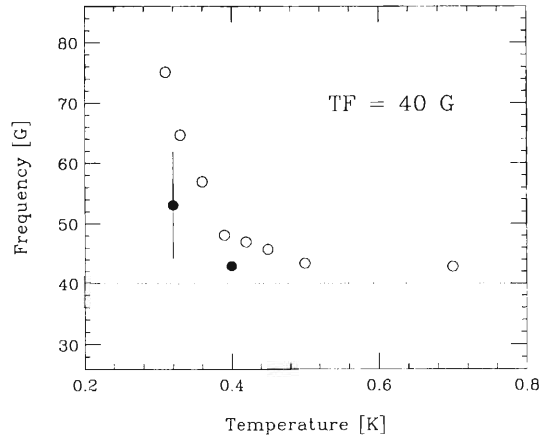

Fig. 2. Temperature dependence of the precession frequency which is not due to the diamagnetic muon spin precession, under TF of 40 G. Open and closed circles respectively show the results for **1** and **2**.

* University of Electro-Communications

dence of the latter precession frequency under the TF of 40 G, for both derivatives.

The internal fields observed in LF- and TF-μSR have the similar magnitude and temperature dependences. Therefore, both the random static internal fields observed in LF-μSR and the additional field in TF-μSR are expected to originate from the same magnetic property. Either a low-dimensional fluctuation or else a hyperfine field from the radical and the electron which forms muonium ($\mu^+ + e^-$) can be a candidate to explain the unusual magnetic state just above T_C observed in these μSR studies.

References

1) T. Nogami et al.: Chem. Lett. **1995**, 635.
2) R. Imachi et al.: Chem. Lett. **1997**, 233.
3) T. Nogami et al.: Bull. Chem. Soc. Jpn. **69**, 1841 (1996).
4) S. Ohira et al.: to be submitted.

Muon Studies on Weak Organic Charge Transfer Compounds

R. M. Macrae, I. D. Reid,[*1] R. Kadono, K. Nagamine, and J. U. von Schütz[*2]

Weak organic charge transfer compounds formed by 1 : 1 co-crystallisation of planar aromatic molecules (Fig. 1) are of interest from the perspective of molecular dynamics and, through the behaviour of triplet excitons in these systems, as models of low-dimensional excitation transport.[1] Muon techniques offer a unique "handle" on these properties in that a single μ^+-generated free radical probe can be utilised to study *both* thermal excitations and molecular reorientational dynamics (using conventional μSR techniques) *and* photoinduced behaviour and excitonic dynamics (using synchronous excitation μSR[2]), separating two influences the effects of which are usually superposed. Initial tests were carried out on the system anthracene/tetra- cyanobenzene (A/TCNB) at PSI and RIKEN, and preliminary reports of the results are available.[3] To summarise, μSR is sensitive to quite subtle changes in the molecular dynamics, and also — apparently— to changes in the degree of static order. Synchronous excitation studies await the development of a suitable laser setup at RIKEN/RAL.

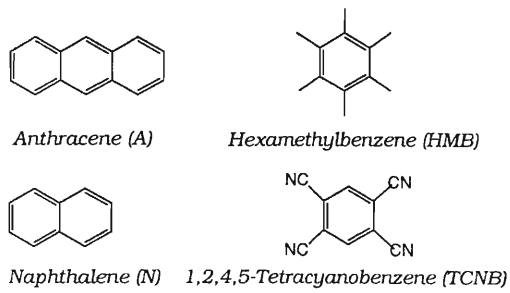

Fig. 1. Donors and acceptors.

Subsequently, studies on A/TCNB were extended to include temperature-dependent high-resolution TF μSR on a single crystal sample, and ALC-μSR measurements were carried out on polycrystalline samples of two other systems in which the "acceptor" molecule remains TCNB, but the "donor" molecule has been replaced by naphthalene (N/TCNB) and hexamethylbenzene (HMB/TCNB) respectively. (Through systematic changes of donor and acceptor, the properties can to a certain extent be "tuned".) The free radical species formed were identified through their characteristic values of B_0, the $\Delta M = 1$ lineshape envelope origin, by comparison with values of A_μ, the isotropic component of the muon-electron hyperfine coupling, to which it is proportional. Values were taken both from the experimental literature[4,5] and from the results of first principles calculations using the density-functional-based method B-PW91.[6]

The results were striking in two major ways. Firstly, in no case was the adduct to the TCNB moiety observed. This can be only partially due to the somewhat greater steric freedom of the donor species and the concomitant stabilisation of radical adducts to it, and must have implications with regard to the formation mechanism of the radical, suggesting that in systems of this type, at least in the solid state, ionic intermediates are not involved. Secondly, the results, particularly in N/TCNB in which the lineshape is highly complex and undergoes subtle temperature-dependent changes (see Fig. 2), indicate that ALC-μSR is particularly effective in distinguishing changes in static order in these systems, implying, in the cases of A/TCNB and N/TCNB, in which the parent molecule lies in an only slightly unsymmetric double potential well, that small intermolecular effects have a considerable influence on the radical hyperfine interaction.

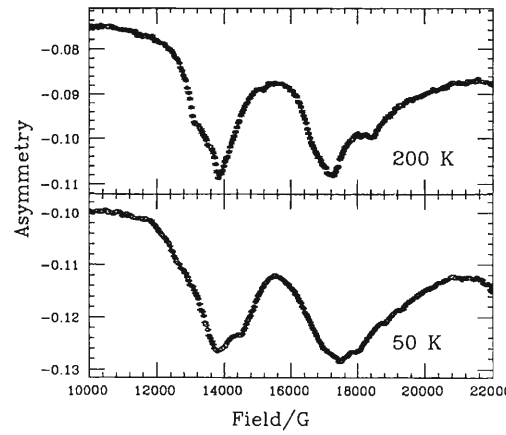

Fig. 2. ALC-μSR spectra for N/TCNB at 200 K and 50 K.

*1 Paul Scherrer Institut, Switzerland
*2 3. Physikalisches Institut, Universität Stuttgart, Germany

References

1) J. Krzystek and J. U. von Schütz: Adv. Chem. Phys. **86**, 167 (1993); and refs. within.
2) R. Kadono, A. Matsushita, R. M. Macrae, K. Nishiyama, K. Nagamine: Phys. Rev. Lett. **73**, 2724 (1994).
3) R. M. Macrae, T. M. Briere, C. J. Rhodes, I. D. Reid, J. U. von Schütz: Proc. Int. Workshop on JHF Science (JHF98), in press; also see PSI and RIKEN reports 1997.
4) I. D. Reid and E. Roduner: Struct. Chem. **2**, 419 (1991).
5) E. Roduner: Hyperfine Interact **65**, 857 (1990).
6) L. A. Eriksson, O. L. Malkina, V. G. Malkin, and D. R. Salahub: J. Chem. Phys. **100**, 5066 (1994).

Development and Test of the RF-μSR System at RAL

I. Watanabe, F. L. Pratt, and K. Nagamine

Muon spin resonance technique using a radio frequency (RF-μSR) field together with a static longitudinal magnetic field (LF) is a powerful method to investigate hyperfine interactions at muon sites in magnetic materials.[1] A pulsed muon facility has certain advantages in carrying out the RF-μSR. The detail design of the RF-system and the first report of the development work have been reported in the previous RIKEN Accel. Prog. Rep.[2] In this letter, we report test results of applications with a real muon beam using the developed RF system.

The RF-μSR on carbon powder was tested first to check the effect of the temperature on the probe. Figure 1 shows the field dependence of the RF-μSR time spectrum of the carbon powder at 280 K. The output power from the RF amplifier was 50 W and the RF frequency was 47.000 MHz. The RF pulse width was 30 μsec. The ^{4}He gas with the pressure of 1 atm was used as an exchange gas to cool down the probe. The absolute value of the LF is not correct because of an offset on a read-back system of the field.

Clear muon spin precession pattern around H_1 was observed near the resonance field of 3.5 kG. The precession frequency showed a minimum on the resonance condition. The estimated strength of H_1 was about 6 Gauss because of the restriction of the discharge. It was found that the discharge was suppressed when the N_2 gas with the pressure of 1 atm was used instead of the ^{4}He gas. In this case, about 17 Gauss of the H_1 was obtained in maximum. However, ^{4}He gas must be used below about 80 K to cool down the probe. As long as the ^{4}He gas is used, the H_1 is restricted to be a couple of Gauss because of the discharge. This restriction is one of the problems which we have to solve out as soon as possible.

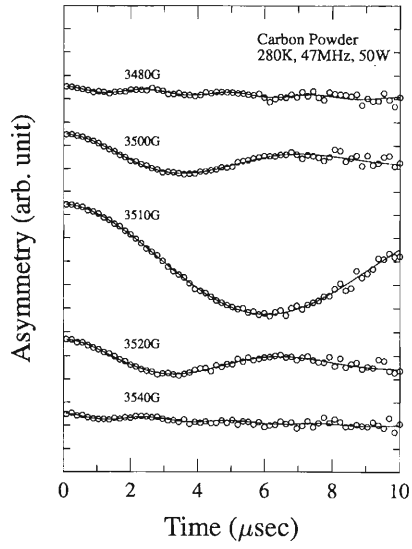

Fig. 1. Field-dependence of the RF-μSR time spectrum of the carbon powder at 280 K.

The resonance frequency and other physics information are obtained by calculation of the double ratio of the time spectrum, i.e. the ratio of the time averaged asymmetry in field to the time averaged asymmetry in zero field. Figure 2 shows a resonance curve which was determined by the double ratio calculation at 280, 100 and 5.3 K. The time range for averaging was from 0 to 15 μsec. The resonance position was obtained from the fitting of the resonance curve assuming the Lorentzian-type function. Tanking into account the offset field, it was found that the resonance position showed the zero temperature shift.

The width of the resonance curve is mainly determined by the inhomogeneity and the amplitude of H_1. If the RF coil deforms at low temperatures, the deformation causes a change in the homogeneity of H_1 leading to a change in the resonance curve width. However, no evidence of the deformation of the RF coil was observed down to 2 K.

The probe was also tested with other materials as follows.

(1) Oxides:
La-Co-O, La-Sr-Nd-Mn-O
(2) Low dimensional materials:
Tl-Cu-Cl, Ni-C-O, NEMP
(3) Organic materials:
polyaniline, polybutadiene,
polypyridine, cytochrome-C

On behalf of these systems, a representative test result of the RF-μSR study on $LaCoO_3$ is simply reported in this letter.

$LaCoO_3$ shows the temperature dependence of the

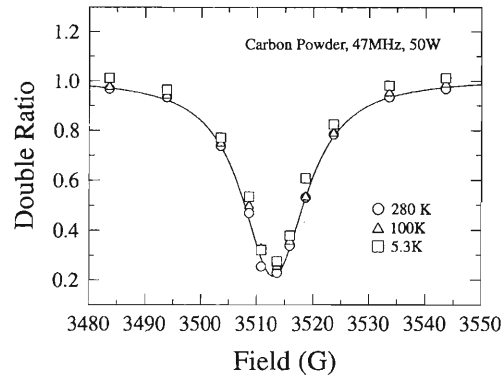

Fig. 2. Resonance curve of the carbon powder sample at 280, 100 and 5.3 K obtained from the double ratio calculation.

Co-spin state, going from a high-temperature high-spin state ($S = 1$) to a low-temperature low-spin state ($S = 0$). Detail of the physics background is reported in other papers.[3-5] The susceptibility of the system shows a maximum around 90 K and vanishes below 20 K. Thus, this system is a good example to check the performance of the newly developed system and to test whether the RF system can detect a change in the magnetic properties from the measurement of the diamagnetic shift of the resonance frequency.

Figure 3 shows the resonance curves obtained at 280, 100 and 5.6 K. Solid lines in the figure are the best fit results. Figure 4 shows the temperature dependence of the resonance frequency. A small shift in the positive direction was observed, indicating the existence of a positive hyperfine field at the muon site. The shift is less than 1%, but it is still observable. This result shows that the system can be used to measure diamagnetic shifts as small as 0.1%.

The test results show good performance of the developed RF probe around 50 MHz. However, it was found that there were still some problems and requirements on this test probe as follows:

(1) Much higher H_1 is required
(2) Low frequency RF-μSR system is desired
(3) Discharge should be prevented

The requirement (1) is correlated to (3) because the discharge is the factor restricting the maximum voltage applied to the RF coil. This restriction

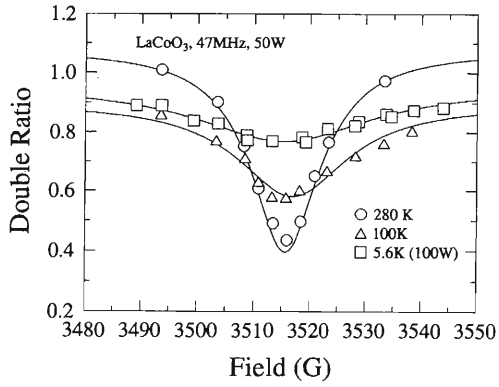

Fig. 3. Resonance curve of $LaCoO_3$ at 280, 100 and 5.6 K. The RF frequency was 47.000 MHz.

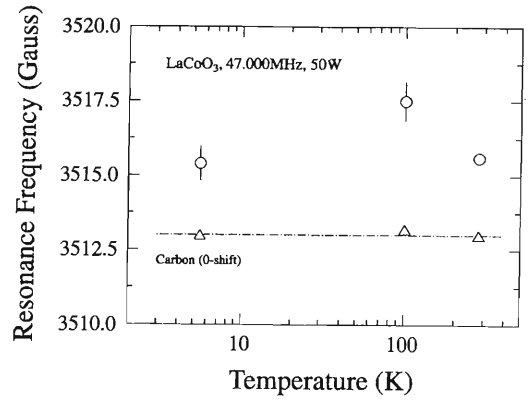

Fig. 4. Temperature dependence of the diamagnetic shift in $LaCoO_3$.

suppresses the strength of H_1. We need more treatments and tests on matching capacitors to prevent the discharge. The higher H_1 more than 20 Gauss is especially needed in the time-delayed RF-μSR measurement, changing the timing of the RF trigger. The time evolution of the state of the muon can be investigated by this measuremant.

The requirement (2) was needed to carry out the field dependence (RF frequency dependence) of the RF-μSR. The electric circuit of the probe has to be changed to another type when the RF frequency is lower than about 20 MHz, which corresponds to an external field of about 2 kG. The "high-impedance" matching method adopted in the present test probe is not efficient for the lower frequency, so that we have to use a "low-impedance" matching method in which the matching capacitor and the RF coil are connected in series. The field variable RF-μSR is the next step of the development work which will be started soon.

References

1) K. Nishiyama: in *Perspectives of Muon Science*, edited by T. Yamazaki, K. Nakai, and K. Nagamine (North-Holland, Amsterdam, 1992), p. 199.
2) I. Watanabe et al.: RIKEN Accel. Prog. Rep. **31**, 116 (1998).
3) K. Asai et al.: Phys. Rev. B **50**, 3025 (1994).
4) M. Itoh et al.: J. Phys. Soc. Jpn. **64**, 3967 (1995).
5) M. A. Korotin et al.: Phys. Rev. B, in press

3. Radiochemistry and Nuclear Chemistry

Comparative Regional Uptake Behaviors of a Radioactive Multitracer in Brain of the Young and Aged C57BL/6N Mice

R. Amano, S. Oishi, T. Tarouda,* and S. Enomoto

The unique properties of cerebral capillary endothelial cells restrict the passage of water and nutrients selectively between blood and brain, by forming the blood-brain barrier (BBB). We focused on studies of the transportation of various trace elements through BBB and of their retainment in the brain, utilizing the radioactive multitracer technique.[1-4] In the preceding reports, we compared the uptake behaviors of radioactive Sc, Mn, Fe, Co, Zn, Se, Rb, and Zr in the brain and other organs of C57BL/6N mice.[3,4] The present work aims to study regional cerebral uptake behaviors of a multitracer of ^{46}Sc, ^{48}V, ^{54}Mn, ^{58}Co, ^{65}Zn, ^{75}Se, ^{83}Rb, and ^{88}Zr among 7 brain regions (corpus striatum, cerebellum, cerebral cortex, hippocampus, midbrain, olfactory, and pons and medulla) and blood of the young and aged C57BL/6N mice. The multitracer solution is expected to give us new findings concerning the relationship between the regional BBB function and the uptake behavior of some trace elements.

Four groups of male C57BL/6N mice having different ages (6, 10, 28, and 52 weeks after birth) were used. The mice had been purchased from Charles River Japan, Inc. These groups were then housed in the plastic and steel cages at the Laboratory for Experimental Animals, Kanazawa University. They were fed on a standard laboratory diet and had free access for drinking water during more than 1 week prior to administration of multitracer. Five of the mice were used in each group. A carrier-free multitracer solution was obtained from an Ag (purity: better than 99.99%) target irradiated by the heavy-ion beam from RIKEN Ring Cyclotron. The multitracer solution was prepared after the method by Ambe et al.[1,2] at the Radioisotope Center, Kanazawa University. The solution contained 12 radioisotopes of 10 elements at 3 weeks after the beam bombardment. For injection to mouse, the physiological saline solution (0.001N HCl, pH 2-3) containing the radioactive multitracer was prepared. An appropriate amount (0.2 ml) of the multitracer solution was intraperitoneally(i.p.) injected into each mouse. At 48 h after this i.p. injection, the mice were sacrificed under ether anesthesia, and about 0.2 ml of blood was collected in a test tube. Then, brains were excised and separated into 7 regions (corpus striatum, cerebellum, cerebral cortex, hippocampus, midbrain, olfactory bulb, and pons plus medulla). These separated regions were weighed immediately and freeze-dried. The dried samples were measured by γ-ray spectrometry with pure Ge detectors in reference to an appropriate standard to obtain "the regional uptake rate" (percentage of injected dose per gram of the region: %dose/g of region) for different tracers. We carefully avoided the adhesive water in weighing the regional samples.

As the results, the multitracer solution enabled a simultaneous tracing of the elements Rb, Zn, Se, Mn, Sc, and Zr elements in each region and a strict comparison of their biobehavior. The regional uptake rates of Rb, Zn, Se, Mn, Sc, and Zr tracers at 48 h after the i.p. injection are shown in Fig. 1. Rubidium, Zn and Se in aged mice were found to be distributed fairly evenly in the regions, and the uptake rates of these elements are higher in aged mice than in young ones. However, the uptake rates of Mn, Sc, and Zr tracers in aged mice have a fairly-large difference among regions, and those of Sc and Zr in aged mice are higher than in young ones, and highly concentrated in certain regions. The behaviors of Sc, Mn, and Zr may be ascribed to the degenerative variation of the function of BBB due to aging.

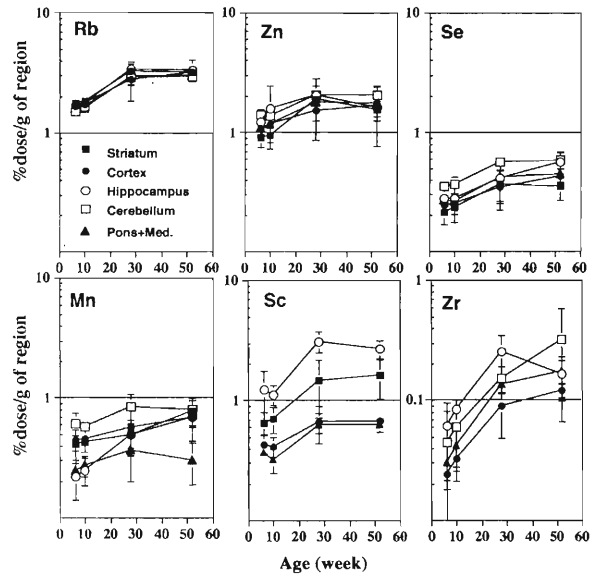

Fig. 1. Aging effect on the regional uptake rates of 6 elements in the brain of normal C57BL/6N mice.

References

1) S. Oishi et al.: J. Radioanal. Nucl. Chem. **239**, 411 (1999).
2) R. Amano et al.: On line Proc. 5th Internet World Congr. on Biomedical Science '98.
3) R. Amano et al.: RIKEN Accel. Prog. Rep. **31**, 126 (1998).
4) S. Oishi et al.: RIKEN Accel. Prog. Rep. **31**, 127 (1998).

* Asanogawa General Hospital, Kanazawa

Metabolic Study of Trace Elements in Se-Deficient Rats (III)

R. Hirunuma, K. Endo, S. Enomoto, S. Ambe, and F. Ambe

Selenium has a property to interact with several metals in mammals.[1,2] Therefore, it is quite interesting and important to compare the distribution of trace elements in various organs between Se-deficient and Se-sufficient rats. However, no systematic study has been performed on the behavior of trace elements in Se-deficient rats. In the present study, the uptake and distribution of trace elements in control and in two types of Se-deficient rats were examined by the multitracer technique, a useful technique to evaluate the behavior of many elements under the identical experimental condition. The rats bred on Se-deficient diet from fetus were used in experiments as Se-deficient (I) rats. Se-deficient (II) rats were fed on Se-deficient diet from the weanling period.

A multitracer solution containing 20 elements of radioisotopes was prepared from an Ag target irradiated by a heavy-ion beam of 135 MeV/nucleon accelerated by RIKEN Ring Cyclotron. Wistar male rats born to Se-deficient dam were fed on Se-deficient diet (produced by Oriental Yeast Co., Ltd.) for 12 weeks after birth to convert them Se-deficient rats (I). Wistar male rats (4 weeks old) were fed on Se-deficient diet for the next 8 weeks to convert them Se-deficient rats (II). Four-week-old Wistar male rats were fed on Se-sufficient (containing 0.2 ppm of Se) diet for 8 weeks to convert them control rats. The multitracer solution was injected intravenously (0.1 ml/rat). The rats were sacrificed at 72 hrs after injection, and the radioactivity of their organs was determined by a γ-ray spectrometry. The observed γ-rays were assigned in terms of their energies and half-lives. The individual behavior of Be, Na, Ca, Sc, V, Cr, Mn, Fe, Co, Zn, Ga, As, Se, Rb, Sr, Y, Zr, Tc, Ru, and Rh was examined.

The influence exerted by Se-deficiency was observed on the behavior of Se, As, Fe, and Sc in various organs of Se-deficient rats (I) or (II). Figure 1 shows the uptake of Se in the brain, testicles, and liver of the Se-deficient (I), (II), and control rats. The uptake of Se was higher in the brain of the Se-deficient rats (I) and (II) than in that of the control ones. On the other hand, the uptake of Se in the testicles was higher only for the Se-deficient rats (II) than that for the control ones. And, there was almost no influence on the uptake for the Se-deficient rats (I). In the liver, the uptake of Se in the control rats was the highest, and that in the Se-deficient (II) was higher than that in the Se-deficient ones (I). It is suggested that the organs such as brain and testicles need Se even a small amount: Se plays a very important and acute role in these organs. It is considered that the morphology of the spermatozoa of Se-deficient rats (I) has changed because they were maintained for a prolonged period on a Se-deficient status. As a result, we suggest that the spermatozoa of Se-deficient rats (I) can not uptake Se.

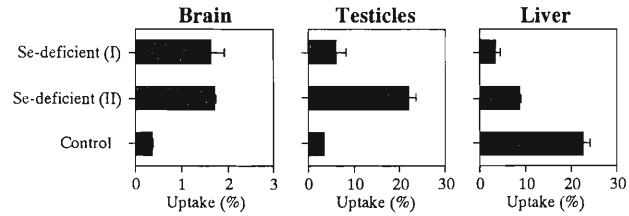

Fig. 1. Uptake of Se in the brain, testicles, and liver of the Se-deficient (I), (II), and control rats.

The characteristic results obtained on As, Fe, and Sc in the liver are shown in Fig. 2. The uptake of As, Fe, and Sc was larger in the liver of the Se-deficient rats (I) than that of the Se-deficient (II) and control ones. Selenium enhances As excretion in to bile in the rats.[3,4] The observed accumulation of As in Se-deficient rats (I) suggests that the bile excretion of As was decreased by Se-deficiency. Increase of Fe uptake in the liver of Se-deficient rats (I) suggests an accumulation of the Fe-binding protein, such as catalase or ferritin. Interestingly, the uptake behavior of Sc and Fe was similar in the liver of the Se-deficient (I), (II) and control rats. One of the reasons why the uptake behavior is similar between Sc and Fe is presumably due to the similarity of their ionic valence and of their ionic radii (0.73 Å for Sc^{3+} and 0.64 Å for Fe^{3+}).

The behavior of trace elements except Se in the Se-deficient rats (II) was not different from that in the control ones. The uptake of As, Fe, and Sc was higher in the Se-deficient rats (I) than in the control ones. It is suggested that the metabolism of these elements is affected by Se-deficiency for fetus.

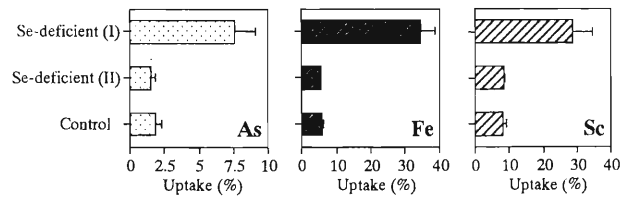

Fig. 2. Uptake of As, Fe, and Sc in the liver of the Se-deficient (I), (II), and control rats.

References

1) T. Urano, N. Imura, and A. Naganuma: Biochem. Biophys. Res. Commun. **239**, 862 (1997).
2) J. P. Berry, L. Zhang, and P. Galle: J. Submicrosc. Cytol. Pathol. **27**, 21 (1995).
3) O. A. Levander and C. A. Baumann: Toxicol. Appl. Pharmacol. **9**, 98 (1966).
4) O. A. Levander and C. A. Baumann: Toxicol. Appl. Pharmacol. **9**, 106 (1966).

Multitracer Study on the Soil-to-Plant Transfer of Radionuclides in *Brassica rapa* L. var. *perviridis* Bail (Komatsuna) at Different Growth Stages

S. Ambe, T. Ozaki, S. Enomoto, and T. Shinonaga

The transfer factor, which is defined as the ratio of the radioactivity concentration in plant to that in soil, is widely used for the evaluation of the uptake of radionuclides by plants from the soil. The transfer factor is greatly affected by growth conditions such as composition of soil, particle size of soil, soil pH, climate, and so on. Most of the transfer factors have been reported for the edible parts of mature plants. Some leafy vegetables are harvested as foods from young to mature growth stages. It was shown that the translocation rate of ^{134}Cs from leaves to tubers is greatly affected by the development stages when radioisotopes are applied to potato plants.[1] This suggests the importance of studies on the uptake of radionuclides by various plants at different development stages. However, the variability of transfer factors depending on the growth stage has not been studied comprehensively. In this study, the uptake of radionuclides of Na, Mn, Co, Zn, Se, Rb, Sr, Y, Zr, Tc, Rh, and Cs by komatsuna (*Brassica rapa* L. var. *perviridis* Bail) was determined simultaneously by the multitracer technique.

Commercially available Kureha soil was mixed well with the multitracer solution and the pH of the soil solution (soil water volume ratio: 1 : 2.5) was determined to be 6.0. About ten seeds of komatsuna were sown and cultured on the soil (about 2 kg dry weight of soil) in a pot. Five pots for the transfer factor study and three pots as control were placed in a plant-growth chamber maintained at 23°C and 70–80% relative humidity under about 13000 lx-light exposure from fluorescent lamps 16 h a day. The komatsuna plants were grown for 14, 20, 26, and 33 days from sowing. Two to 4 plants on day 14, 2 plants on day 20, and one plant each on days 26 and 33 were harvested, and then they were divided into leaves and roots. The samples were dried at 60°C for one day. The dry samples mounted in a plastic vessel (60 mmϕ) were subjected to γ-ray measurement.

The transfer factors were obtained as average values of five samples with standard deviations. Figure 1 shows the time dependence of the transfer factors of these elements except Co, Se, Y, Zr, and Rh. The decrease in the transfer factors from 1.9 to 1.3 for Rb, from 50 to 17 for Tc, and from 0.016 to 0.0065 for Cs was observed in the leaves of komatsuna with increasing culture period with the multitracer, while those of Na (1.3), Co (0.03), Se (0.06), and Sr (0.28) in leaves remained almost constant. In contrast, the transfer factor of Mn increased from 0.11 to 0.25 with time. The transfer factor of Zn (0.52) on day 14 (the youngest stage) was higher than that on other days, although the standard deviation was large. Technetium gave the highest transfer factor among the elements studied, followed by a marked decrease in the transfer factor with time. The radioactivities of Y and Zr in the leaves collected from the plants cultured for 14, 20, 26, and 33 days were below the detection limit. A small amount of Rh was found in the leaves of the plants cultured for 33 days and its transfer factor was 0.003.

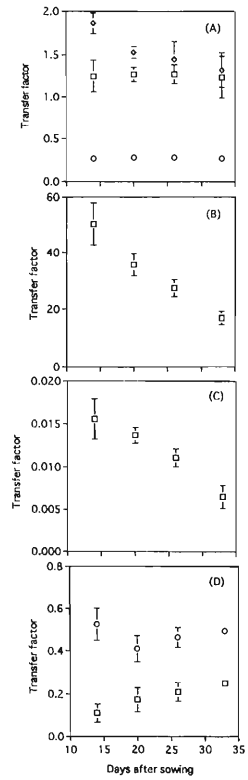

Fig. 1. Time dependence of the transfer factors of Na (□), Rb (◇), and Sr (○) (A), Tc (B), Cs (C), and Mn (□) and Zn (○) (D) obtained from komatsuna leaves. If error bars are not shown, the standard deviations are within symbols.

Extraction of multitracer from the soil was carried out in order to study the correlation between the transfer factor and the aging effect of the tracers in soil. The transfer factors for leaves and roots exhibit no correlation with the extractability of the tracers from soil.

References

1) T. K. Riesen, J. Egli, and R. Y. Andres: Radiat. Environ. Biophys. **36**, 293 (1998).

Reduced Uptake of Mn in Cd-Resistant Metallothionein Null Fibroblast

S. Himeno, T. Yanagiya, N. Imura,* R. Hirunuma, and S. Enomoto

Cadmium (Cd) is a heavy metal known as a causative agent of Itai-itai disease. Orally ingested Cd is preferentially accumulated in the kidney, thus leading to a characteristic nephrotoxicity known as Fanconi's syndrome. Metallothionein (MT) is a low-molecular-weight cysteine-rich protein that can efficiently bind to metals such as Zn, Cu, and Cd. Important roles of MT in the detoxification of Cd have been well documented. However, other factors that can modulate the toxicity of Cd have not yet been fully elucidated. Recently, MT null mice in which MT-I and II genes were disrupted have been developed.[1,2] We established a SV40-transformed embryonic fibroblast cell line from MT null mice so as to obtain apparently immortalized cells lacking MT expression.[3] Furthermore, we developed a Cd-resistant cell line from the SV40-transformed MT null cells to investigate the resistance factors to the Cd irrelevant to MT. This Cd-resistant MT null cells (Cd-r) showed a markedly reduced accumulation of Cd compared to the parental cells. In the present study, we have investigated the uptake of various kinds of metals in Cd-r cells using a multitracer technique, and found a marked decrease of Mn uptake in Cd-r cells.

Cd-r and parental MT null cells were exposed to a multitracer dissolved in the serum-free medium. After the incubation for 2 h, cells were washed twice with PBS(−) and the radioactivities of metals including Zn, Fe, Mn, Co, Be, Sc, Cr, Se, Rb, Y, and Zr in the cells were determined. As shown in Fig. 1, Mn uptake in Cd-r was as low as about 10% of that in the parental cells. The uptake of Co in Cd-r was also reduced to about 70% of the parental cells. Other metals including Zn and Fe did not show any significant difference between the two cell lines. Since the accumulation of Cd in Cd-r cells was also reduced to about 10% of the parental cells, it is suggested that Cd and Mn may share the similar system for their incorporation into the cells and that this system may be disrupted in Cd-r cells.

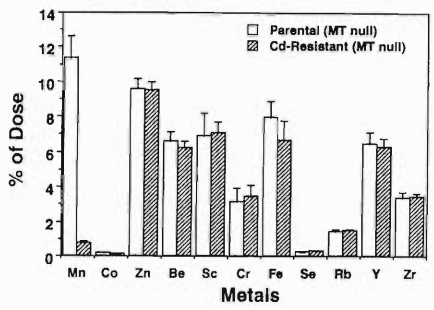

Fig. 1. Uptake of various elements into the Cd-resistant and parental metallothionein null cells. A multitracer was added in the medium of Cd-resistant and parental metallothionein null cells, and incubated for 2 h. The uptake of each element was expressed by the % of added dose.

To further clarify the incorporation system common for Cd and Mn, we have examined inhibitory effects of Mn on the uptake rate of ^{109}Cd. Addition of Mn into the medium efficiently inhibited the uptake of Cd in the parental cells, while no inhibition of Cd uptake by Mn was observed in Cd-r cells. These results strongly suggest that the major part of Cd is incorporated into the cells via a pathway inhibited by Mn and that this pathway is suppressed in Cd-r cells.

Therefore, we have next examined the accumulation of Mn in the Cd-r and parental cells using ^{54}Mn as a tracer. Mn was incorporated into the cells time-dependently, but the rate of uptake is markedly reduced in Cd-r cells. However, this reduction was observed only in the low concentrations of Mn (less than 300 nM), and no difference was observed at concentrations higher than 1 μM, suggesting that there may exist at least two pathways for Mn to incorporate into the cells, and that only the high-affinity pathway for low Mn concentrations may be disrupted in Cd-r cells. In support of this hypothesis, inhibition experiments showed that the addition of Cd into the medium efficiently inhibited the uptake of Mn (100 nM) even at the equimolar concentration. Therefore, it is suggested that Cd may be transported into the cells via the high-affinity uptake system for Mn.

The mechanism of Cd uptake into cells has not yet been fully understood. Based on the facts that the ionic radius of Cd is very close to that of Ca, and that Cd is an efficient blocker of Ca channel, it has been considered that Cd traverses the cell membrane via Ca channel. However, the present study to have used the multitracer technique suggested a possibility that a high-affinity transportation system of Mn could be the major pathway for Cd uptake into cells. Further study is required for the identification of the transporter that we have characterized here.

* School of Pharmaceutical Sciences, Kitasato University

References

1) A. E. Michalska et al.: Proc. Natl. Acad. Sci. USA **90**, 8088 (1993).
2) B. A. Masters et al.: Proc. Natl. Acad. Sci. USA **91**, 584 (1994).
3) Y. Kondo et al.: Life Sci. **64**, PL145 (1999).

Influence of Citrate Ions on the Complex Formation of Lanthanide Ions with Bovine Serum Albumin and Transferrin

K. Endo, N. Sotogaku, K. Matsumoto, R. Hirunuma, S. Enomoto, S. Ambe, and F. Ambe

A number of low molecular-weight ligands, such as citrate, lactate, hydrogen carbonate, amino acids, polyphosphates etc. are contained in blood as well as serum proteins, and these compounds coordinate to metal ions. Several biologically important compounds with low molecular weight have been shown to form stable complexes with metal ions, and many of them have been implicated to play some roles in the absorption of metal ions. For example, lactate appears to take part in specific protein binding, and citrate in protein and metal binding.[1] It seems that metal ions are present as coordination chemical species in equilibrium with serum proteins and low molecular weight ligands in living body. Although transferrin has been known to be the predominant transporter for iron ions in blood, it may be also considered to be important for Ln (lanthanide) ions.[2,3] In the present study, the influence of citrate on the complex formation of bovine serum albumin and transferrin with metal ions was examined using the Ln multitracer.

The Ln multitracer was prepared from gold foil irradiated with a 135 MeV/nucleon N-14 beam at RIKEN Ring Cyclotron. The preparation of the multitracer solution was followed by the established procedure.[4] Fatty acid free bovine serum albumin (BSA) was dissolved in 50 mM HEPES/NaOH (pH 7.4). Apotransferrin was dissolved in 50 mM HEPES/NaOH and 5 mM $NaHCO_3$ (pH 7.4) since synergistic CO_3^{2-} ion is required for metal ion binding to transferrin. Sodium citrate of 0.01 M buffered with 50 mM HEPES/NaOH was used. The ionic strength was adjusted to 13 mM with NaCl. Each protein solution (0.9 mL) was mixed with the Ln multitracer solution (0.1 mL) containing citrate, the final concentration of the protein being 1.49 μM. For carrier free experiment, the protein and the Ln multitracer solutions were mixed together and incubated at 37°C for 2 h. In order to estimate the complex stability constants, the carriers for the Ln multitracers were added, where $CeCl_3$, $EuCl_3{\cdot}6H_2O$, $GdCl_3{\cdot}6H_2O$, Tm_2O_3, $YbCl_3$, and Lu_2O_3 were used. The weighted oxides or chlorides were mixed together, and dissolved in 6 M HCl. After being evaporated into dryness, the Ln carriers were dissolved in HEPES/NaOH (pH 7.4). This Ln carrier solution was added to the reaction mixture. The final concentration of each Ln^{3+} (Ln = Ce, Eu, Gd, Tm, Yb, and Lu) was 50 nM. The concentration of NaH_2 citrate was 10 mM and the ionic strength of the solution being adjusted to be 13 mM with NaCl. The mixture was then incubated at the same condition. After incubation, the mixture was ultrafiltered using a millipore filter of Molcut II (the molecular cut-off of the filter was 10000 Da). The γ-ray spectra of the filters were measured by pure Ge detectors and were compared with those of the standard Ln multitracer solution.

The binding percentages of the Ln ions to serum albumin without citrate are shown in Fig. 1(a) and those with 10 mM sodium citrate in Fig. 1(b). Similar results were obtained for the binding affinity of Ln ions to transferrin. The affinity without carriers was higher than that with carriers for most of the Ln^{3+} studied. Apparently, the lower affinity observed for the sample with carriers can be explained in terms of the lowered specific activity in the Ln-protein complex. In the presence of citrate, the binding percentage increased with increasing atomic number, while in the absence of citrate such tendency was small. The results clearly show that the complex formation of Ln^{3+} with albumin and transferrin are influenced by citrate. The trend was remarkable for the lighter Ln^{3+}. It is known that the stability constants of Ln ions with simple ligands such as OH^-, CO_3^{2-}, and $(COO)_2^{2-}$ increase with an increase in the atomic number of the Ln^{3+} ions, which is due to the Ze_{eff}/r, i.e., the complex formation enthalpy is more favored for heavier Ln^{3+}. In the presence of multidentate ligand, the complex formation is favored further by the chelating effect (entropy effect). In fact, the complex formation of Ln-citrate has been explained by an increase in the freedom by the replacement of monodentate ligands such as H_2O and OH^- with a multidentate citrate ion.[5] However, in the case of protein being ligand molecule, the formation of metal-protein complex gives unfavorable entropy

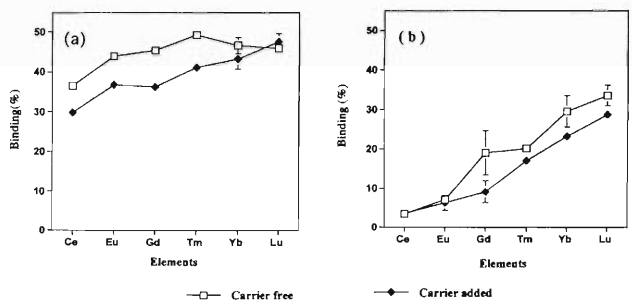

Fig. 1. Binding percentages of the Ln ions to serum albumin without citrate (a), and those with 0.01 M sodium citrate (b). Open squares show the results obtained for the carrier free sample, and filled ones for the sample with 50 nM carriers. Each datum represents the mean value ± standard deviation obtained by five measurements.

effects involving conformational change of flexible ligand on complexation. In addition, the citrate chelate is formed through 7-membered ring. The 7-membered ring is more compatible geometrically for Ce ions with a larger ionic radius, although the stability constant of $Ln(cit)_2^{3-}$ goes greater for heavier Ln^{3+} due to an increase in Ze_{eff}/r. It is also noted that N-atom with a stronger ligand field is involved in the ligating atoms of protein, which contributes to form more covalent (and stable) bonding than O-atom in carboxyl group in Ln citrate complex. It is, therefore, concluded that the geometrical compatibility of lighter Ln^{3+} ions for forming citrate chelate will be a dominant factor for explaining the affinity dependence under the presence of citrate ions. These will be possible reasons responsible for the fact that the formation of Ln protein complex for the lighter Ln^{3+} was affected more remarkably than the heavier one under a presence of citrate.

Similar values of the binding affinity observed for albumin and transferrin may indicate that both serum proteins are good transporter for Ln ions in blood if they are present equally in amount. Actually albumin concentration is 3500–5500 mg in 100 mL of blood plasma, and transferrin 200–400 mg.[6] These indicate that roughly 11 times larger amount of albumin is present than transferrin in blood plasma, and that albumin is the major transporter for Ln ions.

References

1) J. D. Bell, C. C. Brown, and P. J. Sadler: FEBS Lett. **235**, 81 (1988).
2) A. Bezkorovainy: in *Biochemistry of Nonheme Iron* (Plunum Publ., New York, 1980), p. 127.
3) T. Yamamura et al.: Nippon Kagaku Kaishi, No. 4, p. 452 (1988), in Japanese.
4) S. Ambe, S. Y. Chen, Y. Ohkubo, Y. Kobayashi, H. Maeda, and M. Yanokura: J. Radioanal. Nucl. Chem. **195**, 305 (1995).
5) H. Li, P. J. Sadler, and H. Sun: Eur. J. Biochem. **242**, 387 (1996).
6) O. Yamauchi: in *Seitai to Kinzoku Ion* (Gakkai Shuppan Center, Tokyo, 1991), p. 187, in Japanese.

Behavior of Various Trace Elements in Zinc Deficient Mice

M. Yanaga, T. Ohyama, M. Iwama, T. Yoshida, M. Noguchi,[*1]
T. Omori,[*2] R. Hirunuma, and S. Enomoto

Zinc is one of the most important essential elements in living organisms and it influences on the activity of more than 300 enzymes that participate in a wide variety of metabolic processes, such as, the metabolism and the synthesis of proteins and nucleic acid etc. Therefore, it is known that deficiency of this element leads to skin injury, alopecia, loss of senses, growth retardation and so on.

In the present work, the multitracer technique was applied for investigation of the behavior of trace elements in zinc deficient mice. The technique is thought to be suitable for this purpose because zinc interacts with many other trace elements and various kinds of elements are dealed with simultaneously using this technique. Neutron activation analysis is also useful method for analysing multielement simultaneously in organs and tissues of living bodies in order to investigate the behavior and roles of Zn. Yanaga et al. determined six elements in ten organs and tissues of Zn deficient adult mice by means of instrumental neutron activation analysis.[1] They reported that Zn concentrations in organs of Zn deficient mice were not distinctly lower than those of control mice except for bone and pancreas indicating that Zn had been supplied from these organs, mainly bone, to other organs and tissues. They also reported that Co content increased significantly in all organs and tissues of Zn deficient mice compared with control mice indicating the partial substitution of Co with Zn in metal proteins or other materials in the Zn deficient mice. It is considered that there is a possibility that other metal elements substitute with Zn. However, contents of many metal elements are larger than content of Co, then, the slight change of concentration of the other elements is not readily detectable in analytical experiment. On the other hand, tracer experiment may avoid this problem.

In the present tracer experiment, multitracer solution was prepared as following procedures. Silver target was irradiated with $^{12}C^{6+}$ beam (135 MeV/nucleon) accelerated by RIKEN Ring Cyclotron. The irradiated target was first dissolved in (1 : 1) HNO_3. Then, Ag was precipitated as AgCl with conc. HCl. After the precipitate was filtered out, remained multitracer solution was evaporated under reduced pressure. The residue was dissolved in physiological saline for administration.

Twenty-one male mice of the ICR strain, 7-week old (32–34 g), were purchased. These mice were raised in a facility with 12-h light-dark cycle at 24 ± 1°C with commercial food pellet and tap water ad libitum. After a week, they were divided into two groups. Eleven mice were fed with Zn deficient diet pellets and distilled water, and the other ten with control diet pellets and distilled water. After three weeks of feeding, an appropriate amount of the multitracer physiological saline solution was injected intraperitoneally into each mouse. One day after injection, about 1 ml of blood was collected from heart under diethyl ether anesthesia, and then, 10 organs and tissues, such as brain, liver, kidney, spleen, pancreas, testis, skeletal muscle, bone, small intestine, and skin and hair, were removed. They were weighed and bottled. The radioactivities of the samples were measured with HP Ge detectors. Behaviors of various elements, such as, V, Mn, Co, Zn, Se, Rb, Sr, Ru, etc., in Zn deficient mice were satisfactory traced.

References

1) M. Yanaga, M. Iwama, K. Takiguchi, M. Noguchi, and T. Omori: J. Radioanal. Nucl. Chem. **231**, 187 (1998).

*1 Department of Biology and Geosciences, Faculty of Science, Shizuoka University
*2 Radiochemistry Research Laboratory, Faculty of Science, Shizuoka University

Uptake and Distribution of Trace Elements in Yeast *Saccharomyces cerevisiae*

Y. Nose and I. Yamaguchi

Disposal of the radioactive wastes and nuclear facility accidents are serious problem in worldwide. It has been known that nuclear facilities produce not only ^{90}Sr and ^{137}Cs but also various radionuclides. In addition, several radionuclides, including ^{99m}Tc, ^{57}Co and ^{97}Ru, have been used in radiotherapy. Therefore, it is necessary to construct a recover system of various radionuclides for nuclear pollution countermeasures. To achieve this aim, metal uptake by microorganisms has been researched by many investigators for its potential application to remove the radionuclides from radioactive wastes and environment.[1-3] Recently, we tested the uptake of various radionuclides by yeast *Saccharomyces cerevisiae*, as a model of RI accumulating microbe using a multitracer technique,[4,5] and found that radionuclides of Be, Sc, V, Cr, Mn, Fe, Co, Zn, As, Se, Sr, Y, Zr, Ru and Rh were taken up by the yeast.[5] In this paper, we show that tracers of Be, Sc, Mn, Co, Zn, Se, Sr, Y and Zr were present both on the cell surface and inside the cell.

S. cerevisiae (JCM7255) was grown in Difco Yeast Nitrogen Base (Difco) with 0.5% (w/v) glucose at 25 °C in a shaker. The cells of 700 ml of cultures (OD_{660} = 1.0) were collected, washed twice with a 5 mM 2-(*N*-morpholino) ethanesulfonic acid (MES)-NaOH (pH 5.4), and suspended in 30 ml of the same buffer. An aliquot of multitracer solution was added, and the yeast suspension was then incubated for 30 min at 25 °C in a shaker. After incubation, spheroplasts were prepared as described by Bowser and Novick.[6] The spheroplasts were homogenized, centrifuged at 1,000, 3,000, 10,000 and 100,000×g to produce precipitate (ppt) 1, 2, 3 and 4, supernatant (sup) 4 and floating substances, respectively. Each sample was subjected to γ-ray measurement with high-purity Ge detectors.

Figure 1 shows the distribution of 9 tracers in the yeast. All tracers were detected from both digested cell wall fraction and spheroplasts fraction. In spheroplast, tracers of Sc, Mn, Co, Zn, Se, Sr and Y were mainly detected from ppt 1 and sup 4 fractions. On the other hand, tracers of Be and Zr were detected from ppt 1, and little or no tracers were detected from ppt 4 and sup 4. These data suggested that all tracers tested were present both on the cell wall and inside the cells. Inside cells, tracers of Sc, Mn, Co, Zn, Se, Sr and Y were present partly as insoluble form possibly bound to organelles, and those of Be and Zr were mainly present as insoluble form.

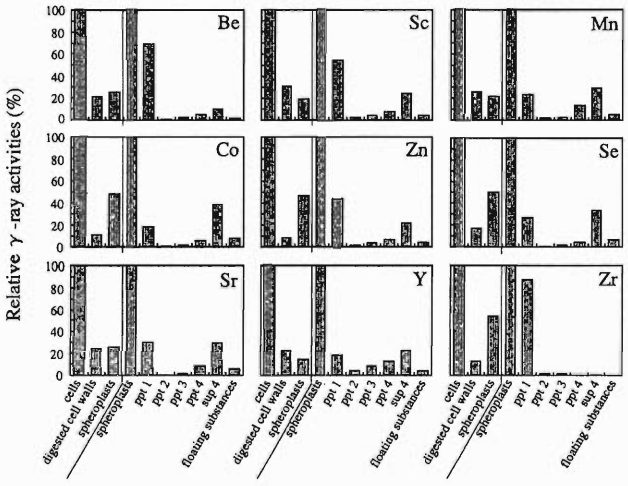

Fig. 1. Typical pattern of distribution of 9 tracers in the yeast *S. cerevisiae*. Each datum represents the relative γ-ray activities.

Next step is to identify the transport systems of tracers from outside to inside the cell.

References

1) L. E. Macaskie and A. C. R. Dean: Biotechnol. Lett. **7**, 627 (1985).
2) J. S. Watson et al.: Appl. Biochem. Biotechnol. **20**, 699 (1989).
3) G. W. Granham et al.: J. Appl. Phycol. **5**, 307 (1993).
4) S. Ambe et al.: Anal. Sci. **7**, Suppl., p. 317 (1991).
5) Y. Nose et al.: RIKEN Accel. Prog. Rep. **31**, 141 (1998).
6) R. Bowser and P. Novick: J. Cell Biol. **12**, 1117 (1991).

Bioaccumulation and Distribution of Sr, Tc and Cs in Soybean

Y. Nose and I. Yamaguchi

Various radionuclides released from nuclear facilities into the atmosphere can be accumulated in human body through food chains. Especially, radioactive Sr, Tc and Cs have been regarded as the most hazardous radionuclides, because of its high yields in products of nuclear facilities and its long half lives. For nuclear safety assessment, it is necessary to research behaviors of these 3 radionuclides from soil to crops. In this experiment, we studied the bioaccumulation and distribution of ^{85}Sr, ^{95m}Tc and ^{137}Cs from soil to soybean in short term (0–480 hr) exposure to a multitracer. Soybean plants *Glycine max* were cultured in pots for 2 months. The multitracer containing ^{85}Sr, ^{95m}Tc and ^{137}Cs dissolved in distilled water was applied to the pots. After several hours incubation, the plants were harvested, dried, and subjected to γ-ray measurement with high-purity Ge detectors.

Figure 1 shows the bioaccumulation (% dose/g dry weight) of 3 radionuclides from soil to soybeans. The bioaccumulation reached the maximal levels at around 20 hr incubation with a multitracer, but more than 24 hr incubation ($\leqq$ 480 hr) led no significant changes in the levels.

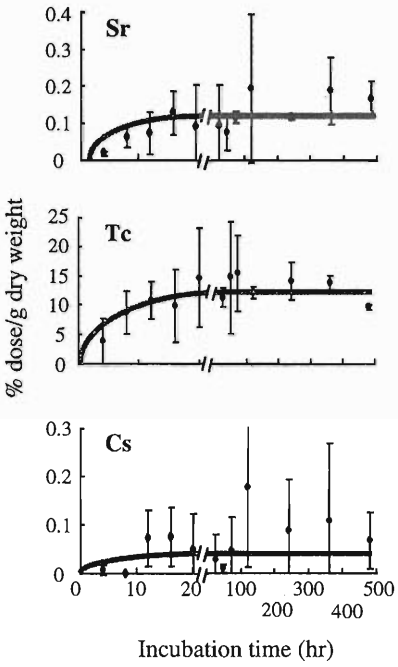

Fig. 1. Time dependent bioaccumulation of ^{85}Sr, ^{95m}Tc and ^{137}Cs from soil to soybean. Each datum represents the mean of three trials ± standard deviation.

Figure 2 shows distribution ratios of 3 radionuclides in fruits, leaves, stems and roots. Radioactive Sr was detected from all tissues, but its distribution rate was varied irrespective of the incubation time. In Tc, relative amounts in roots were decreased from 70 to 10%, but that in other tissues increased from 25 to 80% dependent on the incubation time. More than 80% of Cs were distributed into roots, and little amount were detected from fruits, leaves and stems.

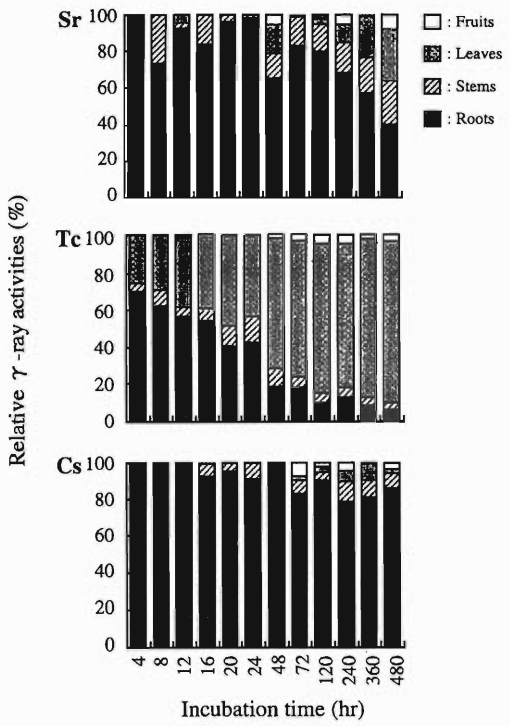

Fig. 2. Time dependent distribution of ^{85}Sr, ^{95m}Tc and ^{137}Cs in soybean. Each datum represents the mean of three trials.

In this experiment, we show that soybean plants took up radioactive Sr, Tc and Cs by several hours exposure to these radionuclides. More than 48 hr incubation resulted in the contamination of edible parts (fruits) by these radionuclides. In addition, the affinity of soybean for Tc was relatively high: about 60% of Tc administered into soil was taken up, whereas 0.25–3% of other elements (data not shown). This property may be possible to apply to phytoremediation of soil Tc. That is, soybean leaves accumulate Tc from soil, and those are harvested and insulated.

Uptake of Rare Earth Elements by Plants

T. Ozaki, S. Enomoto, and Y. Makide*

Under natural conditions, plants absorb a very small amount of rare earth elements (REEs). The most stable oxidation state of REEs is trivalent, and they are tightly bound to surfaces of rocks and organic substances such as humic acid. Under natural conditions, plants absorb a very small amount of REEs. However, some plant species, such as *Dryopteris erythrosora*, absorb a large amount of REEs.[1] Considering the low availability of these elements under natural conditions, some special mechanism, involved in the uptake of the elements, is expected to exist in the accumulating species.

In the present investigation, we have studied the uptake behavior of REEs by several kinds of plant species, including accumulating and non-accumulating species for REEs, using the multitracer technique.

Eleven plant species listed in Table 1 were grown on soil, being kept under the controlled climatic conditions (day/night 16/8 h; light intensity 10000 lux; temperature 25 ± 2°C; and relative humidity 70–80%) until the shoot length became about 7 cm. Before the uptake experiment, they were kept in the ultrapurified water for 1 week to reduce the influence of adhering soil. During this period, the water was changed every several hours. The pH of the water was adjusted to 5.8 ± 0.1 using 0.01 M of HCl, and the volume was adjusted to 50 ml. After this period, the roots of plants were kept in a multitracer solution with the same pH and volume as the preceding treatment. After 1 week, the roots were washed with 0.1 M HCl to get rid of the REEs adhered to the surface of roots. Gamma-ray from both roots and leaves of the plant samples was counted with a germanium detector.

Table 1. Names of the plant species used for the study.

Plant species (common name)
(a) *Luffa cylindrica* Roem. (sponge gourd)
(b) *Antirrhium majus* (snapdragon)
(c) *Pisum sativum* (pea)
(d) *Abelmoschus esculentus* Moench (okra)
(e) *Nicotiana tabaccum* (tabacco)
(f) *Cucumis melo* (melon)
(g) *Amaranthus mangostanus* (edible amanranthus)
(h) *Poa pratensis* (kentuchy blue grass)
(i) *Colysis pothifolia* (fern)
(j) *Cyrtomium fortunei* (fern)
(k) *Dryopteris erythrosora* (fern)

A multitracer of REEs was produced by the irradiation of Au with a 135 MeV/nucleon ^{14}N ion beam accelerated by the RIKEN Ring Cyclotron. Additional details are described in the literatures.[2,3]

As shown in Fig. 1(A), no appreciable difference was observed among the plant species in the uptake of REEs into their roots. For leaves, 9 plant species (a, b, c, d, e, f, g, h, and i), which do no accumulate REEs[4] showed an anomalously high uptake of Y among REEs (Fig. 1(B)). On the other hand, accumulating species for REEs (j and k) showed no anomaly with Y. From this, it is suggested that some unknown mechanisms should exist for the uptake of REEs in *Dryopteris erythrosora* and *Crytomium fortunei*.

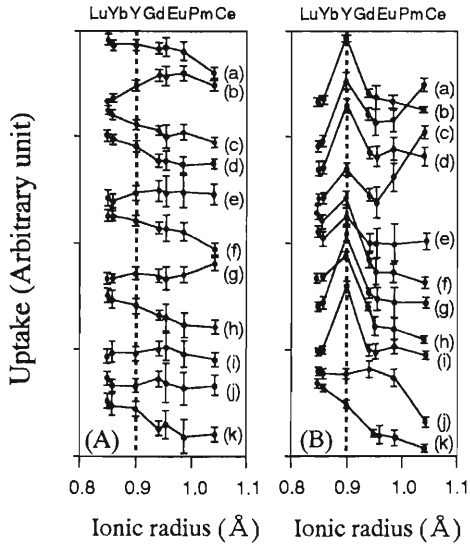

Fig. 1. Uptake of rare earth elements into roots (A) and leaves (B) of plant species. Dotted lines correspond to the ionic radius of Y.

References

1) T. Ozaki et al.: J. Radioanal. Nucl. Chem. **217**, 117 (1997).
2) S. Ambe et al.: Anal. Sci. **7**, Suppl., p. 317 (1991).
3) F. Ambe ed.: RIKEN Rev. No. 13 (1996).
4) T. Ozaki: unpublished data.

* Radio Isotope Center, University of Tokyo

Study on the Uptake of Various Elements into Arbuscular Mycorrhizal Marigold by Multitracer Technique

H. Suzuki,[*1] H. Kumagai,[*1] K. Oohashi,[*2] S. Enomoto, and F. Ambe

The roots of most higher plants are colonized by specific soil fungi to form the arbuscular mycorrhizae which is an important part of the absorbing root system of the plant. It is well known that the arbuscular mycorrhizal (AM) colonization enhances the uptake of phosphorus by plants.[1] A few papers have suggested that AM colonization can also promote the uptake of other elements.[2] In the present study, we have examined the effect of AM colonization on the uptake of various elements in the symbiotic system of marigold (*Tagetes patula* L. cv. Bonanza spray) and *Glomus etunicatum* (Becker and Gerd) using a multitracer technique.

Seeds of marigold were sowed in the autoclaved river sand inside a 9 cm pot (240 ml in volume). One ml of the spore suspension (containing approximately 200 spores) of *Glomus etunicatum* was pipetted to the center of the hole (2 cm in depth) of the growth medium, prior to sowing, for the mycorrhizal inoculation. A non-mycorrhizal plant was used as control plant. Plants were grown in an RI-biotron with 16/8 hr day/night regime, 15000 lux, 65% relative humidity, and 25 °C. The marigold seedlings were thinned to one per pot on the 7th day after sowing. The experiment was carried out at 55% of the water holding capacity of the growth medium.

A multitracer solution was prepared from a Ag foil which was irradiated with a 135 MeV/nucleon ^{14}N beam accelerated by RIKEN Ring Cyclotron. The Ag foil was dissolved in HNO_3, and then the Ag itself was separated from the multitracer by the form of AgCl precipitate. The filtrate was evaporated to dryness and dissolved in fertilizer solution. A multitracer solution containing the radionuclides of ^{7}Be, ^{22}Na, ^{46}Sc, ^{51}Cr, ^{54}Mn, ^{59}Fe, ^{56}Co, ^{65}Zn, ^{74}As, ^{75}Se, ^{83}Rb, ^{85}Sr, ^{88}Y, ^{88}Zr, and ^{95m}Tc was administered on the 29th day after sowing. The plants containing root, shoot, and flower were sampled for analysis on the 7th and 21st days after the administration of a multitracer solution.

The effect of AM colonization on the uptake of multitracer elements was complex (Fig. 1). On 36th day after sowing (7 days after multitracer application), the uptake rate (% of dose) of Zn and Tc in the mycorrhizal plant was approximately 2 and 1.5 times large compared with that in the control plant. On the other hand, the uptake rate of Sc, Co, and Sr in the mycorrhizal plant was lower than that in the control plant. On 50th day after sowing (21 days after multitracer application), the uptake rate of Be, Na, Cr, Fe, Zn, and Tc in the mycorrhizal plant was higher than that in the control plant, while the rate of Sc, Co, and Rb in the mycorrhizal plant was lower than that in the control plant. The uptake rate of Mn, As, Se, Y, and Zr of the mycorrhizal plant was similar to that in the control plant on 36th and 50th days after sowing.

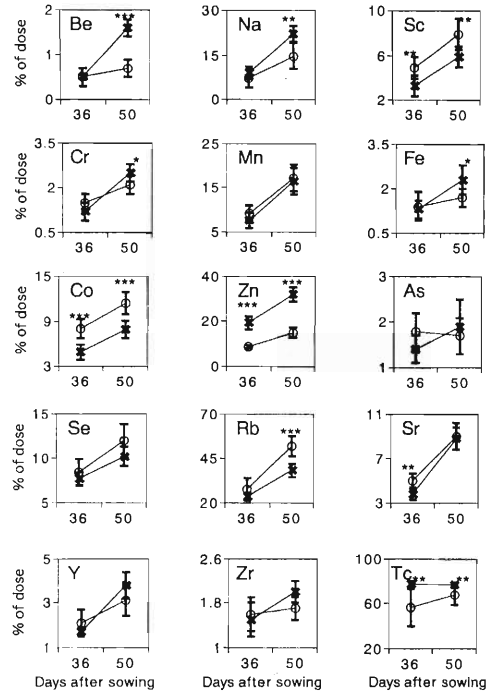

Fig. 1. Uptake rate (% of dose) of various elements in the mycorrhizal (✖) and control plants (○) at two cultivated stages. Each data point in the figure represents the mean value ± standard deviation obtained from at least seven preparations ($^{*}P < 0.05$; $^{**}P < 0.01$; $^{***}P < 0.001$).

The results show that AM colonization affects the uptake of Be, Na, Sc, Cr, Fe, Co, Zn, Rb, Sr, and Tc in marigold. The enhancement of uptake of Zn by AM colonization is probably based on the well-established activity of external mycelium.[2] However, the decrease in the uptake of Sc, Co, Rb, and Sr by AM colonization is not clear. To elucidate this point, further investigation is required.

References

1) K. M. Cooper and P. B. Tinker: New Phytol. **81**, 43 (1978).
2) H. Marschner and B. Dell: in *Management of mycorrhizas in agriculture, horticulture and forestry*, edited by A. D. Robson, L. K. Abbott, and N. Malajczuk (Kluwer Acad. Publ., Netherlands, 1994), p. 89.

*1 Radioisotope Research Center, Chiba University
*2 Faculty of Pharmaceutical Sciences, Chiba University

Study on the Distribution of Various Elements in Arbuscular Mycorrhizal Marigold by Multitracer Technique

H. Suzuki,[*1] H. Kumagai,[*1] K. Oohashi,[*2] S. Enomoto, and F. Ambe

As shown in the preceding paper, the arbuscular mycorrhizal (AM) colonization increased the uptake of Be, Na, Cr, Fe, Zn, and Tc in a multitracer solution, while it inhibited the uptake of Sc, Co, Rb, and Sr. In this report, we have investigated the effect of AM colonization on the translocation of various elements. The experiments were carried out like described in the preceding paper.

Figure 1 shows the distribution of elements (% of dose) in the root. On 36th day after sowing (7 days after multitracer application), the distribution of Sc, Co, and Rb in the root of the mycorrhizal plant was lower than that of the non-mycorrhizal (control) plant, and the distribution of Zn in the root of the mycorrhizal plant was higher than that of the control plant. The distribution of Be, Na, Cr, Fe, Zn, Sr, and Y in the root of the mycorrhizal plant was higher than that of the control plant on 50th day after sowing (21 days after multitracer application). These results show that AM colonization can promote the accumulation of Be, Na, Cr, Fe, Zn, Sr, and Y in the root.

The distribution of elements in the shoot is shown in Fig. 2. The distribution of Co, Sr, and Y in the shoot of the mycorrhizal plant was lower than that of the control plant on 36th and 50th days after sowing, while the distribution of Zn and Tc in the shoot of the mycorrhizal plant was higher than that of the control plant. The distribution of Se and Rb in the shoot of the mycorrhizal plant was lower than that of the control plant on 50th day after sowing. These results suggest that AM colonization affects the translocation of Co, Zn, Se, Rb, Sr, Y, and Tc from the root to the shoot in plants.

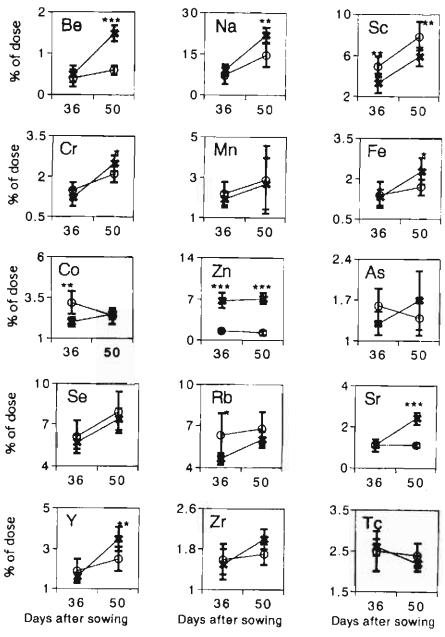

Fig. 1. Distribution (% of dose) of various elements in the root of the mycorrhizal (✖) and control plants (○) at two cultivated stages. Each data point in the figure represents the mean value ± standard deviation (S.D.) obtained from at least seven preparations ($^{*}P < 0.05$; $^{**}P < 0.01$; $^{***}P < 0.001$).

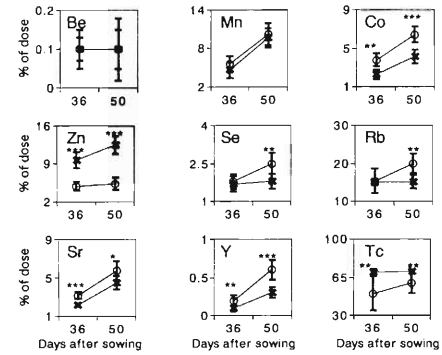

Fig. 2. Distribution (% of dose) of various elements in the shoot of the mycorrhizal (✖) and control plants (○) at two cultivated stages. Each point is the same as described in the legend to Fig. 1.

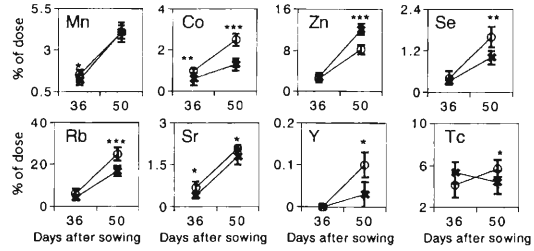

Fig. 3. Distribution (% of dose) of various elements in the flower of the mycorrhizal (✖) and control plants (○) at two cultivated stages. Each point is the same as described in the legend to Fig. 1.

The distribution pattern of Mn, Co, Se, Rb, Sr, and Y in the flower was similar to that in the shoot (Fig. 3). The distribution of Zn in the flower of the mycorrhizal plant was higher than that of the control plant, and the distribution of tracers except Mn and Zn in the mycorrhizal plant was lower than that in the control plant on 50th day after sowing.

Our results show that AM colonization affects on the translocation of Co, Zn, Se, Rb, Sr, Y, and Tc in marigold. To elucidate the inhibition of translocation of these elements except Zn by AM colonization, further investigation is required.

*1 Radioisotope Research Center, Chiba University
*2 Faculty of Pharmaceutical Sciences, Chiba University

Formation of Metallofullerenes Studied by the Multitracer Technique

K. Sueki, K. Kikuchi, K. Akiyama,* T. Sawa,* H. Nakahara,
S. Ambe, S. Enomoto, and F. Ambe

Formation of metallofullerenes, especially stable in air and in organic solvents, has been reported only for the group 2 elements (Ca, Sr and Ba), and for the group 3 elements (Sc, Y, and lanthanoids). In this study, formation of metallofullerenes was examined for a large number of elements belonging to the various groups in the periodic table.

Experiments were performed by use of the multitracer[1] prepared from the ^{197}Au target bombarded with ^{12}C heavy-ion beam at the Ring Cyclotron. After chemical separation from the target material, the tracer was found to contain 33 kinds of radioisotopes of 28 elements with the number of atoms of each isotope ranging from 2×10^{10} to 6×10^{12}. The amount of each isotope was monitored and determined by γ-ray measurements with an HPGe detector. The multitracer and 3 grams of La nitrate were dissolved in ethanol and adsorbed into a porous carbon rod (1.24 g/cm^3). Platinum was not adsorbed into the rod. After proper heat treatment of the rod, it was used as an electrode for fullerene production by the arc discharge method in a vacuum chamber designed for safe handling of radioactive soot. Sodium and Rb were lost by the heat treatment at 1200°C. The soot produced inside the chamber was washed out by CS_2 solvent. No Cr and Os found in the extract. The fraction of each element in the fullerene-like species extracted into CS_2 was quantitatively determined by γ-ray spectrometry.

The results are shown in Fig. 1 by solid points against the group number of each element in the periodic table. The CS_2 extract was injected into an HPLC column (5PBB column, 10 mm$\phi \times$250 mm) and eluted with CS_2 at the flow rate of 1.98 ml/min. The elution was monitored on-line by UV absorption, and the eluted fractions were collected for every one-minute for γ-ray measurements.

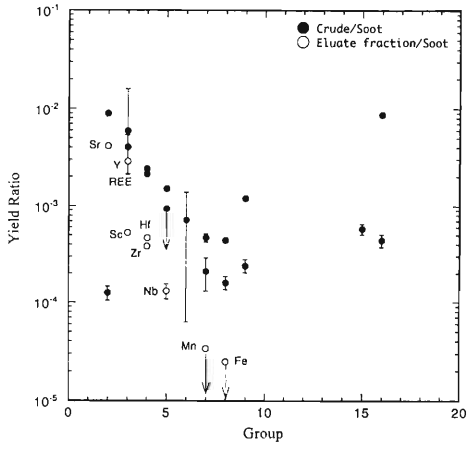

Fig. 1. Yield of each element extracted into CS_2 solvent and those of metallofullerenes as a fraction of the respective radioactivity initially present in the soot.

Observed elution curves are given in Fig. 2 (a), (b) and (c). In the last figure is included the elution curves of the newly discovered metallofullerenes of Zr, Hf and Nb. The elution peaks were also observed for trivalent Sc and lanthanoid elements of La, Ce, Pm and Gd and divalent Eu and Yb,[2] whereas their curves were similar to those for Y and Sr, respectively. The sum of the radioactivity observed in the column fractions for Sr, Sc, Y and the lanthanoid, and for Zr, Hf and Nb is shown in Fig. 1 by open circles. The upper limits of the yields for Mn and Fe were also estimated from the background radioactivity and shown in the figure for comparison.

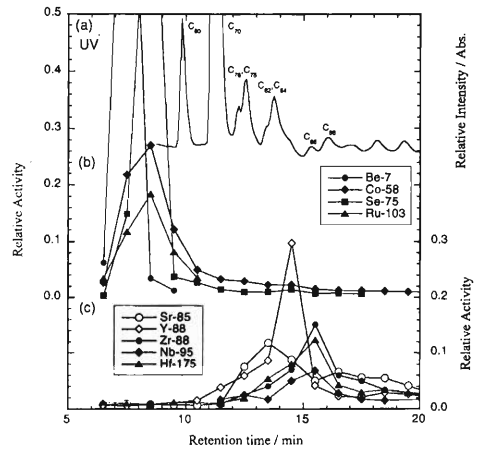

Fig. 2. Elution curves for (a) empty fullerenes, (b) the radioisotopes mostly eluted before C_{60} (^{7}Be, ^{58}Co, ^{75}Se and ^{103}Ru), and (c) those eluted at the retention time expected for the known metallofullerenes.

* Graduate School of Science, Tokyo Metropolitan University

References

1) S. Ambe, S. Y. Chen, Y. Ohkubo, Y. Kobayashi, M. Iwamoto, M. Yanokura, and F. Ambe: Chem. Lett. **1991**, 149.
2) K. Kikuchi, K. Sueki, K. Akiyama, T. Kodama, H. Nakahara, I. Ikemoto, and T. Akasaka: in *Fullerenes 4: Recent Advances in the Chemistry and Physics of Fullerenes*, edited by K. Kadish and R. S. Ruoff (1997), p. 408.

Application of the Multitracer for Substoichiometric Determination of Trace Elements: A Proposal

Y. Minai and S. Enomoto

Isotope dilution analysis has been regarded as a successful application of radioisotopes in analytical chemistry.[1] This technique has been used for determining a single element or component because radioassay was usually achieved by using NaI(Tl) gamma spectrometry or β-counting techniques conventional in tracer studies. Recent development of multitracer technique allows simultaneous application of various radiotracers in a particular system. This implies that isotope dilution analysis, a classical method in radiometric analysis, can revive as a sophisticated method in multielemental or multicomponent analysis by application of the multitracer detectable by γ-ray spectrometer using Ge semiconductor detector.

One of the difficulties in application of multitracer technique to isotope dilution analysis is that the specific activities of the radioisotopes in the multitracer solution are unknown or diffcult to be determined. Isotope dilution analysis has some variations like the direct dilution, reverse dilution, and double dilution methods. Direct dilution method is applied for determination of a non-radioactive component. It is necessary to know, in application of this method, the specific activity of the radioisotope or labelled compound spikes in the sample solution. Radiochemical separation of radioisotopes in preparation of the multitracer solution needs application of various reagents in glassware under ambient atmosphere. Potentially, contamination takes place from the reagents, target material, glasswares, and laboratory air. This implies that monitoring of the level of non-radioactive components in the multitracer solution is necessary in application of the solution to isotope dilution analysis. However, the non-radioactive components are sometimes difficult to be determined because of higher detection limit than in radioassay.

In substoichiometric analysis developed by Suzuki,[2] and independently by Zimakov and Rozhavskii,[3] it is unnessary to know the specific activity applied in the system. Radioassay after chemical separation is the only procedure required in this method. It is obvious that substoichiometric method allows us to avoid tedius determination of the specific activities of the components. The most important point in substoichiometric analysis is the choice of reagent reacting with the element or component determined. Principal requirements for the reagent are as follows:

- High stability of the reaction product in solutions,
- Moderate or high reaction rate,
- Negligible adsorption on surface of vessels, etc.

Use of multitracer is particularly beneficial for determination of the elements or components whose properties in solutions are quite similar: e.g., lanthanides(III), platinum group elements, Zr-Hf pair, Nb-Ta pair, and actinides of the same oxidation state. Due to their similarlity, we can determine those elements or components by applying such a single reagent that fulfill the requirements mentioned above. As the first stage of this research project, simultaneous determination of lanthanides by substoichiometric analysis using di(ethylhexyl)phosphoric acid will be studied in the 1999.

References

1) J. Tölgyessy and W. Kyrs: *Radioanalytical Chemistry I* (Ellis Horwood Ltd., Chichester, 1989).
2) N. Suzuki: Nippon Kagaku Zasshi **80**, 370 (1959), in Japanese.
3) I. E. Zimakov and G. S. Rozhavskii: Zavodsk. Labs. **24**, 922 (1958).

Intense ^{18}F Positron Beam Source Electro-deposited on Graphite

Y. Itoh, I. Fujiwara, Y. Nagashima, F. Saito, T. Kurihara, N. Suzuki, T. Hyodo, R. Iwata, and A. Goto

An positron source of ^{18}F (half-life 110 min) has been developed for a polarized slow positron beams. The radioactive ^{18}F was produced in 2 ml of ^{18}O-water target via the ^{18}O (p, n)^{18}F reaction. A 14 MeV proton beam from the AVF cyclotron at a current of 1 μA was used. The water containing the produced ^{18}F was diluted and was electro-deposited in a cell on a carbon rod, which serves as a positron source.

The positron emission yield was investigated as functions of applied voltage and deposition time. Graphite rods (diameter 3 or 5 mm) or a glassy carbon rods (diameter 3 mm) were used for the anode. The voltage was varied from 100 to 180 V. The deposition time was varied from 5 to 30 min (Fig. 1). The positron emission yield is defined as the product of the electro-deposition efficiency and the fraction of the positrons emitted from the anode rod surface. It represents the fraction of the positrons available for the slow positron beam.

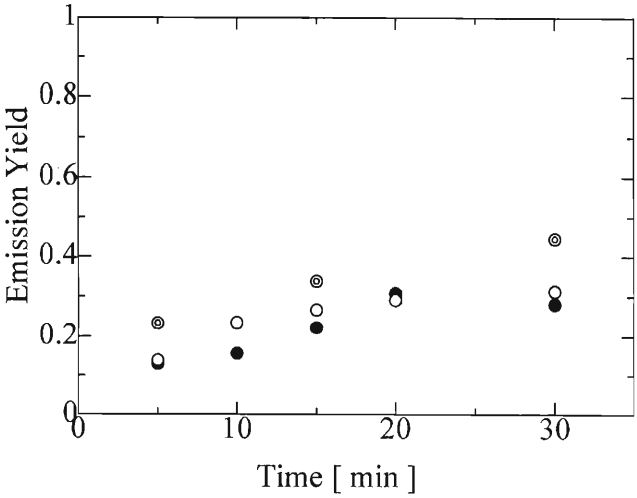

Fig. 1. Deposition time dependence of the positron emission yield. The results obtained by using graphite rod 3 mmϕ, 5 mmϕ and glassy carbon rod 3 mmϕ are indicated by ●, ◎ and ○, respectively. The deposition was performed applying 120 V.

To measure the electro-deposition efficiency, the 0.511 MeV annihilation γ rays from the carbon electrode were counted with a high-purity Ge detector at a fixed distance. The electro-deposition efficiency calculated from the obtained counts was independent of the applied voltage in the voltage range investigated. Electro-deposition efficiency increases as a function of the deposition time, up to 30 min, as expected. The best result of 83% was obtained for the 5 mm graphite rod with 30 min deposition. The result with the 3 mm graphite rod was 58%. The result with the 3 mm glassy carbon was a little better than that with 3 mm graphite.

Fraction of the positrons emitted from the electrode surface was measured with a brass positron annihilation target was visible through a 5 mm gap of a lead slit. The result shows that the fraction of positron emission was about 51% for the 3 and 5 mm graphite, and about 53% for the 3 mm glassy carbon rods. Multiplying these values by the corresponding electro-deposition efficiency, the positron yield of the present system was 44, 30 and 35% for the 5 mm, 3 mm graphite rod and 3 mm glassy carbon rod, respectively.

For high activity ^{18}F electro-deposition in the future, an automated electro-deposition and source- supply system designed (Fig. 2). In this system, several electro-deposition cells are placed on a turn table. The cells are made of copper gilded with rhodium. They serve both as cathodes and vessels for the ^{18}F water. The carbon rod anodes are arranged on the side of a vertical rotatable disc, whose center is directly below the source window of the slow positron beam apparatus. After the cathode cell is filled with the irradiated ^{18}F water, it is moved to the position right below the center of the vertical disc. The vertical disc is then lowered for the electro-deposition. After the deposition, the disc is raised to its home position, rotated by 180 degrees, and then raised for the carbon rod to face the positron incidence window.

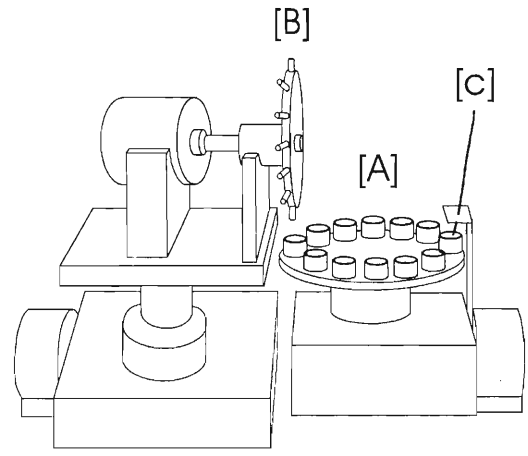

Fig. 2. Design of an automated electro-deposition and source supply system. Cells [A] are placed on turn table. Carbon rods [B] are placed on the side of a vertical rotatable disc. ^{18}F solvent is transferred through the capillary [C].

4. Radiation Chemistry and Radiation Biology

A New 100 ps-Lived Luminescence in Ion Irradiated Insulator Crystals

K. Kimura, S. Sharma, J. Kaneko, and N. Itoh

Ion irradiation ionizes solid materials at extremely high density. Except metals, ejected electrons and holes may relax immediately into electron-hole pairs in one case, and into recombination giving rise to atomic displacement in another case. The electron-hole pairs, which are often free excitons, relax by self-trapping, defect formation, photo-emission, or energy transfer (to defect sites or impurities and to phonon). Ion irradiation adds the density effect to each of all the above steps. This may induce quite different irradiation effect from that by photon and electron irradiation. It is our objective to observe these steps directly. Our interest is concentrated in dynamics of the excited states (excitons). So far, the luminescence and its decay have been measured for ion-irradiated alkali, alkaline-earth halides, rare gases, and ion-irradiated oxides using a fast decay measurement technique with time resolution of 100 ps.[1)] We have found characteristic phenomena of the high-density excitation by ion irradiation.[1)] In this report, finding of a new extremely-fast-decaying (less than 100 ps) luminescence band is described. We could observed such band in many insulator crystals of KBr, KI, RbI, CsCl, CsBr, CsI, NaCl, and Al_2O_3, but it has not been reported in case of photo- and electron-irradiation of these crystals. This extremely short-lived broad band may be ascribed to the collective states of electron-hole pairs. Such finding can evolve not only new track-effect of ions but also new primary excitation mode in the wide band-gap materials. Now, let us present the result of RbI single crystal as an example.

A photo- and electron-excited RbI single crystal is well known to give rise to luminescence bands with peaks at 320, 400, and 540 nm due to three self-trapped excitons,[2)] and the weak free exciton band at 213 nm.[3)] The lifetime of the 320 nm-band (named σ) is 3 ns; 400 nm-bands are 16 ns (singlet) and 22 μs (Ex); 540 nm-bands, 100 ns (singlet) and 11 μs (π).[2)] By contrast, the time-resolved luminescence spectra of heavy ion-irradiated RbI revealed a 100 ps-lived broad luminescence band in addition to the σ band at 320 nm; the other bands aforementioned were not recognized in the range of 20 ns. Figure 1 shows the time-resolved spectra obtained by Ar-, Kr- and Xe-ion irradiation at 6 K. The 100 ps-lived luminescence band was too weak in case of He-ion irradiation to be discerned from the noise level of the base line. In addition, the new 100 ps-lived luminescence band showed the large enhancement by excitation-density. The ratio of the luminescence efficiency at time $t = 0$ (actually, in 20 ps) was 1 : 7.6 : 53 for Ar : Kr : Xe ions, respectively.

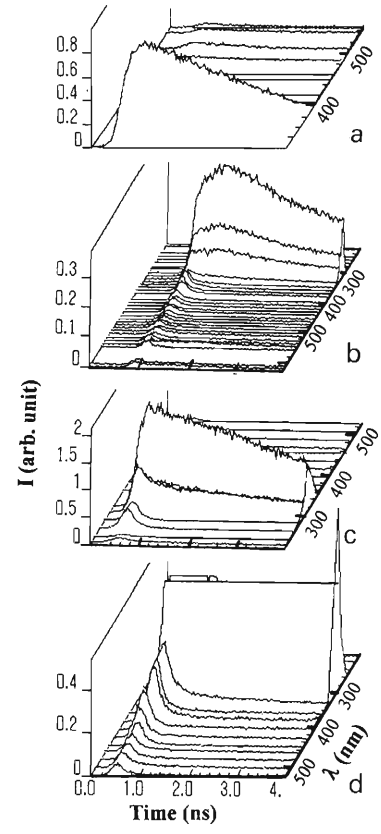

Fig. 1. Wavelength-dependent luminescence decay-curves Ar-, Kr-, and Xe-ion irradiated RbI at 6 K. a: Ar-ion irradiation; b: Kr ion; c: Xe ion; d: an expanded plot of c.

This ratio is large far beyond the square of the excitation density ratio, 1 : 1.8 : 2.4.[4)] This suggests the bindings among many excitons: that is, probably a collective phenomenon like electron-hole plasma in the ion track.

References

1) K. Kimura, K. Mochizuki, T. Fujisawa, and M. Imamura: Phys. Lett. A **78**, 108 (1980); K. Kimura and J. Wada: Phys. Rev. B **48**, 15535 (1993); K. Kimura: Nucl. Instrum. Methods Phys. Res. B **90**, 100 (1994); K. Kimura: Phys. Rev. A **47**, 327 (1993); K. Kimura and W. Hong: Phys. Rev. B **58**, 6081 (1998).
2) K. S. Song and R. T. Williams: *Self-trapped excitons*, edited by M. Cardona (Springer, 1995).
3) H. Nishimura, C. Ohhigashi, and Y. Tanaka: J. Phys. Soc. Jpn. **43**, 157 (1977).
4) K. Kimura, S. Sharma, J. Kaneko, and N. Itoh: to be published on Nucl. Instrum. Methods Phys. Res. B.

Ion-Induced Stimulated Emission of 326 nm Band in α-Alumina

S. Sharma, J. Kaneko, and K. Kimura

Numerous spectroscopic studies on the α-alumina irradiated with electrons, photons, and low and high energy ions have been carried out in the last decade.[1,2] This crystal is a radiation resistive material and also an efficient base material for excitation energy donor for lasers. Ion irradiated α-alumina shows luminescence bands at 280, 326, 422, 688, and 709 nm. We report here that out of these bands the 326 nm band shows stimulated emission.

The luminescence decay was measured using the single ion hitting single photon counting (SISP) technique with a time resolution of 100 ps.[3] The projectile ions He^{1+}, N^{3+}, Ar^{8+}, and Kr^{13+} accelerated by the RILAC were used and the ion energies were 2.0 MeV/nucleon. Though the time integrated luminescence spectrum of ion irradiated α-alumina is almost similar to that obtained by electron irradiation, the decay curves are very different. As mentioned above, ion irradiated α-alumina shows several luminescence bands though, the decay measurements of each luminescence band showed no appreciable intensity from 0 to 25 μs except the decay of the 326 nm band and of a new extremely short-lived band. The decay curve of the 326 nm band was different from that obtained by electron irradiation. In the case of ion irradiation the decay curve was quite different from a single exponential, and the initial change was much larger than that of an exponential. The decay curves consisted of a main part (which can be simulated by a double exponential) and a fast decaying part (Fig. 1a). The fast decay component is reported in another paper in this progress report. As can be seen from the figure, the rate of decay increases with increasing the ion mass, which is equivalent to excitation density. Curve fitting gave the following values for the lifetimes τ_1 and τ_2 : 1.4 and 8.2 ns (N ions), 1.2 and 4.4 ns (Ar ions), and 0.76 and 2.6 ns (Kr ions), respectively. Namely the values of τ_1 and τ_2 decreased with increasing excitation density. This result implies that the excited states decay by a strong interaction between themselves or with the other intermediates.

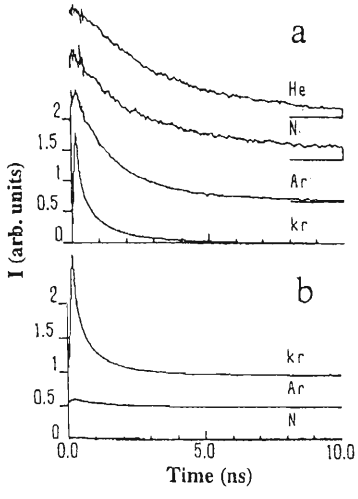

Fig. 1. a: Equi-height decay curves of α-alumina at 330 nm obtained by He-ion irradiation at 170 K, N-ion at 150 K, and Ar- and Kr-ions at 293 K. b: Ion dependent decay curves of α-alumina measured at 330 nm, where the intensity was normalized for ion count.

The luminescence efficiency per ion was also found to enhance with increasing excitation density as shown in Fig. 1b. The ratio of the luminescence efficiency at the time t = 0 is 1 : 3.4 : 44 for N : Ar : Kr ions respectively, while the corresponding ratio of the excitation density is 1 : 3 : 5.5. The ratio of the luminescence efficiency is much larger than that of the square of the excitation density. This super-linear increase as well as the increase in the decay rate indicates that emission may be enhanced by the radiative interaction between the excited states. Since this radiative interaction is still inadequate to explain the observed luminescence efficiency ratio, the stimulated emission by the emitted photons can be considered.

The decay rate was found to increase with decreasing temperature in the case of Ar and Kr ion irradiation, and had a maximum value at 6.7 K at which the trapped excited states and trapped centers are frozen. Therefore, not only the luminescence from the recombination of the trapped centers but also the radiative contact interaction due to the diffusion of the excited states are ruled out. Hence, the interaction must be a distant interaction: i.e., the interaction being effective without contact collisions, similar to exchange[4] and/or dipolar interaction,[5] and stimulated emission by the emitted photons. The excitation density-enhanced stimulated emission through a distant interaction is the first finding and is contrary to the usual results of scintillation research.

References

1) V. I. Baryshnikov, E. F. Martynovich, T. A. Kolensnikova, and L. I. Shchepina: Sov. Phys. Solid State **30**, 868 (1988); E. D. Aluker, V. V. Gavrilov, and S. A. Chernov: Phys. Stat. Sol. (b) **171**, 283 (1992).
2) A. Al Ghamdi and P. D. Townsend: Nucl. Instrum. Methods Phys. Res. B **46**, 133 (1990); K. Kimura, W. Hong, J. Kaneko, and N. Itoh: Nucl. Instrum. Methods Phys. Res. B **141**, 425 (1998).
3) K. Kimura, K. Mochizuki, T. Fujisawa, and M. Imamaura: Phys. Lett. A **78**, 108 (1980).
4) D. J. Dexter: J. Chem. Phys. **21**, 836 (1953).
5) Th. Foerster: Ann. Physik **2**, 55 (1948).

Luminescence Spectra and Decay Curves of Ion Irradiated CVD Diamond

J. Kaneko and K. Kimura

Cathode luminescence is a standard method for characterization of diamond crystals, because it is possible to extract some information about band-gap energy, centers of impurities and vacancies. A high purity Chemical Vapor Deposition (CVD) diamond polycrystal was irradiated by several kinds of ions, i.e., He, Ar and Kr from the RIKEN Linear Accelerator. The luminescence from the CVD diamond crystal irradiated by ions was measured at room temperature and at around 77 K. Moreover, a time-resolved spectrum was measured by using Single Ion hitting and Single Photon counting (SISP) system[1] whose time resolution was better than 100 ps.

A high purity CVD diamond polycrystal which was produced by a plasma assisted chemical vapor deposition technique was used in this experiment. The CVD diamond crystal was estimated to contain fewer impurities than a type IIa single diamond crystal produced by a High Temperature and High Pressure (HTHP) method. Each grain of the CVD diamond crystal had size of several μm. A full width at half maximum of Raman peak of the CVD diamond crystal was the same as that of a type Ib single diamond crystal produced by the HTHP method; besides, any carbide component was not observed in a Raman spectrum of the CVD diamond crystal.

In general, a luminescence band called as a band 'A' is predominant in cathode luminescence spectra of diamond crystals. The CVD diamond crystal had a luminescence center of the band 'A' at 350 nm at 80 K. On the other hand, a high purity type IIa single diamond crystal had the luminescence center of the band 'A' at 545 nm at the same temperature.[2] The origin of the band 'A' in the cathode luminescence spectrum of diamond is not clear at present. Therefore, it is difficult even to make a qualitative understanding on the difference of the band 'A' of these two diamond crystals. However, each grain size of the CVD diamond was bigger enough than an effective volume in diamond that suffered an influence of an ion bombardment, i.e., ionization. Therefore, it probably caused by a difference in quality of single crystals, not caused by a difference between a single crystal and a polycrystal, i.e., existence of grain boundaries.

Figure 1 shows a time-resolved spectrum of the CVD diamond bombarded by Ar^{8+} ions whose energy was 2.0 MeV at 74 K. Usually, luminescence in the band 'A' has a long decay constant in the order of ns. This time-resolved spectrum was measured in the time range of 20 ns. Hence, the band 'A' luminescence was not observable in this spectrum. A peak located at around 235 nm was caused by the recombination of free-excitons. This free-excition recombination luminescence reflects band-gap energy of diamond: thus, it is considered as an index of diamond crystal perfection. Figure 2 shows a decay curve of free-exciton recombination luminescence. It consisted of two decay constants of 0.32 and 4.8 ns. The time resolution of the SISP measurement system was about 100 ps. Therefore, there was a possibility that the fast decay constant of 0.32 ns slightly deteriorated. The slower component with decay time of 4.8 ns had the same luminescence structure to continue up to 400 nm as seen in Fig. 1.

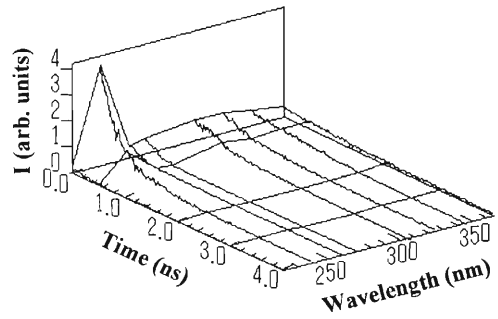

Fig. 1. Time-resolved spectrum of the CVD diamond crystal irradiated by Ar^{8+} at 74 K.

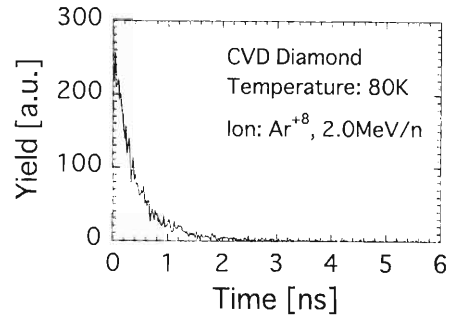

Fig. 2. Decay curve at the 240 nm line from the CVD diamond irradiated by Ar^{8+} ions at 74 K.

References

1) K. Kimura and J. Wada: Phys. Rev. B **48**, 15535 (1993).
2) J. Kaneko and K. Kimura: RIKEN Accel. Prog. Rep. **31**, 153 (1998).

Intramolecular Electron Transfer in Cytochrome c Observed by the Muon Spin Relaxation Method

K. Nagamine, F. L. Pratt, S. Ohira, I. Watanabe, K. Ishida, S. N. Nakamura, and T. Matsuzaki

Electron transfer in macro-molecules such as protein is the most important mechanism for various biological phenomena. A number of experimental investigations have been carried out to explore the electron transfer phenomena in proteins and related chemical compounds. However, almost all the existing informations on the electron transfer has been obtained by essentially macroscopic methods, which measure the evolution of the complete electron transfer from donor to acceptor.

Among various types of proteins, cytochrome c attracts much attention, since it plays an essential role e.g. in the respiratory electron transport chain in mitochondria; it holds a position next to the final process of the cycle and transfers electrons to the surrounding oxidase complex.

In order to obtain microscopic information on electron transfer in the macro-molecule, the muon spin relaxation (μSR) method, offers a great potential. Depending upon the nature of the molecule, the electron picked-up by the μ^+ during the slowing-down process in the molecule can take characteristic behaviours including a localization to form a radical state, and/or a linear motion along the molecular chain, etc. These behaviours can most sensitively be detected by measuring the spin relaxation process of the μ^+ using the μSR method.

Experiments on the μ^+ relaxation in cytochrome c have been conducted by using an intense pulsed beam (70 ns pulses at 50 Hz repetition rate) of 4 MeV μ^+ at the RIKEN-RAL.

At each of the measurement temperatures, the μ^+ relaxation function which corresponds to a time-dependent change of the μ^+ polarization, was found to have an external field dependence (see Fig. 1). The observed relaxation functions G(t) were fitted with the relaxation function proposed by Risch and Kehr and the longitudinal relaxation parameter Γ obtained at various temperatures is seen to decreases monotonically with increasing B_{ext} (Fig. 2). On closer inspection of the B_{ext} dependence of Γ, there seems to be two components, (1) a region of weak-field dependence region (lower field) and (2) a (B_{ext}) dependence region (higher field). The latter region exhibits the characteristic μ^+ spin relaxation behaviour due to a linear motion of a paramagnetic electron. The critical field (hereafter, we refer to this as the cutoff field) where the second region becomes significant over the first region has a significant temperature dependence; the cutoff field is seen to reduce with decreasing temperature (Fig. 3). It can be seen that the temperature dependence of the cutoff field can be represented by the sum of two activated components of the form $\exp(-E_a/kT)$, where E_a is an activation energy; one with an activation energy of 150 meV (dominant above 200 K) and the other with an activation energy of less than 2 meV (dominant below 200 K). A naive picture based upon the previous μ^+SR studies on high molecular weight conducting polymers would suggest an increase in the effective dimensionality of the diffusion rate. In the context of protein such as cytochrome

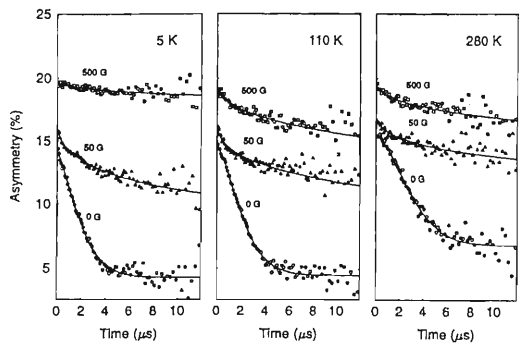

Fig. 1. Typical μ^+ spin relaxation time spectra in cytochrome c at 5, 110 and 280 K under external longitudinal fields of 0, 50 and 500 G (above). For finite fields the curves show best fits using the R-K function.

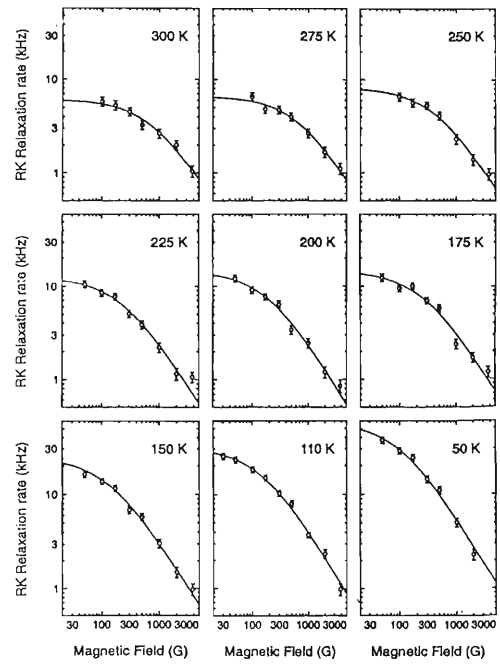

Fig. 2. The R-K relaxation parameter Γ versus external longitudinal magnetic field for the μ^+ in cytochrome c at various temperatures.

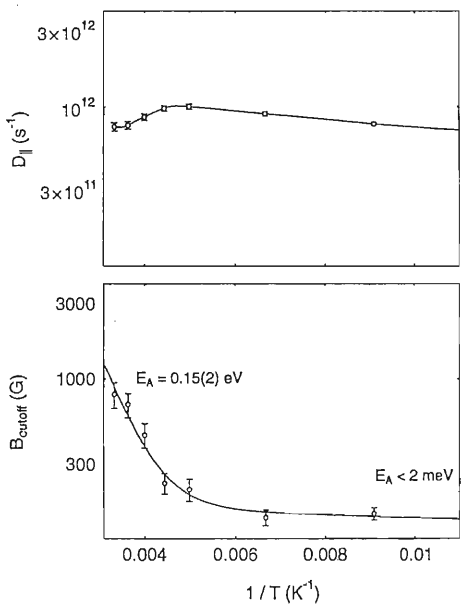

Fig. 3. The upper plot shows the temperature dependence of the inter-site diffusion rate of electron derived from B^{-1} dependent part of Γ and the lower plot shows the cutoff field against inverse temperature.

c with coils and folds in its structure, the 'inter-chain' diffusion might perhaps be interpreted as 'inter-loop' jumps, which could well be strongly activated by the increased thermal displacement of the polymer occurring above the glass transition.

The most important unknown factors in the present μ^+SR studies are the distribution of locations of the μ^+ bonding-sites with corresponding uncertainty in the electronic structure of the μ^+ and the site from where the electron starts its liner motion. For this purpose, muon spin RF resonance as well as level crossing reasonance will be most helpful. These experiments are now in progress.

Although, as mentioned above, there are still some unknown factors at this stage concerning the detailed nature of the probe state, it is clear that the electron transfer process through a microscopic section of cytochrome c was directly detected in the present experiment. The μ^+SR measurement, where high efficiency of the measurements should be emphasized, is easily able to be extended to cytochrome c in various chemical and biological environments. Most importantly, because of original high energy nature of the probe, this method can be applied to a protein *in vivo*.

Translocation Behavior of Sr, Rb, and Zn in Soybean†

S. Gouthu, T. Arie, and I. Yamaguchi

Monitoring the uptake and translocation behavior of radionuclides in plants is important to know how nuclides with contrasting behavior enter through the plant system and ultimately reach edible parts. The ready mobility coupled with the demand by the growing parts of the plant can carry some nuclides to edible parts in high quantities. In this study we monitored translocation of strontium (^{85}Sr), manganese (^{83}Rb.), and zinc (^{65}Zn) in soybean plant with plant growth.

Soybean (*Glycine max* Merr.) seeds were germinated on sterile sand supplemented with nutrient solution made from Gamborg's B5 medium salt mixture (Wako Pure Chem. Indust., Ltd.). Fresh nutrient solution was added every 4 days until the seedlings were 2 weeks old. Then the plants were removed from the sand and were kept in aerated deionized water for 1 week to facilitate rapid absorption of radionuclides later. From deionized water plants were transferred to nutrient solution in 300 ml flasks. Each plant was supplied equal amount of multitracer solution. The plants were maintained in the growth chamber at 24°C, 75% humidity, and 9000 lux light intensity with a 16 h photoperiod for 10 days. The volume of nutrient solution in the flasks was maintained with deionized water. After 10 days the plants were removed from the multitracer solution and were transplanted to soil (Kureha Eng. Co. Ltd., Kureha Chem. Indust. Co., Ltd.). Soybean developmental stages at the time of sampling were described following the scheme of Fehr et al.[1] V4, V5, and V7 indicate the plant vegetative stages with 4, 5 and 7 nodes on the main stem respectively. R1 indicates the starting of flowering; R3, emergence of pod; R5, beans just beginning to develop; and R6, pod containing full size green beans. Thirty-one day old plants at V4 stage, recovered from multitracer and transplanted to soil, as mentioned above, were allowed one week for acclimatization. From V5 stage, plants were sampled six times (three replicates) at 6 day intervals up to the fruiting stage (R6). Ten days were allowed between R5 and final sampling at R6 stage to complete seedfill in the pods. The sampled plants were separated into root, stem, leaf, flower, pod, and seed and were dried at 50°C for 4 days. Translocation of absorbed nuclides within the plant was assessed by measuring the activity of the nuclides in the samples harvested at different growth stages. Activity measurements were performed using hyper-pure Ge-detectors. The amount of each nuclide was expressed as percentage of the total nuclide absorbed by the whole plant.

Figure 1 shows the partitioning of Sr, Zn, and Rb among different organs of soybean with plant maturation. At 1st sampling (V5 stage) more than 95% of the absorbed Sr was already translocated from the root. Stem and leaves were the primary sinks until R3 stage. During this vegetative period the leaf biomass was increasing and there was clear movement of Sr from stem to developing leaves. As flowering progressed (R3 to R6), most of the Sr was remobilized into the inflorescence with leaf and stem activity decreasing concomitantly. At the time of the final sampling (R6), the Sr partitioning in the inflorescence was as much as 70%, with only 10% moving into the pod and none into seed. Zinc showed the same type of trend throughout

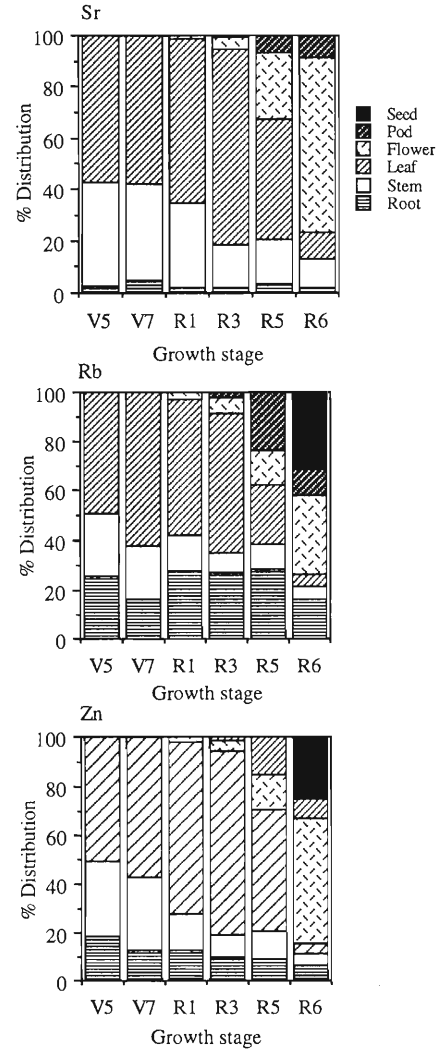

Fig. 1. Distribution of total accumulated Sr, Rb, and Zn in soybean tissues at different growth stages. Distribution is expressed as percentage of plant accumulated nuclide partitioned in root, stem, leaf, flower, pod, and seed. Each value is the mean of three replicates.

† Condensed from the article submitted to Environ. Toxicol. Chem.

the vegetative stage, but once flowers and fruits were formed about 33% was translocated into the fruits, of which 8% was in the pod and 25% in the seed. Rb showed a similar trend of partitioning, but the content of Rb in the root fluctuated with plant growth stage. At R6 stage about 43% was partitioned into the fruit with 31% in the seed and the rest in the pod.

From Fig. 1, mobilization of Sr, Rb, and Zn from the older parts to new growth with plant maturity was clear. The initial increase observed in the leaves was due to the movement of these nuclides from stem to newly formed and rapidly growing leaves. As the plant entered reproductive growth (R3 to R6) there was relatively little increase in the leaf biomass. Substantial amounts of these nuclides were then lost from the leaves and transported into flower and fruit parts. This suggests that these elements are mobile and physiologically important in the actively growing plant tissues. Pod and seed acted as a sink for 40% of the Rb and 30% of the Zn with most activity concentrating in the seed, whereas Sr was not translocated to fruits in significant quantities.

References

1) W. R. Fehr, E. Caviness, D. T. Burmood, and J. S. Pennington: Crop Sci. **11**, 929 (1971).

LET Dependence of Survival in *Arabidopsis thaliana* Irradiated with Accelerated Heavy Ions

N. Shikazono, A. Tanaka, Y. Hase, H. Watanabe, S. Tano,* N. Fukunishi, and S. Kitayama

The biological effects of heavy charged particles, measured by the relative biological effectiveness (RBE) on lethality as a function of linear energy transfer (LET), have been extensively studied in bacteria, yeast, and mammalian cells. In these unicellular systems, it was observed that the RBE on reproductive death was found to peak around 100 keV/μm.[1)]

The effects of heavy ions on multicellular organisms are still not fully understood. The *Arabidopsis thaliana* (L.) Heynh. is a particularly suitable multicellular organism for studying the effects of heavy ions and other kinds of radiation because its seeds and plants are small, it produces a large number of seeds, and because its life cycle is short.[2)] We had investigated the effects of heavy ions on the survival of *Arabidopsis* using various kinds of ions with LETs of 17–549 keV/μm, and reported that the highest RBE value was obtained by Ar ion irradiation (LET 252 keV/μm.[3)] More recently, using Ne and Ar ions at the RIKEN Ring Cyclotron, we elucidated that RBE value of survival seems to have a peak at LET over 300 keV/μm. To further investigate the dependence of RBE on LET in *Arabidopsis*, we used carbon (C) ions at various LETs.

For irradiation, the dry seeds of *Arabidopsis thaliana* ecotype Columbia were carefully sandwiched as a single layer between kapton films (7.5 μm thickness). Seeds were exposed to the C ions accelerated by RIKEN Ring Cyclotron or by AVF Cyclotron at JAERI (Takasaki). The LETs for C ions (72, 113, 152, 214 keV/μm) were varied by placing absorbers in front of the irradiation site. The plants were grown at 23°C under continuous light (40 μE/m^2/s). One month after sowing, plants with expanded rosette leaves were scored as survivors. RBE value was estimated by comparing D_{37} for electrons with that for C ions.

The survival curves for C ions with LET 72, 113, 152 and 214 keV/μm are shown in Fig. 1. C ions with LETs of 214 keV/μm had the smallest shoulder and the highest RBE. The RBE increased with LET. In Fig. 2, RBEs of C ions are plotted as a function of LET, together with those of Ne and Ar ions which were measured previously. The RBE for lethality of *Arabidopsis* seems to have a peak at LET over 300 keV/μm.

Recently, it was reported that the peak of RBE on the interphase death compared to the reproductive death is shifted to a larger LET (around 230 keV/μm) in mammalian cells.[4)] The difference in LETs of the peak of RBE between unicellular systems and *Arabidopsis* may be explained by assuming that the interphase death rather than the reproductive death of cells have major influence on lethality of *Arabidopsis* plants. Alternatively, different repair mechanism(s) may be the main cause of the different LETs to give the peak of RBE on survival in unicellular systems and in *Arabidopsis*.

To verify the latter possibility, RBE values on chromosome aberrations are now being investiagted by varying the LETs.

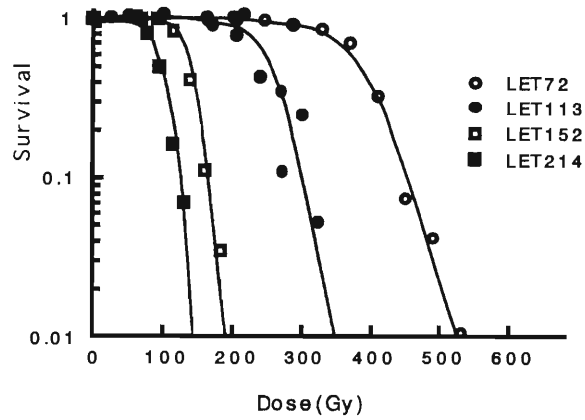

Fig. 1. Effects of C ion beams with different LETs on survival. ○: LET 72 keV/μm, ●: LET 113 keV/μm, □: LET 152 keV/μm, ■: LET 214 keV/μm.

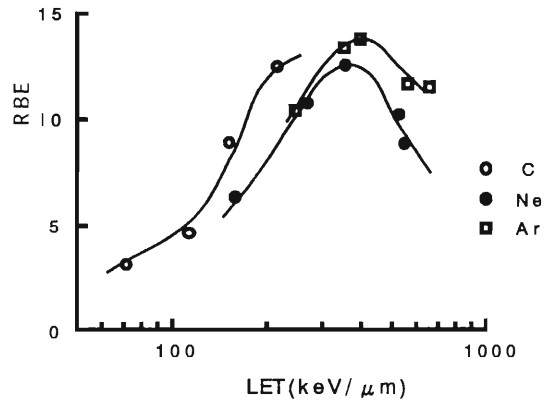

Fig. 2. RBE for lethality with C(○), Ne(●) and Ar(□) ions as a function of LET.

References

1) G. Kraft: Nucl. Sci. Appl. **3**, 1 (1987).
2) U. Bork et al.: Adv. Space Res. **9**, 117 (1989).
3) A. Tanaka et al.: Int. J. Radiat. Biol. **72**, 121 (1997).
4) H. Sasaki et al.: Radiat. Res. **148**, 449 (1997).

* JAERI, Takasaki Radiation Chemistry Research Establishment

Effective Plant-Mutation Method Using Heavy-Ion Beams (III)

T. Abe, S. Sekido, I. Yamaguchi, and S. Yoshida

In the previous paper[1] we have reported that the fertilization cycle of tobacco is quite sensitive to the irradiation of heavy-ion beams. However, it is difficult to use this special stage for the plants that have several seeds per flower. In this paper we report the effect of heavy-ion beams on imbibition seeds, and on selection of chlorophyll mutants in M_2 progeny.

The rice seeds (*Oryza sativa* cv. koshihikari) were soaked for 3 days in water with 0.8% agar at 30 °C under dark. The imbibition seeds were irradiated by Ne-ion beams (135 MeV/u) within a dose range of 5 to 100 Gy. Linear energy transfer of the Ne ion was 63.4 keV/μm. After the irradiation, seedlings were transplanted into soil in pots, and grown in a greenhouse at 20–26 °C. One month after the irradiation, numbers of the survival plants and morphologically abnormal plants were counted. M_2 seeds from selfed M_1 strains were harvested approximately four months after the irradiation. M_2 seeds were sown on seed beds, and grown in a greenhouse. After 3-weeks, the number of chlorophyll mutants was recorded.

High irradiation dose caused a decrease in the survival rate and an increase in the frequency of morphologically abnormal plants (Fig. 1). The morphologically abnormal plants had a retarded growth, a dwarfism, or white stripes or split shape of leaves in the M_1 progeny. There were 8 sterile plants in 36 typical abnormal plants. Thirty-seven M_2 progeny out of 730 treated-strains were segregated into green and chlorophyll mutants as the albino or the striped-leave phenotypes (Table 1). The heigher frequencies of chlorophyll mutants (CM) 11.6 and 6.12% are obtained by the irradiation of M_1 strains with 20 and 10 Gy, respectively, whereas the frequency was 2.18% with γ-ray irradiation of dry seeds.[2] Although mutants with the yellowish green or pale green leaves were more frequent by γ-rays than by ion-beams, the albino phenotypes were more frequent by ion-beams than by γ-rays. Above work has shown that ion-beams irradiation on imbibition seeds can give a higher mutation rate and a wider range in the type of mutants compared to the case of γ-ray irradiation.

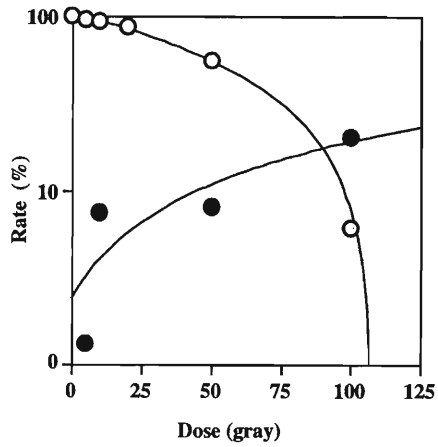

Fig. 1. Effects of imbibition seeds with Ne-ion beams on the suvival rate (○) and on the frequency of morphologically abnormal M_1-plants (●).

Table 1. Frequency of chlorophyll mutants (CM) induced by ion-beam treatment.

Dose (Gy)	No. of M_1 strains	No. of M_2 strains		total No. of CM	Frequency of CM (%)
		Albino	White stripes		
5	225	2	0	2	0.89
10	196	11	1	12	6.12
20	181	21	0	21	11.60
50	115	0	2	2	1.74
100	13	0	0	0	0
Total	730	34	3	37	5.07

References

1) T. Abe et al.: in *Modification of gene expression and non-mendelian inheritance*, edited by K. Oono and F. Takaiwa (NIAR, 1995) p. 469.
2) H. Nakai et al.: Breed. Sci. **44**, Suppl. 1, p. 290 (1994).

Isolation of the Flower-Color Changing Mutant Using Heavy-Ion Beam Irradiation

K. Suzuki, T. Abe, Y. Katsumoto,* Y. Fukui,* S. Yoshida, and T. Kusumi*

Flower color is the most important characteristics of floricultural crops. Isolation of mutants with a high-frequency is a powerful tool to generate new kind of flower colors. The newly identified mutations could be later transported to other plants by a traditional breeding system. *Petunia altiplana*, one of the parent of *P. hybrida*, shows a dominant purple flower color. It is, however, difficult to isolate the plants which contain homozygous recessive mutant alleles, because of the self-incompatibility found in many native *Petunia* species.

Using the ovaries with pistil excised after pollination, we first found that the expected time for fertilization following pollination in *P. altiplana* was about 36 to 48 h. We tried to use ethyl methanesulfonate (EMS), a common and quite efficient chemical mutagen in plants. The *P. altiplana* pollinated ovaries were incubated on a 10% EMS solution. However, no mutant phenotype was observed among the flowering plants derived from EMS mutagenized seeds. As an alternative, we used a method involving the heavy-ion beam irradiation on fertilized egg cells for the isolation of flower color mutants in *P. altiplana*. After 44 h of pollination, ovaries were irradiated with 5 to 200 Gy of the ^{20}Ne heavy-ion beam at 135 MeV/u. The linear energy transfer (LET) of the Ne ion was adjusted to be 63.0 keV/μm. In the irradiation with a dose above 100 Gy, ovaries to develop for mature fruits were not observed. In contrast, many mature seeds were derived from the ovaries irradiated with a dose less than 50 Gy. The germination rate of the mutagenized seeds decreased with the intensity of the irradiation (Fig. 1).

Out of the 102 M1 plants, derived from the 5 Gray-irradiated ovaries and cultivated in a green house, we isolated one flower-color changing mutant called *pne1*. The *pne1* flower presented a whitish pink color with pink veins in its corolla tube. High performance liquid chromatography (HPLC) analysis of the anthocyanins extracted from limbs and corolla tubes indicated a very significant reduction in the amount of malvidin 3-(*p*-coumaroyl)-rutinoside-5-glucoside, final product in the anthocyanin pathway, in the *pne1* mutant compared with the wild-type (Fig. 2). The *pne1* mutation has a dominant character as determined from the result of

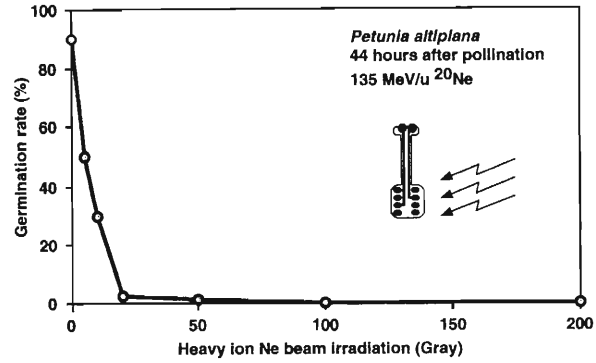

Fig. 1. Germination rate from the seeds derived from irradiated ovules of *P. altiplana*.

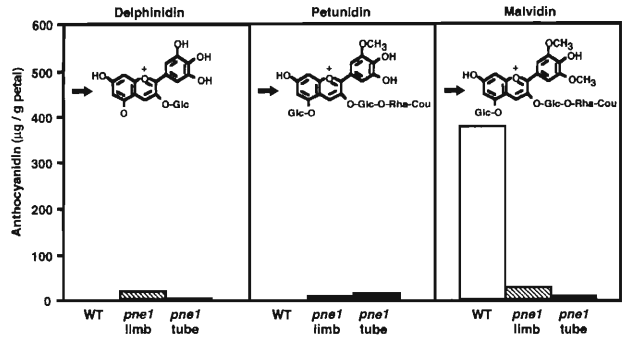

Fig. 2. Accumulation of anthocyanidins in wild-type and *pne1* mutant. The structures of anthocyanin which derive from each anthocyanidin and mainly accumulate in *P. altiplana* flower are shown.

backcrossing *pne1* with wild-type *P. altiplana*. Previously, we identified some vein-type mutants, similar to *pne1* among natural population. The mutations presented in these plants were also dominants. The frequency of flower-color changing mutants following the irradiation of 5 Gy ^{20}Ne heavy-ion beam was about 1% in our petunia system, indicating an increase in the mutation rate about 100 times compared with natural conditions in petunia (0.01%).

References

1) T. Abe et al.: RIKEN Accel. Prog. Rep. **31**, 148 (1998).

* Institute for Fundamental Research, Suntory Ltd.

Produciton of Non-Organogenic and Loosely-Attached Callus in Leaf Disk Culture of Haploid *Nicotiana plumbaginifolia* by ^{14}N Ion Beam Irradiation

H. Iwai, T. Abe, S. Yoshida, H. Kamada,* and S. Satoh*

Leaf disks of the haploid and diploid *Nicotiana plumbaginifolia* were irradiated by ^{14}N heavy-ion beam, and then they were cultured in shoot-inducing medium in order to produce mutants for the elucidation of the functions of the cell wall in plant morphogenesis. Haploid plants are desirable for making mutants in tissue culture because recessive mutations appear directly in the phenotype in such plants.

All samples were irradiated with a 135 MeV/u ^{14}N ion beam accelerated by the RIKEN Ring Cyclotron. Linear energy transfer (LET) of the ^{14}N ion corresponded to 34 keV/μm. Leaves placed in plastic petri dishes aseptically were exposed to the ^{14}N ion beam for specific periods of time, corresponding to doses ranging from 1.25 to 40 Gy. Then the leaves (including veins) were immediately cut into pieces (approximately 6 × 6 mm). The leaf disks were cultured on the Murashige and Skoog's agar media containing 1 mg/l benzyl adenine for shoot induction under a continuous light conditions for three months. The normal callus formed hard cell-clusters with multiple shoots, but a paste-like callus with weak intercellular attachments was found in the irradiated culture.

We confirmed the characteristics of the paste-like loosely-attached callus by touching it with tweezers. The survival rate was defined as the percentage of the leaf disks that avoided entire browning. The frequency of cell proliferation was defined as the percentage of the leaf disks on which callus and/or adventitious shoot are formed.

Normal leaf disks began to form the callus with multiple shoots and adventitious shoot after about ten days of culture. The frequency of cell proliferation decreased in parallel to increasing dose in both haploid and diploid leaf disks. The frequency of cell proliferation in diploid was higher than that in haploid, as shown in Fig. 1. A decrease in survival rate (up to 80%) was observed at 40 Gy in the haploid plants; there was no change in the diploid plants. The frequency of formation of non-organogenic and loosely-attached callus in the culture of haploid leaf disks was much higher than that of the diploid disks (Fig. 2). The highest frequency was obtained at 5 Gy of irradiation in the cultures of both haploid (11.8%) and diploid (4.1%) leaf disks. The cells stimulated by the heavy-ion beam were observed with a scanning electron microscope to be loosely attached to each other, resulting in a random morphology of cell clusters.

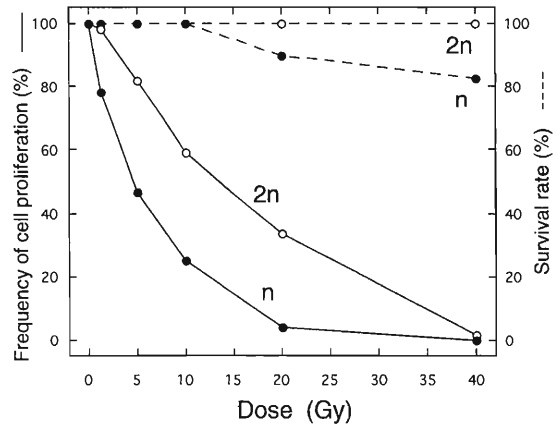

Fig. 1. Effects of the dose of ^{14}N-ion beam on the leaf disks of haploid (n) and diploid (2n) *Nicotiana plumbaginifolia*. Results are expressed by the percentages of non-browning leaf disks (survival rate) and that of callus- and/or shoot-forming leaf disks (frequency of cell proliferation).

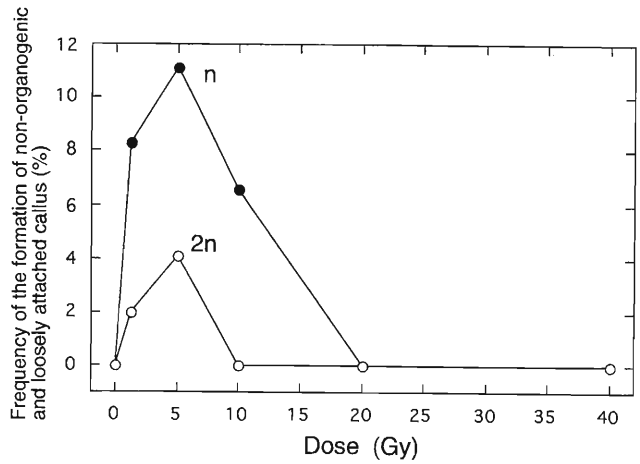

Fig. 2. Effects of the dose of ^{14}N-ion beam on the production of non-organogenic and loosely-attached callus. Results are expressed by the as percentage of the leaf disks on which the non-organogenic and loosely-attached callus are formed.

On the other hand, the normal cells formed a tight callus with multiple shoots. These results show that the ^{14}N ion beam irradiation is a powerful tool for obtaining mutants at a high occurrence rate if the haploid plants are used.

* Institute of Biological Sciences, University of Tsukuba

Biological Effects of Heavy-Ion Beam on Budding Yeast Cells

M. Yoshimasu, T. Abe, S. Yoshida, T. Inoue,* F. Ling, and T. Shibata

Mutants are required for identifying novel genes and their roles. Many mutants have been isolated from budding yeast *Saccharomycese cerevisiae*, which is regarded as a model of eukaryotes. Generally, this process starts by treating yeast cells with mutagens such as ethylmethansulfonate (EMS), nitrosoguanidine, or ultraviolet (UV) light. For the isolation of different mutations, the kind of mutagen is an important factor. Recent studies showed that the exposure of cells to the heavy-ion beam introduced DNA double-strand breaks in diploid yeast cells or in a human tumor cell line.[1,2] Double-strand breaks are known to be repaired by error-free recombinational repair or by error-prone (i.e., mutable) end-joining.

First, we examined the relative biological effects on the survival of yeast cells (IL166-6b, a *leu2, ura3, trp1* [ρ^+]).[3] The cells, grown in glycerol medium at 30°C for 3 days, were spread on an 1% agar containing plate without the required amino acids for its growth. These cells were then irradiated by N-ion beam within the range of dose 20 to 1000 Gy or by Ne-ion beam within the range of 5 to 200 Gy using RIKEN Ring Cyclotron. The linear energy transfer (LET) of the N and Ne ions were adjusted to be 28.5 and 63.0 keV/μm, respectively. After the irradiation, cells were suspended in sterilized water, and then spread on glucose plates to form about 300 colonies per plate at 30°C for 4 days. As shown in Fig. 1, when cells were irradiated by the N ion, viable cells decreased exponentially in the range from 0 to 250 Gy. In the case of Ne-ion irradiation, we observed exponential decrease in the viability in the range from 0 to 50 Gy. This result suggests that the yeast cells were differently susceptible to the two types of heavy ion used in this study. Next, we compared the effects of irradiation of Ne ion with those of EMS treatment or UV irradiation on the induction of temperature sensitive (TS) mutations (Table 1). After the treatments with various mutagens, cells at the same mortality (31.8 ± 1.8%) were selected and spread on glucose plates. After incubation at 30°C for 4 days, colonies on each plate

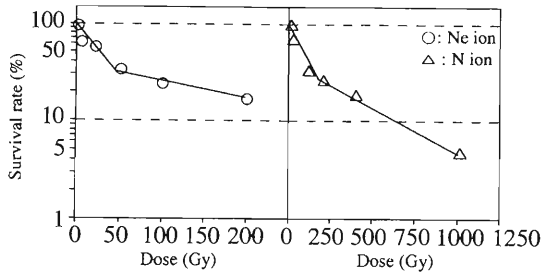

Fig. 1. Survival curves of yeast cells after irradiation of heavy-ion beam.

Table 1. Induction of TS mutations by various mutagens.

Mutagen	Viable cells	TS mutants	Mutation rate (10^{-2})
Ne beam	10,795	7	0.064
EMS	2,060	32	1.6
UV	2,490	49	2.0

TS : Temperature Sensitive

were replicated to other three glycerol plates. These plates were independently incubated for 5 days at 16, 30, and 37°C. The cells that were able to grow at 30°C, but not at 16 or 37°C, were counted as the TS mutants. We observed that the mutation rate induced by the irradiation of Ne ion was 25 or 31-fold lower than that treated by EMS or UV irradiation. We can consider a possibility that the heavy ion caused mutations by an mechanism different from the cases of UV and EMS.

Then, we examined effects of irradiation of Ne ion on induction of the respiration-deficient progenies from FL67 (*mhr1-1*) mutant. The higher rate of such induction than the case of wild type cells was regarded due to a deficiency in mitochondrial DNA repair.[3] We observed that a very low fraction (less than 3%) of viable cells lost its respiration function at a mortality of 30% (Fig. 2). However, at the same mortality caused by UV irradiation, the FL67 mutant produced more than 45% of respiration-deficient progenies.[3] This result has suggested that heavy-ion beam induced such damages of cells that can not be repaired by mitochondrial recombination. DNA double-strand breaks were shown to be repaired by the genetic recombination in various organisms. Thus, our results suggest either that the double-strand breaks are not major DNA lesions, or that the DNA damages are not a major cause of the degenerative effect of heavy-ion beam in mitochondria.

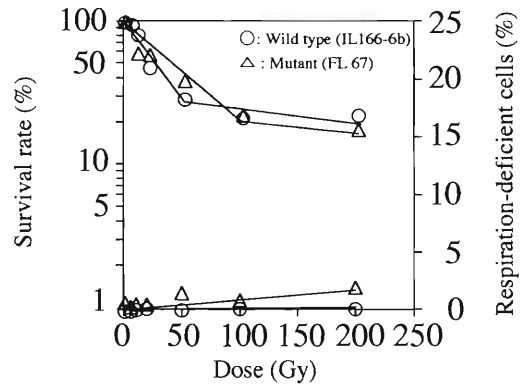

Fig. 2. Effect of heavy-ion beam on induction of respiration deficient cells.

References

1) T. C. Akpa et al.: Int. J. Radiat. Biol. **62**, 279 (1992).
2) K. J. Weber et al.: Int. J. Radiat. Biol. **64**, 169 (1993).
3) F. Ling et al.: EMBO J. **14**, 4090 (1995).

* College of Bioresource Sciences, Nihon University

Effects of Heavy-Ion Beams on Radio-Sensitive Mutant Cell Lines

K. Eguchi-Kasai, H. Itsukaichi, M. Murakami, T. Kanai, F. Yatagai, and K. Sato*

Main cause of severe lethal effect by the high Linear Energy Transfer (LET) radiation to include heavy ion beams is due to a high induction of non-repairable double strand breaks (dsb). The Relative Biological Effectiveness (RBE) of the high LET radiations for total dsb induction is not large compared with their lethal effect. The ratio of non-repairable dsb to total dsb increases with LET. But the nature of non-repairable dsb is not clear, nor is it that repair system really acts with the strand breaks induced by ion beams with very-high LET, because every method which is employed to detect dsb actually detects not only dsb but single strand breaks (ssb) etc. Here, we compared the effects of charged particles on cell killing in a pair of the mouse cell lines which are normal (LTA) or defective in the repair of DNA dsb (SL3-147).

Charged-particle beams used were Ne ion of 135 MeV/u, Ar ion of 83 or 90 MeV/u, and Fe ion of 90 MeV/u. Inactivation cross sections were calculated from 37% survival dose of the survival curves fitted by a linear regression analysis to the linear quadratic model.

In the dsb repair deficient cells, the RBE values were close to unity for the cell killing induced by charged particles with the LET up to 200 keV/μm, and were even smaller than unity at the LET region larger than 300 keV/μm (Fig. 1). The inactivation cross section (ICS) increased with LET for both cell lines (Fig. 2). The ICS of dsb repair deficient mutants is larger than that of their parents for the LET up to 2000 keV/μm. With increasing LET, the difference of ICS between the mutant and its parent became smaller. This suggests that the repair system of parent cell line did not work well for the breaks induced by high LET ion beams. That is, repairable dsb decreases, and the ratio of non-repairable dsb to total dsb increases with increasing LET. This difference in ICS disappeared at the LET of about 3000 keV/μm.

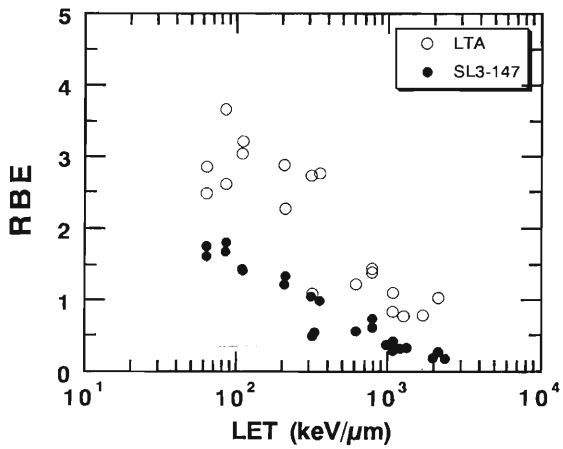

Fig. 1. RBE of heavy ion beams for cell inactivation. Closed symbols represent the dsb repair deficient cells (SL3-147) and open symbols the wild type cells (LTA).

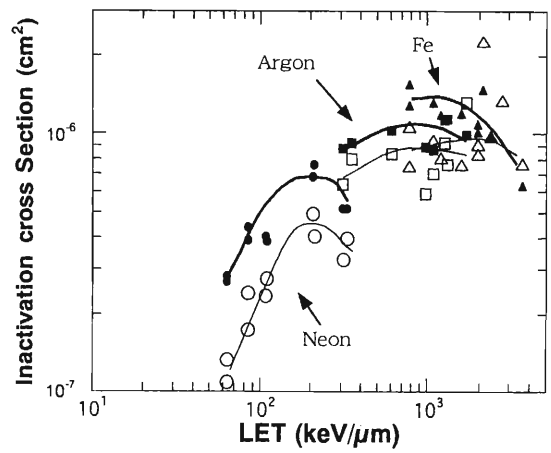

Fig. 2. Inactivation cross section of heavy ion beams. Symbols are the same as in Fig. 1.

* School Biology-Oriented Science and Technology, Kinki University

Potentially Lethal Damage Repair on the Human Skin Fibroblasts Irradiated with Ar Ions

H. Maezawa and F. Yatagai

Previously it was reported that the carbon ions above 58 keV/μm produced less repairable damage in fibroblasts.[1)] For C ions (135 MeV/nucleon) the LET from 22 to around 300 keV/μm was available. Higher LET ions around 1000 keV/μm, which is given by Ar ion, might produce different types of damage from around 100 keV/μm. Present study was conducted to find the relative biological effectiveness (RBE) of lethal sensitivity and potentially lethal damage repair (PLDR) in normal human skin fibroblasts after the irradiation of Ar ions.

Fibroblasts were grown (at 37°C) to a stationary phase in plastic flasks (T25), and were irradiated (at room temperature) with the Ar ions accelerated to 95 MeV/nucleon by RIKEN Ring Cyclotron. Using the quasi-monoenergetic ion beam, different LETs (296–1597 keV/μm) were produced by inserting absorber plates of appropriate thicknesses. Cells were resuspended by trypsinization immediately after irradiation, and were plated for colony formation. In PLDR assay cells were incubated for 24 h at 37°C after irradiation, and then plated.

Figure 1 shows the survival of fibroblasts with and without PLDR. At 306 keV/μm cells were killed exponentially with increasing dose. There appeares a shoulder on the survival curve at 1597 keV/μm. After repair-incubation for 24 h the survival increased at 1597 keV/μm, but did not at 306 keV/μm. These results indicate that the characteristics of damage are different between 306 and 1597 keV/μm. It is interested that the particular group of damage produced by Ar ions at 1597 keV/μm is repairable. RBE (which is the ratio of the dose required for 10% survival with Ar ions to that with Co-60 gamma-rays) at a given LET is shown in Fig. 2. RBE decreased with increasing LET values from 296 to 1597 keV/μm and reached to around 1 at 1000 keV/μm.

Present results suggest a possibility that the radiation, such as Ar ions, above 1000 keV/μm produces less-cytotoxic and more-repairable damages as compared with the radiation at lower LET (100–300 keV/μm).

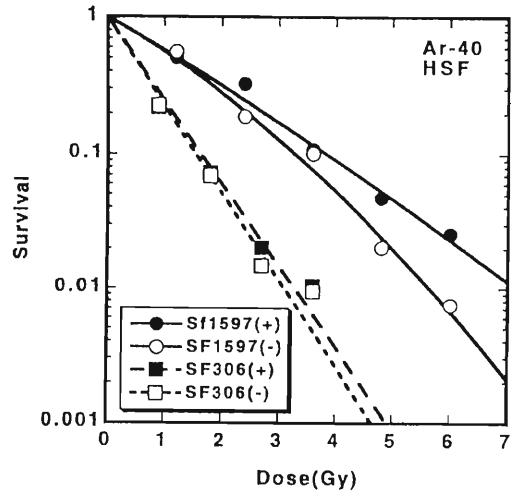

Fig. 1. Survival curves with (closed) and without (opened) PLDR of human fibroblasts irradiated with Ar ions.

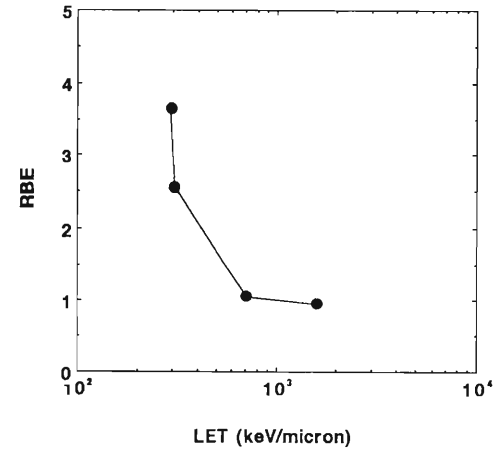

Fig. 2. LET-RBE relationship of fibroblasts exposed to Ar ions.

References

1) H. Maezawa and F. Yatagai: RIKEN Accel. Prog. Rep. **28**, 116 (1995).

Judgement on "Hit or Non-Hit" by Time-Lapse Observations of CHO Cells Exposed to Accelerated Iron-ions

H. Sasaki, P. Mehnati,* F. Yatagai, and F. Hanaoka

It is well known that the cell killing effect of ionizing radiation depends on the linear energy transfer (LET) and that its relative biological effectiveness(RBE) reaches a maximum at an LET of around 100–200 keV/μm and then decreases with further increase in LET. To answer why the cell killing effect decreases with extremely high-LET radiation, an "Over Killing Effect" hypothesis has been proposed. However, an alternative explanation is possible on the basis of microdosimetric points of view. Since the distribution of ionization is sparse and homogeneous for low-LET radiations but it is dense and concentrated for high-LET radiations, the probability that no ionization occurs within the cell target is much higher for the latter than for the former radiation when compared at the same dose level. Assume that cells (target = nucleus : ~130 μm^2) are exposed to 4 Gy of accelerated iron-ions (LET: 2000 keV/μm). After converting the dose (4 Gy) to the fluence ($1.25 \times 10^{-2}/\mu m^2$) and assumming a Poisson distribution of hit-events, the fraction of cells whose targets are not transversed by iron-ions (non-hit) was calculated to be about 20%. This value is roughly equal to the surviving fraction (about 30%) of cells after exposure to 4 Gy of iron-ions.

Division delay is an early cellular response in which all irradiated cells, except those in late G_2/M phase, are temporarily prevented from undergoing G_2/M transition and cell division. In this study, we have tried to measure the fraction of non-hit cells using the division delaly as an indicator of a "hit". Whether division delay did occur or did not occur (hit or non-hit) was determined for individual cells which were observed with time-lapse photography before and after exposure to 4 Gy of iron-ions (LET: 2000 keV/μm). Results are shown as pedigrees of individual CHO (Chinese hamster ovary) cells in Fig. 1. In Fig. 1, arrows indicate the point where cells were exposed to iron-ions and the numbers on the left and right sides of the arrows correspond to the time after division at irradiation (cell age) and the time interval from irradiation to post-irradiation first division, respectively. Therefore, the sum of these two numbers correspond to the cell cycle time at the irradiated generation. As seen for No. 5, 6 and 7 cells, the cell cycle time at the irradiated generation is apparently prolonged as compared to that before irradiation (12–13 h). Furthermore, the cell abnormality such as incomplete division leading to sister-cell fusion and binucleate-cell formation took place for No. 7 cell. Therefore, these cells were judged as hit-cells. Whereas, No. 8 cell showed no division delay at the irradiated generation, and continued dividing with cell cycle time similar to those of non-irradiated cells. Consequently this was judged as a non-hit cell. Twenty five non-hit cells were found in a total of 136 cells. The fraction of non-hit cells (25/136: 18%) is comparable to the value calculated according to a Poisson distribution of hit-events (about 20%) but slightly lower than the surviving fraction (about 30%). This suggests that some hit-cells can survive even after exposure to an extremely high-LET radiation. An example of the pedigree of surviving hit cell is shown in Fig. 2. On the other hand, CHO cells exposed to 4 Gy of X-rays (30% survival) were also observed by the time-lapse photography. However, non-hit cells such as those found in the iron-irradiated cells could not be identified.

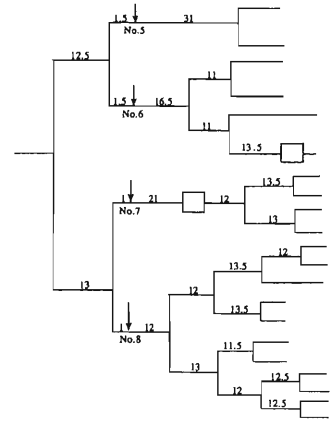

Fig. 1. Pedigrees of CHO Cells Exposed to 4 Gy of accelerated iron-ions (LET: 2000 keV/μm).

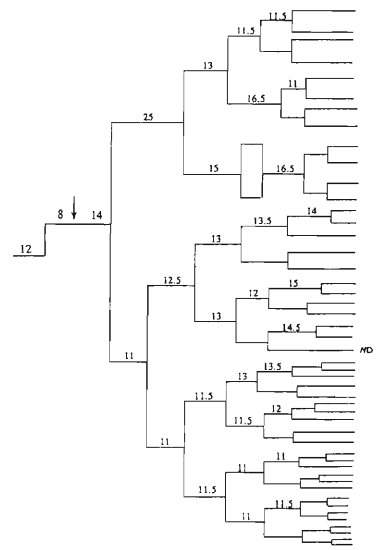

Fig. 2. A pedigree of CHO Cell which retained a reprodutive capacity after exposure to 4 Gy of accelerated iron-ions.

* Faculty of Medicine, Kyushu University

Apoptosis Induction and Cell-Cycle Change of Human Cancer Cell-Line Caused by Heavy-Ions and X-Rays

N. Shigematsu,* S. Yamashita, N. Ihara,* T. Kawata,* S. Kutsuki,* K. Toya,*
A. Kubo,* H. Ito, T. Kanai, Y. Furusawa, and F. Yatagai

A number of studies have been carried out about apoptosis by applying X-ray irradiation thus far, but the studies reporting about the apoptosis induction after heavy-ion irradiation is very few. This article is a preliminary report for comparison between heavy-ion beam and X-rays over the apoptosis induction ability on cultured cells. Previously, we reported that heavy-ion beams (carbon and neon) showed much more powerful cell-killing effects than X-rays, and showed the higher frequency of DNA mutation compared with X-rays.[1] During this reporting period, we investigated the apoptosis induction and cell-cycle change after irradiation using three human cell-lines: MDA-MB231 (breast cancer origin), T24 (bladder cancer origin) and KB3-1 (epidermoid cancer origin). JURKAT (human T-cell lymphoma origin) was used as a control to see the apoptotic effect. The heavy-ion beam which we employed this time was a carbon beam at the energy of 290 MeV/u. Cell apoptosis was detected by flow-cytometer using APO2.7 monoclonal antibody. APO2.7 is an antibody against the 7A6-antigen which is 38kD protein and appears at mitochondrial membrane of apoptotic cells.[2,3] Cell-cycle was also analyzed by flow-cytometer. Cells were harvested and then analyzed by flow-cytometer, by the procedure as shown in Fig. 1. Typical charts of flow-cytometer is shown in Fig. 2.

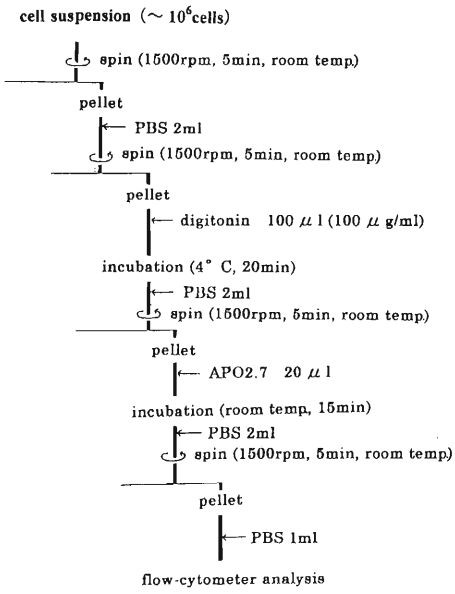

Fig. 1. The procedure outline of detecting apoptosis.

Big shift to G2 was observed after X-ray (150 kV) irradiation, and this effect was dose-dependent. Apoptotic fraction increased with dose, but it reached to a plateau around 50–60% at the dose of approximately 15 Gy. These effects were observed also in the other cell lines we used (Fig. 3).

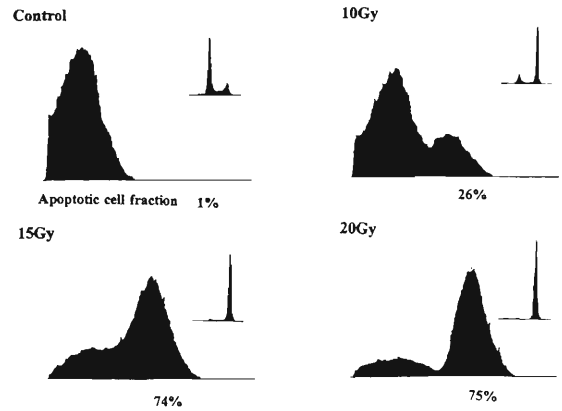

Fig. 2. Apoptosis induction and cell-cycle change in the MDA-MB231 cell-line at the time 72 h after X-ray irradiation.

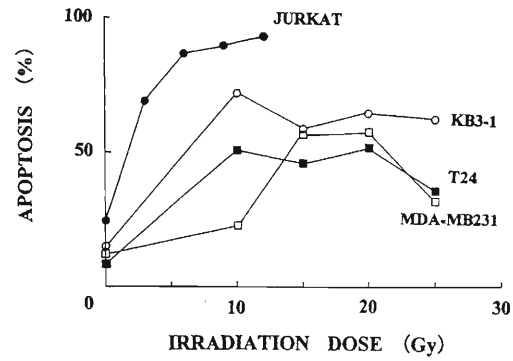

Fig. 3. Apoptosis induction curves of MDA-MB231, T24, and KB3-1 against X-ray dose, comparing with JURKAT as a control.

This observation was not caused by the procedure itself, since the similar experiment using JURKAT cell showed a quite high frequent apoptosis with this method. The effect of carbon beam irradiation on these cell-lines was very similar to that of X-ray. In summary, G2-block was observed after carbon beam irradiation, and apoptosis occurred with dose dependent and then reached to a plateau around 60–80% at the dose of approximately 4-6 Gy (Fig. 4).

* Department of Radiology, School of Medicine, Keio University

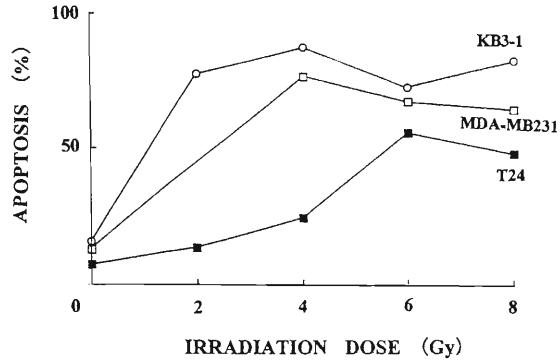

Fig. 4. Apoptosis induction curves of MDA-MB231, TE24, and KB3-1 against the carbon beam dose.

The reason why such a different effect was observed by heavy-ion beam and X-ray can not be explained now, since a number of cell lines is too small to explain whether it was caused from specific cell-line or specific heavy-ion particle. Elaborate analysis will be continued by using other human cell-lines and with other kinds of heavy-ions (e.g., neon- and argon-beams).

References

1) T. Kawata et al.: RIKEN Accel. Prog. Rep. **31**, 149 (1998).
2) S. K. Koester et al.: Cytometry **29**, 306 (1997).
3) C. Zhang et al.: J. Immunol. **157**, 3980 (1996).

Influence of p53-Gene Function on the Specificity in *hprt* Mutations Induced by Heavy-Ions

S. Morimoto, A. Gordon, N. Fukunishi, F. Hanaoka, and F. Yatagai

An attempt has been made to elucidate the mutational specificity of the heavy-ions at various LET (Linear Energy Transfer), which may contribute to the estimation of radiation risk as well as to the basic understanding of mutation induction mechanisms. The LET is defined as the energy deposition along the heavy-ion truck and usually considered as an expression of the status of initial interaction with the matter. Since the risk of exposure to high-LET heavy-ions seems to be increased in recent days, we have focused our effort on such radiation-induced mutations in human cells. It is also of our interest to study the nature of mutations caused by such a high-LET radiation, which is suggested to produce a DNA damage different from that produced by conventional ionizing radiation. In fact, our analyses of hypoxanthine phosphoribosyltransferase (*hprt*) mutations in human cultured cells revealed the heavy-ion energy dependent mutational spectra. For example, this is a high frequency recovery of the point mutations caused by a high-level of LET, in which ions will lose most of their total energy and stop shortly after passing the cells.[1-3] In this same energy region, we have also observed the mutational events that represent complex loss of multiple non-contiguous exon regions.[3]

Recently, the tumor suppressor gene p53 has come to be regarded as a guardian of cells against not only radiation but also various chemicals. Along this line, the influence of mutant p53 gene on X-ray-induced mutagenesis has been studied by some groups using the human lymphoblastoid cell lines derived from the same human spleen, WI-L2-NS (mutant p53) and TK6 (wildtype p53). We extended this type of approach to the *hprt* mutational peculiarity studies for heavy-ions. Similar to the results of X-ray irradiation,[4] WI-L2-NS was more radioresistant and mutable than TK6 after the C-, Ne-, and Fe-ion irradiations at a particular level of high beam-energy (LET: 22, 67, and 1000 keV/μm, respectively). (Fig. 1 and Table 1). The *hprt* mutations obtained after the irradiations of above ions were analyzed mainly by the multiplex PCR of exon region. After the C- and Fe-ion irradiations, a relatively frequent recovery of point mutation was observed in WI-L2-NS compared to the TK6 cells (Fig. 2). A majority of the mutations recovered after exposure to Ne-ion was a partial deletion event in both two cell lines, but deletion events on the 5'-side of the gene were found in only TK6 cells (data not shown). Since characteristic of the Ne-ion induced *hprt* mutation is quite peculiar, we plan to do the experiment to confirm the results. The peculiar differences of the p53 gene function are significant, which requires further study.

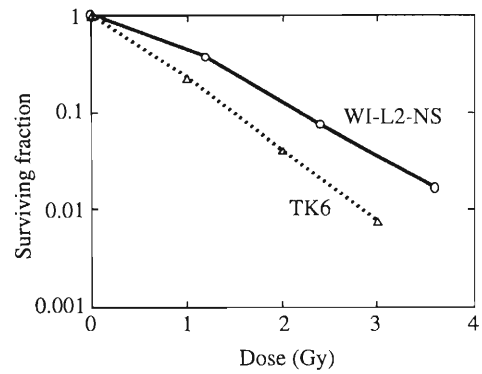

Fig. 1. Survival curves against 22 keV/μm C-ions.

Table 1. *hprt* mutation induction after the exposure of heavy-ions.

Ion (LET: keV/μm)	TK6			WI-L2-NS (WTK1)		
	Dose (Gy)	SF	MF ($\times 10^{-6}$)	Dose (Gy)	SF	MF ($\times 10^{-6}$)
C (22)	2.0	0.058	7.2	2.4	0.068	9.8
Ne (67)	1.0	0.056	9.9	1.2	0.14	31
Fe (1000)	2.0	0.24	7.6	2.4	0.27	17

SF: Surviving fraction
MF: Mutation frequency

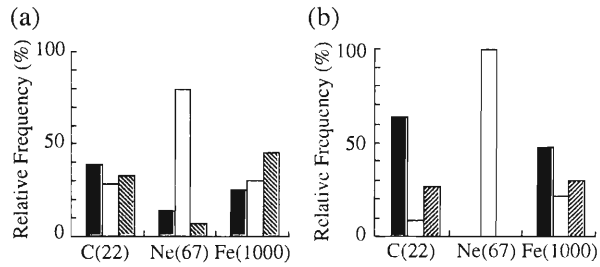

Fig. 2. Relative distribution of the *hprt* mutational classes determined by multiplex PCR pattern: (a) TK6 and (b) WI-L2-NS. Here, ■: point mutation (normal amplification), □: partial deletion (some regions are amplified), and ▨: complete deletion (no amplification).

References

1) M. Suzuki et al.: Adv. Space Res. **18**, 127 (1995).
2) Y. Kagawa et al.: J. Radiat. Res. **36**, 185 (1995).
3) Y. Kagawa et al.: Mutagenesis, in press.
4) E. N. Phillips et al.: Radiat. Res. **143**, 255 (1995).

Induction of p53 and p21 in Human Cells after Heavy-Ion Irradiations

A. Gordon, N. Fukunishi, and F. Yatagai

Recently, the tumor supressor gene p53 has come to be regarded as a guardian of cells against not only radiation but also various chemicals. Damaged DNA can trigger the p53 checkpoint response, p53 centered stress signaling can determine the fate of a stressed cell. As a transcription factor, p53 upregulates many genes including WAF-1 (p21). To assess the influence of mutant p53 gene on mutagenesis, we have undertaken the elucidation of the mutational specificity of heavy ions of various LET (Linear Energy Transfer). The induction of p53 and p21 after X-ray irradiation has been extensively studied by many groups using human lymphoblastoid cell lines derived from the same human spleen, namely, cell lines WI-L2-NS (mutant p53) and TK6 (wildtype p53).[1] After irradiation (C-ion of 22 keV/μm and Fe-ion of 1000 keV/μm as well as X-ray irradiation), both p53 and p21 proteins were induced in the TK6 cell line (Fig. 1). However, p53 and p21 were not induced in the WI-L2-NS cell line after any type of irradiation including the above heavy-ion; p53 was constitutively expressed and p21 was not produced (due to the mutant nature of p53). This is consistent with the results of Little.[2] for the same/or similar cell lines. The type of irradiation did not alter the p53/p21 response of each cell line. The significance of this response in relation to the specificity of heavy-ion induced *hprt* mutations is now under study.

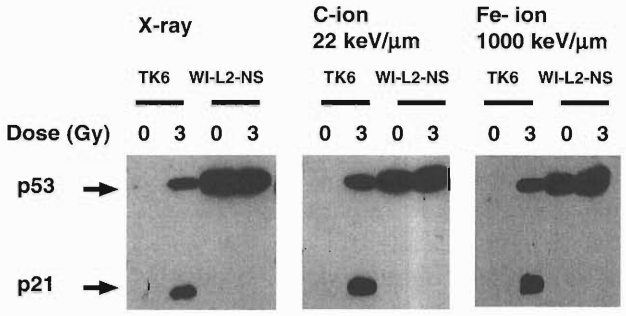

Fig. 1. Western Blot analysis. The protein was extracted 2 h after 3 Gy irradiation of 2×10^7 cells. Equal amounts of protein (60 μg) were loaded into each lane in a 15% SDS-PAGE mini-gel, electrophoresed, and blotted onto a PVDF membrane and probed with monoclonal antibodies against p53 (**DO-1**, Santa Cruz Biotech) and p21 (**EA10**, Oncogene Sciences). Each panel represents an independently processed blot and therefore only qualitative comparison may be made between panels.

References

1) S. A. Amundson, F. Xia, K. Wolfson, and H. L. Liber: Mutat. Res. **286**, 233 (1993).
2) J. B. Little, H. Nagasawa, P. C. Keng, Y. Yu, and C. Li: J. Biol. Chem. **270**, 11033 (1995).

Heavy Ion Beams: An Application to Mouse Mutagenesis

A. Yoshiki, N. Hiraiwa, T. Tsukada, Y. Yoda, C. Poirier, F. Ike,
N. Fukunishi, M. Kase, Y. Yano, and M. Kusakabe

Mouse mutants are a quite useful animal model to study the gene functions and pathogenesis of human diseases. However, we do not have enough kinds of mutants with phenotypes which reveal functions of all the genes and which correspond to every human diseases. For this reason, we need more effort to create and find new phenotypes in mouse mutagenesis. In this paper we report an application of heavy ion beams for mouse mutagenesis.

C57BL/6J (B6) mice were used for this experiment. Mature males were sacrificed by cervical dislocation after anesthesia, and the cauda epididymidis were removed from the testes. Postmeiotic incapacitated spermatozoa were collected from the cauda epididymidis by a fine-needle, suspended in 1.5 ml centrifuge tubes containing 1 ml of M2 medium,[1] and stored at 4 °C until irradiation. The tubes were centrifuged briefly at room temperature, and were exposed to heavy ion beams (^{40}Ar at 95 MeV/u, ^{56}Fe at 90 MeV/u, and ^{20}Ne, ^{14}N and ^{12}C at 135 MeV/u) with dose ranges of 5, 10, 20, 30, 50, 75, and 100 Gy at RIKEN Ring Cyclotron Facility. After irradiation, sperm suspensions were stored at 4 °C until manipulation. Mice were created artificially *in vitro* by using a micromanipulator as shown in Fig. 1. Mouse eggs were collected from oviducts after treating females with pregnant mare's serum gonadotropin and human chorionic gonadotropin. The eggs were held by a holding pipette, a single spermatozoon was picked up by another micropipette and injected into the egg cytoplasm (Fig. 1A). Manipulated eggs were incubated in M16 medium[1] overnight, then successfully cleaved 2-cell embryos (Fig. 1B) were transferred into oviducts of pseudopregnant mothers to produce G1 mice. G1 mice were crossed with wild type B6 mice to produce G2 mice. G2 mice were backcrossed to G1 to produce G3 mice. G1 and G2 mice were screened for dominant mutations, and G3 for recessive mutations. So far we found external anomalies in G1, G2, and G3 generations as summarized in Table 1.

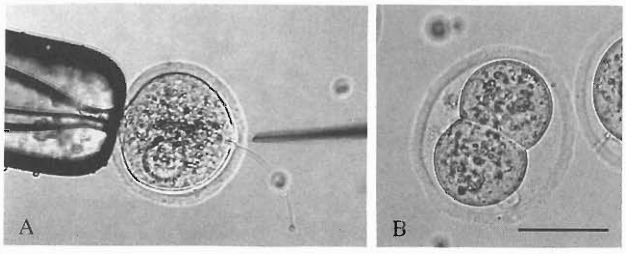

Fig. 1. (A) Microinjection of irradiated sperm cells into the egg cytoplasm. (B) A successfully cleaved 2-cell embryo after sperm injection. Length of bar: 50 μm.

We have also tried to induce mutations in male premeiotic germ cells. B6 male mice were deeply anesthetized with 10% nembutal solution, and their hypogastric and scrotum regions were exposed to heavy ion beams (^{40}Ar, ^{56}Fe, ^{20}Ne, ^{14}N, and ^{12}C) with dose ranges of 0.5, 1, 3, and 5 Gy. Testis tissues were severely damaged after irradiation. Germ cells in seminiferous epithelium decreased significantly with a higher dose of heavy ion beams. Following the sterile periods, some male mice could restart reproduction. We have paired irradiated males with untreated females to produce G1 mice. We examined these G1 generation during embryonic periods for morphological anomalies to assess which male mice have high potential to produce mutants more effectively. In G1 embryos morphological anomalies were found in different organs and systems, such as microphthalmia, anophthalmia, exencephaly, edematous skin, and pale anemic embryos. In further study we plan to select several irradiated male mice as potential breeders for efficient mutant production.

Table 1. The LET of ^{12}C, ^{14}N, ^{20}Ne, and ^{56}Fe ion beams were 23, 31, 61, and 620 keV/μm, respectively. Here, Gen. denotes the generation of mice.

Beam	Dose	Gen.	Affected tissue/ organ/system	Anomaly	No. of mice
^{12}C	30	G1	coat color	non-pigmented hair around eyes and on the back	2
^{14}N	10	G1	eye	cataract	1
^{14}N	50	G1	reproduction	sterile female	1
^{20}Ne	10	G1	skin, eye	dermatitis and corneal inflamation	1
^{20}Ne	10	G1	reproduction	sterile male	3
^{20}Ne	10	G1	hair, eye	complete loss of hair and microphthalmia	1
^{20}Ne	10	G1	hair, skin, eye	complete loss of hair, dermatitis and cataract	1
^{20}Ne	50	G1	tail	round tail tip	1
^{20}Ne	50	G1	eye	cataract and anophthalmia	2
^{12}C	30	G2	coat color	many non-pigmented hairs	2
^{12}C	30	G2	hair	loss of hair or naked	1
^{12}C	30	G2	hair, eye	microphthalmia and hair loss	1
^{56}Fe	75	G2	tooth	long teeth	1
^{14}N	50	G2	eye	cataract	1
^{14}N	50	G2	tooth	long	4
^{14}N	50	G2	reproduction	vagina not open	1
^{14}N	50	G2	tail	kinky	1
^{14}N	30	G3	brain, eye	hydrocephalus and anophthalmia	1
^{14}N	50	G3	skin	hypopigmentation until 10 days of age	1
^{20}Ne	20	G3	tooth	long	2
^{20}Ne	20	G3	eye	microphthalmia	1
^{20}Ne	20	G3	skeleton	abnormal shape of vertebrate	1

References

1) B. Hogan et al.: in *Manipulating the mouse embryo*, 2nd ed. (Cold Spring Harbor Laboratory Press, New York, 1994), p. 385.

5. Instrumentation

Measurement and Simulation of the GARIS Quadrupole Magnet

K. Uchiyama, K. Morita, and Y. Tagaya

For the past few years, several experiments for producing and identifying new isotopes have been performed using the GAs-filled Recoil Isotope Separator (GARIS).[1] The GARIS consists of three magnets which are arranged in a D-Q-Q configuration. It was found recently that the maximum magnetic field gradients of these two quadrupole magnets are not high enough to focus the recoils heavier than transactinide region onto a proper point. Trajectory of the $^{272}108$ which can be produced by the reaction ^{238}U (^{40}Ar, α2n) was calculated using the TRANSPORT code.[2] The magnitude of the dipole magnet field was estimated to be 15.21 kG under the assumption that the recoil energy of $^{272}108$ is 29.0 MeV in the laboratory frame and equilibrium charge is 5.84. The values of field gradient of the quadrupole magnets are set to the maximum ones, 52.0 kG/m. From the results of this calculation, the image size on the focal plane of GARIS was found to become 13.4 cm horizontally and 48.8 cm vertically. This does not satisfy the double focusing condition at all. Obviously, an improvement of focusing elements is needed for the GARIS. Thus, we have performed a simulation of magnetic field of the quadrupole magnet in order to search for the method how to improve the GARIS.

Both quadrupole magnets are identical, whose pole length is 500 mm and bore radius is 150 mm. The pole length is much shorter compared with the bore radius. Therefore, a three dimensional simulation is required to take into account of the fringing-field correctly. Figure 1 shows the magnitude of vertical component of the magnetic field in the median plane at 108 mm away from the center point, as a function of the current drawn by the coils of quadrupole magnet. The open squares denote the measured values, while the solid line shows the three dimensional calculation result obtained by using the computer code TOSCA. The calculation well reproduces the measured values. The error of these simulation results is less than 1%. The saturation occurs at and over 200 A.

In order to achieve the double focusing condition for the case of $^{272}108$, the field gradient 85.6 kG/m for the Q1 and 83.3 kG/m for the Q2, that is 9.24 kG and 8.99 kG at 108 mm away from the center respectively, are required. The double focusing condition was calculated by the TRANSPORT code. But, it is not a realistic solution to increase the current drawn by the coils. Figure 2 (B) shows the magnitude of magnetic field of the iron and air regions along the center line of the pole piece. The current for the coils was the maximum current, 350 A. It was found that the saturation mainly occurs in the pole piece which is wrapped by the coil. Therefore, it is impossible to add the iron to the saturated place, although this is one of the solutions to ease the saturation usually. Consequently, if we stay with the same geometry, we should change the design of the quadrupole magnet to the one whose pole piece is thick enough not to cause a saturation. It will be then possible to achieve the double focusing condition using the same magnets. But, in the latter case we will lose the total collection efficiency due to the smaller acceptance angle. The future plan of the GARIS is under discussion.

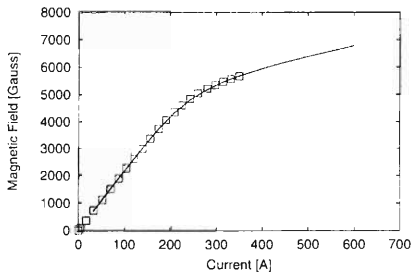

Fig. 1. The magnitude of vertical component of the magnetic field in the median plane at 108 mm away from the center as a function of the input current. The open square and the solid line denote the measured and calculated values, respectively.

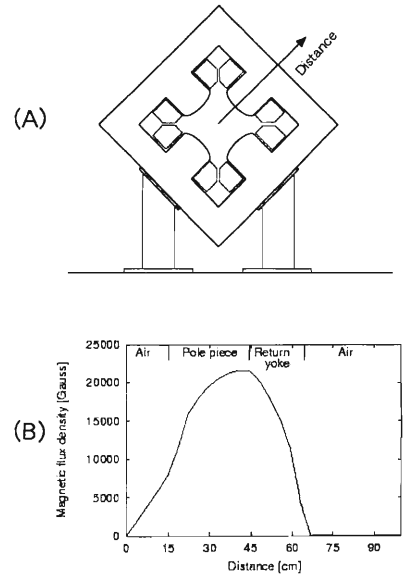

Fig. 2. (A): Schematic of the quadrupole magnet. The eight pentagons show the cross sections of the coils. The arrow corresponds the abscissa for Fig. 2B. (B): Magnetic field strength in the iron and in the air along the center line of the pole piece. The current drawn by the coils was 350 A. The abscissa shows the distance from the center of the quadrupole magnet. The four regions of quadrupole magnet (air region inside the magnet, pole piece, return yoke, and outer air region) are indicated in the upper part of this figure.

References

1) K. Morita et al.: Nucl. Instrum. Methods Phys. Res. B **70**, 220 (1992).
2) K. L. Brown et al.: SLAC-91, Rev. 1 (1974).

Simulation of the Ion Trajectories in the Gas-filled Recoil Separator

Y. Tagaya, K. Morita, K. Uchiyama, and T. Nomura*

The RIKEN gas-filled recoil separator (GARIS)[1] was designed to separate the fusion reaction products from the primary beam with a high transmission efficiency. Many new isotopes have been produced and their decay properties determined in those experiments[2] using the GARIS. Cross-sections besides their decay properties of isotopes are of great physical interest. However, we can not discuss them because of the ambiguous transmission efficiency of the GARIS. Therefore, we are currently improving the simulation code[3] of the ion trajectories in the GARIS in order to calculate its transmission efficiency followed by the experimental cross-sections. The code is also useful to determine the parameters of: the dipole magnet, two quadrupole magnets, and gas pressure of the GARIS prior to the experiment.

Trajectory of ions is governed by

$$m\frac{d\vec{v}}{dt} = q\vec{v} \times \vec{B},$$

where m is the ion mass, $\vec{v}$ the ion velocity, q the ion charge and $\vec{B}$ the magnetic flux density. This equation can be solved by the Runge-Kutta method, and the whole trajectory from the target position to the focal plane can be calculated. The images of particles at the various planes can be drawn by the two-dimensional plots. The energy and angular spreads of the ion in the energy degrader and target material, both of which are at the target position, are taken into account to calculate the image size correctly. The vertical components of magnetic flux density at the medium plane (B_{y0}) were calculated to fit with the measured data and all the other components were calculated from the B_{y0} by the expansion equations.

To check the magnetic flux density in the code, we performed the simulation of the experiment, in which $^{36}Ar^{5+}$ ions passed through 1.5 μm Al foil at the target position and various charge states of ^{36}Ar were created. In the experiment, the magnetic flux density was changed for each charge state of ^{36}Ar, so that the image center appears at the focal position of the GARIS and the transmission efficiency becomes maximum. The GARIS was kept in vacuum, so the collisions of the ions with the gaseous molecules can be ignored. The step size of the calculation $|d\vec{x}|$, in which $\vec{x}$ is the ion position, was fixed to 1 cm which was small enough not to introduce much of calculation error.

Figure 1 shows the calculated image of $^{36}Ar^{13+}$ ions. The calculated image size (FWHM) was 0.7 cm in horizontal direction and 0.9 cm in vertical direction, while the measured image size (FWHM) was 1.0 cm in both directions. This discrepancy is probably due to the calculation of the angular spreads of ions,[4] which is not optimized for the Ar-Al combinations at the energies of this experiment.

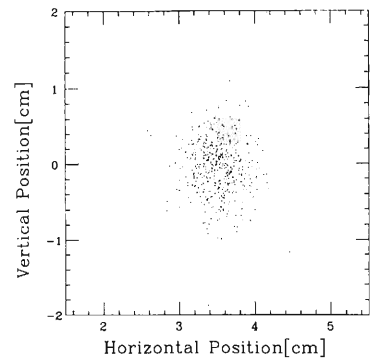

Fig. 1. Calculated image of $^{36}Ar^{13+}$ ions at the focal plane. The horizontal position of the image increases as the value of the magnetic rigidity increases.

Figure 2 shows the calculated horizontal positions of the image center at the focal plane for all charge states. The deviations of the calculated positions from the experimental ones were between 3 cm and 5 cm on the high magnetic rigidity side. This suggests that the magnetic flux density in the code is slightly weaker than the actual field at the same current. Change of the fringing magnetic flux density of the GARIS dipole magnet at a high current, which is not included in the code, probably causes the enhanced shifts for the low charge state ions. We are now modifying the magnetic flux density in the code to reproduce the experimental results.

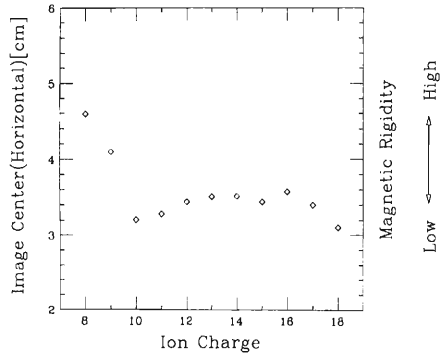

Fig. 2. Calculated horizontal positions of the center of the image at the focal plane as a function of the ion charge state. The horizontal positions derived from the experiment were at 0 cm for all charge states.

References

1) K. Morita et al.: Nucl. Instrum. Methods Phys. Res. B **70**, 220 (1992).
2) For example, K. Morita et al.: Z. Phys. A **352**, 7 (1995).
3) A. Yoshida: Tokyo Inst. Technol., Master thesis (1989).
4) J. D. Jackson: Classical Elecrtodynamics, Chapter 13.

* KEK Tanashi

New Data Acquisition Systems for the Spectrograph SMART

H. Okamura

Two types of data acquisition (DAQ) system have been introduced for the experiments at E4 area. Their common features are: (a) the cost-effectiveness realized by the use of personal computers (PC) running a free UNIX-clone, Linux, (b) the network capabilities which allow on-line analyses and/or the data recording on remote machines, and (c) the graphical user interface (GUI) composed by using Tcl/Tk.[1)]

The first type is a high-speed DAQ system, about ten times faster than the previous one,[2)] but dedicated to the use of LeCroy 4300B (FERA) and FERA compatible modules, such as LeCroy 3377 drift-chamber TDC. These modules are reasonably fast and commonly used in medium-scale experiments, but the low band-width of CAMAC bus becomes a "bottle-neck" limiting the total DAQ speed. In the present system, instead, data are accumulated in a CES High Speed Memory (HSM) 8170 on VME through the FERA bus (20 MB/sec at maximum), and are DMA-transfered to a PC through a Bit3 617 VME/PCI interface (and optionally through a Bit3 400-5/50 optical link) at each time when a 64-kB block is filled (Fig. 1). The device driver for Bit3 617, developed at NIKHEF, is used,[3)] but modified to handle interrupts from the VME bus. It should be noted that there is no CPU on the VME bus, and the resource additionally required is very small.

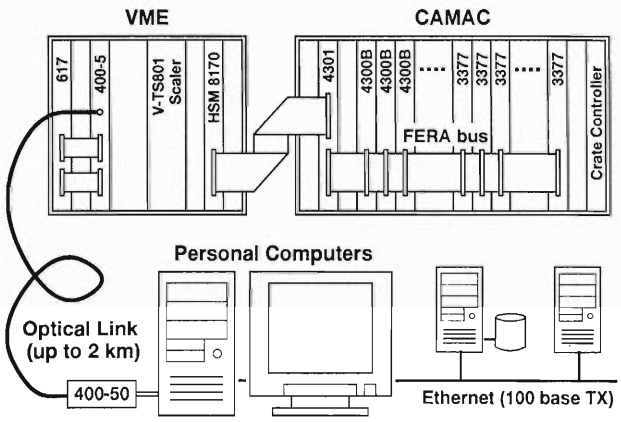

Fig. 1. A simplified scheme of the FERA/VME-based data acquisition system. For polarization experiments, the 4-gate 16-channel VME scaler, V-TS801, has been newly fabricated by Technoland Corp.

Since HSM 8170 allows a memory access from the FERA bus even when a DMA transfer is in progress on the VME bus (i.e. "double-buffer" mode), the DAQ speed is not affected by the system load in spite of the fact that Linux is not a real-time OS. The DMA speed, instead, considerably depends on the event rate as well as on the system load, as summarized in Fig. 2.

The second type DAQ system is a conventional one using an intelligent auxiliary crate controller (ACC) on the CAMAC bus. It is a renewal of the previous system[2)] which consists of a CES 2180 ACC, a Kinetic 2922 Q-bus interface, and a VAX/VMS host computer. They were replaced with a Kinetic 3976 68030-based ACC, a Kinetic 2915 PCI interface, and a PC running Linux, respectively. The Kinetic 3922 crate controller is still used because of its cable-driver (up to 90 m) and DMA capabilities.

The source code, previously running on CES 2180, has been ported to Kinetic 3976 by K. Yoshida, [4)] and is assembled by the assembler written by M. Iwasaki.[5)] The device driver for Kinetic 2915 developed at NIAS and Jefferson Lab. is used,[6)] but was extensively modified for stable and efficient DMA operations.

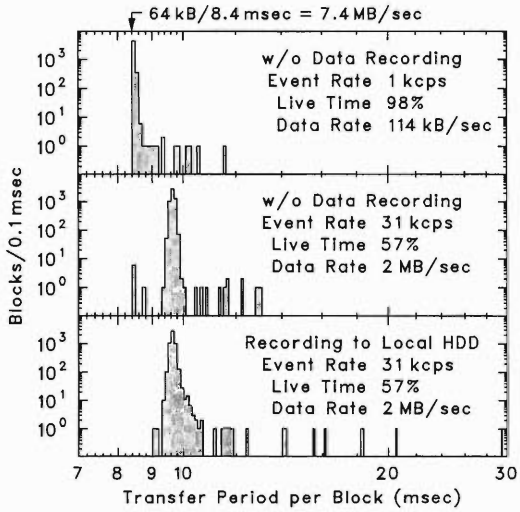

Fig. 2. Typical distribution of DMA-transfer period under various conditions. Triggers were generated by a random pulser with an event-length of 57 (16-bit) words. The block size is 64 kB.

References

1) Tcl/Tk, http://www.tclconsortium.org.
2) T. Ichihara et al.: IEEE Trans. Nucl. Sci. NS-36, 1628 (1989).
3) N. Kruszynska: vmehb-1.2, ftp://ftp.nikhef.nl/pub/projects/vmehb.
4) K. Yoshida: private communications.
5) S. N. Nakamura and M. Iwasaki: RIKEN Accel. Prog. Rep. **30**, 152 (1997).
6) Y. Tanaka et al.: k2915_v2.00, http://www.elc.nias.ac.jp/~daq/software/k2915.

Improvement of Polarized ^{3}He Target

T. Uesaka, S. Yamamoto, T. Wakui, H. Sakai, and Y. Yano

The RIKEN spin-exchange-type polarized ^{3}He target was applied to a nuclear physics experiment for the first time in 1996.[1] At that time the fraction of polarization was about 12%. Such a small fraction of polarization was due to a loss of pumping-laser light at the surface of target cell. Because transmission of the laser light through the glass surface decreases with the incident angle, the cell should have a small curvature in order to achieve an efficient optical pumping. The target cell which was used in the experiment had a cigar shape of 15 mm radius.

Recently we therefore introduced a double-cell design[2] to ease the difficulty. A schematic view of the cell is shown in Fig. 1. Target and pumping cells are connected with a 8 mmϕ glass tube. The pumping cell has a flat surface to where the laser light is incident. The old cell design which was used in the prior experiment is shown with broken line in Fig 1.

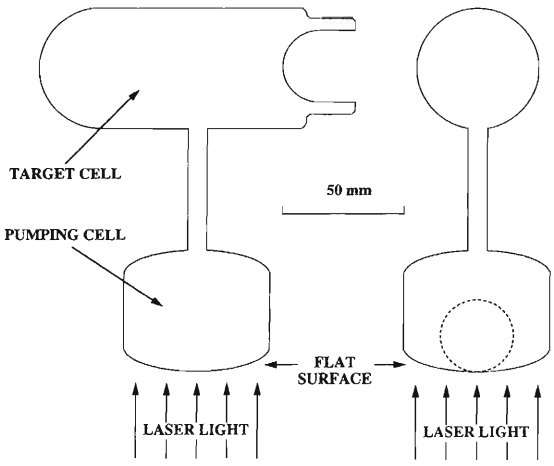

Fig. 1. Schematic view of the new cell.

We have measured the ^{3}He polarization enclosed in the cell. Density of ^{3}He gas was 8.9×10^{19} cm^{-3}. The result of measurement is plotted in Fig. 2. The horizontal axis is the amplitude of NMR signal which is proportional to the ^{3}He polarization. To obtain the absolute value of polarization, calibration by a proton NMR method is necessary. Though we have not yet carried out the calibration for the present cell, a rough estimation can be done on the basis of the calibration made for the old cell. Here we took the difference of the cell size into account and neglected the difference of the cell shape. The ^{3}He polarization thus estimated at equibrillium is thus estimated to be 40–50%.

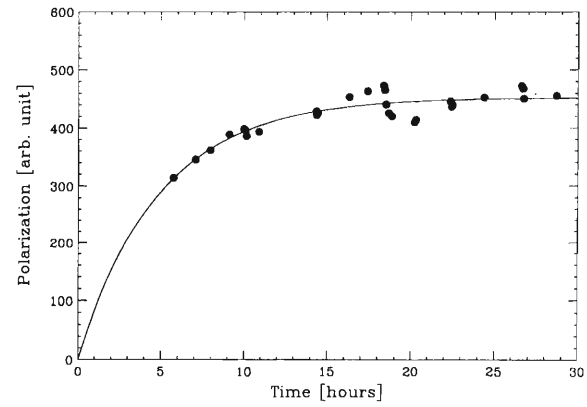

Fig. 2. The results of polarization measurement. Solid line represents the fitting.

References

1) T. Uesaka et al.: RIKEN Accel. Prog. Rep. **30**, 139 (1997).
2) H. Middleton et al.: AIP Conf. Proc. **293**, 244 (1993).

Construction of a New Low-Energy Deuteron Polarimeter

T. Uesaka, H. Okamura, Y. Satou, T. Ohnishi, K. Sekiguchi, K. Yakou, S. Sakoda, N. Sakamoto, T. Wakasa, K. S. Itoh, K. Suda, and H. Sakai

Since the polarized deuteron ion source began to provide the beams at RARF in 1992, our group has concentrated in experiments with a 270-MeV polarized deuteron beam. Therefore, a high-energy deuteron polarimeter which was constructed in the beam delivery room has been calibrated only at $E_d = 270$ MeV. The vector and tensor analyzing powers were determined as $\Delta A_y/A_y \sim 1\%$ and $\Delta A_{yy}/A_{yy} \sim 2\%$, respectively. Recently, however, polarized deuteron beam at the other energies (i.e., $E_d = 140$ and 200 MeV) came to be in demand, and the high-energy polarimeter have to be calibrated at these lower energies with a precision as high as at $E_d = 270$ MeV.

Because there are no standard polarimetry for high-energy deuteron, the high-energy polarimeter has to be calibrated by using a polarized deuteron beam whose polarization is determined prior to the acceleration in Ring cyclotron. In the low energy region ($E_d < 15$ MeV), the ^{3}He$(\vec{d},p)^4$He reaction is known to be a well-established polarimetry for deuteron.[1,2] Both vector and tensor analyzing powers have been determined with a statistical precision of 1%.

We have constructed a new low-energy deuteron polarimeter at the C03 beam-line in the AVF-Cyclotron room. The schematic view of the polarimeter is shownin Fig. 1. Two sets of detectors, 0° and backward-angle detectors, were used to measure the tensor and vector analyzing powers, respectively.

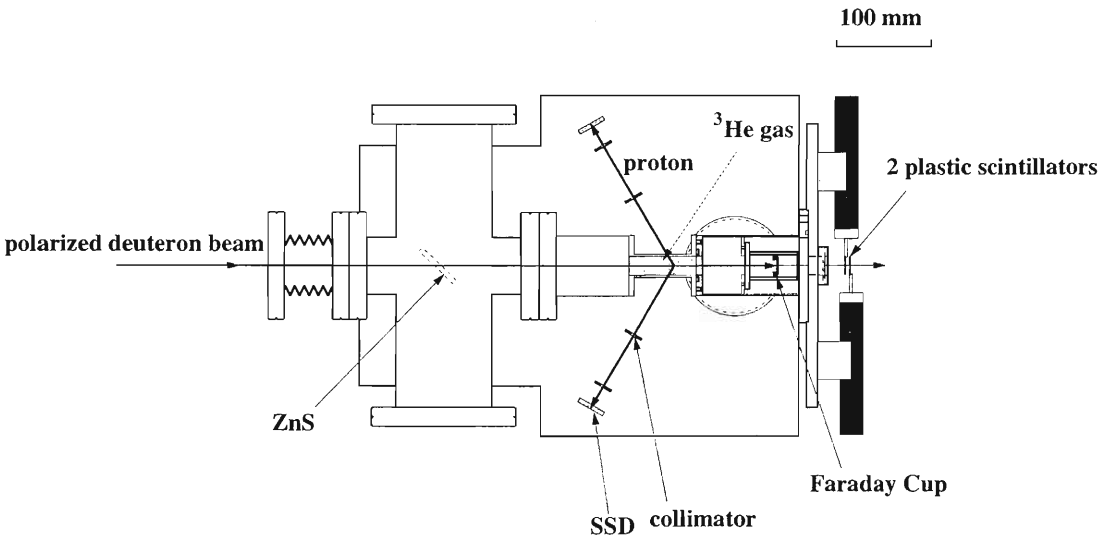

Fig. 1. Schematic view of the new low-energy deuteron polarimeter.

At 0°, two 1 mm-thick plastic scintillators were placed downstream from the beam stopper. Because of a large positive Q-value (18.4 MeV) of the ^{3}He$(d,p)^4$He reaction, the incident beam and any other reaction product can be stopped in the beam stopper or an energy degrader placed in front of the detectors, and only protons from the ^{3}He$(d,p)^4$He reaction reaches to the detector.

At backward angles, two 0.5 mm-thick silicon detectors were used to detect protons. In the both cases of 0° and backward angles, hardware discrimination of the ^{3}He$(d,p)^4$He event was successful, and no software gate was used to obtain the beam polarization.

The first measurement was carried out by using a 8-MeV polarized deuteron beam. The target density was 2.7×10^{19} cm^{-3}. Typical counting rate was about 1 kcps and 25 cps for 0° and backward angles, respectively, when the beam intensity was ~350 nA. The vector and tensor polarizations were determined with statistical errors of 1% and 0.7%, respectively, in an eight-minute measurement.

References

1) W. Grüebler et al.: Nucl. Instrum. Methods Phys. Res. **203**, 235 (1982).
2) N. Nishimori: Kyushu University, Ph. D. thesis (1996).

Beam Calibration of Heavy Ion Telescope on Board MIDORI Satellite

H. Miyasaka, T. Kohno, T. Goka, and H. Matsumoto

The satellite MIDORI was launched by NASDA for the Earth observation. A Heavy Ion Telescope (HIT) was on board this satellite to observe the galactic cosmic rays and the geomagnetically trapped particles.[1] Geometric factor of HIT is ~25 cm^2·sr and observable energy range is e.g. 18–53 MeV/nucleon for oxygen.

The ^{40}Ar beam with energy of 95 MeV/nucleon was irradiated to examine the particle identification ability of the HIT. Figure 1 shows the configuration of this beam test with cross sectional view of telescope. As Fig. 1 shows, HIT consists of two position sensitive detectors (PSD) and four pin type detectors. The PSD has 62 mm × 62 mm effective area with 0.4 mm thickness and the pin type detectors has 85 mm diameter circular effective area and 0.5 mm thickness. The telescope is optically shielded by 0.1 mm aluminum foil. A collimator was placed in front of the telescope. The collimator has 5 mm thickness of brass with 13 × 13 grid of nallow holes at 5 mm interval.

Figure. 2 shows the histogram of atomic number resolution obtained by ΔE-E method. The mean charge is 17.9 and resolution is 0.66 (FWHM). This result demonstrate the satisfactory performance of HIT.

We examined the distortion of PSD with this collimator. Center panel of Fig. 3 shows the distortion of PSD1. The circles represent the locations of holes

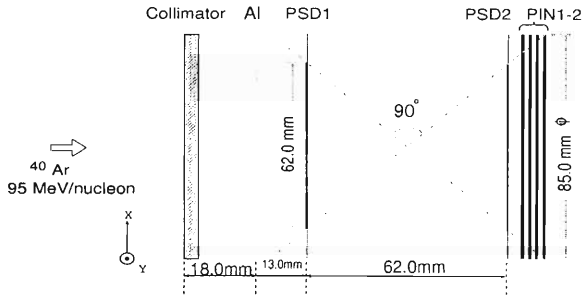

Fig. 1. Cross sectional view of the telescope and the beam arrangement.

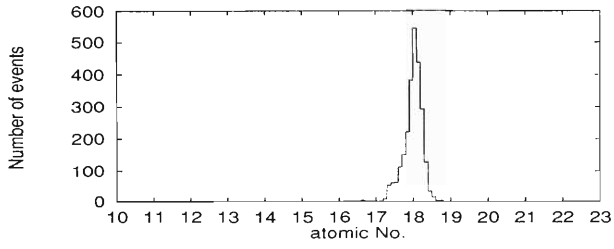

Fig. 2. The atomic number histogram.

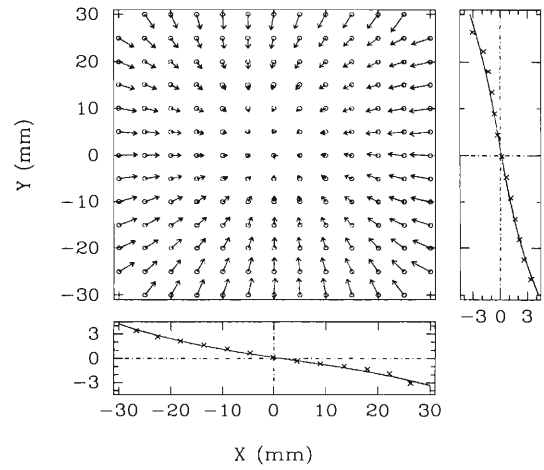

Fig. 3. Position distribution of PSD1. The vector represent the distortion of observed position. Mean deviation lengths projected at X and Y-axis are also shown with fitting curves.

of collimator and arrows represent the difference between observed position and position of the hole of the collimator. Cross marks at right and bottom panel of Fig. 3 shows the mean deviation length projected at Y-axis and X-axis respectively. Fitting curves of deviation length are also shown with solid lines. Using this fitting curve, we can correct this PSD distortion.

From two PSD position information, we determine the particle incidence angle. Figure 4 shows the distribution of observed particle incidence angle in the tilted beam measurement at 20° (top) and 35° (bottom). The broken lines represent the non-corrected results and solid lines represent the corrected results. Mean angle of each corrected case is 20.1° and 34.5° and the FWHM is 0.9° and 1.3° respectively.

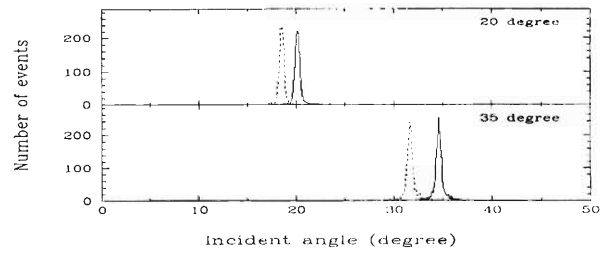

Fig. 4. Histogram of observed incident angle for 20° (top) and 35° (bottom). Solid lines and broken lines represent corrected and non-corrected for PSD distortion respectively.

References

1) T. Kohno et al.: Proc. 25th Int. Cosmic Ray Conf. **2**, 317 (1997).

Calibration Test of Dose Monitor on Board the ADEOS-II

Y. Kimoto, H. Matsumoto, T. Goka, T. Kohno, S. Badono, Y. Ushio, and M. Kobayashi

Calibration test of a radiation monitor for spacecraft was done. By the calibration test, most of the function of detectors and of the signal circuit of radiation monitor were confirmed. This radiation monitor named dose monitor (DOM) on board the ADEOS-II will be launched by NASDA into a sun synchronous orbit at 800 km with an inclination of 98 degree in the year 2000. The DOM measures the energy spectrum of the electron, proton, alpha particle and of the heavy ions heavier than Li. The sensor of DOM consists of seven PIN-type detectors (PINs) and an anti-coincidence detector (ANTI). The telescope is optically shielded by 0.1 mm thick aluminum foil. The nuclide is discriminated by ΔE-E method. The discrimination data were translated as telemetry data.

The H_2 beam with energy of 70 MeV/nucleon was irradiated in order to confirm the function of the sensor and electronics. Figure 1 shows the configuration used for the beam test and shows the cross sectional view of DOM. In this test, the output of each detector was obtained. The beam was irradiated to the aluminum shields with various thicknesses from the front of DOM. Various thicknesses were 0, 9.5, 11.0, 13.0, 15.0, 16.5 and 18.5 mm. The beam size was made as small as possible. The electronics parts were shielded. DOM is expected to be exposed to about 4.22×10^3 rad(Si) for three years in this orbit.

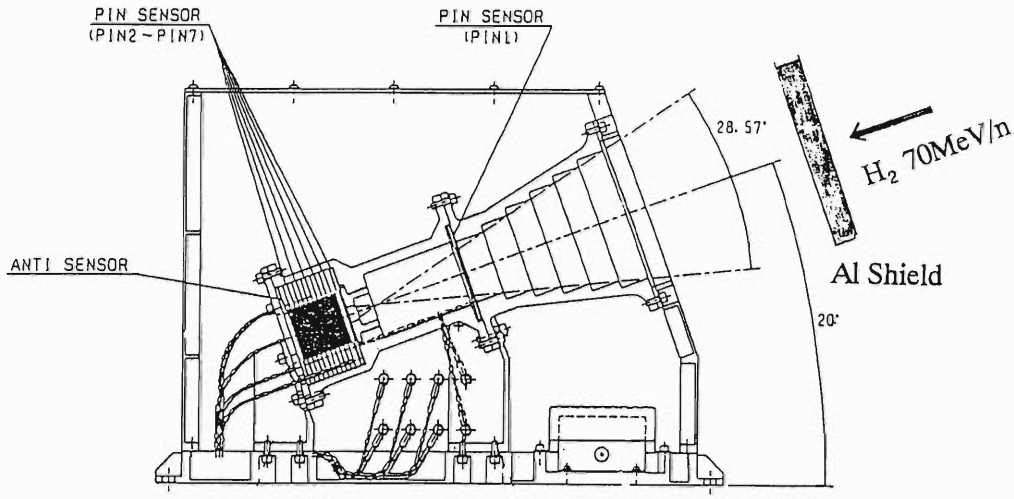

Fig. 1. The configuration of the beam test and DOM.

Figure 2 shows the simulated-pulse height distribution of each PIN detector observed by the pulse height analyzer. The thickness of aluminum shield was 0 mm. Most of the peak voltages of each PIN were consistent with the expectation values. Some PIN data showed two peaks because it detected two particles incident in to the detector at the same time. Figure 3 shows the pulse height distribution for the case of Al-thickness of 9.5 mm. Some peaks in each PIN were consistent with the expectation values, but some were not.

Then, the experiment and expectation values for each shields were compared. Figures 4 and 5 show the PIN1 & PIN3 deposition energy peak values of the experiment and expectation for each shield. From these charts, the experimental data are found to correspond to the expectation values except for thick shields. In the PINs and ANTI, some detectors had good corre-

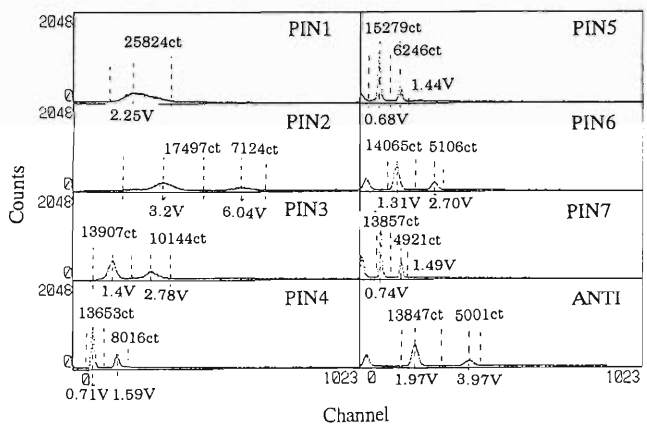

Fig. 2. The pulse height distribution from each PIN detector (Shield = 0 mm).

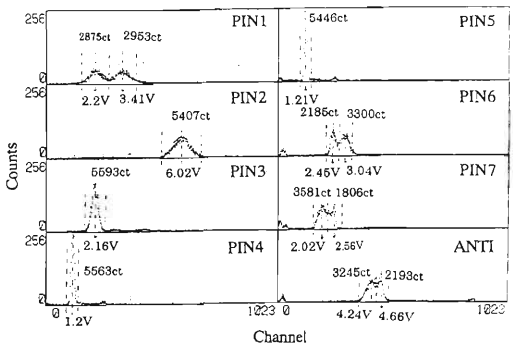

Fig. 3. The count data from each PIN (Shield = 9.5 mm).

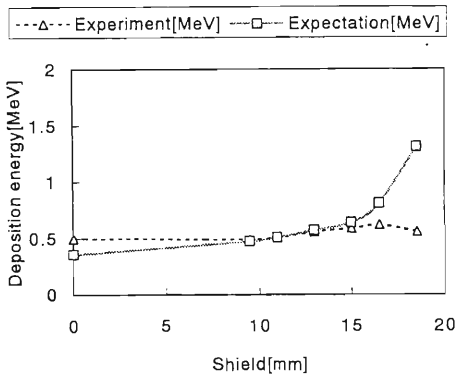

Fig. 4. The experimental and expectation values of deposition energy peak versus shield thickness (PIN1).

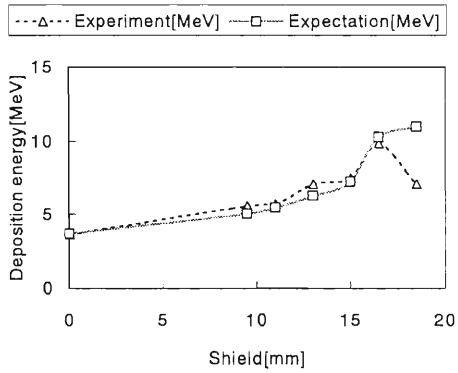

Fig. 5. The experimental and expectation values of deposition energy peak versus shield thickness (PIN3).

spondence between the experiment and expectation, others did not. When the outputs of the preamp were analyzed after the experiment, it was found that this disagreement was caused by the interference from other detectors. The configurations of the lines and circuits were rearranged. Each crosstalk was thus improved after that which was confirmed by electronic pulse test. In electronic pulse test, pulses with different energies were simulated. Then the output of the energy deposition was confirmed too. The leak current of the each PIN detectors was measured. There was no difference between the peak currents before and after the irradiation experiment.

Performance Study of the Plastic Scintillator for BESS Experiment with Heavy-Ion Beams

H. Fuke, T. Kaneko, A. Matsuda, Y. Yamamoto, K. Yoshimura, and H. Sakurai

BESS (Balloon-borne Experiment with a Superconducting Magnet Spectrometer)[1] has been performed since 1993 in order to measure the precise energy spectrum of cosmic-ray particles. Figure 1 shows the cross-sectional view of the BESS spectrometer. It has a large acceptance (0.3 m^2Sr.) and a wide energy range (0.2–100 GeV). Most of scientific data were collected at altitudes of about 36 km during the balloon flights over the northern Canada.

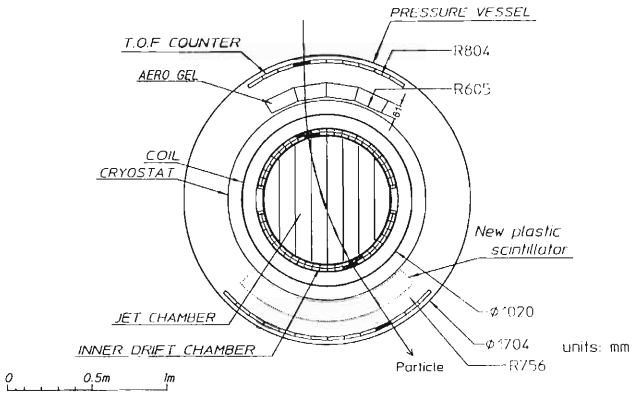

Fig. 1. BESS spectrometer. The dotted line shows where the new counter will be placed.

It is important to measure fluxes of cosmic heavy-ions ($3 \leq Z \leq 30$) for determination of the cosmic-ray propagation mechanism. It is also of interest to search for cosmic strange matters.[2] The present BESS $\frac{dE}{dx}$ range is, however, specialized in the $1 \leq Z \leq 8$ region. Therefore, a prototype of a new plastic scintillation counter to use on board the BESS has been developed and tested with RIPS produced heavy-ion beam. In this report we present data for the luminescent response of the plastic scintillator to heavy ions.

Figure 2 shows an overview diagram of the plastic scintillation counter, where the counter consists of a large diffusion box made from aluminium. It contains plastic scintillator (BC408) viewed by eight 2-inch diameter fine-mesh PMTs at the both ends. The surface of the inner side is covered with a reflector (Goretex). The dotted line in Fig. 1 shows where the new counter will be placed in the BESS spectrometer. The following are the characteristics of the counter.

(1) Thin plastic scintillator: 3 mm thick
(2) Large sensitive area; but light in weight
(3) Good uniformity
(4) Good energy response resolution
(5) Wide range in charge state ($3 \leq Z \leq 30$) by one single setup before PMTs' saturation.
(6) The counter should operate in the fringe magnetic field of ~0.2 T when the counter is incorpolated into the BESS spectrometer. The angle between PMT axes and the horizontal axis is not zero but finite.

The experiment was carried out using RIKEN Projectile-fragment Separator (RIPS). The beam was obtained from the fragmentation of ^{58}Ni projectiles at 90 MeV/nucleon on a Beryllium target, by selecting the emission angle and momentum. The beam was detected by a 0.5 mm thick silicon detector and a 0.5 mm thick plastic scintillator (PL) located at the final focal plane (F3) of RIPS. The magnetic rigidity of RIPS was set to be 2.4 or 2.6 Tm. The particle-identification of the fragments was carried out event-by-event by means of measurement of time-of-flight (TOF) and energy deposit (ΔE). The TOF of fragments between the production target and F3 was obtained from the PL timing and RF signal of the cyclotron. The ΔE of heavy ion was obtained from the silicon detector.

Figure 3 shows four data points where the beam was spotted.

Figure 4 shows a scatter plot of the light signal from our scintillator versus ΔE of the silicon detector, each in units of minimum ionization. The response resolu-

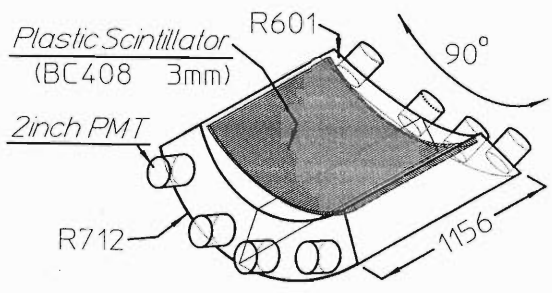

Fig. 2. Overview of the plastic scintillation counter.

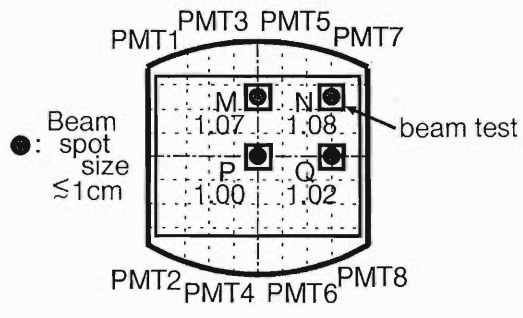

Fig. 3. Locations where the beam was spotted.

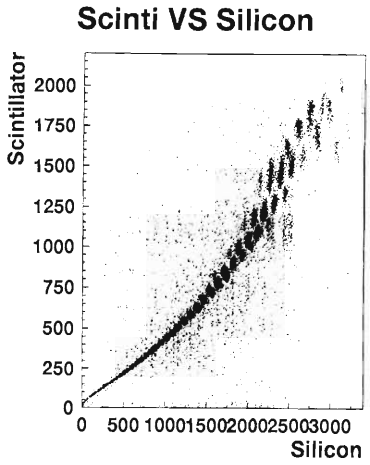

Fig. 4. Scatter plot of scintillator light output vs. silicon ΔE.

tion of the scintillator is better than 4% for the particles which passed through the plastic, which is similar to the resolution of the silicon detector.

Again in Fig. 4, the light signal from the scintillator was calculated as a simple sum of 8-PMTs' signals. This value shows the following relationship among different beam spots in Fig. 3, which is independent of $\frac{dE}{dx}$.

$$\mathrm{M} : \mathrm{N} : \mathrm{P} : \mathrm{Q} = 1.067 : 1.078 : 1.000 : 1.015 \quad (1)$$

Thus, the counter has a small un-uniformity of less than 4%.

In recent years, a number of considerable works have been done to understand the scintillation response, which is a function of the incident particle's energy, charge, and mass. The complex response, however, poses a challenge in their calibration. Birks[3] proposed a simple expression which took into account the quenching of the light output for the cases of very large energy loss. Meyer and Murray[4] suggested a model which also took high energy electrons into account, or "delta rays," which escape from the primary inonization column (MM-model). Here, we present an interpretation of the scintillator response data based on the MM-model. In this model, the differential light output $\frac{dL}{dx}$ arises from the two sources:

(1) A primary column of ionization centred along the path of the incident particle.

(2) Energetic secondary electrons which escape the primary column.

The scintillation efficiency in the primary column is taken to be a saturation function of $\frac{dE}{dx}$ such as the Birks' formula ($\frac{dL}{dE} < 1$), while delta rays produce light with high efficiency ($\frac{dL}{dE} \approx 1$). If F represents the fraction of the energy carried away by delta rays, then the differential light output may be expressed as

$$\frac{dL}{dx} = \frac{S(1-F)\frac{dE}{dx}}{1+(1-F)kB\frac{dE}{dx}} + SF\frac{dE}{dx}, \quad (2)$$

$$F = \frac{1}{2}\frac{\ln(2m_e c^2\beta^2\gamma^2/T_0) - \beta^2}{\ln(2m_e c^2\beta^2\gamma^2/I) - \beta^2}, \quad (3)$$

where β and γ are calculated from the velocity of the incident particle, m_e is the electron rest mass, I is the ionization potential of the scintillator, and T_0 is the minimum electron energy needed to escape from the primary column.

Thus, there are three parameters in this expression: the scintillation constant S, the quenching factor kB, and the electron kinetic energy cutoff T_0. We fitted these 3 parameters to the data with the χ^2 minimization technique, and obtained the following values: $kB = 12$ mg/cm^2 MeV, $T_0 = 3.8$ keV, and residual errors $\leq 1\%$ for $Z \geq 4$ particles (S depents on the device).

Figure 5 shows the predicted (doughnut marks) and measured (filled circles) peak values of some nuclei. The horizontal and vertical axes show the theoretical ΔE and the light output data, each in units of minimum ionization. It is obvious that the scintillation light output is not a simple single-variable function of ΔE but a two-variable function of β and charge state Z, which we succeeded in describing precisely.

Although the above mentioned analysis is not yet final, it can be concluded that our plastic scintillation counter has a good response resolution ($\leq 4\%$) and a small un-uniformity ($\leq 4\%$). In addition, we could reproduce the data by a model which takes both quenching and delta-ray effects into account.

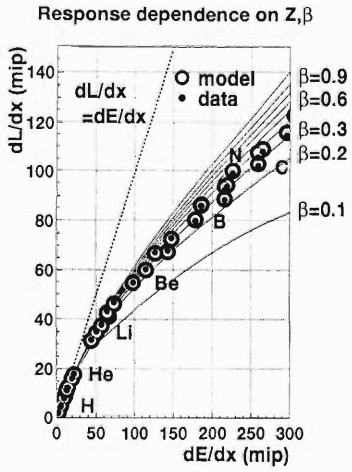

Fig. 5. The result of 3-parameters fitting. The scintillation light output is a two-variable function of β and charge state Z, and the fit can reproduce it precisely.

References

1) S. Orito et al.: Phys. Rev. Lett. **75**, 3792 (1995); Phys. Lett. B **422**, 319 (1998); Phys. Rev. Lett. **81**, 4052 (1998).
2) T. Saito et al.: Phys. Rev. Lett. **65**, 2094 (1990).
3) J. B. Birks: Proc. Phys. Soc. A. **64**, 874 (1951).
4) A. Meyer et al.: Phys. Rev. **122**, 815 (1961).

Construction of a Liquid Hydrogen Target

H. Akiyoshi, K. Sagara, and T. Motobayashi

A liquid hydrogen target for the experiments with secondary beam has been designed and is currently under construction. The design has been made to meet the following requirements. The thickness of hydrogen is typically 100 mg/cm^2. The ratio of hydrogen to other materials should be by far larger than that of polyethylene foil which is a typical hydrogen target. The target system should be easy to mount and dismount.

Figure 1 shows a schematic view of the liquid hydrogen target. The target cell is attached to the cold-head through a copper-rod. The target cell is connected to a gas reservoir with a thin stainless steel pipe. The volume of the reservoir is 10 ℓ. The cryogenic refrigerator cools hydrogen gas in the target cell down to about 20 K, and liquefies it. The hydrogen gas is sealed in the closed system, so the gas pressure decreases steeply when the hydrogen is liquefied. The gas pressure is measured by a pressure transducer. Temperature of the target cell is measured by a Si diode thermometer. Another Si diode thermometer is attached on the copper-rod (see Fig. 1). Excitation current for the Si diode thermometers is supplied by battery powered current sources. The room-temperature is measured by a thermocouple on the reservoir. A heater is mounted on the copper-rod. The temperature is controlled by changing the power to heater.

The target cell, the copper-rod, and the cold-head are surrounded by an aluminum heat shield at the temperature of about 80 K. The shield has two 25 mm diameter holes for the beam entrance and exit. The target can be lifted up by 10 cm, so that one can use other foil targets.

Figure 2 shows a cross section of the target cell. The window foils are made of 12.5 μm thick aramid foil. The window foil is pressed by a foil-cover which has a 24 mm diameter hole for beam. Due to the inner gas pressure of 1500 hPa, the window foils swell out. Thickness of the hydrogen is designed to be 14 mm. The thickness can be changed by replacing the target cell.

Digitized data on the data acquisition/switch unit which is connected to the thermometers and pressure transducer are acquired by a computer located outside of the experimental hall. Remote control of the DC power supply for heater is possible by the computer. The data acquisition and the control of heater power are made by a software on LabVIEW[1] which sends GPIB commands through Ethernet.

When the output from one of the Si diode thermometers become smaller than the lower limit of temperature, an alarm system is turned on and the refrigerator is turned off. When the output from one of the Si diode thermometers reaches beyond the higher limit, an alarm is turned on and the heater power is turned off. The safety system is deployed locally, so as to work even when the computer or network downs.

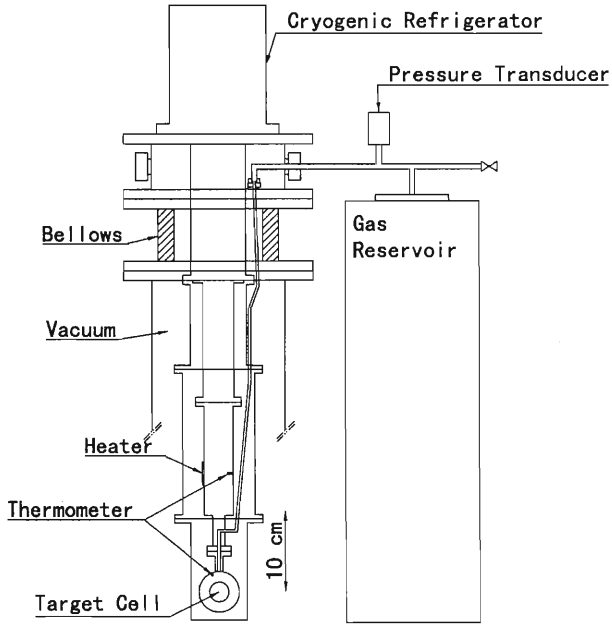

Fig. 1. Schematic front view of the liquid hydrogen target system.

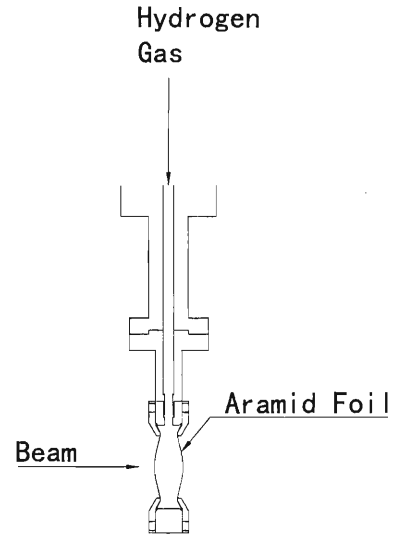

Fig. 2. Schematic side view of the target cell cross section.

References

1) LabVIEW 5.0.1, National Instrument Corporation.

High Resolution MUltiple Sampling Ionization Chamber (MUSIC) Sensitive to Position Coordinates

H. Petrascu, H. Kumagai, I. Tanihata, and M. Petrascu*

A new type of MUSIC sensitive to position coordinates has been developed recently. The development is based on the theoretical analysis of Ref. 1. This detector will be used in experiments on fusion to use radioactive beams, and is suitable, due to the high resolution, for identification and tracking of low Z (down to $Z = 1$) particles. One of our goals, when we started to work, was to reduce, as much as possible, the Z value of particles that can be "seen" by an ionization chamber.

The resolution was improved by connecting preamplifiers directly to the MUSIC's pads. These preamplifiers are able to work in the vacuum and very low gas pressure. In this way the value of S/N ratio was increased by a factor of $\sim$10.

The detector is a Frisch grid type, with the anode splitted into 10 active pads. It is the first model of the ionization chamber with the field shared between the position grid and the anode pads. The Frisch grid was necessary because the detector is originally designed for very accurate energy measurements and particle identification. A drawing of this detector is shown in Fig. 1.

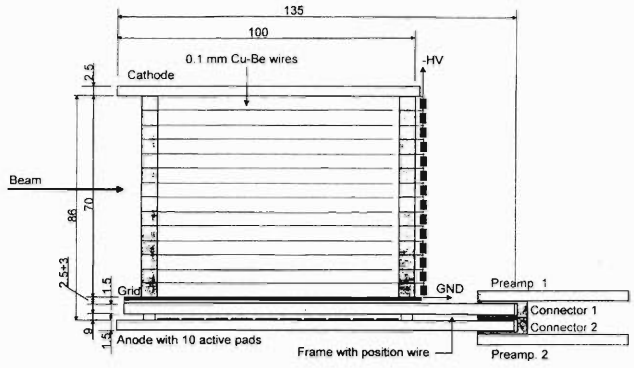

Fig. 1. Schematic picture of MUSIC.

The detector itself consists of four main parts. The first one is the constant field-gradient cage, sandwiched in between the cathode and the Frisch grid. The second is the Frisch grid. The third is the position grid located under the Frisch grid. The last one is the plate with the anode pads. The cage is 60 mm wide and is made of 100 μm Cu-Be wires. Every wire is tensioned with the weight representing a half of its breaking limit. The Frisch grid was fabricated using an aluminum frame for the support of the 20 μm W wires spaced by 0.3 mm. For the position grid we used 10 groups of wires made from Au-plated W with 20 μm in diameter. Every group is composed from 5 wires spaced by 0.9 mm connected in parallel. Both Frisch grid and position grid wires are parallel to the beam direction. The anode pads are transversal to the beam direction, and each of them has an area of 7.8 mm $\times$ 60 mm. Every pad and every group of wires from position grid is directly connected to a charge sensitive preamplifier.

The chamber's energy resolution was first tested using a P-10 gas (Ar 90% + CH_4 10%) at the pressures between 200–300 Torr. As a radioactive source we used a ^{241}Am α source with an activity of 5 kBq. We used also a 4 mm diameter collimator for beam, located at 20 mm away from the α source. The drift velocity of the electrons in cage was selected to be 5 to 8 cm/μs.

A typical pulse distribution in the chamber is shown in Fig. 2. When P = 250 Torr, we obtained FWHM value of 10.4% on the 7th pad, and 8.5% on the 9th pad. One may recognize a "Bragg curve" behavior of the peaks over different pads.

Determination of the position resolution is in progress.

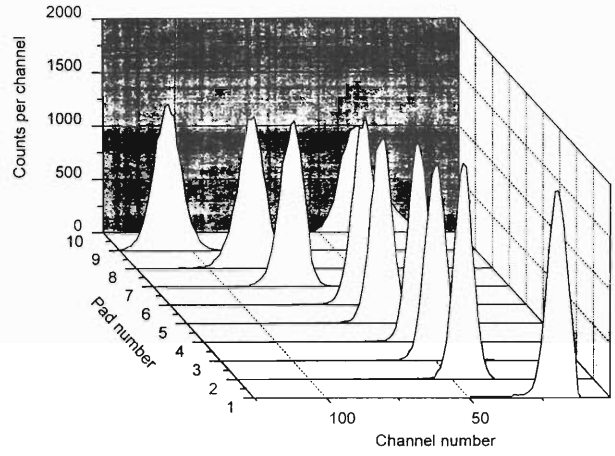

Fig. 2. Pulse distribution at P = 250 Torr. The pulse height is near approximately 5 V.

References

1) G. D. Badhwar: Nucl. Instrum. Methods **109**, 119 (1973).

* Horia Halubei National Institute of Nuclear Physics and Engineering, Romania

Fast-Neutron Measurement Using a Scintillating Fiber Stack with Neutron Beam From ^{7}Li(p, n)^{7}Be Reaction

K. Terasawa, T. Doke, J. Kikuchi, S. Takenaka, M. Yamashita, M. Kase, T. Uesaka, and T. Ohnishi

Radiation dosimetry in space is essential for astronauts in spacecraft. The measurement of radiation dose from ionizing radiation has been made by various detectors.[1,2] However, contribution from the fast neutrons has not been measured well, because the neutron dosimetry in space is not so easy as the ionizing radiation dosimetry. To evaluate neutron dose more accurately, the 3-dimensional imaging detector consisting of a scintillating fiber stack has been developed.

Generally, fast neutrons are efficiently scattered by light nuclei. The energy of recoil nucleus is given by

$$E_r = 4A(\cos^2\theta)E_n/(1+A)^2, \quad (1)$$

where, E_r and E_n are the energies of the recoil nucleus and incident neutron, respectively; θ is the recoil angle of the nucleus; and A the mass number of the target nucleus. The recoil nuclei produced by the collision with fast neutron can be identified from the penetrating charged particles by observing the track of the recoil nuclei appearing inside the stack. Then, the recoil nuclei and electrons produced from γ rays can be identified by observing each scintillation intensity per unit length along the track. The lower threshold energy measurable by a neutron dosimeter is determined by the technical limit of n-γ discrimination.

So far, it is confirmed that identification of penetrating protons and recoil protons from neutron interaction can be made easily and that lower energy limit to identify neutrons and γ rays is estimated to be 1–2 MeV in the scintillating fibers of 0.5 × 0.5 mm.[3] Here, we report the energy calibration for fast neutrons and its lower energy limit by using ~66 MeV neutron beam produced from ^{7}Li(p, n)^{7}Be reaction with proton energy of 70 MeV in the E4 beam line of RIKEN cyclotron. Using the information on the incident direction of neutrons, the recoil angle of protons and the range of recoil protons in the stack, the relation between recoil proton energy and recoil angle given by Eq. (1) was experimentally checked, and the result is shown in Fig. 1. Here, it was assumed that all tracks originating from the inside of the stack were considered as the tracks of recoil protons for simplicity. If the energy of neutrons was completely monochromatic, data points would have been concentrated near the line of neutron 66 MeV, within the resolution of the detector, in Fig. 1. However, data are widely scattered below the line because they have wide energy spectra and because the range of the recoil protons with higher energy is frequently over the detector size. Taking the above considerations into account, Eq. (1) can be confirmed roughly on its validity. Figure 1 depicts no data

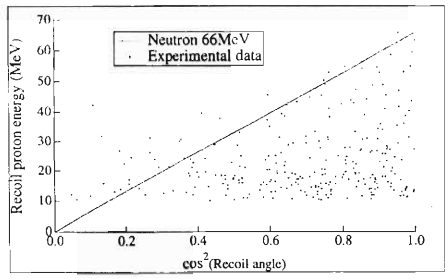

Fig. 1. Relation between recoil angle and recoil proton energy.

below 10 MeV, because the image intensifier was triggered by coincident signals from two photomultipliers. Therefore, no event with the range less than ~1 mm was recorded. If the image intensifier was triggered by signals from a single photomultiplier, the recoil protons with the energy lower than 10 MeV could be detected.

The data plotted in Fig. 1 include only recoil protons which stopped inside the stack. In order to evaluate the recoil protons penetrated the stack, the relation between the light yield and the light intensity per CCD pixel is plotted in Fig. 2. The range of the electrons at the energy from ~1 MeV to ~10 MeV is several ten times longer than that of proton at the same energy. The difference of the light intensity per CCD pixel between electrons and protons in Fig. 2 is consistent with that expected from the range-energy relation. The experiment using the neutrons produced by the D-D or D-T reaction, which is scheduled for the near future, will clarify the response of this method in the low energy region and will find lower energy limit for identifying neutrons and electrons.

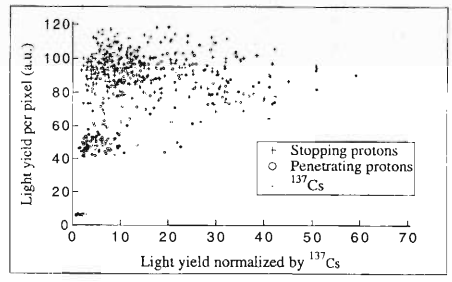

Fig. 2. Light intensity per unit length along the track.

References

1) G. D. Badhwar et al.: Nucl. Tracks Radiat. Meas. **20**, 13 (1992).
2) T. Doke et al.: Nucl. Instrum. Methods Phys. Res. A **365**, 524 (1995).
3) K. Terasawa et al.: Ioniz. Radiat. **24**, 119 (1998).

Position Sensitive Detector Using Scintillation Fiber

K. Morimoto, F. Tokanai, and M. Kurata

A Scintillating Fiber Imager (SFI)[1] has been developed for the Restriction Landmark Genomic Scanning (RLGS)[2] technology. The RLGS technology is a powerful and relatively rapid method for the genetic analysis of mouse and human genome as well as that of other animals and plants. RLGS employs a direct end labeling of the genomic DNA digested with a restriction enzyme, high resolution two-dimensional gel electrophoresis, and *autoradiography*. The restriction enzyme site labeled with beta-emitting radionuclide of ^{32}P can be used as landmark loci. Hereafter we call the restriction enzyme as genome spot. There are more than two thousand genome spots in a single dried gel of 40×40 cm^2. Film-based autoradiography is one of the most useful methods to obtain the genomic information, because of its large detection area and excellent spatial resolution. However, it has two disadvantages: i.e., (1) long exposure time (about two weeks) due to the low sensitivity, and (2) lack of quantitative information due to the non-linear response and limited dynamic range. The present system, on the other hand, offers a real time acquisition and easy quantification of RLGS data compared to film-based autoradiography, and it is proved to be a powerful position sensitive detector for measurements in nuclear physics. Test measurements have been carried out with genomic linkage map labeled with ^{32}P (β-ray emitter) and ^{58}Ni beam at 90 A MeV as well. The RLGS map used in the detector test was processed at the Genomic Science Laboratory of RIKEN. The map was electrophoresised to two dimensional and dried on filter paper. We carried out the observation of the genome spots labeled with ^{32}P one day after the RLGS process. Figure 1 shows the image of genome spots in a single dried gel sheet. The genomic spots are clearly seen and each one can be distinguished. It took about 50 h to accumulate the statistics applicable to quantitative analysis. This shows that SFI shall need much shorter time to measure the RLGS map compared to the film-based autoradiography, since the autoradiography takes about two weeks to obtain the image.

However, the detection efficiency was smaller than expected (roughly 12 h). This lack of detection effi-

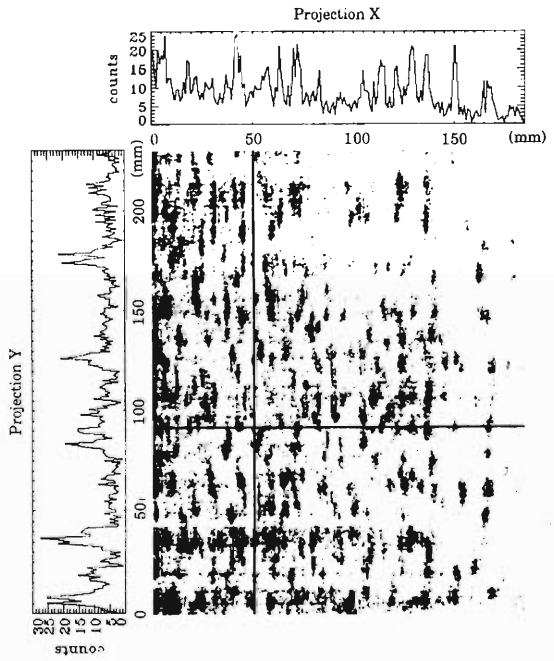

Fig. 1. Image of RLGS map labeled with ^{32}P. The genome spots are clearly seen.

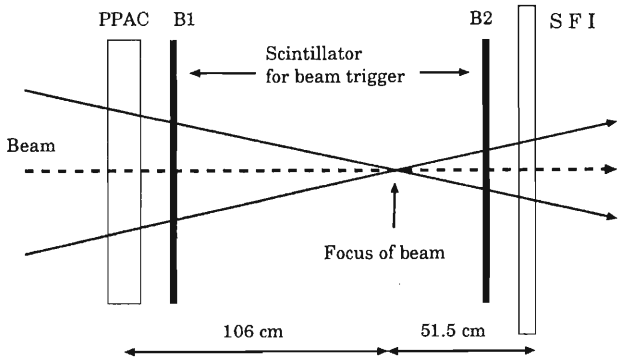

Fig. 2. Layout of detectors in ^{58}Ni beam measurement. PPAC is the position sensitive Parallel Plate Avalanche Counter. B1 and B2 are plastic scintillation beam counters.

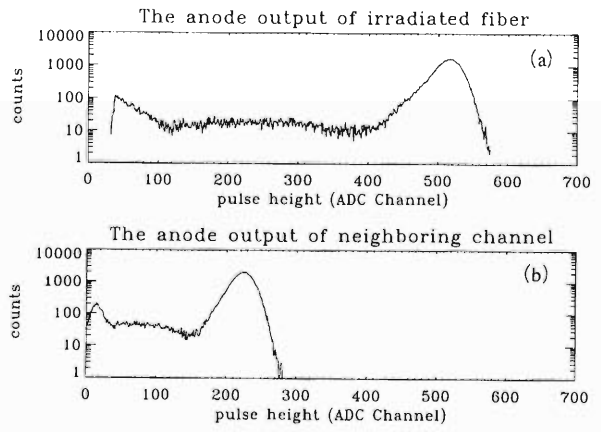

Fig. 3. Pulse height spectra of ^{58}Ni beam: (a) Spectrum of output from the anode watching the irradiated fiber. (b) Spectrum from the anode watching the neighboring fiber.

ciency could be explained by the cross-talk of scintillating photons at joining points between the fibers and the photo-cathode of Multi Anode Photo Multiplier Tube (MAPMT), since the anode pitch of this MAPMT is too narrow to collect all of the photons emitted by corresponding fibers. In order to investigate a detection efficiency of SFI and a cross talk between fibers and the photo-cathode of MAPMT, we carried out a test measurement with the heavy ions produced by the RIKEN Ring Cyclotron. The incident beam was ^{58}Ni at 90 A MeV of energy. The layout of the detectors is illustrated in Fig. 2. Figure 3(a) shows an example of pulse height distribution obtained with one anode watching the irradiated fiber, where the highest pulse is selected in all anodes for one beam event. Then, Fig. 3(b) shows the pulse height distribution of output from the anode watching the neighboring fiber at the same event. We found that 40–50% the scintillated photons from the edge of the fiber were collected by neighbors. If we could avoid this cross-talk, the detection efficiency for the RLGS map would increase. The detection efficiency of SFI is 70% of the beam trigger. The main reason of the reduced detection efficiency is due to the 74% effective area of SFI against the beam of vertical incidence. We have shown that the SFI is applicable to not only the β-ray but also heavy-ion detections.

References

1) K. Morimoto et al.: RIKEN Accel. Prog. Rep. **31**, 163 (1998).
2) Y. Hayashizaki et al.: Genet. Soc. Am. **138**, 120 (1994).

Measurement of the Energy of Heavy Ions at Around 100 MeV/nucleon with Allene-Doped Liquid Argon Ionization Chamber

A. Yunoki, T. Doke, M. Kase, T. Kato, J. Kikuchi, K. Masuda,[*1] M. G. Niimura, K. Ozaki,[*2] E. Shibamura,[*3] M. Tanaka,[*2] and I. Tanihata

An allene-doped liquid argon ionization chamber with 48 mm × 48 mm × 40 mm sensitive volume has been constructed for precise energy measurement of heavy ions at around 100 MeV/nucleon. The energy resolution of 0.6% (FWHM) was achieved for ^{40}Ca ions at 94 MeV/nucleon.[1,2] We expected that a better energy resolution would be obtained for lighter ions such as O and Ne because Hitachi and coworkers obtained better energy resolution for ^{16}O ions than that for ^{36}Ar ions at around 30 MeV/nucleon.[3]

The detector system was the same as that used in the experiment with ^{40}Ca ions. Allene concentration into liquid argon (LAr) was 10, 20, and 80 ppm.

Energy resolution of the gridded ionization chamber was investigated with O (▲) and Ne (●, ■) ions at around 100 MeV/nucleon. Figure 1 shows the fraction of collected charge Q/Q_0 as a function of an external electric field (E). The Q/Q_0 was obtained from the collected charge (Q) divided by the total ionization yield (Q_0), which was given from the total absorbed energy in the LAr divided by the W-value in LAr. The maximum value of Q/Q_0 was 40% which was obtained under E = 4 kV/cm for ^{16}O ions at 133 MeV/nucleon in 20 ppm allene-doped LAr. Figure 2 shows the energy resolution as a function of the E. The energy resolution was obtained by subtracting in quadrature the width of test pulses from that of the charge signal and dividing it by the peak channel of the charge signal. The best energy resolution in Fig. 2 is 1.1% (FWHM) under E = 1 kV/cm for ^{20}Ne at 133 MeV/nucleon in 10 ppm allene-doped LAr. The energy resolution was improved as E was increased from 0.5 kV/cm to 1 kV/cm, and was degrading as E was increased from 1.5 to 4 kV/cm. Figure 3 shows the energy resolution as a function of the beam intensity under E = 1.5 kV/cm, which includes the energy resolution for ^{40}Ar at 94 MeV/nucleon (◆). The energy resolution started degrading as the beam intensity increases.

Contribution of the fluctuation of energy loss in the material existing upstream of the chamber to the energy resolution was estimated to be 0.2% (FWHM). The experimental result was worse than this estimation by a factor of 5. The reason why the energy resolution would not improve with increase of the external electric field is not understood yet. The degradation of the energy resolution may be due to the variation of the Q/Q_0 made by positive ions left in the sensitive volume of the chamber. Based on a simple model, an additional electric field is estimated to be an order of 1 kV/cm for a beam intensity of 100 cps.

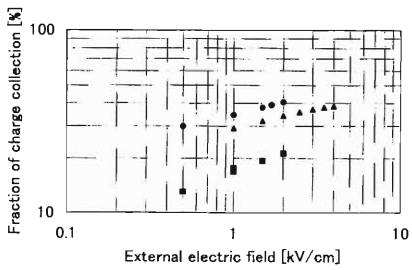

Fig. 1. Fraction of charge collection (Q/Q_0) as a function of the E. Symbols of (●), (▲) and (■) represent the data of 10, 20, and 80 ppm, respectively.

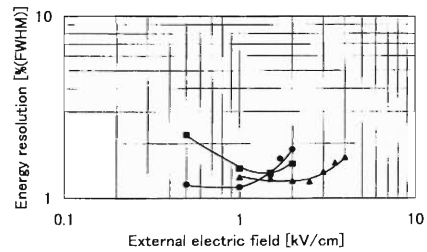

Fig. 2. Energy resolution as a function of the E.

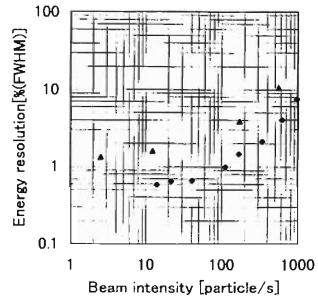

Fig. 3. Energy resolution as a function of the beam intensity at E = 1.5 kV/cm. Symbols of (◆) represent the data of ^{40}Ar ions in 80 ppm allene-doped LAr.

*1 Solar-Terrestrial Environment Laboratory, Nagoya University
*2 Advanced Research Institute for Science and Engineering, Waseda University
*3 Saitama College of Health

References

1) A. Yunoki et al.: RIKEN Accel. Prog. Rep. **30**, 148 (1997).
2) A. Yunoki et al.: to be published in Nucl. Instrum. Methods Phys. Res. A.
3) A. Hitachi et al.: Nucl. Instrum. Methods Phys. Res. A **340**, 546 (1994).

Multiwire Proportional Chamber Read-Out System for Pulsed Muon Facilities

S. N. Nakamura, Y. Matsuda, K. Ishida, T. Matsuzaki, K. Nagamine, D. Tomono,* and M. Iwasaki

Multiwire Proportional Chamber (MWPC) is a gas chamber with thin wires on which high voltage applied to. It provides us a good spatial resolution (determined by a wire pitch, typically ~2 mm) of the particle tracks as well as a good timing resolution (~10 ns).

With its spatial and timing resolution, it can serve for many applications at a pulsed muon facility. For example:

- precise measurement of muon lifetime,
- test of the exponential decay law,
- muon tomography, and
- advanced μSR experiments.

However, conventional MWPCs are designed for continuous beam facility or for pulsed beam facility to study short-life particles. They are not suitable at pulsed muon facilities where the time structure of signals is quite unique. Emission of the $e^{\pm}$ from $\mu^{\pm}$ decay distributes upto several 10 μs ($\tau_{\mu} = 2.2$ μs), and signal rate is quite high (2×10^3/100 ns/total solid angle ~20 GHz/total solid angle at the RIKEN-RAL Muon Facility) just after a burst of muon beam. Therefore, dead time of read-out system of conventional MWPC is too long to use at pulsed muon beam facilities. We have been developing a MWPC system with multi-hit capability, which can be used at a pulsed beam facility such as the RIKEN-RAL Muon Facility.[1)]

We have fabricated two sets of MWPCs (C1 and C2) with 320 mm × 320 mm effective area. Each MWPC had X and Y planes and each plane consisted of 160 anode wires (gold plated tungsten of 20 μm diameter) with 2 mm spacing. Each wire planes were separated by the cathode planes made of aluminized mylar sheet (12 μm thick) and the distance between anode wires and cathode plane was 4 mm. Typical operational voltage was −3 kV.

Two types of gases (Magic Gas, Ar + Ethane 50/50) were tested. Magic Gas (Ar, Freon, and Isobutane gas mixture) allowed a higher operational voltage and a higher gain output. However, a change of gas mixture leads to an efficiency drift, and thus the gas mixture should be carefully controlled. On the contrary, the gas mixture control was not required for Ar + Ethane 50/50 gas, which was pre-mixed at a factory, but it gives a smaller gain output and a slightly poorer time resolution. Now, we are testing both gases and further study is in progress.

Figure 1 shows a schematic diagram of MWPC read-out circuit. The induced charge at each wire was pre-amplified and transferred to the amp-discriminator, where the signals were shaped and converted to be logic signals.

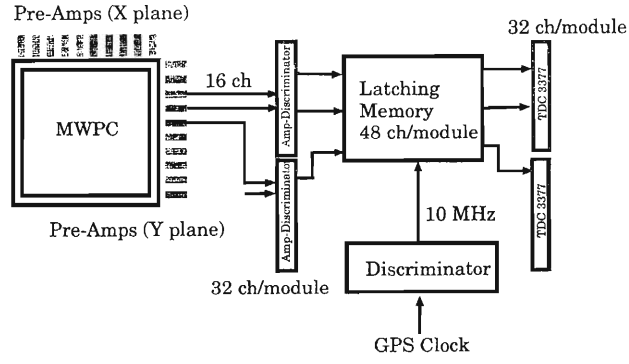

Fig. 1. Schematic diagram of the MWPC read-out circuit.

Two types of time to digital converters (TDC) have served to obtain position and timing information from the MWPC. The first one is used to receive fired-wires information from a particle passed position, and the other is for very precise timing experiments. The first one should have small least-significant bit (LSB, or time binning) to select simultaneous hits on X and Y wires which give particle hit positions. However, excellent integral and differential linearities are not required. We adopted LeCroy long-range multi-hit CAMAC-TDC 3377 for this purpose. It has 16 multi-hit capability and 32 μs time range with 500 ps LSB. Each module contains 32 channel and we will use 20 modules of them.

One the contrary, some experiments require very accurate time information (*e.g.*, μ^+ lifetime measurement), and TDC3377 cannot serve for this purpose. In this case, very accurate integral and differential linearities are essential, but modest LSB (50–100 ns) is enough. We are developing latching memory with global positioning system (GPS) for this purpose (Fig. 2).

The GPS receiver (Hewlett Packard HP58503A) has a very accurate quartz clock, and furthermore it is continuously calibrated by atomic clocks (10^{-12} accuracy) on GPS satellites. The latching memory records the wire information (fired or not-fired) at the timing of sampling clock which is provided by the GPS frequency receiver. Therefore, integral and differential linearities are expected to be extremely good. One module accumulated 48-wires information to 2048 samples. The external clock was 10 MHz, and thus the time window was able to open up to 200 μs.

Overall accuracy of our clock system is better than ~20 ps (r.m.s.) which is restricted by an instability of the discriminator rather by than the accuracy of the GPS clock itself.

The MWPCs have 640 wires in total and each of

* Department of Physics, Tokyo Institute of Technology

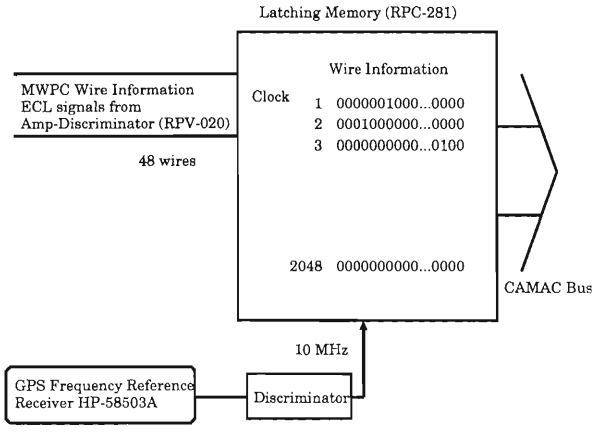

Fig. 2. MWPC wire information is sampled by a latching memory at the timing of an external clock provided by the GPS frequency reference receiver.

them provides 1 bit of information (hit or no-hit) in every 100 ns for 100 μs. Therefore, we have 80 kB data in every 20 ms (4 MB/s) and it is not trivial to read all the data without a serious dead time. A CAMAC block read-action takes typically 1.5 μs/16 bits and hence ~60 ms is necessary for just reading all the wire information. Therefore, we have divided the latching memory modules into four CAMAC crates and each equipped with an Auxiliary Crate Controller (ACC), Kinetics Model K3976, which was a single-board computer with MC68030 CPU (40 MHz) and 1 MB memory. The basic concept of the data acquisition system was already reported in another paper.[2] We used four of such system in parallel. Figure 3 shows schematically the data acquisition system.

Signals from C1-X, C1-Y, C2-X, and C2-Y planes of MWPCs were distributed to four CAMAC crates, and each CAMAC crate contained the latching

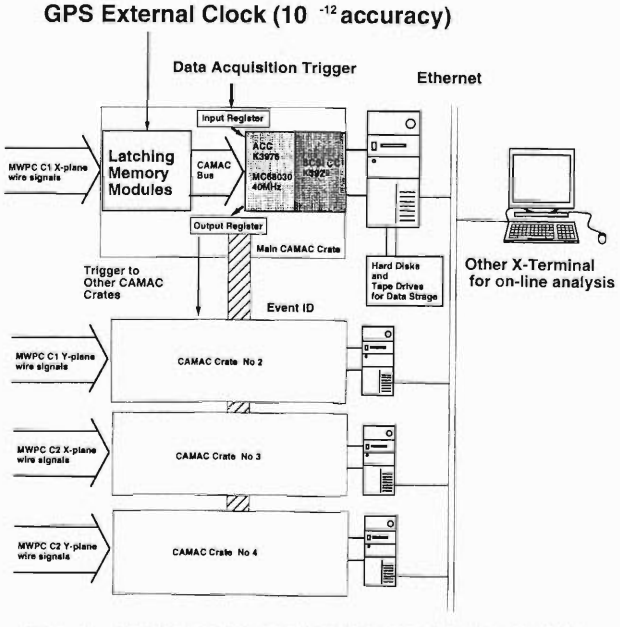

Fig. 3. Configuration of the data acquisition system.

memory modules which recorded the wire information. The ACC read and compressed the recorded data. After closing the time window, the trigger logic issued a trigger signal to one CAMAC crate (named the main crate) and it provided trigger signals to the other ones. Receiving the trigger signal, the ACC started to collect the wire information from the latching memory modules and compressed data to store in its memory. When the memory of the ACC became full, it transfered data to a host computer for the on-line analysis and data storage. In order to associate recorded data separately in different CAMAC modules, the main crate issued an event identifier (14 bits digit = 0 16383) to the other three CAMAC crates at every trigger. Therefore, the data which belonged to the same time-window had the same event identifier even though they were recorded in different CAMAC crates and in host computers. The event identifier was an unique number in the last 5.5 minutes acquired data at the repetition rate of ISIS. Thus we were able to gather separately accumulated data without a confusion in the off-line analysis.

We have developed a multiwire proportional chamber system for pulsed muon beam facilities. It was equipped with an excellent integral and differential linearity clock system. In order to handle a large amount of data from MWPC system, we have also developed a parallel CAMAC data acquisition system.

The system is being checked with a test beam at port 3 of the RIKEN-RAL Muon Facility (Fig. 4).

The system will be used for the measurement of the precise μ^+ lifetime and for the test of the exponential decay law which will start in early 1999.

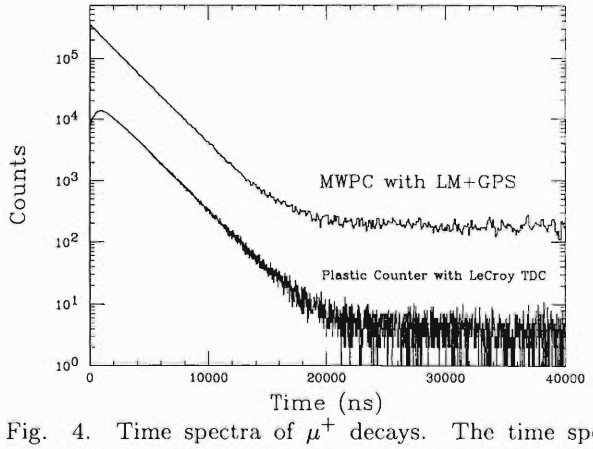

Fig. 4. Time spectra of μ^+ decays. The time spectrum measured by a plastic counter with LeCroy TDC (20 ns/bin) has a large distortion at $t \sim 0$ due to a count loss, while such a problem cannot be seen for the time spectrum measured by the present MWPC with latching memory + GPS clock system (100 ns/bin).

References

1) K. Nagamine et al.: Hyperfine Interact. **101/102**, 521 (1996).
2) S. N. Nakamura and M. Iwasaki: Nucl. Instrum. Methods Phys. Res. A **388**, 220 (1997).

6. Material Analysis

Chemical Shift Measurements of $K\alpha_{1,2}$ Lines Using an In-Air High-Resolution PIXE System

K. Maeda, A. Tonomura, H. Hamanaka,* and K. Hasegawa*

High-resolution PIXE (particle induced X-ray emission) spectroscopy using crystal spectrometers is quite suitable for investigation of the chemical environments of atoms in small amounts of target materials. Recently we have developed a compact crystal spectrometer equipped with a position-sensitive proportional counter (PSPC) for high-resolution PIXE analysis in atmospheric air.[1] Utility of this spectrometer system for *in situ* chemical state analysis was demonstrated by measuring fine structures in $K\beta$ spectra of third period elements.[2]

Although the chemical effects reflected on $K\alpha$ spectra are not so prominent as those on the $K\beta$ spectra, the production cross sections of $K\alpha$ X-rays are one or two orders of magnitude larger than those of $K\beta$ X-rays. Energies of $K\alpha_{1,2}$ line in spectra of chemical compounds differ slightly, e.g. 0-2 eV for third period elements, one from the other. It is expected that chemical state analysis of the minor elements of 10^{-1}-10^{-2}% concentration is possible if the $K\alpha$ line shift can be measured with the precision of ~0.1 eV. We examine here the ability of the in-air high-resolution PIXE system for measurements of chemical shifts of $K\alpha_{1,2}$ lines, taking PIXE spectra of various samples containing Si or P.

Details of the experimental setup are described in the previous papers.[1-3] A target sample was placed in air and bombarded with a 2.1 MeV proton beam of 1 mm × 1.5 mm rectangle. The emitted X-rays were diffracted by a flat analyzing crystal, detected by a PSPC and recorded on a 512 multichannel analyzer. Two laser pointers were set in front of the target for exact target positioning. The sample was set on an Al target holder attached on an X-Y-Z stage. The stage was adjusted so as to converge the two laser beams on the surface of the target.

The chemical shifts of $K\alpha_{1,2}$ lines were measured with respect to the $K\alpha_{1,2}$ line of a reference material. A silicon crystal (c-Si) was used as reference for Si $K\alpha$ and BP powder for P $K\alpha$. PIXE spectra from the sample and reference targets were recorded in succession in order to minimize experimental errors. Measured samples were powders of chemicals of SiC, Si_3N_4, $Ca_3(PO_4)_2$, $CaHPO_4{\cdot}2H_2O$, $Ca(H_2PO_4)_2{\cdot}H_2O$, plates of fused quartz (SiO_2), stainless steel NAS126 (Si 3.5%), duralumin JIS2017 (Si 0.2-0.8%) and GaP, P doped hydrogenated amorphous silicon deposited on quartz substrate (a-Si:H(P), P 0.7%), a fragment of an earthenware of 2500 B. C. (P 0.8%) and a darkened part in the inner bottom of an Al pan.

* College of Engineering, Hosei University

Some of the measured Si $K\alpha_{1,2}$ and P $K\alpha_{1,2}$ spectra are shown in Fig. 1. An InSb(111) crystal was used for Si $K\alpha$ as the analyzing crystal and a Ge(111) crystal for P $K\alpha$. One channel of the PSPC corresponds to 0.106 eV in the region of Si $K\alpha_{1,2}$ and 0.137 eV in the region of P $K\alpha_{1,2}$. As seen in the figure, energy shifts of the $K\alpha_{1,2}$ peak position were clearly observed not only for main components but also for minor components of the order of 10^{-1}%.

The measured chemical shifts of Si $K\alpha_{1,2}$ and P $K\alpha_{1,2}$ lines are listed in Table 1. The precision of measurements (standard deviation) of less than 0.1 eV

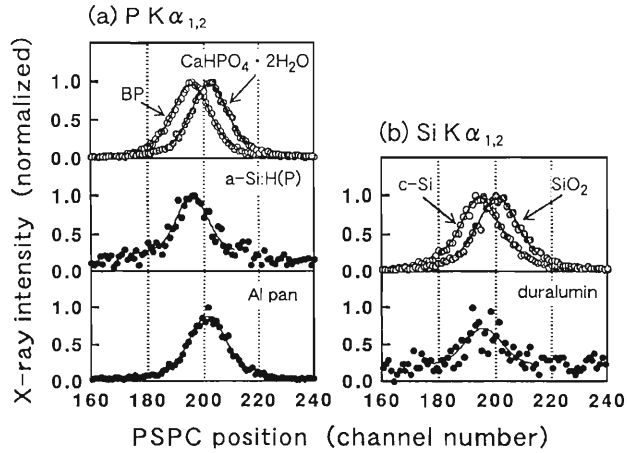

Fig. 1. $K\alpha_{1,2}$ spectra of P and Si.

Table 1. Chemical shift (ΔE) of $K\alpha_{1,2}$ lines. n is the number of measurements and S. D. is the standard deviation. The reference material is c-Si for Si $K\alpha$ and BP for P $K\alpha$.

Element	Sample	n	ΔE (eV)	S. D. (eV)
Si	SiO_2	5	0.68*	±0.09
	Si_3N_4	5	0.47*	±0.05
	SiC	5	0.21*	±0.05
	duralumin (JIS2017)	2	0.14, 0.16	
	steel (NAS126)	2	0.20, 0.26	
P	$Ca_3(PO_4)_2$	4	0.85*	±0.04
	$CaHPO_4{\cdot}2H_2O$	4	0.88	±0.07
	$Ca(H_2PO_4)_2{\cdot}H_2O$	4	0.84*	±0.14
	GaP	8	-0.06*	±0.06
	a-Si:H(P)	4	-0.03	±0.07
	Al pan	4	0.81	±0.06
	earthenware	2	0.82, 0.83	

*The shifts are similar to those obtained by X-ray fluorescence method.[3]

was obtained except for $Ca(H_2PO_4)_2 \cdot H_2O$. This precision is enough for estimation of chemical bonding states of the third period elements. This is, to our knowledge, the first experiment in which the chemical state analysis of minor elements (10^{-1}% order) contained in small amount of samples (10^{-1} mg order) was directly performed in atmospheric air.

References

1) K. Maeda, K. Hasegawa, H. Hamanaka, and K. Ogiwara: Nucl. Instrum. Methods Phys. Res. B **134**, 418 (1998).
2) K. Maeda, K. Hasegawa, H. Hamanaka, and M. Maeda: Nucl. Instrum. Methods Phys. Res. B **136/138**, 994 (1998).
3) K. Maeda, A. Tonomura, H. Hamanaka, and K. Hasegawa: Nucl. Instrum. Methods Phys. Res., in press.

Trace-Element Analysis of Feathers Using PIXE

H. Yoshiki, K. Maeda, A. Tonomura, T. Tsuruda, and H. Higuchi*

It is known that birds molt their feathers every year and remove wastes such as heavy metals through the feathers from the body.[1,2] Therefore, feathers may have any information concerning annual emission of toxic substances to air, water, and land. In this study, we tried to analyze trace elements in feathers using particle induced X-ray emission (PIXE).

Three individuals used in this study and their sampling locations are follows: adult jungle crow (*Corvus macrorhynchos*) in Tokyo; adult bonin petrel (*Pterodroma hypoleuca*) on Haha Jima; adult white's thrush (*Zoothera dauma*) on Haha Jima. The biological data of each species lists in Table 1. After being cleansed with an ultrasonic cleaner in a commercial neutral detergent (Iuchi Seieido Co., Clean Ace S) for 1 h, the feather was bombarded in air by 1.6 MeV proton beam of 3 mm diameter. A Si(Li) solid state detector with 8 μm thick Be window (EG & G Co.) and a graphite sheet with 0.3 mm diameter pinhole (graphite pinhole absorber) or 74 μm thick Al absorber was used to detect the X- rays emitted from the feathers.

Table 2 represents the concentrations of trace elements detected in the feathers. The concentration of each trace element was estimated from the sulfur concentration determined by an ion gas chromatograph, the peak area, and the ratio of X-ray yield. The feathers contained Ca on the order of 10^3 ppm dry weight, Fe and Zn on the order of 10^2 ppm dry weight, Ti and Sr on the order of 10^1 ppm dry weight, and Cu, Pb, Se, Br on the order of 10^0 ppm dry weight except for several data.

Table 1. Biological data of species used as samples.

Species	Distribution and habitat	Food	Total length (cm)	Body weight (g)
Jungle crow	Southeastern Asia, Forests and Cities	Animal carcasses, Garbage, etc.	56.0	600 ~ 750
Bonin petrel	Ogasawara Islands, Sea	Fishes, Cuttle fishes, etc.	30.0	150 ~ 200
White's thrush	Old World, Forests	Earth-worms, Insects, Fruits in forest, etc.	29.5	130

Table 2. Concentrations of trace elements in feathers.

Species	Ca	Ti	Mn	Fe	Ni	Cu	Zn	Se	Br	Sr	Pb
	(ppm dry weight)										
Jungle crow	4500	45	58	240	2	30	400	3	4	31	64
Bonin petrel	400	15	4	150	n.d.	8	51	16	33	12	<4
White's thrush	1200	<6	180	19	n.d.	2	61	1	4	5	<2

There existed significant differences in the concentrations of trace elements in the individual feathers. The jungle crow's feather had higher concentrations of Cu, Zn, and Pb than those in other feathers. In particular, the concentration of Pb was much higher in comparison with other feathers which contained Pb less than minimum detectable concentration. A similar result has been obtained from the analysis of the feathers of birds living in urban and rural areas using an atomic absorption spectrometry.[1] Taking consumption and disposal of many chemical substances around Tokyo into account, these results indicate that the detected trace elements with high concentrations result from man-made pollution.

On the other hand, the feather of the bonin petrel had higher concentrations of Se and Br. It is known that marine products are rich in Se and Br. Since the bonin petrel inhabits the sea and eats fishes and cuttle fishes mainly, these differences seem to originate from food. The differences of concentrations of Ti, Mn, and Fe between the bonin petrel and the white's thrush seem to be related with the life environment such as soil and water. However, since there is no reliable data about the environment of Haha Jima, it is difficult to discuss in detail.

In summary, the usefulness of PIXE was demonstrated for the multi-element analysis in the feathers without any complex pre-treatment. In future, we would like to apply the PIXE analysis of feathers to the evaluation of environmental pollution.

References

1) L. L. Getz, L. B. Best, and M. Prather: Environ. Pollut. **12**, 235 (1977).
2) K. Dmowski and M. A. Karolewski: Ekol. Pol. **27**, 333 (1979).

* School of Agriculture and Life Sciences, University of Tokyo

IV. DEVELOPMENT OF ACCELERATOR FACILITIES

Improvement of Sextupole Magnet for RIKEN 10-GHz ECRIS

M. Kidera, T. Kageyama, T. Nakagawa, J. Fujita, M. Kase, A. Goto, and Y. Yano

The 10-GHz Electron Cyclotron Resonance Ion Source (ECRIS) at RIKEN is used as the injector of AVF cyclotron accelerator.[1] Various heavy ions such as C, N, O, and Ar are produced by this ion source, and are supplied for various experiments. For a long-time operation, a main problem of this source was a lack of stability in the beam intensity. Supply of a stable beam is quite important for better experiments.[2]

In order to improve the performance of this ECRIS we have designed a new sextupole magnet, and installed it in September '98. The maximum strength of the new sextupole magnet is about 1.6 times that of the old one. Cross-sectional view of the new sextupole magnet is shown in Fig. 1. The specifications for the new magnet are described in Ref. 2.

From September to October, the ^{11}B, $^{12,13}C$, ^{14}N, ^{20}Ne, ^{40}Ar, ^{56}Fe, and ^{84}Kr beams were stably supplied from the mew ECRIS for users via AVF. The stability of the ECR plasma has clearly increased. Moreover, the stable beam eased the transportation of extracted beam, because the beam tuning is usually done by monitoring the change of the beam current received by the Faraday-cup in the beam-line. A comparison in the beam intensity before and after the improvement is shown in Table 1. Extracted beam intensity was about 1.5 times greater than the old one for the low charge state, and was about 5 times for the high charge state(Kr^{20+}). The ECR plasma was tuned to supply a specified ion beam for the user for a limited beam time only. Therefore, the beam intensities in Table 1 are not yet optimized for the each charge states of ions.

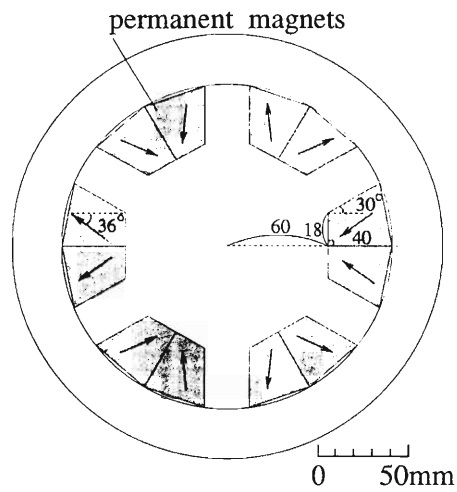

Fig. 1. Cross-sectional view of the new sextupole magnet.

Table 1. Intensity of ion beams from RIKEN 10-GHz ECRIS.

sextupole magnet	$^{11}B^{3+}$	$^{12}C^{4+}$	$^{13}C^{4+}$	$^{14}N^{5+}$	$^{20}Ne^{7+}$	$^{40}Ar^{11+}$	$^{84}Kr^{20+}$
Old type	20	35	35	60	37	20	0.6
New type	36	74	75	135	68	35	3.0

References

1) T. Nakagawa et al.: Jpn. J. Appl. Phys. **32**, 1335 (1993).
2) M. Kidera et al.: RIKEN Accel. Prog. Rep. **31**, 182 (1998).

Off-Centered Compact Duoplasmatron Negative Hydrogen Ion Source with Small Permanent Magnets

H. Tawara, K. Hosaka, and T. Tonuma

Experiments on the electron detachment from H^- ions under collisions with high-energy (MeV/amu) highly-charged ions are under way,[1] and we need a reliable, compact H^- ion source. Generally, negative ions can be obtained either through the double electron capture into positive ions, or by the direct ion extraction from plasma sources. But the qualities of directly extracted beam are known to be much better than those formed by electron capture. The direct extraction of negative ions from electric-discharge plasma sources is always accompanied with an intense electron current which is usually more than three orders of magnitude larger than the extracted H^- ion current (in hydrogen discharge plasmas), requiring a huge extraction power supply for the ion source. Thus it is always a serious problem how to maximize the extracted negative ions and how to simultaneously minimize the loading electron beam current.

The most important processes in H^- ion production in hydrogen plasma sources can be separated into the following three steps:[2] The first step is the process of production of the vibrational excited hydrogen molecules (H_2^*), which requires relatively high energy electrons:

$$e + H_2(v = 0) \rightarrow H_2^*(v). \quad (1)$$

The second step is the process of slow electron attachment onto the vibrationally excited hydrogen molecules $H_2^*(v)$. The cross sections for forming the transient negative hydrogen molecular ions H_2^- (for example at v = 5–6) are known to become large resonantly more than six orders of magnitude than those for the vibrationally ground state molecules:

$$e + H_2^*(v = 5\text{–}6) \rightarrow H_2^-. \quad (2)$$

The third step is the process of dissociation of these resonant state negative hydrogen molecular ions (H_2^-) into the H^- ion plus the ground state H(1s) atom:

$$H_2^- \rightarrow H^- + H(1s). \quad (3)$$

In the present collision experiments, small-scaled negative ion sources with small arc power are more convenient. One of such negative hydrogen ion sources was to use duoplasmatron ion source. It was noted sometime ago that proper displacement of the snout relative to the anode (ion exit) aperture position in the duoplasmatron ion source had resulted in the production of relatively intense H^- ions, while significantly reducing the electron current.[3,4] Now this feature can be understood due to the fact that the $H_2^*(v)$ molecules which are responsible to the production of H^- ions concentrate near the relatively cold, arc-edge region, and that at the arc-center region where the plasma is hot, the positive ions such as protons are dominant.

The present air-cooled, compact off-centered duoplasmatron ion source is shown in Fig. 1, where two small ferrite permanent magnets (each 60 mm diameter and 5 mm thick) are used to focus the arc, flowing out of the snout (intermediate electrode with a 2 mm diameter hole), onto the anode aperture (0.3 mm diameter) made of a 0.5 mm thick Ta plate which is inserted onto a soft iron plate. The maximum arc current which can run on this source is about 0.5 A. Its basic features of construction of the ion source are the same as those described before.[5]

A few parameters can be used to optimize the H^- ion output from the duoplasmatron ion source. One of them, which are most often used, is to change the relative position of the arc from snout against the anode aperture. Most of the observations performed thus far had confirmed that the ratios of the extracted negative ion current to the electron beam current can be maximized: (1) by displacing the arc position relative to the anode aperture, (2) by changing the gas pressure in the ion source and (3) by changing the distance between the snout and the anode aperture. But the most important parameter is the displacement of the snout position relative to the anode aperture. It should be noted that even at the optimum displacement, the ratio of H^- ion current to electron current is a few % at best. It has also been confirmed in the present ion source that the relative

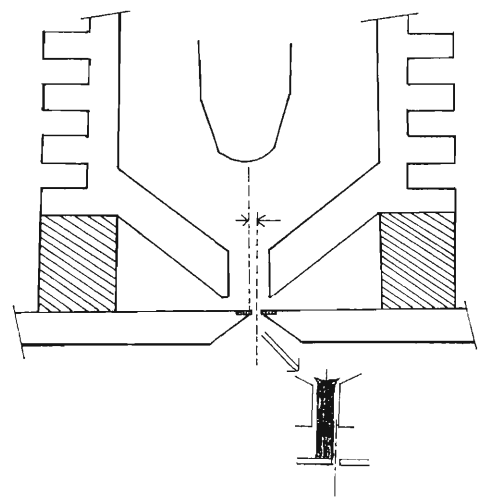

Fig. 1. Schematic of the present off-centered duoplasmatron ion source for producing H^- ions.

position of the arc from snout against the anode aperture is quite sensitive to the H^- ion production, as observed previously. But the movement of the arc or snout during the operation is quite cumbersome and sometimes not reproducible.

Moving the position of the snout is complicated, in particular when the ion source is at a high voltage terminal. We have found that another procedure is more convenient and reproducible. It is to change the arc current, which results in the change of the arc position as well as the arc-column size. This is in principle equivalent to moving the snout. Typical results are shown in Fig. 2, where the H^- ion current is shown as a function of the arc current and also as a function of the gas pressure in the ion source. As seen in Fig. 2(a), as the arc current increases, the drained current increases steadily, meanwhile there is a sharp optimum arc current which is equivalent to an optimum displacement of the snout and at the optimum H^- ion current is enhanced by a factor of roughly 10. Also, some optimum gas pressure in producing H^- ions was found, as seen in Fig. 2(b).

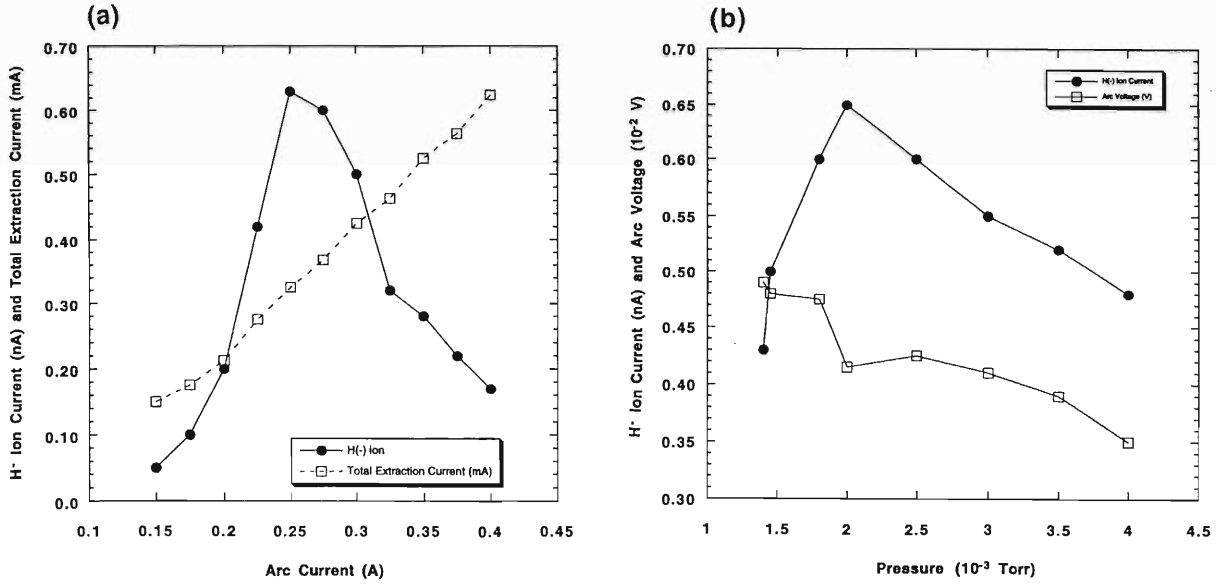

Fig. 2. (a) H^- ion current as a function of the arc current. Also the total drained current (mostly due to the electron current) is shown by dotted line. (b) H^- ion current as a function of the gas pressure in the ion source at a constant arc current. Variation of the arc voltage as a function of pressure is also shown by open squares.

These observed features can be qualitatively understood through our present knowledge of H^- ion production mechanisms described above.[2] Namely, because the electron attachment to the vibrationally excited hydrogen molecules, step (2) process, is strongly enhanced at the low temperature plasma region, the maximum H^- ions are naturally expected to be obtained at the plasma outer edges, instead of the plasma center. Since the electron attachment to the vibrationally excited hydrogen molecules is expected to occur more abundantly near the circular, cold arc edge region, we have also tried to extract H^- ions from multi-apertures (6 holes each 0.15 mm diameter) cocentered with the snout hole along 1 mm radius located on the anode. More ion beam has been extracted but its quality was not always good.

By shifting the snout position toward the anode aperture center, intense proton beam up to 10–50 μA is easily obtainable from this compact duoplasmatron ion source.

References

1) T. Tawara, T. Tonuma, H. Kumagai, T. W. Imai, D. B. Uskov, and L. P. Presnyahkov: Phys. Scripta T, in press.
2) J. M. Wadera and J. N. Bardsley: Phys. Rev. Lett. **41**, 1795 (1978).
3) G. P. Lawrence, R. K. Beauchamp, and J. L. McKibben: Nucl. Instrum. Methods **32**, 357 (1965).
4) L. E. Collins and R. H. Gobbett: Nucl. Instrum. Methods **35**, 277 (1965).
5) H. Tawara, S. Suganomata, and S. Suematsu: Nucl. Instrum. Methods **31**, 353 (1964).

Advanced Acceleration Concept Taking Place in ECRIS (I)

M. G. Niimura, A. Goto, and Y. Yano

For designing the next-step ECR ion sources (ECRIS) that can meet goals in upcoming projects, a profound understanding of the physics taking place inside the source is essential. The so-called third generation ECRIS is required to deliver beams of highly-charged ions (HCI) at ever higher intensity, efficiency, and stability for the high-brightness hadron collider, spallation and/or ECRIS-on-line radioisotope (RI) beam generation, and precision atomic physics data acquisition, respectively.

Answer to the above requirements should be possible if the electron temperatures and their spatial distributions are programmable based on the knowledge of the electron acceleration mechanisms leading to the electron heating. As for this knowledge, however, we are still on a half way at most, since the established theory can not always predict what we observe: e.g., the radially hallow structure in the density as well as temperature distributions of electrons in ECRIS. Throughout the history, the stochastic acceleration (STA) of gyrating electrons has been considered as the only mechanism leading to the electron heating. Naturally, this process should not be all. Because, not all EM-waves propagate in parallel to MMF particularly in a multimode cavity, not all wave elctric fields are of the EM-waves in a plasma medium, and not all electrons are drifting along the magnetic field lines.

We have hence suggested another mechanism called the cross-field acceleration (CFA),[1,2] which we found comlementary to STA. For an example, the abovementioned hallow structure is impossible to explain without a second harmonic ($2\omega_c$) heating for the case of axisymmetric ECRIS. However, the $2\omega_c$ (or $B_{ECR}/2$ resonance) heating should not become obsevable before raising the electron temperature (T_e) above 200 keV or unless $k\rho_L \geq 1.5$, since the heating rates are proportional to the squared Bessel functions: ${J_1}^2(k\rho_L)$ and ${J_o}^2(k\rho_L)$ for the $2\omega_c$ and ω_c heatings, respectively. The authours anticipate that STA alone would not achieve this T_e within the time scale the hollow structure becomes observable.

The CFA can quickly raise T_e of background electrons for STA. It is because CFA has two characteristic features: one is the ability to accelerate cold electrons even those at room temperature, and another is, unlike to the case of STA, the fast process that does not need to wait the slow bouncing period before the next heating takes place.

CFA is the result of an extraordinary (X) wave, propagating perpendicular to the MMF, $\mathbf{B}_{zo}$. X-wave can form regions of compression and rarefaction in electron density, thereby generating ES potentials along the radial (r) direction of propagation. Oscillating ES potential means oscillating longitudinal electric field, E_r^{ES}. This E_r^{ES} and $\mathbf{B}_{zo}$ are cross fields each other, basic configuration for CFA. Figure 1 shows schematic views of the three acceleration mechanisms: Ion Cyclotron, STA, and CFA neglecting the scale of their orbitals. Only the STA and CFA are taking place inside of ECRIS, of course. Unlike the other two, the CFA is an advanced acceleration concept because the strength of acceleration field does not directly depend on the imposing rf-power. It is internally generated together with ES waves by a collective motion of charged particles. Internally generated E_r^{ES} can grow significantly larger than the externally applied rf wave electric field ($E_\perp^{EM}$) by increasing the electron density (n_{el}). [See, Eq. (15)]

For the ion cyclotrons, as is well known, the energy gain per evolution is $Ze\,E_r^{EM}l$ which is constant for a given device. Here, l is the total length of acceleartion gap. For the STA, on the other hand, the gain in the transverse velocity ($\Delta v_\perp$) is constant per evolution. From Fig. 1 we can express

$$\Delta v_\perp = \frac{eE_\perp^{EM}}{m_e} t_e = \frac{E_\perp^{EM}}{B_{zo}} \omega_c t_e. \qquad (1)$$

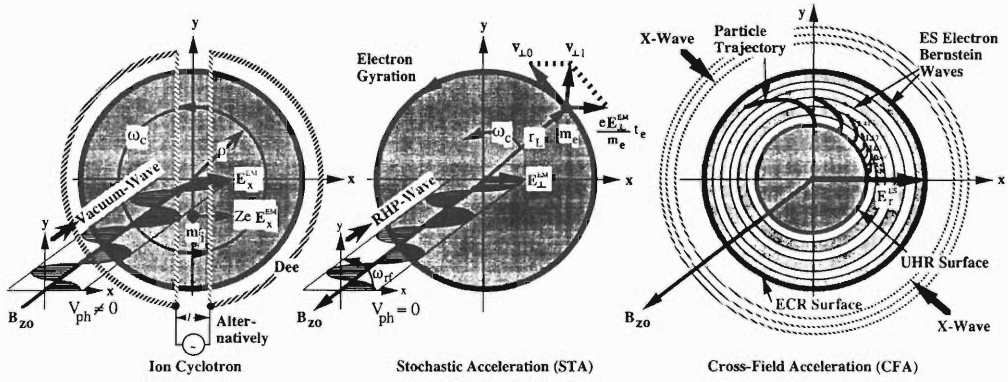

Fig. 1. Acceleration mechanisms taking place in ECRIS, to be compared with ion cyclotron accelerator.

Table 1. Difference and similarity of three acceleration mechanisms.

Accelerators:	Cyclotron Accelerator:	Stochastic Accelerator (STA):	Cross-Field Accelerator (CFA):
Imposed RF Waves:	Vacuum-Wave (High Cavity-Q)	RHP-Wave (Low Cavity-Q)	X-Wave (Low Cavity-Q)
Wave Electric Fields:	Linearly Polarized, E_x^{EM}	Circularly Polarized Field, $E_\perp^{EM}$	ES-Radial Field, E_r^{ES}
Direction of Propagation:	$\mathbf{k}//\mathbf{B}_{zo}$	$\mathbf{k}//\mathbf{B}_{zo}$	$\mathbf{k}\perp\mathbf{B}_{zo}$
Motion of Particle:	Force: $e\,E_x^{EM}$ (Spiral across $\mathbf{B}_{zo}$)	Force: $e\,E_\perp^{EM}$ (Gyration around $\mathbf{B}_{zo}$)	Force: $e(\mathbf{v}_{ph}\times\mathbf{B}_{zo})$ (Spiral across $\mathbf{B}_{zo}$)
Drift during Acceleration	No drift during azimuthal acceleration	Axial drift during gyration acceleration	Radial drift during azimuthal acceleration

When an electron gyrates synchronously with $E_\perp^{EM}$ of the right-hand polarized (RHP) wave [See, Table 1], the effective interaction time (t_c) is $2\pi/\omega_c$ per evolution. Then, Eq. (1) gives the velocity gain:

$$\Delta v_\perp = 2\pi\frac{E_\perp^{EM}}{B_{zo}} \quad \text{per evolution.} \tag{2}$$

Since $E_r^{EM} \sim 30$ kV/m and $B_{zo} \sim 0.5$ T typically, Eq. (2) gives $\Delta v_\perp = 3.76\times10^5$ m/s per evolution. However, notice that $\Delta v_\perp = 0$ if B_{zo} is uniform and if the parallel drift velocity ($v_{//}$) is much faster than the phase velocity of EM-wave, i.e., if $v_{//} \gg \omega/k$. Another difficulty for STA to explain $2\omega_c$ heating or hollow structure.

We have extended our previous works[2] treating the problem of CFA by mathematically-rigorous and fully-relativistic manners.

We have investigated the collective electron motion when perturbed by the rf-field $\mathbf{E}_{1r}(\equiv E_r^{ES})$ of X-wave ($\mathbf{E}_{1r} \perp \mathbf{B}_{zo}$). Such a system may be described by a set of the linearlized fluid equations in cylindrical coordinates:

$$-i\omega m v_{1r} = -eE_{1r} - ev_{1\theta}B_{zo} \tag{3}$$

$$-i\omega m v_{1\theta} = -ev_{1r}B_{zo} \tag{4}$$

$$-i\omega m v_{1z} = 0 \tag{5}$$

$$-i\omega n_{el} = -ik\cdot n_{eo}v_{1r} \quad (\dot{n}_e = -n_e\nabla\cdot\mathbf{v}) \tag{6}$$

$$i\mathbf{k}\cdot\varepsilon_o\mathbf{E}_{1r} = -en_{el} \quad (\nabla\cdot\mathbf{D} = \rho) \tag{7}$$

Here, the suffixes zero ($_0$) and one ($_1$) indicate the equilibrium and perturbed quantities, respectively. Perturbed electron density is thus in the form: $n_{el} = \hat{n}_{el}e^{i(kr-\omega t)}$. Equations (6) and (7) tell that the propagation direction of ES-waves is 1D or $k_\theta = k_z = 0$ when $\mathbf{E}_1 = E_{1r}\hat{\mathbf{r}}$ is the only driving field considered.

Substitution of the $v_{1\theta}$ of Eq. (4) into Eq. (3) gives $v_{1r} = (eE_{1r}/im\omega)(1-\omega_c^2/\omega^2)^{-1}$, with which Eq. (6) yields:

$$n_{el} = \frac{k}{\omega}n_{eo}\frac{eE_{1}r/im\omega}{1-\omega_c^2/\omega^2}, \quad (\omega/k = V_{ph}). \tag{8}$$

Substitution of Eq. (8) into Eq. (7) tells us that the system oscillates at the upper hybrid resonance (UHR) frequency

$$\omega = \omega_h \equiv (\omega_{po}^2+\omega_c^2)^{1/2}, \tag{9}$$

where $\omega_{po} \equiv \sqrt{n_{eo}e^2/\varepsilon_o m}$ and $\omega_c \equiv eB_{zo}/m_e$ of plasma.

In order to investigate the relativistically accelerated 2D-motion of electrons under the cross-field condition, we rewrite Eqs. (3) and (4) back to the original forms:

$$\frac{dv_{1r}}{dt} = -\frac{e}{\gamma m_o}[E_{1r}+v_{1\theta}\times B_{zo}] \tag{10}$$

$$\frac{dv_{1\theta}}{dt} = -\frac{e}{\gamma m_o}[-v_{1r}\times B_{zo}] \tag{11}$$

$$\gamma \equiv 1/\sqrt{1-\beta_r^2-\beta_\theta^2}, \quad (\beta_r \equiv \frac{v_{1r}}{c},\ \beta_\theta \equiv \frac{v_{1\theta}}{c}). \tag{12}$$

Now, we imagine a radially-moving frame moving at the phase velocity V_{ph}, where variables are expressed by the prime ($'$) mark. Then, the particles are rest in the r-direction or $v_{1r}' = 0$. Since, $r' = \gamma_{ph}(r - V_{ph}t)$ by Lorentz transform, we have $v_{1r}' = \gamma_{ph}(v_{1r} - V_{ph}) = 0$ and thus obtain $v_{1r} = V_{ph}$ in Eq. (11). Here, $\gamma_{ph} \equiv 1/\sqrt{1-\beta_{ph}^2}$ and $\beta_{ph} \equiv V_{ph}/c$. Equation (11) gives azimuthal electric field, along the wave front:

$$\mathbf{E}_\theta \equiv -\mathbf{v}_{1r}\times\mathbf{B}_{zo} = -V_{ph}B_{zo}\hat{\theta} \tag{13}$$

Integration of Eq. (11) gives $\mathbf{v}_{1\theta}'$ in the moving frame:

$$\mathbf{v}_{1\theta}' = V_{ph}\omega_c^*t',\ \omega_c^* \equiv \frac{\omega_c}{\gamma},\ t' = \gamma_{ph}\left(t - \frac{V_p r}{c^2}\right) \tag{14}$$

However, $\mathbf{v}_{1\theta}' = \mathbf{v}_{1\theta}$ because the frame is moving only in the r-direction, and $t' \approx \gamma_{ph}t$ if $t \gg 0.3$ ns, because $r/c \le 0.3$ ns in our geometry and because $V_{ph}/c \le 1$ always.

Now that we know $\omega_h/k = V_{ph}$, Eq. (8) can be used to obtain the amplitude of ES drive wave $E_{1r} = \hat{E}_{1r}e^{i(kr-\omega t+\frac{\pi}{2})}$:

$$-i\hat{E}_{1r} = \frac{\hat{n}_{el}}{n_{eo}}\frac{m\omega_{po}V_{ph}}{e}\left[1+\frac{\omega_c^2}{\omega_p^2}\right]^{-1/2} \tag{15}$$

Here we used Eq. (9) for ω, and $\hat{n}_{el}/n_{eo} \equiv \delta$ is the fraction of the electron density participating the longitudinal oscillation. Notice that the phase of E_{1r} is advanced by $\pi/2$ against the wave-potential, $\phi = -\int eE_{1r}dr = -(\lambda/2)eE_{1r}$.

Since general operation condition of ECRIS is $\omega_c \sim \omega_p \sim \omega_{rf}$, one can evaluate Eq. (15) in the form:

$$\hat{E}_{1r} \cong \frac{\delta}{\sqrt{2}}\frac{m\omega_{po}V_{ph}}{e} \cong 2.26\ \delta V_{ph}, \tag{16}$$

if $n_e \cong 10^{12}$ cm^{-3}. The value of V_{ph} can grow by the background electron temperature according to the dispersion relation of Bn-waves.[3] For the Case 1 of Fig. 2 in Part II we have $V_{ph} = 6.47\times10^7$ m/s, with which Eq. (16) gives

$$\hat{E}_{1r} \cong 1.46\delta\times10^8\ \text{V/m} = 146\delta\ \text{MV/m}. \tag{17}$$

Therefore, the internally generated $\hat{E}_{1r}$ is much bigger than the externally imposed rf field (= 23 kV/m for Minimafios) when $\delta \sim 0.01\%$ or larger.

References

1) K. S. Golovanivsky: Rev. Sci. Instrum. **63**, 2886 (1992).
2) M. Niimura: Int. Workshop on ECRIS, **INS-J-182**, 141 (1995); also, *ECRIS-13th*, Texas, p. 52 (1997).
3) I. Bernstein: Phys. Rev. **109**, 10 (1958).

Advanced Acceleration Concept Taking Place in ECRIS (II)

M. G. Niimura, A. Goto, and Y. Yano

Mechanism of detrapping: Using the notations of (I), the radial force exerting on a trapped electron can be expressed by $F'_{lr} = -e(E_{lr} + v_{l\theta}'B_{zo})$, and Lorentz transform for the phase of $E_{1r} \equiv \hat{E}_{lr}\cos(kr - \omega t + \pi/2)$ is given by $kr - \omega t + \pi/2 = kr'/\gamma_{ph} + (kV_{ph} - \omega)t' + \pi/2 = kr'/\gamma_{ph} + \pi/2$. Then, using the $v_{l\theta}'$ given by Eq. (14) in (I), we have

$$F'_r = -e\left[-\hat{E}_{lr}\sin\frac{kr'}{\gamma_{ph}} + V_{ph}B_{zo}\omega_c^* t'\right]. \quad (1)$$

The first term of Eq. (1) is the drive field, which can accelerate the electrons trapped inside the space where $\mathbf{E}_{lr} \leq 0$ or $-\sin kr'/\gamma_p \leq 0$ towards the positive r-direction. However, the second term is a deceleration field: $-\mathbf{E}_{1r} \equiv \mathbf{v}_{1\theta}' \times \mathbf{B}_{zo}$. Therefore, as the time passes, not only the $|F'_{lr}|$ but also the radial size where $\mathbf{E}_{1r} \leq 0$ decreases [Fig. 1], thereby detrapping some of electrons from the beginning ($t \geq 0$). Namely, all particles will be detrapped if

$$\hat{E}_{lr} \leq \gamma_{ph}V_{ph}B_{zo}\omega_c^* t, \quad (0.3\ \text{ns} \ll t \leq t_o) \quad (2)$$

and the time of detrapping is given by

$$t_o = \frac{\hat{E}_{lr}}{\gamma_{ph}V_{ph}B_{zo}\omega_c^*}. \quad (3)$$

Since $c \geq V_{ph}$ and $t \geq 1/\omega_c$, if $\hat{E}_{lr}$ is large enough to satisfy

$$\hat{E}_{lr} \geq \gamma_{ph}cB_{zo} \geq \gamma_{ph}V_{ph}B_{zo}\omega_c^* t, \quad (4)$$

then once trapped particles will never be detrapped before reaching the ECR-zone from inside.

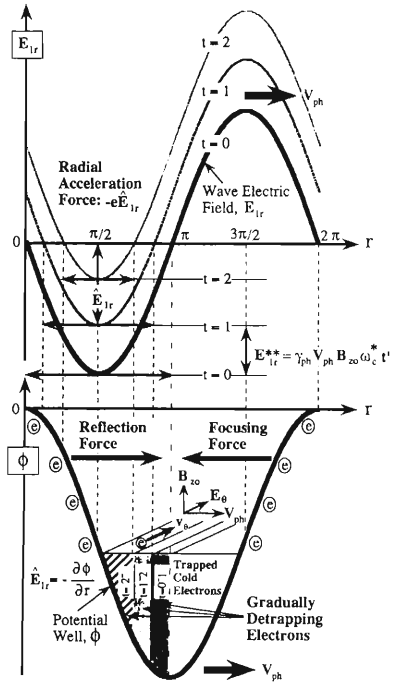

Fig. 1. Detrapping dynamics of wave-trapped electrons.

Figure 1 illustrates the dynamics of the particle detrapping, step by step: Oscillation in electron density creates an ES potential (ϕ) wave, which can trap cold electrons whose energy $\varepsilon \leq \phi = -(\lambda/2)eE_{lr}$. Due to the finite thermal energy of trapped electrons and due to the focusing force of potential-well, only the domain $[\pi/2, \pi]$ is considered as the useful phase. In the frame moving with V_{ph}, trapped electrons feel a dc azimuthal electric field $E_\theta = (V_{ph} \times B_{zo})/(-e)$ which accelerates them along the wave-front. However, a radially deceleration field, $-\mathbf{E}_{1r}$, is generated because of the V_{ph}. Because this $-\mathbf{E}_{1r} \equiv E_{lr}^{**}$ in Fig. 1 and $E_{lr}^{**} = -V_{ph}B_{zo}\omega_c^* t'$ from the second term of Eq. (1), the magnitude grows linearly with time ($t = 0, 1, 2, \ldots$). Consequently, as seen from Fig. 1, the radial domain where $\mathbf{E}_{1r} \leq 0$ as well as the magnitude $|F'_{lr}|$ decreases gradually, thereby detrapping the trapped-electrons in the layer marked by $t = 0 \sim 1$ first, and $t = 1 \sim 2$ next, followed by the layer $t = 2 \sim$.

Skipping the mathematical details, here we will explain only what happens for trapped electrons during the transient phase before the trapped particles can reach the ECR zone. Figure 2 displays total 9-trips of the longitudinal waves being launched from the UHR-surface. The very first trajectory had $t_o = 0.123$ ns. The numbers indicate the V_{ph} of the ES wave deduced from dispersion relation of the electron Bernstein (Bn) wave. This is a single particle simulation, where r'(coordinates from the origin of moving frame) $= 0$. Trajectory of a trapped electron is governed by the set of equations:

$$r(t) = V_{ph}t + r'/\gamma_{ph} + r_{UHR} \quad (5)$$

$$\theta_s(t) = V_{ph}\omega_c^* t^2/2r + \theta_{s-1}. \quad (6)$$

The figure plots the 2D-positions of a trapped-electron by the time-step of $T_c/10$ or of $\tau \equiv t/T_c = 0.1, 0.2, \ldots$, till the detrapping time t_o. After each trip, the new values of $\hat{E}_{lr}$, t_o, and V_{ph} were re-calculated with the new T_c resulted.

Forced detrapping on ECR-surfaces at ω_c, $2\omega_c$,

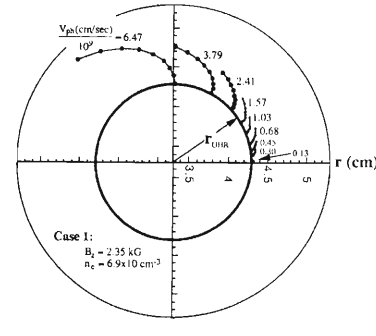

Fig. 2. Trajectories of trapped electrons for increasing V_{ph}.

...: Let us consider the case of strong-$\hat{E}_{lr}$, so that the detrapping radius (r_o) exceeds the ECR radius: i.e., $r_o \equiv \Delta r_o + r_{UHR} \geq r_{ECR}$, since we define: $\Delta r_o \equiv r_o - r_{UHR}$. In this case, $\hat{E}_{lr}$ is forced to decay at $r = r_{ECR}$ because there Bn-waves can satisfy the resonance ($V_{ph} = 0$) condition: $\omega_{Bn} = \omega_c^{ECR}/q$, where $q = 1, 2, ...$ These particles have experienced the maximum acceleration time, until the forced detrap at $r = r_{ECR}$, given by

$$t_{max} = \frac{r_{ECR} - r_{UHR}}{V_{ph}} \quad (\hat{E}_{lr} \gg \gamma_{ph} B_{zo} \omega_c^* \Delta r_{ECR}) \tag{7}$$

Since $v_{l\theta} = V_{ph}\omega_c^* t$ from Eq. (14) in (I), we have at $t = t_{max}$

$$v_{l\theta}^{max} \equiv V_{ph}\omega_c^* t_{max} = \omega_c^* \Delta r_{ECR}, \tag{8}$$

where $\Delta r_{ECR} \equiv r_{ECR} - r_{UHR}$. The kinetic energy at shell is

$$W_\theta^{max} = \frac{1}{2} m^* (\omega_c^* \Delta r_{ECR})^2 = \frac{m_o}{2\gamma} (\omega_c \Delta r_{ECR})^2. \tag{9}$$

Thus, we obtain a formula for the shell energy calculation:

$$\gamma_\theta^o - 1 = \frac{W_\theta^{max}}{m_o c^2} = \frac{1}{2} \frac{(eB_{zo}/m_o)^2}{\gamma c^2} (\Delta r_{ECR})^2 \tag{10}$$

Here, the γ is given by Eq. (12) in (I), and obviouly $\gamma \cong \gamma_\theta$ for the present case. Since $\beta_\theta = v_{l\theta}^{max}/c \cong omega_c \Delta r_{ECR}/\gamma_\theta$, we have $\gamma_\theta = \sqrt{1 + (\omega_c \Delta r_{ECR})^2/c^2}$. Therefore, Eq. (10) can be written as

$$\gamma_\theta^o - 1 = \frac{W_\theta^{max}}{m_o c^2} = \frac{1}{2c} \frac{(\omega_c \Delta r_{ECR})^2}{\sqrt{c^2 + (\omega_c \Delta r_{ECR})^2}}. \tag{11}$$

This gives a convenient formula to calculate W_θ^{max} (keV):

$$W_\theta^{max} = \frac{8.79 \times 10^{-5} B_{zo}^2(G)(\Delta r_{ECR})^2}{\sqrt{1 + 3.43 \times 10^{-7} B_{zo}^2(G)(\Delta r_{ECR})^2}} \tag{12}$$

Here, we take B_{zo}(G) in Gauss unit and Δr_{ECR} in cm. Equation (12) was evaluated for three different cases listed in Table 1. These 3-cases are when the acceleration length (Δr) is equal to $\Delta r_{ECR} = 0.4$ cm.

Figure 3 plots Eq. (12) for different Δr_{ECR}. It is seen that W_θ increases quadratically with B_{zo} in the beginning, but increases linearly later for a large B_{zo}. $W_\theta = 1$ MeV is found possible from Fig. 3 if $B_{zo} = 3$ kG and $\Delta r_{ECR} = 2.5$ cm.

It is interesting to find that Eq. (9) is in the form:

Table 1. Hot electron energy W_θ at the shell for three cases.

	Case 1	Case 2	Case 3
B_{zo} (kG) in the core:	2.35	3.41	3.50
ω_c(rad/s) in the core:	4.14×10^{10}	6.0×10^{10}	6.16×10^{10}
n_e(cm^{-3}) in the core:	6.9×10^{11}	1.1×10^{11}	4.8×10^{10}
ω_c/ω_u in the core:	0.88	3.21	4.96
V_{ph}^o(cm/sec) initial:	1.31×10^8	1.35×10^9	2.10×10^9
W_θ (keV) at Δr =0.4 cm:	68	128	133

Here: $v_{th}^o = 4.2 \times 10^8$ (cm/s), $\omega_{rf}^2 = \omega_h^2 \equiv \omega_c^2 + \omega_p^2 = 2\pi \times 10^{10}$

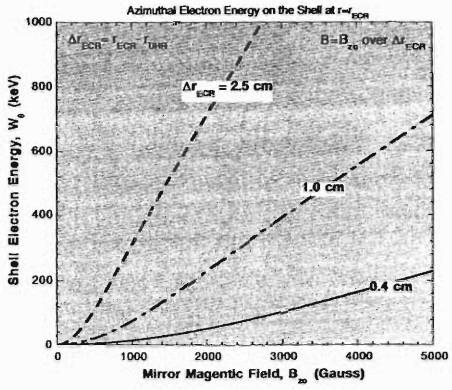

Fig. 3. Hot electron energy on the ECR-surface as a function of the MMF, B_{zo}.

$$W_\theta^{max} = \frac{1}{2m^*} (eB_{zo}\Delta r_{ECR})^2 \equiv \frac{p^2}{2m^*} \tag{13}$$

and $p \equiv eB_{zo}\Delta r_{ECR}$. Since the magnetic rigidity is equal to a relativistic momentum, i.e., $eB_{zo}\Delta r_{ECR} = \gamma mv$, Eq. (13) is a relativistically valid formula. CFA has the same formula as the ion cyclotron to determine energy provided that $\Delta r_{ECR} \equiv r_{ECR} - r_{UHR}$ is used rather than the radius (r) itself for the magnetic rigidity.

CFA mechanism can explain the formation of a closed-shell (ring) and discrete spots of hot electrons for the axisymmetric (or radially max-B_{zo}) ECRIS and non-axisymmetric (min-B) ECRIS, respectively. In the axisymmetric case, only the $2\omega_c$ surface is resonant for radially expanding cyclindrical waves, thereby creating a single hot-electron ring on the midplane (where $\mathbf{B}_{zo} \perp \nabla \mathbf{B}_{zo}$) eventually due to a restoring force of the inflated line of force of MMF there. In the min-B case, the ω_c surface is not always a circle but often follows the multi-cusp geometry, to which cylindrical waves are expanding. Then, the contact points of the wavefront and ω_c surface are discrete spots, not a ting, as observed.[1)]

Cnclusions are: (1) Expression of the longitudinal wave electric field valid under B_{zo} was derived, (2) Detrapping dynamics was clarified, (3) The resonantly detrapped electron energy was formulated relativistically for the first time; (4) Most significantly, strong B_{zo} was found to heat up the hot electrons effectively.

If hot electrons form a ring and if its current is large, the diamagnetism depletes the B_{zo} field inside of it: then cooling of hot electron ring starts and all other parameters start oscillating.[2)] Presence of a hot electron ring surrounding ECR-zone in the mid-plane means an extra space charge, creating a deeper and wider potential well. Axial e-beam injection seems to enhance this effect.[3)]

References

1) J. Vamosi et al.: *ECRIS-13th*, Texas, p. 206 (1997).
2) M. Lamoureux et al.: *ECRIS-13th*, Texas, p. 67 (1997).
3) T. Nakagawa: private communication.

Model Study of a Resonator for Flat-Top Acceleration System in the RIKEN AVF Cyclotron

S. Kohara, O. Kamigaito, M. Kase, E. Ikezawa, Y. Miyazawa, T. Chiba, and A. Goto

A full-scale model of the flat-top resonator to be used for a flat-top acceleration system in the RIKEN AVF Cyclotron was fabricated, and was coupled to the existing main resonator in order to verify the design.[1,2] The flat-top accelerating voltage is generated by a superimposition of the fundamental-frequency and 5th-harmonic-frequency voltages. The flat-top resonator is used to generate the 5th-harmonic-frequency voltage. The fundamental-frequency voltage is generated by the main resonator. The fundamental-frequency range is from 12 to 23 MHz. Due to the 5th-harmonic-frequency the frequency range is required to be from 60 to 115 MHz. Result of the cold model test performed with the flat-top acceleration system is described in this report.[3]

The cross-sectional views of the main resonator and flat-top resonator are shown in Fig. 1. The flat-top resonator shown inside the square of dashed line is designed to be a coaxial resonator with a movable shorting plate, and is coupled with the main resonator shown in the left hand side of Fig. 1 via the coupling capacitor (Cc). A photograph of the flat-top resonator prototype installed on the existing main resonator is shown in Fig. 2.

In the cold model test, the resonant frequency of 5th-harmonic voltage was measured to see if the required frequency range can be achieved. In the measurement,

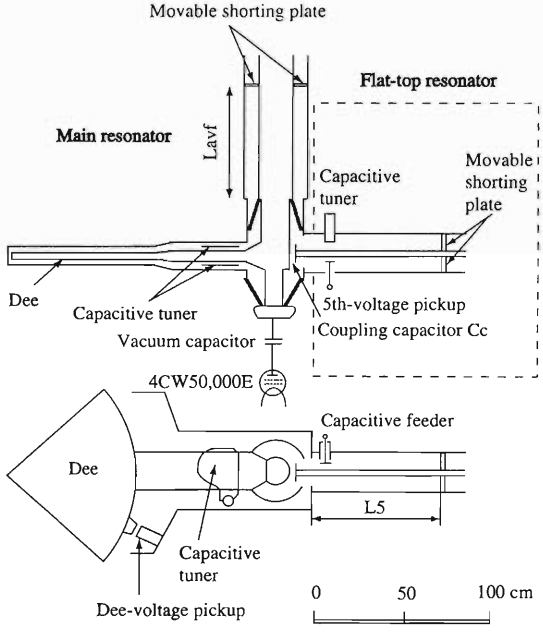

Fig. 1. Cross-sectional view of the resonators of flat-top acceleration system for the RIKEN AVF Cyclotron.

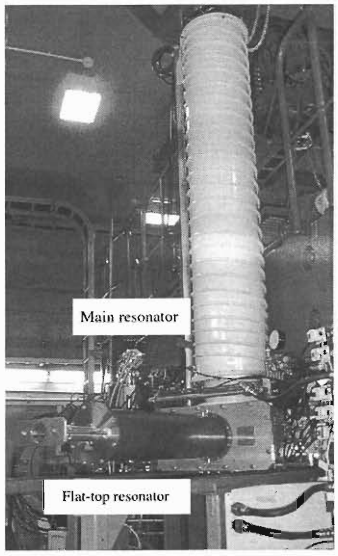

Fig. 2. Photograph of the model flat-top resonator installed on the existing main resonator.

both the coupling capacitor (Cc) and the movable shorting plate of flat-top resonator (L5) were adjusted after the movable shorting plate of main resonator (Lavf) was set for the fundamental frequency. In this case, the 5th-harmonic-frequency signal was fed into the flat-top resonator through the voltage pick-up of 5th-harmonic frequency and was monitored by the dee-

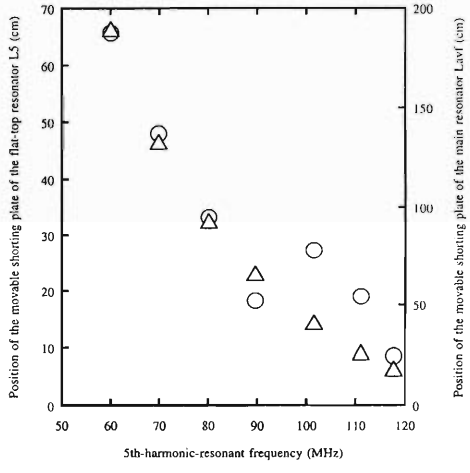

Fig. 3. Positions of the movable shorting plates of the flat-top and main resonators as a function of the 5th-harmonic resonant frequency. The capacitance of the coupling capacitor (Cc) was 16 pF. Circles represent the position of the shorting plate of the flat-top resonator. Triangles represent the position of the shorting plate of the main resonator.

voltage pickup. It was found that the 5th-harmonic-resonant frequency was successfully generated on the dee in the whole required frequency-range along with the fundamental-resonant frequency. The measured positions of the movable shorting plates of the flat-top and main resonators are shown in Fig. 3 as a functio of the 5th-harmonic-resonant frequency. This result gives the specifications of flat-top resonator, which proves achievement of the required frequency range. The moving distance of shorting plate and the length of resonator should be at least 57 and 66 cm, respectively, when the coupling capacitance (Cc) is set to be 16 pF. The measured 5th-harmonic-resonant frequency was found to be very close to the frequency 5 times as large as the fundamental frequency. The measured Q-values of the fundamental and 5th-harmonic modes as a function of the resonant frequency are shown in Fig. 4 (a) and (b), respectively. The measured Q-value (Q1) of the fundamental mode was found to vary from 1500 to 2400, while the measured Q-value (Q5) of the 5th-harmonic mode was from 300 to 740.

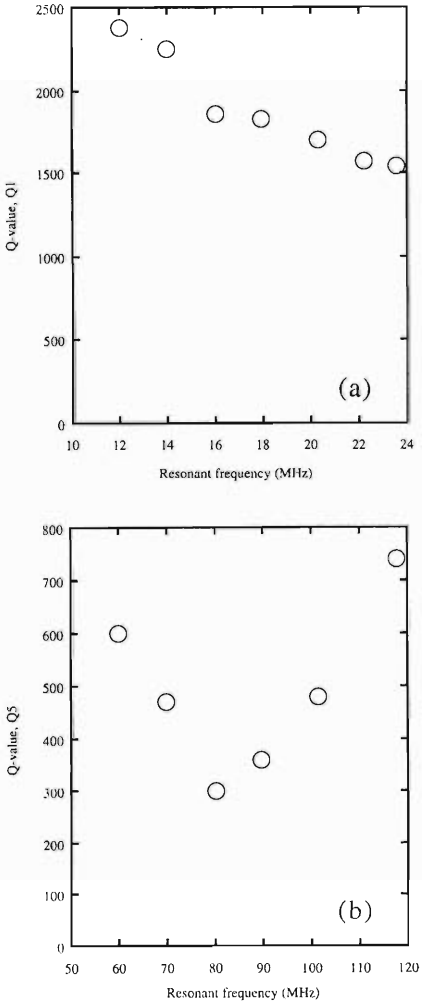

Fig. 4. (a) Q-value of the fundamental mode as a function of the resonant frequency. (b) Q-value of the 5th-harmonic mode as a function of the resonant frequency.

In the cold model test, the flat-top accelerating voltage was generated by feeding low-level signals of the fundamental and 5th-harmonic frequencies at the same time. In this case, the fundamental-frequency signal was fed into the resonator through the vacuum capacitor, while the 5th-harmonic-frequency signal was fed into the resonator through the capacitive feeder of the flat-top resonator. The flat-top accelerating voltage generated on the dee was measured by the dee-voltage pickup. The amplitude and phase of the 5th-harmonic-frequency signal were adjusted to obtain the flat-top voltage on the dee after those of the fundamental-frequency signal were fixed. It was found that the flat-top voltage can be generated in the whole frequency range. The typical wave form of the flat-top voltage is shown in Fig. 5. Design of the real resonator is under progress.

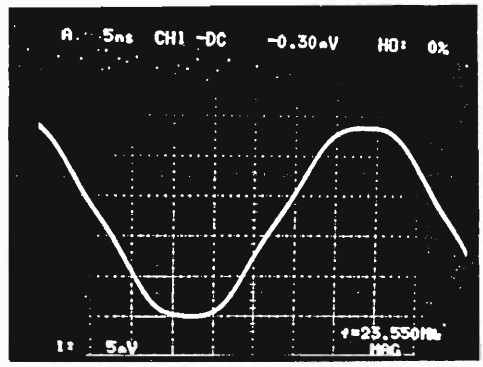

Fig. 5. Typical wave form of the flat-top voltage measured by the dee-voltage pickup. The fundamental frequency was 23.55 MHz and the 5th-harmonic frequency was 117.75 MHz. Horizontal time scale: 5 ns/div., Vertical voltage scale: 5 mV/div.

References

1) S. Kohara et al.: Proc. 11th Symp. on Accelerator Science and Technology, Harima, p. 194 (1997).
2) S. Kohara et al.: RIKEN Accel. Prog. Rep. **31**, 198 (1998).
3) S. Kohara et al.: Proc. 15th Int. Conf. on Cyclotrons and Their Applications, to be published.

Measurement of the Pumping Speed and Pumping Capacity for Photon Detection System

K. Ikegami, D. Wu, and M. Wakasugi

The pumping speed and pumping capacities of a photon detector[1] were measured. The photon detector (PD) in question is the one developed to measure the atomic transition energy precisely in the high-energy and highly-charged ion beams. Technology of a cryopump was applied for this detector to reduce the background produced by collisions between the ion beam and residual gas. This detector has two cylinders inside the vacuum chamber as shown in Fig. 1. The inner cylinder was made of copper and painted black, and charcoal chips were pasted at its central region. The inner cylinder was connected to the second stage of refrigerator of the cryopump and was cooled down to 18 K. The size of the inner cylinder was 112 mm in inner diameter and 960 mm in length. The outer cylinder is a heat shield to protect the inner cylinder from any thermal radiation. Diameter of the outer cylinder was 150 mm. This was also painted black and cooled down to 80 K by connecting it to the first stage of refrigerator. These cylinders have 22 holes at the detection region in order to mount ten photon-counting units (two holes for each unit) and two vacuum gauges. The total radiation power on the surface of the inner cylinder was estimated to be 9.5 W. The refrigerator has a cooling capacity of 10.5 W for the second stage at 18 K and of 68 W for the first stage at 80 K.

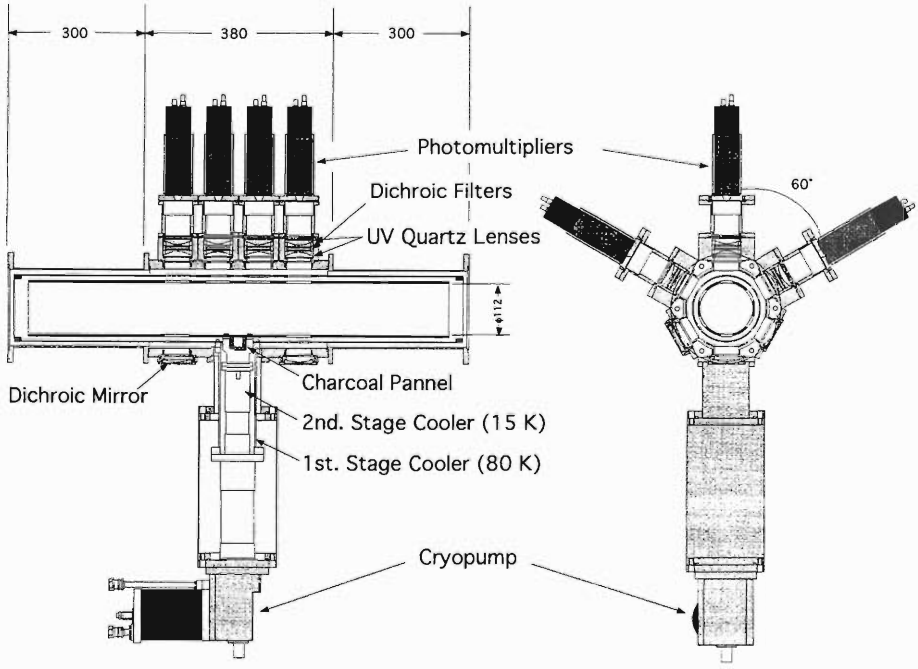

Fig. 1. The photon detector.

One side port of the PD was connected to a calibrated gas flow controller and another side port was to a turbo-molecular pump through a valve. To measure the characteristics of performance of the PD we first evacuated the detector with the turbo-molecular pump and then started a cryopump.

The cool down time of the second stage to 17 K was 7 hours as shown in Fig. 2, while the pressure was below 1.8×10^{-6} Pa. After closing the valve the pumping speed of cryopump was determined from the pressure and gas flow rate. The measured pumping speeds for nitrogen and hydrogen were 7×10^5 l/sec and 80 l/sec, respectively.

We have also measured the pumping capacities for nitrogen and hydrogen keeping the flow rate of gases constant. In the case of nitrogen, after keeping a constant flow rate of 9.52×10^{-6} m^{3}Pa/sec for 195 hours, pressure and temperature rose slowly at first and rapidly later. Figures 3 and 4 show the changes of temperature and pressure with time when nitrogen gas was admitted at a constant flow rate. Pumping capacity for nitrogen was estimated to be 6.7 m^{3}Pa. In the

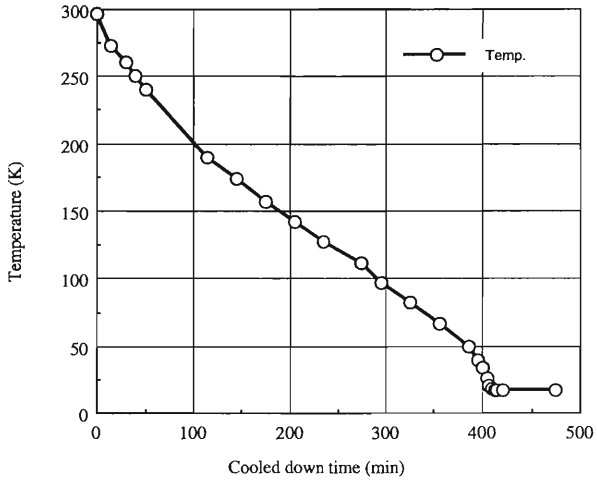

Fig. 2. The cool down time of the second stage for the photon detector.

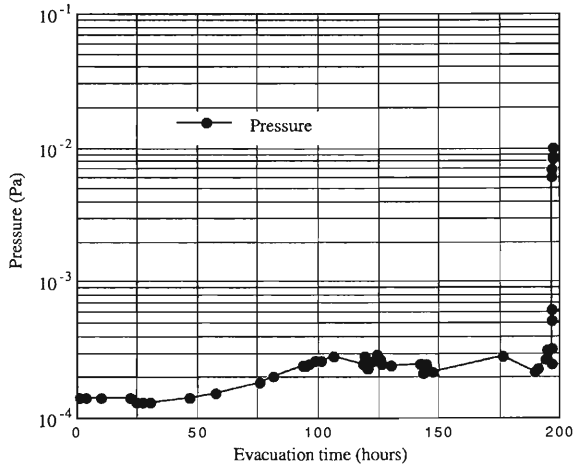

Fig. 3. Pressure rise with time when nitrogen was admitted at a constant flow rate.

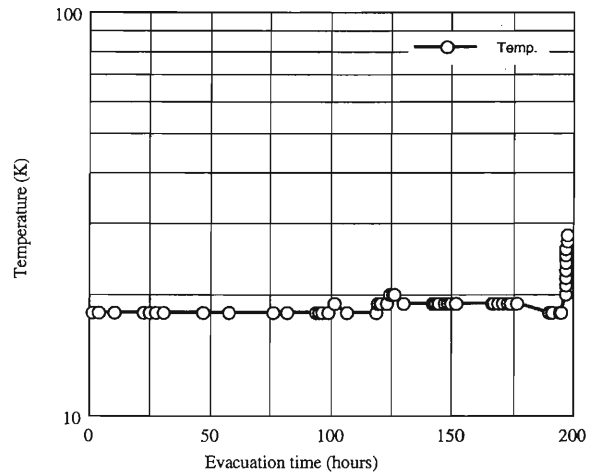

Fig. 4. Temperature rise with time when nitrogen was admitted at a constant flow rate.

case of hydrogen, after keeping a constant flow rate of 3.33×10^{-8} m^3Pa/sec for 240 minutes, the pumping capacity was estimated to be 2.6×10^{-4} m^3Pa.

The pumping speed and pumping capacity of the hydrogen were much smaller than those of the nitrogen gas due to a small amount of activated charcoal chips pasted. Nevertheless, it was found sufficient to keep the operating pressure of order of 10^{-6} Pa for 2 or 3 weeks (in the case of long machine time). Because, in general, the main component of residual gases in the unbaked chamber is the water vapor.

If hydrogen is assumed to be the main component of residual gases at the pressure of 5×10^{-6} Pa, we can expect that the pressure can be kept constant for more than 3000 hours.

References

1) M. Wakasugi et al.: Nucl. Instrum. Methods Phys. Res. A **419**, 50 (1998).

Present Status of RIKEN Microbeam Project

N. Fukunishi, M. Kobayashi, A. Yoneda, M. Kase, and Y. Yano

We have made several researches to realize a heavy-ion microbeam which is a new powerful tool in biophysics. To start with the project, we chose a beam collimation method for the purpose to produce a heavy-ion microbeam. In this method, we inserted a very fine collimator just before a target and ideally speaking, a very small part of the beam should have passed through the collimator before hitting the target. We tried this method, but failed to obtain a fine beam. The heavy ions scattered from the collimator might have worsen the beam quality. Thus, we have tried an alternative method as follows.

We employed an energy degrader with a very small hole instead of a collimator. Some heavy ions will lose their energies here, but a few ions may pass through the hole without losing energies. We separate the energy-lowered ions by using the slits inserted on the dispersive focal point of the beam course. The ions which passed through the hole are collected on the target. The energy degrader and the slits are inserted in the upper stream of the beam course (Fig. 1), and therefore the scattered ions will give little effect on the target. The size of the beam is determined by the size of the hole times the magnification factor of the beam transport system.

We made an experiment to testify the effectiveness of the method. We chose a 80 μm-thick Cu foil as the energy degrader, which had many holes (see Fig. 2). The diameter of the hole was 100 μm. The 135 MeV/nucleon $^{20}Ne^{10+}$ ion will lose 1% of its energy when passing through the energy degrader. On the dispersive focal point, the separation of the beam is

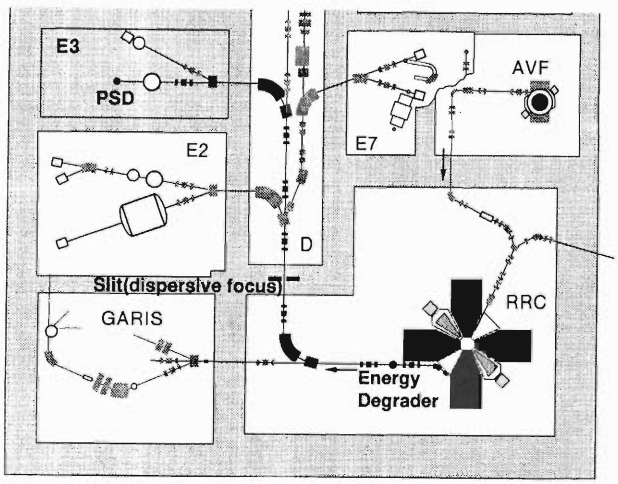

Fig. 1. Setup of the test experiment.

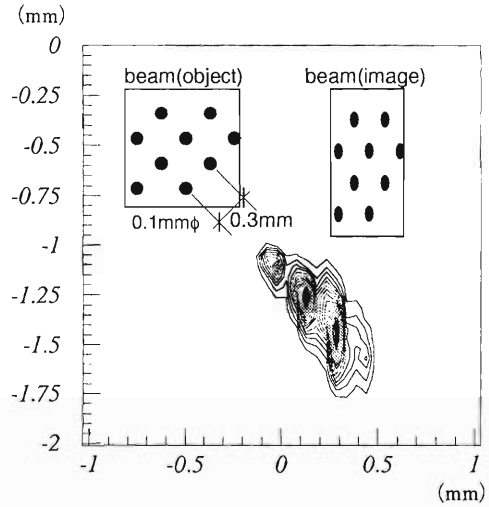

Fig. 2. Result of the experiment of beam size in x(mm)-y(mm) coordinates. The energy degrader is placed at the object point of the ion optical system. The energy degrader has many holes as shown in the figure(object). The ideal image of the beam at the PSD position(image) is also shown.

26 mm, much larger than the beam extent. The magnification of the beam was 0.63 for the horizontal direction and 1.26 for the vertical direction in present case. Position-sensitive Si detector (PSD, S2044 HAMAMATSU) was set at the end of the E3A beam course to measure the size of the beam. The position of the ion was determined based on the charge division method. The sensitive area of the PSD is 4.7 mm $\times$ 4.7 mm. The experimental setup is summarized schematically in Fig. 1.

The performance of the PSD was examined by using ^{241}Am-α source. The result showed a good position-linearity even if an ion hit the edge of the detector. We also found that the PSD had a sufficient position resolution at least for the α-particle emitted from ^{241}Am.

We obtained very sharp peaks as shown in Fig. 2. Each peak corresponds to a hole of the energy degrader. The size of the peak is roughly 70 μm(horizontal) $\times$ 300 μm(vertical). The result shows that the new method works well, basically. On the other hand, the beam size in the vertical direction is much larger than the ideal value (126 μm). We also found by moving the slits that image of the holes is rotated by nearly 45 degrees. It means that the optical system for ions and/or its tuning is poor. We are now investigating these points.

Design of a Charge-State Multiplier System for the RIKEN RI-Beam Factory Project

O. Kamigaito, M. Kase, Y. Miyazawa, T. Chiba, M. Hemmi,
S. Kohara, E. Ikezawa, A. Goto, and Y. Yano

In the RIKEN RI-Beam Factory project, a Charge-State Multiplier (CSM) system is planned to be placed between the existing heavy-ion linac (RILAC) and ring cyclotron (RRC) in order to increase the charge-to-mass ratio (q/m) of the heavy-ion beams. It consists of an accelerator, a charge stripper, and a decelerator.[1] The accelerator section increases the stripping energy further and the decelerator section brings the beam energy down to the initial value. For the accelerator and decelerator sections, drift tube linacs of variable-frequency type will be used. The total voltage-gain required for the accelerator and decelerator sections are 25.6 and 12.5 MV, respectively.

In the initial design,[2] four accelerator tanks and two decelerator tanks were proposed, where 16 or 18 rf-gaps were included in each tank. The resonator is based on the Interdigital H-mode (IH) structure with a movable shorting plate. The maximum gap voltage was chosen 430 kV in order to put the whole CSM system within the present RILAC building. However, the estimated power consumption per tank becomes too high to be provided with a conventional rf-amplifier. Moreover, the calculated current density reaches 90 A/cm, which is quite high, on the sliding contact around the corner of ridge of the IH-structure.

Therefore, we have changed the configuration of the CSM as shown in Fig. 1. Now the accelerator and decelerator sections are divided into eight and four tanks, respectively. Each tank has now only eight rf-gaps in it. The tanks are independently operated at the second harmonic frequency of the fundamental, which means that the frequency of the CSM ranges from 36 to 76 MHz. The last single tank of the decelerator covers the same energy-range as the first two tanks of the accelerator. In the same way, there are a pair of accelerator tanks and a decelerator tank which work in the same energy region. A quadrupole triplet is placed between every two tanks.

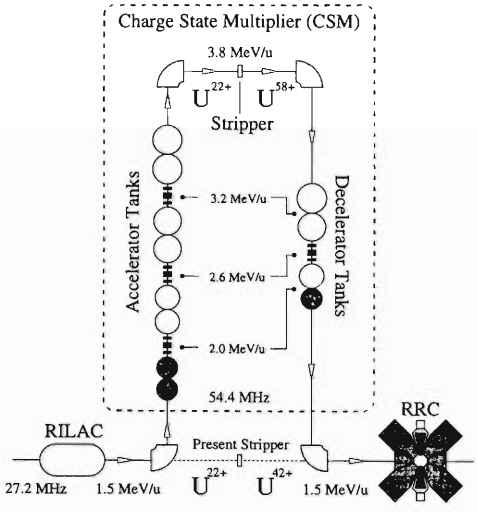

Fig. 1. Schematic layout of the CSM. The beam energies shown are those at the frequency of 54.4 MHz.

The synchronous phase of the accelerator tanks is chosen to be $-25°$, while that of the decelerator tanks is 25°. The total length of the accelerator and that of the decelerator will be about 16 meters and 8 meters, respectively. The drift-tube parameters have been optimized by using a beam simulation program which was newly developed based on a first-order calculation procedure. According to the simulation, the beam transmission through the CSM is fairy good for the assumed transverse emittance of $\varepsilon_n = 1.8\ \pi$ mm·mrad and longitudinal one of $\varepsilon_L = 500\ \pi$ keV/u·deg at 54.4 MHz.

Construction of the low energy part of the CSM, indicated by the three hatched circles in Fig. 1, has started, and the mechanical design of the resonators has been almost finished. The main parameters of the low energy part are listed in Table 1. The resonator is based on a quarter-wavelength resonator of circular cylinder, as shown in Fig. 2. The resonant frequency

Table 1. Main parameters of the low energy part of the CSM tanks. Acc1 and Acc2 are the accelerator tanks, and Dec is the decelerator tank. ϕ_s denotes the synchronous phase. The input (E_{in}) and output (E_{out}) energies correspond to the acceleration condition at 54.4 MHz. The effective shunt impedance (Z_{eff}) is estimated at this frequency. The maximum current density on the sliding contacts (J) and the power loss (P) are estimated at the highest frequency of 76 MHz.

Tank	Acc1	Acc2	Dec
Frequency (MHz)	36-76	36-76	36-76
Mass to charge (m/q)	26-6	26-6	12-2.7
Input energy* (MeV/u)	1.48	1.74	2.01
Output energy* (MeV/u)	1.74	2.01	1.48
Inner length (m)	1.3	1.3	1.3
Number of gaps	8	8	8
Bore radius (cm)	1.75	1.75	1.75
Synchronous phase (ϕ_s)	-25°	-25°	+25°
Max. gap voltage (kV)	450	450	450
Max. power loss (P: kW)**	50	52	50
Z_{eff} (MΩ/m)*	171	178	169
Max. current (J: A/cm)**	58	61	58

* : At 54.4 MHz

** : At 76 MHz (the highest frequency)

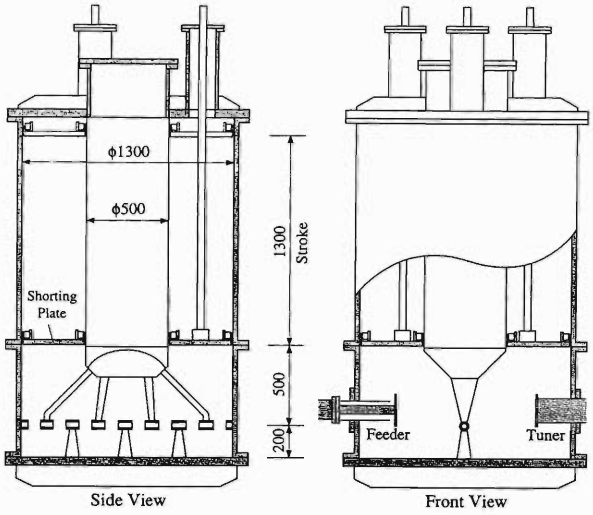

Fig. 2. Schematic drawing of a tank of the low energy part.

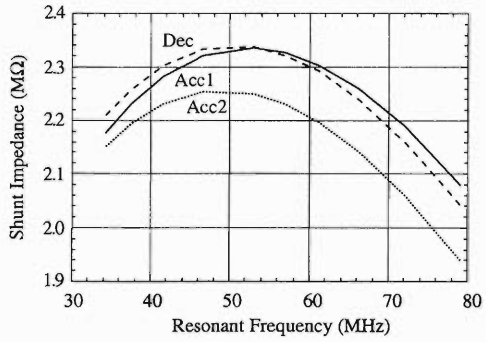

Fig. 3. Calculated shunt impedances of the resonators of the low energy part. The solid, dotted, and dashed curves represent the impedance of the accelerator1, accelerator2, and the decelerator tank of the CSM, respectively.

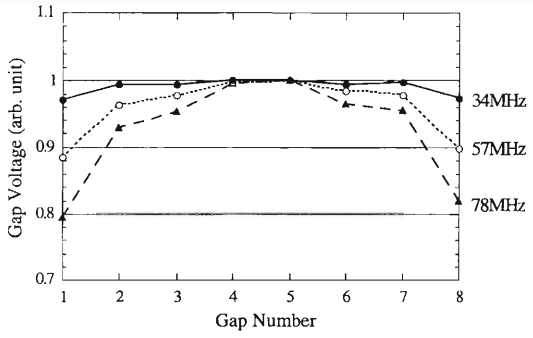

Fig. 4. Calculated gap voltage in the second accelerator tank. The resonant frequencies are indicated ouside of the frame of graph.

can be changed by a movable shorting plate. The rf-power is fed through a capacitive feeder. A capacitive tuner is used for the fine tuning of the resonant frequency. The rf-characteristics of the resonators have been studied with the MAFIA code. All the three resonators have the same dimensions except for the drift tubes and their stems. The size of the coaxial part as well as the shape of the stems for the first and final drift tubes were optimized so that the current density on the sliding contact becomes minimal. The calculation predicts that a stroke of 1300 mm of the movable shorting plate can cover the required frequency-range from 36 to 76 MHz. The current density on the sliding contacts is estimated to be 60 A/cm at the maximum gap voltage of 450 kV.

Figure 3 shows the calculated shunt impedances. The shunt impedance R_s is defined in present paper by $V^2/(2P)$, where P is the rf-power consumption and V is the peak value of the gap voltage. From this result, the maximum power loss is calculated to be about 50 kW per tank. The actual shunt impedances of the resonators will be, however, less than the calculated ones, mainly due to the sliding contacts around the inner conductor of the coaxial part. Therefore, we are planning to construct the amplifiers whose maximum power is 100 kW in the required frequency-range. The calculated Q-values are about 30000, and they are almost constant over the frequency range of our interest.

The gap voltage distribution is not flat along the beam direction in these resonators, particularly not at the high frequency. As shown in Fig. 4, the gap voltage in the end cells is only about 80% of that in the inner cells at the highest frequency (78 MHz). The effect of this voltage distribution on the beam transmission has been estimated with the beam simulation. According to the simulation, the transmission will become good enough if the average gap voltage is made larger than the designed value.

Construction of the low energy part will be completed in 1999. The three tanks will be installed and tested in the beam line between the RILAC and the RRC within the same year. The rest of the CSM tanks will be designed based on the test results of the low energy part.

References

1) Y. Yano et al.: Proc. PAC97, TRIUMF, May 12–16, 1997, in press.
2) A. Bandyopadhyay et al.: RIKEN Accel. Prog. Rep. **31**, 203 (1998).

Status of the Two Booster Ring Cyclotrons for RIKEN RI Beam Factory

A. Goto, H. Okuno, T. Kawaguchi, J. Ohnishi, T. Mitsumoto, T. Tominaka, S. Fujishima, J.-W. Kim, K. Ikegami, N. Sakamoto, K. Sugii, T. Wada, T. Morikawa, Y. Miyazawa, O. Kamigaito, M. Kase, and Y. Yano

Construction of both of IRC (Intermediate Ring Cyclotron) and SRC (Superconducting Ring Cyclotron) has been approved to start from the fiscal year of 1998.

Fabrication of the sector magnets of IRC has already started. Each of the upper and lower poles of IRC is designed to be divided into two slices for the simplification of assembly of the sector magnet in the cyclotron vault: i.e. the two slices faced to each other with respect to the median plane are assembled together with a vacuum chamber at the factory, and the whole assembled components are to be delivered to the cyclotron vault (see Fig. 1). A Purcell gap of 1 mm is designed between the pole and the yoke. Fabrication of the materials of the poles and yokes has been almost completed.

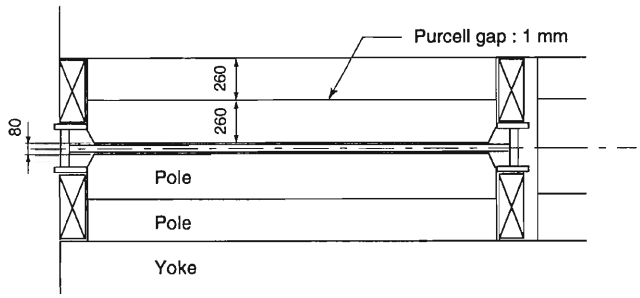

Fig. 1. Cross section of the pole part of IRC along the sector center line.

SRC has been redesigned to have four main rf resonators from three in previous design (see Fig. 2). This decision was made to obtain a better beam extraction efficiency by enlarging the turn separation, despite that design of the components such as injection and extraction elements, a flattop resonator, and beam diagnostic devices becomes tight due to the lack of available space. These components have been redesigned accordingly.

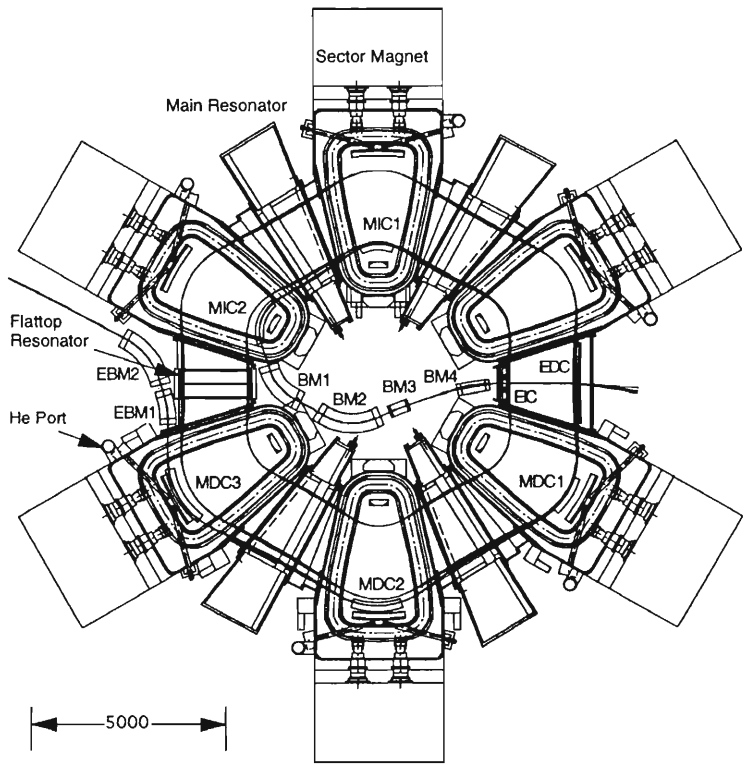

Fig. 2. Plan view of the redesigned SRC with four main rf resonators.

Fabrication of the prototype sector magnet of SRC is still being continued. In spring 1998, two sets of the models of main coil assembly in the straight section, which have a real-size cross section and are 60 cm in length, were made to study the assembling and mechanical stiffness in the two adopted schemes (screw-type and hook-type).[1] A photograph of the model of the screw-type is shown in Fig. 3. The main coil winding of the prototype sector magnet started in August 1998. As of December 1998, the winding has been completed and the final assembling of the remaining coil vessel plates is being made. Figure 4 shows a photograph of the main coil vessel where several turns of main coils are being wound. Three sets of 1/6-scaled sector magnets with normal conducting coils, which are to be operated in a pulse mode, are being constructed to measure the unbalanced magnetic forces in x, y, and z directions. Its testing will be completed around the end of December 1998. The results will be utilized for the design of thermal-insulation supports of the cold mass. Fabrication schedule for the whole system of the prototype is delayed: cool down test of the whole system and measurement of magnetic fields have been rescheduled to be made in the summer of 1999.

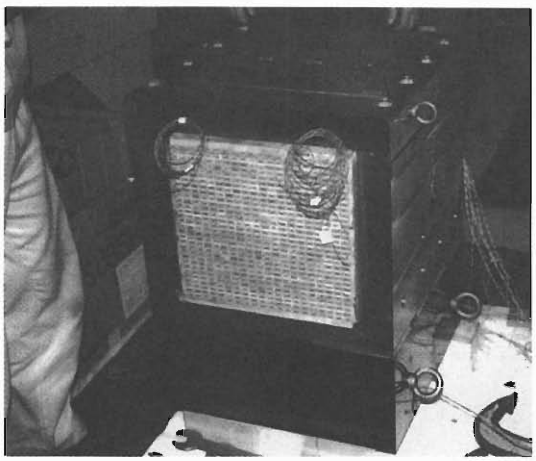

Fig. 3. Photograph of a model of main coil assembly in the straight section (screw-type).

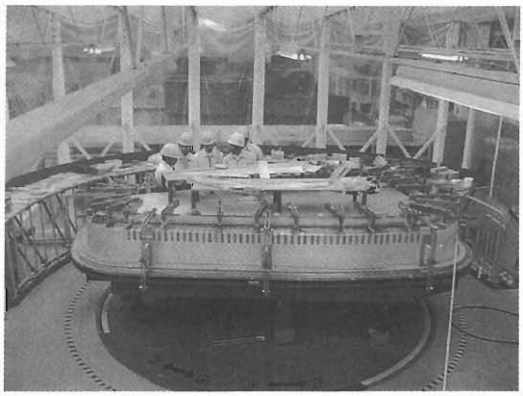

Fig. 4. Photograph of the main coil vessel where several turns of main coils are to be wound (hook-type).

An international technical advisory committee (TAC) was held in May 1998 for the review of design of the superconducting sector magnet of SRC. Details of each component are given elsewhere in this progress report.

References

1) T. Kubo et al.: RIKEN Accel. Prog. Rep. **31**, 210 (1998).

Design Study of the IRC for RIKEN RI-Beam Factory

T. Mitsumoto, A. Goto, M. Kase, H. Okuno, J. Ohnishi, O. Kamigaito,
N. Sakamoto, Y. Miyazawa, and Y. Yano

The RIKEN Intermediate Ring Cyclotron (IRC) is a booster ring cyclotron for the RIKEN RI-Beam Factory,[1] which accelerates the extracted beam from the existing RIKEN Ring Cyclotron (RRC). Required performance for the IRC is shown in Fig. 1 by light-gray area. The maximum energy and the maximum magnetic rigidity is 126.7 MeV/nucleon and 4.57 Tm, respectively.

Figure 2 shows a plan view of the IRC. Four sector magnets, two main RF resonators, one flat-top resonator, and injection and extraction devices are shown.

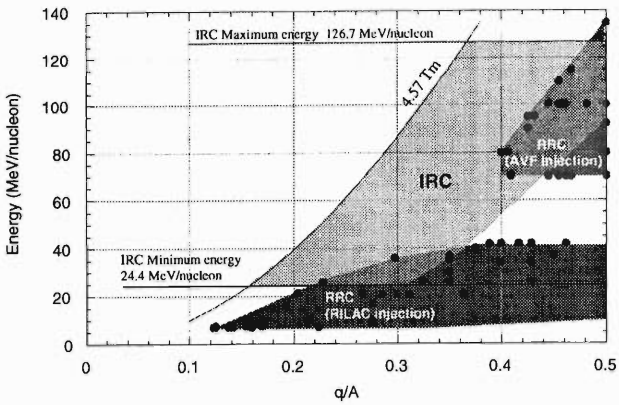

Fig. 1. Required performance for the IRC is shown by light-gray area. The performance of the RRC is shown by dark-gray areas.

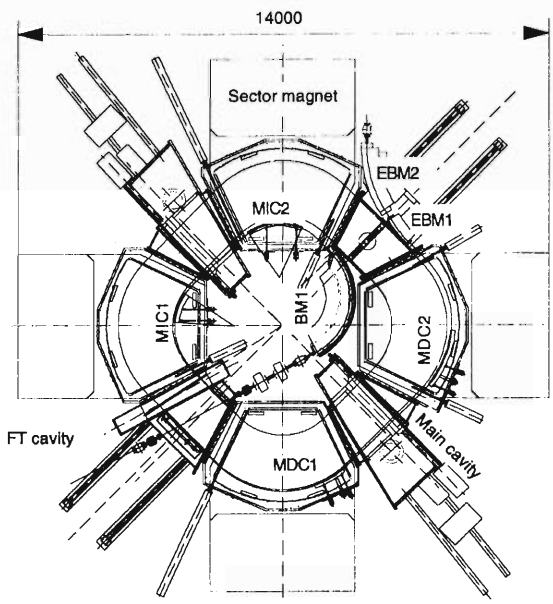

Fig. 2. Plan view of the IRC.

Diameter of the cyclotron is 14 meters. Main parameters of the IRC are listed in Table 1.

Table 1. Main parameters of the IRC.

Number of sectors		4
Harmonics		7
Average radius:	Injection	2.77 m
	Extraction	5.36 m
Velocity gain factor		1.5
Number of cavities	Main	2
	Flat-top	1
Gyration frequency		2.57-5.45 MHz

The fundamental structure of the sector magnets of the IRC is quite similar to that of the RRC. Parameters of the sector magnets are listed in Table 2. Cross-sectional size of the main coil is 160 mm (width) by 390 mm (height). Overall current density of the main coil becomes less than 1.5 A/mm^2. This realizes low power consumption of main coils. The magnet is equipped with 20 sets of trimcoils. The trimcoils are attached on the pole pieces, where the vacuum is separated from that for the beam by stainless steel membrane. The trimcoils are carefully designed to be of low power consumption. A so-called Purcell gap of 1 mm

Table 2. Main parameters of the sector magnets.

Pole gap	8 cm
Sector angle	53 degree
Total hight	5.2 m
Weight	640 × 4 ton
Maximum magnetic field	1.9 T
Main coil	
Maximum current	450 A
Maximum excitation current	1.78×10^5 At
Current stability	2×10^{-5}
Power consumption of main coils	82 × 4 kW
Trimcoil	
Number of trimcoils	20
Maximum current	500 A
Current stability	5×10^{-4}
Power consumption of trimcoils	45 × 4 kW

is designed to be set between the pole and the yoke. The pole gap of 80 mm is estimated to decrease by 0.4 mm at maximum due to a bend of the pole, which is caused by the magnetic and vacuum forces.

Magnetic field of the IRC was calculated by using TOSCA-3D magnetic field calculation program.[2)]

Equilibrium orbits and isochonous conditions were then calculated by using the result of magnetic field calculation. The main coil and trimcoil currents are optimized by several iterations of the field calculations. Figure 3 shows the tune diagram of the IRC. By optimizing 20 sets of trimcoil currents, errors to isochronous condition can be less that ±0.05 % for all acceleration regions.

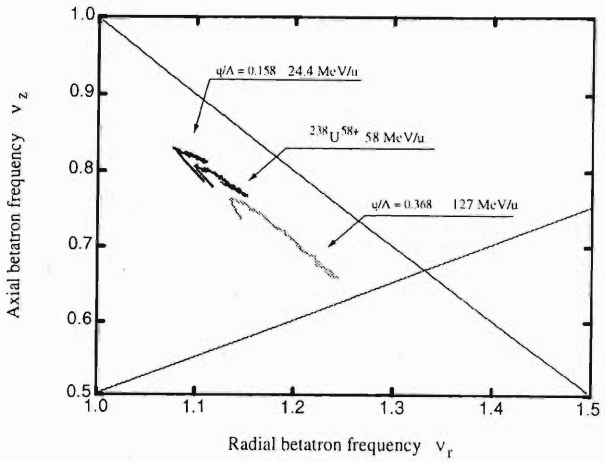

Fig. 3. Tune diagram of the IRC.

Figure 4 shows the model for calculation of the sector magnet with TOSCA.

For the main RF resonators, a single gap type resonator was adopted. Frequency is adjusted by the flap of two panels in the cavity. This type of resonator has a large advantage in that the area of sliding RF contact can be minimized. The maximum voltage is supposed to be 600 kV for one resonator.

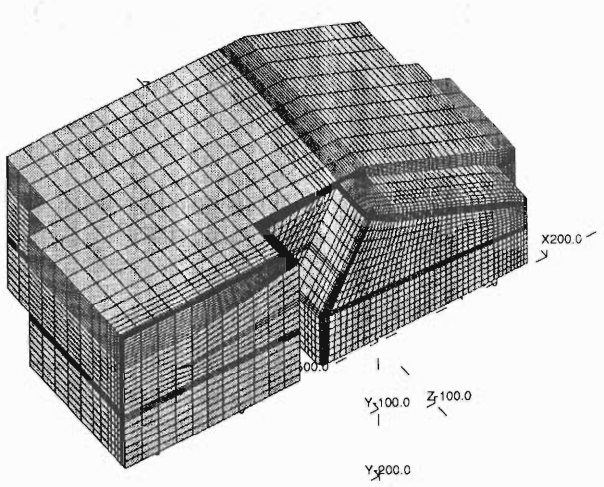

Fig. 4. Geometrical sizes of the sector magnet of the IRC for calculation.

For the flat-top cavity, however, a single gap type with conventional short plates was adopted because of limited space. Required voltage is about 1/9 of the voltage needed originally by two main resonators.

Construction of the sector magnets has been started. The whole components of the IRC will be completed at the end of the fiscal year 2000.

References

1) A. Goto et al.: RIKEN Accel. Prog. Rep. **31**, 205 (1998).
2) Vector Fields Limited, Oxford, England.

Orbit Analysis of RIKEN Superconducting Ring Cyclotron

T. Mitsumoto, A. Goto, J. W. Kim, T. Kawaguchi, H. Okuno, J. Ohnishi, S. Fujishima, T. Tominaka, N. Sakamoto, Y. Miyazawa, and Y. Yano

The RIKEN Superconducting Ring Cyclotron (SRC) utilizes the leakage magnetic field in its valleys in order to increase the vertical focusing force. The leakage field is still large outside of the cyclotron vault. At the points 50 m away from the SRC center, it is estimated that more than 1 Gauss will be observed.[1] In order to cancel the field outside the cyclotron vault, two methods are considered. One method is to use an iron plate surrounding the vault. Thickness of the iron plate is required to be 16 cm. Total weight of the iron plate is approximately 2600 tons. The other method is to use shielding coils. The shielding coils will be put on the wall of the vault. Radius of the coil is 12 meters. Required current is 360 kA.[2]

From the orbit analysis point of view, both methods affect on the field distributions and beam dynamics. Figure 1 shows the influence of two shielding methods on the betatron frequencies. In the case of the iron plate method, vertical betatron frequency decrease by 0.01 because the plates work as a return yoke. The shield coil method does not change the betatron frequency much.

We plan to adopt the shield coil method from the view point of construction cost.

During mechanical design of the sector magnet, we have to be careful about difference between the calculation model and the real magnet. We started from a simple calculation model. For example, iron poles

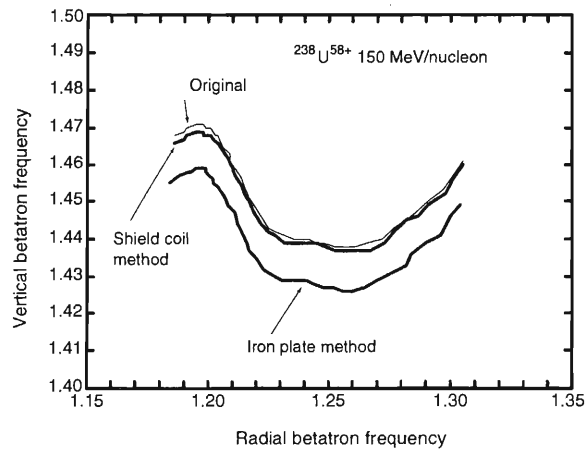

Fig. 1. Influence of the magnetic shielding on betatron frequencies.

were considered to be solid plates. The real iron poles, however, have many holes and cuts for fixing the main coil vessels, trim coil vessels, pole links and so on. It is difficult to make a model which adopts all these with accurate shapes because of limited node numbers of the program by TOSCA.[3] So, equivalent BH curves are used for modeling the holes of the iron pole. Figure 2 shows the regions used for equivalent BH curves in the iron pole. In these regions, new BH curve is calculated by taking the volume ratio of the iron to air into

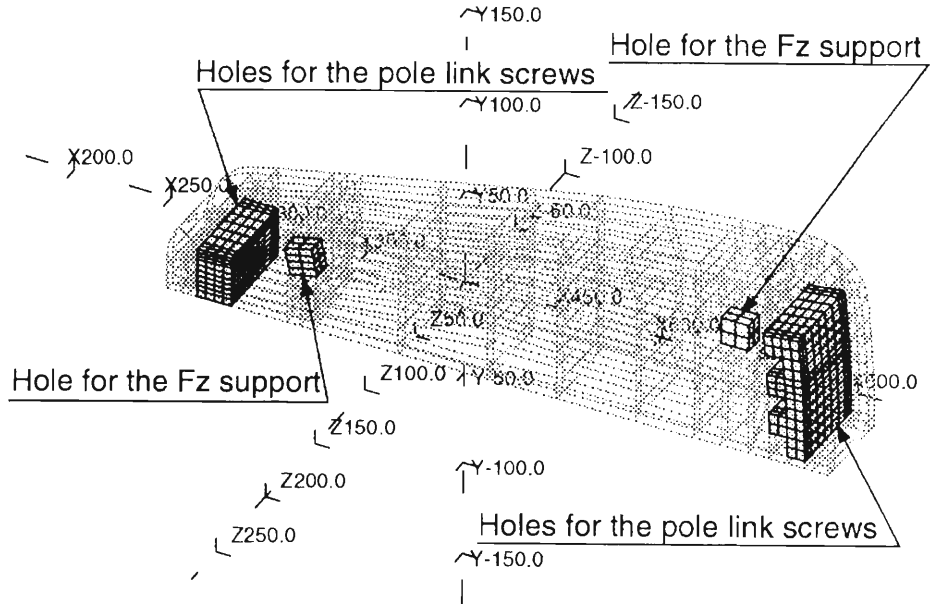

Fig. 2. Calculation model of the iron pole. In hatched regions, equivalent BH curves are used.

account.

Figure 3 shows a model of iron yoke of the sector magnet. Holes of Fz supports and holes of position monitors are considered for the iron pole.

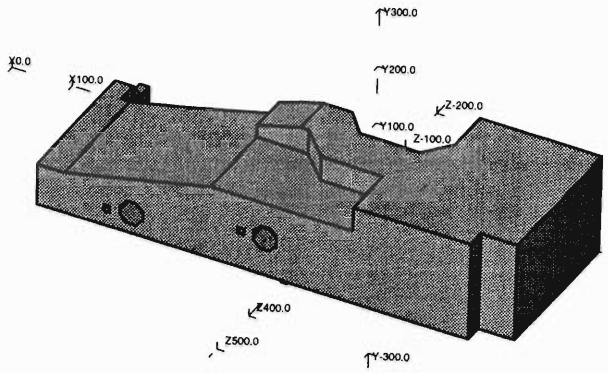

Fig. 3. Calculation model of the yoke.

The BH curve is also important to decide the structure of the magnet. Iron which has high saturation magnetic flux will reduce the vertical betatron frequency as well as the excitation current.

The final structure of the sector magnet will be determined soon to satisfy the condition that the minimum value of the vertical betatron frequency should be larger than 1.05 and that the maximum should be smaller than 1.5. This adjustment can be accomplished by changing the cross-sectional size of the upper and lower yokes.

References

1) T. Mitsumoto et al.: Proc. 12th Int. Conf. on Cyclotrons and Their Applications, Caen, to be published.
2) J. Onishi et al.: RIKEN Accel. Prog. Rep. **32**, 205 (1999).
3) Vector Fields Limited, Oxford, England.

Beam Optics Study on Single-Turn Extraction for RIKEN Superconducting Ring Cyclotron

J.-W. Kim, T. Mitsumoto, A. Goto, and Y. Yano

Beam dynamics has been examined for the RIKEN Superconducting Ring Cyclotron (SRC) to assess the single-turn extraction. In fact, evaluations on optics in the SRC alone can not assert a full assessment because optics calculations are made upon rather idealized conditions, and because the SRC is a high-energy end of the accelerator chain so that instabilities in a preceding machine will affect on the extraction. Nevertheless it is essential that a single turn extraction is assured for the SRC in terms of beam optics. The last-turn separation should be sufficiently larger than the beam width, and the beam quality should be well preserved throughout the acceleration. Usually, the turn separation is enhanced by off centering the beam. The beam in the SRC is to be off-centered at injection.

Design particle is the O^{7+} accelerating from 127 to 400 MeV/u because of its largest turn number i.e. the smallest last-turn separation. The last-turn separation is plotted in Fig. 1 as a function of the energy gain per turn (ΔE) when the turn separation is determined only by the rf acceleration, and when enhanced by the off-centering injection, which induces a precession. A larger amplitude of precession can be induced with a larger ΔE.

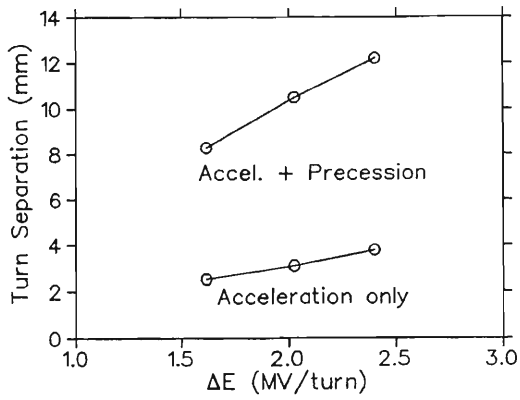

Fig. 1. The turn separation at extraction versus the energy gain per turn when the beam is injected centered (acceleration only) and off-centered (accel. + precession).

The orbit tracings have been carried out using the particles randomly distributed in a 4-D phase space involving longitudinal and transversal phase spaces. The vertical phase space is not included because the effects on beam behavior by coupling to other phase spaces are considered to be weak. Figure 2 shows the last five turns prior to the extraction with 200 particles tracked. The transverse emittance is 3.4 π mm·mrad, the energy spread is $\pm$0.05%, and the initial phase

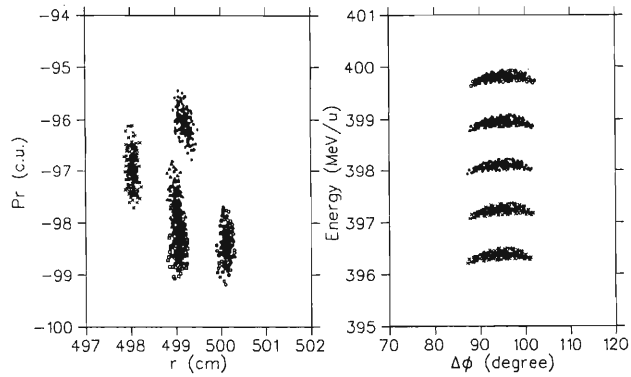

Fig. 2. Phase space motion of the last five turns in the transversal and longitudinal phase spaces.

width is assumed as 20°. The energy gain per turn is 1.6 MV which is obtainable when three rf cavities are arranged. If four cavities are employed, the minimum last-turn separation increases from 8 mm to 11 mm, while other beam behaviors remain essentially the same. By adopting a third harmonic flat-topping cavity the phase acceptance is larger than 20°, so that the beam phase width can be widened to lessen longitudinal space-charge forces.

A major resonance to affect the beam quality is $\nu_r = 1.5$ for the light nuclei accelerating to 300–400 MeV/u. The gradient of the third harmonic field causes the resonance in lowest order, and its constant field component in the next lowest order. The static phase trajectories are plotted in Fig. 3 below and above the resonance. The eigen-ellipse changes its shape at traverse of the resonance. As a result, the beam

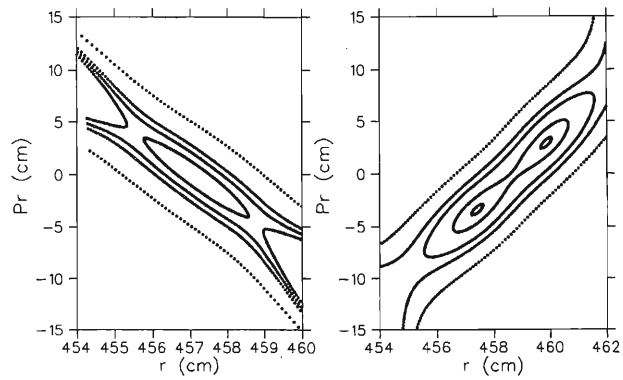

Fig. 3. Static phase-space trajectories below and above the resonance shown in the left and right hand frames, respectively. Beam energies of the O^{7+} are 306 and 308 MeV/u, where the tunes are 1.496 and 1.503, respectively.

phase space becomes mismatched, by which the effective beam width broadens. When the error of field gradient is 0.4 gauss/cm, the phase space motions near the extraction will become the like displayed in Fig. 4 when the beam at the injection is centered without precession and off-centered with precession. The phase

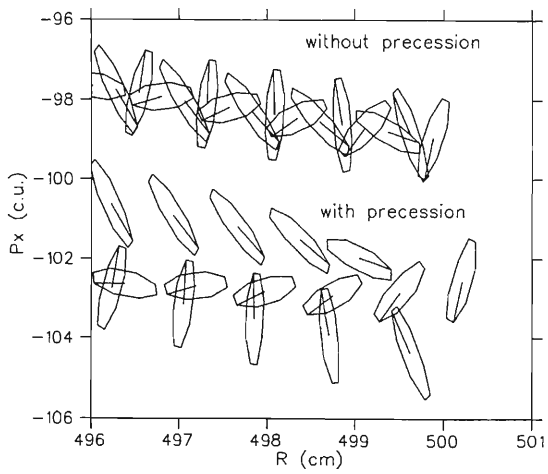

Fig. 4. The phase space motions near the extraction radius when a third harmonic field gradient is 0.3 gauss/cm, with and without an off-centered injection. Due to a mismatch with a new eigen-ellipse above the resonance, phase ellipses oscillate.

space oscillates due to a mismatch with a new eigen-ellipse after traverse of the resonance, and the last-turn separation can not be effectively enlarged even with off-centering. The gradient error allowable is thus considered to be below 0.1 gauss/cm under a conservative estimation.

The limiting current due to longitudinal space-charge forces has been evaluated using a uniform ellipsoidal beam charge distribution. The electric field at the azimuthal edges of the beam is then given by[1)]

$$E_\theta = \frac{\rho a}{2\epsilon_0} g, \tag{1}$$

where a is a half of the beam vertical width, g is a form factor, and ρ is the charge density. For O^{7+} beam, a is roughly 0.25 cm, and g is 1.4. At 1 pμA of beam current, E_θ is calculated to be 9 V/m near the extraction. The energy spread accumulated throughout the acceleration is about ± 54 kV/u. Upon orbit tracings in a 4-D phase space such as shown in Fig. 2, the last-turn separation disappears by $\Delta E/E$ of about 2×10^{-3} even with an off-centered injection. The limiting current is then calculated to be 10 pμA assuming that the initial energy spread is $\pm 5 \times 10^{-4}$.

References

1) W. Joho: Proc. 9th Int. Conf. Cyclotrons and Their Applications, p. 337 (1981).

Design and R&D Works for SRC Sector Magnets

T. Kawaguchi, H. Okuno, A. Goto, J. Ohnishi, T. Tominaka, T. Mitsumoto, and Y. Yano

The RIKEN superconducting ring cyclotron, SRC, has been started already in its construction.[1] Six superconducting sector magnets[2] are one of the main components of the SRC, and a prototype superconducting sector magnet[3] is now under fabrication. Figure 1 shows a cross-sectional view of the sector magnet, and a photograph of the main coil winding for the prototype magnet is shown in Fig. 2. Main parameters of the sector magnets are following. The maximum magnetic field in the beam orbit: 4.5 T, maximum operation current: 5000 A for the main coil and 500 A for the trim coils, and the total weight of the six sector magnets including yokes: 4300 tons. To avoid a coil quench, a cryogenic stabilizing method is applied to both of the main and trim coils.[4]

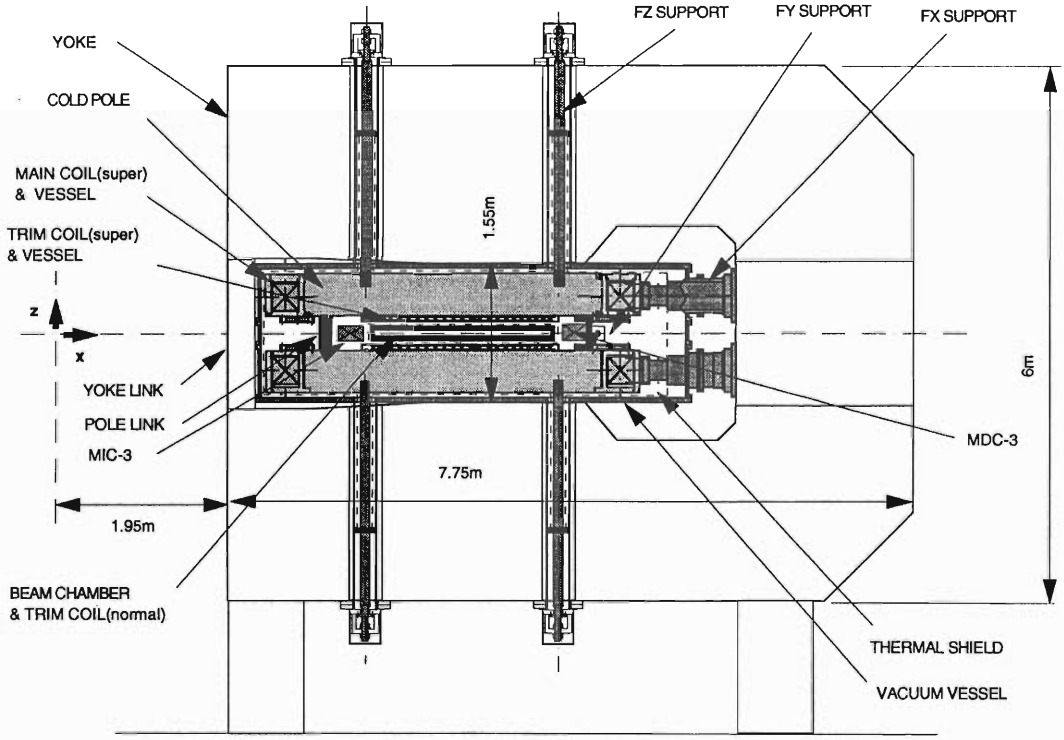

Fig. 1. Cross-sectional view of the SRC sector magnet.

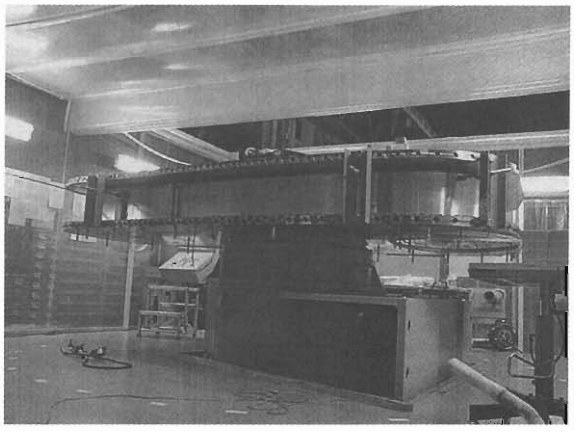

Fig. 2. A photograph of the coil winding for the prototype sector magnet.

Design and R&D works completed and/or achieved during 1998 are summarized as follows: (1) Detailed design for fabrication of the cold mass (main and trim superconducting coils, coil vessels, and cold-pole). (2) Mechanical and thermal analyses of the cryostat (vacuum vessel, thermal shield, and thermal insulating support system) and determination of their dimensions. The detailed design work for their fabrication is under going. (3) Detailed configuration and dimensions of the yoke. Effect of iron purity of yoke material on the magnetic field was investigated. Pure iron as the material for the yoke is being ordered for its fabrication. (4) A design review meeting for the sector magnets was held for 3 days in April '98 by an international technical advisering committee (TAC) which consisted of

four experts on superconducting magnets. (5) A cooling system for the six sector magnets was redesigned after a further study of the system's reliability referring to the TAC review. Two cold-box type arrangement of the previous design[2] was changed to one cold-box type to make the system simpler and less expensive. Figure 3 shows the cooling system diagram for the sector magnets and for the active-shield-coils. Six sector magnets generate a leakage magnetic field in the areas not only inside but also outside of the SRC-room. Therefore, a pair of superconducting active-shield-coils is being planned in order to minimize the leakage magnetic field, especially in the outside area of the SRC-room. Superconducting magnets for the injection and extraction beam channels of the SRC will be cooled down by a separate cooling system. (6) The mechanical rigidity of the main coil was studied by measuring various small straight coils (pack of wires and G11-spacers) and two cross-section-models. We found that the compressive Young's modulus of the main coil is three to four times lower than the calculated value which was obtained by assuming an ideal surface contact between wires and spacers. Compressive pre-stress for the main coil fabrication was decided to be 1 kg/mm^2. (7) Mechanical properties of the Al-stabilized superconducting wire such as static strength, fatigue strength, and creep characteristics were measured at room temperature and at 78 K to investigate and confirm the mechanical design. (8) Some important elements of the main coil vessels were mechanically tested at 78 K, and the results were satisfactory with our design. (9) Two cross-section-models,[1] based on the two different designs[3] about the main coil/vessel configuration, were fabricated at Hitachi Ltd. and Mitsubishi Electric Corporations in order to assure the assembly process and to measure the mechanical rigidity. (10) Three sets of the 1/6-size Cu/Iron magnets were fabricated, and a measurement of the unbalanced magnetic forces in x, y, and z directions was started in December '98 and will be finished in January '99. The magnets are cooled down to 78 K to reduce the electric resistance of the Cu coil, and excited by pulse for one to two seconds with a direct current generator which has a capacity of 750 V and 5000 A. The maximum current density of the coil will reach 200 A/mm^2. The coil/pole assembly unit is supported by the yoke with the rods arranged in x, y, and z directions, and magnetic forces exerted on the coil/pole unit are measured by using strain gages on the rods. The measured results will be compared with the calculation results,[2] and will be used to finalize the designs of the prototype and six sector magnets. Figure 4 shows the photograph of the one magnet on a preliminary measurement test at room temperature. (11) Protection analysis at coil quench was made,[5] and effect of the eddy current in cold-pole due to a change in coil current is under study.

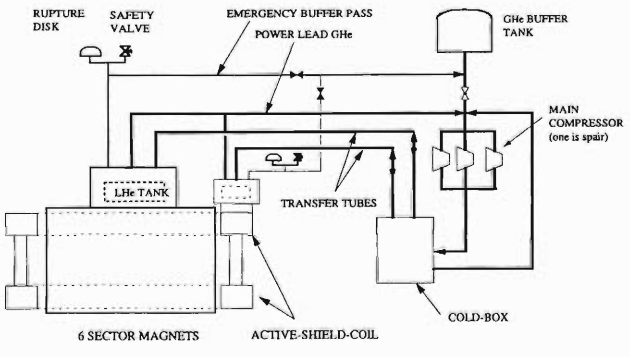

Fig. 3. Cooling system diagram.

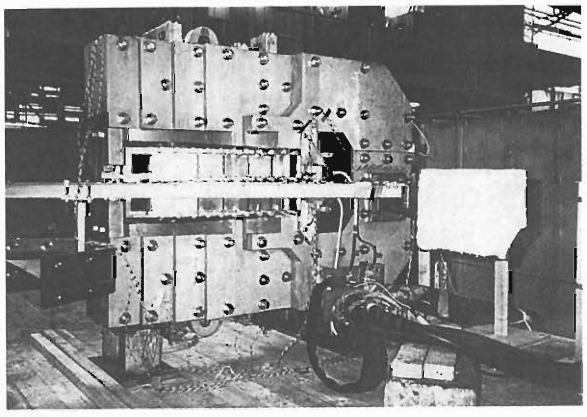

Fig. 4. A photograph of the one set of the 1/6-scale Cu/Iron magnets for the magnetic force measurement.

References

1) A. Goto et al.: RIKEN Accel. Prog. Rep. **32**, 193 (1999).
2) T. Kawaguchi et al.: RIKEN Accel. Prog. Rep. **31**, 208 (1998).
3) T. Kubo et al.: RIKEN Accel. Prog. Rep. **31**, 210 (1998).
4) T. Kawaguchi et al.: RIKEN Accel. Prog. Rep. **31**, 212 (1998).
5) T. Tominaka et al.: RIKEN Accel. Prog. Rep. **32**, 203 (1999).

Quench Analysis for Magnet Protection of RIKEN Superconducting Ring Cyclotron

T. Tominaka, T. Kawaguchi, J.-W. Kim, A. Goto, and Y. Yano

The quench characteristics of the superconducting main and trim coils of the RIKEN Superconducting Ring Cyclotron (SRC) were studied, using the computer program "QUENCH-M" which was developed on the basis of the program "QUENCH".[1,2] In this calculation, it was assumed that the normal zone propagates adiabatically and its shape is ellipsoidal. Since the whole protection circuit of the superconducting main and trim coils is complicated, the analysis of the magnet protection was made only for some simplified circuits.

The principal circuit diagram for the superconducting main coils of the SRC which consists of 6 sectors can be divided into 2 sections in order to protect the main coil more safely during the quench without a violation of the balance of electromagnetic force (Fig. 1).

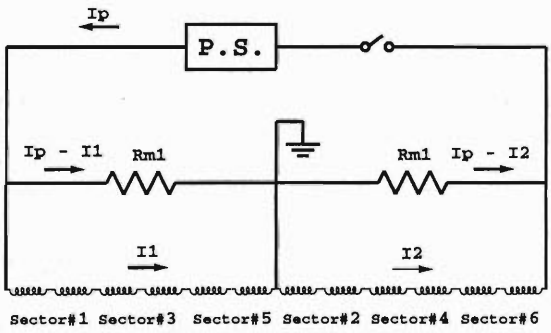

Fig. 1. Protection circuit for the whole 6-sector superconducting main coils of RIKEN SRC.

Inductive coupling between the two sections (3 sector magnets per section) is small: namely the calculated value of the coupling constant is $k = -0.034$ (without iron). As a result, it was confirmed that the coupling effect is negligible in the quench characteristics.

Therefore, the circuit diagram for only the 3 sector magnets as shown in Fig. 2 was analyzed extensively for the purpose of protection of the superconducting main coils. In this analysis, it was assumed that either the upper or lower coil quenches.

Inductance of the superconducting main coil of RIKEN SRC depends on the exciting current because of the presence of the iron pole and yoke. The nonlinear inductance depending on the current L(I) (= dE/IdI), can be calculated from the stored energy E. The nonlinear inductance L(I) is shown in Fig. 3, together with two constant inductances L_0 (dashed line) calculated from the stored energy at I = 5 kA for the case with iron, and L_{air} (dotted line) calculated for the

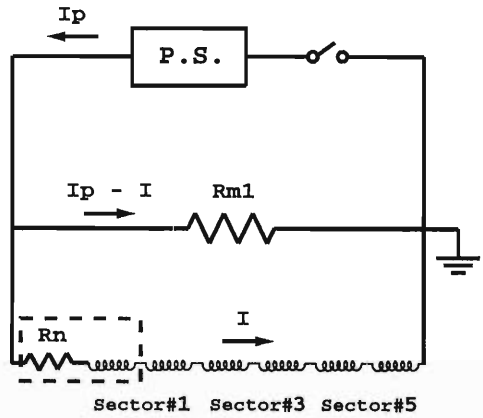

Fig. 2. Protection circuit for the 3-sector superconducting main coils for the purpose of quench analysis.

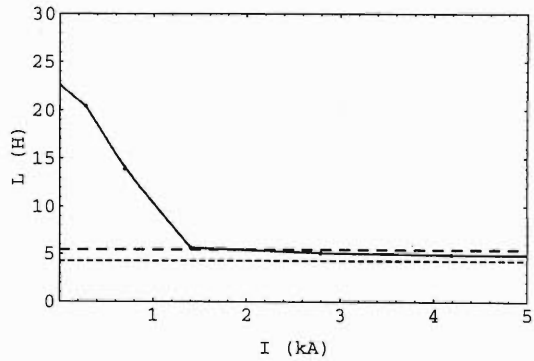

Fig. 3. Inductance of the 1-sector superconducting main coil. The approximated nonlinear inductance, L(I), is shown by solid line; the constant inductance L_0 for the case with iron is shown by dashed line; and the constant inductance L_{air} without iron is by dotted line.

case without iron. It seems reasonable that the nonlinear inductance L(I) approaches L_{air} as the exciting current increases.

The results calculated for three extreme cases are shown in Table 1 and in Figs. 4, 5, and 6. In these calculations, Run#1 (black curve) corresponds to the case with the nonlinear inductance and with the initial normal zone propagation velocity of $v_i = 7.6$ m/s; Run#2 (gray curve) is the case with the constant inductance; and Run#3 (dashed curve) is the case with $v_i = 0.1$ m/s. The calculated current decays shown in Fig. 4 are consistent with the expectation from the inductance and the total resistance, $R_{m1} + R_n$ (sum of the dump resistor and the resistance of normal zone of quenched coil). The time variations of the maximum temperatures shown in Fig. 5 are also consistent with the change expected from each current decay. The

Table 1. Calculated results of the quench analysis for the circuit shown in Fig. 2.

Run#	L (H)	R_{m1} (Ω)	v_i (m/s)	T_{max} (K)	V_{max} (kV)	$V_{l..max}$ (V)	E_{in} (MJ)	E_{out} (MJ)	$R_{n.f}$ (Ω)	t_{sw} (s)
1	L(I) × 3	0.3	7.6	140	1.5	42	87	120	0.57	1.0
2	5.4 × 3	0.3	7.6	140	1.6	48	85	120	0.56	1.0
3	5.4 × 3	0.3	0.1	300	1.5	17	0.72	200	0.006	1.0

L : Inductance of 3 sectors,
R_{m1} : Dump resistance,

v_i : Initial propagation velocity of normal zone,
T_{max} : Maximum temperature,
V_{max} : Maximum voltage in the circuit,

$V_{l..max}$: Maximum voltage between layers,
E_{in} : Dissipated energy in the superconducting coil,
E_{out} : Dissipated energy in the dump resistors,
$R_{n.f}$: Final resistance of normal zone, and
t_{sw} : Swich-off time of power supplies.

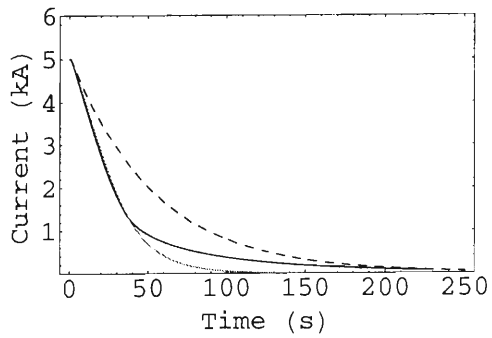

Fig. 4. Current decays of the superconducting main coil of the SRC during quench: black curve (Run#1), gray curve (Run#2), and dashed curve (Run#3) with dump resistor of $R_{m1} = 0.3\ \Omega$.

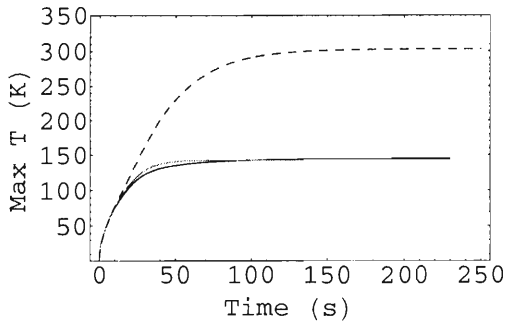

Fig. 5. Temperature rise of the superconducting main coil of SRC during quench: black curve (Run#1), gray curve (Run#2), and dashed curve (Run#3) with dump resistor of $R_{m1} = 0.3\ \Omega$.

maximum temperature of Run#3 is equivalent to the so-called hot spot temperature. The maximum voltages during the quench shown in Fig. 6 are almost the same to $V_{max} \approx 1.5$ kV $\approx R_{m1} \cdot I_0$, which is determined

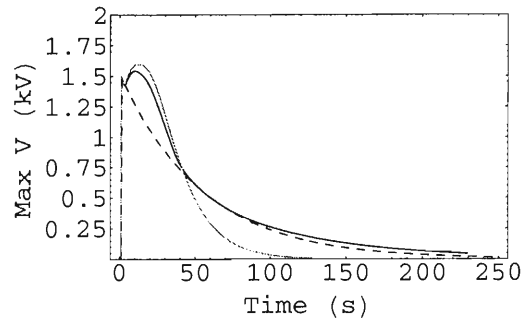

Fig. 6. Time dependence of the maximum voltage of the superconducting main coil of SRC during quench for the circuit shown in Fig. 2: black curve (Run#1), gray curve (Run#2), and dashed curve (Run#3) with dump resistor of $R_d = 0.3\ \Omega$.

by the dump resistor $R_{m1} = 0.3\ \Omega$. For the smaller dump resistor, $R_{m1} < 0.3\ \Omega$, the calculated maximum temperature reaches to a dangerous range hotter than the room temperature. On the other hand, for the larger dump resistor $R_{m1} > 0.3\ \Omega$, the maximum voltage becomes too high to treat. Therefore, the dump resistor of $R_{m1} = 0.3\ \Omega$ was chosen in Table 1 and in Figs. 4, 5, and 6.

Furthermore, the quench analysis for system of the main and trim superconducting coils was also studied. The dump resistors of 5 trim coils are determined so that the current will not increase when the power supply is switched off after the quench of main coil. In addition, effect of the cold iron pole as a secondary circuit for the superconducting coil system is to be taken into account.

References

1) M. N. Wilson: Rutherford Laboratory Report, RHEL/M-151 (1968).
2) T. Tominaka et al.: IEEE Trans. Magn. **28**, 727 (1992).

Leakage Magnetic Field from RIKEN Superconducting Ring Cyclotron

J. Ohnishi, T. Mitsumoto, A. Goto, and Y. Yano

When the light ions such as carbon are accelerated in the RIKEN Superconducting Ring Cyclotron (SRC), the axial betatron frequency decreases in the extraction side of the cyclotron, and approaches to the integer resonance at $\nu_z = 1.0$.[1] To keep the axial betatron frequency away from the resonance, we need to have a strong inverse magnetic field in the valley regions so that the edge-focusing force increases. Since the shape of yoke of the sector magnet is designed according to the above strategy, the SRC produces a large leakage magnetic field around it.

The magnetic field strength is about 4 T in the beam accelerating regions in the pole gap when the SRC sector magnets are excited at the maximum current. As the area of the pole where these fields are induced is about 7 m^2, the total amount of magnetic flux is estimated to be 28 Wb per sector magnet. On the other hand, as the area of the return yoke is about 6.5 m^2 and as the magnetic field strength there is 2 T due to the magnetic saturation of iron, the return flux becomes 13 Wb. Therefore, the magnetic flux of 15 Wb leaks out from each sector magnet to its outside. This value is nearly equivalent to the amount of the magnetic flux to be produced by the coils.

Although there exists no law in Japan to regulate the strength of the leakage magnetic fields, we set the following two limitations:
(1) The region where the strength of the leakage fields is higher than 5 G should be restricted from entering.
(2) The strength of leakage field should be lower than the earth magnetic field (0.35 G) outside of the institute site.
The leakage fields from the SRC have to be shielded to satisfy above limitations. One method is to cover the whole room of the SRC with iron plates. Another is to place large Helmholtz coils around the SRC.

Figure 1 shows the distributions of the leakage field strengths leaking from the SRC for the following three cases: (1) without magnetic shield, (2) with the passive shield to use iron plates, and (3) with the active shield to use Helmholtz coils. These data were calculated with a three-dimensional magnetic field computation code "Radia".[2] In these calculations the magnetomotive force of the SRC is 5.3 MA turns per sector magnet.

The shape of iron shield assumed for calculations is a cylinder whose diameter, height and thickness are

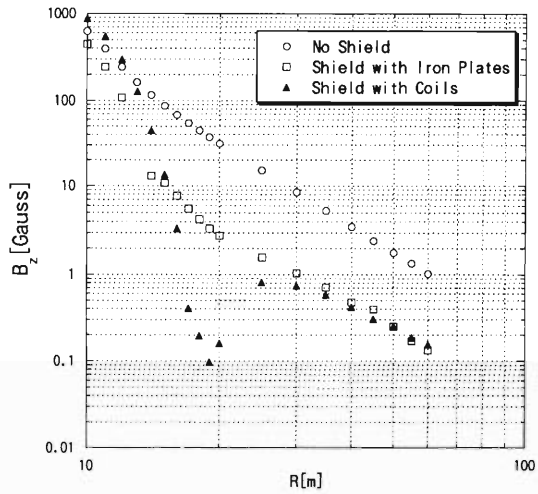

Fig. 1. Leakage magnetic field distributions (B_z) on the median plane with and without magnetic shields when the SRC is operated at the maximum current (5.3 MA/magnet). These data are calculated at the points along the extension of the center line of the sector magnet. The abscissa indicates distance from the center of the SRC.

26 m, 12 m, and 16 cm, respectively. The total weight was calculated to become about 2600 tons. On the other hand, the diameter of the Helmholtz coils is 24 m and the distance of the two coils is 5.2 m. The magnetomotive force of the coils is 360 kA turns, and the total dissipation of electric power is anticipated to become approximately 1 MW if normal conducting coils are used.

As shown in Fig. 1, the strength of the leakage field is reduced to about one tenth of the case without shielding, and becomes smaller than the earth magnetic field at the distance of 40 m away from the center of the SRC.

We have decided to use the magnetic shield to use a set of Helmholtz coils because there are some difficulties in the construction of the building in the case of the iron shield.

References

1) T. Mitsumoto el al.: RIKEN Accel. Prog. Rep. **31**, 206 (1998).
2) P. Elleaume, O. Chubar, and J. Chavanne: Proc. 17th Particle Accelerator Conference, in press.

Analysis of the Injection and Extraction Systems for RIKEN Superconducting Ring Cyclotron

S. Fujishima, H. Okuno, T. Tominaka, T. Mitsumoto, A. Goto, and Y. Yano

The injection and extraction systems for RIKEN Superconducting Ring Cyclotron (SRC) had been designed as a three-RF-cavity system.[1] But recently, to increase energy gain per turn, the number of the RF-cavities was changed from three to four.[2] To realize the four-RF-cavity system, the injection and extraction systems should be changed significantly. Design of the injection and extraction systems is now more challenging because the space to install the injection and extraction elements has decreased.

The SRC has a strong stray field originated from the sector magnets, and this field depends non-linearly on the magnetic rigidities of the beams. Thus, the trajectories of various beams differ considerably from each other. Besides, the injection and extraction elements should be installed in a small space limited with the sector magnets, RF-cavities, and vacuum chambers. These difficulties make the design of the injection and extraction systems quite challenging.

Purpose of present analysis is to optimize the layout and specification of the injection and extraction elements in the SRC. For optimization, the required fields of the elements and the differences of trajectories in the elements are minimized.

To trace the beam trajectories, an equation of motion was solved with Runge-Kutta-Gill method. In the calculation, electric or magnetic field of each element was superimposed on the field of the sector magnets which was calculated with a three-dimensional computer code, "TOSCA".[3]

Table 1 shows the energies and magnetic rigidities of three typical beams. The beam of $^{16}O^{7+}$ (1) has the smallest magnetic rigidity. On the other hand, the beam of $^{238}U^{58+}$ has the largest one. Between these two beams, the difference of trajectories is most pronounced. The beam of $^{16}O^{7+}$ (2) has the largest

Table 1. Energies and magnetic rigidities of three typical beams.

	Energy [MeV/u]		B ρ [Tm]	
	Inj.	Ext.	Inj.	Ext.
^{16}O 7+ (1)	74.2	200	2.89	4.90
^{16}O 7+ (2)	126.7	400	3.83	7.25
^{238}U 58+	58.0	150	4.57	7.52

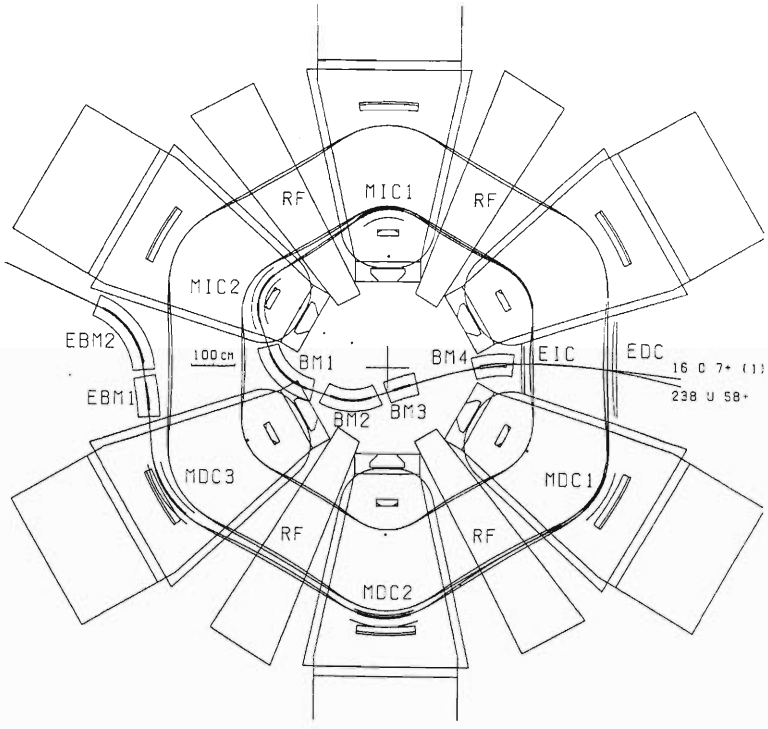

Fig. 1. Schematic layout of the elements, and the trajectories of typical beams.

electric rigidity.

Figure 1 shows a schematic layout of the injection and extraction elements, and shows the trajectories of two typical beams of $^{16}O^{7+}$ (1) and $^{238}U^{58+}$. Because of the stray field in the valley, two trajectories differ considerably from each other. The injection system consists of four bending magnets (BM1, BM2, BM3, and BM4), two magnetic inflection channels (MIC1 and MIC2), and an electrostatic inflection channel (EIC). The extraction system consists of two bending magnets (EBM1 and EBM2), three magnetic deflection channels (MDC1, MDC2, and MDC3), and an electrostatic deflection channel (EDC). The beams from a pre-accelerator are introduced crossing the EIC and EDC, so that the EIC and EDC should have holes to pass the beams. All MICs and MDCs are installed between upper and lower main coils of the sector magnets. And each magnetic element consists of main dipole coils and compensation coils to suppress fringe field on the first or the last equilibrium orbit.

Table 2 shows specification of the injection elements. Required magnetic field of the MIC1 has increased to alomost twice that in the case of previous three-RF-cavity system. Table 3 shows specification of the extraction elements. Length of each element was determined in consideration of the balance between the difference of trajectories in the element and the required field of the element.

Further optimization is in progress.

Table 2. Specification of the injection elements.

	Radius [cm]	Angle [deg.]	Length [cm]	B or E maximum
EIC	1000～4280	variable	102	110 kV/cm
MIC1	108.5	53.2	101	0.32 T
MIC2	96.0	72.0	121	1.12 T
BM1	132.0	52.0	120	4.36 T
BM2	132.0	42.0	97	3.64 T
BM3	466.8	5.0	41	0.50 T
BM4	240.8	14.5	61	-0.91 T

Table 3. Specification of the extraction elements.

	Radius [cm]	Angle [deg.]	Length [cm]	B or E maximum
EDC	1691～4405	variable	213	-110 kV/cm
MDC1	185.0	30.0	97	-0.15 T
MDC2	190.0	37.7	125	-0.27 T
MDC3	221.0	32.0	123	-0.97 T
EBM1	595.0	6.0	62	-0.32 T
EBM2	170.0	54.4	161	-4.20 T

References

1) S. Fujishima et al.: RIKEN Accel. Prog. Rep. **31**, 214 (1998).
2) A. Goto et al.: RIKEN Accel. Prog. Rep. **32**, 193 (1999).
3) T. Mitsumoto et al.: RIKEN Accel. Prog. Rep. **32**, 197 (1999).

Design of the RF Resonators for the New Booster Ring Cyclotrons

N. Sakamoto, O. Kamigaito, T. Mitsumoto, Y. Miyazawa, T. Chiba,
H. Okuno, A. Goto, and Y. Yano

The new booster ring cyclotrons IRC and SRC in the RI Beam Factory require their acceleration resonators to operate with a wide frequency range from 18 to 38.2 MHz in the case of harmonic number 6. It is also needed to obtain a large gap voltage around 600 kV at 38 MHz.[1)]

The present design of the acceleration resonator is a single-gap type whose structure is basically same as that of te RCNP(Osaka Univ.) ring cyclotron.[2)] An effort has been made to modify the frequency range of the former design from 23 to 46 MHz[1)] to the new operation range from 18 to 38.2 MHz. Schematic drawings of the new design are shown in Fig. 1. The sizes of the resonators have become larger than the former ones.

RF characteristics of the new resonators have been investigated by using a three dimensional RF calculation code, MAFIA.[3)] A brief summary on the RF characteristics of resonators with the tuning panel angles of 0° and 90° are shown in Table. 1. The maximum powers for the IRC and the SRC resonators are estimated to be 90 and 50 kW/resonator with a peak voltage of 0.6 MV/gap, respectively, at the highest operational frequency of 38.2 MHz.

The maximum acceleration voltage is anticipated to

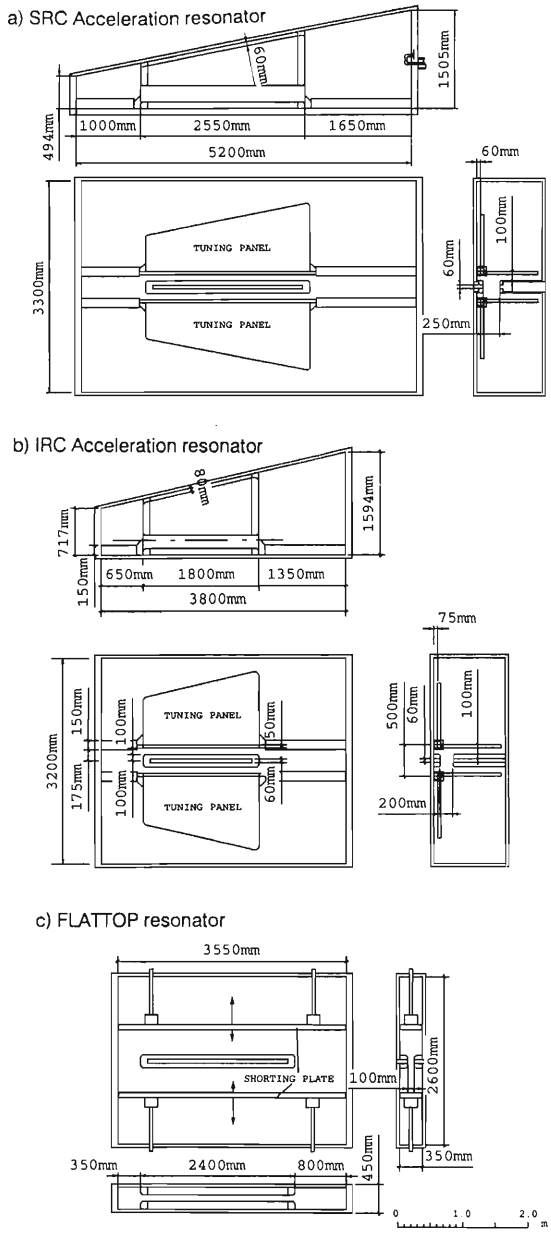

Fig. 1. Schematic drawings of the acceleration and flattop resonators.

Table 1. RF Characteristics of the acceleration and flattop resonators for SRC and IRC.

resonaotrs	SRC accel.		IRC accel.		flattop	
tuner position	0°	90°	0°	90°	1210 mm	110 mm
f_o [MHz]	17.3	38.4	17.95	38.7	53.7	118.4
	(17.8)	(39.0)				
Rs [MΩ]	0.52	2.12	0.69	2.48	0.87	0.72
Q	27000	37000	29000	37000	30000	28000

Date in ( ) were obtained from the measurement with 1/10 scaled model.

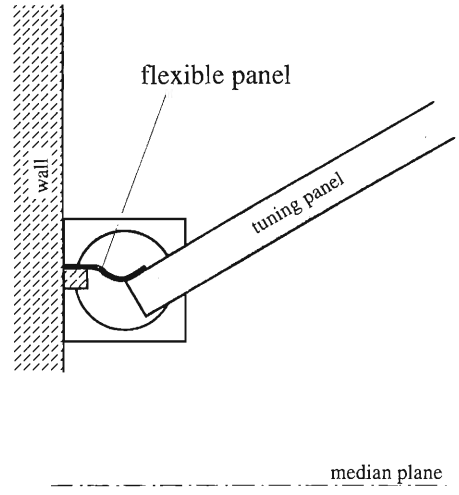

Fig. 2. Flexible panels are used to make contact between the wall and the tuning panel.

be restricted mainly by cooling problem at the flexible panels which are installed to make an electric contact between the tuning panel and the wall (Fig. 2). The power loss limit at the flexible panel is 4.7 W/cm^2 which corresponds tothe current density of 100 A/cm at 100 MHz. In the acceleration resonators, the wall loss at the root of the tuning panel is rather large. From the MAFIA calculation for the SRC resonator, the maximum power loss at the flexible panel is turned out to be 0.4 W/cm^2 at 38 MHz with the gap voltage of 600 kV.

In order to find the accuracy of the resonant frequencies obtained from MAFIA calculations, a 1/10 scaled model of the SRC acceleration resonator was constructed (Fig. 3). The model was made of wood

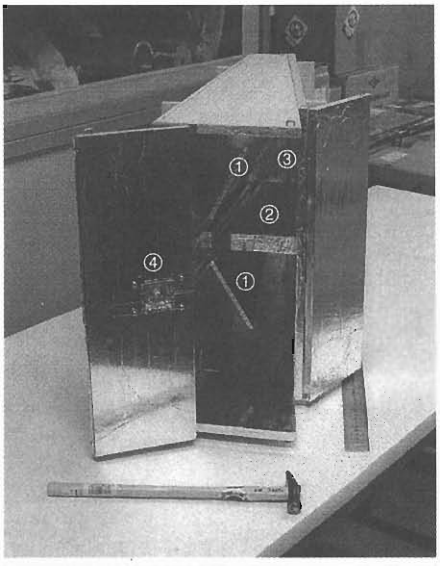

Fig. 3. Photograph of the model of the SRC acceleration resonator. 1: tuning panel, 2: Dee, 3: feeder, 4: pickup.

boards covered with an aluminum foil with a thickness of 15 μm. The resonant frequencies were measured by using a network analyzer for the tuning panel angles of 0° to 90° with a step of 15° (Fig. 4). We estimated the error due to a misalignment of the tuning panels and/or due to a deformation of the cavity to be

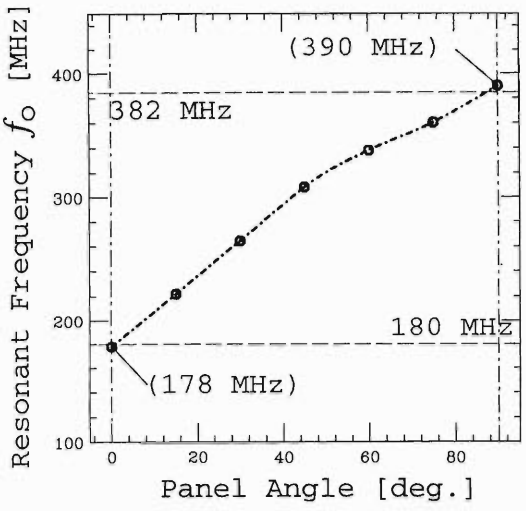

Fig. 4. Measurement of the resonant frequency with the 1/10 scaled model.

less than ±5.0 MHz which corresponds to ±500 kHz for 1/1 scaled cavity. As shown in Fig. 3, the resonant frequency is quasi-proportional to the tuning panel angle. The resonant frequencies at the panel angles of 0° and 90° are well reproduced by the MAFIA calculation with an accuracy of a few percent (see Table 1). The test with the 1/10 scaled model demonstrates the reliability of the MAFIA calculation for this structure. The details of the dimension will be determined from the result of the calculation. Further investigation on the feasibility of our RF system will be made by using a 1/5 scaled model which is now under construction. The size of the inductive coupler will be determined by using the 1/5 scaled model.

References

1) N. Sakamoto et al.: RIKEN Accel. Prog. Rep. **31**, 222 (1998).
2) T. Saito et al.: Proc. 12th Int. Conf. on Cyclotrons and Their Applications, Berlin, 1989, p. 201 (1989).
3) The MAFIA collaboration, User's Guide MAFIA Version 3.2, CST GmbH, Lauteschägerstraße 38, D-64289, Darmstadt, Germany.

Vacuum System for RIKEN Superconducting Ring Cyclotron

K. Sugii, K. Ikegami, S. Yokouchi, A. Goto, and Y. Yano

In this report, we describe the current design of the pumping system for beam chamber and other vacuum chambers of the Superconducting Ring Cyclotron (SRC).[1] Aiming at a beam transmission over 99% for all the ion beams available in the SRC, we have estimated the required pressure of a beam chamber from the relationship between the pressure at beam chamber and the beam loss which is caused by a change of charge state due to collisions of the beam against residual gas.[2] The result shows that the pressure at the beam chamber should be reduced down to the order of 10^{-6} Pa in order to restrict the beam loss within 1% for very-heavy ions. On the other hand, it is presumed that the outgassing rate for the materials exposed to high vacuum is very high since the bake-out of vacuum chamber will not be carried out. The vacuum chamber of the SRC consists of six sector-beam chambers, four rf cavities, one unit of flattop cavity, and one unit of valley chamber. Table 1 shows the total volume of the vacuum chamber and the surface areas of main materials exposed to high vacuum. In order to achieve the required range of pressure described above as quick as possible, we are planning to use sixteen cryopumps with a total pumping speed of 150 m^3/sec as main pump.

Table 1. Total volume of the vacuum chamber and the surface areas of main materials exposed to high vacuum.

Stainless steel	397 m^2
Copper	572 m^2
FPM (O-ring)	5 m^2
Chamber volume	85 m^3

Figure 1 shows the pumping system for the vacuum chamber of the SRC. The pumping system consists of a roughing system, a high vacuum system and an ultra-high vacuum system. The roughing system is composed of a roots pump of 2600 m^3/h and a rotary pump of 290 m^3/h. This roughing system is installed at the flattop cavity and the valley chamber. The high vacuum system is composed of a turbo-molecular pump of 5.5 m^3/sec and a rotary pump of 155 m^3/h. This high-vac system is installed at each rf cavity. The turbo-molecular pump of high-throughput type is to be used. The reason for it is to shorten the pumping time prior to the ultra-high vacuum system by switching the pumping system from the roughing system to

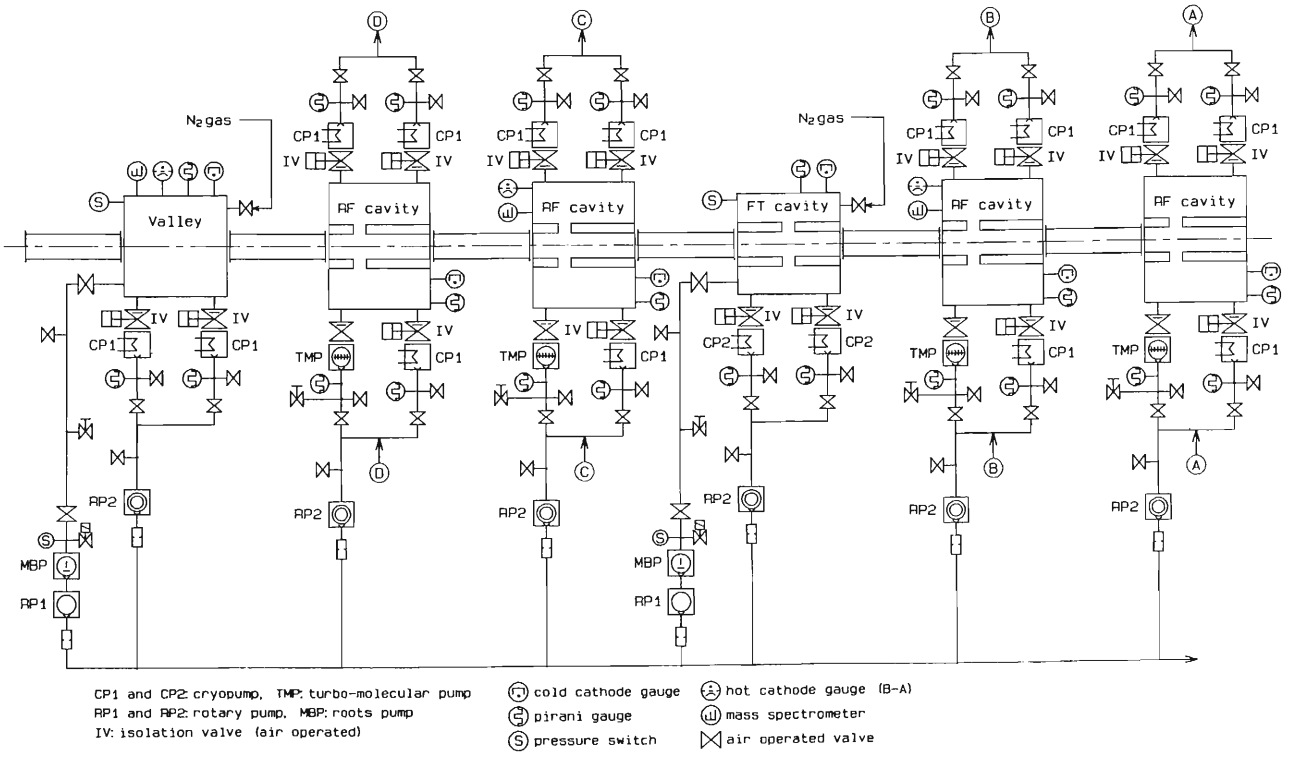

Fig. 1. Pumping system for the vacuum chamber of the SRC.

the high vacuum system at a higher pressure (about 70 Pa). If the ultra-high vacuum system starts to operate at the pressure of 1×10^{-3} Pa, the total pumping time during the operation of the roughing system and high vacuum system is calculated to take about 9 hours (from the atmosphere to 1×10^{-3} Pa).

The ultra-high vacuum system deploys 16 cryopumps: fourteen of 10 m^3/sec and two of 5 m^3/sec. The two cryopumps of 5 m^3/sec are installed at the flattop cavity and those of 10 m^3/sec are distributed to be installed at the valley chamber and to all of the rf cavities. We chose cryopumps as the main pump of ultra-high vacuum system, for they have large pumping speeds against the water vapor and hydrogen gas, both of which are predominant residual gas components in an unbaked vacuum system. Furthermore, they can be operated even in a large environmental magnetic field. Total effective pumping speed of the cryopumps is about 66 m^3/sec at the beam passage. By using this pumping speed and the published data for outgassing rate of materials, the pumping-down time to achieve the order of 10^{-6} Pa is estimated to be more than a few hundred hours.

An isolation valve is installed between the cryopump and the vacuum chamber, so that the maintenance for each of them can be made independently. The isolation valve is required to be compact since the space available for its installation is extremely limited. We are currently making trial of a manufactured valve.

The pressure of the vacuum chamber of the SRC will be measured with a nude type of hot ion gauge during a shutdown period of the SRC. During the SRC operation, since a hot ion gauge is of no practical use due to a large leakage flux from the sector magnet, we are supposed to use a cold cathode gauge. Being constructed with a permanent magnet, it is expected to be usable even in a large external magnetic field. Measurement of pressure using a cold cathode gauge under an external magnetic field is actually reported.[3] We are currently investigating the effect of an external magnetic field on a cold cathode gauge.

References

1) A. Goto et al.: RIKEN Accel. Prog. Rep. **32**, 193 (1999).
2) K. Sugii et al.: RIKEN Accel. Prog. Rep. **31**, 224 (1998).
3) N. Yasumitsu: Proc. 8th Meet. on Ultra High Vacuum Techniques for Accelerators and Storage Rings, KEK, p. 75 (1992).

Development of ACR Electron Cooler (1)

T. Tanabe, K. Ohtomo, T. Rizawa, and T. Katayama

An electron cooler (EC) has been proven to be one of the most effective devices to reduce the phase space volume of charged particle beams in the accelerators. A scheme of adiabatic transverse expansion[1] has been chosen for the Accumulator Cooler Ring (ACR) cooler to further reduce the electron transverse temperature than a normal configuration. It is well known that the average transverse energy of the ensemble of electrons divided by the axial magnetic field is adiabatic invariant:

$$<E_\perp> /B = \text{const.}$$

Therefore, by changing the strength of solenoid field from the gun section to the interaction region adiabatically, where the length of field change is much larger than electron's gyration radius, the transverse temperature of the electron beam could be reduced by a factor of B_f/B_i. Here, the subscript f indicates the final value and i the initial value. The electron kinetic energy E_e can be determined by the nominal energy of the ion beam E_i according to the following relation:

$$E_e\ [\text{MeV}] = (\varepsilon_e/\varepsilon_i)E_i\ [\text{MeV}], \quad (1)$$

where $\varepsilon_e = 0.511$ MeV and $\varepsilon_i = 931.501$ MeV/u. The ion energies in ACR vary from 60 to 400 MeV/u, which translates to the electron energies from 30 to 250 keV to cover the entire range.

The beam diameter of 50 mm is derived from the requirement to cover the horizontal size of ion beams (maximum emittance of 125π mm·mrad and horizontal betatron function of 4.34 m). An axial magnetic field of 0.2 T is chosen to satisfy magnetization condition for the lightest ions. The expansion factor of 25 corresponds to the field of 5 T in the gun section. The maximum available current is determined by the perveance of the gun which is fixed by the geometry and extraction voltage, and it is practically limited by the electrical discharge limit. In our case the electron beam current of 4 A is considered to be viable. Length of the cooler is 3.6 m within ACR perimeter of 168.48 m, which translates to the relative cooler length of 0.02136. Other pertinent parameters are summarized in Table 1.

The result of our initial investigation of the electron gun with the adiabatic beam expansion scheme has been reported elsewhere.[2] Currently, a new design of the gun and accelerating tube is being investigated to reduce the bore radius of a superconducting solenoid surrounding the gun section. The collector design has been chosen similar to the one used for TARN-II with some modifications to accommodate the higher beam current and more vacuum capability. The designs of shakers and clearing electrodes are underway.

Table 1. Other ACR-EC parameters.

Toroidal angle/radius	90°/1200 mm
Field uniformity	0.2% (gun)/$\pm 5 \times 10^{-4}$
HVPS stability	$\pm 1 \times 10^{-5}$
Collector efficiency	> 99.98%
Betatron tunes	$Q_x = 4.555$, $Q_y = 3.540$
Beta functions at EC	$\beta_x = 4.339$, $\beta_y = 3.281$ [m]

Effects of the main solenoid on ion beam have been studied using MAD[3] program. A toroidal field has to be approximated by the combination of 'thin lens' kicker fields (H&V) and two effective solenoid fields on both sides with following relations:

$$B(R) = B_0 R_0/R; R = R_0/\cos\phi, \quad (2)$$

$$B_\nu = B(R)\cdot\cos\phi; B_h = B(R)\cdot\sin\phi, \quad (3)$$

$$s = s(\phi_0) - R_0\cdot\tan\phi, \quad (4)$$

$$\Theta_s = \frac{1}{B\rho}\cdot\int_{\phi 0}^{0} B_h\cdot ds = \frac{B_0 R_0}{B\rho}\phi_0, \quad (5)$$

$$\Theta_h = -\frac{B_0 R_0}{B\rho} ln(\cos\phi_0), \quad (6)$$

$$\Theta_\nu = \frac{(B\rho)_e}{(B\rho)_{ion}}\tan\phi_0. \quad (7)$$

Here, ϕ is the angle from the center of the toroid and ϕ_0 is half the toroidal angle (45°). B_0 is the solenoid field strength and R_0 is the toroidal bending radius. Table 2 summarizes the configuration of the magnets used in the simulation.

Table 2. Configuration of the magnets for CSs and kickers.

ELEMENT	LENGTH[M]	B FIELD [T]	ANGLE
CSOL	Variable	−0.2*1.37124	
DCSOL	0.15		
SD1	0.1		
DDS2	0.35		
BM	1.896	1.5	22.5deg
DD22	0.3		
CHK2	0 (0.2)	(0.254)	7.02mrad
DD22	0.3		
QF	0.4	10.32T/m	
DD1	0.2		
QD	0.4	−10.73T/m	
DSOL	0.5		
CVK1	0 (0.05)	(−0.0348)	−0.24mrad
CHK2	0 (0.2)	(−0.67)	−18.50mrad
DSOL	0.5		
TSOL2	0.6	0.2*0.6435	
SOLVK	0		0.24mrad
SOLHK	0		11.48mrad
TSOL1	0.6	0.2*0.9273	
SOL0	1.8	0.2	

Compensation solenoids (CSs) are located in the adjacent straight sections. Correction kickers are placed in the same straight section as the main solenoid. Single particle tracking with 20000 turns was conducted for each case. The observation point is at the center of the main solenoid. The results are summarized in Table 3, which indicates that the vertical beam size with the presence of the main solenoid increases by more than a factor of two, without any compensation. (Figs. 1 and 2)

The result of a tracking with correction kickers and CSs is shown in Fig. 3. The vertical beam size has been reduced close to the value without the EC. The integrated field of the solenoid for this case turns out to be half a value, which the calculation from Eq. (2)–(7) implies. The reason for this discrepancy is deemed in the following: The calculation assumes that all the compensations are done in the same straight section. However, in the tracking, CSs are placed in the adjacent straight sections. Therefore, the uncompensated beam experiences quadrupole and dipole fields which

Table 3. Ion beam size with varying CS field.

Integrated compensation solenoid field (T)	Beam size in X (mm)	Beam size in Y (mm)
No EC (Fig. 1)	23.5	6.0
0 (Fig. 2)	25.0	13.2
0.25*2[m]*0.274[T]	24.0	10.0
0.5*2[m]*0.274[T] (Fig. 3)	23.5	6.5
0.75*2[m]*0.274[T]	24.0	7.8
1.00*2[m]*0.274[T]	23.7	11.5

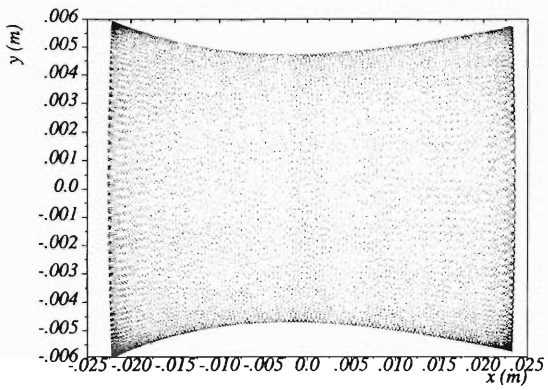

Fig. 1. A single-particle tracking result after 20000 turns without main solenoid.

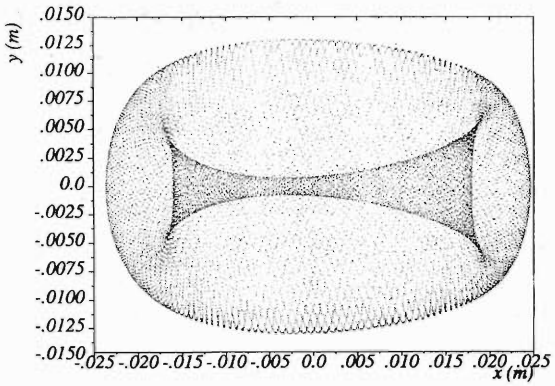

Fig. 2. A single-particle tracking result after 20000 turns with main solenoid, but without any compensation.

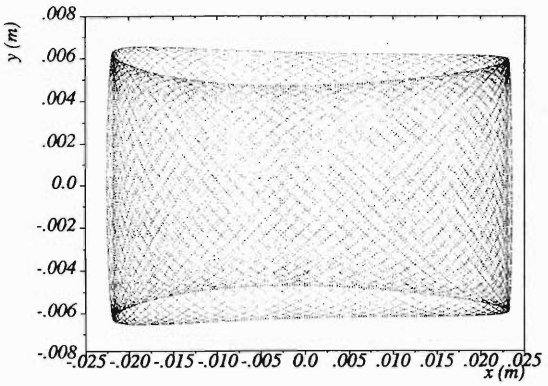

Fig. 3. A single-particle tracking result after 20000 turns with main solenoid, compensation solenoids, and correction kickers with proper strengths.

modify the dynamics of beam before entering a CS. Further investigation on the subject is being undertaken at present.

We have not ruled out the possibility to modify the lattice of ACR to accommodate EC, correction kickers, and CSs in one straight section. In this case, use of superconducting solenoids for CSs is contemplated.

References

1) Y. N. Rao et al.: Electron Cooling at ACR 1996, Proc. EPAC '96, p. 1182 (1996).
2) I. Watanabe et al.: Electron Cooling at ACR in MUSES Project, Proc. EPAC '98, p. 2258 (1998).
3) MAD program, version 8.22., copyright by CERN.

Design Study of Electric Power Station for RIKEN-MUSES Project

S. Watanabe and T. Katayama

The accelerator complex of MUSES project comprises an accumulator ring (ACR), a booster synchrotron ring (BSR), and a double storage ring (DSR). There are so many electric power supplies with an assumption of electric power up to 15 MVA.[1] Considerable line impedance of AC power line branched under the electric- power company will bring unavoidable voltage drop not only at the accelerator complex but also at experimental apparatus. A designed synchrotron power supply of BSR will induce both a large reactive power and a higher ripple current because of the 12-phase thyristor rectifier.[2] An energy bill relating with the operation of BSR will become a large part of considerable running cost. Thus, the design study of site-specific power station is focused on a cleaned AC power line, a good power factor, and an optimized energy bill. The present paper is concerned with the advanced study of BSR power supply and with the brief description of R&D relating with the switch-mode power supply for the ACR lattice magnet.

The operating conditions of BSR have been studied from the power supply point of view. The following operating conditions fulfill the combination of different ion species or of ion-electron acceleration: (1) Polarity change is no longer required in order to inject different ion species; (2) Pulse-to-pulse operation for different ion species requires complicated current pattern control; and (3) Deceleration of an accelerated beam is required to decrease the radioactive contamination at beam-damp courses.[3] Unfavorable remnant field due to a hysteresis loop should be corrected for the dipole, quadrupole, and sextupole families.[4] An example of the measured hysteresis is shown in the literature.[5] The result of analysis shows that the Fourier component of excitation pattern should be optimized since the area of hysteresis curve is proportional to the repetition cycle of magnetic field as is well known. An eddy current in the magnet gap and vacuum chamber of the ring gives an excess of sextupole excitation to the beam optics. The tune tracking and chromaticity control are influenced by the magnetic saturation effects. The study of BSR power supply will be focused in the near future on those tricky problems.

By using the synchrotron power supply of the cooler-synchrotron TARN-II, an R&D has been conducted aiming at the ripple reduction of BSR. The old DCCT to have measured the magnet current was replaced with HOLEC- DCCT. A normal-and-common mode filter was installed in the line circuit of the dipole magnet strings. The new DCCT has the accuracy of 1 ppm during the past one and a half years. The typical ripple current measured by the new pick-up coil in the magnet gap was dramatically reduced by -40 dB compared with the original data.[6]

A line voltage fluctuation called flicker would be deduced from the induced reactive-power due to the pulse operation of BSR. The site-specific power station is subject to stabilize the line voltage of RI-beam

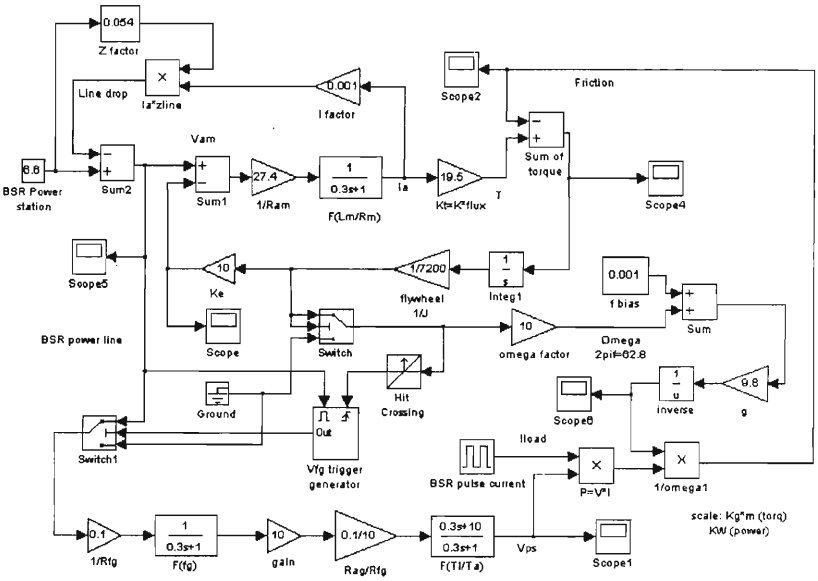

Fig. 1. Flow simulation of the BSR power station.

factory, so that the interference between the electric-power line of BSR and the outside of BSR electric-power line should be minimized. Induced reactive-power is compensated with a hybrid power-saving system located in the BSR power station. The hybrid power-saving system (HPSS) comprises a Static-Var-Compensator (SVC) and motor- generator (MG) to stabilize the primary line-voltage of 6.6 kV and to suppress the 3rd, 5th, 7th and higher harmonic currents. The dipole-magnet power supply is branched directly under the HPSS. The power supplies of quadrupole-magnet group are branched under the HPSS through the sub-power station with local SVC.

The simulation of BSR power station has been done with MATLAB. Figure 1 illustrates the MG with flywheel system, BSR power supply model, line impedance, and turn-on sequence with closed loop circuit.

MG-parameters were estimated as follows: The power ratings of induction motor and AC generator are 1.65 and 12.95 MW, respectively. The inertial moment of flywheel is designed at 7.2 [ton m^2] to achieve the frequency stability of 0.5% at a rotation speed of 600 rpm. The dissipation of stored energy in the flywheel is illustrated as the sum of the negative energies due to the apparent power of BSR. To shorten the calculation time, parameters in the flow simulation was optimized. The examples of simulation are shown in Fig. 2 and 3, respectively. Figure 2 shows the AC line voltage after turn-on and continuous operation of the MG system.

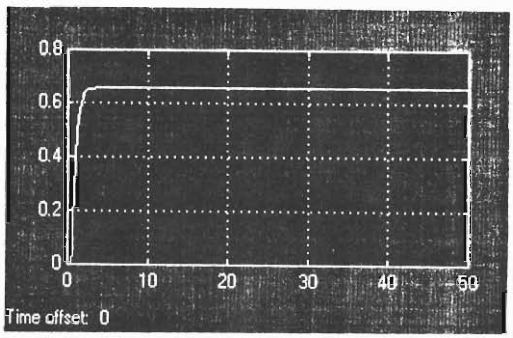

Fig. 2. Rise of AC line voltage after turn-on of MG system.

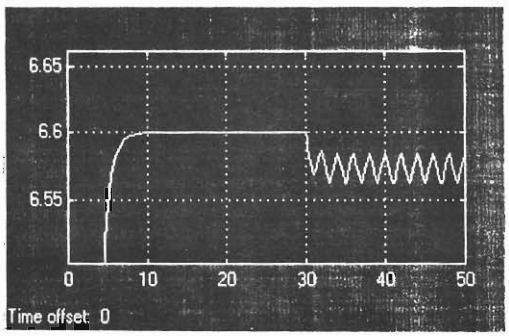

Fig. 3. Voltage drops of the MG output due to repetitive BSR operation.

Fluctuation of the AC line voltage due to the repetitive operation of BSR is calculated as shown in Figure 3. The voltage drops due to the pattern operation are seen in the figure. The apparent power of BSR is calculated at peak.

The power line accident would occur due to any reason. The diesel engines would be used during the peak-electricity days to reduce the energy bill. The solution of redundancy, adapted directly onto the 6.6 kV line of the 10 MVA peak-power requirement, is a new way of supplying electricity to all the sensitive equipments of MUSES complex. Thus, RI-beam factory considers the power plant that is composed of 2 sub units of 1 MVA, each connected in parallel in a $N + 1$ redundant way. The parallelism is performed at the 6.6 kV level. This means that the system is composed of two 6.6 kV bus bars one for the input and another for the output. The motor generator mentioned above is mechanically connected to those diesel engines with the magnetic-crutch.

The design study of ACR magnet power supply has been performed. The lattice structure of ACR is based on the race-track FODO functions with a large beam acceptance. A switching dc-power supply with power rating of 20 or 2 KVA can be used to excite the quadrupole and sextupole magnets. Difficulty for the magnet power supply is to make the ripple field low as required for the beam cooling experiments. Designed switching regulator is described as follows: One AC-DC converter and four inverters comprise a complete unit of switching power supply. The AC-DC converter delivers pre-regulated dc power to each inverter unit. Each inverter unit is a pulse- width-modulation type switched regulator that is composed of insulated-gate-bipolar transistor, coupling transformer, rectifier, and current control loop. To suppress the ripple current, the polyphase technique is applied to the inverter unit. The normal and common mode filters are equipped in the polyphase inverter unit to suppress a ripple current up to 120 KHz. The electromagnetic shielding is subjected to suppress the radiated electromagnetic field from the switching elements. The common-mode filter is equipped in the AC-DC converter to suppress the leak-noise entering into the primary AC lines. A combination of the 12-phase thyristor rectifier and transistor-type series dropper is considered as the ACR dipole-magnet power supply.

References

1) T. Ohkawa et al.: Proc. EPAC98, p. 2123 (1998).
2) S. Watanabe et al.: Proc. EPAC96, p. 2340 (1996).
3) S. Watanabe et al.: Proc. EPAC98, p. 2082 (1998).
4) B. C. Brown et al.: FERMILAB-Conf-97/147 (1997).
5) S. Watanabe: INS-T-533, Accelerator-20 (1995).
6) S. Watanabe et al.: Proc. 11th JPAC, p. 101 (1997).

Design of a Slow Extraction System at Booster Synchrotron for MUSES

T. Ohkawa and T. Katayama

In Booster Synchrotron Ring (BSR) the accelerated ion and electron beams will be fast extracted, and subsequently injected into Double Storage Rings (DSR) by one turn injection. As an alternative mode of operation, the ion beam will be slowly extracted for the experiments. In this paper the slow extraction procedure of ion beam at the BSR is presented.

For slow extraction process, firstly, the sextupole magnets as a resonance exciter are excited. Secondly, the horizontal tune is changed from the operating value 6.691 to a certain value near the third order resonance (20/3) by controlling the excitation currents of the quadrupole magnets. Beams which have deviated more than 25 mm inside from the central orbit at the entrance of the electrostatic septum (ES) are deflected inward as large as 3 mrad by the static high-voltage of ES.

The Hamiltonian can be expressed by the following relation

$$H = -\frac{\varepsilon}{2}(X'^2 + Y'^2) - \frac{\beta g\sqrt{A^2+B^2}}{3\sqrt{1+\alpha^2}}(X'^3 - 3X'Y'^2),$$

from which we can obtain following three unstable fixed points:

$$A:\ (X'_1, Y'_1) = \left(-\frac{\varepsilon\sqrt{1+\alpha^2}}{\beta g\sqrt{A^2+B^2}}, 0\right)$$

$$B:\ (X'_2, Y'_2) = \left(-\frac{1}{2}X'_1, -\frac{\sqrt{3}}{2}X'_1\right)$$

$$C:\ (X'_3, Y'_3) = \left(-\frac{1}{2}X'_1, \frac{\sqrt{3}}{2}X'_1\right).$$

Transforming back to the (x, x') plane, we obtain the following three unstable fixed points:[1)]

$$A:\ (x_1, x'_1) = \left(-G\cos(\Psi-\chi), \frac{\sqrt{1+\alpha^2}}{\beta}G\cos(\Psi+\chi)\right)$$

$$B:\ (x_2, x'_2) = \left(-G\cos\left(\Psi-\chi+\frac{2}{3}\pi\right), \frac{\sqrt{1+\alpha^2}}{\beta}G\cos\left(\Psi+\chi+\frac{2}{3}\pi\right)\right)$$

$$C:\ (x_3, x'_3) = \left(-G\cos\left(\Psi-\chi-\frac{2}{3}\pi\right), \frac{\sqrt{1+\alpha^2}}{\beta}G\cos\left(\Psi+\chi-\frac{2}{3}\pi\right)\right),$$

where

$$\tan\chi = \sqrt{1+\alpha^2} - \alpha$$

and

$$G = \frac{\varepsilon(1+\alpha^2)^{\frac{3}{4}}}{\beta g\sqrt{A^2+B^2}}.$$

The turn separation Δx during three turns can be derived from the Hamiltonian as follows:

$$\Delta x = \frac{[\sqrt{1+\alpha^2}+\alpha]^{\frac{1}{2}}(\Delta X'\cos\Psi - \Delta Y'\sin\Psi)}{\sqrt{2}} + \frac{[\sqrt{1+\alpha^2}-\alpha]^{\frac{1}{2}}(\Delta X'\sin\Psi + \Delta Y'\cos\Psi)}{\sqrt{2}},$$

where

$$\Delta X' \equiv \frac{dX'}{d\nu} = -\frac{\partial H}{\partial Y'} = \varepsilon Y' - \frac{2\beta g\sqrt{A^2+B^2}}{\sqrt{1+\alpha^2}}X'Y'$$

$$\Delta Y' \equiv \frac{dY'}{d\nu} = -\frac{\partial H}{\partial X'} = -\varepsilon X' - \frac{\beta g\sqrt{A^2+B^2}}{\sqrt{1+\alpha^2}}(X'^2 - Y'^2).$$

If we use two sextupole magnets as a resonance exciter, their strengths are given by

$$g_1 = \frac{(A_2\tan 3\Psi + B_2)\cos 3\Psi\sqrt{A^2+B^2}}{A_2B_1 - A_1B_2}g$$

$$g_2 = -\frac{A_1\tan 3\Psi + B_1}{A_2\tan 3\Psi + B_2}g_1.$$

But, there is a little difference between the separatrices obtained by the theory and the orbit tracked with computor, because we take only one of the nonlinear terms which has the largest contribution to the resonance orbit.

For example, if we assume S to be 10π mm·mrad and Δx to be 5 mm, we have[2)]

$$\Psi = 32^\circ$$
$$g_1 = 1.461\ \mathrm{m}^{-3}$$
$$g_2 = -0.333\ \mathrm{m}^{-3}.$$

Result of tracking is shown in Fig. 1, where the outgoing trajectory at the entrance of ES is different from that obtained by the theory.

We therefore tracked of the orbit with computor changing Ψ as a parameter, and chose the best strenghs of the sextupole magnets.

$$\Psi = 29^\circ$$
$$g_1 = 1.166\ \mathrm{m}^{-3}$$
$$g_2 = 0.025\ \mathrm{m}^{-3}.$$

Result of tracking is shown in Fig. 2, where the outgoing trajectory at the entrance of ES is very close to that obtained by the theory.

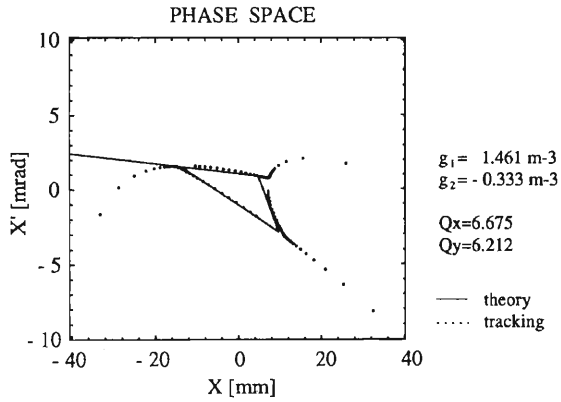

Fig. 1. The separatrices and outgoing trajectories at the entrance of ES ($\Psi = 32°$).

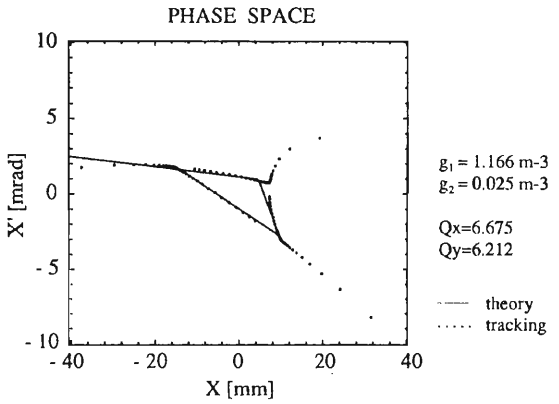

Fig. 2. The separatrices and outgoing trajectories at the entrance of ES ($\Psi = 29°$).

Next, we calculate the number of extracted particles. The area of the triangular separatrix in the (x, x') plane is given by

$$S = \frac{3\sqrt{3}}{4}|\sin 2\chi|\frac{\sqrt{1+\alpha^2}}{\beta}G^2 = \frac{3\sqrt{3}}{4}|\sin 2\chi|\frac{(1+\alpha^2)^2}{\beta^3 g^2(A^2+B^2)}\varepsilon^2.$$

If the area of the triangular separatrix becomes smaller, the particles with larger amplitude will reach the separatrix to escape from the stable region. As soon as single particle escapes from the stable region, its amplitude will blow up rapidly along the out-going separatrix, and will finaly jump into the gap of the ES. The amount of reduction of the triangular separatrix is given by

$$\Delta S = \frac{3\sqrt{3}}{2}|\sin 2\chi|\frac{(1+\alpha^2)^2}{\beta^3 g^2(A^2+B^2)}\varepsilon\Delta\varepsilon,$$

which indicates that the extracted particle numbers can be controlled by the phase shift ε. We have calculated relation between tune and extracted particle numbers. Result of the calculation is shown in Fig. 3.

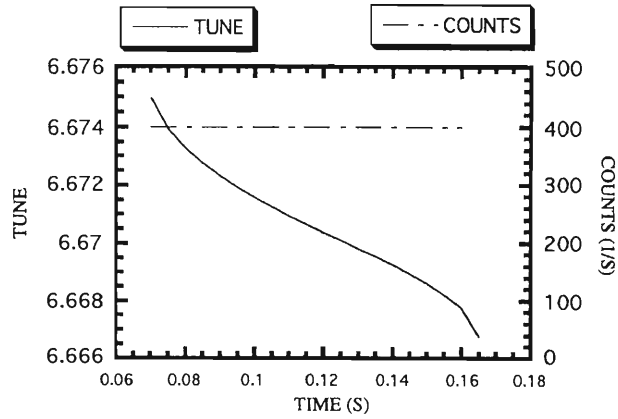

Fig. 3. Tune and extracted particle numbers per second vs. time for Gaussian distribution ($\Delta p/p = 0$).

We have found that a slow extraction of ion beam can be carried out by using the third order resonance ($\nu_{res} = 20/3$). This procedure needs to be investigated further for the installation of all necessary hardwares.

References

1) Y. Kobayashi: Nucl. Instrum. Methods **83**, 77 (1970).
2) T. Ohkawa and T. Katayama: Proc. 6th EPAC, Stokholm (1998).

Ferrite Test Cavity for MUSES†

K. Ohtomo and Y. Chiba

In the project MUSES, it is urgent to develop a ferrite loaded cavity for the Booster Synchrotron Ring. The cavity should operate with the frequency range from 25 to 53 MHz, the voltage 25 kV per cavity, and the repetition frequency 1 Hz. For this purpose, it is necessary to meet the following characteristics of the ferrite material: the relations between permeability (μ) and bias current, magnetic Q-value (Q_m) and RF flux density, and between high loss threshold[1] and bias sweep rate. Moreover, these measurements have to be performed with the real size of ferrite and with real RF power level of operation. We therefore designed and manufactured a test cavity for investigating the RF properties of ferrite. Table 1 shows the parameters of the test cavity.

Table 1. Parameters of the ferrite test cavity.

Cavity type	$\lambda/2$ coaxial resonator loaded with capacitor
Frequency range	20–60 MHz
Ferrite size	5″(I.D.)×8″(O.D.)×1″(thick) 400 mm max. in O.D.
Tuning elements	Bias current, Variable capacitor
Bias conductor	10 turns of water cooled hollow conductor
Cooling of ferrite	Water in cooling plate
RF source	A 3kW solid-state wide-band amplifier
Bias current	2500 A
Impedance matching	Variable capacitor in series

Figure 1 shows a schematic drawing of the ferrite test cavity. It consists of three coaxial arms: F, S, and C arms. The F and S arms are aligned in line and form a $\lambda/2$ resonator loaded with a tuning capacitance in C arm. In order to operate under the above frequency range at high power and high loss threshold, a water cooled vacuum variable capacitor (30–650 pF) is employed. Ferrite is tightly in contact with the cavity wall on both sides, and cooled through the wall by water. The size of ferrite is fixed to be 5 inches in inner diameter, 8 inches in outer diameter (O.D.) and 1 inch in thickness. We can test another size of ferrite with O.D. up to 400 mm by replacing the ferrite vessel.

Conductor for bias current are passing through inside the inner pipe, and wind ten turns around the ferrite ring. The upper parts of conductor are removable for exchange of ferrite. Thus, RF power is confined in the cavity, and does not affect measurement nor biasing system. A water-cooled hollow conductor

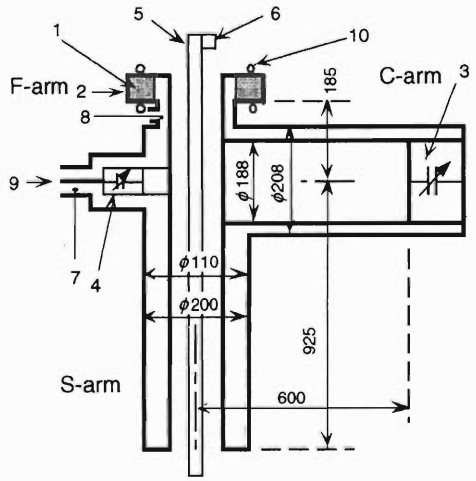

Fig. 1. Schematic drawing of cavity. 1-ferrite ring, 2-ferrite vessel, 3-tunig capacitor, 4-impedance matching section, 5-bias conductor, 6-removable cross bar, 7-voltage and current monitor, 8-2nd voltage monitor, 9-RF input terminal, and 10-water cooling pipe.

is used. Maximum bias current is set to be 2500 A. Most of the material of this cavity including a fixed stub is aluminum except the cooling parts.

Impedance matching between 50 Ω RF source and input impedance of the cavity is necessary to perform the test in high RF power level. Impedance conversion to use a series of variable capacitor (6–500 pF) was adopted. A current transformer and a voltage divider are installed at the entrance of the matching section in order to monitor the input impedance and input RF power. The 2nd voltage monitor is located at the entrance of the ferrite vessel. Figure 2 shows calculated

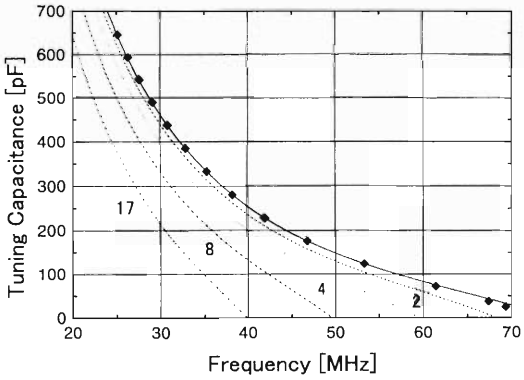

Fig. 2. Tuning capacitance and frequency at resonance. Marks represent experimental data and solid line was obtained by calculation without ferrite. Dashed lines are by calculations with ferrite for different μ as shown in figure.

† Condensed and revised from the article in Proc. 6th Eur. Part. Accel. Conf., p. 1823 (1998)

tuning curves of the system, where a transmission line calculation was used. Measured data on the empty ferrite vessel are plotted by filled squares. Unknown μ can be determined from these tuning curves. For measuring Q_m, input RF power and 2nd monitor voltage are measured, which determines the shunt resistance at the position of the 2nd monitor. Q_m can be calculated from the shunt resistance after corrected with contribution from the cavity system.

Test measurements of μ and Q_m were carried out

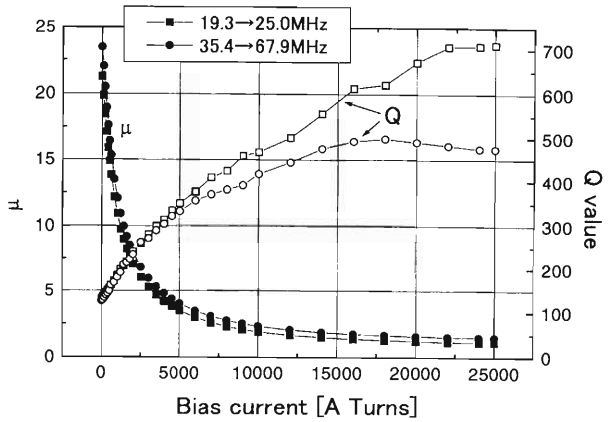

Fig. 3. Ferrite μ and Q_m as a function of bias current under low power test. Filled marks are μ and blank ones Q_m. Resonance frequency range are represented in the inset.

for the ferrite M11E by TDK. It was clarified that the bias current of 1000 A (10000 A-Turns) is enough for this ferrite to reduce the μ to become 2 (i.e., $\mu = 2$). Tentative results are shown in Figs. 3 and 4.

An unstable contact was found at the contact fingers used in the ferrite vessel. An improved vessel is being manufactured.

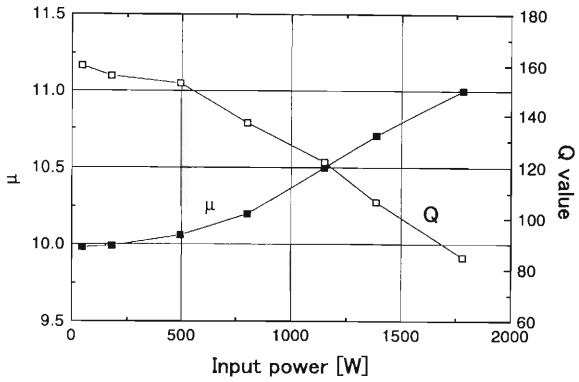

Fig. 4. Ferrite μ and Q_m as a function of the dissipation power at ferrite under high power test. Bias current is 20 A and resonance frequency is 28.6 MHz.

References

1) J. E. Griffin and G. Nicholls: IEEE Trans. Nucl. Sci. **NS-26**, 3965 (1979).

Simulation of Coherent Behavior of Electron-Cooled Bunched Ion Beam at the Ion-Storage Ring of RIKEN RI-Beam Factory Project

M. Takanaka and T. Katayama

Ion-beam bunching under electron cooling was studied by using a computer simulation for realization of the bunched beams required for collision experiments. The simulated results[1] have predicted that (1) the beam has wide tune spreads longitudinally and transversely, (2) the beam is not trapped into resonances due to the nonlinear fields of magnets, and (3) the beam is stable longitudinally under a broad-band impedance based on the broad-band impedance model.

A 150-MeV/u U_{238}^{92+}-ion beam at 3.4 mA has been simulated, and has the profile shown in Fig. 1 under the fundamental-RF (h = 87) voltage 16 kV and the third-RF-harmonic voltage 24 kV. Results of the coherent behavior of the beam are reported here.

The beam has a maximum instantaneous current of 45 mA at the bunch center. The beam has very wide incoherent tune spreads as shown in Fig. 2, because of the intense, small-sized charge distribution which is not flat in the transverse directions and parabolic in the horizontal direction. The spreads make synchrotron-tune multiples overlapped, and make the betatron and synchrotron tunes overlapped at the betatron-side bands. This is why one can not use the Sacherer method as a tool to predict instability phenomena.

Following equations are used to describe the coherent behaviors of the longitudinal beam intensity I and of the transverse dipole moment I_1 (transverse displacement $\times$ I):

$$I(t,s) = \sum_{\Omega,n} A_I(\Omega,n) \exp\left(-i\Omega t + i\frac{ns}{R}\right),$$

$$I_1(t,s) = \sum_{\Omega,n} A_{I_1}(\Omega,n) \exp\left(-i\Omega t + i\frac{ns}{R}\right),$$

where A is the amplitude of the component, t the time, s the longitudinal position, Ω the coherent frequency, n the oscillation mode along a ring, and R is the mean radius of the ring.

The longitudinal spectrum of the coherent behavior, or $A_I(\Omega,n)$ as shown in Fig. 3, has three kinds

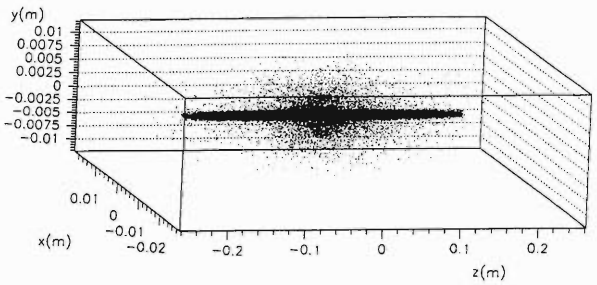

Fig. 1. Beam-bunch profile in the three-dimensional space.

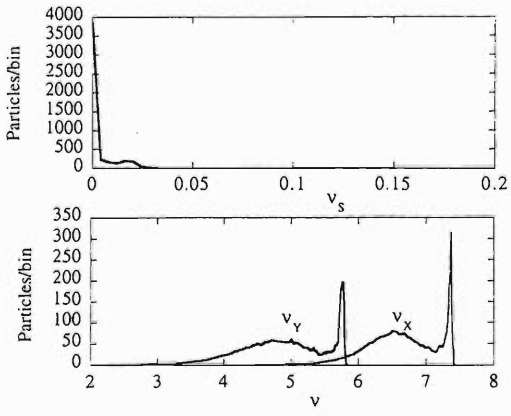

Fig. 2. Tune distributions of 5000 particles .

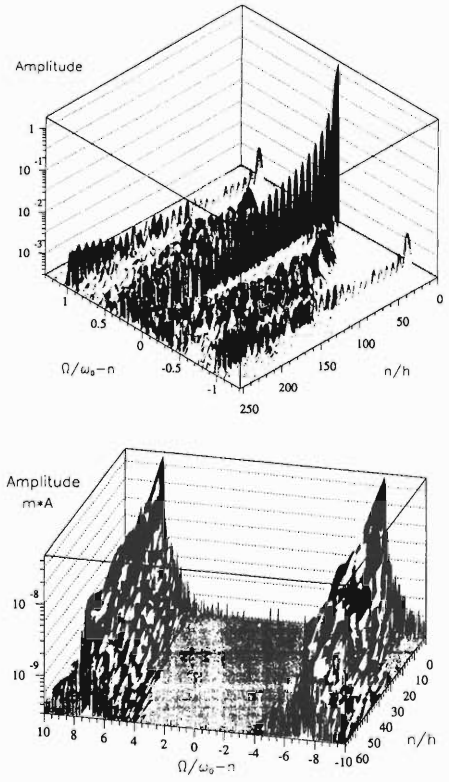

Fig. 3. Spectra of the longitudinal and the transverse oscillations. The upper spectrum is for the longitudinal oscillation, which is normalized so that the DC component is 1. The lower spectrum is for the transverse oscillation. The both spectra have the low signals cut away.

of signals: a signal along $\Omega/\omega_0 - n = 0$ due to the longitudinal parabolic charge distribution (monopole type); signals along $\Omega/\omega_0 - n = \pm 1$ due to the oscillation of the bunch length (quodrupole type), whose frequency is equal to the revolution frequency ω_0 in the case where the RF cavities are installed at a position along the ring; and signals around $\Omega/\omega_0 - n = \pm 1/2$ (dipole type). No signal due to the synchrotron tune is observable here, because of the overlap.

The transverse spectrum, or $A_{I_1}(\Omega, n)$, has two signals of the fast and slow waves along $\Omega/\omega_0 - n = \pm 7.4$.

Behavior of the bunch after shifting the bunch from the synchronous particle by 4 cm has been simulated for the sake of checking the longitudinal stability. As shown in Fig. 4, the longitudinal oscillation is seen to be damped within several periods of synchrotron oscillation.

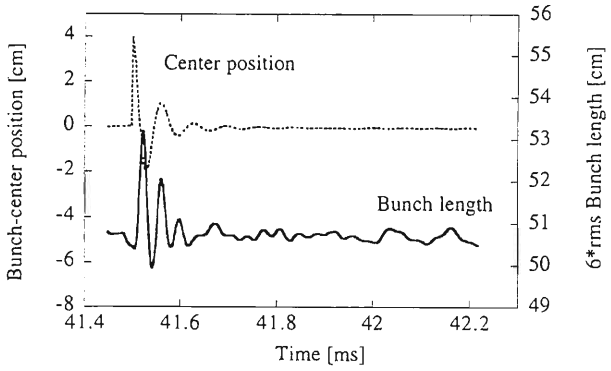

Fig. 4. Damping of the longitudinal oscillations.

Stability of the transverse behavior of the bunch after its shift from the central orbit is seen to be dependent on the shift distance, as shown in Fig. 5. The shift makes a dipole, or a pair of the dense and light spaces in the transverse phase space. In the unstable case of the shift distance of 2 mm, the dipole is incoherently mixed and the dipole moment decreases until 41.52 ms, but after then the dipole is coherently enhanced. The transverse emittance increases simultaneously, as shown by the thick curve in the lower of Fig. 5.

The transverse results have been obtained by using

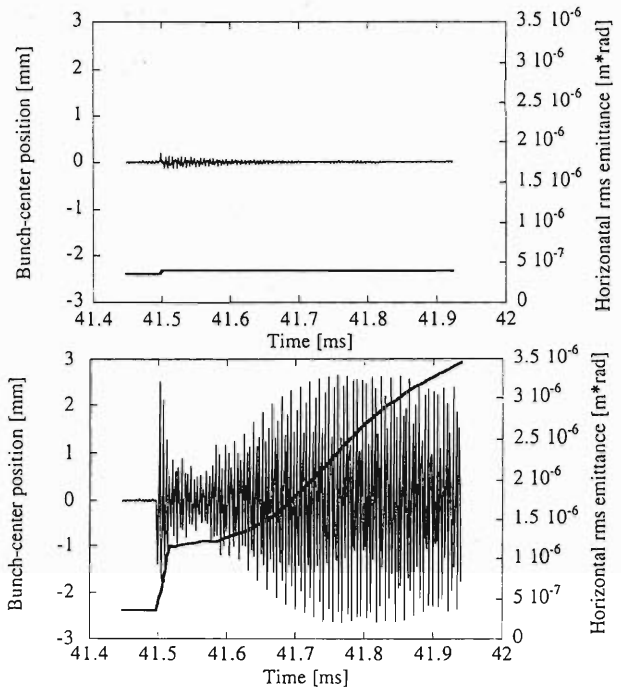

Fig. 5. Transverse oscillations. The upper figure is for the transverse shift distance of 0.5 mm. The lower figure is for the transverse shift distance of 2 mm. The thick curves are for the emittance, and the thin ones for the center position.

the transverse space-charge impedance model based on the following transverse charge distribution of the dipole mode, $\rho(r)$. The $\rho(r)$ is more realistic than the ring-type distribution on the assumption that the transverse charge distribution of the beam is not flat but Gaussian with the deviation σ:

$$\rho(r) = 2I_1 n(r) \cos\theta,$$

where

$$n(r) = \frac{r}{4\pi\sigma^4} \exp\left(-\frac{r^2}{2\sigma^2}\right).$$

References

1) M. Takanaka and T. Katayama: Proc. PAC'97, p. 1807 (1997); M. Takanaka and T. Katayama: Proc. EPAC'98, p. 1014 (1998).

Calculation of Single-Bunch Instability of Electron Beam at DSR

M. Wakasugi and T. Katayama

In the RI beam factory project,[1] we will construct an accelerator complex, which is called MUSES project.[2] At the double storage ring (DSR) in the MUSES, we plan to make unique experiments such as electron to RI collision and X-ray to RI collision experiments. This is why we have to store a high-quality electron beam with a large average current into the DSR. Especially, for the X-ray to RI collision experiment, the electron beam emittance should be on the order of 10^{-9} m·rad to produce a high-brilliance soft X ray by using an undulator.[3] Design of the DSR lattice[4] for a small-emittance electron beam may give us a serious problem of the beam instability. We have to specially care about the instability to achieve the targeted current of 500 mA in the energy range of 0.3–2.5 GeV. As the first step to study the beam instability at DSR, we have calculated the single-bunch instability caused by broadband impedances for a small-emittance mode of operation of the presently designed DSR.

The calculations were performed in both the frequency domain and time domain using a computer code made by ourselves. Various sources of the broadband impedance and their values were referred to thoses of SPring-8[5]; they are listed here in Table 1. Instability calculation in the frequency domain is based on treatment of the eigen-equation derived from well-known Sacherer's equation:

$$(\Omega - m\omega_s)R_m(r) = -i\frac{me^2\omega_0}{ET_0\beta^2}\frac{\varphi_0'}{r}$$
$$\sum_{m'=-\infty}^{\infty}\int_0^{\infty} R_{m'}(r')r'dr' i^{m-m'}\sum_{p=-\infty}^{\infty}\frac{Z_L(\omega')}{\omega'}J_m(\omega' r)J_{m'}(\omega' r') \quad (1)$$

for longitudinal oscillation and

$$(\Omega - \omega_\beta - m\omega_s)R_m(r) = -i\frac{vc^2\omega_0^2\omega_s}{4\pi E\eta\omega_\beta}\varphi_0(r)$$
$$\sum_{m'=-\infty}^{\infty}\int_0^{\infty} R_{m'}(r')r'dr' i^{m-m'}$$
$$\sum_{p=-\infty}^{\infty} Z_T(\omega')J_m(\omega' r - \frac{\xi\omega_0}{\eta}r)J_{m'}(\omega' r' - \frac{\xi\omega_0}{\eta}r') \quad (2)$$

for transverse oscillation, where $\omega' = p\omega_0 + \Omega$, $R_m(r)$ is the radial part of the perturbed quantity $\varphi_1(r)$ of the particle distribution $\varphi(r)$ given by

$$\varphi(r) = \varphi_0(r) + \varphi_1(r) = \varphi_0(r) + \sum_{m=-\infty}^{\infty} R_m(r)e^{im\phi} \quad (3)$$

in the longitudinal phase space, J_m is Bessel function, and the others are conventional notations. Solutions to the frequency shifts $\Omega - m\omega_s$ and $\Omega - \omega_\beta - m\omega_s$ are complex numbers; the imaginary part gives the growth rate of excited m-th mode of instability. Assuming a Gaussian distribution for $\varphi_0(r)$, we can express $R_m(r)$ by the Laguerre polynomial $L_h(R)$. Finally, these equations reduce to an eigen value problem for the frequency shifts.

Table 1. List of sources of broadband impedance.

Elements	No.	$Z_L/n(\Omega)$	Z_T (MΩ /m)
Bellow	50	-0.637 i	-0.087 i
Taper	2	-0.0008 i	-0.0001 i
Vacuum port	90	-0.0027 i	-0.0004 i
Button electrode	20	-0.076 i	-0.0103 i
Flange	300	-0.003 i	-0.0004 i
Weldment	200	-0.0006 i	-0.00008 i
Valve	30	12/n - 0.001 i	14/n - 0.001 i
Space charge	-	-0.0006 i	-0.00008 i
Resistive wall	-	$0.6(1\text{-}i)/\sqrt{n}$	$0.08(1\text{-}i)/\sqrt{n}$
Cavity	2	$8000(1+i)/n\sqrt{n}$	$1098(1+i)/n\sqrt{n}$

For example, one of the results of frequency domain calculation is shown in Fig. 1. This shows the eigen values for modes m = 0, 1, and 2 as a function of the electron beam current at the energy of 1 GeV. The mode coupling, which is a source of strong instability, happens at the single-bunch current of about 0.77 mA. It gives a threshold current of instability. In the same way, we found that the threshold current is 6.6 mA at the energy of 2 GeV. The threshold current depends on the RF voltage, because the bunch length changes by the RF voltage. Relation between the threshold current and the bunch length is shown in Fig. 2. Open circles indicate the threshold current at each RF voltage. The threshold current increase with increasing RF voltage. Its bunch length is, however, getting shorter with RF voltage. This bunch shortening limits the

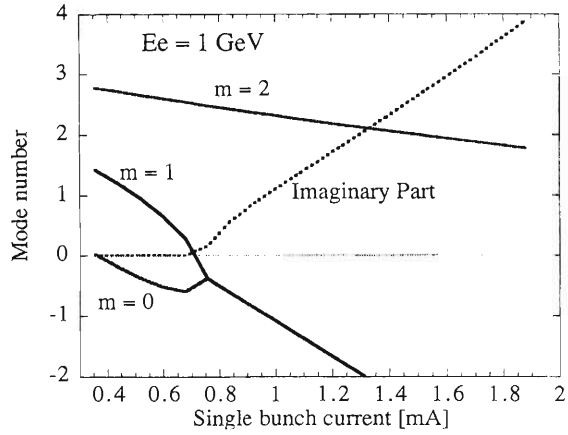

Fig. 1. Eigenvalues of the longitudinal oscillation modes as a function of the single-bunch current at 1 GeV.

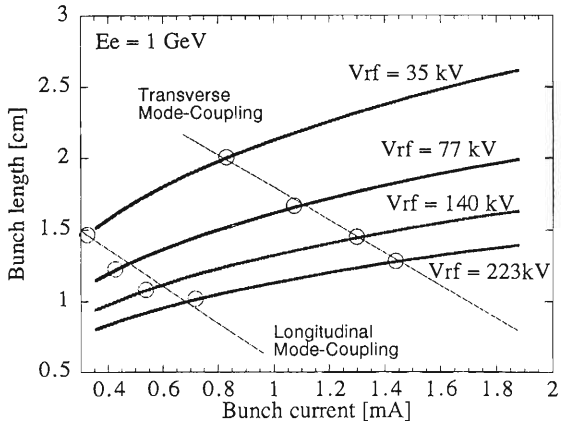

Fig. 2. Bunch lengthening due to the potential-well distortion. The starting points of mode coupling are indicated by open circles together with lines for the guide of eyes.

possible maximum current. It is anticipated from the figure that the maximum would not exceeded 1.5 mA for the case of 1 GeV. That is about one order less than our target current at 1 GeV. We found, however, that the upper limit of the current larger than the targeted current can be expected at 2 GeV.

Another approach adopted here is calculation in the time domain. This calculation is based on the tracking calculation using equations of motion including the wakepotential produced by a bunched beam itself at the source of impedance listed in Table 1. We can make relvant equation of motion for the betatron amplitude $a_i(\theta)$ as:

$$\frac{da_i(\theta)}{d\theta} = i\Delta\nu_{\beta_i} a_i(\theta) + \frac{e}{4\pi iE}\sum_{j=1}^{N_p} q_j a_j(\theta) \sum_{m=1}^{N_z} \beta_m W_{Tm}(\tau_j - \tau_i) \quad (4)$$

for transverse and

$$\frac{d\delta_i}{d\theta} = \frac{eV_0}{T_0}\sin\left(\phi_s + \frac{h\nu}{R}\tau_i\right) - \frac{e}{T_0}\sum_{j=1}^{N_p} q_j \sum_{m=1}^{N_z} W_{Lm}(\tau_j - \tau_i) - \frac{U_0}{T_0}(1 + 2\delta_i),$$
$$\frac{d\tau_i}{d\theta} = -\frac{\eta h\nu}{R}\delta_i, \quad (5)$$

for longitudinal, where N_p is the number of particles in a bunch, q_j the charge of j-th particle, N_z the number of the source of impedance, and β_m the beta function at m-th source. The radiation damping effect has to be taken into account as:

$$\Delta a_i = -i\frac{eV_{rf}}{E}\mathrm{Im}[a_i^* e^{i\theta\nu_\beta}]e^{-i\theta\nu_\beta}, \quad (6)$$

where a_i^* is the amplitude of betatron oscillation at the entrance of the RF cavity. The radiation excitation is also added as:

$$\Delta a_i = \sqrt{\frac{4\Delta T\varepsilon_0}{\tau_\beta}} v_i e^{i2\pi w_i} \quad (7)$$

for transverse and

$$\Delta\delta_i = \sqrt{\frac{4\Delta T}{\tau_\varepsilon}}\left(\frac{\sigma_\varepsilon}{E}\right) u_i \quad (8)$$

for longitudinal, where ΔT is the time advance, ε_0 the equilibrium emittance, τ_β the betatron damping time, τ_ε the synchrotron damping time, σ_ε the equilibrium energy spread, v_i and u_i are the random number forming a Gaussian distribution with rms = 1, and w_i is the random number forming a uniform distribution.

Growth of the amplitude (a_i) at several bunch currents is shown in Fig. 3. The 0 mA means no wakefield; and in this case, the amplitude decreases due to the radiation damping. In the case of 1 mA or 5 mA, it seems that there is no positive growth. Over 10 mA, especially for the case of 20 mA, however, it seems that the amplitude growth starts from about 8 msec. This situation may be made clearer by continuing the calculation for a longer time range. These results mean that the threshold current is supposed to be at around 10 mA.

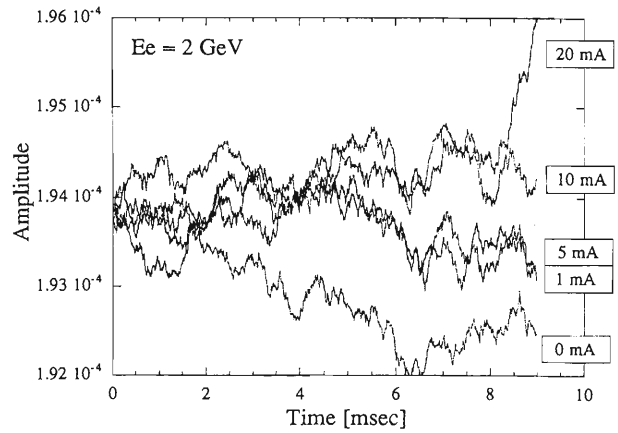

Fig. 3. Amplitude growth as a function of time.

References

1) Y. Yano et al.: Proc. PAC97, Vancouver, p. 930 (1997).
2) T. Katayama et al.: Nucl. Instrum. Methods Phys. Res. A **626**, 545c (1997).
3) M. Wakasugi et al.: Proc. PAC97, Vancouver, p. 3521 (1997).
4) N. Inabe et al.: Proc. PAC97, Vancouver, p. 1400 (1997).
5) T. Nakamura: Proc. EPAC 96, Barcelona, p. 1099 (1996).

Design Study of Superconducting Quadrupoles for RIKEN Big RIPS

T. Tominaka and T. Kubo

For the superconducting quadrupoles of RIKEN Big RIPS, the magnetic characteristics of two types of superconducting quadrupoles, that is, superferric and cos2θ (or shell) types have been studied using the 2D/3D electromagnetic field calculation codes of "PC-OPERA" and "TOSCA/OPERA-3d".[1,2]

For the 2D field calculation of the quadrupole with homogeneous quadrupole field region of r < 100 mm, two superferric type quadrupoles (#1 and #2) shown in Figs. 1 and 2, together with one cos2θ type quadrupole shown in Fig. 3, are compared on the parameters listed in Table 1.

As a result of the field analysis, the following characteristics have become clear for the three quadrupoles. The superferric #1 quadrupole magnet can produce the homogeneous quadrupole field with small multipoles of higher order, but only on the low excitation region as shown in Fig. 4. Contrarily, the superferric

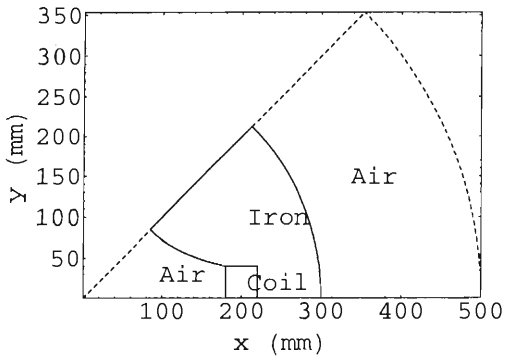

Fig. 1. Cross section (1/8 sector) of a superferric #1 quadrupole magnet for 2D field analysis.

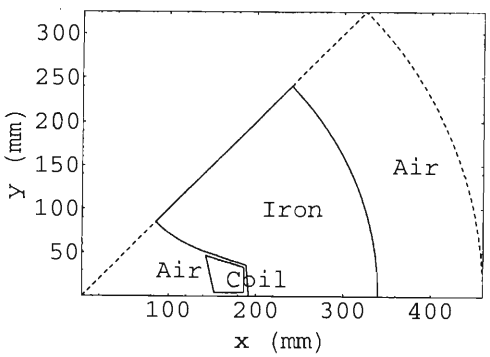

Fig. 2. Cross section (1/8 sector) of a superferric #2 quadrupole magnet (almost equivalent with Q1 at MSU) for 2D field analysis.

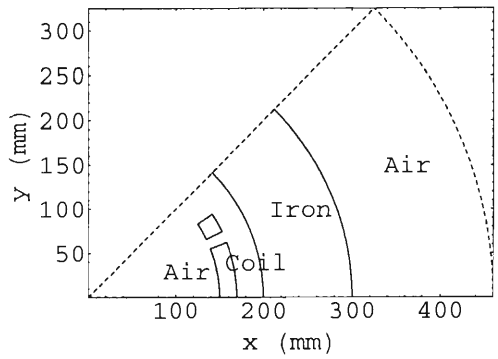

Fig. 3. Cross section (1/8 sector) of a cos2θ type quadrupole magnet for 2D field analysis.

Table 1. Major parameters of superconducting quadrupoles (2D calculation).

Type	superferric (#1)	superferric (#2)	cos(2θ)
Pole tip diameter (mm)	240	240	(300)*
Warm clear bore (mm)	200	200	200
Current density (A/mm^2)	150	100	180
Cross section of current blocks (mm^2)	1600	1340	1630
Total current/pole (A)	2.40×10^5	1.34×10^5	2.93×10^5
Field gradient (T/m)	19.9	19.6	20.4
Maximum field** (T)	4.0	3.1	3.8

*) inner diameter of coil

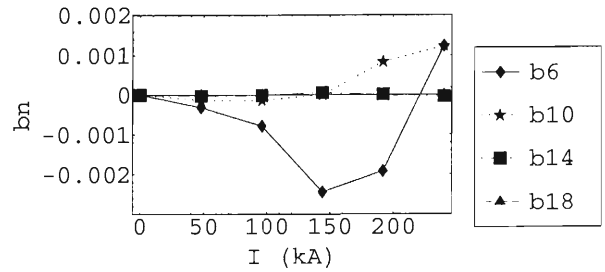

Fig. 4. Allowed normal multipole coefficients vs. exciting current for the superferric #1 quadrupole magnet shown in Fig. 1.

#2 quadrupole magnet (MSU type) can produce the homogeneous quadrupole field only on the high excitation region as shown in Fig. 5.[3] Furthermore, the cos2θ type quadrupole magnet can produce the homogeneous quadrupole field on the almost entire excitation region as shown in Fig. 6. Comparison between MSU and cos2θ types are made in Table 2.

For the RIKEN Big RIPS, approximately 40–50 sets of the triplet quadrupoles are to be operated at different exciting currents. As a result, a low-current operation is indispensable, thereby reducing the heat input through the current leads. Therefore, for the superferric quadrupole at MSU, the major coils were wound by a fine conductor with the diameter of less than 1 mm. On the other hand, for the cos2θ type quadrupole, the multi-strand cable of the so-called Rutherford type[2] with a large current capacity can not be adopted. Instead of the Rutherford cable, the flat cable with parallel unconnected strand (so-called ribbon conductor)[2] become a candidate for the conductor.

Because the winding by a ribbon conductor seems to be costly and difficult for the cos2θ type quadrupole, we are planning to try the superferric type quadrupole first. Now, the triplet set with length of 0.5, 0.8, and 0.5 m of the superferric #2 quadrupole magnets, having a large bore radius for homogeneous quadrupole field region r < 120 mm, is under study, in order to improve the field homogeneity. Characteristics of the quadrupole coil under study are listed, together with those of sextupole and octapole coils are listed in Table 3. A cross-sectional view of their coils is shown in Fig. 7.

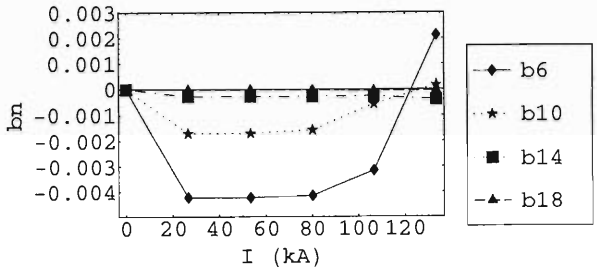

Fig. 5. Allowed normal multipole coefficients vs. exciting current for the superferric #2 quadrupole magnet shown in Fig. 2.

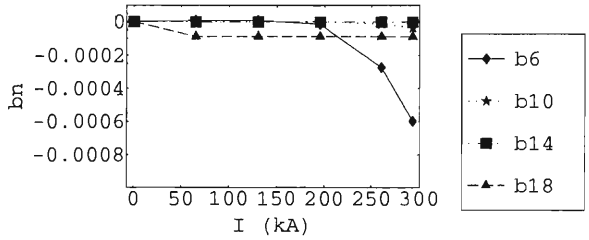

Fig. 6. Allowed normal multipole coefficients vs. exciting current for the cos2θ type quadrupole magnet shown in Fig. 3.

Table 2. Comparison between superferric and cos2θ types (2D & 3D calculation).

Type	superferric (#2)	cos2θ
Homogeneity of gradient field (straight region)	$\lvert g - g_0 \rvert < 4$ %	$\lvert g - g_0 \rvert < 0.5$ %
Contribution of iron	62 %	28 %
Maximum field	3.14 T	3.77 T
Maximum current density	j=100 A/mm^2	j=180 A/mm^2
Winding and conductor types	1) random winding (MSU)	1) ribbon conductor (CERN) 2) automatic winding (BNL)
Magnetic force	small	large
Fabrication cost	small	large

Table 3. Major parameters of a superconducting quadrupole magnet with the effective length of 0.8 m (2D & 3D calculation).

	quadrupole	sextupole	octupole
Field	14.1 T/m	20.8 T/m^2	174 T/m^3
Total current (A) /pole	2.7×10^5	3.9×10^4	2.9×10^4
Length (m) [straight]	0.7	0.7	0.7
Length (m) [end]	0.1 × 2	0.1 × 2	0.1 × 2

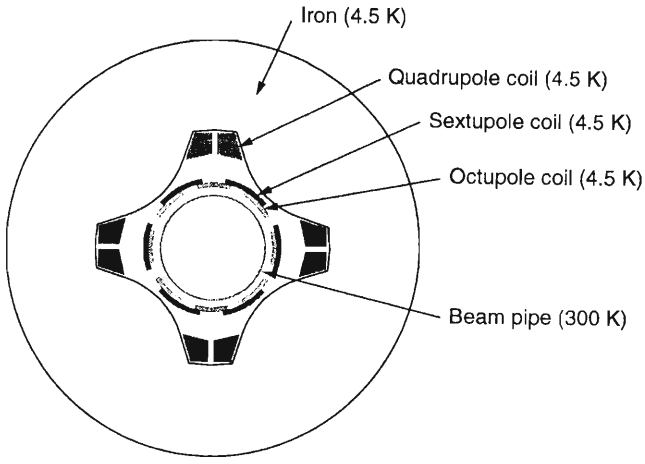

Fig. 7. Cross section of a superconducting quadrupole magnet equipped with the sextupole and octupole coils.

References

1) Vector Fields Limited, Oxford, England.
2) K.-H. Mess, P. Schmüser, and S. Wolff: *Superconducting Accelerator Magnets* (World Scientific, 1996).
3) B. Zhang: Ph. D thesis, MSU (1997).

Symplectification for the Map of Orbital Motion in a Realistic Siberian Snake Obtained by DA Approach

M. Xiao, E. Forest,* and T. Katayama

The issue of symplectic integration has been addressed by several authors.[1-3] Grossly speaking, symplectic integrators can be divided into the explicit and implicit types. Most accelerator physics codes, of the "kick-code" variety, are explicit integrators. These codes are fast and conceptually simple because a variety of effects can be added to them in a more or less self-consistent way. Unfortunately, it seems very hard to produce explicit symplectic integrators for a non-ideal magnetic field, the complexity is compounded by the absence of an analytical representation for the magnetic field.

Therefore, we have opted here to keep using an ordinary integrator, from which we extract a map. This has a small advantage: because the integrator is not symplectic, any violation of the symplectic condition will be a reflection of the integration accuracy or of the non-Maxwellian aspects of the fields. In other words it gives us an idea of the absolute error before any symplectic "fudging" algorithm masks it.

The DA(Differential Algebra) approach pioneered by Berz in beam physics permits the calculation of a truncated Taylor map of an arbitrary element to any order, and the Taylor coefficients of the resulting truncated map will be accurate to machine precision. It is a technique to propagate the derivatives of a function $f(x_i)$ systematically through mathematical transformations on f by simply applying the familiar sum, product and chain rules of differentiation. The derivatives of any complicated function, which may be obtained by successive mapping, can be calculated by extending any function f to a vector $\mathbf{f}$ which contains the value of the function as the first element and the values of the derivatives with respect to all the variables up to the desired order in the subsequent elements. These vectors are called "DA-vectors"[4,5]

$$f(x_i) \to \mathbf{f(x_i)} = \{f, .., \frac{\partial f}{\partial x_i} .., .. \frac{\partial^2 f}{\partial x_i \partial x_j} .., ...\}$$
$$= \{f, .. f_{x_i} .., .. f_{x_i x_j} .., ...\}.$$

For map-tracking, all phase-space coordinates z_i become the DA vectors $\mathbf{z_i}$. The first element of $\mathbf{z_i}$ contains the current value of the coordinates z_i, and the subsequent elements contain the derivatives with respect to the initial values of z_i. The vectors $\mathbf{z_i}$ are initialized by setting the first element to the initial value of z_i, the element which contains the first derivative with respect to the i^{th} initial coordinate is set to be unity(1), and all the other elements are zero. Each mathematical operation which involves phase-space variables is replaced by a vector operation. Then, a truncated Taylor map

$$\vec{z}_{final} = \sum_{j_1+...+j_n \le N} \vec{a}_{j_1,...j_n} \prod_i z_i^{j_i}$$

could be obtained.

The LBNL version of the DA package written by Berz was introduced, and Program SSSTRA was modified into a DA-version, named DA-SSSTRA. Field distribution of the helical magnet in Siberian Snake was given numerically. In order to make use of DA, the magnetic field was reconstructed again to the second order as follows,

$$B_w(x,y,s) = b_w(x,y,s) + \frac{\partial b_w(x,y,s)}{\partial x} \cdot x + \frac{\partial b_w(x,y,s)}{\partial y} \cdot y + \frac{1}{2} \cdot \frac{\partial^2 b_w(x,y,s)}{\partial x^2} \cdot x^2 + \frac{\partial^2 b_w(x,y,s)}{\partial x \partial y} \cdot xy + \frac{1}{2} \cdot \frac{\partial^2 b_w(x,y,s)}{\partial y^2} \cdot y^2 + \ldots$$
$$w = x, y, \text{ or } s$$

Where $b_w(x,y,s)$ as well as its first and second derivatives are expressed by spline interpolation functions[6] fitted from the numerical field data. Since the spline function is smooth in the first derivatives and continuous in the second derivatives, the truncated Taylor map to the second order can be obtained around any ray started from the entrance of the snake.

The field strengths of each helical magnet for Siberian Snake Type I (Spin axis is 45° with respect to s-direction) were optimized first in order to make the spin precession turn 180° at the storage mode (E = 250 GeV). Then, the four-dimensional map to the second order around any ray can be extracted automatically. Linear matrices for the motion at injection mode (E = 25 GeV) and at storage mode around the center ray are given as follows,

$$M_{T_I} = \begin{bmatrix} 0.9971 & 12.2738 & 0.0011 & -0.0255 \\ -0.0004 & 0.9974 & 0.0001 & -0.0050 \\ -0.0038 & 0.0241 & 0.9336 & 11.9255 \\ -0.0002 & 0.0065 & -0.0107 & 0.9347 \end{bmatrix}$$

$$M_{T_S} = \begin{bmatrix} 0.9999 & 12.2799 & 0.0000 & -0.0003 \\ -0.0000 & 0.9999 & -0.0000 & -0.0001 \\ -0.0000 & 0.0001 & 0.9995 & 12.2777 \\ -0.0000 & -0.0001 & -0.0001 & 0.9995 \end{bmatrix}$$

A $2n \times 2n$ matrix, M, is said to be symplectic if

$$M^T \cdot J \cdot M = J,$$

where M^T is the transpose of M, and J is the matrix,

* High Energy Accelerator Research Organization (KEK)

$$J = \begin{bmatrix} 0 & I \\ -I & 0 \end{bmatrix}.$$

Here each entry in J is an $n \times n$ matrix, I denotes the $n \times n$ identity matrix, and all the other entries are zero. It follows that a symplectic matrix has a unit determinant.

Checking of the symplecticity for maps of the snake was made, and the results showed that although a deviation of the determinant of M_{T_I} and M_{T_S} from 1 is as small as $8.6597396 \times 10^{-15}$ and $2.8199665 \times 10^{-14}$ respectively, it does not satisfy the symplectic conditions completely: the maximun error among the matrix elements is 9.1694×10^{-2} for M_{T_I} and -1.2853×10^{-5} for M_{T_S}. The Maxwellian property of the magnetic field around the central ray was checked and it was found that the maximum error is around 10^{-2}, the same order as the symplectic property of the orbital matrix.

The Dragt-Finn factorization states that a map near the identity can be expressed as follows,[1)]

$$M_K = \exp(\vec{F} \cdot \nabla) Id,$$

where Id=identity map. The Poisson bracket operator, $[f, g]$, is a special case of the general vector field operator

$$: f : \vec{g} = [f, g] = \nabla f^T \cdot J \cdot \nabla \vec{g} = \underbrace{-J \nabla f}_{\vec{F}} \cdot \nabla \vec{g} \ ,$$

where $\vec{g}$ is an arbitary vector function of phase space. Then,

$$f = \int_0^x J \cdot \vec{F} \cdot dx'.$$

If $\vec{F}$ is symplectic, then this computation involves an integral of a curl free function. Thus, the function f is unique. If $\vec{F}$ is slightly non-symplectic, then the function f is one of possible symplectifications of the vector field $\vec{F}$, and it will depend on the path of the integration.

We know that the map M (including second order) from the entrance to exit of the snake is nearly the map for a drift of the length equal the full snake. Therefore, one needs to construct a new map M_K given by

$$M_K = D^{-1}(\frac{L}{2}) \cdot M \cdot D^{-1}(\frac{L}{2}),$$

where $D(L/2)$ is a drift of half length of the full snake. So the linear part of the M_K is a matrix near the identity.

In the program DA-SSSTRA, a possible symplectic matrix $\mathcal{M}_\mathcal{K}$ for M_K was computed by an iterative process as follows. First, we compute the vector $\vec{F}$ in such a way that $M_K = \exp\left(\vec{F} \cdot \nabla\right) Id$. Later, we will find a Poisson bracket approximating this general vector field. We then compute

$$vectorm = exp(-\vec{F}_j \cdot \nabla) \cdot M_K - Id$$

as a correction of $\vec{F}$, and check whether $vectorm$ is close enough to zero. If not, then we set

$$\vec{F}_{j+1} \Leftarrow \vec{F}_j + vectorm$$

and repeat the iteration.

Notice that this computation does not separate the map to be symplectified into the first and second orders, so it can be used for the symplectification of arbitrary order.

Once, $: f :$ is obtained from $\vec{F}$, the resulting symplectified map is

$$\begin{aligned} \mathcal{M} &= D(L/2) \cdot \mathcal{M}_K \cdot D(L/2) \\ &= D(L/2) \cdot \exp(: f :) Id \cdot D(L/2). \end{aligned}$$

The maps for the Siberian Snake generated by numerical magnetic field including second order were symplectified, and the following are the symplectified linear matrices M_{T_I} and M_{T_S} obtained by DA

$$\mathcal{M}_{T_I} = \begin{bmatrix} 0.9971 & 12.2740 & -0.0037 & -0.0294 \\ -0.0004 & 0.9975 & -0.0001 & -0.0016 \\ 0.0008 & 0.0273 & 0.9336 & 11.9256 \\ -0.0001 & 0.0029 & -0.0107 & 0.9348 \end{bmatrix}$$

$$\mathcal{M}_{T_S} = \begin{bmatrix} 0.9999 & 12.2799 & -0.0000 & -0.0004 \\ -0.0000 & 0.9999 & -0.0000 & -0.0002 \\ 0.0000 & 0.0002 & 0.9995 & 12.2777 \\ -0.0000 & -0.0001 & -0.0001 & 0.9995 \end{bmatrix}.$$

The symplectification results show that there is a little adjustment for the linear map of the snake calculated by DA to be symplectic, but for the second order map, the elements corresponding to the cross terms such as $x_0 \cdot p_{x_o}$ change significantly.

Further work is being done to put the symplectified map into the full lattice of RHIC for spin tracking. The accuracy will have to be gauged in an actual run.

References

1) A. J. Dragt: AIP Conf. Proc. **87**, 147 (1982).
2) H. Yoshida: in *Celestial Mechanics and Dynamical Astronomy* (1993) p. 56.
3) E. Forest et al.: KEK Report 92-14, Sept. (1992).
4) M. Berz: in *Particle Accelerators*, Vol. 24 (1989) p. 109.
5) F. Willeke: Proc. CAS (CERN Accelerator School) Fifth Advanced Accelerator Physics Course, CERN 95-06, Greece, 1993 (1995).
6) M. Xiao et al.: Spin note AGS/RHIC/SN No. 078, Sept. 10 (1998).

V. RADIATION MONITORING

Routine Works for Radiation Safety in the Ring Cyclotron Facility

S. Fujita, S. Nakajima, S. Ito, T. Arakawa,* A. Fujiwara,* M. Kase, and Y. Uwamino

The radiation safety control system has worked steadily during this year (1998) so as to enable us to execute the radiation monitoring service continuously and automatically.

From the accumulated data of leakage neutrons, the radiation level in the controlled area was found much less than the recommended dose limit (0.3 mSv/week). Leakage of neither γ rays nor neutrons was detected with environmental monitors installed outside the building during this reporting period. Then, we have evaluated the radiation level at the boundary of the accelerator facility. The leakages was recorded with the monitor installed in the ground-floor computer room which is just above a bending magnet that guides the beams from the Ring Cyclotron vault to the distribution corridor. The radiation level (4.5 μSv/year) was much less than the recommended dose limit (1 mSv/year).

Two hand-foot-cloth (HFC) monitors with $\beta(\gamma)$ detector had been used at the entrance of the controlled area before the last winter-98. When one of the HFC monitors was out of order, we could use only one HFC monitor. So many people could not get out smoothly during that period. To improve the situation, we have installed a new HFC monitor which can detect α-rays as well as $\beta(\gamma)$ February-1998. Usually, two HFC monitors are connected to the computer system and one HFC is reserved. Using a newly made switching box, we can easily swap the connection. Therefore, we are able to use two HFC monitors always, even if a trouble occurred to one of the HFC monitors. In addition, the system is able to check α rays for enhanced safety. Figure 1 is the photograph showing the new HFC monitor and the switching box at the entrance into the controlled area.

Around February-1999, we are going to replace the computer system by Radiation Safety Control System[1] with new one.

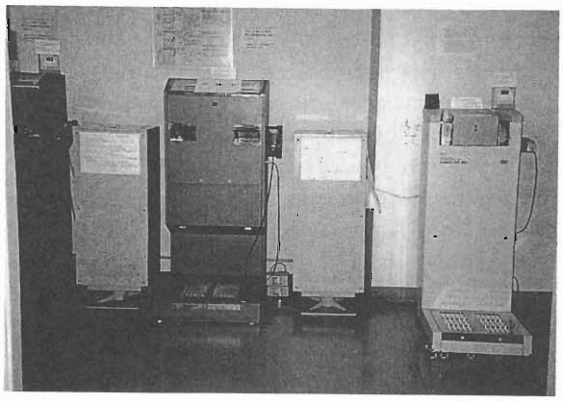

Fig. 1. Photograph of the new hand-foot-cloth monitor on the right hand side which is able to detect both $\beta(\gamma)$ and α rays, and of the new switching box at the foot of the old hand-foot-cloth monitor seen in the left.

References

1) I. Sakamoto, S. Fujita, T. Wada, and H. Takebe: RIKEN Accel. Prog. Rep. **20**, 206 (1986).

* Faculty of Science, Science University of Tokyo

Dose Rates Due to Residual Radioactivity in the Ring Cyclotron Facility

S. Fujita, T. Arakawa,* A. Fujiwara,* S. Nakajima, S. Ito,
M. Kase, and Y. Uwamino

Residual radioactivities in the Ring Cyclotron Facility were measured on the surface at various spots using ionization-chamber survey meters. The measurements were performed during the routine overhaul period as well as after almost every beam time. In the following, we report the significant dose rates observed through measurements.

A client experiment was carried out with an ^{18}O beam of 100 MeV/nucleon in the E6 experimental vault from July 22 to July 31,1998, as the last beam time of the spring term. As the last beam of the term, a proton beam was accelerated up to the energy 14 MeV in the AVF cyclotron vault on Aug. 3. The routine overhaul started just after that date. The dose rates in the Ring cyclotron and in the AVF cyclotron were measured from Aug. 21 till 31 in this period. The results are shown in Figs. 1 and 2.

In addition to the above routine measurement, dose rates inside the AVF cyclotron were measured on June 11 when its acceleration chamber was opened due to a trouble of insulation of the deflector in vacuum. The result is also shown in Fig. 2.

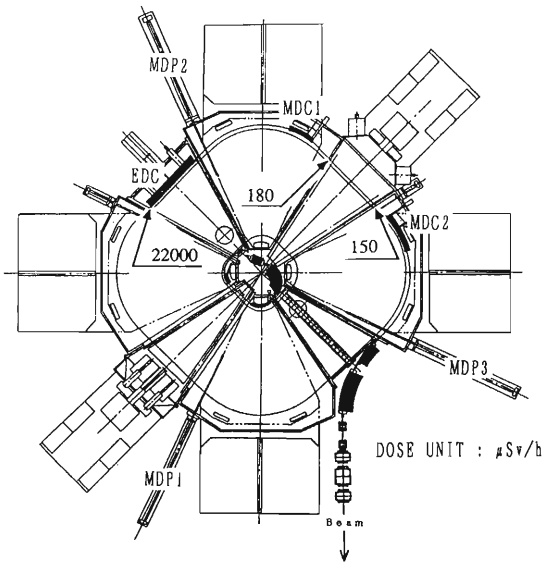

Fig. 1. Measured spots around the RIKEN Ring Cyclotron: EDC, the electrostatic deflection channel; MDC1, the magnetic deflection channel 1; MDC2, the magnetic deflection channel 2; MDP1, the main differential probe 1; MDP2, the main differential probe 2; and MDP3, the main differential probe 3. The numbers are dose rates in units of μSv/h.

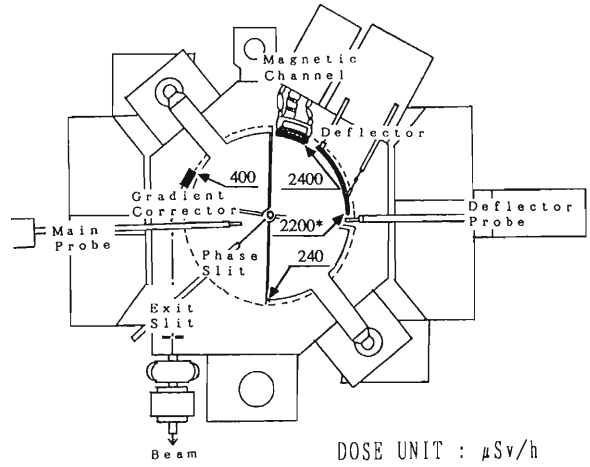

Fig. 2. Dose rates measured inside the injector AVF cyclotron. They are given in units of μSv/h, and asterisk (*) indicates an extra measurement made on June 11.

Table 1. Summary of the dose rates measured along the beam lines with ionization-chamber survey meters. The detection points a-w indicate the measured spots shown in Fig. 3.

Detection point	Measured dose rate (μSv/h)	Date	The experiment preceded			
			particle	energy (MeV/n)	intensity (enA)	period (days)
a	70	Jun 11, '98	d	135	210	4
b	100	Jul 17, '98	O-18	100	1200	6
c	150	Jun 11, '98	d	135	210	4
d	230	Mar 13, '98	Ca-40	100	600	6
e	1200	Jul 2, '98	C-13	115	1200	4
f	1000	Apr 2, '98	O-18	100	3000	13
g	100	Jul 2, '98	C-13	115	1200	4
h	180	Apr 30,'98	N-14	135	1560	1
i	150	Apr 2, '98	O-18	100	3000	13
j	580	Jun 11, '98	d	135	210	4
k	70	Dec 8, '97	Co-59	80	300	5
l	230	Mar 13, '98	Ca-40	100	600	6
m	950	Aug 3, '98	O-18	100	3690	9
n	220	Feb 19, '98	B-11	70	1560	4
o	4000	Apr 6, '98	O-18	100	3000	13
p	400	Jun 11, '98	d	135	210	4
q	80	Dec 8, '97	Co-59	80	300	5
r	1500	May 27,'98	C-12	135	580	5
s	300	Dec 8, '97	Co-59	80	300	5
t	3400	Apr 24,'98	N-14	135	2000	4
u	1500	Apr 24,'98	N-14	135	2000	4
v	450	Oct 16,'97	d	70	310	3
w	700	Jun 29,'98	d	135	940	6

* Faculty of Science, Science University of Tokyo

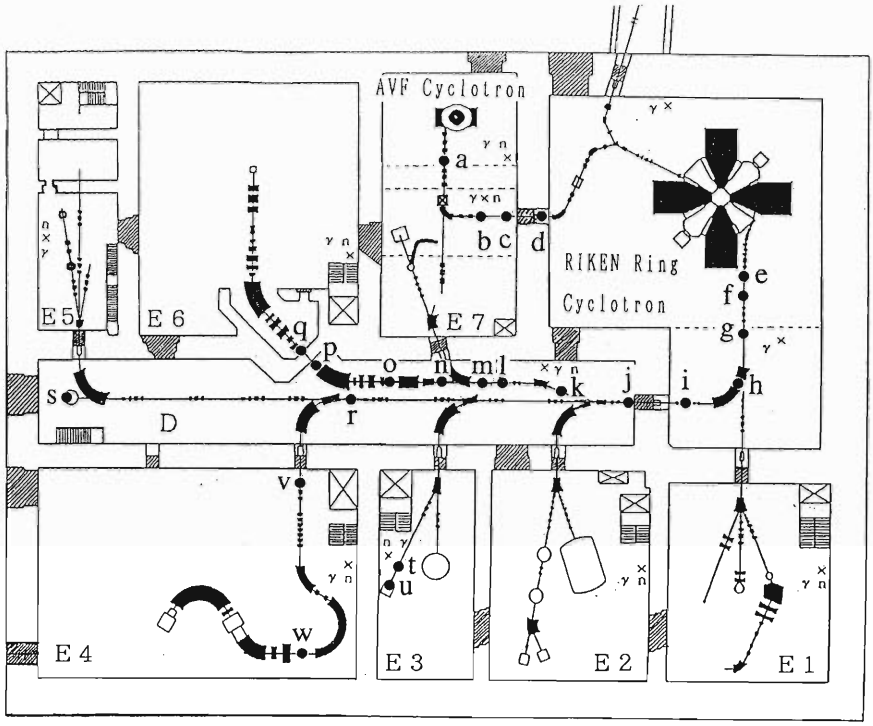

Fig. 3. Layout of the RIKEN Ring Cyclotron Facility as of 1998. Measured spots of residual radio-activities along the beam lines are shown by bullets a-w.

In the period from Oct. 1, 1997 till Sept. 30, 1998, dose rates were measured along the beam lines. The spots a-w marked by bullets in Fig. 3 are the places where the dose rates exceeded 50 μSv/h. Table 1 summarizes the observed dose rates with the dates when the measurements were performed. The maximum dose rate was found to be 4 mSv/h (4000 μSv/h) at the target chamber, denoted by the spot O in Fig. 3. Whenever we observed a high dose rate in some place, we roped the area and posted a sign warning that it was dangerous to stay long in that place.

VI. LIST OF PUBLICATIONS

1. Accelerator development and accelerator physics

A. Goto, Y. Yano, and T. Katayama: "RIKEN RI Beam Factory project", Proc. 6th China-Japan Joint Symp. on Accelerators for Nuclear Science and Their Applications, Chengdu, China, 1996-10, edited by S. Guanqing and L. Zhengda, pp. 28–31 (1996).

A. Goto, Y. Miyazawa, M. Kase, O. Kamigaito, T. Nakagawa, M. Hemmi, T. Chiba, N. Inabe, S. Kohara, T. Kageyama, Y. Batygin, E. Ikezawa, and Y. Yano: "New pre-injector system of the RILAC for the RIKEN RI Beam Factory project", Proc. 6th China-Japan Joint Symp. on Accelerators for Nuclear Science and Their Applications, Chengdu, China, 1996-10, edited by S. Guanqing and L. Zhengda, pp. 161–165 (1996).

T. Nakagawa, M. Kidera, Y. Miyazawa, M. Hemmi, T. Chiba, N. Inabe, M. Kase, T. Kageyama, O. Kamigaito, A. Goto, and Y. Yano: "Production of multicharged Os ion beams from organic metal compounds using a RIKEN 18 GHz electron cyclotron resonance ion source", Jpn. J. Appl. Phys. **36**, 7375–7376 (1997).

T. Nakagawa, J. Ärje, Y. Miyazawa, M. Hemmi, T. Chiba, N. Inabe, M. Kase, T. Kageyama, O. Kamigaito, A. Goto, M. G. Niimura, and Y. Yano: "Production of highly charged metal ion beams from organic metal compounds at RIKEN 18 GHz ECRIS", Nucl. Instrum. Methods Phys. Res. A **396**, 9–12 (1997).

T. Katayama, Y. Batygin, N. Inabe, K. Ohtomo, T. Ohkawa, M. Takanaka, M. Wakasugi, S. Watanabe, Y. Yano, K. Yoshida, J. Xia, Y. Rao, and Y. Yuan: "The MUSES project at the RIKEN RI Beam Factory", Nucl. Phys. A **626**, 545c–560c (1997).

M. Niimura, A. Goto, and Y. Yano: "Structure of the ECRIS-nucleus: Evidence of a high-energy electron layer", Proc. 13th Int. Workshop on ECR Ion Sources, College Station, USA, 1997-02, edited by D. P. May and J. E. Ramirez, pp. 52–66 (1997).

A. Goto, Y. Yano, and T. Katayama: "RIKEN RI-Beam Factory project", J. Phys. G: Nucl. Part. Phys. **24**, 1341–1345 (1998).

J.-W. Kim, A. Goto, T. Mitsumoto, T. Kubo, H. Okuno, T. Kawaguchi, T. Tominaka, S. Fujishima, K. Ikegami, N. Sakamoto, S. Yokouchi, T. Morikawa, and Y. Yano: "Trim coil system for the RIKEN Superconducting Ring Cyclotron", Proc. 1997 Particle Accelerator Conf. (PAC '97), Vancouver, Canada, 1997-05, edited by M. Craddock, pp. 3422–3424 (1998).

J.-W. Kim, T. Kubo, T. Kawaguchi, and T. Kubo: "A superconducting solenoid for heavy ion beam focusing", Proc. 1997 Particle Accelerator Conf. (PAC '97), Vancouver, Canada, 1997-05, edited by M. Craddock, pp. 3425–3427 (1998).

J.-W. Kim and J. S. Chai: "Design study of a linear accelerator system for neutron capture therapy", Proc. 1997 Particle Accelerator Conf. (PAC '97), Vancouver, Canada, 1997-05, edited by M. Craddock, pp. 3825–3827 (1998).

O. Kamigaito, M. Kase, Y. Miyazawa, T. Chiba, M. Hemmi, E. Ikezawa, S. Kohara, A. Goto, and Y. Yano: "Development of a charge-state multiplier system for the RIKEN RI-Beam Factory", Proc. 23rd Linear Accelerator Meeting in Japan., Tsukuba, 1998-09, pp. 399–401 (1998).

T. Nakagawa, J. Ärje, Y. Miyazawa, M. Hemmi, T. Chiba, N. Inabe, M. Kase, T. Kageyama, M. Kidera, A. Goto, and Y. Yano: "Production of intense beams of highly charged metallic ions from RIKEN 18 GHz electron cyclotron resonance ion source", Rev. Sci. Instrum. **69**, 637–639 (1998).

2. Nuclear physics and nuclear instrumentation

I. Yokoyama, T. Otsuka, and N. Fukunishi: "Giant quadrupole excitation in nuclei with neutron skin", Phys. Rev. C **52**, 1122–1125 (1995).

K. H. Kim and T. Otsuka: "Multiphonon structure in a γ-unstable fermionic model", Phys. Rev. C **52**, 2792–2795 (1995).

M. Honma, T. Mizusaki, and T. Otsuka: "Diagonalization of Hamiltonians for many-body systems by auxiliary field quantum Monte Carlo technique", Phys. Rev. Lett. **75**, 1284–1287 (1995).

Y. H. Zhang, Y. Gono, A. Ferragut, K. Morita, C. B. Moon, A. Yoshida, T. Murakami, M. Nakajima, M. Ogawa, T. Morikawa, M. Oshima, H. Kusakari, M. Sugawara, K. Furuno, T. Hayakawa, T. Komatsubara, J. Lu, S. J. Chae, C.-J. Kim, and B.-J. Min: "Study of high spin isomer and its decay level scheme of doubly odd ^{144}Pm nucleus", High Energy Phys. Nucl. Phys. (China) **20**, 385–393 (1996).

M. Shibata, A. Odahara, S. Mitarai, Y. Gono, M. Kidera, K. Miyazaki, and T. Kuroyanagi: "Anomalous Q_{EC}-values of $T_z = 1$ nuclei, ^{80}Y, ^{84}Nb and ^{88}Tc", J. Phys. Soc. Jpn. **65**, 3172–3174 (1996).

N. Sakamoto, H. Okamura, T. Uesaka, S. Ishida, H. Otsu, T. Wakasa, Y. Satou, T. Niizeki, K. Katoh, T. Yamashita, K. Hatanaka, Y. Koike, and H. Sakai: "Measurement of the vector and tensor analyzing powers for the d-p elastic scattering at $E_d = 270$ MeV", Phys. Lett. B **367**, 60–64 (1996).

A. Yoshida, C. Signorini, T. Fukuda, Y. Watanabe, N. Aoi, M. Hirai, M. Ishihara, H. Kobinata, Y. Mizoi, L. Mueller, Y. Nagashima, J. Nakano, T. Nomura, Y. Pu, and F. Scarlassara: "Fusion and breakup at the barrier with ^{11}Be", Phys. Lett. B **389**, 457–462

(1996).

T. Mizusaki, M. Honma, and T. Otsuka: "Quantum Monte Carlo diagonalization with angular momentum projection", Phys. Rev. C **53**, 2786–2793 (1996).

H. Sakurai, N. Aoi, A. Goto, M. Hirai, N. Inabe, M. Ishihara, H. Kobinata, T. Kubo, H. Kumagai, T. Nakagawa, T. Nakamura, M. Notani, Y. Watanabe, Y. Watanabe, and A. Yoshida: "Production and identification of new neutron-rich nuclei, ^{31}Ne and ^{37}Mg, in the reaction 80A MeV ^{50}Ti + ^{181}Ta", Phys. Rev. C **54**, R2802–R2805 (1996).

T. Akiba, E802 Collaboration, K. Kurita, and H. Sakurai: "Production of ϕ mesons in central ^{28}Si + ^{197}Au collisions at 14.6A GeV/c", Phys. Rev. Lett. **76**, 2021–2024 (1996).

K. H. Kim, T. Otsuka, A. Gelberg, P. von Brentano, and P. van Isacker: "Supersymmetric multiphonon structure", Phys. Rev. Lett. **76**, 3514–3517 (1996).

T. Otsuka: "Microscopic basis of the interacting Boson model", Prog. Theor. Phys. Suppl., No. 125, pp. 5–48 (1996).

N. Yoshinaga, T. Mizusaki, A. Arima, and Y. D. Devi: "Microscopic foundations of the interacting Boson model from Shell-model point of view", Prog. Theor. Phys. Suppl., No. 125, pp. 65–96 (1996).

T. Mizusaki and T. Otsuka: "Microscopic calculations for $O(6)$ nuclei by the interacting Boson model", Prog. Theor. Phys. Suppl., No. 125, pp. 97–150 (1996).

M. Honma and T. Otsuka: "Superdeformation in the Hg-Pb region and an extention of IBM", Prog. Theor. Phys. Suppl., No. 125, pp. 165–202 (1996).

Y. Miyake, K. Shimomura, A. Milles, P, and K. Nagamine: "Resonant ionization of thermal muonium produced by 500-MeV protons", Reson. Ioniz. Spectrosc., pp. 259–262 (1996).

A. Odahara, Y. Gono, S. Mitarai, T. Shizuma, E. Ideguchi, J. Mukai, H. Tomura, B.-J. Min, S. Suematsu, T. Kuroyanagi, K. Heiguchi, T. Komatsubara, and K. Furuno: "The β-decay of ^{88}Tc", Z. Phys. A **354**, 231–232 (1996).

A. A. Gusev, T. Kohno, W. Spjeldvik, I. M. Martin, G. I. Pugacheva, and A. Jr. Turtelli: "The 3-9 MeV/nucleon He ion flux dynamics in the inner magnetosphere obtained with OHZORA satellite", Adv. Space Res. **20**, 385–388 (1997).

T. Takashima, T. Doke, T. Hayashi, J. Kikuchi, M. Kobayashi, H. Shirai, N. Takehana, M. Ehara, Y. Yamada, S. Yanagita, N. Hasebe, T. Kashiwagi, C. Kato, K. Munakata, T. Kohno, K. Kondoh, H. Murakami, A. Nakamoto, T. Yanagimachi, D. V. Reams, and T. von Rosenvinge: "The first observation of sulfur in anomalous cosmic rays by the *Geotail* and the *Wind* spacecraft", Astrophys. J. **477**, L111–L113 (1997).

Y. Mochizuki, K. Oyamatsu, and T. Izuyama: "Exotic nuclear rod formation induced by superfluid vortices in neutron star crusts", Astrophys. J. **489**, 848–864 (1997).

Y. H. Zhang, Y. Gono, T. Morikawa, E. Ideguchi, S. Mitarai, A. Odahara, M. Shibata, T. Kishida, K. Morita, A. Yoshida, H. Kumagai, T. Murakami, M. Oshima, H. Iimura, M. Shibata, S. Hamada, H. Kusakari, M. Sugawara, M. Ogawa, M. Nakajima, and M. Ishihara: "Experimental observation of high spin states in ^{146}Sm nucleus", High Energy Phys. Nucl. Phys. (China) **21**, 110–115 (1997).

Z. Ren, T. Otsuka, H. Sakurai, and M. Ishihara: "Skyrme-Hartree-Fock approach to proton halo in ^{26}P and ^{27}S", J. Phys. G: Nucl. Part. Phys. **23**, 597–602 (1997).

H. Miura, T. Tachibana, K. Sumiyoshi, Y. Mochizuki, and T. Ebisuzaki: "Hyzenberg's valley and heavy elements nucleosynthesis: A fine work, the 3rd Nikkei Science computer visualization contest", Nikkei Science **27**, No. 12, p. A14 (1997).

N. Ishida, T. Doke, K. Hasuike, A. Hitachi, M. Kase, T. Kawada, J. Kikuchi, T. Komiyama, K. Kuwabara, K. Masuda, H. Okada, M. Suzuki, T. Takahashi, and Y. H. Qu: "Attenuation length measurements of scintillation light in liquid rare gases and their mixtures using an improved reflection suppresser", Nucl. Instrum. Methods Phys. Res. A **384**, 380–386 (1997).

M. Suzuki, T. Takahashi, K. Kuwabara, H. Okada, and K. Masuda: "A new microdosimetric instrument based on a proportional scintillation imaging chamber for heavy ion track investigation", Nucl. Instrum. Methods Phys. Res. A **392**, 55–61 (1997).

N. Aoi, A. Yoneda, H. Miyatake, H. Ogawa, Y. Yamamoto, E. Ideguchi, T. Kishida, T. Nakamura, M. Notani, H. Sakurai, T. Teranishi, H. Wu, S. S. Yamamoto, Y. Watanabe, A. Yoshida, and M. Ishihara: "β-spectroscopy of ^{11}Li and ^{14}Be: With a β-n-γ triple coincidence method", Nucl. Phys. A **616**, 181c–188c (1997).

S. Shimoura, T. Teranishi, Y. Ando, M. Hirai, N. Iwasa, T. Kikuchi, S. Moriya, T. Motobayashi, T. Murakami, T. Nakamura, T. Nishio, H. Sakurai, T. Uchibori, Y. Watanabe, Y. Yanagisawa, and M. Ishihara: "Charge exchange reaction of the neutron-halo nuleus ^{11}Li", Nucl. Phys. A **616**, 208c–214c (1997).

Y. Ogawa and I. Tanihata: "Momentum distribution of ^{7}Be from (^{8}B, ^{7}Be) reaction within the Glauber model", Nucl. Phys. A **616**, 239c–246c (1997).

T. Suzuki, H. Geissel, O. Bochkarev, L. Chulkov, D. Hirata, M. Golovkov, H. Irnich, Z. Janas, H. Keller, T. Kobayashi, G. Kraus, G. Muenzenberg, S. Neumaier, F. Nickel, A. Ozawa, A. Piechaczeck, E. Roeckl, W. Schwab, K. Suemmerer, K. Yoshida, and I. Tanihata: "Matter radii of Na and Mg isotope", Nucl. Phys. A **616**, 286c–292c (1997).

H. Sakurai, N. Aoi, D. Beaumel, N. Fukuda, M. Hirai, E. Ideguchi, M. Ishihara, H. Iwasaki, T.

Kishida, T. Kubo, H. Kumagai, S. M. Lukyanov, T. Nakamura, M. Notani, Yu. Ts. Oganessian, Yu. E. Penionzhkevich, T. Teranishi, Y. Watanabe, Y. Watanabe, A. Yoneda, and A. Yoshida: "Search for new neutron-rich nuclei with a 70A MeV ^{48}Ca beam", Nucl. Phys. A **616**, 311c–315c (1997).

A. A. Korsheninnikov, E. Y. Nikolskii, C. A. Bertulani, S. Fukuda, T. Kobayashi, E. A. Kuzmin, S. Momota, B. G. Novatskii, A. A. Ogloblin, A. Ozawa, V. Pribora, I. Tanihata, and K. Yoshida: "Scattering of radioactive nulei ^{6}He and ^{3}H by proton: Effects of neutron skin and halo in ^{6}He, ^{8}He, and ^{11}Li", Nucl. Phys. A **617**, 45–56 (1997).

N. Yoshida, A. Gelberg, T. Otsuka, I. Wiedenhöver, H. Sagawa, and P. von Brentano: "IBFM2 description of odd Xe and Cs isotopes", Nucl. Phys. A **619**, 65–87 (1997).

A. Odahara, Y. Gono, S. Mitarai, T. Morikawa, T. Shizuma, M. Kidera, M. Shibata, T. Kishida, E. Ideguchi, K. Morita, A. Yoshida, H. Kumagai, Y. H. Zhang, A. Ferragut, T. Murakami, M. Oshima, H. Iimura, M. Shibata, S. Hamada, H. Kusakari, M. Sugawara, M. Ogawa, M. Nakajima, B. J. Min, J. C. Kim, S. J. Chae, and H. Sagawa: "High-spin isomer and level structure of ^{145}Sm", Nucl. Phys. A **620**, 363–384 (1997).

A. Mengoni, T. Otsuka, T. Nakamura, and M. Ishihara: "Exotic structure of light nuclei and their neutron capture reaction rates", Nucl. Phys. A **621**, 323c–326c (1997).

J. K. Ahn, E224 Collaboration, Y. Goto, and N. Saito: "Scalar and vector meson production and two-step processes in the (K^-, K^+) reaction on ^{12}C", Nucl. Phys. A **625**, 231–250 (1997).

S. Shimoura, T. Teranishi, Y. Ando, M. Hirai, N. Iwasa, T. Kikuchi, S. Moriya, T. Motobayashi, H. Murakami, T. Nakamura, T. Nishio, H. Sakurai, T. Uchibori, Y. Watanabe, Y. Yanagisawa, and M. Ishihara: "Isobaric analog state ^{11}Li", Nucl. Phys. A **630**, 387c–393c (1997).

K. Nagamine: "Probing inner-structure of volcano with muons: Imaging of earth structure with environment radiations", Nyusapouto Koukou Rika, No. 4, pp. 6–8 (1997).

T. Kikuchi, T. Motobayashi, N. Iwasa, Y. Ando, M. Kurokawa, S. Moriya, T. Murakami, T. Nishio, J. Ruan, S. Shirato, S. Shimoura, T. Uchibori, Y. Yanagisawa, T. Kubo, H. Sakurai, T. Teranishi, Y. Watanabe, M. Ishihara, M. Hirai, T. Nakamura, S. Kubono, M. Gai, R. H. III France, K. I. Hahn, Th. Delbar, P. Lipnik, and C. Michotte: "Experimental determination of the E2 component in the Coulomb dissociation of ^{8}B", Phys. Lett. B **391**, 261–266 (1997).

Y. Utsuno, T. Otsuka, and H. Nakada: "Distribution of $E2$ excitations in sd-shell nuclei", Phys. Lett. B **397**, 6–12 (1997).

M. Petrascu, I. Tanihata, T. Kobayashi, A. Isbasescu, H. Petrascu, A. A. Korsheninnikov, E. Nikolski, S. Fukuda, H. Kumagai, S. Momota, A. Ozawa, K. Yoshida, C. Bordeanu, I. David, I. Lazar, I. Mihai, G. Vaman, and M. Giurgiu: "Neutron pre-emission at the fusion of ^{11}Li halo nuclei with Si targets", Phys. Lett. B **405**, 224–229 (1997).

T. Teranishi, S. Shimoura, Y. Ando, M. Hirai, N. Iwasa, T. Kikuchi, S. Moriya, T. Motobayashi, H. Murakami, T. Nakamura, T. Nishio, H. Sakurai, T. Uchibori, Y. Watanabe, Y. Yanagisawa, and M. Ishihara: "Isobaric analog state of ^{11}Li", Phys. Lett. B **407**, 110–114 (1997).

B. Imanishi, V. Denisov, and T. Motobayashi: "Study for the charge symmetric systems, ^{12}C + ^{13}N and ^{12}C + ^{13}C with the orthogonalized coupled-reaction-channel method", Phys. Rev. C **55**, 1946–1963 (1997).

H. Nakada and T. Otsuka: "Microscopic analysis of quadrupole collective motion in Cr-Fe nuclei: II. Doorway nature of mixed-symmetry states", Phys. Rev. C **55**, 2418–2426 (1997).

L. Ahle, E802 Collaboration, K. Kurita, and H. Sakurai: "Baryon emission at taget rapidities in Si + Al, Cu, Au collisions at 14.6A GeV/c and Au + Au collisions at 11.76A GeV/c", Phys. Rev. C **55**, 2604–2614 (1997).

T. Suzuki and T. Otsuka: "Gamow-Teller transitions from ^{11}Li and ^{12}Be", Phys. Rev. C **56**, 847–856 (1997).

Y. Akiba, E802 Collaboration, K. Kurita, and H. Sakurai: "Two-particle rapidity correlations from the Bose-Einstein effect in central ^{28}Si + Au collisions at 14.6A GeV/c and intermittency", Phys. Rev. C **56**, 1544–1552 (1997).

W. Q. Shen, W. Ye, Y. G. Ma, J. Feng, J. S. Wang, K. Yuasa-Nakagawa, T. Nakagawa, K. Yoshida, J. Kasagi, Y. Futami, S.-M. Lee, K. Furutaka, and K. Matsuta: "Azimuthal distribution, azimuthal correlation, and reaction plane dispersion in the reaction 10.6 MeV/nucleon ^{84}Kr on ^{27}Al", Phys. Rev. C **56**, 1996–2002 (1997).

I. Wiedenhöver, A. Gelberg, T. Otsuka, N. Pietralla, J. Gableske, A. Dewald, and P. von Brentano: "2^+ mixed symmetry state in the O(6)-like nucleus ^{128}Xe", Phys. Rev. C **56**, R2354–R2357 (1997).

M. Belbot, J. J. Kolata, M. Zahar, N. Aoi, M. Hirai, M. Ishihara, H. Okuno, H. Sakurai, T. Teranishi, T. Kishida, G. Liu, T. Nakamura, Y. Watanabe, A. Yoshida, E. Ideguchi, H. Miyatake, and S. S. Yamamoto: "β decay of the neutron-rich isotope ^{14}Be", Phys. Rev. C **56**, 3038–3044 (1997).

D. P. Grosnick, E581/704 Collaboration, Y. Goto, and N. Saito: "Measurement of the differences in the total cross-section for antiparallel and parallel longitudinal spins and a measurement of parity nonconservation with incident polarized protons and antiprotons at 200-GeV/c", Phys. Rev. D **55**, 1159–1187 (1997).

K. Kusaka, G. Piller, A. W. Thomas, and A. G. Williams: "Deep-inelastic structure functions in a convariant spectator model", Phys. Rev. D **55**, 5299–5308 (1997).

K. Kusaka, K. Simpson, and A. G. Williams: "Solving the Bethe-Salpeter equation for bound states of scaler theories in Minkowski space", Phys. Rev. D **56**, 5071–5085 (1997).

A. A. Korsheninnikov, E. A. Kuzmin, E. Y. Nikolskii, O. V. Bochkarev, S. Fukuda, S. A. Goncharov, S. Ito, T. Kobayashi, S. Momota, B. G. Novatskii, A. A. Ogloblin, A. Ozawa, V. Pribora, I. Tanihata, and K. Yoshida: "$L = 1$ excitation in the halo nucleus ^{11}Li", Phys. Rev. Lett. **78**, 2317–2320 (1997).

T. Kishida, Y. Gono, E. Ideguchi, T. Morikawa, M. Kidera, M. Shibata, H Tsuchida, K. Miyazaki, H. Watanabe, H. Wu, A. Tanokura, S. S. Yamamoto, A. Yoshida, S. Mitarai, A. Odahara, T. Murakami, M. Oshima, H. Kusakari, M. Sugawara, M. Kubo, T. Murata, M. Shimura, H. Kumagai, and M. Ishihara: "High spin isomer beam line at RIKEN", Proc. Conf. on Nuclear Structure at the Limits (ANL/PHY-97/1), Argonne, USA, 1996-07, pp. 204–208 (1997).

D. Kharzeev: "Charmonium suppression in nuclear collisions", Prog. Theor. Phys. Suppl., No. 129, pp. 73–81 (1997).

Y. Yoshida, Y. Kobayashi, K. Hayakawa, K. Yukihira, J. Nakamura, S. Nasu, E. Yagi, and F. Ambe: "In-beam Mössbauer study on ^{57}Fe jumps in solid Ar and solid Xe after Coulomb-excitation and recoil-implantation", RIKEN Rev., No. 16, pp. 19–20 (1997).

Y. Pu, K. Morita, M. G. Hies, K. O. Lee, A. Yoshida, T. Nomura, Y. Tagaya, T. Motobayashi, M. Kurokawa, T. Minemura, T. Uchibori, T. Ariga, K. Sueki, and S. A. Shin : "New α-decaying neutron-deficient isotope ^{196}Rn", Z. Phys. A **357**, 1–2 (1997).

N. Aoi, K. Yoneda, H. Miyatake, H. Ogawa, Y. Yamamoto, E. Ideguchi, T. Kishida, T. Nakamura, M. Notani, H. Sakurai, T. Teranishi, H. Wu, S. S. Yamamoto, Y. Watanabe, A. Yoshida, and M. Ishihara: "β-delayed neutron decay of drip line nuclei ^{11}Li and ^{14}Be", Z. Phys. A **358**, 253–255 (1997).

X. Zhou, E. Ideguchi, Y. Gono, T. Kishida, S. Mitarai, T. Morikawa, H. Tsuchida, M. Shibata, H. Watanabe, M. Miyake, A. Odahara, M. Oshima, Y. Hatsukawa, S. Hamada, H. Iimura, M. Shibata, T. Ishii, and M. Ishihara: "Study of high-lying states in ^{147}Eu", Z. Phys. A **358**, 285–286 (1997).

M. R. Ahmady and E. Kou: "Combined $B \to X_s \psi$ and $B \to X_s \eta_c$ decays as a test of factorization", Eur. Phys. J. C **1**, 243–246 (1998).

T. Motobayashi: "Nuclear astrophysics with intermediate-energy RI beams", AIP Conf. Proc. 425, Tours Symp. on Nucl. Phys. III, pp. 362–371 (1998).

K. Ushida, H. Shibata, S. Tagawa, Y. Yoshida, K. Kimura, and A. Kira: "Characteristics of phosphor used for beam monitoring: Intensity growth of scintillation and long-lived residual emission observed on steady state γ-radiolysis", Appl. Radiat. Isot. **49**, 55–58 (1998).

S. Nagataki, M. Hashimoto, K. Sato, S. Yamada, and Y. Mochizuki: "The high ratio of ^{44}Ti/^{56}Ni in Cas A and the axisymmetric collapse-driven supernova explosion", Astrophys. J. **492**, L45–L48 (1998).

O. V. Bochkarev, L. Chulkov, P. Egelhof, H. Geissel, M. Golovkov, H. Irnich, Z. Janas, H. Keller, G. Kraus, T. Kobayashi, G. Muenzenberg, F. Nickel, A. A. Ogloblin, A. Ozawa, A. Piechaczeck, E. Roeckl, W. Schwab, K. Suemmerer, T. Suzuki, I. Tanihata, and K. Yoshida: "Evidence for a neutron skin in ^{20}N", Eur. Phys. J. A **1**, 15–17 (1998).

J. H. Ha, J. C. Kim, C. S. Lee, J. Y. Huh, C. B. Moon, Y. Gono, S. Mitarai, T. Morikawa, M. Shibata, H. Watanabe, M. Miyake, E. Komatsu, A. Odahara, E. Ideguchi, and X. Zhou: "High-spin states in odd-odd ^{168}Lu", Eur. Phys. J. A **1**, 247–248 (1998).

C. Signorini, Z. H. Liu, A. Yoshida, T. Fukuda, Z. C. Li, K. E. G Lobner, L. Muller, Y. Pu, K. Rudolph, F. Soramel, C. Zotti, and J. L. Sida: "Fusion around the barrier in ^{11,9}Be + ^{209}Bi", Eur. Phys. J. A **2**, 227–231 (1998).

A. M. El-Badry, T. Kuroyanagi, S. Mitarai, A. Odahara, Y. Gono, S. Morinobu, and K. Ogawa: "Recoil distance half-life measurements of the excited states in ^{145}Sm", Eur. Phys. J. A **3**, 133–138 (1998).

K. Ishida: "Super high intensity muon channel", KEK Report 98-II, Design Report of M-arena at the North-counter Hall, edited by Y. Miyake, K. Shimomura, and K. Nagamine, High Energy Accelerator Research Organization, Tsukuba, pp. 64–69 (1998).

Y. Mochizuki, T. Izuyama, I. Tanihata, and K. Oyamatsu: "A microscopic model of neutron star glitches", Neutron Stars and Pulsars: Thirty Years after the Discovery, Frontiers Sci. Ser. No. 24, edited by N. Shibazaki et al., Universal Academy Press, Tokyo, pp. 561–564 (1998).

T. Motobayashi: "Coulomb dissociation studies for astrophysical thermonuclear reactions", Nucl. Astrophys.: Proc. Int. Workshop 26th on Gross Properties of Nuclei and Nuclear Excitations, Hirschegg, Austria, 1998-01, edited by M. Buballa et al., GSI, Darmstadt, pp. 394–401 (1998).

T. Uesaka, T. Wakui, T. Ohnishi, H. Okamura, Y. Satou, S. Ishida, N. Sakamoto, H. Otsu, T. Wakasa, T. Nonaka, G. Yokoyama, K. Itoh, K. Sekiguchi, S. Haruyama, T. Ikeda, M. Wakasugi, H. Sakai, and Y. Yano: "Polarized ^{3}He project at RIKEN", Nucl. Instrum. Methods Phys. Res. A **402**, 212–217 (1998).

K. Asahi: "Nuclear and fundamental physics with spin polarized nuclei", Nucl. Instrum. Methods Phys. Res. A **402**, 224–228 (1998).

H. Sato, M. Tsuda, A. Yoshimi, H. Izumi, H. Ogawa, N. Kurokawa, K. Sakai, M. Adachi, K. Asahi,

H. Okuno, T. Kubo, S. Fukuda, A. Yoshida, M. Ishihara, A. Yoneda, and M. Notani: "Polarized ^{129}Xe solid for polarizing unstable nuclei", Nucl. Instrum. Methods Phys. Res. A **402**, 241–243 (1998).

H. Okamura, S. Ishida, N. Sakamoto, H. Otsu, T. Uesaka, T. Wakasa, Y. Satou, H. Sakai, T. Niizeki, H. Ohnuma, and T. Ichihara: "Detector system of the first focal-plane of the spectrometer SMART at RIKEN", Nucl. Instrum. Methods Phys. Res. A **406**, 78–88 (1998).

S. N. Nakamura, M. Iwasaki, K. Bartlett, G. A. Beer, D. R. Gill, R. S. Hayano, T. M. Ito, M. Kuwata, L. Lee, G. Mason, H. Ohkubo, A. Olin, H. Outa, M. Salomon, R. Seki, K. Shibuya, T. Taniguchi, T. P. Terada, G. Trayling, T. Watanabe, Y. Yamashita, and S. Yen: "A new approach to measure kaonic hydrogen X-rays", Nucl. Instrum. Methods Phys. Res. A **408**, 438–452 (1998).

T. Motobayashi: "Coulomb dissociation of unstable nuclei", Nucl. Phys. A **630**, 328c–339c (1998).

V. Tatischeff, J. Kiener, P. Auger, G. Bogaert, A. Coc, D. Disdier, T. Ichihara, L. Kraus, A. Lefebvre, I. Linck, W. Mittig, T. Motobayashi, F. de Oliveira Santos, P. Roussel-Chomaz, C. Stephan, and J. P. Thibaud: "Fragment angular correlation in the breakup of ^{16}O ions at 95 MeV/A", Nucl. Phys. A **633**, 373–387 (1998).

K. Oyamatsu, I. Tanihata, Y. Sugahara, K. Sumiyoshi, and H. Toki: "Can the equation of state of asymmetric nuclear matter be studied using unstable nuclei?", Nucl. Phys. A **634**, 3–14 (1998).

N. Dinh Dang and A. Arima: "Temperature dependence of quantal and thermal dampings of the hot giant dipole resonance", Nucl. Phys. A **636**, 427–451 (1998).

D. L. Adams, Fnal E704 Collaboration, Y. Goto, and N. Saito: "Measurement of single spin asymmetry in η-meson productions in $p_{\uparrow}p$ and $\bar{p}_{\uparrow}p$ interactions in beam fragmentation region at 200-GeV/c", Nucl. Phys. B **510**, 3–11 (1998).

E. Kim, T. Nakamura, A. Konno, Y. Uwamino, N. Nakanishi, M. Imamura, N. Nakao, S. Shibata, and S. Tanaka: "Measurements of newtron spallation cross sections of ^{12}C and ^{209}Bi in the 20- to 150-MeV energy range", Nucl. Sci. Eng. **129**, 209–223 (1998).

Y. D. Devi, A. Arima, and N. Yoshinaga: "Nuclear shell model and interacting Boson Fermion approximation", Phys. Lett. B **418**, 13–19 (1998).

J. Meng, I. Tanihata, and S. Yamaji: "The proton and neutron distributions in Na isotopes: The development of halo and shell structure", Phys. Lett. B **419**, 1–6 (1998).

J. A. Tostevin, S. Rugmai, R. C. Johnson, H. Okamura, S. Ishida, N. Sakamoto, H. Otsu, T. Uesaka, T. Wakasa, H. Sakai, T. Niizeki, H. Toyokawa, Y. Tajima, H. Ohnuma, M. Yosoi, K. Hatanaka, and T. Ichihara: "Coulomb breakup of light composite nuclei", Phys. Lett. B **424**, 219–225 (1998).

M. Sugita, K. Uchiyama, and K. Furuno: "Quadrupole deformation of barium isotopes", Phys. Lett. B **440**, 239–245 (1998).

N. Pietralla, T. Mizusaki, P. von Brentano, R. V. Jolos, T. Otsuka, and V. Werner: "2_1^+ and 2_2^+ states in collectiv nuclei multiple Q-phonon excitations", Phys. Rev. C **57**, 150–158 (1998).

M. Schäfer, W.-D. Schmidt-Ott, T. Dörfler, T. Hild, T. Pfeiffer, R. Collatz, H. Geissel, M. Hellström, Z. Hu, H. Irnich, N. Iwasa, M. Pfützner, E. Roeckl, M. Shibata, K. Asahi, H. Izumi, H. Ogawa, H. Sato, H. Ueno, and H. Okuno: "Polarization in fragmentation and g factor of ^{35}K", Phys. Rev. C **57**, 2205–2214 (1998).

N. Dinh Dang and F. Sakata: "Relation between damping of the hot giant dipole resonance and the complex admittance of an irreversible process", Phys. Rev. C **57**, 3032–3048 (1998).

J. Meng, K. Sugawara-Tanabe, S. Yamaji, P. Ring, and A. Arima: "Pseudospin symmetry in relativistic mean field theory", Phys. Rev. C **58**, R628–R631 (1998).

H. Okamura, S. Ishida, N. Sakamoto, H. Otsu, T. Uesaka, T. Wakasa, H. Sakai, T. Niizeki, H. Toyokawa, Y. Tajima, H. Ohnuma, M. Yosoi, K. Hatanaka, and T. Ichihara: "Mechanism of the forward-angle (d, pn) reaction at intermediate energies", Phys. Rev. C **58**, 2180–2191 (1998).

T. Ito, R. S. Hayano, S. N. Nakamura, T. P. Terada, M. Iwasaki, D. R. Gill, L. Lee, A. Olin, M. Salomon, S. Yen, K. Bartlett, G. A. Beer, G. Mason, G. Trayling, H. Outa, T. Taniguchi, Y. Yamashita, and R. Seki: "Observation of kaonic hydrogen atom X rays", Phys. Rev. C **58**, 2366–2382 (1998).

M. R. Ahmady, E. Kou, and A. Sugimoto: "Intermediate psuedoscalar resonance contributions to $B \to X_s \gamma\gamma$", Phys. Rev. D **57**, 1997–2000 (1998).

R. L. Jaffe, X. Jin, and J. Tang: "Interference fragmentation functions and valence quark spin distributions in the nucleon", Phys. Rev. D **57**, 5920–5922 (1998).

K. Bora and R. L. Jaffe: "Double-scattering contribution to $b_1(x, Q^2)$ in the deuteron", Phys. Rev. D **57**, 6906–6911 (1998).

N. Dinh Dang and A. Arima: "Quantal and thermal dampings of giant dipole resonance in ^{90}Zr, ^{120}Sn, and ^{208}Pb", Phys. Rev. Lett. **80**, 4145–4148 (1998).

T. Kohno, H. Miyasaka, H. Kato, C. Kato, T. Goka, and H. Matsumoto: "Heavy ion radiation in space observed by Japanese satellite", Proc. 3rd Int. Workshop on Radiation Effects on Semiconductor Devices for Space Application, Takasaki, pp. 90–95 (1998).

T. Goka, H. Matsumoto, S. Takagi, T. Kohno, and F. Makino: "Empirical radiation belt models based on the Japanese satellites measurements", Proc. 3rd Int. Workshop on Radiation Effects on Semiconductor Devices for Space Application, Takasaki, 1998-10,

pp. 96–101 (1998).
I. M. Martin, A. A. Gusev, T. Kohno, G. I. Pugacheva, and W. Spjeldvik: "Space distribution of energetic He ion flux in magnetosphere: Ohzora observations during 1984-1986", Proc. 5th Cong. Int. Brazilian Geophysical Society, Sao Paulo, 1997-10, edited by Y. R. Marangoni et al., pp. 1085–1088 (1998).
A. A. Gusev, I. M. Martin, G. I. Pugacheva, A. Jr. Turtelli, T. Kohno, and W. Spjeldvik: "The secondary proton radiation belt: Origin and dynamics", Proc. 5th Cong. Int. Brazilian Geophysical Society, Sao Paulo, 1997-10, edited by Y. R. Marangoni et al., pp. 1093–1097 (1998).
K. Ishida, K. Nagamine, T. Matsuzaki, S. N. Nakamura, N. Kawamura, S. Sakamoto, M. Iwasaki, M. Tanase, M. Kato, K. Kurosawa, H. Sugai, I. Watanabe, K. Kudoh, N. Takeda, and G. H. Eaton: "Muon catalyzed fusion (μCF) experiment at the RIKEN-RAL Muon Facility (I): X-ray and neutron measurement of μ to α sticking probability", Proc. Int. Symp. on Laser Application to Muon Science, Tsukuba, 1998-03, edited by Y. Miyake, K. Shimomura, and K. Nagamine, High Energy Accelerator Research Organization, pp. 126–130 (1998).
K. Ishida and K. Nagamine: "Simulation of solenoidal capture of high intensity muon beam at RIKEN/RAL and KEK-MSL", Proc. Int. Workshop on JHF Science (JHF98), Tsukuba, 1998-03, edited by J. Chiba et al., High Energy Accelerator Research Organization, Tsukuba, pp. 12–15 (1998).
J. Kodaira, T. Nasuno, H. Tochimura, K. Tanaka, and Y. Yasui: "Renormalization of gauge-invariant operators for the structure function $g_2(x,Q^2)$", Prog. Theor. Phys. **99**, 315–320 (1998).
E. C. Adelberger, S. M. Austin, J. N. Bahcall, A. B. Balantekin, G. Bogaert, L. S. Brown, L. Buchmann, F. E. Cecil, A. E. Champagne, L. de Braeckeleer, C. A. Duba, S. R. Elliott, S. J. Freedman, M. Gai, G. Goldring, C. R. Gould, A. Gruzinov, W. C. Haxton, K. M. Heeger, E. Henley, C. W. Johnson, M. Kamionkowski, R. W. Kavanagh, S. E. Koonin, K. Kubodera, K. Langanke, T. Motobayashi, V. Pandharipande, P. Parker, R. G. H. Robertson, C. Rolfs, R. F. Sawyer, N. Shaviv, T. D. Shoppa, K. A. Snover, E. Swanson, R. E. Tribble, S. Turck-Chiéze, and J. F. Wilkerson: "Solar fusion cross sections", Rev. Mod. Phys. **70**, 1265–1292 (1998).

3. Atomic and solid-state physics

E. Torikai, K. Nagamine, K. Nishiyama, E. Hirose, Y. Ikedo, T. Hashimoto, P. Birrer , T. Tanaka, H. Kojima, S. Srinivas, T. P. Das, S. Maekawa, K. Yamada, S. Hosoya, and Y. Endoh: "Probing interaction of paramagnetic electron with conduction electrons in high T_c superconductor LaSrCuO by (μ^-O) spin relaxation", Hyperfine Interact. **105**, 175–179 (1997).
R. M. Macrae, R. Kadono, F. L. Pratt, K. Tanigaki, K. Nishiyama, and K. Nagamine: "Longitudinal field repolarization studies of reorientational dynamics in the fullerences C_{60} and C_{70}", Hyperfine Interact. **106**, 175–180 (1997).
A. Matsushita and K. Nagamine: "Muonium desorption to vacuum from hot iridium surface", Hyperfine Interact. **106**, 283–289 (1997).
T. Azuma, T. Ito, K. Komaki, T. Tonuma, M. Sano, A. Kitagawa, E. Takada, and H. Tawara: "Relativistic heavy collisions studies at HIMAC: X-rays from radiative electron capture into continuum and secondary electrons from binary encounter collisions", Nucl. Instrum. Methods Phys. Res. B **132**, 246–249 (1997).
F. L. Pratt, S. J. Blundell, W. Hayes, K. Nagamine, K. Ishida, and A. P. Monkman: "Anisotropic polaron motion in polyaniline studied by muon spin relaxation", Phys. Rev. Lett. **79**, 2855–2858 (1997).
S. Makino, T. Matsuo, M. Mizuno, M. Sano, T. Kohno, T. Tonuma, H. Tawara, A. Kitagawa, and T. Murakami: "Net-ionization cross sections of rare gases by fully-stripped heavy ion impact", Phys. Scr. T **73**, 238–239 (1997).
T. Azuma, T. Ito, K. Komaki, H. Tawara, T. Matsuo, T. Tonuma, K. Shima, A. Kitagawa, E. Takada, T. Murakami, and A. Warczak: "RECC and REC measurements for heavy ion impact on foil targets at relativistic energies", Phys. Scr. T **73**, 250–251 (1997).
E. Yagi: "State of hydrogen in Nb-based Nb-Mo alloys as observed by a channelling method utilizing a nuclear reaction ^{1}H(^{11}B, α)$\alpha\alpha$", RIKEN Rev., No. 16, pp. 3–4 (1997).
K. Tanaka, E. Yagi, N. Masahashi, Y. Mizuhara, K. Tatsumi, and T. Takahashi: "Lattice location of B atoms in an intermetallic compound $Ni_{0.75}Al_{0.15}Ti_{0.10}$ as observed by a channelling method", RIKEN Rev., No. 16, pp. 5–6 (1997).
T. Minamisono, K. Matsuta, M. Fukuda, M. Tanigaki, Y. Nojiri, H. Akai, M. Mihara, T. Yamaguchi, M. Sasaki, T. Miyake, T. Onishi, K. Minamisono, K. Sato, T. Ohtsubo, S. Fukuda, K. Yoshida, A. Ozawa, S. Momota, and I. Tanihata: "β-NMR detections of short-lived β-emitters ^{13}O and ^{23}Mg implanted in Pt for the studies on anomalous Knight shifts", RIKEN Rev., No. 16, pp. 7–8 (1997).
Y. Ohkubo, Y. Kobayashi, K. Harasawa, S. Ambe, T. Okada, K. Asai, S. Shibata, and F. Ambe: "TDPAC and emission Mössbauer studies on ^{99}Ru in $YB_2Cu_3O_{6.8}$ and $YBa_2Cu_3O_6$", RIKEN Rev., No. 16, pp. 11–12 (1997).
T. Okada, Y. Noro, Y. Kobayashi, J. Nakamura, H. Kitazawa, and F. Ambe: "Giant hyperfine magnetic field at ^{61}Ni in spinel-type chromites", RIKEN Rev., No. 16, pp. 23–24 (1997).
J. Nakamura, Y. Noro, T. Okada, Y. Kobayashi, H. Kitazawa, and F. Ambe: "Hyperfine interaction of ^{61}Ni in $Cu_{1-x}Ni_xCr_2O_4$: The effect of unquenched

orbital angular momentum", RIKEN Rev., No. 16, pp. 25–26 (1997).
T. Nishimura: "Vibrationally elastic scattering of positrons from CH_4 molecules", At. Collision Res. Jpn: Prog. Rep. **24**, 7–9 (1998).
Y. Sakurai: "High energy inelastic scattering beamline for electron momentum density study", J. Jpn Soc. Synchrotron Rad. Res. **11**, 114–121 (1998).
T. Kambara, M. Kimura, Y. Awaya, T. M. Kojima, V. Mergel, Y. Nakai, and H. Schmidt-Böcking: "State-selective differential cross sections of electron capture in 10 MeV Ar^{8+} -He collisions", J. Phys. B: At. Mol. Opt. Phys. **31**, L909–L914 (1998).
T. Nishimura : "Theoretical study of electron scattering from CH_2F_2 molecules", J. Phys. B: At. Mol. Opt. Phys. **31**, 3471–3478 (1998).
E. Yagi and S. Koike: "Change of site occupancy of hydrogen in Nb on alloying with undersized Mo", J. Phys. Soc. Jpn. **67**, 340–344 (1998).
E. Yagi: "Studies on hydrogen in metals and alloys by the nuclear reaction channelling method", Met. Technol. **68**, 49–58 (1998).
N. Ishikawa, Y. Chimi, A. Iwase, H. Maeta, K. Tsuru, O. Michikami, T. Kambara, T. Mitamura, Y. Awaya, and M. Terasawa: "Electronic excitation effects in ion-irradiated high-T_c superconductors", Nucl. Instrum. Methods Phys. Res. B **135**, 184–189 (1998).
Y. Sugaya, D. Ashery, J. Chiba, H. Ito, K. Kimura, Y. T. Kiselev, S. Koda, K. Miyano, T. Murakami, J. Murata, T. Nagae, Y. Nakai, M. Nomachi, M. Numajiri, H Ochiishi, S. Sawada, M Sekimoto, T. Shibata, T. Suzuki, K. H. Tanaka, M. K. Vlasov, Y. Yamanoi, K. Yasuda, and Y. Yoshimura: "Sub-threshold antiproton production in pA, dA and αA reactions", Nucl. Phys. A **634**, 115–140 (1998).
I. Shimamura: "Antiprotonic helium", Photonic, Electronic and Atomic Collisions, Vienna, Austria, 1997-07, edited by F. Aumayr and H. Winter, World Scientific, pp. 631–638 (1998).
D. Bakalov, K. Bakalova, V. I. Korobov, H. J. Monkhorst, and I. Shimamura: "Fine and quadrupole structure of the weakly bound systems $(dt\mu)_{11}dee$ and $(dd\mu)_{11}dee$", Phys. Rev. A **57**, 3370–3375 (1998).
A. Igarashi, I. Shimamura, and N. Toshima: "Hyperspherical close-coupling study of hyperfine transitions in low-energy $p + p\mu$ and $e^{\pm}$ + Ps scattering", Phys. Rev. A **58**, 1166–1173 (1998).
V. Mergel, M. Achler, R. Dörner, Kh. Khayyat, T. Kambara, Y. Awaya, V. Zoran, B. Nyström, L. Spielberger, J. H. McGuire, J. Feagin, J. Berakdar, Y. Azuma, and H. Schmidt-Böcking: "Helicity dependence of the photon-induced three-body Coulomb fragmentation of helium investigated by cold target recoil ion momentum spectroscopy", Phys. Rev. Lett. **80**, 5301–5304 (1998).
M. Terasawa, N. Takezawa, K. Fukushima, T. Mitamura, X. J. Fan, H. Tsubakino, T. Kohara, K. Ueda, Y. Awaya, T. Kambara, M. Matsuda, and G. Tatara: "Flux pinning and flux creep in $La_{2-x}Sr_xCuO_4$ with splayed columnar defects", Physica C **296**, 57–64 (1998).
E. Yagi: "Studies of impurities in metals by a channelling method utilizing a nuclear reaction", Proc. Int. Workshop on JHF Science (JHF98), Tsukuba, 1998-03, edited by J. Chiba et al., High Energy Accelerator Research Organization, Tsukuba, pp. 380–383 (1998).
Y. Nakai, A. Itoh, T. Kambara, Y. Bitoh, Y. Awaya, and Y. Yamazaki: "Fragmentation of C_{60} in close collision with fast carbon ions", RIKEN Rev., No. 17, pp. 55–56 (1998).
H. Tsuchida, A. Itoh, Y. Nakai, K. Miyabe, M. Imai, and N. Imanishi: "Effects of collective excitation on ionization and fragmentation of C_{60} by high energy H^+ impacts", RIKEN Rev., No. 17, pp. 57–58 (1998).
T. Nishimura: "Vibrationally elastic scattering of positrons from CH_4 molecules", RIKEN Rev., No. 19, pp. 65–66 (1998).
E. Yagi: "Ion beam analysis with accelerators", Vac. J., No. 56, pp. 20–21 (1998).

4. Radiochemistry, radiation chemistry, and radiation biology

I. Narumi, K. Cherdchu, S. Kitayama, and H. Watanabe: "The *Deinococcus radiodurans uvrA* gene: Identification of mutation sites in two mitomycin-sensitive strains and the first discovery of insertion sequence element from deinobacteria", Gene **198**, 115–126 (1997).
T. Ban-nai, Y. Muramatsu, S. Yoshida, S. Uchida, S. Shibata, S. Ambe, F. Ambe, and A. Suzuki: "Multitracer studies on the accumulation of radionuclides in mushrooms", J. Radiat. Res. **38**, 213–218 (1997).
S. Gouthu, T. Arie, S. Ambe, and I. Yamaguchi: "Screening of plant species for comparative uptake abilities of radioactive Co, Rb, Sr, and Cs from soil", J. Radioanal. Nucl. Chem. **222**, 247–251 (1997).
S. Kitayama, M. Kohoroku, A. Takagi, and H. Itoh: "Mutation of *D. radiodurans* in a gene homologous to *ruvB* of *E. coli*", Mut. Res. **385**, 151–157 (1997).
Y. Ohkubo, S. Uehara, Y. Kawase, J. Nakamura, T. Okada, S. Ambe, and F. Ambe: "Time-differential perturbed-angular-correlation studies on ^{117}In and ^{111}Cd in $Li_{0.995}Cd_{0.005}NbO_3$", Phys. Rev. B **56**, 10730–10733 (1997).
S. Gouthu, T. Arie, S. Ambe, and I. Yamaguchi: "Selection of plants for phytoremediation of soil contaminated with radionuclides and the impact of some parameters on plant uptake", Proc. Int. Meet. on Influence of Climatic Characteristics upon Behavior of Radioactive Elements, edited by Y. Ohmomo and N. Sakurai, Institute for Environmental Sciences, pp. 221–228 (1997).

H. Wang, S. Ambe, N. Takematsu, and F. Ambe: "Influence of acid rain and organic matter on the adsorption of trace elements on soil", Proc. Sci. Meet. on Behavior and Distributions of Trace Substances in the Environment, 1997-12, edited by M. Fukui and H. Matsuzuru, Res. Reactor Inst., Kyoto Univ., No. KURRI-KR-18, pp. 33–38 (1997).

K. Ushida, A. Kira, Y. Yoshida, T. Kozawa, S. Tagawa, and H. Shibata: "Self exchange electron transfer and ultrafast formation of dimer radical ions", RIKEN Rev., No. 15, pp. 59–60 (1997).

K. Ushida, A. Kira, Y. Yoshida, T. Kozawa, and S. Tagawa: "Inter solute hole transfer competing with geminate ion recombination", RIKEN Rev., No. 15, pp. 61–62 (1997).

Y. Hatano and N. Hatano: "Anomalous transport of ions in porous media", RIKEN Rev., No. 15, pp. 91–92 (1997).

Y. Kobayashi, Y. Yoshida, K. Hayakawa, K. Yukihira, J. Nakamura, S. Nasu, N. Inabe, Y. Watanabe, A. Yoshida, M. Kase, A. Goto, Y. Yano, and F. Ambe: "In-beam Mössbauer spectroscopy of ^{57}Fe using a ^{57}Mn beam from RIPS of RIKEN Ring Cyclotron", RIKEN Rev., No. 16, pp. 21–22 (1997).

S. Ambe and F. Ambe: "Emission Mössbauer spectroscopy of ^{119}Sn using ^{119}Sb as the source nuclide: Defect studies", RIKEN Rev., No. 16, pp. 33–34 (1997).

F. Ambe, T. Okada, and S. Ambe: "Emission Mössbauer spectroscopy of ^{119}Sn using ^{119}Sb as the source nuclide: *in situ* surface studies", RIKEN Rev., No. 16, pp. 37–38 (1997).

K. Eguchi-Kasai, M. Murakami, H. Itsukaichi, K. Fukutsu, F. Yatagai, T. Kanai, H. Ohara, and K. Sato: "Repair of DNA double-strand breaks and cell killing by charged particles", Adv. Space Res. **22**, 543–549 (1998).

H. Wang, S. Ambe, N. Takematsu, and F. Ambe: "Model study of acid rain effect on adsorption of trace elements on soils using a multitracer", J. Radioanal. Nucl. Chem. **235**, 295–300 (1998).

T. Shinonaga, S. Ambe, and I. Yamaguchi: "Uptake rate of trace elements by soybean plants", J. Radioanal. Nucl. Chem. **236**, 133–137 (1998).

S. Ambe, K. Yashiki, H. Maeda, S. Enomoto, T. Ozaki, and F. Ambe: "Multitracer study on permeation of rare earth elements through a supported liquid membrane", J. Radioanal. Nucl. Chem. **236**, 181–185 (1998).

T. Abe: "The use of heavy-ion beams for mutation induction", Kagaku To Seibutsu **36**, 477–482 (1998).

S. Ambe, T. Shinonaga, T. Ozaki, S. Enomoto, H. Yasuda, and S. Uchida: "Multitracer study on uptake of elements by komatsuna", Proc. Int. Meet. on Influence of Climatic Characteristics upon Behavior of Radioactive Elements, Rokkashomura, 1997-10, edited by Y. Ohmomo and N. Sakurai, Institute for Environmental Sciences, Japan, pp. 174–180 (1998).

T. Shinonaga, S. Ambe, and I. Yamaguchi: "Uptake and translocation of Sr, Tc, and Cs in soybean plants", Proc. Int. Meet. on Influence of Climatic Characteristics upon Behavior of Radioactive Elements, Rokkashomura, 1997-10, edited by Y. Ohmomo and N. Sakurai, Institute for Environmental Sciences, Japan, pp. 197–204 (1998).

Y. Ohkubo, S. Uehara, S. Shibata, Y. Kawase, J. Nakamura, T. Okada, S. Ambe, F. Ambe, K. Asai, Y. Murakami, and T. Saito: "TDPAC studies on ^{117}In and ^{111}Cd in $Li_{0.995}Cd_{0.005}NbO_3$", Proc. Specialist Res. Meet. on Solid State Physics with Probes of Radiations and Nuclei (II), 1998-02, edited by S. Nasu, Y. Kawase, and Y. Maeda, Res. Reactor Inst., Kyoto Univ., No. KURRI-KR-22, pp. 47–51 (1998).

S. Ambe, T. Okada, and F. Ambe: "*In situ* emission Mössbauer studies on carrier-free $^{57}Co^{2+}$ and $^{119}Sb^{5+}$ ions at interfaces between spinel-type oxides and aqueous solutions", Radiochim. Acta **80**, 101–108 (1998).

T. Shinonaga and S. Ambe: "Multitracer study on absorption of radionuclides in atmosphere-plant model system", Water, Air, Soil Pollut. **101**, 93–103 (1998).

5. Material analysis

W. Hong, S. Hayakawa, K. Maeda, S. Fukuda, M. Yanokura, M. Aratani, K. Kimura, Y. Gohshi, and I. Tanihata: "Development of a high mass-resolution TOF-ERDA system for a wide mass range from hydrogen to middle heavy elements", Anal. Sci. **13**, 365–368 (1997).

K. Katsumata, H. Aruga Katori, S. M. Shapiro, and G. Shirane: "Neutron-scattering studies of a phase transition in the metamagnet $FeBr_2$ under external magnetic fields", Phys. Rev. B **55**, 11466–11470 (1997).

N. Yamada, T. Fuwa, J. Nakamura, and T. Okada: "Mössbauer study on ^{57}Fe in $YSr_2Cu_{3-x}Fe_xO_{7+\delta}$", RIKEN Rev., No. 16, pp. 27–28 (1997).

Y. Takano, T. Okada, and T. Yamadaya: "Antiferromagnetic spin clusters in the 2126 type cuprate", RIKEN Rev., No. 16, pp. 29–30 (1997).

J. Kawai, N. Inada, and K. Maeda: "X-ray emission due to charge-up", Adv. X-Ray Chem. Anal. Jpn. **29**, 203–222 (1998).

K. Maeda, K. Hasegawa, H. Hamanaka, and K. Ogiwara: "Development of an in-air high-resolution PIXE system", Nucl. Instrum. Methods Phys. Res. B **134**, 418–426 (1998).

K. Maeda, K. Hasegawa, H. Hamanaka, and M. Maeda: "Chemical state analysis in air by high-resolution PIXE", Nucl. Instrum. Methods Phys. Res. B **136/138**, 994–999 (1998).

VII. LIST OF PREPRINTS

1998

RIKEN-AF-NP

278 K. Varga, J. Usukura, and Y. Suzuki: "Second bound state of the positronium molecule and biexcitons"

279 M. R. Ahmady, V. Elias, and E. Kou: "Nonperturbative QCD contribution to gluon-gluon-eta vertex"

280 H. Kurasawa and T. Suzuki: "Double giant resonance states"

281 H. Kurasawa and T. Suzuki: "Spin dipole states deformed nuclei"

282 N. Saito: "Spin physics with the PHENIX detector system"

283 N. Saito: "High-energy spin physics with RHIC"

284 H. Okamura, S. Ishida, N. Sakamoto, H. Uesaka, T. Wakasa, H. Sakai, T. Niizeki, H. Toyokawa, Y. Tajima, H. Ohnuma, M. Yosoi, K. Hatanaka, and T. Ichihara: "Mechanism of the forward-angle(d, pn) reaction at intermediate energies"

285 N. D. Dang, K. Tanabe, and A. Arima: "Damping of hot giant dipole resonance due to complex configuration mixing"

286 N. D. Dang, K. Tanabe, and A. Arima: "Contribution of higher-order processes to the damping of hot giant dipole resonance"

287 T. Horibata, M. Oi, and N. Onishi: "Band crossing studied by GCM with 3D-CHFB"

288 M. Oi, N. Onishi, and T. Horibata: "Wobbling motion in band crossing"

289 Y. S. Mochizuki, S. Kumagai, and I. Tanihata: "The half-life of ^{44}Ti and SN 1987A"

290 N. D. Dang, K. Tanabe, and A. Arima: "Width and shape of hot giant dipole resonance"

291 Y. Ogawa, K. Arai, and K. Varga: "Microscopic four-cluster description of ^{10}Be and ^{10}C with the stochastic variational method"

292 M. R. Ahmady and E. Kou: "Possible large direct CP asymmetry in hadoronic $B^{\pm} \to \pi^{\pm}\eta'$ decays"

293 N. Hayashi, Y. Goto, and N. Saito: "RHIC spin physics"

294 A. Ozawa, O. Bochkarev, L. Chulkov, D. Cortina, H. Geissel, M. Hellström, M. Ivanov, R. Jank, K. Kimura, T. Kobayashi, A. A. Korsheninnikov, G. Münzenberg, F. Nickel, Y. Ogawa, A. A. Ogloblin, M. Pfützner, V. Pribora, H. Simon, B. Sitár, P. Strmen, K. Sümmerer, T. Suzuki, I. Tanihata, M. Winkler, K. Yamashita, and K. Yoshida: "Measurements of interaction cross-sections for carbon isotopes at relativistic energies and the halo structure ^{19}C"

295 M. R. Ahmady and V. Elias: "Nonperturbative QCD corrections to the effective coefficients of the four-Fermi operators"

296 N. D. Dang, K. Tanabe, and A. Arima: "Shape evolution of the hot giant dipole resonance"

297 T. Horibata, M. Oi, N. Onishi, and A. Ansari: "Band structures of ^{182}Os studied by GCM based on 3D-CHFB"

298 M. Sambataro and N. D. Dang: "Variational approach to collective excitations"

299 T. Suzuki and H. Sakai: "The landau-migdal parameters, g'NN and g'NΔ"

300 N. D. Dang, K. Tanabe, and A. Arima: "Damping of double giant dipole resonance"

301 H. Toki and T. Tanihata: "Implication of recent (p, n) spin experiments and the necessity of relativity in nuclear physics"

302 K. Kato, T. Yamada, and K. Ikeda: "Dynamical effects on the ^{9}Li-n interaction induced by the pauli-blocking of the $J^{\pi} = 0^{+}$ pairing correlation"

RIKEN-AF-NC

4 G. Shirkov and T. Nakagawa: "Numerical simulation of highly charged ion production in RIKEN 18GHz ECR ion source"

5 G. Shirkov, Y. Batygin, and Y. Yano: "Particle-cell model for numerical simulation of multicomponent ECR plasma and electron-ion beams"

6 O. Kartavisev and G. Shirkov: "Role of charge exchange processes in the plasma of ECR ion sources"

7 E. Syresin, T. Tanabe, and I. Watanabe: "Simulation of electron and collector for ACR electron cooling system"

8 I. Meshkov, E. Syresin, T. Katayama, and Y. Yano: "Single turn injection scheme for ACR"

9 T. Katayama, I. Meshkov, A. Sidorin, and E. Syresin: "Electron cooling at DSR"

10 Y. Batygin and T. Katayama: "Luminosity of particle collider"

11 M. Wakasugi, Y. Batygin, N. Inabe, T. Katayama, K. Maruyama, K. Ohtomo, T. Ohkawa, M. Takanaka, T. Tanabe, I. Tanihata, S. Watanabe, Y. Yano, and K. Yoshida: "Storage rings at RIKEN RI Beam Factory"

VIII. PAPERS PRESENTED AT MEETINGS

1. Accelerator development and accelerator physics

J.-W. Kim, T. Kubo, and T. Kawaguchi: "A superconducting solenoid for heavy ion beam focusing", 1997 Particle Accelerator Conf. (PAC'97), (IEEE, APS), Vancouver, Canada, May (1997).

J.-W. Kim, A. Goto, T. Mitsumoto, T. Kubo, H. Okuno, T. Kawaguchi, T. Tominaka, S. Fujishima, K. Ikegami, N. Sakamoto, S. Yokouchi, T. Morikawa, and Y. Yano: "Trim coil system for the RIKEN Superconducting Ring Cyclotron", 1997 Particle Accelerator Conf. (PAC'97), (IEEE, APS), Vancouver, Canada, May (1997).

J.-W. Kim and J. S. Chai: "Design study of a linear accelerator system for neutron capture therapy", 1997 Particle Accelerator Conf. (PAC'97), (IEEE, APS), Vancouver, Canada, May (1997).

O. Kamigaito, A. Goto, Y. Miyazawa, T. Chiba, M. Hemmi, S. Kohara, M. Kase, T. Nakagawa, Y. Batygin, Y. Yano, E. Ikezawa, T. Aihara, T. Ohki, H. Hasebe, and H. Yamauchi: "Performance tests of a variable-frequency RFQ linac for RILAC", 22nd Linear Accelerator Meet. in Japan, Sendai, Sept. (1997).

T. Takagi, S. Fujiwara, K. Wakashima, S. Eguchi, H. Mukai, and I. Sakamoto: "Radiation safety control system for SPring-8", 11th Symp. on Accelerator Science and Technology, (JASRI), Harima, Oct. (1997).

N. Sakamoto: "Atomic hydrogen beam production at RIKEN polarized ion source", 14th RIKEN Symp. on Atomic Physics Using Accelerators: Atomic Physics with Slow Antiprotons, Wako, Dec. (1997).

A. Goto, Y. Yano, and T. Katayama: "RIKEN RI-Beam Factory project", Int. Workshop on Physics with Radioactive Nuclear Beams, Puri, India, Jan. (1998).

I. Tanihata: "RI Beam Factory project", RIKEN Symp. on Nuclear Chemistry of Heavy Elements at RIKEN RI-Beam Factory, Wako, Jan. (1998).

Y. Yoshida, Y. Mizutani, T. Yamamoto, M. Miki, Y. Izumi, K. Ushida, S. Seki, T. Kozawa, and S. Tagawa: "Improvement of femtosecond laser-synchronized pulse radiolysis system and its application to ultrafast processes", 5th Int. Workshop on Femtosecond Technology, Tsukuba, Feb. (1998).

M. Niimura, A. Goto, and Y. Yano: "Acceleration and heating mechanisms of the hot electron ring and warm core plasma: The consequence on performance of ECRIS", 1st Asian Particle Accelerator Conf. (APAC98), (KEK), Tsukuba, Mar. (1998).

K. Yuasa-Nakagawa: "Reaction mechanism study using total kinetic energy and precision particle multiplicity in medium mass nuclei", RIKEN Symp. on Dynamics in Hot Nuclei, Wako, Mar. (1998).

T. Tominaka, K. Kusaka, and T. Kubo: "Design study of the superconducting quadrupole magnets for RIKEN Big RIPS (1)", 58th Meet. on Cryogenics and Superconductivity, (Cryogenic Association of Japan), Fujisawa, May (1998).

T. Tominaka, H. Okuno, S. Fujishima, A. Goto, and Y. Yano: "Optimization of the superconducting dipole coils for injection system of superconducting ring cyclotron", 58th Meet. on Cryogenics and Superconductivity, (Cryogenic Association of Japan), Fujisawa, May (1998).

K. Ohtomo and T. Katayama: "Injection simulation study at accumulator cooler ring at RI Beam Factory", 6th European Particle Accelerator Conf., (Manne Siegbahn Laboratory), Stockholm, Sweden, June (1998).

A. Goto, H. Okuno, T. Kawaguchi, T. Mitsumoto, T. Tominaka, S. Fujishima, J.-W. Kim, J. Ohnishi, K. Ikegami, N. Sakamoto, S. Yokouchi, K. Sugii, T. Wada, T. Morikawa, T. Kubo, and Y. Yano: "The K2500 superconduction Ring Cyclotron of RIKEN RI Beam Factory", 15th Int. Conf. on Cyclotrons and Their Applications (Cyclotrons'98), (GANIL), Caen, France, June (1998).

T. Tominaka, H. Okuno, S. Fujishima, A. Goto, and Y. Yano: "An optimal design for the injection and extraction elements for the RIKEN Superconducting Ring Cyclotron", 15th Int. Conf. on Cyclotrons and Their Applications (Cyclotrons'98), (GANIL), Caen, France, June (1998).

A. Goto, J.-W. Kim, J. Ohnishi, T. Kawaguchi, H. Okuno, S. Fujishima, T. Tominaka, and Y. Yano: "Orbit analysis of the RIKEN Superconducting Ring Cyclotron", 15th Int. Conf. on Cyclotrons and Their Applications (Cyclotrons'98), (GANIL), Caen, France, June (1998).

S. Kohara, Y. Miyazawa, O. Kamigaito, T. Chiba, E. Ikezawa, M. Kase, and A. Goto: "Model study of a resonator for a flat-top acceleration system in the RIKEN AVF Cyclotron", 15th Int. Conf. on Cyclotrons and Their Applications (Cyclotrons'98), (GANIL), Caen, France, June (1998).

S. Fujishima, H. Okuno, T. Tominaka, T. Mitsumoto, A. Goto, and Y. Yano: "Analysis of the injection and extraction trajectories in the RIKEN Superconducting Ring Cyclotron", 15th Int. Conf. on Cyclotrons and Their Applications (Cyclotrons'98), (GANIL), Caen, France, June (1998).

H. Shibata, K. Kobayashi, T. Iwai, M. Narui, T. Omata, S. Sasaki, Y. Hamabe, A. Fujiwara, S. Hasegawa, T. Nishimura , H. Yano, H. Ohashi, and K. Nogami: "Experiment for dust acceleration", 23rd Ann. Meet. of the Society for Atomic Collision Research, Yokohama, Aug. (1998).

O. Kamigaito, A. Goto, Y. Miyazawa, T. Chiba, M. Hemmi, M. Kase, S. Kohara, E. Ikezawa, T.

Nakagawa, M. Kidera, and Y. Yano: "Recent developments of the folded-coaxial RFQ for the RIKEN Heavy Ion Linac", 19th Int. Linac Conf., (ANL, FNAL), Chicago, USA, Aug. (1998).

O. Kamigaito, A. Bandyopadhyay, M. Kase, Y. Miyazawa, T. Chiba, M. Hemmi, S. Kohara, E. Ikezawa, A. Goto, Y. Yano, and A. Bandyopadhyay: "Design of a charge-state multiplier system for the RIKEN RI-Beam Factory", 19th Int. Linac Conf., (ANL, FNAL), Chicago, USA, Aug. (1998).

O. Kamigaito, M. Kase, Y. Miyazawa, T. Chiba, M. Hemmi, E. Ikezawa, S. Kohara, A. Goto, and Y. Yano: "Development of a charge-state multiplier system for the RIKEN RI-Baem Factory", 23rd Linear Accelerator Meet. in Japan, (Electrotechnical Laboratory), Tsukuba, Sept. (1998).

M. Niimura, A. Goto, and Y. Yano: "Study of the hot-electron acceleration and warm-electron heating mechanisms in an ECR ion source for high-brightness hadron colliders", High Energy Accelerator Conf. (HEACC'98), (Joint Institute of Nuclear Research), Dubna, Russia, Sept. (1998).

T. Kawaguchi, T. Nakagawa, and T. Kurita: "Development of a He-free SCM for ECR ion source", 59th Meet. on Cryogenics and Superconductivity, (Cryogenics Association of Japan), Yamaguchi, Oct. (1998).

T. Kawaguchi, H. Okuno, A. Goto, and Y. Yano: "Development of the sector magnets for the Superconducting Ring Cyclotoron", 59th Meet. on Cryogenics and Superconductivity, (Cryogenics Association of Japan), Yamaguchi, Oct. (1998).

T. Tominaka, M. Okamura, T. Kawaguchi, and T. Katayama: "R&D of helical dipole magnets", 59th Meet. on Cryogenics and Superconductivity, (Cryogenics Association of Japan), Yamaguchi, Oct. (1998).

T. Tominaka, H. Okuno, S. Fujishima, A. Goto, and Y. Yano: "Optimization of the superconducting dipole coils for injection system of Superconducting Ring Cyclotron(2)", 59th Meet. on Cryogenics and Superconductivity, (Cryogenics Association of Japan), Yamaguchi, Oct. (1998).

Y. Mizutani, A. Saeki, K. Okamoto, M. Miki, S. Seki, T. Kozawa, K. Ushida, Y. Yoshida, and S. Tagawa: "Development of picosecond pulse radiolysis by using femtosecond laser synchronized with L-band linac", 41st Symp. on Radiation Chemistry, (Japanese Society of Radiation Chemistry), Kobe, Oct. (1998).

H. Shibata, K. Kobayashi, T. Iwai, M. Narui, T. Omata, S. Sasaki, Y. Hamabe, A. Fujiwara, S. Hasegawa, T. Nishimura, H. Yano, H. Ohashi, and K. Nogami: "Design of electrostatic acceleration system for microparticles to hypervelocites and its application", 41st Symp. on Radiochemistry and Asia-Pacific Symposium on Radiochemistry, (The Chemical Society of Japan), Kobe, Oct. (1998).

2. Nuclear physics and nuclear instrumentation

T. Motobayashi: "New measurement of ^{8}B Coulomb dissociation and E2 component", 4th Int. Conf. on Radioactive Nuclear Beams (RNB4), Omiya, June (1996).

T. Motobayashi: "Measurement of the E2-component in the Coulomb dissociation of ^{8}B", 4th Int. Symp. on Nuclear Astrophysics (NIC96), (Notre Dame University), Notre Dame, USA, June (1996).

T. Motobayashi: "Radiative capture process of astrophysical interest studied by Coulomb dissociation of unstable nuclei", 9th Int. Symp. on Capture γ Rays Spectroscopy and Related Topics (cgs9), Budapest, Hungary, Oct. (1996).

K. Asahi: "Polarized heavy ions and their application", 7th RCNP Int. Workshop on Polarized ^{3}He Beams and Gas Targets and Their Application, Kobe, Jan. (1997).

T. Matsuzaki, K. Nagamine, K. Ishida, S. N. Nakamura, N. Kawamura, S. Sakamoto, M. Tanase, M. Kato, K. Kurosawa, M. Hashimoto, K. Kudoh, N. Takeda, and G. H. Eaton: "Muon catalyzed fusion research at RIKEN-RAL Muon Facility: (5)Target gas purification system and He-3 accumulation effect", 52nd Ann. Meet. of Physical Society of Japan, Nagoya, Mar. (1997).

K. Yoshida: "Search for super heavy compound nuclei", RIKEN Symp. on Dynamics in Hot Nuclei, Wako, Mar. (1997).

H. Sakurai: "RIBF-facility development and unstable nuclear physics", Symp. on RI Beam Factory and Astrophsics, Wako, Apr. (1997).

Y. Mochizuki: "Neutron stars and RI Beam Factory", Symp. on RI Beam Factory and Astrophysics, Wako, Apr. (1997).

T. Kishida: "γ-ray detector for RI Beam Factory", Workshop on Physics in RI Beam Factory, Wako, May (1997).

H. Sakurai: "Particle identification and new isotope search", Workshop on Physics in RI Beam Factory, Wako, May (1997).

H. Sakurai: "Nuclear mass measurement", Workshop on Physics in RI Beam Factory, Wako, May (1997).

Y. Gono: "Position sensitive gamma-ray detection", 3rd Japan China Joint Nuclear Physics Symp. on Recent Topics in Nuclear Physics, Sendai, June (1997).

N. Saito: "Spin physics at PHIC", 1997 QCD in Nuclear Physics Gordon Research Conf., (Salve Regina University in Newport, RI), Rhode, Island, July (1997).

T. Otsuka, T. Mizusaki, and M. Honma: "Monte-Carlo shell model calculations", 3rd Japan China Joint Nuclear Physics Symp. on Recent Topics in Nuclear Physics, Sendai, July (1997).

K. Asahi, K. Sakai, H. Ogawa, A. Yoshimi, M. Tsuda, Y. Uchiyama, T. Suzuki, K. Suzuki, N. Kurokawa, H.

Sato, M. Adachi, A. Yoshida, S. Fukuda, T. Kubo, H. Okuno, N. Fukunishi, M. Notani, N. Aoi, K. Yoneda, H. Iwasaki, N. Fukuda, M. Ishihara, H. Izumi, H. Ueno, T. Shimoda, S. Tanimoto, N. Takahashi, W.-D. Schmidt-Ott, and M. Schäfer: "Experiments with polarized RI Beam Factory at RIKEN", 3rd Japan China Joint Nuclear Physics Symp. on Recent Topics in Nuclear Physics, Sendai, July (1997).

T. Nakamura: "Coulomb excitation of ^{11}Be", 3rd Japan China Joint Nuclear Physics Symp. on Recent Topics in Nuclear Physics, Sendai, July (1997).

H. Sakurai: "New neutron-rich nuclei isotopes close to the neutron drip-line", 3rd Japan China Joint Nuclear Physics Symp. on Recent Topics in Nuclear Physics, Sendai, July (1997).

Y. Ogawa: "The momentum distributions of the core fragment from the nuclear breakup reaction within the glauber model", 3rd Japan China Joint Nuclear Physics Symp. on Recent Topics in Nuclear Physics, Sendai, July (1997).

K. Nagamine: "Muon catalyzed fusion", 9th TRIUMF Summer Institute, Vancouver, Canada, July (1997).

T. Kishida: "RI Beam Factory and γ-ray detector", Workshop on γ Spectroscopy with Using Heavy Ion · Photon · RI Beam, Tokai-mura, July (1997).

Y. Mochizuki, T. Izuyama, I. Tanihata, and K. Oyamatsu: "Exotic nuclear rod formation for the origin of neutron star glitches", 1997 Pacific Rim Conf. on Stellar Astrophysics, Hong Kong, China, Aug. (1997).

Y. Mochizuki and S. Kumagai: "The half-life of titanium 44 and supernova remnants", Int. Astronomical Union General Meet., Symp. No. 188, Kyoto, Aug. (1997).

K. Sumiyoshi, Y. Sugahara, D. Hirata, I. Tanihata, and H. Toki: "Light unstable nuclei in relativistic mean field theory", Workshop for Physics of RI Beams: Physics of Cluster in Unstable Nuclei, Wako, Aug. (1997).

H. Ogawa, K. Asahi, K. Sakai, M. Tsuda, A. Yoshimi, Y. Uchiyama, T. Suzuki, K. Suzuki, N. Kurokawa, M. Adachi, H. Izumi, H. Ueno, T. Shimoda, S. Tanimoto, N. Takahashi, W. D. Schmidt-Ott, M. Schäfer, S. Fukuda, A. Yoshida, T. Kubo, H. Okuno, H. Sato, M. Notani, N. Aoi, K. Yoneda, H. Iwasaki, N. Fukuda, M. Ishihara, and H. Miyatake: "Measurement of the magnetic moment and electric quadrupole moment of a neutron-rich nucleus ^{18}N", 1997 Fall Meet. of Physical Society of Japan, Hachioji, Sept. (1997).

N. Saito: "High energy spin physics with using RHIC", 1997 Fall Meet. of Physical Society of Japan, Hachioji, Sept. (1997).

K. Yoshida, M. Shimooka, T. Nakagawa, K. Nakagawa, I. Tanihata, R. Wada, Y. Aoki, and J. Kasagi: "Construction of a large area PPAC/ion chamber", 1997 Fall Meet. of Physical Society of Japan, Hachioji, Sept. (1997).

K. Kusaka and H. Toki: "Non-perturbative renormalization of the fermion mass term in the Dyson-Schwinger equation", 1997 Fall Meet. of Physical Society of Japan, Hachioji, Sept. (1997).

Y. Mochizuki, T. Izuyama, I. Tanihata, and K. Oyamatsu: "Pycnonuclear fusion reactions as the origin of neutron star glitches", 1997 Fall Meet. of Physical Society of Japan, Hachioji, Sept. (1997).

I. Imaida, Y. Muraki, Y. Matsubara, K. Masuda, T. Koi, H. Tsuchiya, T. Hoshida, T. Goka, H. Matsumoto, T. Omoto, A. Takase, K. Taguchi, M. Nakazawa, I. Tanaka, M. Fujii, T. Kohno, H. Ikeda, and T. Sako: "Beam experiment results of multi anode neutron sensor", 1997 Fall Meet. of Physical Society of Japan, Hachioji, Sept. (1997).

H. Miyasaka, I. Yamagiwa, C. Kato, T. Goka, and H. Matsumoto: "Observation results of heavy ions with ADEOS satellite", 1997 Fall Meet. of Physical Society of Japan, Hachioji, Sept. (1997).

H. Sakurai: "New neutron-rich nuclei found with a 70A MeV ^{48}Ca beam", 6th Int. School-Seminar, Heavy-Ion Physics, Dubna, Russia, Sept. (1997).

T. Suzuki, H. Geissel, O. Bochkarev, L. Chulkov, M. Golovkov, D. Hirata, H. Irnich, Z. Janas, H. Keller, T. Kobayashi, G. Kraus, G. Muenzenberg, S. Neumaier, F. Nickel, A. Ozawa, A. Piechaczeck, E. Roeckl, W. Schwab, K. Suemmerer, K. Yoshida, and I. Tanihata: "Neutron skin of Na isotopes and an application to the EOS", 6th Int. School-Seminar, Heavy-Ion Physics, Dubna, Russia, Sept. (1997).

T. Otsuka, T. Mizusaki, Y. Utsuno, and M. Honma: "Stochastic approach to nuclear shell model", Int. Symp. on Atomic Nuclei and Metallic Clusters: Finite Many-Fermion Systems, Praque, Czech, Sept. (1997).

T. Matsuzaki, K. Ishida, S. N. Nakamura, N. Kawamura, and K. Nagamine: "Muon catalyzed fusion research at RIKEN-RAL Muon Facility", RIKEN Symp. on Muon Science '97: Muon Condensed Matter Studies and Muon Catalyzed Fusion, Wako, Sept. (1997).

K. Nagamine, T. Matsuzaki, K. Ishida, S. N. Nakamura, and N. Kawamura: "Experimental result of RIKEN-RAL Muon Facility: Muon catalyzed fusion", RIKEN Symp. on Muon Science '97: Muon Condensed Matter Studies and Muon Catalyzed Fusion, Wako, Sept. (1997).

H. Sakurai: "Research with radioactive beams at RIKEN", School-Seminar on RI Beams, Lanzhou, China, Sept. (1997).

K. Nagamine: "Muon science", UK-Japan Collaboration Assisted by The British Council, Tokyo, Sept. (1997).

T. Kohno and H. Miyasaka: "Heavy ion observation with ADEOS satellite", Workshop on Dynamics of Magnetospheric High Energy Particles at Solar Terrestrial Environment Laboratoly, (Solar-Terrestrial Environment Laboratory, Nogoya Univer-

sity), Nagoya, Sept. (1997).

Y. Suda, Y. Ogawa, H. Iwasa, F. Hiraga, T. Kamiyama, Y. Kiyanagi, T. Oku, H. Kato, H. M. Shimizu, and T. Wakabayashi: "Focus of cold neutron beam using neutron lens", 1997 Fall Meet. of the Atomic Energy Society of Japan, Ginowan, Oct. (1997).

T. Otsuka, T. Mizusaki, Y. Utsuno, and M. Honma: "Monte Carlo shell model calculations for stable and unstable nuclei", 3rd INFN-RIKEN Meet. on Perspectives in Heavy Ions Physics, (Padova Univ. and National Laboratories of Legnaro), Padova, Italy, Oct. (1997).

T. Kishida: "RI Beam Factory Project at RIKEN", 3rd INFN-RIKEN Meet. on Perspectives in Heavy Ions Physics, (Padova Univ. and National Laboratories of Legnaro), Padova, Italy, Oct. (1997).

M. Ishihara: "Direct reaction spectroscopy of very neutron rich nuclei", 3rd INFN-RIKEN Meet. on Perspectives in Heavy Ions Physics, (Padova Univ. and National Laboratories of Legnaro), Padova, Italy, Oct. (1997).

T. Nakamura: "Coulomb dissociation of halo nuclei", 3rd INFN-RIKEN Meet. on Perspectives in Heavy Ions Physics, (Padova Univ. and National Laboratories of Legnaro), Padova, Italy, Oct. (1997).

Y. Gono: "HSIB and Ge-telescope", 3rd INFN-RIKEN Meet. on Perspectives in Heavy Ions Physics, (Padova Univ. and National Laboratories of Legnaro), Padova, Italy, Oct. (1997).

K. Asahi, H. Ogawa, K. Sakai, A. Yoshimi, M. Tsuda, Y. Uchiyama, T. Suzuki, K. Suzuki, N. Kurokawa, H. Sato, M. Adachi, H. Izumi, H. Ueno, T. Shimoda, S. Tanimoto, N. Takahashi, W. D. Schmidt-Ott, M. Schäfer, S. Fukuda, A. Yoshida, T. Kubo, H. Okuno, N. Fukunishi, M. Notani, N. Aoi, K. Yoneda, H. Iwasaki, N. Fukuda, and M. Ishihara: "Recent results of nuclear moment measurements with polarized radioactive beams", 3rd INFN-RIKEN Meet. on Perspectives in Heavy Ions Physics, (Padova Univ. and National Laboratories of Legnaro), Padova, Italy, Oct. (1997).

A. Ozawa: "Measurement of interaction cross sections for light neutron rich nuclei", 3rd INFN-RIKEN Meet. on Perspectives in Heavy Ions Physics, (Padova Univ. and National Laboratories of Legnaro), Padova, Italy, Oct. (1997).

Y. Mochizuki: "A microscopic model of glitches: Nuclei and superfluidity inside neutron stars", Astrophysics Seminar at Tokyo-Metropolitan University, Tokyo, Oct. (1997).

T. Kohno, H. Miyasaka, I. Yamagiwa, C. Kato, T. Goka, and H. Matsumoto: "Observation results of heavy ions with ADEOS satellite", Plenary Meet. of Society of Geomagnetic and Planetary Physics, Sapporo, Oct. (1997).

Y. Ogawa: "The momentum distributions of the core fragment from the nuclear breakup reaction within the glauber model", Structure and Reaction of Unstable Nuclei, Kyoto, Oct. (1997).

T. Kohno, T. Goka, and H. Matsumoto: "Heavy ion observation with ADEOS satellite", Workshop on Space Radiation Environment Modelling: New Phenomena and Approaches, (Skobeltsyn Institute of Nuclear Physics of Moscow State University, Rusian Foundation for Fundamental Research, COSPAR), Moscow, Russia, Oct. (1997).

T. Nakamura: "Coulomb excitation of neutron rich halo nuclei", YITP Workshop on Structure and Reaction of Unstable Nuclei, Kyoto, Oct. (1997).

Y. Mochizuki, T. Izuyama, I. Tanihata, and K. Oyamatsu: "A microscopic model of neutron star glitches", Int. Conf. on Neutron Stars and Pulsars: Thirty Years after the Discovery, (Rikkyo University), Tokyo, Nov. (1997).

T. Otsuka and T. Suzuki: "Spin-isospin degree of freedom in unstable nuclei", Int. Symp. on New Facet of Spin Giant Resonances in Nuclei, (University of Tokyo), Tokyo, Nov. (1997).

T. Teranishi, S. Shimoura, Y. Ando, M. Hirai, N. Iwasa, T. Kikuchi, S. Moriya, T. Motobayashi, H. Murakami, T. Nakamura, T. Nishio, H. Sakurai, T. Uchibori, Y. Watanabe, Y. Yanagisawa, and M. Ishihara: "Isobaric analog state of ^{11}Li (experiment)", Int. Symp. on New Facet of Spin Giant Resonances in Nuclei, (University of Tokyo), Tokyo, Nov. (1997).

H. Okamura, T. Wakasa, Y. Satou, T. Ohnishi, T. Nonaka, H. Sakai, S. Ishida, N. Sakamoto, T. Uesaka, T. Ichihara, T. Niizeki, and H. Ohnuma: "Spin-dipole resonance studied by the $(\vec{d},{}^2\mathrm{He})$ reaction", Int. Symp. on New Fact of Spin Giant Resonances in Nuclei, (University of Tokyo), Tokyo, Nov. (1997).

Y. Mochizuki, S. Kumagai, K. Nomoto, and I. Tanihata: "The half-life of ^{44}Ti and supernova remnants", Int. Symp. on Origin of Matter and Evolution of Galaxies 97, Atami, Nov. (1997).

K. Nagamine: "Recent progress in muon catalyzed fusion and related muon science: Muons for human life", Oxford Physics Colloquium, (Oxford University), Oxford, UK, Nov. (1997).

Y. Utsuno, T. Mizusaki, T. Otsuka, and M. Honma: "Structure of unstable nuclei studied by Monte Carlo shell model", 17th RCNP Int. Symp. on Innovative Computational Methods in Nuclear Many-Body Problems, (RCNP), Osaka, Nov. (1997).

Y. Ogawa: "The momentum distributions of the core fragment from the nuclear breakup reaction within the glauber model", 17th RCNP Int. Symp. on Innovative Computational Methods in Nuclear Many-Body Problems, Osaka, Nov. (1997).

Y. Mao: "SPIN experiment at PHENIX", RIKEN Symp. on Quarks and Gluons in the Nucleon, Wako, Nov. (1997).

T. Otsuka, T. Mizusaki, Y. Utsuno, and M. Honma: "Monte Carlo shell model calculations for proton-

rich and neutron-rich unstable nuclei", Workshop on the Structure of Atomic Nuclei in Exotic States, (GANIL), Caen, France, Nov. (1997).

Y. Mochizuki: "A microscopic model of glitches: Nuclei and superfluidity inside neutron stars", Hadron Transfer Group Seminar at Japan Atomic Energy Research Institute, Tokai-mura, Dec. (1997).

N. Saito and Collaboration Phenix: "Spin physics with the PHENIX detector system", 13th Int. Conf. on Ultra Relativistic Nucleus-Nucleus Collisions, Tsukuba, Dec. (1997).

D. Kharzeev: "Summary theoretical interpretations of J/Ψ suppression", Quark Matter '97, Tsukuba, Dec. (1997).

K. Nagamine: "New directions in muon atomic physics research", 14th RIKEN Symp. on Atomic Physics Using Accelerators: Atomic Physics with Slow Antiprotons, Wako, Dec. (1997).

I. Tanihata: "RI Beam Factory project", RIKEN Symp. on Materials Science in RIKEN RI Beam Factory, Wako, Dec. (1997).

Y. Kobayashi, Y. Yoshida, A. Yoshida, Y. Watanabe, N. Aoi, K. Hayakawa, K. Yukihira, S. Nasu, J. Nakamura, and F. Ambe: "In-Beam Mössbauer spectroscopy for materials science at RIKEN Accelerator Research Facility", Specialist Res. Meet. on Solid State Physics with Probes of Radiations and Nuclei, (Kyoto University), Kumatori, Dec. (1997).

K. Nagamine: "Recent progress in muon catalyzed fusion and related muon science: Muons for human life", Birmingham University Colloq., Birmingham, UK, Jan. (1998).

K. Yoneda, N. Aoi, H. Iwasaki, H. Sakurai, H. Ogawa, T. Nakamura, W. D. Schmidt-Ott, M. Schäfer, M. Notani, N. Fukuda, E. Ideguchi, T. Kishida, S. S. Yamamoto, and M. Ishihara: "Half-life measurement of the drip line nuclei ^{19}B, ^{22}C and ^{23}N", Int. Workshop on Physics with Radioactive Nuclear Beams, Puri, India, Jan. (1998).

T. Motobayashi: "Coulomb excitation studies with radioactive nuclear beams", Int. Workshop on Physics with Radioactive Nuclear Beams, Puri , India, Jan. (1998).

T. Motobayashi: "Coulomb dissociation studies for astrophysical thermonuclear reactions", Int. Workshop XXVI on Gross Properties of Nuclei and Nuclear Excitations, Hirschegg, Austria, Jan. (1998).

K. Morita: "Experiment for Synthesising heavy elements at RIKEN", RIKEN Symp. on Nuclear Chemistry of Heavy Elements at RIKEN RI-Beam Factory, Wako, Jan. (1998).

T. Matsuzaki, K. Nagamine, K. Ishida, and S. N. Nakamura: "Muon catalyzed fusion research at RIKEN-RAL Muon Facility", RIKEN Symp. on Studies on Condensed Matter Physics, Atomic Physics, Nuclear Chemistry, and Biology and Medicine Using RIKEN Acccelerators, Wako, Jan. (1998).

H. Sakurai: "Search for new neutron-rich isotopes", 6th RIKEN Winter School, Kusatsu, Jan. (1998).

Y. Satou, S. Ishida, H. Sakai, H. Okamura, H. Otsu, N. Sakamoto, T. Uesaka, T. Wakasa, T. Ohnishi, T. Nonaka, G. Yokoyama, T. Ichihara, T. Niizeki, K. Ito, K. Sekiguchi, K. Yako, S. Fukusaka, and K. Hatanaka: "Measurement of the ^{28}Si($\vec{d}, \vec{d}'$) reaction at E_d=270 MeV", 53rd Ann. Meet. of Physical Society of Japan, Funabashi, Mar. (1998).

H. Iwasaki: "E2 strength of neutron-rich neuclei ^{12}Be", 53rd Ann. Meet. of Physical Society of Japan, Funabashi, Mar. (1998).

T. Motobayashi, T. Kikuchi, N. Iwasa, Y. Ando, M. Kurokawa, S. Moriya, H. Murakami, T. Nishio, S. Shirato, S. Shimoura, T. Uchibori, Y. Yanagisawa, T. Kubo, H. Sakurai, T. Teranishi, Y. Watanabe, M. Ishihara, M. Hirai, T. Nakamura, S. Kubono, M. Gai, R. H. III France, K. I. Hahn, Th. Delbar, P. Lipnik, C. Michotte, and J.-Z. Ruan: "S-factor determination of solar neutrino reaction ^{7}Be(p,γ)^{8}B", 53rd Ann. Meet. of Physical Society of Japan, Funabashi, Mar. (1998).

T. Matsuzaki, K. Nagamine, K. Ishida, S. N. Nakamura, N. Kawamura, S. Sakamoto, M. Tanase, M. Kato, K. Kurosawa, K. Kudoh, N. Takeda, G. H. Eaton, M. Hashimoto, and H. Sugai: "Muon catalyzed dt fusion research at RIKEN-RAL Muon Facility(8): Pure T2 Target", 53rd Ann. Meet. of Physical Society of Japan, Funabashi, Mar. (1998).

S. N. Nakamura, K. Nagamine, T. Matsuzaki, K. Ishida, N. Kawamura, S. Sakamoto, M. Tanase, M. Kato, K. Kurosawa, M. Hashimoto, H. Sugai, K. Kudoh, N. Takeda, and G. H. Eaton: "Muon catalyzed dt fusion research at RIKEN-RAL Muon Facility (9): High tritium concentration DT target", 53rd Ann. Meet. of Physical Society of Japan, Funabashi, Mar. (1998).

Y. Mochizuki, T. Izuyama, I. Tanihata, and K. Oyamatsu: "A microscopic model of neutron star glitches", Ann. Meet. of Astronomy Society of Japan, Hachioji, Mar. (1998).

Y. Mochizuki and I. Tanihata: "The half-life of ^{44}Ti and supernova remnants", Ann. Meet. of Physical Society of Japan, Funabashi, Mar. (1998).

K. Ishida: "Solenoid capture/phase rotation simulation at RIKEN/RAL", Int. Workshop on JHF Science (JHF98), (KEK), Tsukuba, Mar. (1998).

T. Otsuka: "What are interesting in nuclear physics?", Int. Workshop on JHF Science (JHF98), (KEK), Tsukuba, Mar. (1998).

K. Ishida: "Beams in future-solenoid capture at RIKEN/RAL", Int. Workshop on JHF Science (JHF98), (KEK), Tsukuba, Mar. (1998).

T. Otsuka, T. Mizusaki, Y. Utsuno, and M. Honma: "Monte Carlo shell model calculations", Int. Workshop on Mean-Field Methods in Low-Energy Nuclear Structure, (ECT*), Trento, Italy, Mar. (1998).

K. Sumiyoshi: "Systematic study of structure of unstable nuclei: Quest for the shape of nucleus", RIKEN Symp. on Computational Science with Supercomputer and Special-Purpose, Wako, Mar. (1998).

K. Varga: "Applications of the stochastic variational method", RIKEN Symp. on Computational Science with Supercomputer and Special-Purpose, Wako, Mar. (1998).

K. Sumiyoshi, S. Sugimoto, D. Hirata, H. Toki, and I. Tanihata: "Systematic study of structure of unstable nuclei: Shape of nuclei", RIKEN Symp. on Computational Science with Supercomputer and Special-Purpose, Wako, Mar. (1998).

K. Sugawara-Tanabe and K. Tanabe: "Some aspects in thermal field theory and its application", RIKEN Symp. on Dynamics in Hot Nuclei, Wako, Mar. (1998).

N. Dinh Dang and A. Arima: "Temperature dependence of quantal and thermal dampings of hot giant dipole resonance", RIKEN Symp. on Dynamics in Hot Nuclei, Wako, Mar. (1998).

S. Yamaji: "Temperature dependence of friction", RIKEN Symp. on Dynamics in Hot Nuclei, Wako, Mar. (1998).

K. Yoshida: "Search for super heavy compound nuclei", RIKEN Symp. on Dynamics in Hot Nuclei, Wako, Mar. (1998).

H. Sakurai: "New neutron rich isotopes close to the neutron drip line", RIKEN Symp. on Dynamics in Hot Nuclei, Wako, Mar. (1998).

T. Matsuzaki, K. Ishida, S. N. Nakamura, N. Kawamura, and K. Nagamine: "Results on muon catalyzed fusion experiments in solid/liquid D-T and T2 at RIKEN-RAL", RIKEN Symp. on Muon Life Science, Muon Catalyzed Fusion and Muon Fundamental Physics, Wako, Mar. (1998).

K. Ishida: "Muon catalyzed fusion (μCF) experiment at the RIKEN-RAL Muon Facility: (1) X-ray and neutron measurement of μ to α sticking probability", Symp. on Laser Application to Muon Science, (Meson Science Laboratory, IMSS, KEK(KEK-MSL)), Tsukuba, Mar. (1998).

T. Matsuzaki: "Facility and Apparatus for muon catalyzed fusion research at RIKEN-RAL Muon Facility", Symp. on Laser Muon Science, (KEK), Tsukuba, Mar. (1998).

N. Dinh Dang, K. Tanabe, and A. Arima: "Temperature dependence of quantal and thermal dampings of the hot giant dipole resonance", 6th Int. Spring Seminar on Nuclear Physics 'Highlights in Modern Nuclear Structure', (INFN Napoli and Universita di Napoli), Varenna, Italy, May (1998).

Y. Satou, S. Ishida, H. Sakai, H. Okamura, H. Otsu, N. Sakamoto, T. Uesaka, T. Wakasa, T. Ohnishi, T. Nonaka, G. Yokoyama, T. Ichihara, T. Niizeki, and N. Nishimori: "Study of isoscalar spin strength via the ^{12}C $(\vec{d},\vec{d})$ reaction", Topical Conf. Giant Resonances, (Istituto Nazionale di Fisica Nucleare), Varenna, Italy, May (1998).

N. Dinh Dang, K. Tanabe, and A. Arima: "Temperature dependence of quantal and thermal dampings of the hot giant dipole resonance", Topical Conf. on Giant Resonances, (Istituto Nazionale di Fisica Nucleare), Varenna, Italy, May (1998).

K. Sugawara-Tanabe, A. Arima, and N. Yoshida: "The deformation effect on the pairing gap", Int. Conf. on Nuclear Structure at the Extremes, Lewes, UK, June (1998).

K. Sugawara-Tanabe, A. Arima, S. Yamaji, and J. Meng: "The pseudo-spin symmetry in Dirac equation", Int. Conf. on Nuclear Structure at the Extremes, Lewes, UK, June (1998).

T. Horibata, M. Oi, and N. Onishi: "Band crossing studied by GCM with 3D-CHFB", Nuclear Structure at the Extremes, Lewes, UK, June (1998).

T. Goka, H. Matsumoto, S. Takagi, and T. Kohno: "Empirical radiation belt models based on the Japanese satellites measurements", 1998 Western Pacific Geophysics Meet., (American Geophysical Union), Taipei, Taiwan, July (1998).

T. Kohno, H. Miyasaka, C. Kato, I. Yamagiwa, T. Goka, and H. Matsumoto: "Heavy ion observation with MIDORI satellite", 1998 Western Pacific Geophysics Meet., (American Geophysical Union), Taipei, Taiwan, July (1998).

K. Nagata, T. Kohno, H. Murakami, A. Nakamoto, N. Hasebe, J. Kikuchi, and T. Doke: "Pitch angle distributions of the low latitude precipitation electrons", 1998 Western Pacific Geophysics Meet., (American Geophysical Union), Taipei, Taiwan, July (1998).

H. Miyasaka, T. Kohno, I. Yamagiwa, H. Kato, C. Kato, T. Goka, and H. Matsumoto: "Observation of trapped anomalous cosmic rays with MIDORI satellite", 32nd COSPAR Scientific Assembly, (The International Council of Scientific Unions), Nagoya, July (1998).

C. Kato, K. Munakata, T. Kohno, H. Miyasaka, I. Yamagiwa, T. Goka, and H. Matsumoto: "Pitch angle distribution of He observed at MIDORI satellite", 32nd COSPAR Scientific Assembly, (The International Council of Scientific Unions), Nagoya, July (1998).

G. I. Pugacheva, A. A. Gusev, T. Kohno, I. M. Martin, and W. Spjeldvik: "An investigation of the spatial and time variations of the energetic trapped helium ions with Japanese OHZORA and AKEBONO satellites", 32nd COSPAR Scientific Assembly, (The International Council of Scientific Unions), Nagoya, July (1998).

A. A. Gusev, T. Kohno, I. M. Martin, G. I. Pugacheva, and W. Spjeldvik: "The spatial distribution and dynamics of MEV proton fluxes under earth's radiation belt", 32nd COSPAR Scientific Assembly, (The International Council of Scientific Unions), Nagoya, July (1998).

K. Uchiyama, M. Sugita, and K. Furuno: "Systematic study of $B(E2;0_1^+ \rightarrow 2_1^+)$ for the Ba isotopes", JAERI Symp. on Frontier of Gamma-Ray Spectroscopy, (Japan Atomic Energy Research Institute), Tokai-mura, July (1998).

H. Madokoro, J. Meng, M. Matsuzaki, and S. Yamaji: "Relativistic mean field description of the identical bands and band crossing in superdeformed Eu-Gd nuclei", JAERI Symp. on Frontier of Gamma-Ray Spectroscopy, (Japan Atomic Energy Research Institute), Tokai-mura, July (1998).

K. Ishida, K. Nagamine, T. Matsuzaki, S. N. Nakamura, N. Kawamura, S. Sakamoto, M. Iwasaki, M. Tanase, M. Kato, K. Kurosawa, H. Sugai, I. Watanabe, K. Kudoh, N. Takeda, and G. H. Eaton: "Measurement of X-rays from muon to alpha sticking and fusion neutrons in solid/liquid D-T mixtures of high tritium concentration", Monte Verità Workshop on Exotic Atoms, Molecules and Muon Catalyzed Fusion, (Paul Scherrer Institute and the University of Fribourg), Ascona, Switzerland, July (1998).

S. N. Nakamura, K. Bartlett, G. A. Beer, D. R. Gill, R. S. Hayano, T. M. Ito, M. Iwasaki, L. Lee, G. Mason, A. Olin, H. Outa, M. Salomon, R. Seki, T. Taniguchi, T. P. Terada, G. Trayling, Y. Yamashita, and S. Yen: "Observation of kaonic hydrogen atom X rays", Monte Verità Workshop on Exotic Atoms, Molecules and Muon Catalyzed Fusion, (Paul Scherrer Institute and the University of Fribourg), Ascona, Switzerland, July (1998).

S. N. Nakamura, K. Nagamine, T. Matsuzaki, K. Ishida, N. Kawamura, S. Sakamoto, M. Iwasaki, M. Tanase, M. Kato, K. Kurosawa, H. Sugai, I. Watanabe, K. Kudoh, N. Takeda, and G. H. Eaton: "K_β/K_α ratio of muon to alpha sticking X-ray in muon catalyzed dt fusion at RIKEN-RAL Muon Facility", Monte Verità Workshop on Exotic Atoms, Molecules and Muon Catalyzed Fusion, (Paul Scherrer Institute and the University of Fribourg), Ascona, Switzerland, July (1998).

K. Sugawara-Tanabe: "Pseudospin-orbit interaction and normal spin-orbit interaction", Predeal Int. Summer School on Structure and Stability of Nucleon and Nuclear Systems, Predeal, Romania, Aug. (1998).

A. Ozawa: "Measurement for interaction cross-sections for carbon isotopes at relativistic energy and the halo structure in ^{19}C", '98 Seminar on Nuclear Physics with Radioactive Ion Beam and High Spin Nuclear Structure, Lanzhou, China, Sept. (1998).

K. Ishida: "Projects of high-intensity muon channels at RIKEN-RAL and KEK-MESON Facilities", PRISM KUICR98 Workshop, (Institute for Chemical Research, Kyoto University), Uji, Sept. (1998).

Y. Mochizuki, K. Takahashi, T. Janka, W. Hillebrand, and R. Diehl: "The long half-life of highly ionized ^{44}Ti", 1998 Fall Meet. of the Physical Society of Japan, Akita, Oct. (1998).

H. Madokoro, J. Meng, M. Matsuzaki, and S. Yamaji: "Relativistic mean field description of the identical bands and band crossing in superdeformed Eu-Gd nuclei", 1998 Fall Meet. of the Physical Society of Japan, Akita, Oct. (1998).

K. Nagamine, T. Matsuzaki, K. Ishida, S. N. Nakamura, Y. Matsuda, S. Sakamoto, M. Tanase, M. Kato, K. Kurosawa, H. Sugai, K. Kudo, N. Takeda, and G. H. Eaton: "Muon catalyzed fusion experiment for D-T system at RIKEN-RAL Muon Facility (10): Helium accumulation effect", 1998 Fall Meet. of the Physical Society of Japan, Akita, Oct. (1998).

K. Nagamine, K. Shimomura, S. Sakamoto, and K. Nishiyama: "Study of the energy spectrum emitted from the nuclear-captured μ^-", 1998 Fall Meet. of the Physical Society of Japan, Akita, Oct. (1998).

K. Ishida, K. Nagamine, T. Matsuzaki, S. N. Nakamura, N. Kawamura, Y. Matsuda, S. Sakamoto, M. Tanase, M. Kato, K. Kurosawa, H. Sugai, K. Kudoh, N. Takeda, and G. H. Eaton: "Muon catalyzed dt fusion research at RIKEN-RAL Muon Facility (11): Muon sticking probability", 1998 Fall Meet. of the Physical Society of Japan, Akita, Oct. (1998).

H. Fuke and K. Yoshimura: "Response of the BESS scintillator for heavy ions", 1998 Fall Meet. of the Physical Society of Japan, Akita, Oct. (1998).

K. Uchiyama, M. Sugita, and K. Furuno: "Systematic study of $B(E2;0_1^+ \rightarrow 2_1^+)$ for the Ba isotopes", 1998 Fall Meet. of the Physical Society of Japan, Akita, Oct. (1998).

C. Kato, K. Munakata, T. Kohno, H. Miyasaka, I. Yamagiwa, T. Goka, and H. Matsumoto: "The pitch angle distributions of trapped particles observed with MIDORI", 1998 Fall Meet. of the Physical Society of Japan, Akita, Oct. (1998).

T. Goka, H. Matsumoto, S. Takagi, T. Kohno, and F. Makino: "Empirical radiation belt models based on the Japanese satellites measurements", 3rd Int. Workshop on Radiation Effects on Semiconductor Devices for Space Application, (Japan Atomic Energy Research Institute, National Space Development Agency of Japan), Takasaki, Oct. (1998).

T. Kohno: "Heavy ion radiation in space observed by Japanese satellite", 3rd Int. Workshop on Radiation Effects on Semiconductor Devices for Space Application, (Japan Atomic Energy Research Institute, National Space Development Agency of Japan), Takasaki, Oct. (1998).

Y. Mochizuki, K. Takahashi, T. Janka, W. Hillebrand, and R. Diehl: "The long half-life of highly ionized ^{44}Ti and cassiopeia A", Nihon Tenmon Gakkai 1998nen Syuki Nenkai, Yamagata, Oct. (1998).

K. Ishida: "X-ray and neutron studies on α-sticking in D-T μCF", RIKEN Symp. on Muon Science '98: New Direction in Muon Catalyzed Fusion μSR Studies and Fundamental Muon Physics, Wako, Oct. (1998).

H. Madokoro and M. Matsuzaki: "The superdeformed bands in proton rich A=60 nuclei", YITP Workshop on Structure and Reaction of Unstable Nuclei, Kyoto, Nov. (1998).

Y. Mochizuki: "A microscopic model of neutron star glitches", Workshop on the Birth and Evolution of Neutron Stars, (Tokyo University), Tokyo, Dec. (1998).

Y. Mochizuki: "^{44}Ti: Its effective half-life in young supernova remmants and abundance in Cas-A", Workshop on the Birth and Evolution of Neutron Stars, (Tokyo University), Tokyo, Dec. (1998).

3. Atomic and solid-state physics

Y. Yamazaki: "Interaction of highly charged ions with matter from meV to TeV", 3rd RIKEN Symp. on Studies on Condensed Matter Physics, Atomic Physics, Nuclear Chemistry, and Biomedical Science using RIKEN Accelerators, Wako, Jan. (1997).

I. Shimamura: "Rich structure in atomic photoionisation cross sections", Congr. 97(The Institute of Physics Ann. Congr.), Leeds, UK, Mar. (1997).

T. Matsuo, T. Kohno, S. Makino, M. Sano, T. Tonuma, H. Tawara, A. Kitagawa, and T. Murakami: "Net ionization cross sections for molecular targets in 6 MeV/amu fully-stripped ion impact", 20th Int. Conf. on Physics of Electronic and Atomic Collisions, Vienna, Austria, July (1997).

I. Shimamura: "Long-lived antiprotonic helium", 20th Int. Conf. on the Physics of Electronic and Atomic Collisions, Vienna, Austria, July (1997).

I. Shimamura: "Antiprotonic atoms", 7th Asia Pacific Physics Conf., Beijing, China, Aug. (1997).

Y. Kobayashi, Y. Yoshida, K. Hayakawa, K. Yukihira, J. Nakamura, H. Haesslein, R. Sielemann, S. Nasu, N. Inabe, Y. Watanabe, A. Yoshida, M. Kase, A. Goto, Y. Yano, E. Yagi, and F. Ambe: "In-beam Mössbauer spectrometers for materials science at RIKEN Accelerator Research Facility", Int. Conf. on the Applications of the Mössbauer Effect, (ICAME97), Rio de Janeiro, Brazil, Sept. (1997).

M. Matsumoto, E. Idesawa, K. Makishima, M. Kokubu, M. Tashiro, T. Murakami, K. Takizawa, Y. Saito, and Team Hxd: "Development of a fine X-ray collimator for the hard X-ray instrument on board ASTRO-E", Nihon Tenmon Gakkai 1997nen Syuki Nenkai, Utsunomiya, Sept. (1997).

S. Sakamoto and A. Matsushita: "Experimental result and proposal of RIKEN-RAL Muon Facility: Elementary Particle, Nuclear and Atomic Physics", RIKEN Symp. on Muon Science '97: Muon Condensed Matter Studies and Muon Catalyzed Fusion, Wako, Sept. (1997).

W. Higemoto: "Experimental result and proposal of RIKEN-RAL Muon Facility: μSR(2)", RIKEN Symp. on Muon Science '97: Muon Condensed Matter Studies and Muon Catalyzed Fusion, Wako, Sept. (1997).

V. Krishnamurthy: "Experimental result and proposal of RIKEN-RAL Muon Facility: μSR(1)", RIKEN Symp. on Muon Science '97: Muon Condensed Matter Studies and Muon Catalyzed Fusion, Wako, Sept. (1997).

K. Nagamine: "Direct observation of electron transfer in protein by muon", 3rd RIKEN Symp. on Studies on Condensed Matter Physics, Atomic Physics, Nuclear Chemistry and Biomedical Science Using RIKEN Accelerators, Wako, Jan. (1998).

Y. Yoshida: "Materials science at the RI Beam Factory", 3rd RIKEN Symp. on Studies on Condensed Matter Physics, Atomic Physics, Nuclear Chemistry and Biomedical Science Using RIKEN Accelerators, Wako, Jan. (1998).

E. Yagi: "Analysis of the state of hydrogen by the nuclear-reaction channelling method", Symp. on the Suppression of the Degradation on Highly Strengthened Materials used under the Environmental Conditions, (The Iron and Steel Indtitute of Japan), Awaji, Feb. (1998).

T. Nishimura: "Elastic scattering of positrons from methane molecules", 53rd Ann. Meet. of Physical Society of Japan, Funabashi, Mar. (1998).

Y. Kobayashi, Y. Yoshida, K. Hayakawa, A. Yoshida, Y. Watanabe, Y. Yano, and F. Ambe: "^{57}Fe Mössbauer spectroscopy using ^{57}Mn nuclei by a projectile-fragment reaction", 53rd Ann. Meet. of Physical Society of Japan, Funabashi, Mar. (1998).

Y. Yoshida, Y. Kobayashi, K. Hayakawa, K. Yukihira, F. Ambe, and S. Nasu: "The dynamic behavior of Fe atoms in solid Ar depending on both the specimen-thickness and the measuring-time", 53rd Ann. Meet. of Physical Society of Japan, Funabashi, Mar. (1998).

M. Kitajima, Y. Nakai, Y. Kanai, Y. Yamazaki, and Y. Itoh: "Present status of the differential cross section measurement experiment of multi-electron capture in the low energy ion-atom collision", 53rd Ann. Meet. of Physical Society of Japan, Funabashi, Mar. (1998).

Y. Takabayashi, T. Ito, T. Azuma, K. Komaki, Y. Yamazaki, M. Torikoshi, A. Kitagawa, E. Takada, and T. Murakami: "Okorokov effect with relativistic heavy ions (3)", 53rd Ann. Meet. of Physical Society of Japan, Funabashi, Mar. (1998).

S. Kaneko, H. Sakata, Y. Ono, Y. Taguchi, N. Nishida, and T. Kambara: "STS observations of columnar defects in layered materials", 53rd Ann. Meet. of Physical Society of Japan, Narashino, Mar. (1998).

N. Kuroda, N. Ishikawa, S. Okayasu, A. Iwase, H. Ikeda, R. Yoshizaki, and T. Kambara: "AC susceptibility measurements in Bi-based oxide superconductors irradiated with GeV heavy ions", 53rd Ann. Meet. of Physical Society of Japan, Narashino, Mar. (1998).

T. Kamei, T. Takayanagi, K. Wakiya, Y. Nakai, Y. Kanai, and T. Kambara: "Measurement of angular distribution in collision of N^{5+}-Ar by Toroidal Spectrometer", 53rd Ann. Meet. of Physical Society of Japan, Narashino, Mar. (1998).

S. Uramoto, I. Krajcar-Bronic, and M. Kimura: "Charge transfer process of O^{+}+H collision near threshold", 53rd Ann. Meet. of Physical Society of Japan, Narashino, Mar. (1998).

K. Kuroki, Y. Turuta, N. Okabayashi, T. Azuma, Y. Yamazaki, and K. Komaki: "Proton spattering by slow multiply charged ions", 53rd Ann. Meet. of Physical Society of Japan, Narashino, Mar. (1998).

T. Kambara: "Atomic collision study with recoil ion momentum spectroscopy", Int. Symp. on Atomic Process of Highly Charged Heavy Ions and Cluster Ions, (Himeji Institute of Technology), Himeji, Mar. (1998).

Y. Yamazaki: "Potential sputtering of hydrogen atoms on a surfaces with slow highly charged ions", Int. Symp. on Atomic Process of Highly Charged Heavy Ions and Cluster Ions, (Himeji Institute of Technology), Himeji, Mar. (1998).

E. Yagi: "Studies of impurities in metals by a channelling method utilizing a nuclear reaction", Int. Workshop on JHF Science (JHF98), (KEK), Tsukuba, Mar. (1998).

J. Nakamura, K. Asai, N. Yamada, Y. Noro, H. Kitazawa, T. Okada, Y. Kobayashi, and F. Ambe: "The studies on magnetics materials by means of ^{121}Sb and ^{61}Ni Mössbauer spectroscopy", RIKEN Symp. on RI as Probes and Tracers '98, Wako, Mar. (1998).

Y. Yoshida, K. Hayakawa, K. Yukihira, Y. Kobayashi, F. Ambe, and S. Nasu: "Direct observation of the jump processes of ^{57}Fe atoms in solids by in-beem Mössbauer spectroscopy", RIKEN Symp. on RI as Probes and Tracers '98, Wako, Mar. (1998).

Y. Kobayashi, A. Yoshida, Y. Watanabe, N. Aoi, J. Nakamura, Y. Yano, F. Ambe, Y. Yoshida, K. Hayakawa, and K. Yukihira: "^{57}Fe in-beam Mössbauer spectroscopy using ^{57}Mn nuclei by a projectile-fragmentation", RIKEN Symp. on RI as Probes and Tracers '98, Wako, Mar. (1998).

E. Yagi: "Feasibility of channelling experiments utilizing a short-lived radioactive ion beam", KEK Seminar, Tanashi, Apr. (1998).

A. Iwase, N. Ishikawa, Y. Chimi, K. Tsuru, O. Michikami, and T. Kambara: "High energy heavy ion irradiation damage in oxide superconductor $EuBa_2Cu_3O_y$", 4th Int. Symp. on Swift Heavy Ions in Matter(SHIM98), Berlin, Germany, May (1998).

N. Kuroda, N. Ishikawa, S. Okayasu, A. Iwase, H. Ikeda, R. Yoshizaki, and T. Kambara: "Pinning and Vortex dynamics in Bi-based oxide superconductors irradiated with heavy-ions", 4th Int. Symp. on Swift Heavy Ions in Matter(SHIM98), Berlin, Germany, May (1998).

T. Nishimura: "Interest in positron-molecule collision", The Society for Atomic Collision Research, The Meet. for Youth, '98 Summer School', Oarai, July (1998).

A. Igarashi, I. Shimamura, and T. Tonuma: "Hyperfine transitions in low-energy p + pμ scattering: A hyperspherical close-coupling study", Monte Verità Workshop on Exotic Atoms, Molecules and Muon Catalyzed Fusion, Ascona, Switzerland, July (1998).

Y. Takabayashi, T. Ito, K. Komaki, Y. Yamazaki, T. Azuma, H. Tawara, M. Torikoshi, A. Kitagawa, E. Takada, and T. Murakami: "Convoy electron prodution with relativistic heavy ions", 23rd Ann. Meet. of the Society for Atomic Collision Research, Yokohama, Aug. (1998).

Y. Yamazaki: "Historical review and perspective of atomic collision research from atomic physics and particle-beam physics views", 23rd Ann. Meet. of the Society for Atomic Collision Research, Yokohama, Aug. (1998).

B. Nyström: "Noise reduction of CCD-images used in VUV-spectroscopy: A statistical approach", 23rd Ann. Meet. of the Society for Atomic Collision Research, Yokohama, Aug. (1998).

T. Azuma, T. Ito, Y. Takabayashi, K. Komaki, Y. Yamazaki, M. Sano, M. Torikoshi, A. Kitagawa, E. Takada, and T. Murakami: "Observation of Okorokov effects with relativistic heavy ions", 23rd Ann. Meet. of the Society for Atomic Collision Research, Yokohama, Aug. (1998).

T. Ito, K. Komaki, Y. Yamazaki, T. Azuma, M. Torikoshi, A. Kitagawa, E. Takada, and T. Murakami: "Energy loss measurements of charge-state-frozen Ar^{17+} ions", 23rd Ann. Meet. of the Society for Atomic Collision Research, Yokohama, Aug. (1998).

B. Nyström, T. Kambara, Y. Kanai, and Y. Nakai: "Double electron capture vs. target excitation in slow He^{2+} + He collisions", 23rd Ann. Meet. of the Society for Atomic Collision Research, Yokohama, Aug. (1998).

S. Uramoto, H. Sato, and I. Shimamura: "Two-electron excited states of the hydrogen molecule", 23rd Ann. Meet. of the Society for Atomic Collision Research, Yokohama, Aug. (1998).

T. Ichioka, H. Higaki, H. Matsushima, Y. Yamazaki, K. Komaki, M. Hori, K. Yamashita, N. Oshima, A. Mouri, and K. Kuroki: "Developments of charged particle trap of ultra slow antiproton experiments", 23rd Ann. Meet. of the Society for Atomic Collision Research, Yokohama, Aug. (1998).

T. Nishimura: "Polarization effects on the vibrationally elastic scattering of positrons from methane molecules", 23rd Ann. Meet. of the Society for Atomic Collision Research, Yokohama, Aug. (1998).

E. Yagi, T. Sasahara, T. Joh , M. Hacke, T. Urai, T. Sasamoto, T. Watanabe, and S. T. Nakagawa: "State of Xe atoms implanted in Fe", 1998 Fall

(123rd) Meet. of Japan Institute of Metals, Matsuyama, Sept. (1998).

H. Yamada, T. Hasegawa, N. Komuro, T. Maruyama, K. Akimoto, and E. Yagi: "Characterization of undoped ZnSeTe by RBS, PIXE/channelling measurements", 1998 Fall Meet. of Japan Society of Applied Physics, Higashihiroshima, Sept. (1998).

Y. Chimi, A. Iwase, N. Ishikawa, N. Kuroda, and T. Kambara: "Electronic excitation and atomic displacements induced by high-energy heavy ion irradiation in Fe", 1998 Fall Meet. of the Physical Society of Japan, Nishiharacho, Sept. (1998).

Y. Takabayashi, T. Ito, T. Azuma, K. Komaki, Y. Yamazaki, H. Tawara, M. Torikoshi, A. Kitagawa, E. Takada, and T. Murakami: "Convoy electron production with relativistic heavy ions", 1998 Fall Meet. of the Physical Society of Japan, Nishiharacho, Sept. (1998).

T. Ichioka, M. Hori, K. Yamashita, H. Matsushima, H. Higaki, N. Oshima, Y. Yamazaki, K. Komaki, and R. Hayano: "Experiments with electrons confined in a penning trap", 1998 Fall Meet. of the Physical Society of Japan, Ginowan, Sept. (1998).

Y. Morishita, S. Ninomiya, Y. Yamazaki, K. Kuroki, K. Komaki, H. Masuda, and M. Sekiguchi: "Visible light emission from slow highly charged ions transmitted through Ni microcapillary", 1998 Fall Meet. of the Physical Society of Japan, Nishiharacho, Sept. (1998).

M. Kitajima, Y. Nakai, Y. Kanai, Y. Yamazaki, and Y. Itoh: "Doubly differential cross section measurements of multi-electron capture in the low energy ion-atom collision", 1998 Fall Meet. of the Physical Society of Japan, Nishiharacho, Sept. (1998).

T. Kamei, K. Ogura, T. Takayanagi, K. Wakiya, Y. Nakai, and Y. Kanai: "Angular dependence of the emitted electron spectrum in the collision of N^{5+} and Ar", 1998 Fall Meet. of the Physical Society of Japan, Nishiharacho, Sept. (1998).

Y. Nakai, T. Kambara, A. Itoh, H. Tsuchida, and Y. Yamazaki: "Ionization and fragmentation of C_{60} by fast ion impact in MeV region-TOF spectrum profile", 1998 Fall Meet. of the Physical Society of Japan, Nishiharacho, Sept. (1998).

T. Ito, Y. Takabayashi, K. Komaki, Y. Yamazaki, T. Azuma, M. Torikoshi, A. Kitagawa, E. Takada, T. Murakami, and S. Datz: "Okorokov effect with relativistic heavy ions (4)", 1998 Fall Meet. of the Physical Society of Japan, Nishiharacho, Sept. (1998).

T. Azuma, T. Ito, Y. Takabayashi, K. Komaki, Y. Yamazaki, M. Sano, M. Torikoshi, A. Kitagawa, E. Takada, and T. Murakami: "Observation of Okorokov effect with relativistic heavy ion beams", 1998 Fall Meet. of the Physical Society of Japan, Nishiharacho, Sept. (1998).

Y. Yamazaki: "Production of ultra slow antiprotons and atomic physics/atomic collisions", 1998 Fall Meet. of the Physical Society of Japan, Nishiharacho, Sept. (1998).

E. Yagi: "State of inert gas atoms and hydrogen in metals as observed by the channelling method", 1998 Fall Meet. Phys. Soc. Jpn., Lattice Defect Symp. on Recent Progress in Experimental Studies on Point Defects and the Related Problems, Naha, Sept. (1998).

T. Maruyama, T. Hasegawa, N. Komuro, H. Yamada, W. Ohtsuka, K. Akimoto, Y. Kitajima, E. Yagi, and K. Maeda: "Analysis of Cl-doped ZnSeTe using EXAFS, RBS and PIXE", 2nd Int. Symp. on Blue Laser and Light Emitting Diodes(2nd ISBLLED), Kisarazu, Sept. (1998).

E. Yagi: "Analysis of the state of hydrogen dissolved in metals by means of a nuclear-reaction-channelling method", 136th Fall Meet. of The Iron and Steel Institute of Japan, Symp. on Studies on the Effect of Hydrogen on the Embrittlement of, Matsuyama, Sept. (1998).

N. Ishikawa, Y. Chimi, N. Kuroda, A. Iwase, and T. Kambara: "Ion-velocity effects on defect production in metals and high-Tc superconductors irradiated with swift heavy ions", 9th Int. Conf. on the Physics of Highly Charged Ions (HCI-98), Bensheim, Germany, Sept. (1998).

K. Ishii, S. Kawae, T. Nakano, K. Ando, H. Oyama, and T. Kambara: "Beam-foil spectra of highly charged Neon ion in visible region", 9th Int. Conf. on the Physics of Highly Charged Ions (HCI-98), Bensheim, Germany, Sept. (1998).

Y. Zou, R. Hutton, S. Huldt, I. Martinson, K. Ando, T. Kambara, B. Nyström, and Y. Awaya: "limitations of the beam-foil method in lifetime measurements", 9th Int. Conf. on the Physics of Highly Charged Ions (HCI-98), Bensheim, Germany, Sept. (1998).

R. Hutton, Y. Zou, S. Huldt, I. Martinson, K. Ando, T. Kambara, B. Nyström, H. Oyama, and Y. Awaya: "A CCD detector system for beam-foil spectroscopy", 9th Int. Conf. on the Physics of Highly Charged Ions (HCI-98), Bensheim, Germany, Sept. (1998).

T. Kamei, K. Ogura, K. Wakiya, T. Takayanagi, Y. Kanai, and Y. Nakai: "Angular distribution of Auger electrons from doubly-excited N^{3+} produced by 50 keV N^{5+} -Ar collisions", 9th Int. Conf. on the Physics of Highly Charged Ions (HCI-98), Bensheim, Germany, Sept. (1998).

M. Kitajima, Y. Nakai, Y. Kanai, Y. Yamazaki, and Y. Itoh: "Crossed beam experiment for multi-electron capture in ion atom collision in the energy range of 10-100 eV/q", 9th Int. Conf. on the Physics of Highly Charged Ions (HCI-98), Bensheim, Germany, Sept. (1998).

K. Tőkési, Y. Awaya, T. Kambara, Y. Kanai, and B. Sulik: "Double K-shell vacancy production in N^{7+} + Ti collisions", 9th Int. Conf. on the Physics of Highly Charged Ions (HCI-98), Bensheim, Germany,

Sept. (1998).

N. Okabayashi, K. Kuroki, Y. Turuta, T. Azuma, K. Komaki, and Y. Yamazaki: "Two dimensional velocity distribution of potential sputtered hydrogen ions with slow highly charged ions", 9th Int. Conf. on the Physics of Highly Charged Ions (HCI-98), Bensheim, Germany, Sept. (1998).

K. Kuroki, T. Takahira, Y. Turuta, N. Okabayashi, T. Azuma, K. Komaki, and Y. Yamazaki: "Charge state dependence of proton sputtering from solid surfaces with slow highly charged ions", 9th Int. Conf. on the Physics of Highly Charged Ions (HCI-98), Bensheim, Germany, Sept. (1998).

Y. Morishita, S. Ninomiya, Y. Yamazaki, K. Komaki, K. Kuroki, H. Masuda, and M. Sekiguchi: "Visible light emission from slow highly charged ions transmitted through a Ni microcapillary", 9th Int. Conf. on the Physics of Highly Charged Ions (HCI-98), Bensheim, Germany, Sept. (1998).

Y. Takabayashi, T. Ito, T. Azuma, K. Komaki, Y. Yamazaki, H. Tawara, M. Torikoshi, A. Kitagawa, E. Takada, and T. Murakami: "Convoy electron production in 390 MeV/u Ar^{17+} ion collisions with thin foils", 9th Int. Conf. on the Physics of Highly Charged Ions (HCI-98), Bensheim, Germany, Sept. (1998).

T. Ito, T. Azuma, K. Komaki, Y. Yamazaki, M. Torikoshi, A. Kitagawa, E. Takada, and T. Murakami: "Direct observation of energy loss of charge-frozen hydrogen-like Ar ions", 9th Int. Conf. on the Physics of Highly Charged Ions (HCI-98), Bensheim, Germany, Sept. (1998).

I. Shimamura: "Atomic physics of muon-catalyzed fusion", Symp. on Supercomputing, Collision Processes and Applications, Belfast, UK, Sept. (1998).

Y. Yamazaki: "Atomic physics and related fields", 1998 Fall Meet. of the Physical Society of Japan, Akita, Oct. (1998).

Y. Yamazaki, N. Okabayashi, K. Kuroki, and K. Komaki: "Angular distribution of potential sputtered hydrogen ions with slow highly charged ions", 2nd Japan-Russia Symp. on Interactions of Fast Charged Particles with Solids, (Nagoya University and Atomic Energy Society of Japan), Nagoya, Oct. (1998).

I. Shimamura: "Extraordinarily long-lived hadronic helium", Int. Meet. on Frontiers of Physics (IMFP98), Kuala Lumpur, Malaysia, Oct. (1998).

Y. Yamazaki: "Aiming at antimatter production: Developments of slow antiproton beams and atomic physics·atomic collisions", Rikkyo Daigaku Rigakubu Butsuri Danwakai, Tokyo, Nov. (1998).

K. Ishida, K. Nagamine, and T. Matsuzaki: "Topics on muonic atoms and molecules and muon catalyzed fusion", ISAS 1998 Workshop on Atomic and Molecular Processes in Space 'Atomic and Molecular Processes Involving Exotic Particles', (The Institute of Space and Astronautical Science), Sagamihara, Dec. (1998).

Y. Yamazaki: "Developments of new fields with ultra slow highly charged ions and antiprotons", Nihon Butsuri Gakkai Kyushu-shibu Reikai, (The Physical Society of Japan), Miyazaki, Dec. (1998).

I. Shimamura: "Atomic physics of exotic atoms", Uchu-Kagaku Kenkyuusyo Uchu Kuukan Genshi Bunshi Katei Kenkyuukai, (The Institute of Space and Astronautical Science), Sagamihara, Dec. (1998).

A. Igarashi, I. Shimamura, and N. Toshima: "Atomic collisions involving positrons and muons", Uchu-Kagaku Kenkyuusyo Uchu Kuukan Genshi Bunshi Katei Kenkyuukai, (The Institute of Space and Astronautical Science), Sagamihara, Dec. (1998).

Y. Yamazaki: "Production of slow antiprotons and atomic collisions: Ionization and antiprotonic atom formation", Uchu-Kagaku Kenkyuusyo Uchu Kuukan Genshi Bunshi Katei Kenkyuukai, (The Institute of Space and Astronautical Science), Sagamihara, Dec. (1998).

T. Nishimura: "Elastic scattering of positron from atoms and molecules", Uchu-Kagaku Kenkyuusyo Uchu Kuukan Genshi Bunshi Katei Kenkyuukai, (The Institute of Space and Astronautical Science), Sagamihara, Dec. (1998).

4. Radiochemistry, radiation chemistry, and radiation biology

Z. Du, I. Narumi, S. Kitayama, and H. Watanabe: "Molecular cloning of the *Deinococcus radiodurans pprA* gene involved in DNA repair", Ann. Meet. of Japan Society for Bioscience, Biotechnology, and Agrochemistry, Tokyo, Apr. (1997).

I. Narumi, Z. Du, S. Kitayama, and H. Watanabe: "A new DNA repair gene, *pprA* of *Deinococcus radiodurans* is functional in *E. coli*", Ann. Meet. of Japan Society for Bioscience, Biotechnology, and Agrochemistry, Tokyo, Apr. (1997).

S. Ambe, H. Maeda, S. Enomoto, T. Ozaki, and F. Ambe: "Multitracer study on permeation of rare earth elements through a supported liquid membrane", 4th Int. Conf. on Methods and Applications of Radioanalytical Chemistry, (American Nuclear Society), Hawaii, USA, Apr. (1997).

H. Wang, S. Ambe, N. Takematsu, and F. Ambe: "Multitracer study of acid rain effect on adsorption of trace elements on soils", 4th Int. Conf. on Methods and Applications of Radioanalytical Chemistry, (American Nuclear Society), Hawaii, USA, Apr. (1997).

I. Narumi, K. Cherdchu , S. Kitayama, and H. Watanabe: "*uvrA* gene of radioresistant bacterium, *Deinococcus radiodurans* and mutation site in two radiosensitive mutants", 70th Ann. Meet. of Japanese Biochemical Society, Kanazawa, Sept. (1997).

W. Hong, J. Kaneko, and N. Ito: "Extremely fast decay component of UV luminescence from 2 MeV/amu ion irradiated alumina", 9th Int. Conf. on Radiation Effects in Insulators-9 (REI-9), Knoxville, USA, Sept. (1997).

F. Ambe: "Multitracer-A tracer technique developed by using RIKEN Ring Cyclotron", Asia-Pacific Symp. on Radiochemistry '97 (APSORC'97), (Kumamoto University), Kumamoto, Oct. (1997).

Y. Kobayashi, Y. Yoshida, K. Hayakawa, K. Yukihira, J. Nakamura, H. Haesslein, R. Sielemann, S. Nasu, N. Inabe, Y. Watanabe, A. Yoshida, M. Kase, A. Goto, Y. Yano, E. Yagi, and F. Ambe: "In-beam Mössbauer spectroscopy in materials science at RIKEN Accelerator Research Facility", Asia-Pacific Symp. on Radiochemistry '97 (APSORC'97), (Kumamoto University), Kumamoto, Oct. (1997).

S. Gouthu, T. Arie, and I. Yamaguchi: "Selection of plants for phytoremediation of soil contaminated with radionuclides and the impact of some parameters on plant uptake", Int. Meet. on Influence of Climatic Characteristics upon Behavior of Radioactive Elements, (Institute for Environmental Sciences), Rokkashomura, Oct. (1997).

S. Kitayama, I. Narumi, and H. Watanabe: "RecR mutation of *D. radiodurans*", 40th Ann. Meet. of Japan Radiation Research Society, Kyoto, Nov. (1997).

K. Funayama, M. Kikuchi, S. Kitayama, and H. Watanabe: "Analysis of the contriol region of genes in a radioresistant bacterium, *Deinococcus radiodurans*", 40th Ann. Meet. of Japan Radiation Research Society, Kyoto, Nov. (1997).

I. Narumi, O. Kou, S. Kitayama, and H. Watanabe: "Induction of a new DNA repair gene, *pprA* of *Deinococcus radiodurans*", 40th Ann. Meet. of Japan Radiation Research Society, Kyoto, Nov. (1997).

M. Kikuchi, I. Narumi, S. Kitayama, and H. Watanabe: "New style of genome formation estimated by physical mapping of genomes in radioresistant bacterium *Deinococcus radiodurans*", 40th Ann. Meet. of Japan Radiation Research Society, Kyoto, Nov. (1997).

K. Satoh, I. Narumi, M. Kikuchi, T. Yanagisawa, S. Kitayama, and H. Watanabe: "Molecular analysis of the *cinA-recA* operon of *Deinococcus radiodurans*", 20th Ann. Meet. of Japanese Society of Molecular Biology, Kyoto, Dec. (1997).

I. Narumi, S. Kitayama, and H. Watanabe: "Analysis of DNA-binding ability of *Deinococcus radiodurans pprA* gene product", 20th Ann. Meet. of Japanese Society of Molecular Biology, Kyoto, Dec. (1997).

S. Kitayama, I. Narumi, M. Kikuchi, T. Funayama, and H. Watanabe: "DNA recombination and Repair in *Deinococcus radiodurans*", 20th Ann. Meet. of Japanese Society of Molecular Biology, Kyoto, Dec. (1997).

F. Ambe: "Nuclear Chemistry in the last decade '88-'98", 3rd RIKEN Symp. on Studies on Condensed Matter Physics, Atomic Physics, Nuclear Chemistry and Biomedical Science Using RIKEN Accelerators, Wako, Jan. (1998).

S. Yoshida: "An effective mutation method for plants using heavy-ion beams", 3rd RIKEN Symp. on Studies on Condensed Matter Physics, Atomic Physics, Nuclear Chemistry and Biomedical Science Using RIKEN Accelerators, Wako, Jan. (1998).

S. Enomoto, R. Hirunuma, J. Chou, S. Ambe, and F. Ambe: "Transfers of various elements from the placenta to the fetus of pregnant rat", 118th Ann. Meet. of the Pharmaceutical Society of Japan, Kyoto, Mar. (1998).

F. Ambe, S. Enomoto, R. Hirunuma, and S. Ambe: "Uptake of various trace elements in HeLa cell", 118th Ann. Meet. of the Pharmaceutical Society of Japan, Kyoto, Mar. (1998).

R. Hirunuma, S. Enomoto, S. Ambe, F. Ambe, and K. Endo: "Dynamics of various trace elements in Se-deficient rats", 118th Ann. Meet. of the Pharmaceutical Society of Japan, Kyoto, Mar. (1998).

K. Matsumoto, N. Sotogaku, S. Ueda, K. Endo, S. Enomoto, S. Ambe, and F. Ambe: "Affinity of biotrace elements to cell componet, *in vivo* study using multitracer", 118th Ann. Meet. of the Pharmaceutical Society of Japan, Kyoto, Mar. (1998).

N. Sotogaku, K. Matsumoto, K. Endo, R. Hirunuma, S. Enomoto, S. Ambe, and F. Ambe: "The influence of citrate acid on the complex formation of serum protein with various trace elements", 118th Ann. Meet. of the Pharmaceutical Society of Japan, Kyoto, Mar. (1998).

M. Miki, Y. Mizutani, K. Okamoto, Y. Izumi, T. Kozawa, K. Ushida, Y. Yoshida, and S. Tagawa: "Study on the behavior of geminate ion pair in alkane by using picosecond pulse radiolysis: Electron scavenging effect", 74th Natl. Meet. of the Chemical Society of Japan, Kyoto, Mar. (1998).

S. Enomoto: "Biological application of the multitracer technique", RIKEN Symp. on RI as Probes and Tracers '98, Wako, Mar. (1998).

S. Ambe: "Applications studies on environmental science by using the multitracer technique", RIKEN Symp. on RI as Probes and Tracers '98, Wako, Mar. (1998).

Z. Chang: "A study of metal-ion bindings to humic acid by multitracer", RIKEN Symp. on RI as Probes and Tracers '98, Wako, Mar. (1998).

Y. Einaga: "The ^{57}Fe Mössbauer studies of light-induced magnetic properties of cobolt-iron cyano complexes", RIKEN Symp. on RI as Probes and Tracers '98, Wako, Mar. (1998).

R. Amano: "Behavior of trace elements in the brain", RIKEN Symp. on RI as Probes and Tracers '98, Wako, Mar. (1998).

Y. Takahashi, Y. Minai, Y. Makide, S. Ambe, and F. Ambe: "Multitracer study for chemical speciation

of various elements on the environment: Focusing on their complexation with humic acid", RIKEN Symp. on RI as Probes and Tracers '98, Wako, Mar. (1998).

R. Hirunuma, S. Enomoto, K. Endo, S. Ambe, and F. Ambe: "Behavior of trace elements in Se-deficient rats", RIKEN Symp. on RI as Probes and Tracers '98, Wako, Mar. (1998).

T. Ozaki, Y. Makide, S. Enomoto, S. Ambe, F. Ambe, and Y. Minai: "Study on the uptake of rare earth elements by *Dryopteris erythrosora*", RIKEN Symp. on RI as Probes and Tracers '98, Wako, Mar. (1998).

N. Sotogaku, K. Matsumoto, K. Endo, R. Hirunuma, S. Enomoto, S. Ambe, and F. Ambe: "Binding properties of various metals to serum proteins", RIKEN Symp. on RI as Probes and Tracers '98, Wako, Mar. (1998).

S. Gouthu, T. Arie, and I. Yamaguchi: "Role of plants in bioremediation of soils and the influence of soil-types and soil-microbes", RIKEN Symp. on RI as Probes and Tracers '98, Wako, Mar. (1998).

F. L. Pratt, S. Ohira, and K. Nagamine: "Electron transfer in cytochrome-c observed by μ^+ spin relaxation", 7th RIKEN-RAL PAC, Wako, Mar. (1998).

H. Iwai, T. Abe, S. Yoshida, and S. Satoh: "Production and morphological analysis of the mutants correlated with intercellular attachment in haploid *Nicotiana plumbaginifolia*", 1998 Ann. Meet. of the Japanise Society of Plant Physiologists, Sapporo, May (1998).

R. Hirunuma, S. Enomoto, T. Ozaki, S. Ambe, and F. Ambe: "Transfers of trace elements from the placenta to the fetus of pregnant rat using the multitracer technique", 9th Symp. on Roles of Metals in Biological Reactions, Biology and Medicine, (The Pharmaceutical Society of Japan), Kumamoto, May (1998).

R. Hirunuma, K. Endo, S. Enomoto, S. Ambe, and F. Ambe: "Study of behavior of trace elements in Se-deficient rats", 8th Ann. Meet. of the Japan Society for Biomedical Research on Trace Elements, Sapporo, June (1998).

F. Yatagai, Y. Kagawa, A. Gordon, N. Fukunishi, T. Shimazu, K. Tatsumi, A. Fujie , and F. Hanaoka: "Mutational events after heavy-ion exposure", 32nd Scientific Assembly of COSPAR, Nagoya, July (1998).

Y. Furusawa, M. Saitou, K. Fukutsu, F. Yatagai, M. Vazquez, T. C. Yang, and T. Kanai: "Different cellular effects of heavy ions at the same LET", 32nd Scientific Assembly of COSPAR, Nagoya, July (1998).

K. Suzuki, T. Abe, Y. Katsumoto, Y. Fukui, S. Tuda, S. Yoshida, and T. Hisazumi: "Isolation of flower color changing mutants using heavy-ion beams irradiation", 16th Ann. Meet. and Symp. of Japanese Society for Plant Cell and Molecular Biology, Sendai, July (1998).

C. H. Bae, T. Abe, T. Matsuyama, T. Nakano, and S. Yoshida: "Production of tobacco mutants induced with heavy-ion beams irradiation", 16th Ann. Meet. and Symp. of Japanese Society for Plant Cell and Molecular Biology, Sendai, July (1998).

T. Abe, S. Yoshida, N. Fukunishi, N. Inabe, M. Kase, A. Goto, and Y. Yano: "An effective mutation method of plants using heavy-ion beams", 16th Ann. Meet. and Symp. of Japanese Society for Plant Cell and Molecular Biology, Sendai, July (1998).

F. Yatagai, A. Gordon, S. Morimoto, N. Fukunishi, M. Honma, T. Sofuni, and F. Hanaoka: "HPRT mutation induced by heavy-ion irradiation, the effect of p53", Gordon Reseach Conf. on DNA Alterations in Transformed Cells, New Hampshire, USA, Aug. (1998).

K. Ushida: "New phorochemistry and new radiation chemistry: Beyond Synchrotron Radiation", 9th Riron Kagaku Symp., Seto, Aug. (1998).

K. Ishioka, K. Ushida, S. Hishita, K. Nakamura, and M. Kitajima: "Phonon dynamics in ion-irradiated bismuth", 1998 Fall Meet. of the Physical Society of Japan, Naha, Sept. (1998).

S. Ambe, T. Ozaki, T. Shinonaga, H. Wang, and S. Enomoto: "Factors affecting the absorption of trace elements by plants", 42nd Symp. on Radiochemistry, Sendai, Sept. (1998).

Z. Chang, S. Ambe, N. Takematsu, K. Takahashi, Y. Takahashi, and F. Ambe: "Multitracer study on the binding of trace elements to humic acid", 42nd Symp. on Radiochemistry, Sendai, Sept. (1998).

F. Yatagai, T. Saito, A. Takahashi, and T. Ohnishi: "Mutation induction in the rpsl gene on an *E. coli-B. subtillis* shuttle vector by space flight on MIR", 49th IAF Cong., (The International Astronautical Federation, The International Academy of Astronautics, and The International Institute of Space Law), Melbourne, Australia, Sept. (1998).

I. Fujiwara, Y. Itoh, R. Iwata, F. Saito, and A. Goto: "^{18}F intense spot positron source for spin polarized positron beam", 8th Int. Workshop on Slow Positron Beam Techniques for Solid and Surfaces, (Union of Cape Town), Cape Town, South Africa, Sept. (1998).

I. Fujiwara, Y. Itoh, R. Iwata, T. Nozaki, and A. Goto: "Preparation of an intense positron source by electro-deposition of ^{18}F on a graphite-electrode", OECD/NEA Workshop on Ion and Slow Positron Beam Utilization, Lisbon, Portugal, Sept. (1998).

S. Yoshida and T. Abe: "Plant biotechnology using heavy-ion beams", 1998 Fall Meet. of the Physical Society of Japan, Akita, Oct. (1998).

C. H. Bae, T. Abe, T. Matsuyama, T. Nakano, K. Miyoshi, and S. Yoshida: "Mutants induction using heavy-ion beams irradiation in ovules and cultured anthers of tobacco plants", 94th Congr. of the Breeding Society of Japan, Iwate, Oct. (1998).

T. Matsuyama, T. Abe, Y. Takahashi, C. H. Bae, T. Nakano, T. Asami, and S. Yoshida: "RLGS analysis in plant genome: Preliminary studies for mutant

analysis", 94th Congr. of the Breeding Society of Japan, Iwate, Oct. (1998).

M. Miki, Y. Mizutani, K. Okamoto, Y. Izumi, T. Kozawa, K. Ushida, Y. Yoshida, and S. Tagawa: "Study on the behavior of geminate ion pair in alkane by using picosecond pulse radiolysis: Measurement by using white light continuum", 41st Symp. on Radiation Chemistry, Kobe, Oct. (1998).

K. Ushida, K. Ishioka, S. Hishita, K. Nakamura, and M. Kitajima: "Coherent phonon spectroscopy on ion-beam irradiated solids", 41st Symp. on Radiation Chemistry, Kobe, Oct. (1998).

S. Morimoto, A. Gordon, N. Fukunishi, M. Honma, T. Sofuni, F. Hanaoka, and F. Yatagai: "HPRT mutation induction by heavy-ion irradiation: The effect of mutant p53 gene", 27th Ann. Meet. of the Japan Environmental Mutagen Research Society, Osaka, Nov. (1998).

T. Arie, S. Gouthu, S. Ambe, and I. Yamaguchi: "Plant uptake of radionuclides and rhizosphere factors", A Nuclear Cross-Over Research Symp.: New Approaches in Environmental Radioactivity, (Promotion Committee on Nuclear Cross-Over Research, Japan and Specialist Committee on Assessment and Reduction of Radiation Risks, Japan), Wako, Nov. (1998).

M. Yoshimasu, T. Abe, S. Yoshida, T. Inoue, F. Ling, and T. Shibata: "Biological effects of heavy-ion beam on budding yeast cells", 20th Ann. Meet. of Japanese Society of Molecular Biology, Yokohama, Dec. (1998).

P. Mehnati, F. Yatagai, F. Hanaoka, T. Tsuzuki, and H. Sasaki: "Judgement on 'Hit or Non-hit' by time-lapse observations on CHO cells", 41st Ann. Meet. of the Japan Radiation Research Society, Nagasaki, Dec. (1998).

T. Kato, H. Tauchi, K. Komatsu, K. Ishizaki, F. Yatagai, and M. S. Sasaki: "Mutation spectrum for human tumor cell deficient in mismatch repair gene hMSH3", 41st Ann. Meet. of the Japan Radiation Research Society, Nagasaki, Dec. (1998).

M. Saitou, Y. Furusawa, T. Kanai, M. E. Vazguez, T. C. Yang, F. Yatagai, and F. Soga: "RBE of lethal effects on V79 cells by high-LET heavy-ions", 41st Ann. Meet. of the Japan Radiation Research Society, Nagasaki, Dec. (1998).

T. Kanai, N. Matsufuji, Y. Futami, and F. Yatagai: "Radiation dosimetry and LET estimation for biological irradiation with heavy charged particles", 41st Ann. Meet. of the Japan Radiation Research Society, Nagasaki, Dec. (1998).

S. Morimoto, A. Gordon, N. Fukunishi, M. Honma, T. Sofuni, F. Hanaoka, and F. Yatagai: "Analysis of HPRT mutation induced by heavy-ion irradiation", 41st Ann. Meet. of the Japan Radiation Research Society, Osaka, Dec. (1998).

5. Material analysis

A. Tonomura, K. Maeda, H. Hamanaka, and K. Hasegawa: "Chemical shift measurements using high-resolution PIXE system with position-sensitive crystal spectrometer", 45th Spring Meet., 1998, The Japan Society of Applied Physics and Related Societies, Hachioji, Mar. (1998).

H. Yoshiki, K. Maeda, A. Tonomura, T. Tsuruda, and H. Higuchi: "PIXE Analysis of trace element in feathers", 4th Asian Symp. on Academic Activities for Waste Management, (Asian Association of Academic Activities for Waste Management), Seoul, Korea, Aug. (1998).

T. Kobayashi, G. Dorenbos, C. F. McConville, M. Iwaki, and M. Aono: "Depth profiling and lattice location of Sb atoms in a Si/Sb(δ-doped)/Si structure formed by solid phase epitaxy using a ME-CAICISS", 59h Autumn Meet., 1998, The Japan Society of Applied Physics, Higashihiroshima, Sept. (1998).

K. Maeda, K. Hasegawa, A. Tonomura, H. Hamanaka, and M. Maeda: "Chemical state analysis by in-air high-resolution PIXE(1): Kβ spectra", 16th PIXE Symp., Hachimantai, Oct. (1998).

A. Tonomura, T. Hasegawa, H. Hamanaka, K. Hasegawa, and K. Maeda: "Chemical state analysis by in-air high-resolution PIXE(2): Kα spectra", 16th PIXE Symp., Hachimantai, Oct. (1998).

Y. Tokimitsu, K. Maeda, S. Murao, and E. Henseler: "External-PIXE identification of material for popular music pipes during the late Meiji era, Japan", 16th PIXE Symp., Hachimantai, Oct. (1998).

H. Yoshiki, K. Maeda, A. Tonomura, and H. Higuchi: "PIXE analysis of lead in Jungle Crow's feather", 16th PIXE Symp., Hachimantai, Oct. (1998).

T. Kobayashi, T. Sakurai, T. Matsuo, H. Matsuda, M. Iwaki, and M. Aono: "Medium-energy coaxial impact-collision ion scattering spectrometer", Symp. on Charged Particle Optics, (132nd Committee, Japan Society for the Promotion of Science), Tsukuba, Oct. (1998).

J. Kawai, K. Hayashi, T. Yamamoto, M. Yamaguchi, A. Nisawa, K. Okuda, and K. Maeda: "EXEFS of Al in TiAl", 34th Meet. for X-Ray Chemical Analysis Japan, Sendai, Nov. (1998).

IX. LIST OF SYMPOSIA

(Jan.–Dec. 1998)

1) RIKEN Symp. on Studies on Condensed Matter Physics, Atomic Physics, Nuclear Chemistry, and Biomedical Science Using RIKEN Accelerators
26 Jan., Wako, RIKEN, Nuclear Chemistry Lab.

2) RIKEN Symp. on Nuclear Chemistry of Heavy Elements at RIKEN RI-Beam Factory
27–28 Jan., Wako, RIKEN, Nuclear Chemistry Lab.

3) RIKEN Symp. on Dynamics in Hot Nuclei
13–14 Mar., Wako, RIKEN, Cyclotoron Lab.

4) RIKEN Symp. on RI as Probes and Tracers '98
17 Mar., Wako, RIKEN, Nuclear Chemistry Lab.

5) Int. Technical Advisory Committee Meet. on the Sector Magnets of RIKEN Superconducting Ring Cyclotron (SRC)
11–13 May, Wako, RIKEN, RI Beam Factory Project Office

6) RIBF Workshop on Effective Interaction and Unstable Nuclei
14 Sept., Wako, RIKEN, Cyclotoron Lab.

7) RIKEN Symp. on Muon Science '98, New Direction in Muon Catalyzed Fusion and μSR Studies and Fundamental Muon Physics
7–8 Oct., Wako, RIKEN, Muon Science Lab.

8) RIBF Workshop on Structure of Unstable Nuclei
16–18 Nov., Wako, RIKEN, Cyclotron Lab.

9) RIKEN Symp. on The Theory of Atomic and Molecular Processes (VI)
19 Nov., Wako, RIKEN, Atomic Physics Lab.

10) RIKEN Symp., A Nuclear Cross-Over Research Symposium: New Approaches in Environmental Radioactivity
26–27 Nov., Wako, RIKEN, Microbial Toxicology Lab.

11) RIKEN Symp. on Space Charge Dominated Beam Physics for Heavy Ion Fusion
10–12 Dec., Wako, RIKEN, RI Beam Factory Project Office

12) Symp. on Present Status and Future of the RIKEN-RAL Muon Facility Project
14 Dec., Wako, RIKEN, Muon Science Lab.

X. LIST OF SEMINARS

(Jan.–Dec. 1998)

Radiation Lab., Cyclotron Lab., and Linear Accelerator Lab.

1) R. Suda, Tokyo Metropolitan University (Tokyo), KEK B-factory BELLE Group (Ibaraki), 24 Feb.
"The development of low-refractive-index silica Aerogel Cerenkov Counter (ACC)"

2) A. Kohama, RIKEN (Saitama), 9 Mar.
"Nuclear transparency in a relativistic quark model"

3) Y. M. Zhao, RIKEN (Saitama), 23 Mar.
"Regional regularities of low-lying excitations in nuclei"

4) H. Geissel, GSI (Germany), 25 Mar.
"Precision experiments with relativistic heavy ions at the FRS-ESR facilities"

5) K. Suemmerer, GSI (Germany), 26 Mar.
"Recent results from Ar-40 fragmentation at 1000 MeV/nucleon studied at GSI"

6) N. van Do, National Center for Natural Science and Technology (Vietnam), 30 Mar.
"Some aspects on the exploitation of small accelerators in Vietnam"

7) G. Kalinka, Institute of Nuclear Research of the Hungarian Academy of Sciences (Hungary), 28 Mar.
"Development of high performance CsI(Tl) scintillator + Si pin photodiode charged particle detectors for the EUROBALL"

8) N. Pietralla, University of Koeln (Germany), 6 May
"Low-lying collective dipole modes and isovector excitations in the valence shell of heavy nuclei"

9) H. Madokoro, RIKEN (Saitama), 18 May
"Relativistic mean field description of nuclear collective rotation"

10) Xu Shuwei, IMP (CHINA), 19 May
"Decay properties of neutron-deficient nuclei and new nuclides near the proton-drip line"

11) E. A. Cherepanov, Flerov Laboratory of Nuclear Reactions, Joint Institute for Nuclear Research (Russia), 22 May
"The role of the quasi-fission in the reactions used for the synthesis of superheavy elements"

12) G. I. Kosenko, Flerov Laboratory of Nuclear Reactions, Joint Institute for Nuclear Research (Russia), 22 May
"Use of the combined dynamical evaporation approach to the calculations of the characteristics of fission of excited nuclei"

13) T. Tanimori, Department of Physics, Tokyo Institute of Technology (Tokyo), 22 May
"The new gas PSD applicable to high count rate"

14) B. R. Barrett, Department of Physics, University of Arizona (USA), 26 May
"Large-Basis No-Core Shell-Model calculations for light nuclei"

15) T. Kifune, Institute for Cosmic Ray Research, University of Tokyo (Tokyo), 16 June
"Superhigh energy gamma ray astronomy by the ground observation"

16) N. Ohnishi, Graduate School of Arts and Sciences, University of Tokyo (Tokyo), 29 June
"Pairing correlation studied in generator coordinate method"

17) A. Ansari, Institute of Physics, Bhubaneswar (India), 27 July
"Calculation of nuclear level densities incorporating corrections for thermal and quantum fluctuations"

18) T. Nakatsukasa, University of Manchester (UK), 12 Aug.
"Selfconsistent determination of collective coordinates in nuclear collective motion"

19) C. Samanta, Saha Institute of Nuclear Physics (India), 7 Sept.
"^{6}Li projectile breakup reaction at 0.1 A GeV"

20) A. Krasznahorkay, Institute of Nuclear Research (Hungary), 8 Sept.
"Super- and Hyperdeformed states in the Actinide Region"

21) K. Hara, Technische Universität of München (Germany), 16 Sept.
"How the Projected Shell Model (PSM) works"

22) M. Tanaka, Kobe Tokiwa College (Kobe), 21 Sept.
"Production of polarized ^{3}He beam and its application"

23) M. Schaedel, GSI (Germany), 28 Sept.
"Nuclear reaction paths into the region of superheavy elements and prospects of heavy element

research with radioactive beams"

24) M. Iinuma, Advanced Sciences of Matter, Hiroshima University (Hiroshima), 8 Oct.
"Dynamic nuclear polarization in the high-temperature low-magnetic-field condition for polarized proton target"

25) H. Kamada, Ruhr University (Germany), 14 Oct.
"The proton-deutron scattering and the three body effect"

26) M. N. Harakeh, KVI Groningen University (The Netherlands), 24 Nov.
"Recent results from AGOR"

27) G. M. Jin, Institute of Modern Physics, Chinese Academy of Science (China), 30 Nov.
"The progress of physics research in IMP"

28) G. M. Jin, Institute of Modern Physics, Chinese Academy of Science (China), 2 Dec.
"Study on the properties of hot nuclei in IMP"

29) R. Seki, California State University, Kellogg Radiation Laboratory (USA), 8 Dec.
"Model-independent determination of matter distributions of neutron-rich nuclei"

Atomic Physics Lab.

1) H. Shibata, RCNST, University of Tokyo (Ibaraki), 30 Jan.
"Production, acceleration, and detection of charged fine particles"

2) B. H. Gilbody, Queen's University (UK), 10 Feb.
"State-selective charge transfer collisions involving slow multiply charged ions"

3) P. C. Stancil, Oak Ridge National Laboratory (USA), 11 Mar.
"Low-energy atomic collisions in astrophysics"

4) T. Kitamori, University of Tokyo (Tokyo), 13 Mar.
"Photothermal spectroscopy and ultimate measurements —Single molecule detection in liquids and femtosecond time resolved measurement— "

5) N. Watanabe, Hokkaido University (Hokkaido), 13 Mar.
"Formation of H_2 molecules on the amorphous water ice"

6) M. Stockli, Kansas State University (USA), 19 Mar.
"New experiments and developments with the KSU-EBIS"

7) P. H. Mokler, GSI (Germany), 26 Mar.
"The two-photon decay in heavy He-like ions"

8) H. Geissel, GSI (Germany), 27 Mar.
"Slowing down of relativistic heavy ions and new applications"

9) T. Goto, Nagoya Institute of Technology (Nagoya), 27 Mar.
"Absolute measurements of Auger electrons"

10) S. Datz, Oak Ridge National Laboratory (USA), 17 Apr.
"Atomic collision physics at ultra-relativisic energies"

11) K. Kageyama, Saitama University (Saitama), 1 May
"Basis of non-destructive inspections by ultrasonic waves"

12) M. Lamoureux (University of Paris) and M. Niimura RIKEN (Saitama), 8 May
"ECRIS oscillatory regime discussed in relation with their performances"

13) N. Kabachnik, Moscow State University (Russia), 19 May
"Multiple ionization of atoms and molecules by fast ion impact"

14) H. M. Shimizu, Cosmic Radiation Laboratory, RIKEN (Saitama), 21 May
"Development of superconducting tunnel junctions"

15) B. Sulik, ATOMKI (Hungary), 5 June
"Experimental separation of two- and three- body effects in the ionization of Li by the impact of fast, highly charged ions: Analogies between photon- and ion-impact ionization"

16) T. Ishikawa, SPring-8, RIKEN (Saitama), 19 June
"Study of X-ray optics at SPring-8"

17) H. Dezso, RMKI (Hungary), 26 June
"Brief review of anticyclotron"

18) H. Tsuchida, Nara Women's University (Nara), 28 July
"Mechanisms of ionization and fragmentation in fast ion-C_{60} collisions"

19) T. Azuma, University Tsukuba (Ibaraki), 18 Aug.
"Correlation between radiative electron capture

into continuum and convoy electron"

20) A. Dalgarno, Harvard-Smithsonian Center for Astrophysics (USA), 6 Oct.
"Ultra-cold collisions of atoms and molecules"

21) J. S. Cohen, Los Alamos National Laboratory (USA), 9 Oct.
"Isotope effects on capture of exotic particles"

22) M. Inokuti, Argonne National Laboratory (USA), 10 Dec.
"Electron degradation in gaseous media"

23) K. Ueda, Toyota Technological Institute (Nagoya), 17 Dec.
"Behavior of hydrogen on metallic and semiconductor surface studied by electron -excited ion detachment"

24) Chii-Dong Lin, Kansas State University (USA), 18 Dec.
"Visualization of correlations in triply excited states of atoms"

25) Chii-Dong Lin, Kansas State University (USA), 18 Dec.
"Weakly-bound atomic and molecular systems"

RI Beam Factory

1) T. Saitoh, RCNP, Osaka University (Osaka), 8 Jan.
"Present Status of the RCNP Ring Cyclotron"

2) F. Caspers, CERN (Switzerland), 21 Jan.
"Topics around stochastic cooling"

3) N. Takahashi, Okayama University (Okayama), 5 Feb.
"Overview of calculation of electromagnetic force in three dimensional analysis on magnetic fields and calculation of electromagnetic forces of the Superconducting Ring Cyclotron"

4) G. Wei, Institute of Modern Physics, Chinese Academy of Science (China), 9 Feb.
"About stochastic cooling"

5) E. Syresin, JINR(Russia),11 Mar.
"Theory and experimental investigations of EBIS in the reflection operation mode"

6) V. Mirnov, JINR(Russia), 14 May
"Plasma investigation in PPL"

7) S. Pal, VECC(India),15 May
"Cryogenic system for K-500 Superconducting Cyclotron at VECC"

8) M. Lamoureux, University of Pierre and Marie Curie (France), 4 June
"Characteristics and role of the hot electrons in the ECR ion sources"

9) P. Sigg, PSI(Switzerland), 28 July
"Recent experimence with high beam power operation and improvements of the PSI RF-System"

10) V. Shevtsov, JINR(Russia), 26 Aug.
"Numerical simulation of charged particle dynamics in transportation"

11) A. Denker, Hahn Meitner Institute(Germany), 22 Oct.
"Inverstigation of objets d'Art with PIXE using 68 MeV protons"

12) U. Trinks, University of München(Germany), 27 Oct.
"Superconducting cyclotron development in Munich"

13) E. Baron, GANIL(France), 29 Oct.
"Status of the GANIL operation and of the SPIRAL project"

14) E. Baron, GANIL(France), 4 Nov.
"Heavy ions traversing foils: Charge state distribution, energy spread, emittance growth and foil lifetime"

15) G. Ryckewaert, Louvain-la-Neuve(Belgium), 9 Dec.
"Status of the cyclotrons at the University in Louvain-la-Neuve: Uses for research and development"

Muon Science Lab.

1) G. zu Putlitz, University Heidelberg (Germany), 14 Dec.
"Report of the external review committe on RIKEN-RAL Muon Facility Project"

Microbial Toxicology Lab.

1) E. E. T. Smolders, Leuven University (Belgium), 16 Dec.
"Transfer of radionuclides and related elements from soil to plant and their mobility in soil"

XI. LIST OF PERSONNEL

RIKEN Accelerator Research Facility

TANIHATA Isao 谷畑勇夫 (Facility Director)
YANO Yasushige 矢野安重 (Vice Facility Director)

Linac Division

IKEZAWA Eiji 池沢英二
KOHARA Shigeo 小原重夫
KASE Masayuki 加瀬昌之*1

Ring Cyclotron Division

FUJITA Jiro 藤田二郎
IKEGAMI Kumio 池上九三男
KAGEYAMA Tadashi 影山 正
KASE Masayuki 加瀬昌之
KUBO Toshiyuki 久保敏幸
NAKAGAWA Takahide 中川孝秀
OKUNO Hiroki 奥野広樹
GOTO Akira 後藤 彰*1
INABE Naohito 稲辺尚人
KAMIGAITO Osamu 上垣外修一
KOHARA Shigeo 小原重夫
NAGASE Makoto 長瀬 誠
OGIWARA Kiyoshi 荻原 清
YOKOYAMA Ichiro 横山一郎

Experimental Support Division

ICHIHARA Takashi 市原 卓
KANAI Yasuyuki 金井保之
MATSUZAKI Teiichiro 松﨑禎市郎
WATANABE Yasushi 渡邊 康
KAMBARA Tadashi 神原 正*1
KUMAGAI Hidekazu 熊谷秀和
MORITA Kosuke 森田浩介
YATAGAI Fumio 谷田貝文夫

Radioisotope Facilities Division

KOBAYASHI Yoshio 小林義男
YATAGAI Fumio 谷田貝文夫*1

Radiation Protection Group

FUJITA Shin 藤田 新*1
NAKAJIMA Shunji 中島諄二
ITO Sachiko 伊藤祥子
OGIWARA Kiyoshi 荻原 清

Administration Division

NAKAMURA Toshiko 中村とし子
NUMATA Shigeo 沼田茂男
NISHIGUCHI Fumiyoshi 西口文彬*2

Steering Committee

GOTO Akira 後藤 彰
ISHIHARA Masayasu 石原正泰
KASE Masayuki 加瀬昌之
MATSUOKA Masaru 松岡 勝
NAGAMINE Kanetada 永嶺謙忠
SAWA Hiroshi 澤 宏
TANIHATA Isao 谷畑勇夫
YAMAZAKI Yasunori 山崎泰規*3
YATAGAI Fumio 谷田貝文夫
HANAOKA Fumio 花岡文雄
KAMBARA Tadashi 神原 正
KATSUMATA Koichi 勝又紘一
MATSUZAKI Teiichiro 松﨑禎市郎
NISHIGUCHI Fumiyoshi 西口文彬
TAKAMI Michio 高見道生
YAGI Eiichi 八木栄一
YANO Yasushige 矢野安重
YOSHIDA Shigeo 吉田茂男

*1 Group Leader, *2 Manager, *3 Chairperson

RI Beam Factory Project Office

Head

YANO Yasushige　矢野安重

Members

IKEGAMI Kumio　池上九三男
KAMIGAITO Osamu　上垣外修一
OHNISHI Jun-ichi　大西純一
SAKAMOTO Naruhiko　坂本成彦
WAKASUGI Masanori　若杉昌徳
INABE Naohito　稲辺尚人
KUBO Toshiyuki　久保敏幸
OKUNO Hiroki　奥野広樹
TANABE Toshiya　田辺敏也

Visiting Members and Postdoctoral Fellows

AMANO Ryohei　天野良平　(Fac. Med., Kanazawa Univ.)
ARAKAWA Kazuo　荒川和夫　(JAERI, Takasaki Rad. Chem. Res. Estab.)
BANDYOPACHYAY Arup　(Variable Energy Cycl. Cen., India)
BATYGIN Yuri
CHATTOPADHYAY Subrata　(Variable Energy Cycl. Cen., India)
CHIBA Toshiya　千葉利哉
CHIBA Yoshiaki　千葉好明　(Tokyo Electr. Tech. Serv.)
DINH DANG Nguyen
ENDO Kazutoyo　遠藤和豊　(Showa Coll. Pharm. Sci.)
ENOMOTO Shuichi　榎本秀一
FUJISAWA Takashi　藤沢高志　(Denki Kogyo Co., Ltd.)
FUJISHIMA Shiro　藤島史郎　(I.H.I.)
FUKUDA Mitsuhiro　福田光宏　(JAERI, Takasaki Rad. Chem. Res. Estab.)
FUKUNISHI Nobuhisa　福西暢尚
HEMMI Masatake　逸見政武
HIMENO Seiichiro　姫野誠一郎　(Kitasato Univ.)
HIRUNUMA Rieko　蛭沼利江子
HONMA Toshihiro　本間寿広　(N.I.R.S.)
INAMURA Takashi T.　稲村卓
IWAMA Motonori　岩間基訓　(Shizuoka Univ.)
KATAYAMA Takeshi　片山武司　(Cen. Nucl. Study, Grad. Sch., Sci. Univ. Tokyo)
KAWAGUCHI Takeo　川口武男　(Mitsubishi Elec. Co., Ltd.)
KIM Jong-Won
MATSUMOTO Ken-ichiro　松本謙一郎　(Showa Coll. Pharm. Sci.)
MINAI Yoshitaka　薬袋佳孝　(Musashi Univ.)
MINAMI Takeshi　南武志　(Nara Medical Univ.)
MIRONOV Vladmir　(J.I.N.R., Dubna, Russia)
MITSUOMOTO Toshinori　密本俊典　(Sumitomo Heavy Ind., Ltd.)
MIYAZAWA Yoshitoshi　宮澤佳敏
MORIKAWA Tetsuya　森川鐵也
MOTONAGA Shyoushichi　元永昭七
NAGAFUCHI Teruyasu　永渕照康　(Toshiba Corp.)
NIIMURA Masanobu　新村正信　(Sch. Sci. Eng., Waseda Univ.)
NODA Kouji　野田耕司　(N.I.R.S.)
OHKAWA Tomohiro　大川智宏　(Mitsubishi Heavy Ind., Ltd.)
OHTOMO Kiyotaka　大友清隆　(Sumitomo Heavy Ind., Ltd.)
OHYAMA Takuya　大山拓也　(Shizuoka Univ.)
OKAMOTO Youichi　岡本洋一　(Showa Coll. Pharm. Sci.)
OKAMURA Masahiro　岡村昌宏
OKUMURA Susumu　奥村進　(JAERI, Takasaki Rad. Chem. Res. Estab.)
SAITO Fuminori　斉藤文修
SEKINE Hirotaka　関根弘隆
SIDORIN Anatoly　(J.I.N.R., Dubna, Russia)
SUGII Kazuo　杉井一生　(Osaka Vacuum, Ltd.)
SUZUKI Hiroyuki　鈴木弘行　(Chiba Univ.)

TAKAHASHI Masaaki 高橋正昭 (Osaka Prefect. Univ.)
TAKANAKA Masao 高仲政雄
TAKEUCHI Suehiro 竹内末広 (JAERI, Tokai Res. Estab.)
TANAKA Yasushi 田中保志 (Kyokuto Boeki Kaisha, Ltd.)
TOMIMASU Takio 富増多喜夫 (Free Electrons Laser Res. Inst.)
TOMINAKA Toshiharu 冨中利治 (Hitachi, Ltd.)
TOMIZAWA Masato 冨澤正人 (KEK)
WATANABE Shin-ichi 渡辺伸一 (Cen. for Nucl. Study, Grad. Sch., Sci. Univ. Tokyo)
WATANABE Ikuo 渡辺郁男 (Toshiba Corp.)
WU Dezhong (Inst. Modern Phys., Academia Sinica, China)
XIA Jia-Wen 夏佳文 (Inst. Modern Phys., Academia Sinica, China)
YANAGA Makoto 矢永誠人 (Shizuoka Univ.)
YANAGIYA Takahiro 柳谷隆宏 (Kitasato Univ.)
YOKOUCHI Shigeru 横内茂 (Osaka Vacuum, Ltd.)
YOKOYAMA Ichiro 横山一郎
YONEDA Akira 米田晃 (Houshin Corp.)
YOSHIDA Tsutomu 吉田努 (Shizuoka Univ.)
YOSHIDA Yutaka 吉田豊 (Shizuoka Inst. Sci. Tech.)

Cosmic Radiation Laboratory

Members

KATO Hiroshi 加藤博
KOHNO Tsuyoshi 河野毅
YOSHIDA Atsumasa 吉田篤正

Visiting Members and Postdoctoral Fellows

BADONO Shinro 馬殿進路 (Mitsubishi Elec. Corp.)
GOKA Tateo 五家建夫 (NASDA)
HASEBE Nobuyuki 長谷部信行 (Waseda Univ.)
KASHIWAGI Toshisuke 柏木利介 (Fac. Eng., Kanagawa Univ.)
KATO Chihiro 加藤千尋 (Fac. Sci., Shinshu Univ.)
KIMOTO Yugo 木本雄吾 (NASDA)
KOBAYASHI Motohiro 小林基宏 (Mitsubishi Elec. Corp.)
MATSUMOTO Haruhisa 松本晴久 (NASDA)
MUNAKATA Kazuoki 宗像一起 (Fac. Sci., Shinshu Univ.)
MURAKAMI Hiroyuki 村上浩之 (Fac. Sci., Rikkyo Univ.)
NAGATA Katsuaki 永田勝明 (Fac. Eng., Tamagawa Univ.)
NAKAMOTO Atsushi 中本淳 (Fac. Sci., Rikkyo Univ.)
TAKASHIMA Takeshi 高島健 (Fac. Sci., Nagoya Univ.)
USHIO Youji 海塩洋史 (Mitsubishi Elec. Eng. Corp.)
YAMAGIWA Iwao 山極巖 (Tobu High School)
YANAGIMACHI Tomoki 柳町朋樹 (Fac. Sci., Rikkyo Univ.)

Trainees

HOSHIDA Takashi 星田貴志 (Grad. Sch. Fac. Sci., Nagoya Univ.)
MIYASAKA Hiromasa 宮坂浩正 (Grad. Sch. Sci. Eng., Saitama Univ.)

Cyclotron Laboratory

Head

YANO Yasushige 矢野安重

Members

FUJIMAKI Masaki 藤巻正樹
FUJITA Jiro 藤田二郎
FUJITA Shin 藤田新
GOTO Akira 後藤彰
IKEZAWA Eiji 池沢英二
ITO Sachiko 伊藤祥子

KAGEYAMA Tadashi 影山 正
KASE Masayuki 加瀬昌之
KIMURA Kazuie 木村一宇
KOHARA Shigeo 小原重夫
MORITA Kosuke 森田浩介
NAGASE Makoto 長瀬 誠
NAKAGAWA Takahide 中川孝秀
NAKAJIMA Shunji 中島諄二
OGIWARA Kiyoshi 荻原 清
USHIDA Kiminori 丑田公規
WADA Takeshi 和田 雄
YAMAJI Shuhei 山路修平
YOKOYAMA Ichiro 横山一郎

Visiting Members and Postdoctoral Fellows

ABE Yasuhisa 阿部恭久 (Yukawa Inst. Theor. Phys., Kyoto Univ.)
ABURAYA Takashi 油谷崇志 (NASDA)
AKIYOSHI Hiromichi 秋吉啓充
ARIGA Takehiro 有賀健博 (Fac. Sci., Saitama Univ.)
BABA Shinji 馬場信次 (NASDA)
BAN Shuichi 伴 秀一 (KEK)
BANDYOPACHYAY Arup (Variable Energy Cycl. Cen., India)
BANDYOPACHYAY Tapas (Variable Energy Cycl. Cen., India)
BANERJEE Vaishali (Variable Energy Cycl. Cen., India)
BHATTACHAYA Sankar (Variable Energy Cycl. Cen., India)
BIRI Sandor (ATOMKI, Hungary)
CHAKRABARTI Alok (Variable Energy Cycl. Cen., India)
CHEVTSOV Uladmir (J.I.N.R., Dubna, Russia)
DATE Schin 伊達 伸 (JASRI)
DINH DANG Nguyen (Fac. Sci., Saitama Univ.)
EJIRI Hiroyasu 江尻宏泰 (Fac. Sci., Osaka Univ.)
EN'YO Hideto 延与秀人 (Fac. Sci., Kyoto Univ.)
FUJIOKA Manabu 藤岡 学 (Cycl. Radioisot. Cen., Tohoku Univ.)
FUJITA Yoshitaka 藤田佳孝 (Fac. Sci., Osaka Univ.)
FUJIWARA Ichiro 藤原一郎 (Dept. Economy, Otemon Gakuin)
FUJIWARA Mamoru 藤原 守 (RCNP, Osaka Univ.)
FURUNO Kohei 古野興平 (Tandem Accel. Cen., Univ. Tsukuba)
FURUSE Kaoru 古瀬 馨 (NASDA)
FUTAMI Yasuyuki 二見康之 (N.I.R.S.)
GOKA Tateo 五家建夫 (NASDA)
GRUBER Bruno (Tech. Univ. Clausthal, Germany)
GU Wei (Inst. Modern Phys., Academia Sinica, China)
HAMA Hiroyuki 浜 広幸 (I.M.S.)
HARADA Toru 原田 融 (Sapporo Gakuin Univ.)
HASHIMOTO Miwa 橋本美和 (NASDA)
HASHIMOTO Osamu 橋本 治 (Fac. Sci., Tohoku Univ.)
HATANAKA Kichiji 畑中吉治 (RCNP, Osaka Univ.)
HATSUKAWA Yuichi 初川雄一 (JAERI, Tokai Res. Estab.)
HATTORI Toshiyuki 服部俊幸 (Res. Lab. Nucl. React., T.I.T.)
HAYANO Ryugo 早野龍五 (Fac. Sci., Univ. Tokyo)
HIEDA Kohtaro 檜枝光太郎 (Coll. Sci., Rikkyo Univ.)
HIGUCHI Tatsuro 樋口達郎 (NASDA)
HIRAO Yasuo 平尾泰男 (N.I.R.S.)
HIROSE Takayuki 広瀬孝幸 (NASDA)
HIRUNUMA Rieko 蛭沼利江子
HONMA Michio 本間道雄 (Aizu Univ.)
HORIBATA Takatoshi 堀端孝俊 (Fac. Eng., Aomori Univ.)
HORIGUCHI Takayoshi 堀口隆良 (Fac. Sci., Hiroshima Univ.)
HORIUCHI Hisashi 堀内 昶 (Fac. Sci., Kyoto Univ.)
HOSONO Kazuhiko 細野和彦 (Dept. Eng., Sci., Himeji Inst. Tech.)
HUGIWARA Ichiro 藤原一郎 (Dept. Economy, Otemon Gakuin)
HYODO Toshio 兵頭俊男 (Grad. Sch. Arts Sci., Univ. Tokyo)
IDESAWA Masanori 出澤正徳 (Univ. Electro-Commun.)
IGARASHI Toshio 五十嵐敏雄 (NASDA)

IKEDA Akitsu 池田秋津 (Shizuoka Inst. Sci. Technol.)
IKEDA Kiyomi 池田清美 (Fac. Sci., Niigata Univ.)
IKEDA Nobuo 池田伸夫 (Fac. Sci., Kyushu Univ.)
IKEZOE Hiroshi 池添博 (JAERI, Tokai Res. Estab.)
IMAI Kenichi 今井憲一 (Fac. Sci., Kyoto Univ.)
IMAMURA Mineo 今村峯雄 (National Museum of Japanese History)
INOUE Makoto 井上信 (Inst. Chem. Res., Kyoto Univ.)
ISHIDA Satoru 石田悟
ISHIZUKA Takeo 石塚武男 (Fac. Sci., Saitama Univ.)
ITO Yasuo 伊藤泰男 (Atomic Energy Res. Cen., Univ. Tokyo)
ITOH Hiroshi 伊藤寛 (KEK)
ITOH Kazuya 伊藤和也
ITOH Yoshiko 伊東芳子 (Adv. Res. Cen. Sci. Eng., Waseda Univ.)
IWAMOTO Akira 岩本昭 (JAERI, Tokai Res. Estab.)
IWASA Naohito 岩佐直仁
IWASHITA Yoshihisa 岩下芳久 (Inst. Chem. Res., Kyoto Univ.)
IWATA Ren 岩田錬 (Cycl. Radioisot. Cen., Tohoku Univ.)
IZUMOTO Toshiaki 泉本利章 (Coll. Sci., Rikkyo Univ.)
JEONG S. C. (KEK)
JIN Weigou 金衛国 (Fac. Sci., Toho Univ.)
KAMIMURA Masayasu 上村正康 (Fac. Sci., Kyushu Univ.)
KANAZAWA Mitsutaka 金沢光隆 (N.I.R.S)
KANEKO Junichi 金子純一 (JAERI, Tokai Res. Estab.)
KATAYAMA Ichiro 片山一郎 (KEK)
KATO Kiyoshi 加藤幾芳 (Fac. Sci., Hokkaido Univ.)
KATO Shohei 加藤昌平 (Fac. Sci., Osaka Univ.)
KATORI Kenji 鹿取謙二 (Fac. Sci., Osaka Univ.)
KATSURAGAWA Hidetsug 桂川秀嗣 (Fac. Sci., Toho Univ.)
KAWAZU Akira 河津璋 (Techno Riken Co., Ltd.)
KIDERA Masanori 木寺正憲
KITAGAWA Hisashi 北川尚 (KEK)
KLUGE Thomas (Liptih Univ., Germany)
KOHAMA Akihisa 小濱洋央
KONDO Michiya 近藤道也 (RCNP, Osaka Univ.)
KOTAJIMA Kyuya 古田島久哉 (Fac. Eng., Tohoku Univ.)
KOYEN Ali (Univ. Texas, Arlington, USA)
KUBOYAMA Satoshi 久保山智司 (NASDA)
KUDO Hisaaki 工藤久昭 (Fac. Sci., Niigata Univ.)
KUMATA Masayuki 熊田雅之 (N.I.R.S.)
KURIHARA Toshikazu 栗原俊一 (KEK)
KURITA Tetsurou 栗田哲郎 (Inst. Phys., Univ. Tsukuba)
KUROKAWA Meiko 黒川明子
LEE Kong-Ok 李康王 (Rika Women's Coll., Korea)
LEE Sang Mu 李相茂 (Inst. Phys., Univ. Tsukuba)
LIU Sheng Li (Inst. Modern Phys., Academia Sinica, China)
MADOKORO Hideki 間所秀樹 (Interdisciplinary Grad. Sch. Eng. Sci., Kyushu Univ.)
MAEDA Kazuhide 前田和秀 (Fac. Sci., Kyushu Univ.)
MATSUDA Sumio 松田純夫 (NASDA)
MATSUI Yoshiko 松井芳子 (Fac. Technol., Tokyo Univ. Agric. Technol.)
MATSUKI Seishi 松木征史 (Inst. Chem. Res., Kyoto Univ.)
MATSUMOTO Akihiro 松本暁洋 (NASDA)
MATSUSE Takehiro 松瀬丈浩 (Fac. Textile Sci. Technol., Shinshu Univ.)
MATSUYANAGI Kenichi 松柳研一 (Fac. Sci., Kyoto Univ.)
MATSUZAKI Kazuhiro 松崎一浩 (NASDA)
MATUZAKI Masayuki 松崎昌之 (Fukuoka Univ. Educ.)
MENG Jie (Peking Univ., China)
MINAMISONO Tadanori 南園忠則 (Fac. Sci., Osaka Univ.)
MIURA Iwao 三浦岩 (RCNP, Osaka Univ.)

MIYATAKE Hiroari 宮武宇也 (KEK)
MIZOTA Takeshi 溝田武志 (Free Electr. Laser Res. Inst. Inc.)
MIZUNO Yoshiyuki 水野義之 (RCNP, Osaka Univ.)
MIZUSAKI Takahiro 水崎高浩 (Fac. Sci., Univ. Tokyo)
MORI Yoshiharu 森義治 (KEK)
MUKHOPADHYAY Tapan (Variable Energy Cycl. Cen., India)
MURAKAMI Hideoki 村上英興 (Tokyo Gakugei Univ.)
MURAKAMI Tetsuya 村上哲也 (Fac. Sci., Kyoto Univ.)
MURAYAMA Toshiyuki 村山利幸 (Tokyo Univ. Mercantile Marine)
MUTO Kazuo 武藤一雄 (Fac. Sci., T.I.T.)
NAGAI Yasuki 永井泰樹 (Fac. Sci., T.I.T.)
NAGAI Yuki 永井由紀 (NASDA)
NAGASHIMA Yasuyuki 長嶋泰之 (Grad. Sch. Arts Sci., Univ. Tokyo)
NAKADA Hitoshi 中田仁 (Coll. Art Sci., Chiba Univ.)
NAKAGAWA Keiko 中川恵子
NAKAHARA Hiromichi 中原弘道 (Fac. Sci., Tokyo Metrop. Univ.)
NAKAI Ko-zi 中井浩二 (Fac. Sci. Technol., Sci. Univ. Tokyo)
NAKAMURA Hiroyuki 中村裕之 (Fac. Sci., Kyushu Univ.)
NAKAMURA Ichiro 中村市郎 (Fac. Sci., Saitama Univ.)
NAKAMURA Takashi 中村尚司 (Cycl. Radioisot. Cen., Tohoku Univ.)
NAKAO Noriaki 中尾徳晶 (KEK)
NAKASHIMA Hiroshi 中島宏 (JAERI, Tokai Res. Estab.)
NEMOTO Norio 根本規生 (NASDA)
NODA Akira 野田章 (Inst. Chem. Res., Kyoto Univ.)
NOMURA Toru 野村亨 (KEK)
NOZAKI Tadashi 野崎正 (Kagami Memorial Lab., Mater. Sci., Waseda Univ.)
OGAWA Kengo 小川健吾 (Dept. Eng. Sci., Himeji Inst. Technol.)
OHIRA Hideharu 大平秀春 (NASDA)
OHNISHI Naoki 大西直毅 (Coll. Art Sci., Univ. Tokyo)
OHNISHI Tetsuya 大西哲哉 (Fac. Sci., Univ. Tokyo)
OHTSUKI Tsutomu 大槻勤 (Lab. Nucl. Sci., Tohoku Univ.)
OHYA Jiro 大矢次郎 (NASDA)
OKAMOTO Hiromi 岡本宏巳 (Inst. Chem. Res., Kyoto Univ.)
OKAMURA Hiroyuki 岡村弘之 (Fac. Sci., Saitama Univ.)
OOTOMO Hiromitu 大友洋光 (NASDA)
OTA Kiyoshi 太田清 (Fac. Sci., Saitama Univ.)
OTSUKA Takaharu 大塚孝治 (Fac. Sci., Univ. Tokyo)
OZAWA Shuichi 小沢修一 (Coll. Sci., Rikkyo Univ.)
SAGARA Kenshi 相良建至 (Fac. Sci., Kyushu Univ.)
SAITO Motozo 斉藤始三
SAKAI Hideyuki 酒井英行 (Fac. Sci., Univ. Tokyo)
SAMBATARO Michelangelo (I.N.F.N., Catania, Italy)
SATO Ken-ichi 佐藤憲一 (Dept. Phys., Tohoku Coll. Pharm.)
SATO Kenji 佐藤健次 (RCNP, Osaka Univ.)
SATO Yukio 佐藤幸夫 (N.I.R.S.)
SATOU Yoshiteru 佐藤義輝
SEKINE Toshiaki 関根俊明 (JAERI, Tokai Res. Estab.)
SHARMA Sumit (Pune Univ., India)
SHENG Yeng Ching 沈文慶 (Shanghai Inst. Nucl. Res., China)
SHIBATA Tokushi 柴田徳思 (KEK)
SHIKAZONO Naomoto 鹿園直基 (JAERI, Tokai Res. Estab.)
SHIMIZU Akira 清水昭 (RCNP, Osaka Univ.)
SHIMOMURA Kouichiro 下村浩一郎 (Mes. Sci. Lab., KEK Brunch, Univ. Tokyo)
SHIN Kazuo 秦和夫 (Fac. Eng., Kyoto Univ.)
SHIN Seung Ai 辛承愛 (Rika Women's Coll., Korea)
SHINDO Hiroyuki 新藤浩之 (NASDA)
SHINOZUKA Tsutomu 篠塚勉 (Cycl. Radioisot. Cen., Tohoku Univ.)
SHIRAI Toshiyuki 白井敏之 (Nucl. Sci. Res. Fac., Inst. Chem. Res., Kyoto Univ.)

SHIRKOV Grigori (J.I.N.R., Dubna, Russia)
SHUGYO Shin-ichi 修行新一 (NASDA)
SUEKI Keisuke 末木啓介 (Fac. Sci., Tokyo Metrop. Univ.)
SUGAI Isao 菅井 勲 (KEK)
SUGIMOTO Kenji 杉本憲治 (NASDA)
SUGIYAMA Hiroki 杉山大樹 (NASDA)
SUMIYOSHI Hiroyuki 住吉広行 (Matsusho-Gakuen Jr. Coll.)
SUZUKI Takahiro 鈴木隆博 (NASDA)
SUZUKI Toshio 鈴木敏男 (Fac. Eng., Fukui Univ.)
SUZUKI Toshio 鈴木俊夫 (Coll. Sci. Technol., Nihon Univ.)
SYRESSINE Evgucni (J.I.N.R., Dubna, Russia)
TAGAYA Yu 多加谷祐 (Fac. Sci., Univ. Tokyo)
TAGISHI Yoshihiro 田岸義宏 (Tandem Accel. Cen., Univ. Tsukuba)
TAJIMA Naoki 田嶋直樹 (Coll. Art Sci., Univ. Tokyo)
TAKADA Masashi 高田真志 (N.I.R.S.)
TAKAHASHI Takehide 高橋丈英 (NASDA)
TAKEMASA Tadashi 武政尹士 (Kyoto Univ. Educ.)
TAKIGAWA Noboru 滝川 昇 (Fac. Sci., Tohoku Univ.)
TAKIZAWA Yoshiyuki 滝澤慶之
TAMAGAKI Ryouzou 玉垣良三 (Fac. Sci., Kyoto Univ.)
TANABE Kazuko 田辺和子 (Otsuma Women's Coll.)
TANABE Kousai 田辺孝哉 (Fac. Sci., Saitama Univ.)
TANAKA Jinichi 田中仁市 (KEK)
TANAKA Kazuhiro 田中和廣 (Med. Dept., Jyuntendo Univ.)
TANAKA Toshio 田中俊雄
TANIKAWA Masashi 谷川勝至 (Fac. Sci., Univ. Tokyo)
TOHYAMA Mitsuru 遠山 満 (Kyorin Univ.)
TOMITANI Takehiro 富谷武浩 (N.I.R.S.)
TOMODA Toshiaki 友田敏章 (Fac. Eng., Aomori Univ.)
TOPREK Dragan (VINCA, Inst. Nucl. Sci., Yugoslavia)
TORIYAMA Tamotsu 鳥山 保 (Dept. Phys., Musashi Inst. Technol.)
TSUBAKI Noriyuki 椿 則幸 (NASDA)
TSUKINO Akihisa 月野晃久 (NASDA)
UCHIYAMA Koji 内山浩志 (Inst. Phys., Univ. Tsukuba)
UESAKA Tomohiro 上坂友洋
UTSUNO Yutaka 宇都野穣 (Fac. Sci., Univ. Tokyo)
UTSUNOMIYA Hiroaki 宇都宮弘章 (Fac. Sci., Konan Univ.)
WADA Michiharu 和田道治 (KEK)
WADA Ryoichi 和田良一 (Texas A & M Univ., USA)
WADA Takahiro 和田隆宏 (Fac. Sci., Konan Univ.)
WAKAI Masamiti 若井正道 (Fac. Sci., Osaka Univ.)
WAKUTA Yoshihisa 和久田義久 (Fac. Eng., Kyushu Univ.)
XIAO Meigin (Dept. Phys., Grad. Sch. Sci., Univ. Tokyo)
YABANA Kazuhiro 矢花一浩 (Fac. Sci., Niigata Univ.)
YAMANOUCHI Mikio 山内幹雄 (Inst. Phys., Univ. Tsukuba)
YAMAZAKI Hirohito 山崎寛仁 (Lab. Nucl. Sci., Tohoku Univ.)
YAMAZAKI Takashi 山崎 魏 (PCNP, Osaka Univ.)
YONEMARU Mitsunori 米丸充規 (NASDA)
YOSHIDA Nobuaki 吉田宣章 (Fac. Sci., Univ. Tokyo)
YOSHINAGA Naotaka 吉永尚孝 (Fac. Sci., Saitama Univ.)
YOSHIOKA Yasuhiro 吉岡康弘 (NASDA)
YOSHIZAWA Yasukazu 吉沢康和 (Fac. Sci., Kyushu Univ.)
YUAN Ping (Inst. Modern Phys., Academia Sinica, China)
ZHANG Wenzhi (Inst. Modern Phys., Academia Sinica, China)
ZHAO Yu Min
ZHOU Shan-Gui (Peking Univ., China)

Trainees

AOKI Yuka 青木由香 (Grad. Sch. Sci., Tohoku Univ.)
ARIGA Takehiro 有賀健博 (Fac. Sci., Saitama Univ.)
FUJISAKI Takayuki 藤崎貴之 (Coll. Sci., Rikkyo Univ.)
FUJITA Tatsuru 藤田建 (Interdisciplinary Grad. Sch. Eng. Sci., Kyushu Univ.)
HARUYAMA Seigo 春山征伍 (Dept. Phys., Grad. Sch. Sci., Univ. Tokyo)
HASHIMOTO Satoshi 橋本賢 (Dept. Phys., Grad. Sch. Sci., Univ. Tokyo)
IWASE Hiroshi 岩瀬広 (Grad. Sch. Sci., Tohoku Univ.)
KIM Eunjoo 金琅珠 (Grad. Sch. Sci., Tohoku Univ.)
KINOSHITA Tadashi 木下忠 (Grad. Sch. Sci., Tohoku Univ.)
KUROSAWA Tadahiro 黒澤忠弘 (Grad. Sch. Sci., Tohoku Univ.)
NAKAJIMA Takao 中島隆夫 (Fac. Sci., Saitama Univ.)
NAKAO Makoto 中尾誠 (Grad. Sch. Sci., Tohoku Univ.)
NUNOMIYA Tomoya 布宮智也 (Grad. Sch. Sci., Tohoku Univ.)
OGATA Kentaro 緒方研太郎 (Fac. Sci., Kyushu Univ.)
OI Makito 大井万紀人 (Grad. Sch. Arts Sci., Univ. Tokyo)
OKAMOTO Tomoko 岡本知子 (Fac. Sci. Technol., Sci. Univ. Tokyo)
OKUDA Hikaru 奥田光 (Fac. Sci., Kyushu Univ.)
OSHIMA Nagayasu 大島永康 (Grad. Univ. Adv. Studies)
SASAKI Michiya 佐々木道也 (Grad. Sch. Sci., Tohoku Univ.)
SHIGENAGA Kouichi 重永晃一 (Fac. Sci., Kyushu Univ.)
SONE Hayato 曽根逸人 (Fac. Sci. Technol., Sci. Univ. Tokyo)
SUDA Kenji 須田健嗣 (Fac. Sci., Saitama Univ.)
SUZUKI Naoki 鈴木直毅 (Grad. Sch. Arts Sci., Univ. Tokyo)
TANIGUCHI Shingo 谷口真吾 (Grad. Sch. Sci., Tohoku Univ.)
TANIKAWA Atsushi 谷川篤司 (Fac. Sci., Saitama Univ.)
TOKUNAGA Youji 徳永洋治 (Grad. Sch. Eng., Osaka Univ.)
TSURUTA Kaoru 鶴田薫 (Interdisciplinary Grad. Sch. Eng. Sci., Kyushu Univ.)
WAKUI Takashi 涌井崇志 (Fac. Sci., Toho Univ.)
YAGITA Takanori 八木田貴典 (Fac. Sci., Kyushu Univ.)
YAMAMOTO Sumiko 山本純子 (Fac. Sci., Toho Univ.)

Linear Accelerator Laboratory

Head

TANIHATA Isao 谷畑勇夫

Members

KORSHENINNIKOV Alexei A.
KUMAGAI Hidekazu 熊谷秀和
MORIMOTO Koji 森本幸司
OZAWA Akira 小沢顕
SUMIYOSHI Kohsuke 住吉光介
TONUMA Tadao 戸沼正雄
YOSHIDA Koichi 吉田光一

Visiting Members and Postdoctoral Fellows

ADACHI Shizuko 安達静子 (ICFD)
AHMADY Mohammad (Western Ontario Univ., Canada)
ARATANI Michi 荒谷美智 (Inst. Environ. Sci.)
BOLBOT Michael (Notre Dame Univ., USA)
BORDEANU Cristina (Horia Hul. Natl. Inst., Romania)
BOYD Richard (Ohio Univ., USA)
BROCKMANN Roff (Inst. Phys., Univ. Mainz, Germany)
DATAR Vivek (Bhabha Atomic Res. Cen., India)
DAVID Dean J. (CALTEC, USA)
DEMYANOVA Alla S. (Kurchatov Inst. Atomic Energy, Russia)
DOKE Tadayoshi 道家忠義 (Adv. Res. Inst. Sci. Eng., Waseda Univ.)
FUJIWARA Mamoru 藤原守 (RCNP, Osaka Univ.)
FÜLÖP Zsolt (ATOMKI, Hungary)

GEISSEL Hans (GSI, Germany)
GOLOVKOV Mkheil S. (Kurchatov Inst., Russia)
GONCHAROV Sergei A. (Kurchatov Inst., Russia)
GOSWAMI Ranjana (Variable Energy Cycl. Cen. Calcutta, India)
HIRENZAKI Satoru 比連崎悟 (Fac. Sci., Nara Women's Univ.)
HORIUCHI Hisashi 堀内 昶 (Fac. Sci., Kyoto Univ.)
IWAMOTO Akira 岩本 昭 (JAERI, Tokai Res. Estab.)
IZUYAMA Takeo 伊豆山健夫 (Fac. Sci., Toho Univ.)
KANUNGO Rituparna (Saha Inst. Nucl. Phys., Calcutta, India)
KATORI Kenji 鹿取謙二 (Fac. Sci., Osaka Univ.)
KIKUCHI Jun 菊地 順 (Sci. Eng. Res. Lab., Waseda Univ.)
KIMURA Kikuo 木村喜久雄 (Fac. Eng., Nagasaki Inst. Appl. Sci.)
KOBAYASHI Toshio 小林俊雄 (Fac. Sci., Tohoku Univ.)
KOLATA James (Notre Dame Univ., USA)
KUMAR, Suresh (Bhabha Atomic Res. Cen., India)
KURATA Mizuki 倉田美月 (JST)
KUSAKA Kensuke 日下健祐
LE Hong Khiem (Inst. Phys., Natl. Cen. Sci. Technol., Vietnam)
MARUYAMA Tomoyuki 丸山智之 (Fac. Sci., Kyoto Univ.)
MATSUTA Kensaku 松多健策 (Fac. Sci., Osaka Univ.)
MATSUYAMA Yoshitaka 松山芳孝 (Inst. Nucl. Study, Univ. Tokyo)
MATUOKA Nobuyuki 松岡伸行 (RCNP, Osaka Univ.)
MINAMISONO Tadanori 南園忠則 (Fac. Sci., Osaka Univ.)
MITTING M. (GANIL, France)
MIYAKE Yasuo 三明康郎 (Fac. Sci., Univ. Tsukuba)
MIYAMURA Osamu 宮村 修 (Fac. Sci., Hiroshima Univ.)
MOCHIZUKI Keiko 望月圭子 (Fac. Sci., Osaka Univ.)
MOCHIZUKI Yuko 望月優子
MOMOTA Sadao 百田佐多生 (Kochi Univ. Technol.)
MURAOKA Mitsuo 村岡光男 (Fac. Eng., Aomori Univ.)
NOJIRI Yoichi 野尻洋一 (Kochi Univ. Technol.)
OGAWA Kengo 小川健吾 (Coll. Arts. Sci., Chiba Univ.)
OGAWA Yoko 小川洋子 (Fac. Sci., Osaka Univ.)
OGLOBLIN Alexei A. (Kurchatov. Inst., Russia)
OHNISHI Akira 大西 明 (Fac. Sci., Hokkaido Univ.)
OHTSU Hideaki 大津秀暁 (Fac. Sci., Tohoku Univ.)
OHTSUBO Takashi 大坪 隆 (Fac. Sci., Niigata Univ.)
OJIMA Minoru 小嶋 稔 (Fac. Sci., Osaka Univ.)
OMATA Kazuo 小俣和夫 (Inst. Nucl. Study, Univ. Tokyo)
ONISHI Takashi 大西 崇
ORYU Shinsho 尾立晋祥 (Fac. Sci. Technol., Sci. Univ. Tokyo)
OYAMATSU Kazuhiro 親松和浩 (Dept. Energy Eng. Sci., Nagoya Univ.)
PETRASCU Horia (Inst. Phys. Nucl. Eng., Romania)
PETRASCU Marius (Inst. Phys. Nucl. Eng., Romania)
SAGAWA Hiroyuki 佐川弘幸 (Cen. Math. Sci., Aizu Univ.)
SAKAI Hideyuki 酒井英行 (Fac. Sci., Univ. Tokyo)
SATO Kazuhiro 佐藤和広 (Tokyo Fire Dept.)
SEKI Ryoichi 関 亮一 (California Univ., USA)
SHERRIL B. (Michigan State Univ., USA)
SUDA Toshimi 須田利美 (Fac. Sci., Tohoku Univ.)
SUGANUMA Hideo 菅沼秀夫 (RCNP, Osaka Univ.)
SUGAWARA Masahiko 菅原昌彦 (Fundam. Sci., Chiba Inst. Technol.)
SÜMMERER Klaus (GSI, Germany)
SUZUKI Hideyuki 鈴木英之 (KEK)
SUZUKI Takeshi 鈴木 健 (Fac. Sci., Niigata Univ.)
SUZUKI Tsuneo 鈴木恒雄 (Fac. Sci., Kanazawa Univ.)
SUZUKI Yasuyuki 鈴木宣之 (Fac. Sci., Niigata Univ.)
TACHIBANA Takahiro 橘 孝博 (Senior High Sch., Waseda Univ.)

TAKAHASHI Yoshiyuki 高橋義幸 (Alabama Univ., USA)
TAKAHASHI Yutaka 高橋 豊 (Fac. Sci., Osaka Univ.)
TOKANAI Fuyuki 門叶冬樹 (JST)
TOKI Hiroshi 土岐 博 (RCNP, Osaka Univ.)
TORBJOEN Baeck (Stochholm Univ., Sweden)
VARGA Kalman (Inst. Nucl. Res., Hungarian Acad. Sci., Hungary)
WADA Takahiro 和田隆宏 (Fac. Sci., Konan Univ.)
WINKLER Martin (GSI, Germany)
YAGI Hirosuke 八木浩輔 (Fac. Sci., Univ. Tsukuba)
YORANN Alhassid (Yale Univ., USA)
ZAHAR Mohamed (Dept. Phys., Notre Dame Univ., USA)

Trainees
HIBINO Masaru 日比野優 (Fac. Sci. Eng., Waseda Univ.)
KATO Tomomi 加藤智美 (Fac. Sci., Niigata Univ.)
KATO Toshiyuki 加藤俊幸 (Fac. Sci. Eng., Waseda Univ.)
KAWA Tadahisa 河 忠久 (Fac. Sci., Osaka Univ.)
MINAMISONO Kei 南園 啓 (Fac. Sci., Osaka Univ.)
OKUDA Takashi 奥田貴志 (Fac. Sci., Tohoku Univ.)
OZAKI Kiminori 尾崎公教 (Fac. Sci. Eng., Waseda Univ.)
SAKAGUCHI Takao 坂口貴男 (Fac. Sci. Eng., Waseda Univ.)
SASAKI Makoto 佐々木誠 (Fac. Sci., Osaka Univ.)
SATO Kazunori 佐藤和則 (Fac. Sci., Osaka Univ.)
SEKIGUCHI Masatugu 関口昌嗣 (Fac. Sci., Tohoku Univ.)
SHIMIZU Noritaka 清水則孝 (Fac. Sci., Univ. Tokyo)
SHIMOOKA Masaaki 下岡正明 (Fac. Sci., Kyoto Univ.)
TAKAHASHI Yoshiyuki 高橋義幸 (Fac. Sci. Eng., Waseda Univ.)
TAKENAKA Sunao 竹中 直 (Fac. Sci. Eng., Waseda Univ.)
TAKEUCHI Satoshi 武内 聡 (Fac. Sci., Rikkyo Univ.)
TANAKA Motoyuki 田中基之 (Fac. Sci., Waseda Univ.)
TERASAWA Kazuhiro 寺沢和洋 (Adv. Res. Inst. Sci. Eng., Waseda Univ.)
TERUHI Shigeru 照日 繁 (Fac. Sci. Eng., Waseda Univ.)
WAKASAYA Yoshiaki 若狭谷義朗 (Fac. Sci. Technol., Sci. Univ. Tokyo)
WANG Haiming 王 海鳴 (Fac. Sci., Univ. Tokyo)
YAMAGUCHI Yoshitaka 山口由高 (Fac. Sci., Niigata Univ.)
YAMASHITA Masaki 山下雅樹 (Adv. Res. Inst. Sci. Eng., Waseda Univ.)
YUZUKI Akira 柚木 彰 (Grad. Sch., Waseda Univ.)

Radiation Laboratory

Head
ISHIHARA Masayasu 石原正泰

Members
ICHIHARA Takashi 市原 卓
KISHIDA Takashi 岸田 隆
SAITO Naohito 斉藤直人
SAKURAI Hiroyoshi 櫻井博儀
TAKETANI Atsushi 竹谷 篤
WATANABE Yasushi 渡邊 康
YOSHIDA Atsushi 吉田 敦

Visiting Members and Postdoctoral Fellows
ABE Yasuhisa 阿部恭久 (Yukawa Inst. Theor. Phys., Kyoto Univ.)
ADACHI Minoru 足立 實 (Fac. Sci., Tokyo Inst. Technol.)
ANDO Yoshiaki 安藤嘉章 (Coll. Sci., Rikkyo Univ.)
AOI Nori 青井 考 (Dept. Phys., Grad. Sch. Sci., Univ. Tokyo)
ASAHI Koichiro 旭 耕一郎 (Fac. Sci., Tokyo Inst. Technol.)
ASAI Masato 浅井雅人 (JAERI)
AWAYA Yoko 粟屋容子 (Musashino Art Univ.)

BEAUMEL Didier (Div. Phys. Theor. IPN, Inst. Phys. Nucl., France)
BECK F. A. (CRN, France)
BROGLIA R. (Univ. Milano, Italy)
BROOKS Melynda (Los Alamos Natl. Lab., USA)
CASTEN Rick (Phys. Dept., BNL, USA)
CRIST Norman (Columbia Univ., USA)
DEVI Yelamanchili Durga
DOOI Makoto 堂井 真 (Inst. Phys., Univ. Tsukuba)
ENYO Hideto 延与秀人 (Fac. Sci., Kyoto Univ.)
FLOCARD Hubert (Div. Phys. Theor. IPN, Inst. Phys. Nucl., France)
FORTIER Simone (Div. Phys. Theor. IPN, Inst. Phys. Nucl., France)
FUCHI Yoshihide 渕 好秀 (KEK, Tanashi)
FUKE Hideyuki 福家英之 (Fac. Sci., Univ. Tokyo)
FUKUDA Mitsunori 福田光順 (Grad. Sch. Sci., Osaka Univ.)
FUKUDA Naoki 福田直樹
FUKUDA Tomokazu 福田共和 (KEK)
FURUTAKA Kazuyoshi 古高和禎 (JAERI)
GELBERG Adrian (Koln Univ., Germany)
GONO Yasuyuki 郷農靖之 (Fac. Sci., Kyushu Univ.)
GOTO Yuji 後藤雄二
HAMAGAKI Hideki 浜垣秀樹 (Cen. Nucl. Study, Univ. Tokyo)
HAMAMOTO IKUKO 浜本育子 (Lund Inst. Technol., Univ. Lund, Sweden)
HASEGAWA Takeo 長谷川武夫 (Fac. Eng., Miyazaki Univ.)
HATSUDA Tetsuo 初田哲男 (Fac. Sci., Kyoto Univ.)
HAYASHIGAKI Arata 林垣 新 (Yukawa Inst. Theor. Phys., Kyoto Univ.)
HAYASHI Naoki 林 直樹
HEENEN Paul-Henri (Univ. Libre Bruxelles, Belgium)
HIRAI Masaaki 平井正明
HOSAKA Masahito 保坂将人 (KEK, Tanashi)
ICHIMURA Munetake 市村宗武 (Grad. Sch. Arts Sci., Univ. Tokyo)
IDEGUCHI Eiji 井手口栄治 (Phys. Dept. Frescati, Royal Inst. Technol., Sweden)
IEKI Kazuo 家城和夫 (Coll. Sci., Rikkyo Univ.)
IMAI Kenichi 今井憲一
IMOTO Michiko 井本道子 (Lab. Phys. Coll. Sci. Technol., Nihon Univ.)
ISHII Tetsuro 石井哲朗 (JAERI)
ITAKURA Kazunori 板倉和記 (Yukawa Inst. Theor. Phys., Kyoto Univ.)
IWASAKI Haironori 岩崎弘典
IWASA Naohito 岩佐直仁 (Lab. Nucl. Studies, Fac. Sci., Osaka Univ.)
IZUMI Hideaki 出水秀明 (Grad. Sch. Sci., Osaka Univ.)
JIN Genming 靳 根明 (Inst. Modern Phys., Chinese Acad. Sci., China)
KAKI Kaori 嘉規香織 (Fac. Sci., Shizuoka Univ.)
KAMAE Tsuneyoshi 釜江常好 (Fac. Sci., Univ. Tokyo)
KANEKO Tomohiro 金子智博 (Fac. Sci., Univ. Tokyo)
KASAGI Jirota 笠木治郎太 (Lab. Nucl. Sci., Tohoku Univ.)
KATAYAMA Ichiro 片山一郎 (Cen. Nucl. Study, Univ. Tokyo)
KATAYAMA Takeshi 片山武司 (Cen. Nucl. Study, Univ. Tokyo)
KATO Seigo 加藤静吾 (Fac. Educ., Yamagata Univ.)
KATORI Kenji 鹿取謙二 (Fac. Sci., Osaka Univ.)
KAWASHIMA Hideo 川島英雄 (KEK, Tanashi)
KIM Jong Chan (Dept. Phys., Seoul Natl. Univ., Korea)
KISTENEV Edouard (Phys. Dept., BNL, USA)
KITAGAWA Hisashi 北川 尚 (KEK)
KITAO Kensuke 喜多尾憲助 (Data Eng. Inc.)
KODAIRA Jirou 小平治郎 (Fac. Sci., Hiroshima Univ.)
KOHAMA Akihisa 小濱洋央 (Fac. Sci., Univ. Tokyo)
KOIKE Yuji 小池裕司 (Fac. Sci., Niigata Univ.)
KUBONO Shigeru 久保野茂 (Cen. Nucl. Study, Univ. Tokyo)
KUMANO Shunzo 熊野俊三 (Fac. Sci. Eng., Saga Univ.)

KUNIHIRO Teiji 國弘悌二 (Ryukoku Univ.)
KURITA Kazuyoshi 栗田和好
KUSAKARI Hideshige 草刈英榮 (Fac. Educ., Chiba Univ.)
LEE Sang Mu 李相茂 (Inst. Phys., Univ. Tsukuba)
LI Zhihong 李志宏 (China Inst. Atom. Energy, China)
LIU Guanhua 劉冠華 (Inst. Modern Phys., Chinese Acad. Sci., China)
LUCCIO Alfredo
LIU Zhong (Inst. Modern Phys., Chinese Acad. Sci., China)
LUKIANOV Serguei (Flerov Lab. Nucl. React., Joint Inst. Nucl. Res., Russia)
MAEDA Kazushige 前田和茂 (Grad. Sch. Sci., Tohoku Univ.)
MAO Yajun (Phys. Dept., BNL, USA)
MATSUDA Atsushi 松田充史 (Fac. Sci., Univ. Tokyo)
MATSUDA Satoshi 松田哲 (Fac. Integr. Human Studies, Dept. Fundamental Sci., Kyoto Univ.)
MATSUI Tetsuo 松井哲男 (Yukawa Inst. Theor. Phys., Kyoto Univ.)
MATSUKI Tsuneki 松木常樹
MATSUYANAGI Kenichi 松柳研一 (Fac. Sci., Kyoto Univ.)
MEISON Jean-Marie (Div. Phys. Theor. IPN, Inst. Phys. Nucl., France)
MENGONI Alberto (Phys. Div., ENEA, Italy)
MIN Byung-Joo 閔丙珠 (Korea Atomic Energy Res. Inst., Korea)
MITARAI Shiro 御手洗志郎 (Fac. Sci., Kyushu Univ.)
MITSUOKA Shinichi 光岡真一 (JAERI)
MIYACHI Takashi 宮地孝 (Cen. Nucl. Study, Univ. Tokyo)
MIYATAKE Hiroari 宮武宇也 (KEK, Tanashi)
MIZOI Yutaka 溝井浩
MORII Toshiyuki 森井俊行 (Fac. Human Dev., Kobe Univ.)
MORIKAWA Tsuneyasu 森川恒安 (Fac. Sci., Kyushu Univ.)
MORINOBU Shunpei 森信俊平 (Fac. Sci., Kyushu Univ.)
MOTOBAYASHI Tohru 本林透 (Coll. Sci., Rikkyo Univ.)
MOTTELSON Ben R. (Nordisk Inst. Theor. Fusik, Denmark)
MUELLER Ludwig (Phys. Dept., Univ. Padoba, Italy)
MURAKAMI Takeshi 村上健 (Natl. Inst. Radiol. Sci.)
NAGAI Yasuki 永井泰樹 (Fac. Sci., Tokyo Inst. Technol.)
NAGAMIYA Shoji 永宮正治 (JHF Project Office, KEK)
NAGASHIMA Yasuo 長島泰夫 (Univ. Tsukuba)
NAKAJIMA Mitsuo 中島充夫 (Interdiscplinary Grad. Sch. Sci. Eng., Tokyo Inst. Technol.)
NAKAMURA Shogo 中村正吾 (Fac. Ed., Yokohama Natl. Univ.)
NAKAMURA Takashi 中村隆司 (Natl. Supercond. Cycl. Lab., Michigan State Univ., USA)
NAKAMURA Masanobu 中村正信 (Fac. Sci., Kyoto Univ.)
NAKAYAMA Shintaro 中山信太郎 (Fac. Integr. Arts Sci., Univ. Tokushima)
NIIZEKI Takashi 新関隆 (Fac. Sci., Tokyo Inst. Technol.)
NORO Tetsuo 野呂哲夫 (RCNP, Osaka Univ.)
NOTANI Masahiro 野谷将広
ODAHARA Atsuko 小田原厚子 (Nishinippon Inst. Technol.)
OGAWA Masao 小川雅生 (Interdiscplinary Grad. Sch. Sci. Eng., Tokyo Inst. Technol.)
OHTA Shigemi 太田滋生 (KEK)
OKAMURA Hiroyuki 岡村弘之 (Dept. Phys., Grad. Sch. Sci., Univ. Tokyo)
OKAMURA Masahiro 岡村昌宏
ONUMA Hajime 大沼甫 (Chiba Inst. Technol.)
OOISHI Ryutaro 大石竜太郎 (Inst. Phys., Univ. Tsukuba)
OOYAMA Ken 大山健
ORIHARA Hikonojyo 織原彦之丞 (Cycl. Radioisot. Cen., Tohoku Univ.)
OSHIMA Masumi 大島真澄 (JAERI)
OTSUKA Takaharu 大塚孝治 (Fac. Sci., Univ. Tokyo)
OYAIZU Michihiro 小柳津充広 (KEK, Tanashi)
PENIONZHKEVICH Iouri (Flerov Lab. Nucl. React., Joint Inst. Nucl. Res., Russia)
PETROVICH Ilya (Flerov Lab. Nucl. React., Joint Inst. Nucl. Res., Russia)
RAURENT Henri (Div. Phys. Theor. IPN, Inst. Phys. Nucl., France)
REN Zhongzhou 任中洲 (Nanjing Univ., China)

RUAN (GEN) Jian-Zhi 阮 建治 (Coll. Sci., Rikkyo Univ.)
SAGAWA Hiroyuki 佐川弘幸 (Cen. Math. Sci., Univ. Aizu)
SAKAGUCHI Harutaka 坂口治隆 (Fac. Sci., Kyoto Univ.)
SAKAI Mitsuo 坂井光夫 (KEK, Tanashi)
SAKAI Kenji 酒井健二 (Tokyo Inst. Technol.)
SAKURAGI Hiroyuki 櫻木弘之 (Fac. Sci., Osaka City Univ.)
SAMANTA Chhanda (Theory Group, Saha Inst. Nucl. Phys., India)
SATO Hikaru 佐藤 皓 (KEK)
SATO Hiroki 佐藤博紀
SCHAEFER Markus (Phys. Inst., Univ. Goettingen, Germany)
SCHMIDT-OTT Wolf-Dieter (Phys. Inst., Univ. Goettingen, Germany)
SEDERWALL Bo (Royal Inst. Technol., Sweden)
SHIBATA Toshiaki 柴田利明 (Tokyo Inst. Technol.)
SHIMIZU Hajime 清水 肇 (Fac. Educ., Yamagata Univ.)
SHIMIZU Yoshifumi 清水良文 (Fac. Sci., Kyushu Univ.)
SHIMODA Tadashi 下田 正 (Grad. Sch. Sci., Osaka Univ.)
SHIMOURA Susumu 下浦 享 (Coll. Sci., Rikkyo Univ.)
SIGNORINI Cosimo (Phys. Dept., Univ. Padoba, Italy)
SOKOL Evgueni (Flerov Lab. Nucl. React., Joint Inst. Nucl. Res., Russia)
SUGAWARA Masahiko 菅原昌彦 (Chiba Inst. Technol.)
SUN Zuxun
SUZUKI Yasuyuki 鈴木宜之 (Fac. Sci., Niigata Univ.)
SUZUKI Katsuhiko 鈴木克彦 (RCNP, Osaka Univ.)
TAJIMA Yasuhisa 田島靖久 (Cycl. Radioisot. Cen., Tohoku Univ.)
TAKADA Eiichi 高田栄一 (Natl. Inst. Radiol. Sci.)
TAKAHASHI Noriaki 高橋憲明 (Grad. Sch. Sci., Osaka Univ.)
TAKAHASHI Tadayuki 高橋忠幸 (Inst. Space Astro. Sci.)
TAKAKU Seisaku 高久清作 (KEK, Tanashi)
TAKIGAWA Noboru 滝川 昇 (Grad. Sch. Sci., Tohoku Univ.)
TAKIZAWA Makoto 瀧澤 誠 (Showa Coll. Pharm. Sci.)
TAMII Atsushi 民井 淳 (Fac. Sci., Univ. Tokyo)
TANAKA Masahiko 田中雅彦 (KEK, Tanashi)
TANOKURA Atsushi 田野倉敦 (Fac. Sci. Technol., Sophia Univ.)
TENDOW Yoshihiko 天道芳彦
TERAKAWA Atsuki 寺川貴樹 (Cycl. Radioisot. Cen., Tohoku Univ.)
TERANISHI Takashi 寺西 高 (Cen. Nucl. Study, Univ. Tokyo)
THOMPSON J. I. (Univ. Surry, UK)
TOKI Hiroshi 土岐 博 (RCNP, Osaka Univ.)
TOYAMA Takeshi 外山 毅 (KEK)
UENO Hideki 上野秀樹 (Fac. Sci., Osaka Univ.)
UNO Masahiro 宇野正宏 (Min. Educ., Sci. Culture)
WAKAMATSU Masashi 若松正志 (Fac. Sci., Osaka Univ.)
WATANABE Yutaka 渡辺 裕
WHITE Sebastian (Phys. Dept., BNL, USA)
WU Heyu 吳 和宇 (Inst. Modern Phys., Chinese Acad. Sci., China)
XU Shuwei 徐 樹威 (Inst. Modern Phys., Chinese Acad. Sci., China)
YAMAMOTO Sukeyasu 山本祐靖 (Fac. Sci. Technol., Sophia Univ.)
YAMANISHI Teruya 山西輝也 (Fac. Eng., Fukui Univ. Technol.)
YAMASHITA Yoshiki 山下芳樹 (Hirosaki Univ.)
YANAGISAWA Yoshiyuki 柳沢善行
YAZAKI Koichi 矢崎紘一
YOSHIMURA Koji 吉村浩司 (Int. Cen. Element. Part. Phys., Univ. Tokyo)
YOSHINAGA Naotaka 吉永尚孝 (Fac. Sci., Saitama Univ.)
YOSOI Masaru 與曽井優 (Fac. Sci., Kyoto Univ.)
ZHOU Xiaohong 周 小紅 (Inst. Modern Phys., Chinese Acad. Sci., China)

Trainees
CHIKU Suenori 知久季倫 (Inst. Phys., Univ. Tsukuba)

FOUBERT Luc (Coll. Sci., Rikkyo Univ.)
FUKE Hideyuki 福家英之 (Fac. Sci., Univ. Tokyo)
FUKUCHI Tomonori 福地知則 (Fac. Sci., Kyushu Univ.)
FUKUSAKA Shouichi 福坂将一 (Dept. Phys., Grad. Sch. Sci., Univ. Tokyo)
FUTAKAMI Udai 二上宇内 (Coll. Sci., Rikkyo Univ.)
GOMI Tomoko 五味朋子 (Coll. Sci., Rikkyo Univ.)
GOTO Atsudhi 五島 敦 (Tokyo Inst. Technol.)
HIGURASHI Yoshihide 日暮祥英 (Coll. Sci., Rikkyo Univ.)
HIRAI Masanori 平井正紀 (Fac. Sci. Eng., Saga Univ.)
HORII Hideyuki 堀井英行 (Coll. Sci., Rikkyo Univ.)
HORIKAWA Hirotsugu 堀川博嗣 (Fac. Human Dev., Kobe Univ.)
IMAI Nobuaki 今井伸明 (Dept. Phys., Grad. Sch. Sci., Univ. Tokyo)
IWATA Yoshiyuki 岩田佳之 (Coll. Sci., Rikkyo Univ.)
KANAZAWA Yasunobu 金澤康信 (Fac. Sci., Niigata Univ.)
KANEKO Tomohiro 金子智博 (Fac. Sci., Univ. Tokyo)
KATO Hiromitsu 加藤裕充 (Dept. Phys., Grad. Sch. Sci., Univ. Tokyo)
KINUGAWA Hiroto 衣川裕人 (Coll. Sci., Rikkyo Univ.)
KOBAYASHI Hiroshi 小林 寛 (Coll. Sci., Rikkyo Univ.)
KOMIYA Takefumi 小宮丈史 (Coll. Sci., Rikkyo Univ.)
MAEDA Yukie 前田幸重 (Dept. Phys., Grad. Sch. Sci., Univ. Tokyo)
MATSUDA Atsushi 松田充史 (Fac. Sci., Univ. Tokyo)
MAMURO Erika 間室映里香 (Coll. Sci., Rikkyo Univ.)
MINEMURA Toshiyuki 峯村俊行 (Coll. Sci., Rikkyo Univ.)
MIYACHI Yoshiyuki 宮地義之 (Cen. Integrated Res. Sci. Eng., Nagoya Univ.)
MIYAKAWA Takahiko 宮川貴彦 (Fac. Sci., Tokyo Metropol. Univ.)
MIYAMA Masanori 深山正紀 (Fac. Sci. Eng., Saga Univ.)
MIZUMURA Yuuki 水村祐記 (Tokyo Inst. Technol.)
MOTOMURA Shinji 本村信治 (Fac. Sci., Kyushu Univ.)
NAGAKURA Masaki 長倉正樹 (Tokyo Inst. Technol.)
NAKANO Joe 中野 譲 (Cen. Nucl. Study, Univ. Tokyo)
NAKANO Eiji 仲野英司 (Fac. Sci., Tokyo Metropol. Univ.)
NISHIYAMA Naoki 西山直樹 (Fac. Sci., Niigata Univ.)
OGAWA Hiroshi 小川博嗣 (Tokyo Inst. Technol.)
OHKUMA Kazumasa 大熊一正 (Fac. Human Dev., Kobe Univ.)
OONISHI Tetsuya 大西哲哉 (Dept. Phys., Grad. Sch. Sci., Univ. Tokyo)
SAITOU Akito 斎藤明登 (Coll. Sci., Rikkyo Univ.)
SAKODA Seitaro 迫田誠太郎 (Dept. Phys., Grad. Sch. Sci., Univ. Tokyo)
SAKUMA Tai 佐久間泰 (Tokyo Inst. Technol.)
SATO Miki 佐藤美紀 (Tokyo Inst. Technol.)
SAWADA Hirokazu 澤田弘一 (Coll. Sci., Rikkyo Univ.)
SEKIGUCHI Kimiko 関口仁子 (Dept. Phys., Grad. Sch. Sci., Univ. Tokyo)
SERATA Masaki 世良田真来 (Coll. Sci., Rikkyo Univ.)
SHIBATA Masataka 柴田雅隆 (Fac. Sci., Kyushu Univ.)
SUETSUGU Kentaro 末次健太郎 (Tokyo Inst. Technol.)
SUGA Toshitaka 須賀敏孝 (Tokyo Inst. Technol.)
SUIGIOKA Makoto 杉岡 誠 (Tokyo Inst. Technol.)
SUZUKI Takayuki 鈴木孝幸 (Tokyo Inst. Technol.)
TAKRUCHI Takeshi 竹内 猛 (Fac. Sci., Konan Univ.)
TANIGUCHI Etsuji 谷口悦史 (Tokyo Inst. Technol.)
TOJO Junji 東城順治 (Fac. Sci., Kyoto Univ.)
TORII Hisayuki 鳥井久行 (Fac. Sci., Kyoto Univ.)
TSUTSUMI Takeshi 堤 剛志 (Fac. Sci., Kyushu Univ.)
UCHIYAMA Yasuhito 内山靖仁 (Tokyo Inst. Technol.)
UEHARA Ayaka 上原亜矢佳 (Coll. Sci., Rikkyo Univ.)
WATANABE Hiroshi 渡邉 寛 (Fac. Sci., Kyushu Univ.)
YAKO Kentaro 矢向謙太郎 (Dept. Phys., Grad. Sch. Sci., Univ. Tokyo)
YAMADA Kazunari 山田一成 (Coll. Sci., Rikkyo Univ.)
YAMAMOTO Yasuchika 山本康史 (Fac. Sci. Technol., Sci. Univ. Tokyo)

YOGO Katsunori　余語克紀　(Coll. Sci., Rikkyo Univ.)
YONEDA Kenichiro　米田健一郎　(Dept. Phys., Grad. Sch. Sci., Univ. Tokyo)
YOSHIMI Akihiro　吉見彰洋　(Tokyo Inst. Technol.)

Atomic Physics Laboratory

Head

YAMAZAKI Yasunori　山崎泰規

Members

ANDO Kozo　安藤剛三
KANAI Yasuyuki　金井保之
NAKAI Yoichi　中井陽一
OURA Masaki　大浦正樹
SHIMAMURA Isao　島村　勲
KAMBARA Tadashi　神原　正
KOJIMA Takao M.　小島隆夫
NISHIDA Masami　西田雅美
OYAMA Hitoshi　大山　等

Visiting Members and Postdoctoral Fellows

AZUMA Toshiyuki　東　俊行　(Inst. Appl. Phys., Univ. Tsukuba)
CHIMI Yasuhiro　知見康弘　(JAERI, Tokai Res. Estab.)
DATZ Sheldon　(Oak Ridge Natl. Lab., USA)
DePAOLA Brett D.　(Kansas State Univ., USA)
FUJIMA Kazumi　藤間一美　(Fac. Eng., Yamanashi Univ.)
HARA Shunsuke　原　俊介　(Dept. Gen. Educ., Tsukuba Coll. Technol.)
HATTORI Toshiyuki　服部俊幸　(Res. Lab. Nucl. React., Tokyo Inst. Technol.)
HINO Ken-ichi　日野健一　(Inst. Appl. Phys., Univ. Tsukuba)
HIRAYAMA Takato　平山孝人　(Dept. Phys., Gakushuin Univ.)
HITACHI Akira　月出　章　(Kochi Med. Sch.)
HULDT Sven　(Lund Univ., Sweden)
HUTTON Roger
ICHIMURA Atsushi　市村　淳　(Inst. Space Astro. Sci.)
ICHIOKA Toshiyasu　市岡利康　(Grad. Sch. Arts Sci., Univ. Tokyo)
IGARASHI Akinori　五十嵐明則　(Fac. Eng., Miyazaki Univ.)
ISHII Keishi　石井慶之　(Fac. Sci. Eng., Ritsumeikan Univ.)
ISHIKAWA Norito　石川法人　(JAERI, Tokai Res. Estab.)
ITOH Akio　伊藤秋男　(Fac. Eng., Kyoto Univ.)
ITOH Yoh　伊藤　陽　(Fac. Sci., Josai Univ.)
IWASE Akihiro　岩瀬彰宏　(JAERI, Tokai Res. Estab.)
KAGEYAMA Kensuke　蔭山健介　(Fac. Eng., Saitama Univ.)
KANEKO Shinichi　金子眞一　(Fac. Sci., Tokyo Inst. Technol.)
KAWATSURA Kiyoshi　川面　澄　(Fac. Eng. Design, Kyoto Inst. Technol.)
KIKIANI Boris　(Tbilisi State Univ., Georgia, USA)
KIMURA Masahiro　木村正廣　(Kochi Univ. Technol.)
KIMURA Mineo　季村峯生　(Sch. Allied Health Sci., Yamaguchi Univ.)
KINK Ilmar　(Lund Univ., Sweden)
KITAJIMA Masashi　北島昌史　(Fac. Sci. Technol., Sophia Univ.)
KOBAYASHI Nobuo　小林信夫　(Dept. Phys., Tokyo Metrop. Univ.)
KOHARA Takao　小原孝夫　(Fac. Sci., Himeji Inst. Technol.)
KOIKE Fumihiro　小池文博　(Sch. Med., Kitasato Univ.)
KOIZUMI Tetsuo　小泉哲夫　(Dept. Phys., Rikkyo Univ.)
KOMAKI Ken-ichiro　小牧研一郎　(Grad. Sch. Arts Sci., Univ. Tokyo)
KORENMAN Grigori　(Moscow State Univ., Russia)
KOWARI Kenichi　小割健一　(Dept. Appl. Phys. Chem., Univ. Electro-Commun.)
KUROTA Naoshi　黒田直志　(JAERI, Tokai Res. Estab.)
KUROKI Kenro　黒木健郎　(Natl. Res. Inst. Police Sci.)
MARTINSON Indrek　(Lund Univ., Sweden)
MATSUO Takashi　松尾　崇　(Dept. Pathol., Tokyo Med. Dent. Univ.)
MATSUZAWA Michio　松澤通生　(Dept. Appl. Phys. Chem., Univ. Electro-Commun.)

MITAMURA Tohru 三田村 徹 (Fac. Eng., Himeji Inst. Technol.)
MIZOGAWA Tatsumi 溝 川 辰 巳 (Nagaoka Coll. Technol.)
MOHRI Akihiro 毛 利 明 博 (Fac. Integrated Human Studies, Kyoto Univ.)
MUKOYAMA Takeshi 向 山 毅 (Inst. Chem. Res., Kyoto Univ.)
NAKAMURA Masato 中 村 正 人 (Coll. Sci. Technol., Nihon Univ.)
NISHIDA Nobuhiko 西 田 信 彦 (Fac. Sci., Tokyo Inst. Technol.)
NISHIMURA Tamio 西 村 民 男
NYSTRÖM Bosse
OHTANI Shunsuke 大 谷 俊 介 (Inst. Laser Sci., Univ. Electro-Commun.)
OKAYASU Satoru 岡 安 悟 (JAERI, Tokai Res. Estab.)
OKUNO Kazuhiko 奥 野 和 彦 (Dept. Phys., Tokyo Metrop. Univ.)
OSHIMA Nagayasu 大 島 永 康
SAKATA Hideaki 坂 田 英 明 (Fac. Sci., Tokyo Inst. Technol.)
SAKURAI Makoto 桜 井 誠 (Fac. Sci., Kobe Univ.)
SATO Hiroshi 佐 藤 浩 史 (Fac. Sci., Ochanomizu Univ.)
SATOH Kazuhiko 佐 藤 一 彦 (Fac. Sci., Tokyo Inst. Technol.)
SATOH Yukinori 佐 藤 幸 紀 (Res. Inst. Sci. Meas., Tohoku Univ.)
SCHMIDT-BÖCKING Horst (Univ. Frankfurt, Germany)
SEKIOKA Tsuguhisa 関 岡 嗣 久 (Fac. Eng., Himeji Inst. Technol.)
SHIBATA Hiromi 柴 田 裕 実 (Res. Cen. Nucl. Sci., Univ. Tokyo)
SHIMA Kunihiro 島 邦 博 (Tandem Accel. Cen., Univ. Tsukuba)
SHIMAKURA Noriyuki 島 倉 紀 之 (Fac. Sci., Niigata Univ.)
SOEJIMA Kouichi 副 島 浩 一 (Fac. Sci., Niigata Univ.)
SUZUKI Isao 鈴 木 功 (Electrotech. Lab.)
TAKAYANAGI Toshinobu 高 柳 俊 暢 (Fac. Sci. Technol., Sophia Univ.)
TAWARA Hiroyuki 俵 博 之 (Natl. Inst. Fusion Sci.)
TERASAWA Mititaka 寺 澤 倫 孝 (Fac. Eng., Himeji Inst. Technol.)
THURIEZ Sebastien
TOSHIMA Nobuyuki 戸 嶋 信 幸 (Inst. Appl. Phys., Univ. Tsukuba)
TSUCHIDA Hidetsugu 土 田 秀 次 (Fac. Sci., Nara Women's Univ.)
URAMOTO Seiichi 浦 本 聖 一
WAKIYA Kazuyoshi 脇 谷 一 義 (Fac. Sci. Technol., Sophia Univ.)
WATANABE Shinichi 渡 辺 信 一 (Dept. Appl. Phys. Chem., Univ. Electro-Commun.)
YAGISHITA Akira 柳 下 明 (KEK)
YODA Jun 依 田 潤 (Natl. Res. Lab. Metrol.)
YOSHINO Masuhiro 吉 野 益 弘 (Lab. Phys., Shibaura Inst. Technol.)
ZOU Yaming (Shanghai Jiao Tong Univ., China)

Trainees
CHIBA Daisuke 千 羽 大 介 (Fac. Sci. Technol., Sophia Univ.)
FUJINO Atsushi 藤 野 敦 (Dept. Phys., Rikkyo Univ.)
HORI Masaki 堀 正 樹 (Dept. Phys., Grad. Sch. Sci., Univ. Tokyo)
ITO Akira 伊 藤 聡 (Fac. Sci. Technol., Rikkyo Univ.)
IWAI Yoshio 岩 井 良 夫 (Grad. Sch. Arts Sci., Univ. Tokyo)
KAMEI Takehito 亀 井 武 仁 (Fac. Sci. Technol., Sophia Univ.)
KAWAE Sotaro 川江宗太郎 (Dept. Eng. Sci., Kyoto Univ.)
KIMURA Yasuyuki 木 村 恭 之 (Dept. Eng. Sci., Kyoto Univ.)
MATSUSHIMA Hiroshi 松 島 広 (Grad. Sch. Arts Sci., Univ. Tokyo)
NAKANO Tomohide 仲 野 友 秀 (Dept. Eng. Sci., Kyoto Univ.)
OGURA Kunihiro 小 倉 都 宏 (Fac. Sci. Technol., Sophia Univ.)
ONO Yasuhiro 小 野 泰 弘 (Fac. Sci., Tokyo Inst. Technol.)
SUGIYAMA Yukiko 杉 山 幸 子 (Fac. Sci. Technol., Sophia Univ.)
TAGUCHI Yoshio 田 口 義 雄 (Fac. Sci., Tokyo Inst. Technol.)
WHITEHEAD Richard (Dept. Phys., Sci. Lab., Univ. Durham, UK)
YAMASHITA Kenya 山 下 賢 哉 (Dept. Phys., Grad. Sch. Sci., Univ. Tokyo)

Muon Science Laboratory

Head

NAGAMINE Kanetada 永嶺謙忠

Members

ISHIDA Katsuhiko 石田勝彦
MATSUDA Yasuyuki 松田恭幸
NAKAMURA Satoshi N. 中村哲
YAGI Eiichi 八木栄一
KOYAMA Akio 小山昭雄
MATSUZAKI Teiichiro 松﨑禎市郎
WATANABE Isao 渡邊功雄

Visiting Members and Postdoctoral Fellows

AKIMITSU Jun 秋光純 (Coll. Sci. Eng., Aoyama Gakuin Univ.)
AKIMOTO Katsuhiro 秋本克洋 (Inst. Mater., Univ. Tsukuba)
ASAI Kichizo 浅井吉蔵 (Univ. Electro-Commun.)
DAS Prasad Tara (Dept. Phys., State Univ. New York, Albany, USA)
FUJITA Ayumi 藤田あゆみ
FUKAYA Atsuko 深谷敦子
HASHIMOTO Masashi 橋本雅史 (JAERI, Tokai Res. Estab.)
HIGEMOTO Wataru 髭本亘 (KEK)
HIYAMA Emiko 肥山詠美子
IWASAKI Masahiko 岩崎雅彦 (Dept. Phys., Tokyo Inst. Technol.)
KADONO Ryosuke 門野良典 (KEK)
KATO Mineo 加藤峯生 (JAERI, Tokai Res. Estab.)
KAWAMURA Naritoshi 河村成肇
KINO Yasushi 木野康志 (Fac. Sci., Tohoku Univ.)
KRISHNAMURTHY Vemuru
KUROSAWA Kiyoyuki 黒沢清行 (JAERI, Tokai Res. Estab.)
MACRAE Roderick M.
MARUYAMA Takahiro 丸山隆浩 (Inst. Mater., Univ. Tsukuba)
MATSUSHITA Akira 松下明
MIYAKE Yasuhiro 三宅康博 (KEK)
NISHIDA Nobuhiko 西田信彦 (Fac. Sci., Tokyo Inst. Technol.)
NISHIYAMA Kusuo 西山樟生 (KEK)
PRATT Francis L.
SHIMOMURA Koichiro 下村浩一郎 (KEK)
SAKAMOTO Shinichi 坂元眞一 (KEK)
STRASSER Patrick
TANASE Masakazu 棚瀬正和 (JAERI, Tokai Res. Estab.)
TORIKAI Eiko 鳥養映子 (Fac. Eng., Yamanashi Univ.)

Trainees

OOHIRA Seiko 大平聖子 (Grad. Sch., Univ. Tokyo)
TOYODA Akihisa 豊田晃久 (Grad. Sch., Univ. Tokyo)

Magnetic Materials Laboratory

Head

KATSUMATA Koichi 勝又紘一

Members

HAGIWARA Masayuki 萩原政幸
MATSUDA Masaaki 松田雅昌

Computational Science Laboratory

Head
EBISUZAKI Toshikazu 戎崎俊一

Members
SUMIYOSHI Kohsuke 住吉光介

Visiting Members and Postdoctoral Fellows
MIURA Hitoshi 三浦 均
SHIMIZU Tetsuya 清水鉄也

Inorganic Chemical Physics Laboratory

Head
TAKAMI Michio 高見道生

Members
AMBE Shizuko 安部靜子
MAEDA Kuniko 前田邦子
MATSUO Yukari 松尾由賀利

Visiting Members and Postdoctoral Fellows
ARAI Nobuaki 荒井修亮 (Dept. Fisheries, Kyoto Univ.)
KAWAI Jun 河合 潤 (Dept. Metallurgy, Kyoto Univ.)
HUI Qin 恵 秦

Trainees
HASEGAWA Tomotake 長谷川兼丈 (Coll. Eng., Hosei Univ.)
TONOMURA Atsuro 殿村淳朗 (Coll. Eng., Hosei Univ.)

Nuclear Chemistry Laboratory

Head
AMBE Fumitoshi 安部文敏

Members
KOBAYASHI Yoshio 小林義男
TAKEMATSU Noburu 竹松 伸

Visiting Members and Postdoctoral Fellows
ALEXANDER T. Roeck (Max-Planck Inst. Stuttgart, Germany)
BABA Hiroshi 馬場 宏 (Fac. Sci., Osaka Univ.)
CHANG Zheng 常 征
NASU Saburo 那須三郎 (Fac. Eng. Sci., Osaka Univ.)
OHKUBO Yoshitaka 大久保嘉高 (Res. React. Inst., Kyoto Univ.)
OISHI Shigeo 大石茂雄 (Sch. Health Sci., Kanazawa Univ.)
OKAMOTO Yayoi 岡本弥生 (Showa Coll. Pharm. Sci.)
SAITO Tadashi 斎藤 直 (Fac. Sci., Osaka Univ.)
SHIBATA Seiichi 柴田誠一 (Res. React. Inst., Kyoto Univ.)
SHINOHARA Atsushi 篠原 厚 (Fac. Sci., Nagoya Univ.)
YOKOYAMA Akihiko 横山明彦 (Fac. Sci., Osaka Univ.)

Trainees
ABE Daisuke 阿部大輔 (Fac. Sci., Toho Univ.)
ARAKI Hirokazu 荒木宏一 (Fac. Sci., Osaka Univ.)
DAIRAKU Tomohisa 大樂知久 (Fac. Sci., Nagoya Univ.)
HAYAKAWA Nobutaka 早川信隆 (Showa Coll. Pharm. Sci.)
IRIGUCHI Yuko 入口優子 (Fac. Sci. Living, Osaka City Univ.)
MORIMOTO Shinya 森本真哉 (Fac. Sci., Osaka Univ.)

MUKAI Kazuhiko 向 和彦 (Fac. Sci., Osaka Univ.)
MURASE Nobuyuki 村瀬伸幸 (Shizuoka Inst. Sci. Technol.)
MURATA Chihiro 村田千裕 (Fac. Sci., Nagoya Univ.)
MUROYAMA Toshiharu 室山俊浩 (Fac. Sci., Nagoya Univ.)
NAKANISHI Kouichi 中西孝市 (Shizuoka Inst. Sci. Technol.)
ODA Hirotaka 小田寛貴 (Fac. Sci., Nagoya Univ.)
OIKAWA Shinji 及川真司 (Fac. Sci., Kanazawa Univ.)
SANADA Jun 真田 潤 (Fac. Sci., Osaka Univ.)
SOGA Kyoko 曽我恭子 (Fac. Sci., Nagoya Univ.)
SOTOGAKU Naoki 外角直樹 (Showa Coll. Pharm. Sci.)
TAKAHASHI Yoshio 高橋嘉夫 (Fac. Sci., Univ. Tokyo)

Chemical Dynamics Laboratory

Members

KIMURA Kazuie 木村一宇
USHIDA Kiminori 丑田公規

Visiting Members and Postdoctoral Fellows

KAZAMA Shigeo 風間重雄 (Dept. Phys., Chuo Univ.)
SHARMA Sumit

Trainees

ITOH Noriaki 伊藤憲昭 (Osaka Inst. Technol.)
KANEKO Junichi 金子純一 (JAERI, Tokai)

Cellular Physiology Laboratory

Head

HANAOKA Fumio 花岡文雄

Members

KITAYAMA Shigeru 北山 滋
YATAGAI Fumio 谷田貝文夫

Trainees

ANDO Koichi 安藤興一 (Natl. Inst. Radiol. Sci.)
FURUSAWA Yoshiya 古澤佳也 (Natl. Inst. Radiol. Sci.)
HAMA Yoshimasa 浜 義昌 (Sci. Eng. Res. Lab., Waseda Univ.)
HASE Yoshihiro 長谷純宏 (JAERI, Takasaki Rad. Chem. Res. Estab.)
HOSHINO Kazuo 星野一雄 (Natl. Inst. Radiol. Sci.)
ITO Hisao 伊東久夫 (Sch. Med., Chiba Univ.)
ITSUKAICHI Hiromi 五日市ひろみ (Natl. Inst. Radiol. Sci.)
KANAI Tatsuaki 金井達明 (Natl. Inst. Radiol. Sci.)
KASAI Kiyomi 笠井清美 (Natl. Inst. Radiol. Sci.)
KAWACHI Kiyomitsu 河内清光 (Natl. Inst. Radiol. Sci.)
KOBAYASHI Yasuhiko 小林泰彦 (JAERI, Takasaki Rad. Chem. Res. Estab.)
LI Ryonpha 李 玲華 (Natl. Inst. Radiol. Sci.)
MATSUFUJI Naruhiro 松藤成弘 (Natl. Inst. Radiol. Sci.)
MINOHARA Shinichi 簑原伸一 (Natl. Inst. Radiol. Sci.)
MURAKAMI Masahiro 村上正弘 (Natl. Inst. Radiol. Sci.)
SAITO Mizuho 斉藤瑞穂 (Natl. Inst. Radiol. Sci.)
SASAKI Hiroshi 佐々木 弘 (Fac. Med., Kyushu Univ.)
SHIKAZONO Naoya 鹿園直哉 (JAERI, Takasaki Rad. Chem. Res. Estab.)
SOGA Fuminori 曽我文宣 (Inst. Nucl. Study, Univ. Tokyo)
TANAKA Atsushi 田中 淳 (JAERI, Takasaki Rad. Chem. Res. Estab.)
TOMURA Hiromi 外村浩美 (Natl. Inst. Radiol. Sci.)
WATANABE Masami 渡辺正己 (Fac. Pharm., Nagasaki Univ.)

YAMASHITA Shoji　山下昌次　(Natl. Saitama Hospital)

Plant Functions Laboratory

Head
YOSHIDA Shigeo　吉田茂男

Members
ABE Tomoko　阿部知子

Visiting Members and Postdoctoral Fellows
BAE Chang-Hyu　裵　昌烋
HASHIMOTO Takashi　橋本　隆　(Dept. Biosci., NAIST)
MATSUYAMA Tomoki　松山知樹
MIYOSHI Kazumitsu　三吉一光
SATO Fumihiko　佐藤文彦　(Dept. Agric. Chem., Kyoto Univ.)
SATO Shinobu　佐藤　忍　(Inst. Biol. Sci., Tsukuba Univ.)
SUZUKI Kenichi　鈴木賢一　(Suntory Ltd.)
TAKAHASHI Yoshiko　高橋佳子

Trainees
IWAI Hiroaki　岩井宏暁　(Inst. Biol. Sci., Tsukuba Univ.)
MIYAGAI Mashu　宮外麻周　(Dept. Biosci., Teikyo Univ.)
MUTO Sonoko　武藤その子　(Fac. Hortic., Chiba Univ.)
TAKAHASHI Hideki　高橋英樹　(Coll. Agric. Vet. Med., Nihon Univ.)

Microbial Toxicology Laboratory

Head
YAMAGUCHI Isamu　山口　勇

Members
ARIE Tsutomu　有江　力

Visiting Members and Postdoctoral Fellows
GOUTHU Satyanarayana
NOSE Yasuhiro　能勢泰寛

Cellular and Molecular Biology Laboratory

Head
SHIBATA Takehiko　柴田武彦

Members
LING Feng　凌　　楓

Trainees
YOSHIMASU Masatoshi　吉益雅俊　(Sch. Agric., Nihon Univ.)

Division of Experimental Animal Research

Head

KUSAKABE Moriaki　日下部守昭

Members

IKE Fumio　池　郁生
HIRAIWA Noriko　平岩典子
YOSHIKI Atsushi　吉木　淳
TSUKADA Teruyo　塚田晃代

Visiting Members and Postdoctoral Fellows

POIRIER Christophe
YODA Yoshika　依田賀香　(Japan Sci. Technol. Corp.)

Safety Center

Members

HARASAWA Kaoru　原沢　薫
MATSUZAWA Yasuhide　松澤安秀
SHINOHARA Shigemi　篠原茂己
YAMANAKA Akira　山仲　暁
KAGAYA Satoru　加賀屋悟
MIYAGAWA Makoto　宮川真言
UWAMINO Yoshitomo　上蓑義朋
YOSHIKI Hajime　吉識　肇

Radioisotope Technology Division

Head

YATAGAI Fumio　谷田貝文夫

Visiting Members and Postdoctoral Fellows

FUJIE Akio　藤江章雄　(Furuuchi Chemicals)
GORDON Alasdair
KAGAWA Yasuhiro　香川康浩　(Toray Res. Cen. Inc.)
MAEZAWA Hiroshi　前澤　博　(Fac. Med. Technol., Tokushima Univ.)
MORIMOTO Shigeko　森本茂子　(Japan Space Forum)
OGURA Koichi　小倉紘一　(Coll. Ind. Technol., Nihon Univ.)
SUZUKI Makoto　鈴木　任
SUZUKI Masao　鈴木雅雄　(Fac. Pharm., Nagasaki Univ.)

Trainees

KITO Masatoshi　鬼頭昌利　(Fac. Sci. Eng., Waseda Univ.)
INOUE Kensuke　井上憲介　(Fac. Sci. Eng., Waseda Univ.)
OKA Toshitaka　岡　壽崇　(Fac. Sci. Eng., Waseda Univ.)
KUROBE Toshihiro　黒部利博　(Fac. Sci. Eng., Waseda Univ.)

AUTHOR INDEX

RIKEN Accelerator Progress Report Vol. 32

理化学研究所加速器年次報告　第32巻　(1999)

印　刷　平成11年 (1999) 3月20日
発　行　平成11年 (1999) 3月31日

発行者　理化学研究所
代表者　小林俊一
〒351-0198　埼玉県和光市広沢2番1号
電話　(048) 462−1111

編集者　理化学研究所加速器研究施設
運営委員会

印刷所　株式会社ユニバーサル・アカデミー・プレス
〒113-0033　東京都文京区本郷6丁目16番2号BR本郷5ビル

定価5,000円
（消費税別）

理化学研究所

埼玉県　和光市　広沢